Handbook of Electrostatic Processes

edited by
Jen-Shih Chang
Arnold J. Kelly
Joseph M. Crowley

Handbook of Electrostatic Processes

This Page Intentionally Left Blank

Handbook of Electrostatic Processes

edited by

Jen-Shih Chang
McMaster University
Hamilton, Ontario, Canada

Arnold J. Kelly
Princeton University
Princeton, New Jersey

Joseph M. Crowley
Electrostatic Applications
Morgan Hill, California

Marcel Dekker, Inc. New York • Basel • Hong Kong

Library of Congress Cataloging-in-Publication Data

Handbook of electrostatic processes / edited by Jen-shih Chang, Arnold J. Kelly, Joseph M. Crowley.
p. cm.
Includes bibliographical references and index.
ISBN 0-8247-9254-8 (acid-free paper)
1. Electrostatics—Handbooks, manuals, etc. 2. Electrostatics—Industrial applications—Handbooks, manuals, etc. I. Chang, Jen-shih II. Kelly, Arnold J. III. Crowley, Joseph M.
QC571.H25 1995
621.3—dc20 94-46371
CIP

The publisher offers discounts on this book when ordered in bulk quantities. For more information, write to Special Sales/Professional Marketing at the address below.

This book is printed on acid-free paper.

Copyright © 1995 by Marcel Dekker, Inc. All Rights Reserved.

Neither this book nor any part may be reproduced or transmitted in any form or by any means, electronic or mechanical, including photocopying, microfilming, and recording, or by any information storage and retrieval system, without permission in writing from the publisher.

Marcel Dekker, Inc.
270 Madison Avenue, New York, New York 10016

Current printing (last digit):
10 9 8 7 6 5 4 3 2 1

PRINTED IN THE UNITED STATES OF AMERICA

Preface

Electrostatic phenomena have been known for the past few thousand years. In 1600 Sir William Gilbert, the court physician to Queen Elizabeth I wrote a somewhat scientific description of electrostatics called *De Magneto*. From the earliest days of the use of electrostatic processes in industry, however, no comprehensive handbook has existed for someone new to the field who is looking for both an introduction and enough specific information to solve an immediate problem. This handbook was written by practicing engineers and scientists, who are recognized experts in their respective specialties, and has been designed to provide as comprehensive and detailed a description of electrostatic processes and related phenomena as possible within the confines of a single volume. A balance has been established between the competing needs of those individuals requiring reliable information on specific topics for immediate application and those who wish to use this book as a general, central reference. Accordingly, the book has been organized to provide a compendium of our current understanding of the field and accepted practices; to facilitate access to the extensive worldwide literature base; and to introduce the experts in the various disciplines, who collectively form a unique resource base.

Sufficient background or "tutorial" material has been included to make this field accessible to the technically trained individual who is confronting an electrostatically related problem for the first time. Various topic areas are organized to help the reader identify the necessary resource materials

whether they be the text, the literature base, or the individual experts to enlist these resources in the solution at whatever level of sophistication is ultimately required.

Chapters 1 to 11 cover fundamental phenomena and general information. Chapter 1 introduces electrostatic fundamentals. Electrical phenomena for solids and liquids are discussed in Chapters 2 through 5. Numerical techniques for the solution of problems in electrostatics are summarized in Chapter 6. Chapters 7 and 8 deal with fundamental phenomena in electrohydrodynamics. Gas discharge physics and chemistry are summarized in Chapter 9. Generation and measurement techniques for high voltages and electrostatic fields are described in Chapters 10 and 11, respectively.

Chapters 12 to 29 cover the applications area of electrostatics. Chapters 12 and 13 deal with fluid flow measurements using electrostatic techniques. Printers, electrophotography, and displays are summarized in Chapters 14, 15, and 16, respectively. Electrostatic separation and coalescence techniques are introduced in Chapters 17 and 18, respectively. Chapter 19 deals with electrorheological applications. Electrostatic atomization and spraying for agricultural applications is summarized in Chapter 20. Industrial dust particle precipitation and filtering are discussed in Chapters 21 and 22. Applications of electrostatic principles in electronics devices, chemical reactors, and heat exchangers are summarized in Chapters 23, 24, and 25, respectively. Chapters 26 and 27 deal with the application of gas discharges to water and pollutant gas clean-ups. Chapter 28 covers atmospheric electricity, and Chapter 29 introduces electrostatic applications for biomedical engineering.

The final chapters cover static electricity hazards and charge elimination techniques. Electrostatic hazards in electronic industries and in solid and liquid transport processes are summarized in Chapters 30, 31, and 32, and charge elimination techniques are introduced in Chapter 33.

We thank all the authors for their contributions.

Jen-Shih Chang
Arnold J. Kelly
Joseph M. Crowley

Contents

Preface *iii*

Contributors *ix*

1. Electrostatic Fundamentals *Joseph M. Crowley* **1**

2. Electrification of Solid Materials *Alexander A. Berezin* **25**

3. Electrostatic Charging of Particles *Jen-Shih Chang* **39**

4. Electrical Phenomena of Dielectric Materials **51**
R. Tobazéon

5. Flow Electrification of Liquids *G. Touchard* **83**

6. Numerical Techniques for Electrostatics *R. Godard* **89**

7. Dimensionless Ratios in Electrohydrodynamics **99**
Joseph M. Crowley

8. Injection Induced Electrohydrodynamic Flows **121**
P. Atten and A. Castellanos

9. Gas Discharge Phenomena *T. G. Beuthe and Jen-Shih Chang* **147**

10. Generation of High Voltages *A. Chakrabarti and S. Jayaram* **195**

11. Measurement of Electrostatic Fields, Voltages, and Charges *Mark N. Horenstein* **225**

12. Electrostatic Flow Measurement Techniques *Kazutoshi Asano* **247**

13. Electrostatic Multiphase Flow Measurement Techniques *Glenn Harvel and Jen-Shih Chang* **271**

14. Printers *P. T. Krein and K. S. Robinson* **295**

15. Electrophotography *L. B. Schein* **321**

16. Electrostatics in Flat Panel Displays *A. Kitai* **351**

17. Applications of the Electrostatic Separation Technique *K. Haga* **365**

18. Electrostatic Coalescence in Liquid-Liquid Systems *Wuhai He* **387**

19. Electrorheology *J. L. Sproston and R. Stanway* **399**

20. Electrostatic Atomization and Spraying *S. Edward Law* **413**

21. Electrostatic Precipitation *Senichi Masuda and Shunsuke Hosokawa* **441**

22. Modeling of Electrostatic Precipitators and Filters *Phil A. Lawless, Toshiaki Yamamoto, and Yoshio Otani* **481**

23. Transducers *T. Oda* **509**

24. EHD Enhanced Mass Transfer Operations and Chemical Reactions *Wuhai He and Jen-Shih Chang* **527**

25. Heat Engineering *Akira Yabe* **555**

26. Ozone Generation and Applications *U. Kogelschatz and B. Eliasson* **581**

27. Combustion Flue Gas Treatments *Massimo Rea* **607**

28. Atmospheric Electricity *Toshio Ogawa, T. Takeuti, and Z.-I. Kawasaki* **619**

29. Biomedical Engineering *Akira Mizuno and Masao Washizu* **653**

30. ESD Hazards in the Electronics Industry *L. F. DeChiaro and B. A. Unger* **687**

31. Static Electricity Hazards: Solid Surfaces and Gases *István Berta* **703**

32. Electrostatic Hazards During Liquid Transport and Spraying *A. G. Bailey* **723**

33. Electrostatic Charge Elimination Techniques *C. G. Noll* **733**

Index ***749***

This Page Intentionally Left Blank

Contributors

Kazutoshi Asano Yamagata University, Yonezawa, Japan

P. Atten Centre National de la Recherche Scientifique, Grenoble, France

A. G. Bailey University of Southampton, Southampton, England

Alexander A. Berezin McMaster University, Hamilton, Ontario, Canada

István Berta Technical University of Budapest, Budapest, Hungary

T. G. Beuthe McMaster University, Hamilton, Ontario, Canada

A. Castellanos University of Sevilla, Sevilla, Spain

A. Chakrabarti McMaster University, Hamilton, Ontario, Canada

Jen-Shih Chang McMaster University, Hamilton, Ontario, Canada

Joseph M. Crowley Electrostatic Applications, Morgan Hill, California

L. F. DeChiaro Bell Communications Research, Red Bank, New Jersey

B. Eliasson Asea Brown Boveri, Baden, Switzerland

R. Godard Royal Military College, Kingston, Ontario, Canada

K. Haga Fuji Electric CRD Company, Ltd., Kanagawa, Japan

Glenn Harvel McMaster University, Hamilton, Ontario, Canada

Wuhai He McMaster University, Hamilton, Ontario, Canada

Mark N. Horenstein Boston University, Boston, Massachusetts

Shunsuke Hosokawa Masuda Research, Inc., Tokyo, Japan

S. Jayaram University of Waterloo, Waterloo, Ontario, Canada

Z.-I. Kawasaki Osaka University, Osaka, Japan

A. Kitai McMaster University, Hamilton, Ontario, Canada

U. Kogelschatz Asea Brown Boveri, Baden, Switzerland

P. T. Krein University of Illinois at Urbana-Champaign, Urbana, Illinois

S. Edward Law The University of Georgia, Athens, Georgia

Phil A. Lawless Research Triangle Institute, Research Triangle Park, North Carolina

Senichi Masuda Masuda Research, Inc., Tokyo, Japan

Akira Mizuno Toyohashi University of Technology, Toyohashi, Japan

C. G. Noll The Simco Company, Hatfield, Pennsylvania

T. Oda The University of Tokyo, Tokyo, Japan

Toshio Ogawa Science Laboratory International, Kochi, Japan

Yoshio Otani Karazawa University, Karazawa, Japan

Massimo Rea University of Padova, Padova, Italy

K. S. Robinson Eastman Kodak Company, Rochester, New York

L. B. Schein IBM Research Division, San Jose, California

J. L. Sproston University of Liverpool, Liverpool, England

R. Stanway University of Sheffield, Sheffield, England

T. Takeuti Aichi College of Industry and Technology, Aichi, Japan

R. Tobazéon Centre National de la Recherche Scientifique, Grenoble, France

G. Touchard Centre National de la Recherche Scientifique, Poitiers, France

B. A. Unger Burt Unger Associates, Monmouth Beach, New Jersey

Masao Washizu Seikei University, Tokyo, Japan

Akira Yabe Ministry of International Trade and Industry, Tsukuba, Japan

Toshiaki Yamamoto Research Triangle Institute, Research Triangle Park, North Carolina

This Page Intentionally Left Blank

Handbook of Electrostatic Processes

This Page Intentionally Left Blank

1

Electrostatic Fundamentals

Joseph M. Crowley

Electrostatic Applications
Morgan Hill, California

I. INTRODUCTION

Electrostatics is used in a wide range of applications ranging from the calculation of atomic forces to wrapping of leftover food items. All of these applications can be understood by the application of a few principles based on numerous observations. This chapter describes these principles and gives the formulas used to calculate the magnitude of the effects. The ideas presented here will be used repeatedly in the later chapters to discuss particular aspects of electrostatics.

II. COULOMB'S LAW

Electrostatics is based primarily on the observation that like charges repel and unlike charges attract, as indicated in Fig. 1. The force is observed to increase linearly with each of the two charges, so that

$$F_{12} \sim q_1 q_2 \tag{1}$$

The magnitude of the force falls off quadratically as the charges are separated, so the force expression can be further specified as

$$F_{12} \sim \frac{q_1 q_2}{r^2} \tag{2}$$

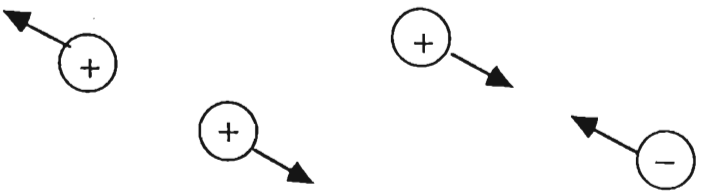


Figure 1 The basic electrostatic interaction.

where r is the distance between the charges. The constant of proportionality in this force expression depends on the units chosen to express the other quantities. For SI units, with charge in coulombs and distance in meters, the force expression becomes

$$F = \frac{q_1 q_2}{4\pi\epsilon_0 r^2} \tag{3}$$

The constant 4π is included because it simplifies some calculations. The other constant, ϵ_0, is called the permittivity of free space and has the value

$$\epsilon_0 \approx 8.854 \times 10^{-12}\, F/m = 8.854 pF/m \tag{4}$$

The force acts along the line of centers of the two charges, so its direction can be included by referring to the vector distance between the two charges, $\mathbf{r}_{12}$. With this addition, the vector force on the first charge caused by its interaction with the second charge can be written as

$$\mathbf{F}_1 = q_1 \left[\frac{q_2}{4\pi\epsilon_0 r_{12}^2} \mathbf{i}_{12} \right] \tag{5}$$

This expression is simple when only two charges are involved, but with many charges the force is expressed as a vector sum of the contributions from all the other charges. The force on the first charge is then

$$\mathbf{F}_1 = \mathbf{F}_{12} + \mathbf{F}_{13} + \mathbf{F}_{14} + \cdots \tag{6}$$

or taking the vectors into account,

$$\mathbf{F}_1 = q_1 \left[\frac{q_2}{4\pi\epsilon_0 r_{12}^2} \mathbf{i}_{12} + \frac{q_3}{4\pi\epsilon_0 r_{13}^2} \mathbf{i}_{13} + \frac{q_4}{4\pi\epsilon_0 r_{14}^2} \mathbf{i}_{14} + \cdots \right] \tag{7}$$

Since any material is composed of numerous positive and negative charges, it is clear that a more compact expression must be used in most applications. This simplified form is obtained by defining the term in the brackets as the electric (force) field acting on the ith charge,

$$\mathbf{E}_i = \sum_{i \neq j} \frac{q_j}{4\pi\epsilon_0 r_{ij}^2} \mathbf{i}_{ij} \tag{8}$$

It contains contributions from all the other charges that interact with the charge of interest. Thus the electric force on the ith charge can be written more simply as

$$\mathbf{F}_i = q_i \mathbf{E} \tag{9}$$

III. DIELECTRIC MATERIALS

So far, the force has been described as acting in a vacuum between discrete charges. In many applications of electrostatics, however, the charges exist in a material medium. Materials contain numerous charged particles such as protons and electrons, and the task of describing all these interactions on an atomic scale is impossible. The principal effect of all the other charges, however, is to decrease the net electric field at the location of the test charge. This occurs because the other charges rearrange themselves so as to neutralize the externally applied fields. For example, positive charges will tend to move toward a negative charge, so the force acts on this intermediate charge, rather than the test charge.

The net decrease in apparent field can be determined experimentally fairly easily. The decrease is expressed by the dielectric constant κ, which is defined by the decrease in apparent force through the relation

$$\kappa = \frac{F_{\text{vac}}}{F_{\text{material}}} \tag{10}$$

Thus the basic expression for the electrostatic force between two charges in a material, when modified to include the effect of the intervening material, becomes

$$\mathbf{F} = \frac{q_1 q_2}{4\pi\kappa\epsilon_0 r^2} \mathbf{i}_r \tag{11}$$

Sometimes the dielectric constant is lumped with the permittivity of free space to give the permittivity of the material as

$$\epsilon = \kappa\epsilon_0 \tag{12}$$

IV. GAUSS'S LAW

The electrostatic force, like gravity, depends on the inverse square of the distance between charges. If we consider a large spherical shell enclosing a single charge, the electric field associated with that charge has the form

$$E \sim \frac{1}{r^2} \tag{13}$$

while the surface of the spherical shell is proportional to the radius,

$$A = 4\pi r^2 \tag{14}$$

Clearly, the product of the two is a constant.

$$EA = \frac{q}{4\pi\epsilon r^2} 4\pi r^2 = \frac{q}{\epsilon} \tag{15}$$

This relation is true regardless of the shape of the enclosing surface, and can be written more generally as

$$\oiint (\epsilon \mathbf{E}) \cdot d\mathbf{S} = q \tag{16}$$

which is called Gauss's law. From this it is clear that the integrand is essentially related to the charge per unit area. It is called the electric displacement field, defined by

$$\mathbf{D} = \epsilon \mathbf{E} \tag{17}$$

The integral form of Gauss's law can be rewritten in the differential form

$$\nabla \cdot \mathbf{D} = \rho \tag{18}$$

where ρ is charge per unit volume.

V. THE ELECTROSTATIC POTENTIAL

While the definition of the electric field vector simplifies writing the Coulomb force equation, it still leaves the problem of finding the vector sum of all of the electric fields in the system. Usually it is easier to work with a single scalar quantity, and this is the role of the electrostatic potential energy. The Coulomb force on a charge is a function of position given by

$$\mathbf{F} = q\mathbf{E} = f(r) \tag{19}$$

The electrostatic force is conservative, so it can be written as the gradient of a scalar function, called the electrostatic potential energy W:

$$\mathbf{F}(r) = -\nabla W(r) \tag{20}$$

The spatial dependence comes only from the electric field, so the charge is usually removed from the equation, giving the electric field as

$$\mathbf{E}(r) = -\nabla\Phi(r) \tag{21}$$

where $\Phi(\mathrm{r})$ is the electrostatic potential energy per unit charge (also called the voltage or electric potential). This defines the potential but does not tell us how to find it.

By combining Gauss's law with the electric potential, we can eliminate the unknown electric field from Eq. 18, yielding a single equation for the scalar electrostatic potential as

$$\nabla\cdot\mathbf{D} = -\nabla\cdot(\epsilon\nabla\Phi) = \rho \tag{22}$$

If the permittivity does not depend on the spatial coordinates (the usual case), this equation simplifies to

$$\nabla^2\Phi = -\frac{\rho}{\epsilon} \tag{23}$$

This is Poisson's equation, which gives the potential in terms of the volume charge density. In regions where there is no net charge density, it simplifies to Laplace's equation,

$$\nabla^2\Phi = 0 \tag{24}$$

This is the equation most often used to find electrostatic fields in practice. It is particularly useful when the fields are generated by electrodes connected to voltage sources. Typically, its solution requires boundary conditions related to the voltage or its derivatives. These boundary conditions must be specified around a surface that completely encloses the region of interest.

Laplace's equation has been extensively studied for over a century, and numerous books have been written to discuss its solution. For most applications, only a few of the simplest solutions are needed. These special cases include most of the basic engineering geometries and shapes and often serve to model the effects expected in practice. If more detailed results are required, numerical techniques must be used.

Both the analytical and the numerical techniques rely heavily on the linearity of Laplace's equation, which allows us to construct complete solutions by adding together partial solutions that satisfy only one boundary condition. For example, the potential between two cylinders at different voltages can be constructed by solving for the potential with first the inner and then the outer cylinder grounded, and then adding the two solutions. These superposed solutions have the general form

$$\Phi = f_1(\mathbf{r})B_1 + f_2(\mathbf{r})B_2 + \cdots \tag{25}$$

Here B_i represents boundary conditions on the ith boundary, and f_i represents the solution for the special case when the condition at the ith boundary is set to unity and the conditions at all the other boundaries are set to zero.

This technique is valid for combinations of different types of boundary conditions, including voltage, charge, surface charge density, volume charge density, and normal electric fields. The tables at the end of this chapter give the partial solutions for a number of common situations.

VI. CAPACITANCE

In practical electrostatics, it is often necessary to connect an electrostatic device to an external electrical circuit. In a circuit context, this requires a relation between the charge supplied to the electrical terminals and the voltage applied there. As an example of how the charge and voltage can be related, consider the basic parallel plate arrangement of Fig. 2. The electric field between the two plates can be obtained by applying the formulas of Table 1 at the end of this chapter. In this example, the boundary conditions are

$$V_1 = 0 \qquad (26)$$
$$V_2 = V$$

and the plates are separated by a distance

$$d = b - a \qquad (27)$$

so the electric field between the plates (Region 1) is given by

$$E = -\frac{1}{b-a} V = -\frac{V}{d} \qquad (28)$$

The total charge on a plate is calculated by using Gauss's law over a

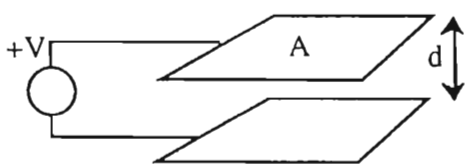


Figure 2 The parallel plate capacitor.

volume that encloses the plate, giving the total charge on the electrode as

$$Q = \oiint \frac{\epsilon V}{d}\, dS = \frac{\epsilon A}{d}\, V \tag{29}$$

Note that the charge is linearly related to the voltage in this example. The constant of proportionality is defined as the capacitance of the device,

$$C = \frac{\epsilon A}{d} \tag{30}$$

It is a measure of the amount of charge that can be stored on an electrode for a given voltage. Much of electrostatics can be explained by considering how such a capacitor behaves as its dimensions are changed, or the dielectric constant varies.

VII. CONSERVATION OF CHARGE

Ultimately, charge is always associated with mass through its association with a proton or electron. Like mass, it is also conserved, but its conservation law needs some additional consideration because charge can be either positive or negative, and opposite charges can neutralize each other even though the associated masses always add together. Consider an enclosed volume in space, as shown in Fig. 3. The net amount of charge inside the volume is denoted by Q. A flow of charge (called an electric current) can enter or leave the volume, leading to an increase or decrease of the net charge inside. This conservation law is written as

$$\frac{dQ}{dt} = i_{\text{in}} - i_{\text{out}} \tag{31}$$

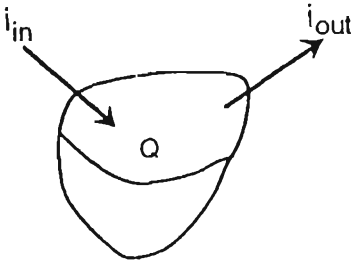


Figure 3 Conservation of charge in a volume.

where i is the electric current, in coulombs per second (amperes). This conservation law can also be written in differential form by defining a current density J that gives the current per unit area at any point. Using this definition, the conservation law first takes the form

$$\frac{d}{dt}\iiint \rho \, dV + \oiint \mathbf{J}\cdot d\mathbf{S} = 0 \tag{32}$$

where the surface integral is positive if the current density J is flowing out of the surface. Using standard vector identities gives the corresponding differential form of charge conservation as

$$\frac{d\rho}{dt} + \nabla\cdot\mathbf{J} = 0 \tag{33}$$

VIII. ELECTRIC CURRENT

The electric current density is a crucial quantity in electrostatics, since it determines where charges are located at any instant. Occasionally, we observe a linear relation between the current and the electric field, of the form

$$\mathbf{J} = \sigma\mathbf{E} \tag{34}$$

where σ is called the conductivity of the material through which the current flows. In most electrostatic applications, however, the relation between current and field is more complicated. To understand why, and to decide which relation is appropriate in a given instance, we need to examine the conduction process more closely.

To begin, we consider the case of unipolar conduction, where only a single type of charge carrier is present. These carriers have a volume density of n per cubic meter, and they are all moving with a velocity u. The current density is given by

$$\mathbf{J} = nq\mathbf{u} \tag{35}$$

There are three quantities that affect the current density, so changes in any one of them will affect the current flow. Note that this current is associated with a local charge density

$$\rho = nq \tag{36}$$

If the moving charge is the only charge present, there will be a net space charge density, which leads to variations in the local electric field. This situation often occurs when current is flowing through good insulators

like gases, oils, or plastics. In other cases, there are additional charges that do not participate in the motion but are available to neutralize the space charge of the carriers. This situation is common in good conductors like metals or water.

The current density is proportional to the velocity of the charge carriers, which is determined by their response to applied forces. They can be swept along by surrounding material, as in a flow of insulating liquid, or they can be moved by a force that acts directly on the associated mass, such as gravity or inertia. They can also be moved by the electric field. When a field is applied, the charge at first accelerates inertially, but it usually reaches a terminal velocity depending on the nature of the surrounding material. After this inertial transient, the charge velocity is related to the applied field by

$$\mathbf{u} = \mu\mathbf{E} \tag{37}$$

where μ is the mobility of the carrier in that material. This relation is only valid after some delay time in normal fluids and solids. In thin materials like gases and vacuum, the delay time may exceed the time available for the experiment. In those cases, mobility has no meaning.

Note that the mobility relation includes the sign of the charge, since the velocity will be reversed if the sign changes. A negative carrier, for example, will have a negative mobility. Often the sign is omitted from discussions, but it must be replaced in the equations when needed to avoid incorrect results.

So far we have seen a number of ways in which the current density can vary in time and space. The number density of carriers, their charge, and their velocity can all vary in a particular situation, invalidating the concept of conductivity. It is still possible to define a material conductivity, however, if these sources of variations are absent or weak. In particular, if the number of available carriers and their charge is constant, and if the velocity is linearly related to the electric field through the mobility relation, then we can write the current as

$$\mathbf{J} = (nq\mu)\mathbf{E} \equiv \sigma\mathbf{E} \tag{38}$$

which serves to define the conductivity.

These considerations remain valid if there is more than one available carrier, since the total current density can be expressed as the sum of contributions from each carrier as

$$\mathbf{J} = \sum_i \mathbf{J}_i = \sum_i n_i q_i \mathbf{u}_i \tag{39}$$

In the mobility limit, this takes the form

$$\mathbf{J} = \sum_i n_i q_i \mu_i \mathbf{E} = \left(\sum_i n_i q_i \mu_i \right) \mathbf{E} \equiv \sigma \mathbf{E} \tag{40}$$

which gives an expanded definition of conductivity. Note that the charge on each particle is multiplied by its mobility, so that the correct result is obtained by taking the magnitude of these quantities.

In some studies, the relation between current density is described by resistivity instead of conductivity. Normally the resistivity is defined by

$$\rho \equiv \frac{1}{\sigma} \tag{41}$$

If resistivity is used, care should be taken not to confuse it with the space charge density, which often uses the same symbol, ρ.

IX. ELECTROSTATIC FORCE EXPRESSIONS

Coulomb's law describes the electrostatic forces exerted between pairs of charges, but practical situations are rarely that simple. A number of alternate formulations have arisen in practice to simplify the task of finding force in a particular situation. The most popular formulations are described below.

A. Monopoles and Dipoles

The force on a single charge in an electric field is given by the monopole force expression as

$$\mathbf{F} = q\mathbf{E} \tag{42}$$

This is often used when there is a single charged object. In many cases, there will be two equal and opposite charges on a single object, as shown in Fig. 4. To first order, the forces on the two charges oppose each other, yielding a net force of zero on the object. If the electric field is stronger at the location of one of the charges, however, it will exert a slightly greater force. The net force on the entire object depends on the size of the object, and on the difference in electric field across the object. In Fig. 4, this gives a net force in the x direction of

$$F_x = qd \frac{\partial E_x}{\partial x} \tag{43}$$

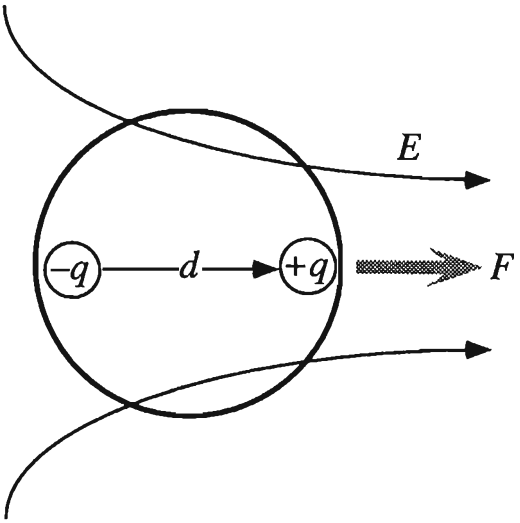


Figure 4 A dipole in a nonuniform field.

The coefficient of the derivative is called the dipole moment of the object. It is a vector quantity, defined by

$$\mathbf{p} = q\mathbf{d} \tag{44}$$

The net vector force on the dipole can therefore be written as

$$\mathbf{F} = (\mathbf{p}\cdot\nabla)\mathbf{E} \tag{45}$$

Since most materials consist of atoms or molecules that contain equal numbers of electrons and protons, the dipole force can always occur if the electric field is nonuniform. In studying dipole forces in bulk materials, it is more convenient to combine the force contributions of all the individual dipoles into a single expression for the dipole force density per unit volume (or dielectrophoretic force),

$$\mathbf{f} = (\mathbf{P}\cdot\nabla)\mathbf{E} \tag{46}$$

Here **P** is the polarization vector, defined as

$$\mathbf{P} = n\mathbf{p} \tag{47}$$

where n is the number density of dipoles.

B. Stress Tensor

When dealing with bulk materials, and when formulating boundary conditions for motion, it is usually simplest to use the Maxwell stress tensor to describe the force. This expression is based on the volume force density expression

$$f = \frac{F}{Volume} = \rho E \tag{48}$$

When the charge density is eliminated by using Gauss's law, this takes the form

$$f = (\nabla \cdot \mathbf{D})\mathbf{E} \tag{49}$$

which can be rewritten using vector identities as

$$f_i = \sum_{j=1}^{3} \frac{\partial T_{ij}}{\partial x_j} \tag{50}$$

Each component of the force is the sum of partial derivatives of a new quantity called the stress tensor. It is defined by

$$T_{ij} = \epsilon E_i E_j - \tfrac{1}{2}\epsilon E_{ij}^2 \delta_{ij} \tag{51}$$

where δ_{ij} is the Kronecker delta,

$$\delta_{ij} = \begin{cases} 1 & i = j \\ 0 & i \neq j \end{cases} \tag{52}$$

This formulation of the electrostatic force has the advantage that only a single quantity, the electric field, need be known in order to apply it.

The stress tensor is widely used to find forces on entire bodies, and also to derive boundary conditions by converting to a surface integral. This conversion relies on vector identities to produce the expression for the net force on a closed volume as

$$F_i = \oiint \left(\sum_{i=1}^{3} T_{ij} n_j \right) dS \tag{53}$$

Just as for the volume force density, this allows calculation of force solely from knowledge of the electric fields, without the need to determine the charge distribution.

C. Lumped Force

When dealing with macroscopic bodies subject to electrostatic forces, a lumped parameter formulation can often be made. This approach assumes

that the charge on an object can be described by a capacitance relation. For a single body, this takes the form

$$Q = CV \tag{54}$$

This approach can also be used when there are multiple charges and voltages by extending the definition. The electrostatic force can be written as a derivative of a potential energy function as

$$f = \frac{\partial W'}{\partial x} \tag{55}$$

The energy function W′ is called the electric coenergy and is calculated for a two-terminal device as (Woodson and Melcher, 1968)

$$W' = \tfrac{1}{2}CV^2 \tag{56}$$

Only the capacitance factor depends on position, so the force has the simpler form

$$f = V^2 \frac{\partial C}{\partial x} \tag{57}$$

Similar expressions can be calculated for forces in other directions. For example, the torque on the object would be given as

$$\tau = V^2 \frac{\partial C}{\partial \theta} \tag{58}$$

if the capacitance varies with the angular position.

NOMENCLATURE

A	area, m^2
C	capacitance, F
D	electric displacement field, C/m^2
d	distance, m
E	electric field, V/m
F	force, N
f	force density, N/m^3
i	current, A
$\mathbf{i}$	unit vector
J	current density, A/m^2
n	number density, $1/m^3$
$\mathbf{n}$	normal unit vector
P	polarization, C/m^2
p	electric dipole, C·m

Q charge, C
q charge on particle, C
r radial distance
S surface area, m^2
T electric stress tensor, Pa
u velocity, m/s
V voltage, V
W potential energy, J
W' electric coenergy, J
δ Kronecker delta, also dielectric thickness, m
ϵ permittivity, F/m
ϵ_0 permittivity of vacuum, 8.854 pF/m
Φ potential, V
κ dielectric constant
μ mobility, m^2/Vs
π 3.14159 ···
ρ charge density, C/m^3, or resistivity, $\Omega \cdot m$
ρ_L linear charge density, C/m
σ conductivity, S/m
τ torque, N·m
θ angular position, radians

TABULATED SOLUTIONS OF LAPLACE'S EQUATION

These tables give the solutions of Laplace's equation for a number of useful geometries and boundary conditions. In each geometry, there are several boundary conditions that can give rise to fields. Each of the partial solutions associated with a boundary condition is given in the table. They may be superposed to find the total solution. An example of the application of these tables is shown in Sec. VI.

Table 1 Flat Parallel Electrodes

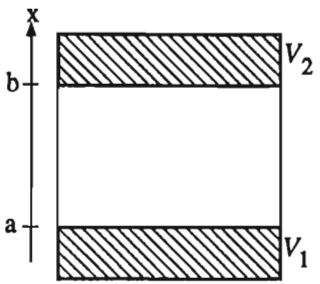
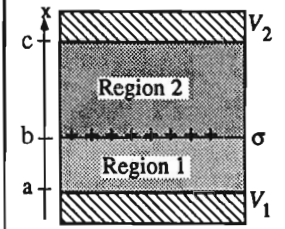
		Boundary Conditions	
		V_1 $x = a$ $-\infty \le y \le \infty$ $-\infty \le z \le \infty$	V_2 $x = b$ $-\infty \le y \le \infty$ $-\infty \le z \le \infty$
Region 1			
$a < x < b$ $-\infty \le y \le \infty$ $-\infty \le z \le \infty$	$\Phi =$	$\dfrac{b-x}{b-a}$	$\dfrac{x-a}{b-a}$
	$E_x =$	$\dfrac{1}{b-a}$	$-\dfrac{1}{b-a}$
	$E_y =$	0	0
	$E_z =$	0	0

Table 2 Parallel Dielectric Sheets

		Boundary Conditions		
		V1 at $x = a$ $-\infty \le y \le \infty$ $-\infty \le z \le \infty$	V2 at $x = c$ $-\infty \le y \le \infty$ $-\infty \le z \le \infty$	σ at $x = b$ $-\infty \le y \le \infty$ $-\infty \le z \le \infty$
Region 1				
$a < x < b$ $-\infty \le y \le \infty$ $-\infty \le z \le \infty$	$\Phi =$	$\frac{\delta_2 + (b-x)/\kappa_1}{\delta_1 + \delta_2}$	$\frac{(x-a)/\kappa_1}{\delta_1 + \delta_2}$	$\frac{\delta_2}{\delta_1 + \delta_2}\frac{(x-a)\sigma}{\kappa_1 \varepsilon_0}$
	$E_x =$	$\frac{1/\kappa_1}{\delta_1 + \delta_2}$	$-\frac{1/\kappa_1}{\delta_1 + \delta_2}$	$-\frac{\delta_2}{\delta_1 + \delta_2}\frac{\sigma}{\kappa_1 \varepsilon_0}$
	$E_y =$	0	0	0
	$E_z =$	0	0	0
Region 2				
$b < x < c$ $-\infty \le y \le \infty$ $-\infty \le z \le \infty$	$\Phi =$	$\frac{(c-x)/\kappa_2}{\delta_1 + \delta_2}$	$\frac{\delta_1 + (x-b)/\kappa_2}{\delta_1 + \delta_2}$	$\frac{\delta_1}{\delta_1 + \delta_2}\frac{(c-x)\sigma}{\kappa_2 \varepsilon_0}$
	$E_x =$	$\frac{1/\kappa_2}{\delta_1 + \delta_2}$	$-\frac{1/\kappa_2}{\delta_1 + \delta_2}$	$\frac{\delta_1}{\delta_1 + \delta_2}\frac{\sigma}{\kappa_2 \varepsilon_0}$
	$E_y =$		0	0
	$E_z =$		0	0

This table uses the definitions $\delta_1 = (b - a)/\kappa_1$ and $\delta_2 = (c - b)/\kappa_2$. The ratio of thickness to dielectric constant is often called the (apparent) dielectric thickness.

Table 3 Coaxial Circular Cylinders

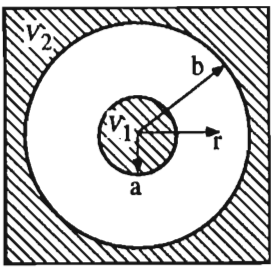
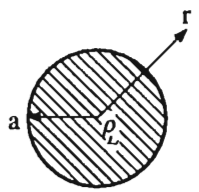
		Boundary Conditions	
		V1 $r = a$ $0 \le \theta \le 2\pi$ $-\infty \le z \le \infty$	V2 $r = b$ $0 \le \theta \le 2\pi$ $-\infty \le z \le \infty$
Region 1			
$a < r < b$ $0 \le \theta \le 2\pi$ $-\infty \le z \le \infty$	$\Phi =$	$\dfrac{\ln(b/r)}{\ln(b/a)}$	$\dfrac{\ln(r/a)}{\ln(b/a)}$
	$E_r =$	$\dfrac{1}{r\ln(b/a)}$	$-\dfrac{1}{r\ln(b/a)}$
	$E_\theta =$	0	0
	$E_z =$	0	0

Table 4 Charged Cylinder

		Boundary Conditions	
		ρ_L $r = a$ $0 \le \theta \le 2\pi$ $-\infty \le z \le \infty$	V $r = \infty$ $0 \le \theta \le 2\pi$ $-\infty \le z \le \infty$
Region 1			
$a \le r \le \infty$ $0 \le \theta \le 2\pi$ $-\infty \le z \le \infty$	$\Phi =$	$\dfrac{\ln(r)}{2\pi\kappa_1\varepsilon_0}$	1
	$E_r =$	$\dfrac{1}{2\pi\kappa_1\varepsilon_0 r}$	0
	$E_\theta =$	0	0
	$E_z =$	0	0

The quantity ρ_L is the net charge per unit length in C/m.

Table 5 Isolated Sphere

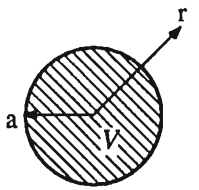
		Boundary Conditions	
		V_1 $r = a$ $0 \le \theta \le \pi$ $0 \le \phi \le 2\pi$	V_2 $r = \infty$ $0 \le \theta \le \pi$ $0 \le \phi \le 2\pi$
Region 1			
$a < r < \infty$ $0 \le \theta \le \pi$ $0 \le \phi \le 2\pi$	$\Phi =$	$\frac{a}{r}$	1
	$E_r =$	$\frac{a}{r^2}$	0
	$E_\theta =$	0	0
	$E_\phi =$	0	0

Table 6 Concentric Spheres

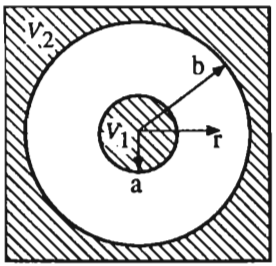
		Boundary Conditions	
		V_1 $r = a$ $0 \le \theta \le \pi$ $0 \le \phi \le 2\pi$	V_2 $r = b$ $0 \le \theta \le \pi$ $0 \le \phi \le 2\pi$
Region 1			
$a < r < b$ $0 \le \theta \le \pi$ $0 \le \phi \le 2\pi$	$\Phi =$	$\frac{b/r - 1}{b/a - 1}$	$\frac{b/a - b/r}{b/a - 1}$
	$E_r =$	$\frac{ab}{(b-a)r^2}$	$-\frac{ab}{(b-a)r^2}$
	$E_\theta =$	0	0
	$E_\phi =$	0	0

Table 7 Surface Charge on Sphere

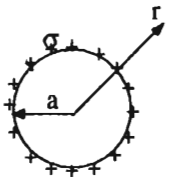
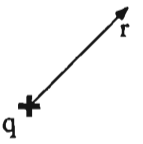
		Boundary Conditions	
		σ $r = a$ $0 \le \theta \le \pi$ $0 \le \phi \le 2\pi$	V $r = \infty$ $0 \le \theta \le \pi$ $0 \le \phi \le 2\pi$
Region 1			
$0 < r < a$ $0 \le \theta \le \pi$ $0 \le \phi \le 2\pi$	$\Phi =$	$\frac{a}{\kappa_2 \varepsilon_0}$	1
	$E_r =$	0	0
	$E_\theta =$	0	0
	$E_\phi =$	0	0
Region 2			
$a < r < \infty$ $0 \le \theta \le \pi$ $0 \le \phi \le 2\pi$	$\Phi =$	$\frac{a^2}{\kappa_2 \varepsilon_0 r}$	1
	$E_r =$	$\frac{a^2}{\kappa_2 \varepsilon_0 r^2}$	0
	$E_\theta =$	0	0
	$E_\phi =$	0	0

Table 8 Point Charge at Origin

		Boundary Conditions	
		q $r = 0$ $0 \le \theta \le \pi$ $0 \le \phi \le 2\pi$	V $r = \infty$ $0 \le \theta \le \pi$ $0 \le \phi \le 2\pi$
Region 1			
$a < r < \infty$ $0 \le \theta \le \pi$ $0 \le \phi \le 2\pi$	$\Phi =$	$\frac{1}{4\pi\kappa\varepsilon_0 r}$	1
	$E_r =$	$\frac{1}{4\pi\kappa\varepsilon_0 r^2}$	0
	$E_\theta =$	0	0
	$E_\phi =$	0	0

BIBLIOGRAPHY

Crowley, J. M. (1986). *Fundamentals of Applied Electrostatics*. Wiley, New York.

Durand, E. (1964). *Electrostatique*. Masson, Paris.

Haus, H., and J. R. Melcher (1989). *Electromagnetic Fields and Energy*. Prentice-Hall, Englewood Cliffs, New Jersey.

Jackson, J. D. (1962). *Classical Electrodynamics*. Wiley, New York.

Melcher, J. R. (1981). *Continuum Electromechanics*. MIT Press, Cambridge, Massachusetts.

Moon, P., and D. E. Spencer (1961). *Field Theory for Engineers*. Van Nostrand, Princeton, New Jersey.

Moon, P., and D. E. Spencer (1961). *Field Theory Handbook*. Springer Verlag, Berlin.

Moore, A. D. (1973). *Electrostatics and Its Applications*. Wiley, New York.
Plonus, M. A. (1978). *Applied Electromagnetics*. McGraw-Hill, New York.
Pohl, H. A. (1978). *Dielectrophoresis*. Cambridge University Press, Cambridge.
Smythe, W. (1939). *Static and Dynamic Electricity*. McGraw-Hill, New York.
Stratton, J. E. (1941). *Electromagnetic Theory*. McGraw-Hill, New York.
Woodson, H. H., and J. R. Melcher (1968). *Electromechanical Dynamics*. Wiley, New York.
Zahn, M. (1979). *Electromagnetic Field Theory*. Wiley, New York.

This Page Intentionally Left Blank

2

Electrification of Solid Materials

Alexander A. Berezin

McMaster University
Hamilton, Ontario, Canada

I. INTRODUCTION

This article provides a brief overview of physical aspects related to the electrification mechanisms of solid materials.

With the exception of lightning, frictional electrification of material objects is probably the earliest electrophysical phenomenon known to people from their direct experience. Yet in contemporary electrical science, engineering, and modern society at large, electrostatics and its applications attract relatively little attention. It is not difficult to indicate several reasons for such an apparent neglect of electrostatics:

(1) Almost all modern technology and the entire society relies on electricity in its, so to say, electrodynamical form. Production, distribution, and utilization of electric power along with many industries related to electronics (computing, musical entertainment equipment, radio and cable communication systems including TV and VCR technologies) employ the lion's share of all electrically related professionals. On the background of these populous occupations and trades, those few who are professionally engaged into electrostatics are almost unnoticeable.

(2) Accumulation of a static charge is often perceived as a source of parasitic and undesirable effects, i.e., largely as a "pest" phenomenon. This is the typical feeling of those involved in the home insulation, stereo equipment, conveyor belts, etc. For them, static charging is primarily

something to avoid rather than a fundamental and applicationally useful physical phenomenon. Effects like electrification due to engine belts are of direct concern to car manufacturers. For the general public, static charging of synthetic cloth and apparel leads to additional (though usually relatively minor) expenditures on antistatic sprays and laundry additives.

(3) Skeptical overtones toward electrostatics have even some effect on electrical and electronics professionals. Many of them perceive the whole lore of static electricity and electrostatic charging in an essentially negative way, sometimes even with near disdain. Such an attitude is easily recognizable from the typical present-day university curriculum in electrical or civil engineering, which as a rule gives almost no serious exposure to electrostatics problems.

(4) Likewise, among "pure" physicists, electrostatically related areas (such as static charging, dielectrics, and breakdown phenomena) are not usually taken as exciting and promising research directions for the near future.

To summarize, electrostatics does not generally enjoy the same level of respect and social support as many other, currently more fashionable, areas of physics and electronics. Few will be willing to support a major electrostatics project with even 1% of the costs of the now notorious superconducting supercollider (its current price tag is about $11 billion). Few believe that electrostatics could be a likely or inspiring source for important breakthroughs in fundamental and applied areas of science and technology. The overview of electrification phenomena presented in this article provides some arguments to offset such a widespread negative image of electrostatics. Following a more optimistic note, this paper emphasizes the present development of new and important links between electrification phenomena and certain fundamental aspects of quantum physics and other key areas of modern science, technology, and engineering.

II. PHENOMENOLOGY OF A STATIC CHARGE

A. Conductors and Insulators

The traditional division of materials into two opposite classes, conductors and insulators, is valid only in a crude sense. In reality there is a tremendous diversity of properties of solid materials in terms of their electrical conductivity characteristics, their dielectric properties, and their ability to accumulate and hold a static electric charge.

B. Electrical Conductivity and Charging

Materials differ in physical types and concentrations of electrical charges and in the ability of these charges to move freely or quasifreely. The latter type of motion means a wide variety of propagation mechanisms of charges, e.g., by quasicontinuous diffusion or by "hopping" over the atomic impurities and other microscopic defects in a crystal lattice. The generation and recombination mechanisms are also quite versatile, as well as the delivery mechanisms of charges from the surrounding objects, which are especially important for the kinetics of static charging (Loeb, 1958; Harper, 1967; Krupp, 1971; Shinbrot, 1985; Schein et al., 1992; Horn and Smith, 1992).

Charging is mainly (but not exclusively) a surface-dominated process. It is, of course, trivial that any local charging is a result of an imbalance between the positive and negative charges at a particular spot. However, the specific mechanisms of this charging allow for numerous scenarios in terms of the nature of the charge carriers, their mobility, their dynamics of accumulation on surfaces and defects, etc.

C. Charge-Holding Characteristics

Conductivity and charge-holding characteristics of solids are, of course, primarily defined by their physical and chemical nature. However, even for a given material (with a specified chemical structure and composition), the nature and magnitude of the fundamental electroconductivity and electrostatic characteristics can exhibit an additional dependence on the size, shape, degree of polycrystallinity, and all possible varieties of chemical impurities and structural imperfections. Among the characteristics showing sample-dependent variability are relaxation ("leaking") times of the accumulated charges, thresholds of breakdown and arcing, and local values of dielectric losses.

The charge-holding capacity of bodies varies greatly and is limited by a whole range of discharge effects. For example, for electrostatic charging of powder-type materials it is quite typical to achieve charge-to-mass ratios on the order of 10^{-4} C/kg. Typical scenarios of electrostatic charging are shown in Fig. 1a,b. Generically, three main types of behavior can be identified:

(a) Linear charge accumulation with a subsequent abrupt ("catastrophic") breakdown (curve Lin-Break in Fig. 1). This type of breakdown happens mostly as a spark-type discharge. The threshold voltage for such a discharge usually has a poor predictability. It may change quite erratically depending on the size and shape of the charging objects, the state of their

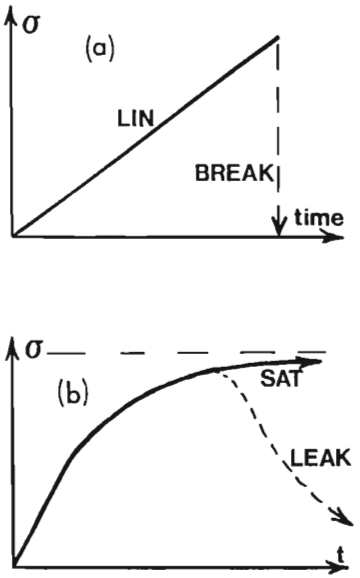


Figure 1 Three scenarios of static charging as functions of time: (a) linear charge accumulation (Lin) followed by an abrupt breakdown discharge (Break); (b) Nonlinear saturation restricted by charge repulsion effects (Sat) or followed by gradual leaking of the charge (Leak). σ is a surface charge density.

surfaces (dry or wet, etc.), the configuration and placement of surrounding objects, and other environmental factors (e.g., presence of moisture or dust particles).

(b) Saturation-type characteristics of charge accumulation. In this case the accumulation of charges on solids during the triboelectrification process saturates in time (curve Sat in Fig. 1). This happens when the effects of electrostatic repulsion noticably precede the spark breakdown. The saturation happens because of the effects of the electrostatic repulsion (Berezin, 1986) that the newly arriving charges experience from the already accumulated charges, which resist their further accumulation. This process can be delayed for some special geometries favoring charge accumulation on the outer surfaces of the charging bodies (e.g., in a van der Graaff electrostatic accelerator or a Leyden jar).

(c) Charge accumulation limited by gradual leaking effects. In this case the nonlinearity of a process arises as a result of a competition between charge arrival and a setup of various leaking currents (curve Leak

in Fig. 1). To some extent, such a scenario can include corona discharge effects.

D. Randomness and Chaos in Charging

Erratic and often highly unpredictable chains of breakdown onsets accompanying triboelectrical charging can lead to chaotic time patterns of discharges as illustrated in Fig. 2. This sketches a typical plot of spark discharges in systems like conveyor belts. Due to sporadic discharges, the total instantaneous charge Q varies. In most cases (but not always) the total charge at each discharge reduces to near zero and then accumulates again. Although the discharges normally happen with a certain average frequency (repetition rate), they as a rule do not form a periodic train and appear to have some stochasticity.

Furthermore, as the discharge events are very sensitive to the initial conditions, the time instances of discharges (t_1, t_2, t_3, etc.) may not be just a random time series but can form (at least sometimes) correlated patterns according to recent theories of chaos and fractal dynamics. These "hidden" correlations are usually described as a presence of some intricate structures in a phase space of a system in question. Such mathematical objects have a fractal-like topology and are presently known under the name of strange attractors (Berezin, 1991).

III. OVERVIEW OF CHARGING MECHANISMS

A. Charge Geometry and Charge Stability

The distribution of static charges on solid or polymer objects is defined by an interplay of several factors: (a) the geometry of charge generation areas (e.g., "hot spots" on surfaces under friction), (b) the degree of ease

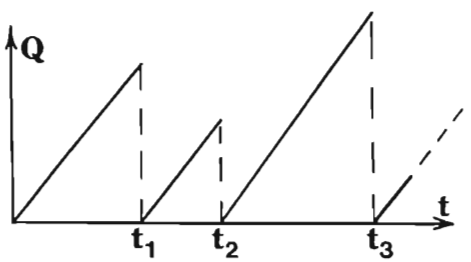


Figure 2 Chaotic sequence of tribochargings and discharge breakdowns.

with which charges move, and (c) the electrostatic (Coulombic) repulsion between charges of a given sign. Additionally, polarization effects (formation of dielectric dipoles) can sometimes play a role in defining the terminal charging pattern.

If charges have some positional flexibility, their distribution can experience sharp spacial rearrangements (Berezin, 1986). This can be interpreted as electrostatic phase transitions, which are similar to structural phase transitions in crystals. Generally speaking, the charges are more stable when they are highly localized (Harper, 1967), and their self-stabilization is often due to polarization effects. Polarization effects can sometime facilitate nonuniform charge distributions and asymmetrical charge clustering. The physical basis for this is illustrated in Fig. 3 with the simple example of two identical neutral impurity atoms immersed in a polarizable insulator. Polarization of a medium by a net electrical charge leads to a decrease of the total potential energy of the system. As a result, it may be energetically advantageous for a system of two neutral atoms (Fig. 3a) to "decay" into the asymmetrical state of one positive and one negative ion. Such a process of spontaneous charge asymmetrization is shown by the dashed arrow in Fig. 3a. Physically, it can proceed by a ("cold") quantum mechanical tunneling or a ("hot") thermally activated hopping process. Either of these routes results in the state shown in Fig. 3b. The polarization energy

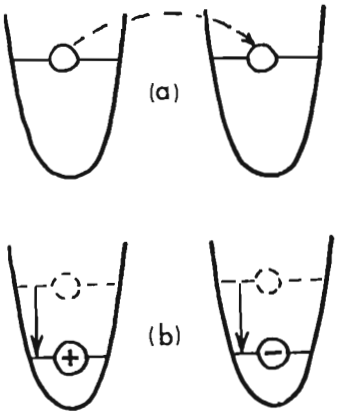


Figure 3 Formation of charge nonuniformities due to polarization effects. Vertical axis indicates the energy of an individual atomic state relative to the energy band structure of a given solid material. (a) Two identical electrically neutral atoms in a polarizable medium. (b) Asymmetrical stable state formed by charge redistribution.

is always negative, as it is proportional to the minus square of the electric field of a net charge, i.e., both $+Q$ and $-Q$ contribute separately to a net decrease of the potential energy. This means that at both (so originating) charged sites the whole system gains negative contributions to the total net potential energy. These energy shifts are shown in Fig. 3b by the two downward-pointing arrows.

The process sketched in Fig. 3 is an example of a general physical phenomenon known as spontaneous symmetry breaking. It is also akin to a polaron effect in solid state physics (Emin, 1982). In the case when such spontaneous charge asymmetrization leads to the formation of a poly-electronic localized charge, the whole phenomenon is refered to as "polarization catastrophe." These aspects of static charging are especially important for electrification effects in microparticles, e.g., in dusty plasmas, aerosoles, sprays.

B. Classification of Charging Mechanisms

It is possible to indicate several distinguishably different mechanisms of the charging process as it applies to solids (Harper, 1967). Any possible classification of charging mechanisms has, of course, some degree of subjectivity and can depend on a desired emphasis under consideration. For instance, the optimal classification of charging mechanisms will likely be different whenever the point of major interest lies in a fundamental microscopic dynamics of charging, the relationship of charging to other physical and chemical processes, or various objectives of engineering related to charging. As a compromise between diverse fundamental and applied aspects of various processes of electrification of solid materials, the following classification of charging mechanisms is adopted in the present review. We can, roughly speaking, separate all charging phenomena into three categories:

1. Charging involving relative mechanical motion of objects and surfaces
2. Charging as a pure contact phenomenon (no relative macroscopic motion occurs)
3. Charging as a primarily chemical (or electrochemical) process

The first category involves various processes like sliding, rolling, the flow of a liquid or a gas around solid objects, etc. (Horn and Smith, 1992). This class of phenomena is generally known as triboelectric (Sec. III.C). It also may include charging by a mechanical collision between particles or between particles and surfaces ("hit-and-run" charging).

The second category encompasses many phenomenologically and microscopically different processes like charge redistribution due to contact

potential difference, charging due to electron tunneling, etc. (Sec. III.D). Formation of regions of spacial net charge and built-in electric fields at semiconductor pn junctions and more complicated semiconductor structures also falls into this category. The latter effects are due to the different electronic affinity of donor- and acceptor-type impurities, with the consequence that their charged (and not neutral) state leads to the configurations of the least potential energy (Streetman, 1990).

The third category includes such phenomena as electrification as a result of electrolytic charge separation (e.g., in batteries) or during some corrosion processes (Sec. III.E). In most cases, charges released in chemical processes do not accumulate in significant quantities but are diffused away by net electric currents.

Additionally to the above categories, the (partial) electrical charging of solids can be achieved through their illumination by light (photoelectric effect) or by a direct extraction of electrons by the application of strong electric fields (autoelectronic emission). These effects are outside the scope of this article.

C. Triboelectric Charging

Triboelectrification or frictional charging is one of the oldest known forms of charging, yet it is perhaps less understood in its fundamental mechanisms than such processes as contact or electrochemical charging. The major body of data related to triboelectrification is mostly of a phenomenological nature. In some cases it is not even clear how to explain the *sign* of a charge on a particular surface for a given pair of surfaces experiencing a frictional contact.

1. Types of Triboelectrification

Generally speaking, frictional charging can happen at any dynamical contact of surfaces. The main forms of such dynamical triboelectric contact (Harper, 1967) are

1. Sliding
2. Rolling
3. Vibration of surfaces at a contact
4. Impact charging
5. Charging at a rupture or a separation of solid/solid or solid/liquid surfaces (Loeb, 1958)
6. Deformation-induced charging due to a charge redistribution at stress
7. Charging at cleavage of crystals (Krupp, 1971)

Additionally, a noticeable charging can sometimes result from a periodi-

cally varying pressure between the two surfaces, even when they are not moving against each other. This is a subcase of case (6) above.

2. Volta-Helmholtz Hypothesis

Experiment generally shows that the level of a triboelectric charging depends on the relative velocity of surfaces moving against each other and on the pressure acting between them. In most cases the accumulated charge increases with pressure at rubbing. This could be simply explained as a multiplication of the density of contact points with pressure increase. This is known as the Volta-Helmholtz hypothesis. Surface charge density at these processes can be up to 10^4 electrostatic units per cm^2, which corresponds to about $2 \cdot 10^{13}$ electronic charges per cm^2. The latter means that the average distance between the two neighboring electrons at the surface is less than 10 interatomic distances. Such charge densities, which are quite rare at frictional electrification processes, can lead to electric fields in the range of thousands of kV/cm near a charged surface.

D. Contact Charging

Contact charging (Volta effect) is a process of charge redistribution resulting from a direct contact of two surfaces without their relative macroscopic motion or application of a pressure (these are at least not the essential aspects of contact charging). Contrary to mechanical triboelectrical charging, the physical mechanisms of contact charging are quite well understood.

The physical reason for contact charging is the gain of potential energy of a system that can be achieved when two surfaces of different chemical and/or structural nature are brought into contact. Usually contact charging is treated as the formation of a double electrical layer (DEL), as shown in Fig. 4. This layer spontaneously originates between (almost) any two

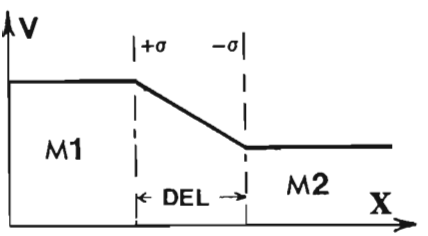


Figure 4 Double dielectric layer between two materials (M1 and M2). Electric potential V changes over the microscopic distance, usually of several atomic layers. Del = double electrical layer.

dissimilar materials (M1 and M2). In Fig. 4 the x-axis shows the direction perpendicular to the interface between both materials. The DEL, also known as a Helmholtz double layer, is somewhat similar to a charged capacitor (Harper, 1967; Loeb, 1958). Its formation is due to the differences in the original energies of mobile electrons in the two contacting materials. For the case of two metals in contact these energies are referred to as the Fermi energies of the two respective metals. The actual charge redistribution is usually described as a quantum mechanical tunneling effect through the potential barrier, as shown in Fig. 5. The potential barrier between two metals is usually caused by a thin layer of oxide forming at the interface.

As such, contact charging does not necessarily involve mechanical motions. In this way it differs from triboelectrical effects. However, the main physical aspect of contact charging (quantum tunneling of electrons) can also be present during the process of frictional charging.

E. Chemically Induced Charging

Contact charging (Sec. III.D) does not as such presume chemical changes in the materials in contact. When such chemical changes have taken place, the charging is referred to as chemically induced charging. This features chemical reactions involving charge transfer and various electrochemical processes when a system is subjected to the voltage differences imposed from outside (external biases). An example is the electrochemical corrosion of a metallic surface or other surface oxidation reactions. Depending on the circumstances, charging or voltage biasing can affect the rate of such processes. Usually, depending on the interplay of the polarity and a magnitude of biasing with the material and environmental parameters (type of metals, acidity of solutions, etc.), both rate-accelerating and rate-inhibiting effects can be actualized.

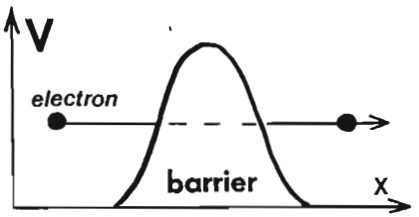


Figure 5 Quantum mechanical tunneling of an electron through the potential barrier.

F. Charging Oscillations and Sign Reversals

Unpredictability of frictional charging can sometime elevate to a random or quasirandom (chaotic) change of the magnitude (and even sign) of a static charge during the charging process. For instance, electrification by repeated contacts of an epoxy resin with a copper plate leads to a nonmonotonic (oscillating) dependence of total charge as a function of the number of contacts made (Kwetkus et al., 1991). Most of these effects remain at a largely phenomenological level and await a truly quantitative theoretical explanation. It is quite likely that many of these observations will require explanation at a quantum mechanical level using theoretical tools such as quantum nonlocalities in electrostatic interactions. The latter are represented, for instance, by an electrostatic version of the Aharonov-Bohm effect (Matteucci and Pozzi, 1990) or some other recent developments in the area of quantum chaos (Gutzwiller, 1991).

G. Triboelectric Series

Mutual charging of two frictionally interacting materials usually preserves the sign of a charge induced on each of the participating surfaces. For example, rubbing of zinc over glass results in the glass being charged positively and the zinc negatively (Harper, 1967). Sometimes (but not always!) several materials can be arranged into a so-called triboelectric series so that each material is charged positively when it is rubbed against the previous. Sometimes these series are closed (i.e., form loops). An example of such a loop involving five materials is (Harper, 1967)

$$\cdots - \text{zinc} - \text{glass} - \text{cotton} - \text{filter paper} - \text{silk} - \text{zinc} - \cdots$$

It should be noted, however, that such loops are reproducible only quite poorly, and often the sign of the induced charge shows the reverse of the expected. This reversal may be influenced by such circumstances as the shape of the surfaces. For example, convex and concave surfaces may acquire different signs of charge. Similar erratic changes of sign ("temperamental charging") may be due to variations in the degree of smoothness of the participating surfaces, etc.

IV. SOME APPLIED ASPECTS OF CHARGING

A. Static Charge Monitoring

In practical static electrification we need means of dealing with essentially opposite tasks:

1. Getting rid of a static charge when it is not needed
2. Keeping a static charge when it facilitates the desired effects

For the first task we need means of suppressing the charge separation in various mechanical processes and/or neutralizing the accumulated charge. For the latter we need various antistatic circuits and other ways of increasing the ambient electrical conductivity (e.g., antistatic sprays). The second task must be accomplished relatively less often and is mostly attained by designing surface geometries that are beneficial for charge accumulation and subsequent charge stabilization. A typical example of the latter is an electrostatic van de Graaff generator.

B. Industrial Implications of Triboelectricity

Along with some applications mentioned in the introduction, the following industries and technologies are fundamentally affected by the effects of static charging: photocopying, laser printing, electrostatic dust collection, electrostatic precipitation, etc. Paper and textile industries have special facilities to reduce static charging. Another problem is a static charge in an aircraft induced during flight. As many areas of manufacturing (like the auto industry) are now moving from metals to plastics and ceramics, the role of static charging is getting more and more important.

C. Electrostatic Effects in Microelectronics and Related Areas

A special facet of electrostatic effects is opened up by microelectronic technology. Here it becomes more and more important to take into account the fundamentally discrete nature of electrical charge. In systems of submicron size the motion and locations of individual electrons can significantly affect the dynamics and the performance of a device. Effects like single electron charging and the Coulomb blockade (when the repulsion between just a few electrons inhibits electrical conductivity) are sometime vitally important in submicron electronics.

Interactions between the individual elementary charges also may be instrumental for some nonelectronic aspects of microelectronics and microtechnology in general (here by "electronics" in a proper sense we mean the processing of information). Examples for such "extended" use of electrostatic charging could be drawn from such different directions as corrosion passivation for microscale devices, implanted charges for structural stabilization in microtechnological applications ("electrostatic glue"), electrostatic effects for controlling the rate of catalytic reactions, and electrostatically operated micromotors (Pool, 1988). The latter may soon find important applications in medicine, e.g., as microdrills to clean clogged blood vessels.

Another area of recent opportunities is opened up by a possibility of electrostatic control of the behavioral response of the so called "smart materials" in their numerous emerging applications for fundamental research and engineering (Newnham and Ruschau, 1991). An example of the latter is electrostatic switching in rheological "smart" materials (Filisko, 1992). Here the application of an electric field induces fast and reversible transitions between liquid and solid phases. This new direction, interdisciplinary between electrostatics, materials science, and control systems, has many potential technical applications ranging from automobile transmissions and house plumbing to some facets of microelectronics and micromanipulators.

V. EPILOG

Electrification of materials can be seen in the wider context of the physics of charge separation. In this way it is akin to a magnetically induced charge separation attained in electrical generators. The latter are, of course, among the main technological instruments of modern civilization.

The classical foundational basis of electrostatic charging is the Coulomb interaction, which defines the kinematics and dynamics of charge separation and subsequent charge holding. Coulomb interaction determines the configurations of charge stability, the thresholds of sudden charge rearrangements and breakdowns, the effects of charge correlations (electrostatic ordering, Coulomb blockade, etc.), and electrostatic instabilities and gradual charge leaking processes. Quantum corrections to these effects are becoming important at the submicron scale and also in the presence of a long-range quantum coherency, as in e.g. the electrostatic Aharonov-Bohm effect mentioned above. As the latter (the change of an electronic interference pattern by an electrostatic field) belongs to the class of macroscopic quantum phenomena, it may have nontrivial implications for the electrostatic charging of macroscopic and mesoscopic solid objects (e.g., dust particles) in the presence of electric fields. Most of these effects are still largely unexplored.

To conclude, electrostatic charging effects are related to many fundamental physical, mechanical, and chemical processes. As is true for many other technological frontiers, the effects related to electrostatic charging have both macroscopic and microscopic terms of reference. On the microscopic side, the study of electrification phenomena is becoming more and more related to quantum mechanical effects. The applicational potential of quantum and chaotic aspects of charging is not yet fully appreciated. However, they are presently becoming more and more visible in microelectronics and other areas.

REFERENCES

Berezin, A. A. (1986). A discontinuous symmetry change in electrostatic systems. *Journal of Electrostatics*, 18, 193–197.

Berezin, A. A. (1991). Isotopic relatives of strange attractors. *Physics Letters A*, 161, 295–300.

Emin, D. (1982). Small polarons. *Physics Today* (June 1982), 34–40.

Filisko, F. E. (1992). Electrorheological materials: smart materials of the future. *Chemistry and Industry* (18 May 1992), 370–373.

Gutzwiller, M. C. (1991). *Chaos in Classical and Quantum Mechanics*, 2d ed. Springer-Verlag, Berlin.

Harper, W. R. (1967). *Contact and Frictional Electrification*. Monographs on the Physics and Chemistry of Materials. Clarendon Press, Oxford.

Horn, R. G., and D. T. Smith (1992). Contact electrification and adhesion between dissimilar materials. *Science*, 256, 362–364.

Krupp, H. (1971). Physical models of the static electrification of solids. *Static Electrification 1971* (Inst. Phys. Conf. Ser. No. 11), pp. 1–16.

Kwetkus, B. A., B. Gellert, and K. Sattler (1991). Discharge phenomena in contact electrification. *Electrostatics 1991* (Inst. Phys. Conf. Ser. No. 118, Sec. 4), pp. 229–234.

Loeb, L. B. (1958). *Static Electrification*. Springer-Verlag, Berlin.

Matteucci, G., and G. Pozzi (1990). The electrostatic Aharonov-Bohm effect. In *Quantum Coherence* (Anandan, J. S., ed.). World Scientific, Singapore, pp. 62–71.

Newnham, R. E., and G. R. Ruschau (1991). Smart electroceramics. *Journal of the American Ceramic Society*, 74, 463–480.

Pool, R. (1988). Microscopic motor is a first step. *Science*, 242, 379–380.

Schein, L. B., M. LaHa, and D. Novotny (1992). Theory of insulator charging. *Physics Letters A*, 167, 79–83.

Shinbrot, T. (1985). A look at charging mechanisms. *Journal of Electrostatics*, 17, 113–123.

Streetman, B. G. (1990). *Solid State Electronic Devices*. Prentice-Hall, Englewood Cliffs, N.J.

3

Electrostatic Charging of Particles

Jen-Shih Chang

McMaster University
Hamilton, Ontario, Canada

I. INTRODUCTION

When particles flow through an ionized zone, some ions will be deposited to the particle's surface and become charged particles. The amount of ion deposition on the particle surface depends on resident time, particle radius and shape, external electric and magnetic fields, particle velocity, etc. In this chapter, the effect of these parameters will be discussed in detail.

The effect of particle size and the ion species can be observed in Fig. 1. Depending on the ion species, the mean free path of the ion varies from 10^{-1} to 10^{-2} μm. Small ions such as O_2^+ and N_2^+ have a longer mean free path ($\sim 10^{-1}$ μm), and larger ions such as $H\text{-}(H_2O)_n^+$ and $NH_4\text{-}(NH_3)_n^+$ have a shorter mean free path ($\sim 10^{-2}$ μm). Hence for larger ions the usual continuum mechanics only apply to the particle size larger than 10^{-1} μm at one atmospheric gas pressure as shown in Fig. 1. For particle size smaller than 10^{-3} μm, the behavior of larger ions must be analyzed by free molecular flow. The effect of particle shape can be observed in Fig. 1 by the κ/κ' ratio, where κ and κ' are the shape factors defined in Sec. II.B; the κ/κ' ratio becomes unity for spherical particles. The effect of particle velocity and external electric field can be observed in Fig. 1 and Table 1, where three dimensionless numbers, *Re* (Reynolds number), *Pe* (Peclet number) and F_E (field charging factor), are introduced (see Secs. II.C and III.A for detailed definitions). Depending on these factors, the

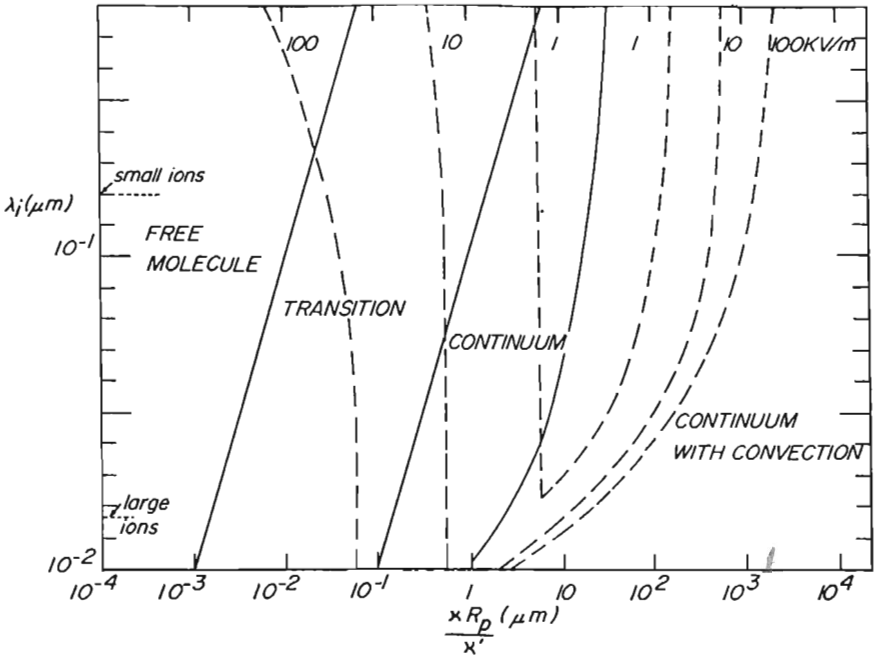


Figure 1 The relations between various charging processes and the effective aerosol particle radius $\kappa R_p/\kappa'$ (μm) for atmospheric pressure at 300K in air.

particle charging process may be controlled by convective motion of ions or drift motion of ions by external electric fields. Typical values of Pe and F_E are compared in Table 1 for atmospheric pressure at 300K in air. Table 1 shows that for aerosol particle size $R_p \geq 10$ μm, the gravitational motion will dominate most charging processes, even under the presence of an external electric field.

II. DIFFUSION CHARGING

The theory of diffusion charging of particles by unipolar ions has been developed by numerous authors (Arendt and Kallman, 1925; White, 1951; Gunn, 1954; Murphy et al., 1959; Natanson, 1960; Gentry and Brock 1967; Liu et al., 1967; Gentry, 1972; Parker, 1975); however, all of these theories assume spherical particles with continuum ($Kn \ll 1$) or free-molecule (Kn

Table 1 Typical values of Peclet number for ions *Pe* and field charging factor F_E for atmospheric pressure at 300K in air, where the value of the diffusion coefficient for small (2×10^{-4} μm), medium (2×10^{-3} μm), and large ions (2×10^{-3} μm) used here are 3.3×10^{-1}, 3.2×10^{-3}, and 4.0×10^{-5} (cm²/sec), respectively.

R_p (μm)	Re	Pe for small ions	Pe for medium ions	Pe for large ions	F_E for 1 kV/m	F_E for 10 kV/m	F_E for 10^2 kV/m	F_E for 10^3 kV/m
1	1.5×10^{-5}	7.3×10^{-6}	7.5×10^{-4}	6.0×10^{-2}	3.3×10^{2}	3.3×10^{-1}	3.3	3.3×10
10	1.5×10^{-2}	7.3×10^{-3}	7.5×10^{-1}	6.0×10	3.3×10^{-1}	3.3	3.3×10	3.3×10^{2}
10^2	1.1×10	5.5	5.5×10^{2}	4.5×10^{4}	3.3	3.3×10	3.3×10^{2}	3.3×10^{3}
10^3	1.2×10^{3}	5.8×10^{3}	5.8×10^{5}	4.8×10^{7}	3.3×10	3.3×10^{2}	3.3×10^{3}	3.3×10^{4}

$\gg 1$) conditions, where *Kn* is the Knudsen number ($= \lambda_i/R_p$; λ_i is the mean free path of the ion, and R_p is the particle radius). However, particles in nature can have a wide variety of shapes and sizes and hence a wide range of the ratio of mean free path to characteristic length. Recently, the theory of diffusion charging on aerosol particles of arbitrary shape has been developed by Chang (1981).

A. Charging of Spherical Particles

Based on the diffusion charging model of Chang (1981), particle charging can be expressed as

$$K_0\tau = \frac{4\pi R_p e^2 N_\infty D t}{C_p k T(1+\kappa)} = \frac{1}{1+\kappa}\sum_{m=1}^{\infty}\left\{\frac{\Phi_p^m}{m\cdot m!} + \frac{\kappa\Phi_p^{m+1}}{(m+1)\cdot m!}\right\} + \frac{\kappa\Phi_p}{1+\kappa} \tag{1}$$

where C_p is the capacitance of particles, k is the Boltzmann constant, T is the temperature, κ is $[(2-\alpha)\langle v\rangle Kn/[3\alpha\langle v_\parallel\rangle J]]$ ($\simeq Kn$ for most cases), $\langle v\rangle$ is the ion thermal velocity $(8kT/\pi m)^{1/2}$, $\langle v_\parallel\rangle$ is the average ion velocity parallel to ion flux, α is the sticking probability of the ion in particle surfaces, e is the elemental charge, N_∞ is the ion density far from particles, D is the ion diffusion coefficient, and $K_0 = 4\pi R_p^3 e^2 N/kT(1+\kappa)\epsilon_0$.

For short charging time t, we obtain

$$\Phi_p = K_0\tau \qquad (\Phi_p < 0.1)$$

$$\Phi_p = \frac{2(1+\kappa)}{1+2\kappa}\left[\sqrt{1+\left(\frac{1+2\kappa}{1+\kappa}\right)K_0\tau} - 1\right] \qquad (\Phi_p < 1) \tag{2a}$$

For the free molecule limit ($Kn \to \infty$) and the continuum limit ($Kn \to 0$), Eq. 1 reduces to

$$\Phi_p = \ln\left(1 + \frac{e^2 R_p \langle v \rangle N_\infty}{4\epsilon_0 kT} t\right) \qquad (Kn \to \infty)$$
$$\Phi_p + \sum_{m=2}^{\infty} \frac{\Phi_p^{m+1}}{m \cdot (m+1)!} = \frac{e^2 N_\infty D t}{\epsilon_0 kT} \qquad (Kn \to 0) \tag{2b}$$

respectively, when $C_p = 4\pi\epsilon_0 R_p$ (M.K.S.). Equation 2a for the free molecule case agrees with White (1951) and Liu et al. (1967).

Nondimensional surface potential is shown as a function of characteristic time $K_0\tau$ in Fig. 2 using Eq. 1 for various effective Knudsen numbers κ. Figure 2 shows that Eqs. 2a and 2b are accurate to within 10% for $K_0\tau$ values up to 0.3 and 2.0, respectively. Here $\Phi_p = 0.3$ and 2.0 are equivalent to $N_p = 3.4$ and 35.7 charges on the surface of $R_p = 1$ (μm) particle at 300 (K), where $\Phi_p = 5.56 \times 10^{-6} N_p / R_p$ (cm).

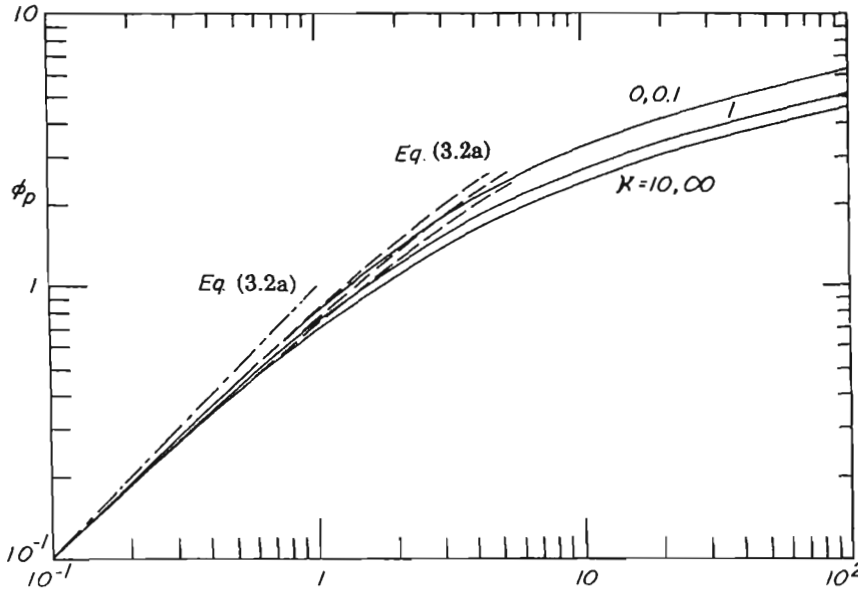


Figure 2 Nondimensional surface potential (or surface charge density) Φ_p as a function of characteristic time $K_0\tau$ for various values of effective Knudsen number.

B. Charging of Arbitrarily Shaped Particles

In the continuum limit ($Kn \to 0$), we obtain (Chang, 1981)

$$K_1\tau = \sum_{m=1}^{\infty} \left\{ \frac{\Phi_p^m}{m \cdot m!} \right\} = \frac{e^2}{kT} \frac{N_\infty Dt}{\epsilon_0} \tag{3}$$

and

$$\begin{aligned} \Phi_p &= \frac{e^2 N_p}{C_p kT} \\ &\simeq K_1\tau \qquad (\Phi_p < 0.1) \\ &\simeq 2[(K_1\tau + 1)^{1/2} - 1] \qquad (\Phi_p < 1) \end{aligned} \tag{4}$$

Equation 3 shows that the number of charges on the aerosol particle surface at any moment can be calculated knowing the capacitance (not the surface area) of aerosol particles in the continuum case.

In the free molecule limit ($Kn \to \infty$) we obtain

$$\begin{aligned} \Phi_p &= \ln(1 + K_2\tau) \\ &\simeq \sqrt{1 + 2K_2\tau} - 1 \qquad (\Phi_p < 1) \\ &\simeq K_2\tau \qquad (\Phi_p < 1.1) \end{aligned} \tag{5}$$

where $K_2\tau = (e^2 N_\infty \langle v \rangle S_p t)/(4kTC_p)$. Equation 4 shows that the number of charges on the aerosol surface at any moment can be calculated knowing the capacitance and surface area of the aerosol particle. However, the effect of capacitance is small as we can see from Eqs. 5.

In the transition region ($0.1 \leq Kn \leq 10$), an exact numerical treatment is required. However, if we may approximate the shape of the aerosol particle by the family of oblate or prolate spheroids (L = major axis/minor axis), the approximate solution can be obtained by modification of the work of Laframboise and Chang (1977) as

$$\begin{aligned} K_3\tau &= \frac{1}{1 + \kappa'} \sum_{m=1}^{\infty} \left\{ \frac{\Phi_p^m}{m \cdot m!} + \frac{\kappa' \Phi_p^{m+1}}{(m+1) \cdot m!} \right\} + \frac{\kappa' \Phi_p}{1 + \kappa'} \\ &= \frac{e^2}{kT} \frac{N_\infty Dt}{(1 + \kappa')\epsilon_0} \qquad \text{(for any } L\text{)} \end{aligned} \tag{6}$$

and

$$\begin{aligned} \kappa' &= \kappa \frac{\cosh^{-1}(1/L)}{\cos^{-1} L} \qquad (L \leq 1) \\ &= \kappa \frac{\cos^{-1}(1/L)}{\ln(L + \sqrt{L^2 - 1})} \qquad (L \geq 1) \end{aligned}$$

For small Φ_p, Eq. 6 reduces to (Chang 1981)

$$\Phi_p = \frac{2[\sqrt{(1+\kappa')^2 + (1+\kappa')(1+2\kappa')K_3\tau} - (1+\kappa')]}{1+2\kappa'} \qquad (\Phi \leq 1)$$

$$= K_3\tau \qquad (\Phi \leq 0.1) \tag{7}$$

where

$$C_p = \frac{4\pi R_p\sqrt{1-L^2}}{\cos^{-1}L} \qquad (L \leq 1)$$

$$= \frac{4\pi R_p\sqrt{1-L^2}}{\ln[L + (L^2-1)^{1/2}]} \qquad (L \geq 1)$$

Equations 4, 5, and 7 show that numerical values for the spherical particle in Fig. 2 can be applied to the arbitrarily shaped particle by replacing K_0 and κ by K_3 and κ', respectively.

The shapes of aerosol particles in nature vary widely. However, it is possible to use a family of oblate or prolate spheroids to approximate the capacitance. For example, a chain of spherical aerosol particles is typical in nature (Fuchs, 1964). The exact solutions of the capacitance for bispheres (Smythe, 1968, p. 138, p. 226) are, for spheres with radii R_a and R_b that intersect orthogonally,

$$C_p = 4\pi\epsilon_0 \frac{(R_a + R_b)\sqrt{R_a^2 + R_b^2 - R_aR_b)}}{\sqrt{R_a^2 + R_b^2}} \tag{8}$$

and for spheres with radii R_a and R_b that are in contact,

$$C_p = \frac{4\pi\epsilon_0 R_aR_b}{R_a + R_b}\left[2C' + \Psi\left(\frac{R_a}{R_a + R_b}\right) + \Psi\left(\frac{R_a}{R_a + R_b}\right)\right] \tag{9}$$

where $C' = 0.5772$ and $\Psi(x) = \Gamma'(z)/\Gamma(z)$.

The case for $R_a = R_b$ is one of the most interesting ones (Megaw and Wiffen, 1963). Equation 9 then becomes

$$C_p = 8\pi\epsilon_0 R_p \ln 2 \approx 5.5\pi R_p\epsilon_0 \tag{10}$$

If we approximate a bisphere of $R_a = R_b = R_p$ by a prolate spheroid of R_p and $L = 2R_p$, we obtain

$$C_p \approx 5.3\pi R_p\epsilon_0 \tag{11}$$

By comparison between Eqs. 10 and 11, it can be seen that differences between the two values are less than 5%.

The other example is wire particles (Cooke et al., 1977). The exact numerical solution of the capacitance of a cylinder is given by Smythe (1968, p. 211) with an error of 0.2% or less in the approximate form of

$$C_p = 4\pi R_p \epsilon_0 (8 + 6.95 L^{0.76}) \tag{12}$$

for $(0 \leq L \leq 8)$.

C. Convection Effect

When the aerosol particle size is larger than 1 μm, gravitational motion becomes more important than random motion. However, the gravitational force balances the drag force, and the particle almost immediately reaches its terminal settling velocity U_g (Fuchs, 1964). In this case, the particle charging equation (Chang, 1981) becomes

$$\Phi_p = \frac{e^2 N_\infty D}{kT\epsilon_0} \left[i_d + i_d^2 \frac{Pe}{8} + i_d^2 (\mathbf{F}\cdot\mathbf{i}) Pe \frac{\ln Pe/2}{16} \right] t \qquad (\Phi_p < 1) \tag{13}$$

where i_d is the nondimensional deposition current for $Pe = 0$, $(\mathbf{F}\cdot\mathbf{i})$ is the dimensionless resistive force, $\mathbf{F}$ is a dimensionless vector equal to the ratio of the resistive force F_0 of the aerosol particle to the Stokes resistive force of a solid sphere of radius R_p, and i is the unit of vector of the rate of flow U_g at infinity. Here we assume that the Reynolds number Re is small enough so that the flow is Stokes flow ($Re \leq 1$), and for small sizes, the Cunningham factor is required ($R_p < 5$ μm). Here, Pe is $2U_g R_p/D_i$ (the Peclet number for ions), and $Re = 2U_g R_p/\nu$, where ν is the kinematic viscosity.

The nondimensional resistive forces $(\mathbf{F}\cdot\mathbf{i})$ for the prolate and oblate spheroid (Happel and Brenner, 1965) are

$$(\mathbf{F}\cdot\mathbf{i}) = \frac{1}{3}\delta_c + \frac{2}{3}\delta_a \tag{14}$$

where

$$\delta_c = \frac{4}{3}(L^2 - 1)\left[\frac{(2L^2 - 1)}{(L^2 - 1)^{1/2}} \ln(L + \sqrt{L^2 - 1}) - L \right]^{-1} \qquad (L \geq 1)$$

$$= \frac{4}{3}(1 - L^2)\left[\frac{(1 - 2L^2)}{(1 - L^2)^{1/2}} \arctan\left(\frac{\sqrt{1 - L^2}}{L^2} \right) + L \right]^{-1} \qquad (L \leq 1)$$

$$\delta_a = \frac{8}{3}(L^2 - 1)\left[\frac{(2L^2 - 3)}{(L^2 - 1)^{1/2}} \ln\left(L + \sqrt{L^2 - 1} \right) - L \right]^{-1} \qquad (L \geq 1)$$

$$= \frac{8}{3}(1 - L^2)\left[\frac{3 - (2L^2)}{(1 - L^2)^{1/2}} \arctan\left(\frac{\sqrt{1 - L^2}}{L^2} \right) - L \right]^{-1} \qquad (L \leq 1)$$

The terminal settling velocity for the prolate and oblate spheroid (Happel and Brenner, 1965) is

$$U_g(\text{spheroid}) = U_g(\text{sphere})L^{1/3}\left[\frac{1}{3}\delta_c + \frac{2}{3}\delta_a\right]^{-1} \tag{15}$$

where the volume of the sphere equals the volume of the spheroid.

For spherical particles, an exact numerical simulation has been conducted by Chang et al. (1978) for wide range of Reynolds and Peclet numbers.

D. Effect of Nonthermal Equilibrium

The surface temperature of dust particles is often not in thermal equilibrium with a surrounding gas when introduced to a hot or cold ionized gas. Therefore a nonuniform temperature field exists about the dust particles. If a temperature gradient exists in space, charged particles will move toward lower temperature locations. This phenomenon is called thermophoresis, and various theories have been proposed (Springer, 1970; Chang, 1986). For a charged aerosol particle, the deposition of the particle can also be controlled by a surface electric potential, since charged particle drift motion, thermophoresis, and natural convection as well as a temperature-dependent charged particle transport coefficient coexist under these conditions. Chang (1991) shows that the particle charging equation under unipolar diffusion charging can be modified simply by replacing Φ_p with $\zeta_p\,(=\Phi_p + \sigma_i)$ in Eqs. 1 through 7, where σ_i is the dimensionless thermophoresis coefficient $(T_p - T_\infty)G/D_\infty$; T_∞ and D_∞ are the temperature and ion diffusion coefficients, respectively, far from the particle surface, and G is the thermophoresis coefficient.

III. FIELD CHARGING

A. Electric Field

In particle charging under an external electric field E, the field charging becomes dominant when the field charging factor F_E becomes much larger than unity (Chang, 1981), where $F_E = eER_p/kT$.

For a pure field charging case with $Kn \to 0$ (Pauthenier and Moreau-Hanot, 1932), the surface charge density becomes

$$N_p = N_s \frac{t}{t + \tau'}$$

$$\tau' = \frac{4\epsilon_0}{eN_i\mu_i} \tag{16}$$

$$N_s = \frac{12\pi\epsilon_0 R_p^2 E\epsilon_s}{\epsilon_s + 2}$$

By solving for the dimensionless surface ion density Φ_p, one can determine the number of elementary charges acquired by the particle.

The theory of unipolar charging of fine particles under an electric field (free molecule limit, $Kn \rightarrow \infty$) has been developed by Brock (1970), Brock and Wu (1973), and Parker (1975); however, all of these theories assume spherical particles at rest conditions. Numerical simulations have been conducted for the unipolar charging of ultrafine aerosol particles under an electric field (Parker, 1975). Numerical simulation of ultrafine particles, which considers particle motion under an electric field, is based on the kinetic theory, since the mean free path of the ion is much longer than the particle radius, and the mobility of the charged ultrafine particles increases with increasing surface charges. Parker (1975) and Chang et al. (1984) used the dimensionless factor $S_i = U_i/(2kT/\pi m_i)^{1/2}$ to analyze the effect of an external field on the particle charging, where $U_i = e\mu_i E$ is the drift velocity of the ion, E is the external electric field, μ_i is the mobility of the ion, and m_i is the mass of the ion.

The effect of an applied electric field on the motion of the ultrafine particles ($R_p < 10^{-2}$ μm) will be an important factor in the charging process, since mobility of charged ultrafine particles increases with increasing surface charge and becomes comparable with the ionic mobility. Here the mobility of the charged aerosol particles is given by

$$\mu_k = \frac{1}{6\pi\mu_g R_p} \frac{N_p^e}{300} \left(1 + \frac{A_0\lambda}{R_p}\right) \quad (\text{cm}^2/\text{V sec}) \tag{17}$$

where μ_g is the viscosity expressed in poise, λ is the mean free path of the gas given in cm, A_0 is the correction factor ($= 1.25 + 0.42 \exp(-0.87 R_p/\lambda)$), and e and R_p are expressed in units e.s.u. and cm, respectively. Therefore U_0 in the charging rate calculation with consideration of charged particle motion is (Chang et al., 1984)

$$U_0 = (\mu_i - \mu_k)E$$

or in nondimensional form

$$S_i = S_{i0}(1 - A_1\Phi) \tag{18}$$

where $S_{i0} = \mu_i E/(2kT/m)^{1/2}$ and $A_i = \mu_i/\mu(N_p = 1)$.

The numerical charging characteristics with and without the aerosol particle's motion for particle radius 10^{-2} μm are shown in Fig. 3 for various values of effective speed ratio S_i for initially uncharged particles, $\Phi_0(t = 0) = 0$. Figure 3 shows that the effect of aerosol particle motion on the charging rate increases with increasing S_{i0} and decreases with particle size, and that the effect of field charging can be neglected when $S_{i0} \leq 0.1$.

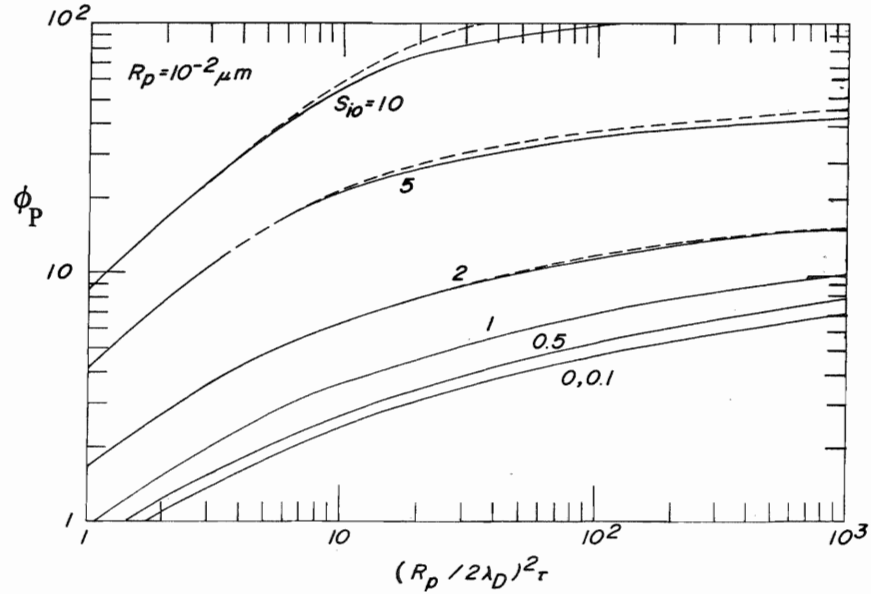


Figure 3 Particle charging characteristics for $R_p = 10^{-2}$ μm aerosol particles at $T_g = 300$K and $\mu_i = 1.4$ cm/Vsec. The dashed line represents the value neglecting the effect of aerosol particle motion, i.e., $S_i = S_{i0}$, where $\tau = t(8kT/\pi m)/R_p$ and $\Phi_p = 1.67 \times 10^{-3}\, N_p/T(K)R_p$ (cm).

B. Magnetic Field

Due to the existence of an external magnetic field, ions near the particle surface are influenced by ion gyromotions, and the charging speed will be reduced. Chang and Ono (1987) and Chang (1992) analyzed particle charging under an external magnetic field and concluded that no significant external magnetic field B exists in particle charging phenomena when the magnetic field charging factor $\beta < 1$ and when $\beta \geq 1$, conditions only exist for electron charging cases where

$$\beta = [\pi kTm/2e^2B^2]^{1/2} \tag{19}$$

REFERENCES

Arendt, P., and H. Kallman (1925). *Z. Phys.*, 35, 421.

Brock, J. R. (1970). *J. Appl. Phys.*, 41, 1940–1944.

Brock, J. R., and M. S. Wu (1973). *J. Colloid Int. Sci.*, 45, 106–114.

Chang, J.-S. (1981). *J. Aerosol Sci.* 12, 19.

Chang, J.-S. (1986). *J. Aerosol Sci.* 17, 423.

Chang, J.-S. (1991). Electrostatics '91. Inst. Phys. Conf. Ser. No. 118, IOP Press, pp. 305–310.

Chang, J.-S. (1992). *J. Aerosol Sci.* 23, S89

Chang, J.-S., and S. Ono (1987). *J. Aerosol Sci.* 18, 765.

Chang, J.-S., K. Kodera, and T. Ogawa (1978). *Proceedings of the Society of Atmospheric Electricity of Japan*, 20, 22.

Chang, J.-S., P. Beckwith, and J. D. Miller (1984). *J. Aerosol Sci.* 15, 270.

Cooke, C. M., R. E. Wootton, and A. H. Cookson (1977). *IEEE Trans. Power Apparatus*, PAS-96, 768.

Fuchs, N. A. (1964). *The Mechanics of Aerosols*. Pergamon Press, Oxford.

Gentry, J. W. (1972). *J. Aerosol Sci.*, 3, 65.

Gentry, J. W., and J. R. Brock (1967). *J. Chem. Phys.* 47, 64.

Gunn, R. (1954). *J. Meteorol.* 11, 339.

Happel, J., and H. Brenner (1965). *Low Reynolds Number Hydrodynamics*, p. 220. Prentice-Hall, New Jersey.

Laframboise, J. G., and J.-S. Chang (1977). *J. Aerosol Sci.* 8, 331.

Liu, B. Y. H., K. T. Whitby, and H. H. S. Yu (1967). *J. Colloid Interface Sci.*, 23, 367.

Megaw, W. J., and R. D. Wiffen (1963). *J. Res. Atmos.*, 1, 113.

Murphy, A. T., F. T. Adler, and G. W. Penney (1959). *AIEE Trans.* 78, 318.

Natanson, G. L. (1960). *Soviet Phys. Tech. Phys.*, 5, 538.

Parker, L. W. (1975). Conference Record of the 68th Air Pollution Control Association, 75-02.2, p. 1.

Pauthenier, M. M., and M. Moreau-Hanot (1932). *J. Phys. Radium* (Paris), 3, 590.

Smythe, W. R. (1968). *Static and Dynamic Electricity*, 3d ed. McGraw-Hill, New York.

Springer, G. S. (1970). *J. Colloid Interface Sci.* 34, 215.

White, H. J. (1951). *AIEE Trans.*, 70, 1186.

This Page Intentionally Left Blank

4

Electrical Phenomena of Dielectric Materials

R. Tobazéon

Centre National de la Recherche Scientifique
Grenoble, France

I. INTRODUCTION

If we exclude metals, all remaining materials are dielectrics, whatever the state of the matter in question (solid, liquid, gas), and a permittivity ϵ can be ascribed to any substance, with vacuum as the reference dielectric.

Dielectrics can be employed either as passive devices (capacitors, cables) or in active devices (electrets, electrostatic motors), and they are required to function in our near or far environment (air, seawater, soil, space). Generally, materials are subjected to a *voltage* (dc, ac, impulse), and, in exceptional cases, to an electromagnetic field produced by, for example, an intense laser beam. The spatiotemporal distribution of the field inside the matter not only is imposed by the geometry of the electrodes (whether to insure a uniform or a nonuniform field) and the shape of the voltage wave but also depends on space charges: charge carriers can be generated or blocked at interfaces or interphases, when different dielectric substances come into contact with each other.

Among environmental constraints, we may consider the actions of pressure, temperature, radiation, chemical attack, etc. *Time* is often a fundamental parameter in the study of dielectrics, e.g.:

A perfect insulator would be a medium through which no conduction current could flow. In fact, the transition from "capacitive" behavior to "resistive" behavior depends on the conduction relaxation time

$\tau_c = \epsilon\rho$ (insofar as a resistivity ρ can be ascribed to the material). Thus a dielectric may behave in a completely different manner under dc, ac, or impulse voltages.

Generally, electrical devices are built to operate over years or decades, which means that they must sustain a voltage without failure despite any possible modifications induced by the combined action of the electric stress and the other constraints (thermal, mechanical, chemical, etc.). It can thus be easily understood that aging of materials is an important subject of research.

The physicist or the engineer tries to employ materials that are as "perfect" as possible. However, imperfections are often present at the molecular or atomic level, and on the macroscopic scale (presence of foreign bodies and voids). The study of dielectrics is characterized by its multidisciplinary nature, since it involves chemistry, electrochemistry, wave theory, fluid mechanics, etc. For a comprehensive and realistic survey of most insulating materials, the reader is referred to the book by Clark (1962).

The aim of this chapter is to describe concisely the various electrical phenomena produced inside materials subjected to an electric field and to give orders of magnitude to the various quantities involved. In Sec. II, we shall present a bird's-eye view of the action of the field on matter. Sec. III considers the "pure" dielectric properties (polarization, relaxation). In Sec. IV, we address conduction and losses in materials (linear or nonlinear effects). Sec. V is dedicated to the most important and most difficult problem, breakdown.

II. EFFECTS OF THE ELECTRIC FIELD ON MATTER

According to the nature of the stressed medium and the amplitude of the field, we can make the following classification of the different effects produced on dielectric materials.

A. Effects Due to Charge Displacement

Effects due to charge displacement result either from the (limited) motion of "linked" charges (polarization phenomena) or from that of "free" charges (conduction phenomena).

1. Linear Phenomena

Linear phenomena take place at "low" fields.

Polarization: electronic polarization is a universal characteristic of dielectrics and is due to the distortion of electron clouds in atoms; ionic

polarization, due to ion displacement, is quite general (it is large in certain solids); dipolar polarization dominates in polar fluids and in certain solids and is due to the rotation of molecules.

Conduction: ionic conduction happens in all liquids and gases and in certain solids; electronic conduction is observed in gases and solids, but only in ultrapure liquids; heterogenous conduction (also called "interfacial polarization" or, rather unfortunately, since there is no space charge, "space charge polarization") results from the association of two (or more) dielectrics of different permittivities and conductivities placed in series.

2. Nonlinear Phenomena

Nonlinear phenomena generally appear for "high" fields.

In polarization, they are usually negligible.

In conduction, they dominate as a general rule; for instance, injection(s) or blocking of charge carriers at the electrode(s), electrohydrodynamic charge transport in fluids (see Chapter 8).

3. Instabilities

Instabilities are most often produced for high field values.

They can lead to breakdown through various mechanisms: electronic (avalanches), thermal (heat generation), mechanical (collapse of soft materials), chemical (degradation).

They can also be limited: partial discharges in voids (in solids), in bubbles (in liquids); oscillations of current (gun mechanism in solids).

B. Coupling Effects

Coupling effects are studied both fundamentally and through their applications mainly to conversion processes.

1. Electrical-Electrical Coupling

The most common example is the capacitor used to store electrostatic energy.

2. Electrical-Thermal Coupling

Pyroelectricity typifies a reversible conversion, whereas electric losses of any kind (dipolar, conduction) cause irreversible dissipation.

3. Electrical-Mechanical Coupling

Reversible conversion takes place in piezoelectric or electrostrictive phenomena, or with electrets, electrostatic motors, or ion drag pump in fluids.

However, turbulence induced in fluids by electrohydrodynamic motion is an irreversible effect.

4. Electrical-Optical Coupling

An electric field induces a birefringence in the medium across which polarized light propagates; the effect is linear (Pockels effect) in some materials and quadratic (Kerr effect) in others; diffusion of ordinary light is another optical effect widely used in liquid crystal displays.

III. POLARIZATION BY AN ELECTRIC FIELD

According to the principle of electroneutrality, any material medium contains in equal quantities—at thermal equilibrium—positive and negative charges, embedded in atoms or molecules. The electric field E produces some displacement of these linked charges (approximately proportional to E); the combined action of these dipoles (in general oriented parallel to the field) produces the polarization of the dielectric. Each elementary dipole, comprising the charges $+q$ and $-q$ separated by a distance l, possesses an electric moment: $\vec{M} = q \cdot \vec{l}$ (directed from $-q$ to $+q$). The sum of these elementary moments is equivalent to a single dipole of moment $\vec{M}$. A simple approach is to define the polarization vector $\vec{\mathbf{P}}$ as the electric moment per unit volume ω: $\vec{\mathbf{P}} = d\vec{M}/d\omega$.

Several mechanisms can produce charge displacement and are causes of polarization. The consequences on the behavior of different kinds of dielectric materials will be outlined in the following sections. For more detailed treatments, the reader is referred to the following books: Anderson, 1964; Böttcher, 1973, 1978; Coelho, 1979; Daniel, 1967; Purcell, 1965.

A. The Mechanisms of Polarization

1. Electronic Polarization

An electric field distorts the electron cloud of any atom with respect to the positive nucleus. The atom acquires an induced dipolar moment $\vec{p} = \alpha_e \vec{E}_i$, where α_e is the electronic polarizability and E_i is the local field to which the atom is subjected. This field is the same as the applied field when dipoles are far from each other (as in gases at low pressure, for instance); otherwise, as will be shown later on, E_i is *higher* than the applied field E because of the polarization of the surroundings. For a given atom or molecule, α_e is a constant even for very high applied fields (MV/cm), but it can vary over two orders of magnitude when comparing different media (Purcell, 1973). For a monoatomic gas, simple models allow the

calculation of α_e (Coelho, 1979): $\alpha_e = 4\pi\epsilon_0 a^3$ for an atom of "radius" a ($a \sim 0.5 \times 10^{-10}$ m for the hydrogen atom). Measured values of α_e are 0.73×10^{-40} C·m²/V for hydrogen and 2.9×10^{-40} C·m²/V for the methane molecule. The moment p is thus very small, and the displacement of charges at high field is generally less than $10^{-2}a$. Indeed, electronic polarization always exists in any material, but the following effects can be superimposed on it.

2. Ionic Polarization

For certain ionic solids, the polarization is created by the displacement of charged atoms. The ionic polarizability α_i varies widely according to the structure of the material, from values comparable to α_e to much higher values, e.g., in ferroelectric materials.

3. Molecular Polarization

Many molecules are disymmetric and possess a permanent dipolar moment. The applied field tends to orient the permanent dipoles in its direction. These polar molecules produce a dipolar polarizability α_d. The electric dipole moments are comparable in many polar media since interatomic distances are close to 10^{-10} m. This moment is expressed in debye units: one debye is equal to 3.33×10^{-30} C·m. The permanent dipole moments are thus several orders of magnitude higher than electronic moments, even those induced by high applied fields.

Remark: We have considered above the motion of linked charges. If the motion of *free* charge carriers is impeded either by traps in the bulk, or on interfaces, or on electrodes, space charges build up. This accumulation of charges behaves like a macroscopic dipole. This mechanism is called space charge (or interfacial) polarization and can be characterized by a space charge polarizability α_s. This subject of relaxing space charges is of major practical importance and will be considered again in Sec. IV.

B. Relation Between Microscopic and Macroscopic Properties

We shall present only a brief outline of how the microscopic parameters relate to those that are experimentally measurable (permittivity, applied field). As a simple model, let us consider the polarization as a vector $\vec{P}$. It is linked to the microscopic parameters N (the number of contributing molecules per unit volume), α (the sum of their polarizabilities) and $\vec{E}_i$ (the local field) by $\vec{P} = N\alpha\vec{E}_i$. We know that the electrical induction $\vec{D}$ is linked to the absolute permittivity $\epsilon = \epsilon_0\epsilon_r$ (ϵ_r: relative permittivity) and to the macroscopic field E by $\vec{D} = \epsilon_0\vec{E} + \vec{P}$. Hence

$$\vec{P} = \epsilon_0(\epsilon_r - 1)\vec{E} = N\alpha\vec{E}_i \qquad (1)$$

Depending on the nature of the dielectric, the calculation of E_i can be quite straightforward or rather complicated. Let us simply point out that the field acting on a dipole sufficiently far from its neighbors is close to the applied field: $E_i = E$; otherwise, the combined action of the other dipoles in the vicinity of the dipole in question would always *increase* the local field: $E_i > E$. A few simple illustrations of these statements are given in the following.

1. Gases

It follows from Eq. 1, since $E_i = E$, that $\epsilon_r = 1 + N\alpha/\epsilon_o$. Thus, ϵ_r is always very close to 1, since both α and N are small ($N = 2.7 \times 10^{25}$ m^{-3} at 0°C and atmospheric pressure).

2. Condensed Nonpolar Phases

The simplest way to calculate E_i is to consider the dipole alone in the center of an empty spherical cavity. On the boundary of the sphere, the charges produced by the oriented dipoles increase the field inside. A classical treatment gives $E_i = E + P/3\epsilon_o$. Then

$$\frac{\epsilon_r - 1}{\epsilon_r + 1} = \frac{N\alpha}{3\epsilon_o}. \tag{2}$$

This relation is valid for nonpolar materials (liquids or solids). Since α is small and $N \sim 10^{28}$ m^{-3}, then $\epsilon_r > 1$ (from 1.5 to 2.2 typically). It applies also to dilute solutions of polar molecules in a nonpolar medium.

3. Other Materials

More refined treatments accounting for the presence of permanent dipoles or specific local interactions are necessary to describe the properties of particular materials, whether liquid (ϵ_r from 3 to 200), solid (ϵ_r over 10,000 for certain ferroelectric materials) or liquid crystals.

4. Influence of Pressure and Temperature

Moderate pressures (up to 10 MPa) have no appreciable effects on the dielectric properties of condensed phases (except piezoelectric solids, as will be seen later on). However, temperature does play an important role, especially in polar materials. The applied field tends to orient the permanent dipoles parallel to its own direction, but this orientation, counteracted by thermal agitation, is only partial. An order of magnitude is easily obtained: a dipole of rather large moment $p_d = 1.6 \times 10^{-29}$ C·m acquires in a field of 100 kV/cm a maximum electric energy of $p_d E_i > 1.6 \times 10^{-22}$ J, whereas at $T = 300$K, $KT \sim 4 \times 10^{-21}$ J. If p_d is unaffected by the field and the temperature and if there is no mutual interaction between

the dipoles, the statistical mean moment $\bar{p}$, using Langevin's calculation, is $\bar{p}/p_d = (\coth x - 1/x) = L(x)$, with $x = p_d E_i/KT$. $L(x)$ is known as the Langevin function. Saturation is approached only for very high field strengths (several MV/cm); for usual fields, $x \ll 1$, $L(x) \sim x/3$, and $\bar{p} \sim p_d^2 E_i/3KT$. The molecular polarizability is then $\alpha_d = p_d^2/3KT$. From Eq. 2 it follows that ϵ_r decreases when T increases. This model has been verified in polar gases and in dilute solutions of polar molecules in nonpolar liquids. For polar liquids, ϵ_r always decreases when T increases (from 80 at 20°C to 56 at 100°C for water). Elaborate models have been established to relate ϵ_r to T in various classes of polar liquids.

It is interesting to note that in Eq. 2, if $N\alpha/3\epsilon_0$ approaches unity, then ϵ_r tends to infinity. This in fact occurs at a critical temperature T_C known as the Curie temperature in ferroelectric materials (which possess spontaneous polarization). This polarization decreases when the temperature is increased, and vanishes at T_C, while ϵ_r goes to a sharp maximum. For $T > T_C$, there is transition to a nonferroelectric phase, and ϵ_r decreases. The most characteristic properties of a ferroelectric are hysteresis of D with E and nonlinearity of the polarization versus the applied field. Ferroelectrics belong to a wider class of materials presenting spontaneous polarization, called pyroelectrics. The prefix *pyro* (from the Greek: fire) indicates that temperature plays a dominant role in their electric properties (for instance, charges appear on each side of an appropriately shaped plate, when heated).

C. Dielectric Response in Variable Fields

1. Relaxation

In the previous sections, α and P were regarded as real quantities resulting from the application of a static (dc) field. If the applied field is a rectangular pulse, a temporal phase shift may occur between the driving field and the resulting polarizability. If the response is linear, the polarizability follows an exponential growth or decay characterized by a relaxation time τ. Indeed, this time is extremely short for α_e, since electrons are quite easily displaced even at optical frequencies ($\tau_e \sim 10^{-16}$–10^{-15} s).

For α_i, the relaxation time is in the range 10^{-15}–10^{-12} s, since ions are less easily displaced. For α_d, τ_d can be as short as 10^{-11} s (for water at room temperature) and as long as 10^{-2} s (for viscous polychlorobiphenyls at −40°C). For space charge polarization, τ_s can reach hours or more. Consequently, the polarization P (and also the electric induction D) will follow the field after a certain delay depending on the nature of the material.

2. Complex Permittivity

A vacuum insulated plane capacitor of capacitance $C_0 = \epsilon_0 S/d$ (S: surface area of the electrodes, d: gap distance) acquires a charge $Q_0 = C_0 V$ on its electrodes, in phase with the applied ac voltage $V = V_m e^{j\omega t}$. The current in the external circuit is a displacement current $I_0 = dQ_0/dt = j\omega C_0 V$, with an advance of $\pi/2$ over V. There are no losses. If a perfectly insulating nonpolar dielectric of permittivity ϵ_r fills the capacitor, its capacitance becomes $C = \epsilon_r C_0$; the charge Q is $\epsilon_r Q_0$ and the current $I = j\omega\epsilon_r C_0 V$. This last is $\pi/2$ ahead of V since, again, there are no losses. However, if the dielectric is not a perfect insulator, a component of the current due to conduction, in phase with V, appears, and this is independent of ω: $I = V/R$ (R is the resistance: $R = \rho d/S$). The resultant current is now $(\pi/2 - \delta)$ ahead of V, δ being the loss angle. Thus $\tan\delta$, the ratio of the conduction current to the displacement current, is simply $\tan\delta = 1/RC\omega$. If the dielectric is a polar material, the orientation of dipoles by the field introduces losses, and therefore a component of current in phase with V. This depends on ω, as does the capacitive component, which decreases from its high static value to a lower value at high frequency (the dipoles no longer being able to keep up with the field reversals). In fact, conduction losses contribute to the in-phase current and can be very high, especially in polar liquids of low viscosity. With a variable frequency bridge, we can measure the real part of the capacitance C' and $\tan\delta$ versus ω, and deduce the imaginary part $C'' = C' \tan\delta$. To the complex capacitance $C^* = C'(\omega) - jC''(\omega)$ corresponds the complex permittivity $\epsilon^* = \epsilon'(\omega) - j\epsilon''(\omega)$.

3. Polar Dielectric with a Single Relaxation Time τ

The dielectric is supposed to be a perfect insulator; ϵ_s is the static permittivity (at very low frequency, or dc); ϵ_∞ is the permittivity at very high frequency. ϵ_∞ lies between 1 and 3, since, at optical frequencies, $\epsilon_r \sim n^2$. This follows from the fact that the refractive index n is the ratio of the velocity of an electromagnetic wave *in vacuo* $1/(\epsilon_0\mu_0)^{1/2}$ to the velocity in the medium $1/(\epsilon\mu)^{1/2}$. In a nonmagnetic material, the magnetic permeability μ is equal to μ_0. It can be shown that $\epsilon^*(\omega) = \epsilon_\infty + (\epsilon_s - \epsilon_\infty)/(1 + j\omega\tau)$, where $\epsilon'(\omega) = \epsilon_\infty + (\epsilon_s - \epsilon_\infty)/(1 + \omega^2\tau^2)$ is the real part of ϵ^* and $\epsilon''(\omega) = (\epsilon_s - \epsilon_\infty)\,\omega\tau/(1 + \omega^2\tau^2)$ is the imaginary part. These are represented in Fig. 1.

A useful representation consists in plotting ϵ'' as a function of ϵ'. If we eliminate $\omega\tau$ from the above expressions, we get $[\epsilon' - (\epsilon_s + \epsilon_\infty)/2]^2 + \epsilon''^2 = [(\epsilon_s - \epsilon_\infty)/2]^2$. This is the equation of a circle. Figure 2 shows the semicircle representing $\epsilon^*(\omega)$. Notice that $\tan\delta$ exhibits a peak: $\tan\delta_m = (\epsilon_s + \epsilon_\infty)/2\sqrt{\epsilon_s\epsilon_\infty}$ when $\omega = \sqrt{\epsilon_s\epsilon_\infty}/\tau$.

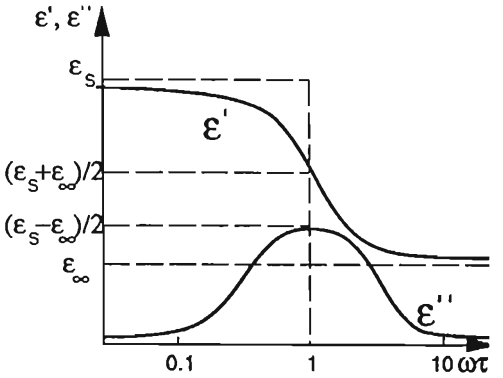


Figure 1 Polar dielectric with a single relaxation time τ.

Such a semicircle is obtained with many pure polar liquids (water, alcohols, nitrobenzene), and τ can vary by several orders of magnitude for liquids of comparable static permittivity (nitrobenzene: $\epsilon_r = 36$, $\tau \sim 10^{-10}$ s; methanol: $\epsilon_r = 33$, $\tau \sim 10^{-6}$ s).

4. Other Materials

Most other materials do not give a semicircle as in the $\epsilon''(\epsilon')$ diagram. Nevertheless, we can separate them into two classes. (1) One class contains those for which $\epsilon''(\omega)$ shows a peak. It is however flattened and broadened. $\epsilon''(\epsilon')$ either approaches a circular arc centered below the ϵ' axis (observed in vulcanized rubber and in polychlorobiphenyl liquids) or is asymmetric, in the form of a half-pear (observed in polychlorobiphe-

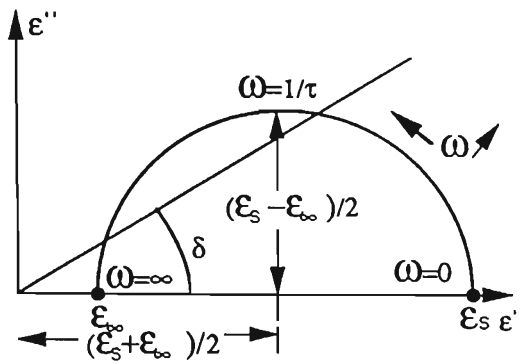


Figure 2 The semicircle representing $\epsilon^*(\omega)$.

nyls). This is usually explained by considering that there is not a single relaxation time, and many distribution functions have been proposed to fit the experimental data. (2) The other class contains those for which there is no marked peak, which is frequently the case for cellulosic materials in electrical engineering.

D. Forces Exerted on Polarized Dielectrics

1. Electrostriction

Solids always have some elasticity and liquids are slightly compressible. The permittivity varies when such deformations take place. This produces an energy variation, and the action of the electric field induces an extra pressure that is linked to the compressibility. This pressure tends to contract the material and is called electrostriction. For nonpolar condensed materials, this excess pressure is comparable to the electrostatic pressure $\epsilon E^2/2$ (~0.1 MPa for $\epsilon_r = 2$ and $E = 1$ MV/cm) and is very weak indeed. On the contrary, the electrostriction of piezoelectric materials is very large and has important applications.

Electrostriction has no "inverse," as far as nonpolar materials are concerned: a mechanical pressure does not induce any dielectric phenomena. In contrast, a compression (or a traction), applied in a specific direction, induces an extra polarization in solid polar materials (a voltage can then be generated). This so-called piezoelectric effect—observed in asymmetrical mineral crystals (quartz, tourmaline) or in semicrystalline polymers (polyvinylidene fluoride: PVDF)—is a reversible one.

2. Dielectrophoresis

This concerns the motion of matter due to the polarization force (*not* the Coulomb force). A demonstrative example, treated in many textbooks, is that of a *plane capacitor* with vertical electrodes, filled with a gas ($\epsilon_r = 1$). If a solid foil or a liquid (of higher permittivity) is allowed to enter the electrode gap, energy considerations show that it will tend to occupy the whole gap.

In a nonuniform electric field, polarization effects may induce vigorous motion of particulate bodies (conducting or insulating), particularly so in fluids. Since a particle is polarized by the field, the separation into positive and negative charges produces a dipole that is subjected to a net force in a divergent field. If its permittivity is higher than that of the host medium, this force tends to pull it toward the region of the higher field (whatever the sign of the field, e.g., even in an ac field). The translation force is given by $\vec{F} = \vec{\mu}_e \cdot \text{grad}\, \vec{E}$, μ_e being the field induced dipolar moment of the particle. This moment can be calculated for objects of particular shape subjected to a field E and is maximum for conducting materials. A classical

result is that for a sphere of radius R in a medium of permittivity ϵ_r, $\mu_c = 4\pi\epsilon_0\epsilon_r R^3 E$. The effect only concerns macroscopic objects and does not apply on a molecular scale. The volumic force density in a homogeneous medium is written $f = -(E^2/2)$ grad ϵ. Thus a thermal gradient will produce a gradient in ϵ. For example, warm liquid of a lower ϵ value will be set in motion toward the low electric field regions.

IV. CONDUCTION CURRENT AND LOSSES IN DIELECTRIC MATERIALS

This section is concerned with the electrical phenomena produced by the motion of *free* charge carriers in dielectric materials. The resulting effects, always dissipative, can be linear or nonlinear (e.g., the conduction current is not proportional to the voltage).

A. Nature, Origin, and Behavior of Charge Carriers

1. Nature

Basically, electrons and ions are the most common charge carriers whatever the nature of the material. In certain solids, holes can also be present. In fluids, aggregates of molecules, inside of which are trapped one or a few elementary charges, are often involved in conduction processes. Excess electrons are observed only in ultrapure liquids, ions being mostly prevalent.

2. Origin

The carriers *may preexist* or they *may appear in the bulk* of the dielectric. The field can displace the thermodynamic equilibrium of generation and recombination of charges. It can also generate excess charge carriers, by enhancing the process of generation.

Carriers can be *generated at the electrodes*: at the cathode, at the anode, or at both. These so-called "injections" (unipolar or ambipolar) are governed by many different mechanisms: for instance, Schottky injection and tunnel injection in solids (O'Dwyer, 1973; Ieda, 1984); electrochemical reactions in polar liquids (Félici, 1971); field emission and field ionization in nonpolar liquids (Halpern and Gomer, 1969; Schmidt, 1984; Denat et al., 1988). Natural radiation or controlled local irradiation (UV, x-rays, etc.) can enhance the charge generation either in the bulk or at the electrodes.

3. Behavior

When subjected to a field E, the charge carriers acquire a drift velocity v. In many materials, and up to very high fields (hundreds of kV/cm), the

ratio $k = v/E$, called the *mobility*, is constant. However, in certain particular cases, the mobility can increase or decrease when the field is increased.

In solids, the mobility of carriers can vary over an extraordinarily wide range: in ordered materials, electron or hole mobility can approach 1 $m^2/V \cdot s$, while in polymers it can be lower by up to twelve orders of magnitude. Ion mobility is lower than electron mobility and varies over a much narrower extent. In liquids, ions are generally solvated, i.e., they attract several neutral molecules and their motion is thus slowed down by the viscosity η of the medium. The relation ηk = constant, known as Walden's rule, is well verified ($k \sim 10^{-8}$ $m^2/V \cdot s$ with $\eta = 10^{-3}$ P), except when specific conduction mechanisms take place (in water, H_+ and OH_- have mobilities around 20 times higher), or in liquid crystals (due to large anisotropic viscosity effects). Electron mobilities are in the range 10^{-7}–10^{-6} $m^2/V \cdot s$ in ultrapure hydrocarbon liquids, and in the range 10^{-2}–1 $m^2/V \cdot s$ in liquefied rare gases. In gases at atmospheric pressure, ion mobility is around 10^{-4} $m^2/V \cdot s$. Since electrons are accelerated by the electric field, we cannot consider an electronic mobility, but we may refer to the electron drift velocity (for typical fields, the apparent mobility is 10^{-1}–1 $m^2/V \cdot s$).

The recombination constant (expressed in m^3/s) between positive and negative carriers present in a gas has been shown by Langevin to reach a maximum value: $K_R = (k_+ + k_-)e/\epsilon$. This has been found to hold for gases, for liquids, and for many solids.

4. Influence of Pressure and Temperature

Pressure p and temperature T play dominant roles for gases, since they are linearly linked to the gas density (via the equation of state of a perfect gas). Charge carrier mobility decreases quasilinearly with an increase in pressure. In fluids, viscosity decreases with an increase in temperature, and then an ionic mobility increase is observed, whereas even a substantial increase in pressure (several tens of bars) has but a negligible effect. For solids, the effect of pressure on mobility is weak in general. The effect of temperature; can be very important, with particularly fast increases in mobility being found in polymers for small increases in temperature.

The diffusion coefficient is linked to the mobility through the relation $D_\pm = k_\pm (KT/e)$, known as the Einstein relation (K: Planck constant; T: absolute temperature; e: electronic charge). At room temperature, the thermal voltage is KT/e = 1/40 volt.

B. Conduction Under Direct Current and Step Voltages

1. Conduction Equations

We shall limit ourselves to the case of plane parallel electrodes with the following assumptions: (1) ϵ is independent of E; (2) only a single type of

carrier of each sign is involved in the conduction process; (3) the dielectric medium is at rest (there is no convective motion, if a fluid is considered); (4) the applied voltage V is much higher than the thermal voltage, and thus diffusion currents can be neglected. The equations are

$$j(t) = (k_+ q_+(x, t) + k_- q_-(x, t))E(x, t) + \epsilon \frac{\partial E(x, t)}{\partial t} \tag{3}$$

$$\frac{dE(x, t)}{dx} = \frac{q_+(x, t) - q_-(x, t)}{\epsilon} \tag{4}$$

$$\int_{x=0}^{x=d} E(x, t)\, dx = V \tag{5}$$

$j(t)$, the current density defined as the ratio of the current I to the surface area of the electrodes, is strictly a function of time t (hence, in the external circuit). The volumic charge densities $q_\pm$ and the electric field are functions both of the distance x and the time t. The gap distance is d. The current-voltage relationships can differ widely according to the mechanisms and location of charge generation, and the steady state (dc) current and the transient current following a voltage step are quite distinctive.

2. Volumic Conduction Due to a Dissociation-Recombination Process

Initially proposed for ionized gases (Thomson and Thomson, 1928), the model may apply to any material. They used the equilibrium reaction between neutral molecules AB (either the molecules of the dielectric itself or those of a dissociable compound) and dissociated charge carriers A^+ and B^-: $AB \rightleftarrows A^+ + B^-$. At thermodynamic equilibrium (with no applied field), the number of generated carriers is equal to the number of those that recombine. If K_D (expressed in s^{-1}) is the kinetic constant of dissociation and ν the number of dissociated carriers per unit volume, this equality is written $K_D \nu = K_R n_+ n_-$, and $n_+ = n_- = \sqrt{K_D \nu / K_R}$.

3. The Steady State Regime

Two distinct situations may be examined.

1. The field is low enough to hardly perturb the thermodynamic equilibrium; Eq. 3 is, with $q_\pm = n_\pm e$,

$$j_0 = (k_+ + k_-)e \sqrt{K_D \nu / K_R} E = \sigma E \tag{6}$$

This is Ohm's law. σ is the characteristic conductivity of the medium. The field is uniform in the bulk ($q_+ = q_-$). In the two layers $\lambda_\pm$, close to the electrodes (see Fig. 3), heterocharges are present, and these increase the field in accordance with Poisson's equation (Eq. 4). Note that

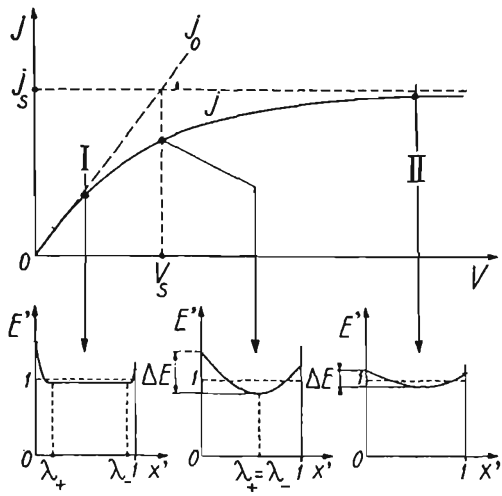


Figure 3 Steady state regime of conduction:ohmic regime (I), and saturation regime (II).

in this Ohmic regime, the conduction relaxation time $\tau = \epsilon\rho$ is much lower than the transit time $t_0 = d/kE = d^2/kV$ (time needed for one carrier of mobility k to cross the gap, since $E \sim V/d$).

In air, a few pairs of ions per cm^3 per sec are typically created by natural radiations, and the calculated resistivity $\rho = 1/\sigma \sim 10^{13}\ \Omega\cdot m$ is in agreement with the measured value.

This is also found to be the case for pure water. The limiting resistivity corresponding solely to the dissociation of water molecules is $2 \times 10^5\ \Omega\cdot m$.

2. The field is high enough so that recombination is weak and can be neglected. All the carriers are readily swept away by the field, and the current reaches a limit (saturation current). Its density is

$$j_s = K_D \nu e d \tag{7}$$

It is reached beyond the saturation voltage: $V_S = \sigma d^2/(k_+ + k_-)\epsilon$ (defined by $j_0 = j_s$).

4. The Transient Behavior

The transient behavior, under a voltage step, is schematically depicted in Fig. 4. If $V < V_s$, the initial current $j_{(t=0)}$ is barely above the steady state value. If $V > V_s$, $j_{(t=0)} = \sigma V/d$ can be much higher than j_s; it decreases to j_s in a time almost equal to the transit time of the slowest carriers.

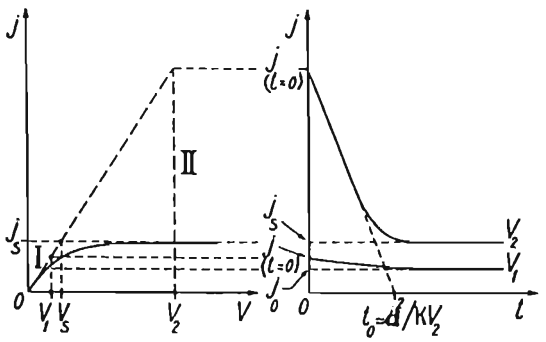


Figure 4 The transient behavior under a voltage step.

The applicability of the Thomson model has been demonstrated in gases and liquids (containing known additives) in both steady and transient states.

5. A Few Remarks on Field-Enhanced Volumic Conduction

Increasing the electric field produces a lowering of the charge separation energy and then an increase in the charge carrier density. This field-enhanced dissociation theory was established for weak electrolytes by Onsager (1934). The dissociation constant is supposed to increase with the field, thus $K_D(E) = K_D(E = 0)\cdot\mathcal{F}(b)$, $\mathcal{F}(b)$ being a function of the field, with $b = e^3E/8\pi\epsilon K^2T^2$. $\mathcal{F}(b)$ can be written $\mathcal{F}(b) = 1 + b + (b^2/3) + (b^3/18) + \cdots$ and at high fields takes the asymptotic form $\mathcal{F}(b) = (2/\pi)^{1/2}(8b)^{-3/4}\exp(8b)^{1/2}$. As an example, for $\epsilon_r = 2$, K_D is doubled for $E \sim 15$ kV/cm.

The ohmic behavior will be modified, since it follows from Eq. 6 that $\sigma(E) = \sigma(E = 0)\cdot[\mathcal{F}(b)]^{1/2}$, whereas from Eq. 7, $j_s(E) = j_s(E = 0)\cdot F(b)$. This has been shown to apply to hydrocarbon liquids containing a single electrolyte. It should also apply to solids in which ionic dissociation takes place.

In solid materials, however, generally only electrons coming from ionizable centers are mobile. The Poole-Frenkel effect refers to a decrease in ionization energy (hence a higher concentration of charge carriers) due to the combined potentials of the ionization center and of the applied field. The increase in conductivity at high fields follows a similar law to that above. This model has undergone many refinements (O'Dwyer, 1973) in order to improve the interpretation of experimental results. Their validity, however, is often restricted to particular materials.

6. Injection of Charge Carriers

Let us suppose that in a perfect insulator ($\sigma = 0$), carriers of the same sign as that of one electrode (located at $x = 0$) are produced at the metal/dielectric interface. If the density of injected charges (of mobility k) is very high ($q_{(x=0)} \to \infty$), then $E_{(x=0)} \sim 0$, and it follows from expressions Eqs. 3 to 5 that the stationary current density is

$$j = \frac{9}{8} \frac{\epsilon k V^2}{d^3} \tag{8}$$

This is the "space charge limited current" (SCLC) law for unipolar injection. The field distribution is now given by $E(x) = \sqrt{2jx/\epsilon k}$. The "strength" of the injection, governed by q_i, is characterized by the nondimensional number $C_i = q_i d^2/\epsilon V$. If $C > 5$, "strong" injection is almost indistinguishable from the SCLC regime. If $C_i < 0.2$ ("weak injection"), the current depends on the injection law. If q_i is a constant (independent of V), at low values of V (high values of C_i), $j \alpha V^2/d^3$, whereas at high values of V (low values of C_i), $j = kq_i V/d$ (e.g., analogous to an ohmic variation). However, if q_i increases with V, the reverse can happen: an ohmic behavior of low V, followed by a regime of sharp increase in current eventually reaching SCLC.

The transient current due to unipolar injection following a voltage step exhibits, according to the value of C, a more or less marked peak (Fig. 5) corresponding to the arrival of the injected carriers on the collecting electrode (Atten and Gosse, 1969).

Since injection can take place at both electrodes, and since bulk and electrode effects are generally combined, experimental studies must be as wide as possible (influence of gap distance, of nonplanar geometry, stationary and transient regimes, etc.), and great care must be taken with the interpretation of results (see also Chapter 8 and references therein).

7. Injection Mechanisms

The mechanisms of charge injection from a metal into a dielectric have received considerable attention. We shall restrict ourselves to discussing some of the more well-documented models. *Schottky injection* is the enhancement of thermoionic emission from a metal cathode due to the lowering of the potential barrier by the field, with the image force correction being taken into account. The injected current I varies as $\exp(E/\epsilon)^{1/2}$. *Field emission* (or Fowler-Nordhein emission) is the tunnelling of electrons from the metal through the potential barrier. At room temperature, this mechanism predicts a much higher current density than Schottky injection, for fields of several hundred kV/cm. Since this model predicts that $I/E^2 \propto \exp(1/E)$, it might appear easy to separate Schottky emission from field

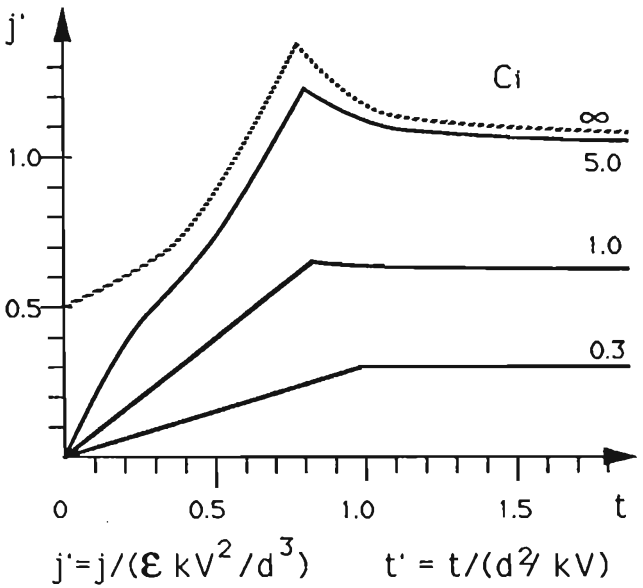


Figure 5 The transient current density due to unipolar injection following a voltage step exhibits a more or less marked peak corresponding to the arrival of the injected carriers on the collecting electrode.

emission. This, in fact, is not often possible. In general, experimental results follow the expected variations qualitatively (with unrealistic barrier heights, for instance), and it can be quite difficult to separate bulk effects from injection effects in solids (O'Dwyer, 1923).

The basic work concerning field-emission in a number of ultrapure liquids and liquefied gases is that of Halpern and Gomer (1969a). It has been recently extended to many other liquids (Denat et al., 1988). Indeed, injection can also take place at the anode: hole injection is possible in solids, and also in certain liquids. In ultrapure liquids, *field ionization* is the process by which the liquid yields electrons to the anode (Halpern and Gomer, 1969b). Field emission and field ionization give rise to high current densities at fields in excess of say 20 MV/cm.

Other mechanisms of charge injection at both electrodes are *electrochemical* in nature. They can take place in solids or liquids, via the intervention of the double layer. In liquids of high permittivity, the "compact" part of the double layer—in which a field on the order of 10^8V/cm is built up between undischarged ions and the metal—facilitates the metal-to-liquid electron exchange. Oxidation of neutral species produces positive

ions at the anode (H_+ in water, for instance), and negative ions are injected at the cathode by reduction (Félici, 1971). In nonpolar liquids, ions are extracted from a charged layer made up of ions coming from the bulk, by a mechanism similar to that used by Onsager (Denat et al., 1982).

8. Multiplication of Charge Carriers

The current-voltage curve for a gas shows that at high field strengths, the current rises rapidly (saturation is no longer observed). This is due to an increase in the number of charge carriers by avalanches (Townsend mechanism). An electron, liberated at (or near) the cathode in a uniform field, acquires energy from the field. When this energy is greater than the ionization energy of the gas molecules, the electron/molecule collision releases a second electron and there are now two electrons that ionize again giving four new electrons, and so on. If α new electrons are created per unit length of path in the field direction, n electrons present at a distance x increase to $n + dn$, where $dn = n\alpha\, dx$ and $n = \exp(\alpha x)$. An electron current I_0 beginning at the cathode will increase as $I = I_0 \exp(\alpha x)$. The first Townsend coefficient α is found to obey a relation, characteristic of each gas, of the form $\alpha/p = A \exp[-B/(E/p)]$, where p is the gas pressure and A and B are constants. The avalanches may develop from one or several initiating electrons, which can be, though not necessarily, produced at the same time. According to the particular conditions of electron production near the cathode, breakdown may or may not ensue (see Sec. V). Since the velocity of electrons is much higher than ionic velocity, the electronic current is followed by an ionic one. Raether (1964) has calculated and measured these currents in different gases in a uniform field. These avalanches are the sites of luminous phenomena. In divergent geometry (point-plane, wire-cylinder), the luminous zone, concentrated near to (or around) the sharp electrode, resembles a "corona." The mechanisms of positive or negative corona are widely different and depend on the nature of the gas. An extensive review of this subject is found in Loeb (1975) and Meek and Craggs (1978).

Multiplication of electrons has also been observed in solids (O' Dwyer, 1973) and very recently in ultrapure liquids and liquefied gases (Denat et al., 1988).

C. Dielectric Losses Under Alternating Fields

Consider a plane capacitor filled with a single or an association of dielectric materials. The permittivity of each material is supposed to be independent of the applied sinusoidal voltage V_e (r.m.s. value) and of the frequency f ($\omega = 2\pi f$), whereas the conduction may possibly depend on them.

1. A Single Dielectric

If the conditions are fulfilled to get ohmic behavior, the material of resistivity ρ will simply behave as a capacitance C in parallel with a resistance R. The amplitude of the conduction current (in phase with the voltage) is V_m/R; that of the displacement current (at $\pi/2$ from the voltage) is $C\omega V_m$, where $V_m = \sqrt{2}\, V_e$. The loss angle between these two components of the total current is such that

$$\tan \delta = \frac{1}{RC\omega} = \frac{1}{\rho\epsilon\omega} \tag{9}$$

The power dissipated by conduction losses is then $P = C\omega V_e^2 \tan \delta$. If we consider the nonlinear conduction due to dissociation/recombination processes, we must compare the transit time of carriers (having the same mobility k) in a uniform ac field ($t_a = (2d^2/k\omega V_m)^{1/2}$) to the half period $T/2 = \pi/\omega$. If $t_a \geq T/2$, the regime remains ohmic. If $t_a \ll T/2$, and if we suppose that the saturation regime is quickly reached, we can evaluate a generalized value of tan δ (ratio of the energy dissipated to the energy stored per cycle) as

$$\tan \delta \propto \frac{K_D \nu d^2}{\epsilon\omega V_m} \tag{10}$$

As for the unipolar injection regime (each electrode is supposed to be an injector during each half wave), if $t_a \ll T/2$, then

$$\tan \delta \propto \frac{kV_m}{\omega d^2} \tag{11}$$

2. Two Dielectrics in Series

The simplest situation is that of two ohmic materials of permittivities ϵ_1, ϵ_2 and resistivities ρ_1, ρ_2. Such a model has been proposed to explain relaxation in heterogeneous materials, e.g., the "response" to an ac voltage of variable frequency. It is also known as the Maxwell-Wagner effect, or interfacial polarization. Very simple arguments allow us to present the main features of the frequency response. Suppose that one of the materials is perfectly insulating and is represented by a pure capacitance C_1 ($R_{1\to\infty}$), whereas the other dielectric is represented by C_2 in parallel with R_2. At very high frequency, the system behaves as capacitances in series. On the Argand plot of the complex capacitance C^*, $C'_\infty = C_1C_2/(C_1 + C_2)$, $C''_\infty = 0$. At very low frequency, only the pure capacitance C_1 is charged, so that $C'_0 = C_1$, $C''_0 = 0$. When the frequency is varied from zero to infinity, C^* is a semicircle centred on the C' axis. The representation is similar to that of Debye relaxation (see Fig. 2), although the mechanisms

are obviously completely different. As a general rule, the study of the variation of the capacitance and of tan δ versus the frequency at low voltage is very useful in characterizing such dielectric associations. If the two dielectrics are not perfectly insulating, C^* follows only the high-frequency part of the semicircle circumference, if the time constants $\tau_1 = R_1 C_1$ and $\tau_2 = R_2 C_2$ are not very different.

More complex situations can result from the different fates of charge carriers at interfaces or in the bulk of the dielectrics. Some examples of nonlinear behavior will be outlined in the following. In a liquid impregnated insulation considered for the sake of simplicity as a liquid and a solid in series, two effects can simultaneously be present, to a greater or lesser extent: ions arriving from the slightly conducting liquid may either be blocked against the solid walls or they may enter the solid through the action of the field. In the former case, named the *barrier effect* or the Garton effect (Garton, 1941), ions swept in from the bulk of the liquid remain stuck on the solid during the greater part of the half wave until reversal of the field. If they cross the liquid gap in a time $t_a \ll T/2$, the losses due to the liquid alone (with some simplifying assumptions) decrease when the voltage applied to the liquid increases according to

$$\tan \delta \propto \frac{\omega^{1/2} d^3}{\epsilon k^{1/2} V_m^{3/2}} \tag{12}$$

Consequently, the losses of the whole insulation decrease. This is currently observed with impregnated cellulosic materials. It must be realized that the blocking effect is not purely a mechanical effect but corresponds to a specific ion/cellulose interaction (acting as a semipermeable material).

In the latter case, the field forces liquid ions to penetrate into the solid; this *field-enhanced absorption effect* (Tobazéon and Gartner, 1975) can produce a drastic reduction in the ionic density in the liquid (and so a considerable decrease in the liquid losses). The ion mobilities in the solid are lower by several orders of magnitude, and the increase in losses in the solid is low, and thus the losses of the whole insulation decrease. The process takes a rather long time (minutes or more) to reach an equilibrium at constant voltage, in contrast with the barrier effect. This effect is mainly observed with impregnated synthetic polymers.

It is also possible, however, that losses may *increase* with the applied voltage. This is typical of "partial discharges" that take place in gaseous cavities accidentally present in solid insulations. When the voltage across each gas cavity exceeds its own "Paschen voltage" (see Sec. V), discharges take place in the gas, which then becomes suddenly conductive. An increase in the applied voltage causes more and more cavities to ignite,

and this lasts a longer time during each period. It can thus be understood that the losses of the whole insulation increase with the voltage.

Finally, it must be mentioned that the brief presentation given above should not give the impression that few other situations can be encountered. For example, dielectric walls can be essentially parallel to the direction of the field, e.g., solid spacers in fluids (or in a vacuum). The mechanisms of conduction along interfaces are governed by electrokinetic phenomena (Hunter, 1981), and the spontaneous presence of excess unipolar charges in these interphase regions may introduce nonlinear losses and can be at the origin of breakdown along spacers. The paper by H. J. Wintle (1990), covering such topics as mathematical and numerical techniques, numerical and analytical results, advances in fundamental understanding of insulators, and new and enhanced experimental techniques, is recommended not only for its content but also for its extensive bibliography.

V. BREAKDOWN OF DIELECTRIC MATERIALS

Electrical breakdown of dielectric media is the ultimate stage of a succession of events that leads to an arc, a luminous channel of high conductivity, passing through the dielectric between conductors once the voltage exceeds a certain value. This *breakdown voltage* depends on the particular situation for which it is measured (geometry, wave form, polarity . . .) and is generally not a characteristic of the dielectric itself. The consequences are more or less catastrophic according to the nature of the material: a fluid can be renewed, whereas a solid (impregnated or not) is locally destroyed and unable to sustain the voltage thereafter. Indeed, breakdown mechanisms are governed by the electric field acting locally rather than on a macroscopic scale. Thus the *breakdown field* (or *rigidity*) of a dielectric material expresses the mean value (processed by statistical analysis) that it is able to sustain under well-specified conditions (generally, between plane electrodes, at a given gap distance, subjected to a certain voltage wave, during a certain lapse of time). The breakdown fields usually observed are always lower by several orders of magnitude than the fields inside atoms or molecules. Although under careful laboratory conditions the impulse strength of thin films can reach 10 MV/cm (10^{-1} V per angström), in industrial practice, working fields are limited (to insure a "life" of several decades to the insulation). Under power frequency, for instance, these values are reduced to a few kV/mm in the windings of power transformers (several cm thickness of oil-impregnated cellulosic materials), but can reach exceptionally high maximum values (100 V/μm or 100

kV/mm) in capacitors using polypropylene films impregnated with new liquid impregnants.

Several features are common to all materials:

Breakdown is localized, the spark or arc being preceded by luminous treelike patterns.

The actual strength depends on the form and the duration of the applied voltage wave, generally being much higher for impulses of short duration.

Scale effects are important: the lower the gap, or the area, or the volume subjected to the field, the higher the strength.

Polarity effects are often very important in divergent fields: the breakdown voltage is generally much lower when the sharp electrode is positive, especially under impulse voltage; this situation, considered the most "dangerous," has been the most widely studied.

The surface state of the electrodes (roughness, presence of oxides, adsorbed layers, etc.) may result in conditioning processes, and contribute to give, especially in uniform fields, a more or less large dispersion in rigidity measurements.

Conducting particles (either isolated or in chains in fluids) can reduce the strength by a tenth or more of the "uncontaminated" value, by locally enhancing the field or by triggering microdischarges when approaching an electrode surface.

Breakdown is facilitated along solid spacers (in fluids or in a vacuum).

A. Gas Breakdown

1. Breakdown in Uniform Fields

In Sec. IV, it was shown how an electron produces an avalanche by impact ionization. One single avalanche does not lead to a breakdown. A subsequent mechanism creating new electrons at the cathode or in the gas is necessary. Then, it can be shown that: $I = I_0\,[\exp(\alpha d)]/(1 - \mu)$, where $\mu = \gamma[\exp(\alpha d) - 1]$ is the number of new electrons capable of producing new avalanches. The coefficient γ (second Townsend coefficient) depends on several mechanisms: e.g., positive ion impact at the cathode (observed preferentially in rare gases); photon-induced electron extraction from the cathode (in common gases); photoionization in the gas. Values of γ depend also on electrode surfaces and on impurities in the gas and often increase with E/p. They lie in the range 10^{-9} to 10^{-1} (the lowest values in hydrocarbon vapors, the highest in rare gases). If $\mu = 1$, the current after a few series of avalanches become constant ("self-sustaining discharge"); if $\mu < 1$, it would decrease to zero, whereas, if $\mu > 1$, it would increase

continuously, resulting in breakdown. This is the Townsend criterion for breakdown:

$$\gamma[\exp(\alpha d) - 1] \sim \gamma \exp(\alpha d) \geq 1 \tag{13}$$

A very important law in practice is Paschen's law, which follows analytically from Eq. 13 and from the functions α/p and γ versus E/p. In a uniform gap either between metallic electrodes or between dielectric surfaces, the breakdown voltage V_p is a function of pd and has a marked minimum (Fig. 6).

The minimum Paschen voltages and the behavior at high pd are widely different in air, in SF_6 (an electronegative gas used in high voltage insulation) and in helium or neon (used in lasers or luminescent light sources). The breakdown voltage of air at atmospheric pressure with $d = 1$ cm is 30 kV (the corresponding field is 30 kV/cm). For SF_6 it is 89 kV (89 kV/cm). However, for the same pressure but at the Paschen minimum on the curve, the breakdown *field* is one order of magnitude higher in each gas. Deviations from Paschen's law have been reported at very high or very low values of p and for small gaps (microns).

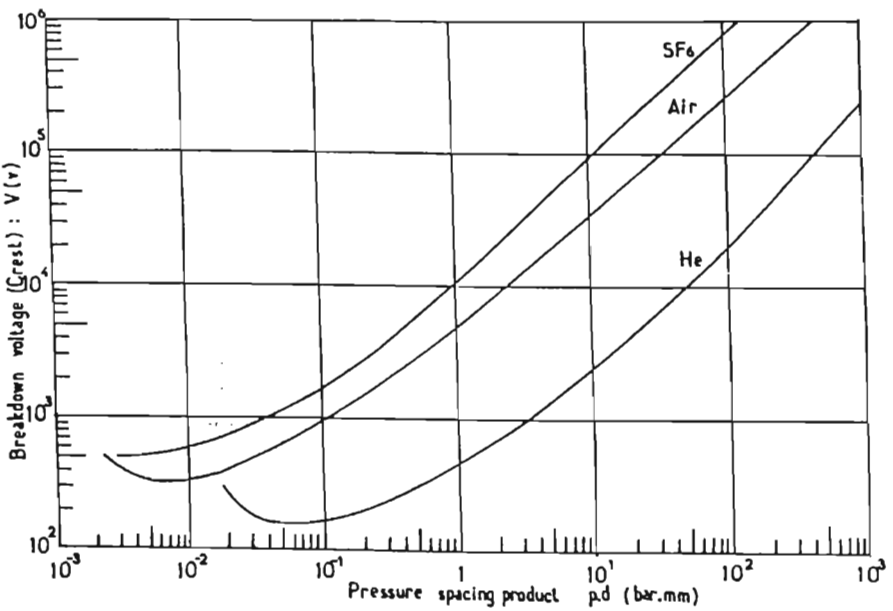


Figure 6 In a uniform gap either between metallic electrodes or between dielectric surfaces, the breakdown voltage V_p is a function of pd and has a marked minimum. (From CIGRE-Working Group 15-03, 1974, 1977.)

There exists a much faster and more localized mechanism of prebreakdown when the space charge at the head of the avalanche transforms it into a *streamer*. A semiempirical criterion for the transition of the streamer mechanism based on the magnitude of the space charge field was proposed by Raether (1964) and by Meek and Craggs (1978):

$$\exp(\alpha d) > 10^8 \quad \text{or} \quad \alpha d > 20 \tag{14}$$

The mechanism is very rapid: the "anode-directed" streamer develops out of the avalanche tip at a velocity $\sim 10^6$ m/s. Further increase in the amplitude of the voltage pulse produces the development of a "cathode directed" streamer, also with a high velocity ($\sim 10^6$ m/s).

2. Breakdown in Nonuniform Fields

The beginning of breakdown takes place at the electrode with the smaller radius of curvature. Due to the field asymmetry, there are major differences with a change in polarity, in both the nature of the breakdown events and in the breakdown voltage values. Streamers originating from the anode or the cathode are luminous filamentary channels of discharges, which propagate partly or fully across the gap (causing breakdown). Streamers may proceed by steps and be followed by leaders in large gaps in air (lightning) or in pressurized SF_6. The extremely great variety of breakdown mechanisms in divergent fields is examined in the book by Meek and Craggs (1978).

It is worth noting that the presence of conducting particles (even of a single particle) in a uniform field can substantially increase the field, particularly at the tips of elongated particles. Such particles can acquire a net charge by contact with the electrodes and move rapidly in the gap. The breakdown voltage can be reduced by a factor of 5 or more.

B. Vacuum Breakdown

If the mean free path of an electron is greater than the distance between the electrodes ($\lambda > 1$ m if $p < 10^{-2}$ Pa), the multiplication of charged carriers by collision cannot occur and then the initiation of breakdown has to be found either in surface effects (metallic or insulating) or in the exchange of micro particles between the electrodes.

1. Prebreakdown

Breakdown is always preceded by prebreakdown currents that can take the form of current pulses due to random bursts of charges. A number of different mechanisms have been put forward to explain the causes of such charge transfer (Meek and Craggs, 1978, Chapter 2): (1) field emission and associated pulse phenomena (for very clean electrodes, in an ultrahigh

vacuum, with a macroscopic cathode field $>10^5$ V/cm); (2) microdischarges, if adsorption on surfaces is likely to occur; (3) microparticle transfer, e.g., extraction from electrode surfaces and movement across the gap of atom clusters, which may occur at any gap spacing. All of these processes can occur simultaneously. The geometrical and physical properties of the electrodes and their surroundings play a considerable role on the performance of a vacuum gap.

2. Breakdown in Uniform Field

Breakdown curves are usually drawn with averaged values, since the breakdown voltage varies with each measurement. The process of reaching relatively constant values for the breakdown is a consequence of electrode surface conditioning. The general form of variation of the breakdown voltage V_B with the spacing d of a uniform field gap is $V_B \propto d^{1/2}$. This variation is followed over a very large range of gap separations; for example, breakdown ($E_B = V_B/d$) is $\sim 10^6$ V/cm for $d \sim 100$ μm; it falls to 10^4 V/cm (or even less) for $d \geq 10$ cm.

3. Breakdown in Nonuniform Fields

The general trends are the same as those for short gaps (<1 cm); the smaller the radius of curvature of the sharp electrode (opposite a plane electrode), the higher the breakdown voltage. This voltage is higher when the sharp electrode is the anode. For larger gaps, this effect is reversed. Such configurations give higher strengths than a uniform field geometry.

4. Vacuum-Solid Insulation Arrangements

There is evidence to indicate that the breakdown is initiated at the junction between the cathode and the insulator. Significant improvement can be achieved in practice by ensuring very close contact between them, and proper choice of shape and properties of the insulator (Birks, 1967, Vol. 7).

C. Liquid Breakdown

In most applications, liquids are used in association with solid insulators. Their main role is to replace air, in order to avoid partial discharges in cavities possibly subjected to voltages above the Paschen threshold. The wide variety of applications of liquid impregnants has led to the use of either natural or synthetic products, polar or nonpolar, of high or low viscosity, etc. Although, for certain applications, liquids offer the advantage of a high permittivity, their breakdown strength is often as low as that of gases under moderate pressure (a few bars). Their conductivity (and the corresponding ac losses) is not negligible (as for gases), and ther-

mal breakdown of the insulation may occur. Compared to gases, breakdown in liquids shows many phenomenological similarities. If there is no doubt that electronic processes are at work, many other specific phenomena take place (thermal, hydrodynamical, mechanical), which have been shown to be at the origin of breakdown (Gallagher, 1975; Sharbaugh et al., 1978). Examples include moisture content, especially in uniform fields when it approaches and exceeds the saturation level (reductions of breakdown voltage by a factor of 3 have been reported); gas extracted from the bulk (dissolved gas), from the electrodes or insulating solids (occluded gas), or gas generated by electrochemical processes, thermal heating, or (as we shall see later) more complicated electronic processes.

1. Prebreakdown Phenomena in Liquids

The statistical study of breakdown time lags in liquids has shown, as in gases, that breakdown takes place after a certain time delay, which includes the following successive steps:

An "initiation phase," which corresponds to the onset and development of a precursor event (or succession of events) capable of giving rise to a following phase

A "propagation phase" of figures identified as luminous and conducting treelike patterns exiting from a highly stressed region (generally called "streamers") and capable of crossing part of all of the gap

An "arcing phase," where the "main stroke" is established, in a very short time 1 ns or less)

This separation into distinct phases is questionable, especially when breakdown takes place within a very short time (ns). Breakdown could then take place via means somewhat different from the so-called streamer mechanism. This term has been used to name the luminous figures preceding the arc in gases, solids, or liquids. In gases, a terminology is well established, and the processes leading to breakdown by the streamer or the leader mechanisms are well documented, whereas, in general, almost any detectable treelike event in a liquid is called a streamer.

In divergent fields, the development of streamers is much less limited before breakdown than in uniform fields, and whatever the liquid, they have the following general characteristics (Tobazéon, 1988): their optical index is different from that of the liquid; their velocity varies over a large range, from lower than acoustic velocities (around 1 km/s), for negative streamers in hydrocarbons (100 m/s) to much higher velocity in halogenated compounds (10–80 km/s) (both polarities); for a given liquid, positive streamers are faster than negative ones; their shapes can be markedly different, but "slow" subsonic figures are bushlike, while "fast" super-

sonic streamers are filamentary. Streamers produce a current composed of either discrete pulses or of a dominant continuous component, and also emit light; current and emitted light signals generally have similar shapes; fast streamers are the seat of energetic processes, a large amount of decomposition products being produced; shock waves are associated with the propagation of streamers; the streamer is arrested if the amplitude or the duration of the voltage is not large enough, and it then decomposes into a string of microbubbles; an increase in the hydrostatic pressure impedes the propagation of slow streamers, the fast form being much less sensitive to pressure.

It has been well established that in point-plane geometry, with a negative point, electron multiplication by avalanches in the *liquid phase* does exist, producing in hydrocarbons a regular current pulse regime under a dc voltage (Denat et al., 1988). Each impulse systematically produces a bubble. The sequence of generation, growth, and collapse of bubbles has been characterized and shown to follow the Rayleigh model (Kattan et al., 1989). The transition to streamer occurs when the voltage is increased: a train of bubbles is produced by successive current pulses, the new growing bubbles being generated ahead of the preceding ones. When the so-called slow bushlike streamer develops, the processes are controlled by discharge in the gas-phase (liquid vapor). The propagation of fast supersonic streamers is more related to ionization in the liquid phase at the tip of the branches of the channel(s), since they are loaded with highly excited and ionized species, reminiscent of "leaders" in gases.

2. Breakdown

This is controlled either by initiation or by propagation of streamers. The lengths streamers travel before stopping as a function of voltage can be widely different according to the nature of the liquid, the polarity, the shape of the voltage wave. Thus not only the velocity of streamers but also their ability to propagate are the factors controlling breakdown.

Under impulse waves, breakdown voltage is usually lower (or much lower) at large gaps for a positive point, which exemplifies the "danger" of easily propagated streamers. Slow negative streamers cannot propagate very far, so the negative lightning impulse breakdown values are high. In uniform fields, the conditions necessary for the streamer to reach the other electrode are generally fulfilled, and breakdown is controlled by initiation either in the bulk of the liquid or at the electrodes. Exceptionally high values (several MV/cm) are attainable for small sphere gaps (tens of microns) and short pulses (microseconds), whereas with large plane gaps it is reduced by around two orders of magnitude. We do not yet possess the quantity of data that we do for gases: there is still no classification of

liquids (there is for gases) according to their density and to their electronic affinity.

Under ac voltage, streamer appearance is randomly distributed in time, the mean appearance frequencies increasing with the applied voltage. In point-plane geometry, both the field divergence and the gap distance control the breakdown voltage. At large gaps (a few cm or tens of cm), since positive streamers are more easily propagated, breakdown takes place when the point is positive at very low mean fields (tens of kV/cm). Such very low values of rigidity have also been reported in transformer oil, with large plane gaps. Any positive streamer generated by a protrusion or a sharp particle is easily propagated and can produce breakdown. Under dc voltages, similar trends to those found under impulse or ac have been reported. However, space charge can significantly modify the actual field on sharp electrodes. The study of high field dc conduction has highlighted many of the basic processes implied in prebreakdown phenomena, as shown in Sec. IV.

D. Solid Breakdown

Failure of solid dielectrics generally results from cumulative effects, producing a gradual formation of one or several conducting channels, in the material, such as discharges in the ambient medium, discharges the dielectric itself, chemical and electrochemical degradation, and thermal runaway. Apart from these extrinsic types of breakdown, there are more intrinsic mechanisms, genuinely characteristic of certain materials, that we shall now consider.

1. Purely Electric Breakdown

Breakdown is considered as a continuation of the conduction processes; thus there are bulk-limited theories, electrode-limited theories, and combinations of the two. For the former theories, an "intrinsic critical field strength" is reached when some instability occurs in the electronic conduction current. Several models have been proposed (Frölich high energy criterion, von Hippel low energy criterion, for instance) which differ by considering different mechanisms of energy transfer from the conduction electrons to the lattice.

Theories of "avalanche breakdown" are basically extensions to solids of the avalanche model for gases: the avalanche arises by field emission from the valence to the conduction band (Zener model), or by collision-ionization. Space charge enhanced critical field theories are developments of the collision-ionization theories. In the book by O'Dwyer (1973), a detailed review of these mechanisms will be found, as well as experimental data on alkali halides, glass, and quartz.

2. Thermal Breakdown

Dielectric losses (either by conduction or by relaxation) produce heat dissipation in a lossy material. If heat is not extracted fast enough by conduction and/or convection, the material temperature rises. Severe damage may occur: chemical decomposition, melting of a solid, boiling of liquid. According to the thermal and electrical properties of the material and its surroundings, breakdown can happen either at very short times ($<10^{-3}$ s) or after a rather long period of voltage application (hours). Breakdown voltage is lower for ac than for dc and decreases when the ac frequency is increased. If Joule heating and thermal conduction are the only processes considered, there exists a critical field strength E_m for which the temperature of the material approaches some critical temperature T_m. For $E > E_m$, the temperature reaches T_m in a fixed time and increases thereafter. Various situations have to be considered: dc, ac, impulse voltages; thin or thick samples; field-independent or field-dependent conductivity; electrode configurations, etc. (O'Dwyer, 1973; Coelho, 1979). It is important to note that a maximum thermal *voltage* is obtained for the frequently encountered situation where one electrode is thermally insulated, the other being maintained at a constant temperature. For thick samples of thermal conductivity Λ, under an ac voltage of frequency f, the maximum thermal voltage varies as $V_m \propto \sqrt{\Lambda/\epsilon f}$. For many low-loss solid insulators, V_m exceeds 1 MV at power frequency, though this voltage is rarely reached. In contrast, thermal breakdown is likely to occur at high frequency; for example, for polyethylene, $V_m \sim 50$ kV at 1 MHz. Indeed, an increase in temperature favors thermal breakdown since, in general, the electrical conductivity increases while the thermal conductivity decreases. Nonuniformity of the electric field may be an important factor in the production of hot spots.

3. Electromechanical Breakdown

The Young's modulus Y of soft materials (especially polymers) decreases when the temperature is raised. The electrostatic pressure causes a compression of the dielectric of initial thickness d_0. If d is the strained thickness, we get $\epsilon V^2/2d^2 = Y \ln(d_0/d)$. Failure occurs due to mechanical collapse at an (apparent) critical field: $E_c = V_c/d_0 = 0.61\sqrt{Y/\epsilon}$. This model, proposed by Stark and Garton, has been shown to apply successfully to many polymers (O'Dwyer, 1973).

4. Partial Discharge Induced Breakdown

This is one of the most frequent causes of failure in high voltage ac insulators. It is always difficult to avoid the presence of gaseous cavities. For plane-shaped cavities, the field in the gas E_G will be higher than in the

solid (or liquid) of relative permittivity ϵ_r: $E_G = \epsilon_r E$ (E being the mean field applied to the insulation). When the voltage V_G across each cavity exceeds its Paschen voltage, which depends on its thickness d and the gas pressure p inside it (Fig. 6), discharges are produced in the gas. Charges are deposited on the cavity walls that tend to reduce (or cancel) the field in the gas. The physics of these partial discharges has recently been investigated in detail (Devins, 1984). Depending on the thickness of the cavity, the overvoltage, and the nature of the gas, Townsend discharges or streamerlike discharges may occur. The dissipated power density can be high, and since it is concentrated on localized areas of the walls, detrimental effects are likely to occur. In addition to the chemical action of aggressive substances (such as ozone) resulting from gas ionization, physical effects favoring the initiation of breakdown take place. In organic products particularly, carbonization occurs, and from some punctured area(s), thin conducting channels (at the tip(s) of which the field is enhanced) propagate until breakdown occurs. In many failures, the final arc may have been preceded by the development of branched hollow channels, resembling trees: this is *electrical treeing*. Trees may be caused by other phenomena, essentially by the field enhanced penetration of water (or other particular substances): *water treeing* and *electrochemical treeing*. An impressive amount of work has been devoted to this subject during the two last decades. It has mainly concerned the dielectric materials used for nonimpregnated power cables (particularly polyethylene). A comprehensive presentation of discharge measurements and their interpretation will be found in the books by Kreuger (1964) and Bartnikas and McMahon (1979).

As a closing remark, new liquid impregnants used for high-voltage impregnated power capacitors possess excellent "gassing" properties. This changes the way a trapped gaseous cavity or one created within a liquid will expand or shrink when subjected to discharges. The collapse of the cavity leads to the extinction of discharges and to an increase of the life of the insulation.

REFERENCES

Anderson, J. C. (1964). *Dielectrics*. Chapman and Hall.

Atten, P., and J. P. Gosse (1969). Transient of one-carrier injections in polar liquids. *J. Chem. Physics*, 51, 2804.

Bartnikas, R., and E. I. McMahon (1979). *Engineering Dielectrics. Vol. 1, Corona Measurement and Interpretation*. American Society for Testing and Materials.

Birks, J. B. (1959–1967). *Progress in dielectrics*. 7 vols. Heywood.

Böttcher, C. J. F. (1973, 1978). *Theory of Electric Polarization*. 2 vols. Elsevier.

CIGRE-Working Group 15-03 (1974, 1977). Breakdown of gases in uniform electric fields. *Electra*. 32, 43; 52, 67.

Clark, F. M. (1962). *Insulating Materials for Design and Engineering Practice*. John Wiley.

Coelho, R. (1979). *Physics of Dielectrics for the Engineer*. Elsevier.

Daniel, V. V. (1967) *Dielectric Relaxation*. Academic Press.

Denat, A., B. Gosse, and J. P. Gosse (1982). High field DC and AC conduction of electrolyte solutions in hydrocarbons. *J. Electrostatics*. 11, 179.

Denat, A., J. P. Gosse, and B. Gosse (1988). Electrical conduction of purified cyclohexane in divergent electric field. *IEEE Trans. Electr. Insul.*, 23, 545.

Devins, J. C. (1984). The physics of partial discharges in solid dielectrics. *IEEE Trans. Electr. Insul.*, EI-19, 475.

Félici, N. J. (1971). Conduction in liquid dielectrics. A survey of recent progress. *Direct Current*, 90.

Gallagher, T. H. (1975). *Simple Dielectric Liquids*. Oxford University Press.

Garton, C. G. (1941). Dielectric loss in thin film of insulating liquids. *Proc. Instn. Electr. Engrs.*, 88, 103.

Haidara, M., and A. Denat (1991). Electron multiplication in liquid cyclohexane and propane. *IEEE Trans. Electr. Insul.*, 26, 592.

Halpern, B., and R. Gomer (1969a). Field emission in liquids. *J. Chem. Phys.*, 51, 1031.

Halpern, B., and R. Gomer (1969b). Field ionization in liquids. *J. Chem. Phys.* 51, 1048.

Hunter, R. J. (1981). *Zeta Potential in Colloid Science*. Academic Press.

Ieda, M. (1984). Electrical conduction and carrier traps in polymeric materials. *IEEE Trans. Electr. Insul.*, EI-19, 162.

Kattan, R., A. Denat and O. Lesaint (1989). Generation, growth and collapse of vapor bubbles in hydrocarbon liquids under a high divergent electric field. *J. Appl. Phys.*, 23, 457.

Kreuger, F. H. (1964). *Discharge Detection in High Voltage Equipment*. Heywood.

Loeb, L. B. (1965). *Electrical Coronas*. University of California Press, Berkeley.

Meek, J. M., and J. D. Craggs (1978). *Electrical Breakdown of Gases*. John Wiley.

O'Dwyer, J. J. (1973). *The Theory of Electrical Conduction and Breakdown in Solid Dielectrics*. Clarendon Press.

Onsager, L. (1934). Deviations from Ohm's law in weak electrolytes, *J. Chem. Phys.*, 126, 599.

Purcell, E. M. (1965). *Electricity and Magnetism*. Berkeley Physics Course, Vol. 2. Educational Development Center.

Raether, H. (1964). *Electron Avalanche and Breakdown in Gases*. Butterworths.

Schmidt, W. F. (1984). Electronic conduction processes in dielectric liquids. *IEEE Trans. Electr. Insul.*, EI-19, 389.

Sharbaugh, A. H. J. C. Devins, and S. J. Rzad (1978). Progress in the field of electric breakdown in dielectric liquids. *IEEE Trans. Electr. Insul.*, 13, 242.

Tobazéon, R. (1988). Streamers in liquids. In *The Liquid State and its Electrical Properties*. Plenum Press.

Tobazéon, R., and E. Gartner (1975). The effect of solid polymeric materials on the ionic conductivity of liquids under high electric stress. *Proceedings of the 5th. Intern. Conf. on Conduction and Breakdown of Dielectric Liquids, Delft, The Netherlands*, pp. 32–35.

Thomson, J. J., and G. P. Thomson (1928). *Conduction of Electricity Through Gases*. Cambridge University Press.

Wintle, H. J. (1990). Basic physics of insulators. *IEEE Trans. Electr. Insul.*, 25, 27.

5

Flow Electrification of Liquids

G. Touchard

Centre Nationale de la Recherche Scientifique
Poitiers, France

I. INTRODUCTION

When a dielectric liquid flows through a pipe from one vessel to another, the potential difference that appears in the collecting vessel is due to the accumulation of charges. These charges result from the convection of a part of the electrical double layer existing in the tube at the contact between the liquid and the inner wall (Boumans, 1957; Klinkenberg, 1967; Gavis, 1964; Gibbings, 1970). Indeed, at the liquid/solid interface, the electrochemical reaction induces an electrical double layer composed of two layers in the liquid: the compact layer very close to the wall (unaffected by the flow), and a diffuse layer that can be convected (Touchard et al., 1985). Then the space charge density Q convected in a pipe by a flow is given by the ratio of the charge convected to the flow rate $Q = \int_s \rho \bar{u} ds / \int_s \bar{u} ds$, where s is the section of the pipe, ρ the space charge density, and $\bar{u}$ the mean axial velocity. To compute this quantity, we need to know the velocity profile and the space charge density profile, which is a function of three parameters: the electrochemical reaction at the interface, the diffuse layer thickness, and the characteristic of the flow. To analyze the phenomenon, first it is important to know the space charge density profile for a diffuse layer at rest in the pipe (without flow), and then we must understand how it is affected by the flow (Touchard, 1978).

II. FUNDAMENTAL EQUATIONS OF A DIFFUSE LAYER AT REST

The phenomenon is controlled by the diffusion and the migration and can be expressed by five fundamental equations (Touchard and Romat, 1981): two equations of current densities, two conservation equations, and the Poisson equation for the potential.

But for a steady state, an infinite length, a cylindrical pipe, and appropriate reference quantities, the five previous equations may be reduced to two nondimensional equations (Touchard, 1978):

$$\frac{d\rho_+}{dr_+} + (\rho_+^2 + \alpha^4)^{1/2} \frac{d\psi_+}{dr_+} = 0 \tag{1}$$

$$\frac{1}{r_+} \frac{d}{dr_+} \left(r_+ \frac{d\psi_+}{dr_+} \right) = -\rho_+ \tag{2}$$

where ρ_+ is the nondimensional space charge density, ψ_+ the nondimensional potential, and $\alpha = 2(D_P D_N)^{1/2}/(D_P + D_N)$, D_P and D_N being the cation and the anion diffusion coefficients. In practice, α is very close to 1, and $\alpha = 1$ is a good approximation.

Then these equations can be solved for different cross-section configurations of the pipe. The nondimensional space charge density is a function of the nondimensional space charge density on the wall ρ_{w+} (which translates the intensity of the electrochemical reaction at the interface) and the geometry of the pipe compared to the diffuse layer thickness. For an example, in the case of circular pipe and for $\rho_{w+} \ll 1$, we have $\rho = \rho_w(I_0 r/\delta_0)/(I_0(R/\delta_0))$, where I_0 is the modified Bessel function of zero order, δ_0 the diffuse layer thickness, and R the radius of the pipe.

III. SPACE CHARGE DENSITY CONVECTED BY A FLOW IN A CIRCULAR PIPE

A. Laminar Flow

For a laminar flow and for a very long pipe, the diffuse layer at the exit of the pipe is fully developed, so the space charge density profile is the same as the one for a diffuse layer at rest. For example, with the same conditions as previously, the space charge density convected Q_1 is given by

$$Q_1 = 8\rho_w \frac{\delta_0^2}{R^2} \left[1 - \frac{2\delta_0 I_1(R/\delta_0)}{R I_0(R/\delta_0)} \right] \tag{3}$$

where I_1 is the Bessel modified function of first order.

B. Turbulent Flow

In the case of a turbulent flow, two different modelizations have already been performed. They both supposed that the space charge density on the inner wall ρ_w remains the same as the one for a laminar flow. One is based on the competition between the fluctuant radial velocity and the diffuse layer relaxation velocity (Touchard, 1978), the other one on the eddy diffusivity (Marcano et al., 1987). For the same example mentioned above, $Q_t = 2\rho_w(\delta_0/R)(I_1(R/\delta_0))/(I_0(R/\delta_0))$.

IV. EXPERIMENTAL APPARATUS

Different equipments can be considered to investigate the flow electrification, which depends on the kind of liquids used (hydrocarbons, liquefied gas, etc.) (Touchard, 1978; Marcano et al., 1987), but some general precautions must be taken in order to keep the liquid in the same state of purity (Touchard et al., 1985). If they are not taken then it will be very difficult to settle precisely the influence of one parameter, because the whole phenomenon can be radically different with only some ppm of impurities added to the liquid. Nevertheless, in industrial installations, where such conditions are impossible, the value of the current taken on an insulated part of the pipe gives an idea of the intensity of the phenomenon (Touchard et al., 1988).

V. DETERMINATION OF THE ELECTRICAL QUANTITIES IN A DIFFUSE LAYER

The conductivity, the ion diffusion constant, and the space charge density on the wall are needed to analyze the flow electrification. The first two quantities can be obtained by experiments in a conductivity cell. The third one is computed from the experimental value of the space charge density convected in a long pipe and for a very low laminar Reynolds number (Touchard and Romat, 1981).

VI. GENERAL RESULTS ON FLOW ELECTRIFICATION

The analysis of both theoretical and experimental results enables us to express some general predictions concerning the evolution of the space charge density convected in terms of different parameters.

A. In Terms of the Reynolds Number

For a laminar flow and for a very long pipe, the space charge density convected is constant in terms of the Reynolds number, as could be pre-

dicted by the theory. Nevertheless, if the pipe is not long enough, it decreases with the mean velocity or the Reynolds number. Then, at the transition, it increases and reaches a new level in turbulent flow two or three times greater than in laminar. Last, for a turbulent flow, it is in many cases nearly constant again in terms of the Reynolds number (Touchard and Dumargne, 1983).

B. In Terms of the Radius of the Pipe

For very small pipe radii (smaller than the diffuse layer thickness), it is nearly constant with the radius; then for large diameters it decreases proportionally to $1/R^2$ (Touchard and Romat, 1981).

C. In Terms of the Length

For lengths smaller than one hundred times the diameter, it is nearly proportional to the length; then it reaches an asymptotic value for very long pipes, in which the diffuse layer is fully developed at the exit (Gibbings, 1970; Touchard and Romat, 1982).

D. In Terms of the Temperature

As the conductivity and the viscosity of the liquid as the electrochemical reactions on the wall are all functions of the temperature, the space charge density convected is also affected by this parameter. When the temperature increases, the rate of reaction increases; thus the charge convected tends to increase, but the resistivity of the liquid decreases as the diffuse layer thickness, which reduces the charge convected. Thus the space charge density passes normally through a maximum when the temperature is increasing. In fact, very often we just observe an increasing of the charge convected (Touchard et al., 1985).

E. In Terms of the Concentration of Additives

If the concentration of additives increases, then the conductivity and the space charge density on the wall increase. But these two parameters act in opposite direction, so the space charge density convected generally passes through a maximum, which is very often observed (Klinkenberg, 1967; Benyamina et al., 1987).

F. In Terms of the Roughness of the Pipe

The charge convected in a rough pipe is smaller than in a smooth pipe for a laminar flow (Touchard et al., 1989) but greater for a turbulent flow

(Gavis, 1964). This phenomenon can be explain by the development of eddies close to the roughness in the case of laminar flows in a rough pipe.

REFERENCES

Benyamina, M., S. Watanabe, G. Touchard, and H. Romat (1987). Étude des courants d'écoulement dans un tube rugueux en régime laminaire. *Revue de Physique Appliquée*, 22, 1071–1074.

Boumans, A. A. (1957). Streaming currents in turbulent flows and metal capillaries. *Physica*, 23, 1007–1055.

Gavis, J. (1964). Transport of electric charge in low dielectric constant fluids. *Chem. Eng. Sci.*, 19, 237.

Gibbings, J. C. (1970). Electrostatic charging in the laminar flow in pipes of varying length. *J. Electroanal. Chem.*, 25, 497–504.

Klinkenberg, A. (1967). On the electric streaming current. *Electrochim. Acta.*, 12, 104–105.

Marcano, L., G. Touchard, and M. F. Morin (1987). Charges électrostatiques convectées par des écoulements hautement turbulents. *Revue de Physique Appliquée*, 22, 1081–1085.

Touchard, G. (1978). Streaming currents developed in laminar and turbulent flows through a pipe. *J. Electrostatics*, 5, 463–476.

Touchard, G., and P. Dumargue (1983). Streaming current in stainless steel and nickel pipes for heptane and hexane flows. *J. Electrostatics*, 14, 209–223.

Touchard, G., and H. Romat (1981). Electrostatic charges convected by flow of dielectric liquid through pipes of different lengths and different radii. *J. Electrostatics*, 10, 275–281.

Touchard, G., and H. Romat (1982). Mechanism of charge formation in double layer appearing at a hydrocarbon liquid-metal interface. *J. Electrostatics*, 12, 377–382.

Touchard, G., J. Borzeix, and S. Saunière (1985). Electrisation des fluides en mouvement dans des conduites. *R. G. E.*, 7/8, 592–602.

Touchard, G., P. Humeau, L. Marcano, Z. H. Wu, J. Borzeix, J. P. Nossent, and S. Watanabe (1988). Static electrification due to liquefied natural gas flows. *Modern Electrostatics, I. A. P. (A Pergamon-CNPIEC Joint Venture)*, 400–403.

Touchard, G., M. Benyamina, J. Borzeix, and H. Romat (1989). Static electrification by laminar flows through artificially roughed pipes. *IEEE-IAS*, 25–6, 1067–1072.

This Page Intentionally Left Blank

6

Numerical Techniques for Electrostatics

R. Godard

Royal Military College of Canada
Kingston, Ontario, Canada

I. INTRODUCTION

A mathematical model is always an approximation to real physical problems. We can distinguish from a mathematical point of view two different kinds of problems that are of interest to electrostatics.

The first one is a time dependent problem or a problem of evolution as a function of time from time t_0. An example of the Cauchy problem is particle kinetics:

$$u'' = f(t, u, u') \qquad u(t_0) = \alpha \qquad u'(t_0) = \beta$$

where u is the dependent variable. This is also called the initial value problem. The generalization in several dimensions would be parabolic equations.

The second kind of problem is a problem of equilibrium. It is also called the boundary value problem. An example of the Dirichlet problem is the computation of electric potentials and particle charging:

$$u'' = f(x, u, u') \qquad u(x_0) = \alpha \qquad u(x_1) = \beta$$

and we seek a solution $\alpha < x < \beta$. The problem is time independent. When generalizing in several dimensions, the mathematical problem is

$$\mathcal{L}(u) = f(u) \quad \text{in} \quad D \qquad B_i(u) = g_i \quad \text{on} \quad C$$

where C is the border of the domain D. $\mathcal{L}$ is an operator applied to the dependent variable u(x, y, z). This operator may be linear or nonlinear. The subscript i may indicate different types of boundary conditions.

The mathematical model is translated into a numerical code that should follow the best algorithm. An algorithm is defined with respect to its robustness, its speed, its flexibility, and its portability, while the program must be readable, user-friendly, and divided into small subroutines. We shall describe only a few basic ideas and basic algorithms with some emphasis toward modern algorithms.

When possible, it is recommended not to write all of the programs but rather to use library programs. They may belong to the IMSL library or the NAG library or to some more specialized library such as the French library MODULEF on finite elements.

In this chapter, we examine in Sec. II the numerical solution of the initial value problem and also the problem of stiff differential equations. In Sec. III, we examine the problem of equilibrium and we introduce the concept of finite differencing and finite elements. In Sec. V, we comment on some basic algorithms for parabolic equations and the stability of the algorithms. In Sec. V, we consider the elliptic problem.

II. THE INITIAL VALUE PROBLEM

The initial value problem for a system of ordinary differential equations, in vector form, is

$$\underline{u}' = \underline{f}(x, \underline{u}) \qquad a \leq x \leq b \qquad \underline{u}(a) = \underline{A} \tag{1}$$

where $\underline{f}$ is a continuous function for $a \leq x \leq b$ and all $\underline{u}$. Equation 1 may have more than one solution, and it is generally assumed that $\underline{f}$ satisfies a Lipschitz condition, i.e., that all the first partial derivatives of $\underline{f}$ are bounded by a constant L.

$$\left|\frac{\partial f_i}{\partial u_i}(x, \underline{u})\right| \leq L \qquad \forall x \epsilon [a, b] \qquad \text{and} \qquad \underline{u} \tag{2}$$

Any differential equation of order $n > 1$ can be transformed into a system of first-order equations. A numerical code will find an approximate solution V_n at step x_n. If $h_n = h$ is the step size, then we seek a solution at the next step $x_{n+1} = x_n + h_n$. The local error is $u_n - V_n$, and indeed the code should control this local error at each step size.

A. The Runge-Kutta Method

The fourth-order Runge-Kutta method (denoted RK4) is based on the Taylor expansion about the current point x_n. Starting at (x_0, u_0), four

function evaluations per step generate the approximation (a_n, V_n),

$$V_{n+1} = V_n + \frac{h}{6}(f_1 + 2f_2 + 2f_3 + f_4)$$

where

$$f_1 = f(x_n, V_n)$$

$$f_2 = f\left(x_n + \frac{h}{2}, V_n + \frac{h}{2} f_1\right)$$

$$f_3 = f\left(x_n + \frac{h}{2}, V_n + \frac{h}{2} f_2\right)$$

$$f_4 = f(x_n + h, V_n + hf_3)$$

The local error is in $O(h^4)$. The control of the local error E_n is the critical step in the algorithm, which has to adapt itself to the rate of variation of the function. Gustafson (1991) analyzed the error control strategies. The step is accepted if $E_n(h)$ is less than a given tolerance. Classical Runge-Kutta codes may be found in the IMSL Library.

Two advantages of the RK method are low storage and good stability. It can treat linear and nonlinear problems as well. Also, RK methods do not use previously computed solution values. Such methods are called *explicit methods*. For special classes of problems, they become unstable.

B. Stiff Problems

Consider the generalized linear constant coefficient system of equations

$$\underline{u}' = A\underline{u} + \underline{\Phi}(x) \qquad \underline{u}, \underline{\Phi} \in \mathbb{R}^n$$

where A is an $n \times n$ matrix. The eigenvalues of the matrix A are λ_i, $i = 1, 2, \ldots, n$. Assume that the eigenvalues are distinct. The differential system is *stiff* (Lambert, 1980) if

(i) $R_e(\lambda_i) < 0 \qquad i = 1,2, \ldots, n$

(ii) $$\frac{\underset{i=1,\,n}{Max} \mid R_e(\lambda_i)\mid}{\underset{i=1,\,n}{Min} \mid R_e(\lambda_i)\mid} = S \gg 1$$

S is called the stiffness ratio. This situation arises if the solution of the differential system has a fast transient and a slow transient. Explicit algorithms have the tendency to become unstable, if it is necessary to utilize an implicit scheme such as the implicit Euler method or the more sophisticated implicit Runge-Kutta (Brenan, 1986).

III. THE BOUNDARY VALUE PROBLEM

Boundary value problems are more complicated than initial value problems. They can be transferred to initial value problems by shooting methods (Fox, 1980). We shall consider here only the finite difference method and the finite element method.

A. The Finite Difference Method

Finite difference approximations are based on the use of the Taylor series:

$$f(x + \Delta x) = f(x) + \Delta x f'(x) + \frac{\Delta x^2}{2!} f''(x) + \cdots \tag{3}$$

The forward and backward approximations to the derivative $f'(x)$ are, respectively

$$f'(x)_+ \simeq \frac{f(x + \Delta x) - f(x)}{\Delta x} \qquad f'(x)_- \simeq \frac{f(x) - f(x - \Delta x)}{\Delta x} \tag{4}$$

The central approximation comes from averaging Eqs. 4, thus obtaining

$$f'(x) \simeq \frac{f(x + \Delta x) - f(x - \Delta x)}{2\Delta x} \tag{5}$$

By using Eq. 5, a central approximation to the second derivative can be obtained, i.e.,

$$f''(x) \simeq \frac{f(x + \Delta x) - 2f(x) + f(x - \Delta x)}{\Delta x^2} \tag{6}$$

when the derivatives are approximated by finite differencing; i.e., by truncating the Taylor series, we introduce a truncating error. This truncation error is local, in the neighborhood of the current point x. If $f \epsilon C^4[a, b]$, the truncation error is $-\Delta x^2/6f^{(3)}(C)$ for Eq. 5. The error is $-\Delta x^2/12f^{(4)}(C')$ for Eq. 4. It is the step size $\Delta x = h$ that controls the local error.

For the solution of the linear second-order boundary value problem,

$$u'' = p(x)u' \; q(x)u + r(x) \qquad u \leq x \leq b \qquad u(a) = \alpha, \; u(b) = \beta \tag{7}$$

The finite difference approximations are used to approximate both u' and u'' (Burden and Faires, 1985, p. 533). We divide the interval $[a, b]$ into $N + 1$ subintervals with $\Delta x = h = (b - a)/(N + 1)$. The numerical grid corresponds to the nodes $x_i = a + ih$, $i = 0, \ldots, N + 1$, and the approximate solution v is computed at each node. Equation 7 becomes the finite difference equation

$$\frac{v(x_{i+1}) - 2v(x_i) + v(x_{i-1})}{h^2} \simeq p(x_i)\frac{[v(x_{i+1}) - v(x_{i-1})]}{2h} + q(x_i)\,v(x_i) + r(x_i) \quad (8)$$

If the resulting system of equations is expressed in matrix form, taking into account the boundary conditions, we obtain *a tridiagonal system of equations that requires small storage*. If $q(x) \geq 0$, the main diagonal is dominant. The system is positive definite and the solution is unique provided that $h < 2/Max|p(x_i)|$, $i = 1, \ldots, N$ (Burden and Faires, 1985, p. 535). The accuracy of the solution is controlled by the step size h and the local truncation errors. The program must be run at least twice, say with a step h_1, and a step $h_2 = h_1/2$. In the Richardson extrapolation technique, we combine the numerical solutions v_1 and v_2 to obtain more accurate results, so that $v = (4v_2 - v_1)/3$, and the truncation error becomes $O(h^4)$.

Indeed, Eq. 7 represents a linear differential equation. If the differential equation is nonlinear, the concept of finite differencing can still be applied except that an iterative process is required for the solution (Burden and Faires, 1985, p. 539).

Another problem requiring some mathematical attention is the treatment of infinite intervals, which often occur in electrostatics. A condition on the electric potential like

$$u(x) \to 0 \qquad \text{as} \quad x \to \infty$$

may be approximated by a finite boundary at a distance sufficiently large. In some cases, a change of variable such as $t = 1/x$ is recommended. Finally, a uniform numerical grid is not always the best way to solve problems that have locally strong rates of variations.

B. Finite Element Methods

The self-adjoint differential equation

$$-\frac{d}{dx}\left(p(x)\frac{du}{dx}\right) + q(x)\,u = f(x) \qquad q(x) \geq 0,\ p(x) > 0, \quad (9)$$

for $0 \leq x \leq 1$

with boundary conditions $u(0) = u(1) = 0$, belongs to an important class of differential equations. The differential equation can be transformed into a minimization of the integral (Burden and Faires, 1985, p. 547)

$$I(u) = \int_0^1 \{p(x)[u'(x)]^2 + q(x)\,[u(x)]^2 - 2f(x)\,u(x)\}\,dx \quad (10)$$

Let us consider $u_n = \sum_{i=1}^{n} C_i \phi_i(x)$ as an approximation to the solution $u(x)$; the functions ϕ_i are linearly independent and constitute a basis. An example of a piecewise linear function ϕ_i is the "chapeau function"

$$\phi_i(x) = \begin{cases} (x - x_{i-1})/h_{i-1} & x_{i-1} \leq x \leq x_i \\ (x_{i+1} - x)/h_i & x_i \leq x \leq x_{i+1} \\ 0 & \text{elsewhere} \end{cases}$$

We now have to find the constants C_i of the combination of the basis functions ϕ_i. Therefore the integral of Eq. (10) is a function of C_1, C_2, . . . , C_n. The values of the coefficients C_i that minimize the integral are given by

$$\frac{\partial I}{\partial C_j} = 0 \qquad \text{for each } j = 1, 2, \ldots, n \tag{11}$$

The following algorithm sets up a tridiagonal linear system. To the contrary of the finite difference technique, where we minimize the local errors, in the Rayleigh-Ritz Method, the method just described, we try to minimize the global error over the interval $[a, b]$.

The main deficiency of the Ritz method is that it is applicable only to self-adjoint differential equations. The Galerkin method is free of this constraint. Let us consider

$$Lu = f \qquad \text{with} \qquad v_n = \sum_{i=1}^{n} C_i \phi_i(x) \tag{12}$$

For the determination of the coefficients C_{ij} we then orthogonalize the residual $(Lv_n - f)$ with respect to all the functions $\phi_j(x), j = 1, \ldots, n$.

IV. THE INITIAL BOUNDARY VALUE PROBLEM: PARABOLIC EQUATIONS

Let us consider the linear diffusion equation

$$\frac{\partial u}{\partial t} = D \frac{\partial^2 u}{\partial x^2} \qquad a < x < b, \; t > 0 \tag{13}$$

subject to the conditions

$$u(0, t) = 0 \qquad u(l, t) = 0 \qquad t > 0 \tag{14}$$

$$u(x, 0) = f(x) \qquad 0 \leq x \leq l \tag{15}$$

Equations 14 constitute the boundary conditions. Equation 15 is an initial condition. D is a diffusion constant. A parabolic equation may be consid-

ered as a stiff problem. The classical way to solve Eq. 13 is by finite differencing in space and time. Standard implicit methods to solve Eq. 13 require the solution of large systems of algebraic equations (Hundsdorfer, 1992). The classical numerical implicit scheme is the Crank-Nicholson representation

$$\frac{D}{2}\left[\frac{v_{j+1,\,k+1} - 2v_{j+1,\,k} + v_{j+1,\,k-1}}{\Delta x^2} + \frac{v_{j,\,k+1} - 2v_{j,k} + v_{j,\,k-1}}{\Delta x^2}\right] = \frac{v_{j+1,\,k} - v_{j,\,k}}{\Delta t} = \frac{v_{j+1,\,k} - v_{j,\,k}}{\Delta t} \tag{16}$$

The left side of the equation is an average of central difference expressions for $\partial^2 u/\partial x^2$ at the points $(j + 1, k)$ and (j, k). The right side is the central approximation of $\partial u/\partial t$ but at a virtual point $(j + 1/2, k)$. The advantage of the Crank-Nicholson method is a relatively small truncation error, and it is unconditionally stable.

A method that has achieved some popularity is the box method developed by Keller. Equation 13 can be written as a system of coupled first-order equations:

$$\psi = \frac{\partial u}{\partial x} \qquad \frac{\partial u}{\partial t} = D\frac{\partial \psi}{\partial x} \tag{17}$$

To discretize these equations, Keller integrates Eq. 5 over a box. It is possible to build algorithms that are almost as efficient as the Crank-Nicholson method. Finally, we can use Galerkin's finite element procedures for the solution of parabolic problems (Dawson and Dupont, 1992). It is recommended to use specialized libraries such as MODULEF for finite element routines.

V. THE ELLIPTIC PROBLEM: THE GENERALIZED BOUNDARY VALUE PROBLEM

Boundary value problems generally model steady-state (time independent) phenomena. Classical examples are the steady-state diffusion-convection equation

$$\nabla^T(D\nabla u) - \nabla^T(uV) + f = 0 \qquad \text{on } D \tag{18}$$

where D is the domain, $u = u(x, y, z)$ is the dependent variable, and $V = V(x, y, z)$ is the velocity.

Another example is the Poisson equation $\nabla^2 u + \rho/\epsilon_0 = 0$. To these equations, we have to associate the appropriate boundary conditions, which may be

(i) The Dirichlet condition: u is specified at the border C of the domain D
(ii) The Newman condition: the normal derivative $\partial u/\partial n$ is specified at the border C
(iii) Mixed conditions: $u + \alpha\, \partial u/\partial n = 0$ is specified on C
(iv) Periodic boundary conditions

In this section, we shall consider only the diffusion problem with no convection.

A. The Finite Difference Method

Consider the two-dimensional linear Poisson equation in a domain D, with boundary C

$$\frac{\partial^2 u}{\partial x^2} + \frac{\partial^2 u}{\partial y^2} = f(x, y) \qquad \text{for } (x, y) \text{ in } D \tag{19}$$

with the Dirichlet boundary condition

$$u(x, y) = g(x, y) \qquad \text{for } (x, y) \text{ on } C \tag{20}$$

A rectangular grid on the region D is set up so that every interior point (i, j) has four neighbors. If the domain is irregular, a special treatment has to be done at the border C.

Approximating Eq. 19 at each interior point by finite difference, we obtain for the approximate solution v_{ij} to $u(x_i, y_i)$:

$$\frac{V_{i+1,j} - 2V_{ij} + V_{i-1,j}}{\Delta x^2} + \frac{V_{ij,j+1} - 2V_{ij} + V_{i,j-1}}{\Delta y^2} = f_{ij} \tag{21}$$

where $f_{ij} = f(x_i, y_i)$; at each boundary point $v_{ij} = g(x_i, y_i)$. After eliminating from Eq. 21 the boundary points, we obtain a sparse system of linear equations where the V_{ij} are the unknowns. This is the generalization of the two point boundary value problem. This system of equations $A\vec{V} = \vec{b}$ can be solved by iterative or direct methods.

1. Iterative Methods

In all iterative methods, we need a guess field, a starting point, and the convergence is independent of the value of this guess field. We transfer

all the nondiagonal elements of $A\underline{V} = \underline{b}$ to the right side, thereby considering that the only unknown at row i is

$$V_i = \frac{b_i - \sum_{\substack{j=1 \\ j \neq i}}^{n} a_{ij} V_j}{a_{ii}} \qquad a_{ii} \neq 0 \tag{22}$$

By a process of updating the current solution, the system of equations converge toward an approximate solution. The advantage of the iterative techniques is small storage and the possibility to treat nonlinear equations while the techniques are easy to code. The main consideration is the rate of convergence. A more powerful version of the classical Gauss-Seidel method of Eq. 22 is the successive overrelaxation method (SOR method), which is an extrapolation method for a system that is already convergent. If k is an index of iteration, we obtain

$$V_i^{(k+1)} = V_i^{(k)} + \omega(\tilde{V}_i^{(k+1)} - V_i^{(k)}) \tag{23}$$

Here ω is called the overrelaxation factor, and for a convergence consideration, $1 \leq \omega < 2$. $\tilde{V}^{(k+1)}$ is the Gauss-Seidel approximation to the $(k + 1)$ iteration. More information about the overrelaxation factor ω can be found in Forsythe and Wasov (1960).

Perhaps just as important is the case of higher nonlinear systems of equations, which have the tendency to diverge. Then $\omega < 1$ has the property of damping the solution.

2. Direct and Semidirect Methods

In elliptic problems, the matrix A of $A\vec{V} = \vec{b}$ is a structured and sparse matrix. An algorithm for block tridiagonal systems can be found in Golub and Van Loan (1983). Finally, a system of linear equations can be transformed into a minimization problem, and a combination of both direct and iterative techniques seems to be the right direction toward robust and fast numerical algorithms.

B. Finite Element Methods

Herein we lack the space to describe in detail the finite element methods. One clear disadvantage of the finite difference method is the treatment of irregular boundaries. If the domain is complex, the finite element method is more flexible. Sewell's (1988) book is a good introduction to finite element methods. We recommend the French finite element library called MODULEF. This library is distributed by INRIA, Rocquencount, France.

VI. CONCLUSIONS

In this brief presentation, we have tried to classify the principal numerical problems that may occur in electrostatics. We have distinguished the linear problem and the nonlinear problems, which are more computer time consuming. The main difficulty is in the choice of stable algorithms and the control of errors. The difficulty in finite element methods is the generation of the grid, and the tendency is to introduce multigrids or windows of importance in the regions where the rate of variation of the function is particularly important. Finally, we omitted discussion of the more complex diffusion-convection process, which has a tendency to destabilize the numerical solution, and which requires a special treatment; and also the particle collection with turbulent gas flow. Finally, the book written by Birdsall and Langdon (1981) links problems of electrostatics and plasma physics.

REFERENCES

Birdsall, C. K., and A. B. Langdon (1985). *Plasma Physics via Computer Simulation*. McGraw-Hill, New York.

Brenan, K. E. (1986). *The Numerical Solution of Higher Index Differential, Algebraic Equations by Implicit Runge-Kutta Methods*. Lawrence Livermore National Laboratories, UCLA, Report UCRL, 95905.

Burden, R. L., and J. D. Faires (1985). *Numerical Analysis*. Prindle, Weber and Schmidt, Boston.

Dawson, C. N., and T. Dupont (1992). Explicit/implicit conservative galerkin domain decomposition procedures for parabolic equations. *Mathematics of Computation*, 1, 21–34.

Forsythe, G. E., and W. R. Wasow (1960). *Finite Difference Methods for Partial Differential Equations*. John Wiley, New York.

Fox, L. (1980). Numerical methods for boundary value problems in computed techniques for ordinary differential equations (I. Gladwell and D. K. Sayers, eds.). Academic Press, New York, pp. 175–216.

Golub, G. H., and C. F. Van Loan (1983). *Matrix Computations*. Johns Hopkins University Press, Baltimore.

Gustafson, K. (1991). Control theoretic techniques for stepsize selection in explicit Runge-Kutta methods. *ACM Transactions on Mathematical Software*, 4, 533–554.

Hundsdorfer, W. (1992). Unconditional convergence of some Crank-Nicholson LOD methods for initial-boundary value problems. *Mathematics of Computation*, 1, 35–53.

Lambert, J. D. (1980). Stiffness in computational techniques for ordinary differential equations (I. Gladwell and D. K. Sayers, eds.). Academic Press, New York, pp. 19–46.

7

Dimensionless Ratios in Electrohydrodynamics

Joseph M. Crowley

Electrostatic Applications
Morgan Hill, California

I. INTRODUCTION

Electrohydrodynamics is often carried out by persons trained in either electrostatics or fluid mechanics, but rarely both. As a result, it is often difficult to foresee how the electrical and mechanical effects will interact in the laboratory. One useful approach to this problem is the comparison of the various forces that arise naturally in electrohydrodynamics. By sorting and comparing these quantities, it is usually possible to predict the overall results of an experiment by using "back of the envelope" calculations. In many cases, the systematic study of dimensionless ratios can also expose the possibility of new interactions not considered in the initial planning.

In this chapter, the principal electrical and mechanical forces are compared, and dimensionless ratios that characterize the relation are formulated. These ratios are then used to explain several experiments taken from the literature.

II. ELECTRIC PRESSURE

In any discussion of fluid mechanics, the most important aspect is the forces or pressures that are exerted on the fluid. In electrohydrodynamics, these forces are ultimately generated by Coulomb interactions between

charges, which can either attract or repel each other. These forces are communicated to the surrounding fluid by the reaction between the charged entities (ions, electrons, particles, etc.) and the fluid. Inside a fluid, the charges move in response to electric forces, dragging the fluid with them. At fluid surfaces, the charges are held in check by the balance between the electric force and the surface forces. In any event, the central idea in electrohydrodynamics is the transfer of force from charges to fluids.

The electrical forces can be expressed in a number of ways that are all equally valid but that involve different physical variables. In electrohydrodynamics, the most convenient variable is the electric field strength E. This is preferred over charge density, voltage, or other possibilities because we observe that the magnitude of the electric field in practical applications is usually confined to a relatively small range, regardless of the size scale. Normally, the electric field is on the order of 0.1 to 50 MV/m. The upper limit is set by the occurrence of electrical breakdown, while the lower gives forces too small to be useful.

The electrostatic force on a fluid can be expressed in terms of electric field strength by using the stress tensor (Crowley, 1986), but for most experimental work it is possible to estimate the magnitude of this force by using a scalar quantity called the electric pressure, which has a magnitude on the order of

$$p_e \approx \epsilon E^2 \tag{1}$$

(Since we are only concerned with estimates of effects, we dispense with the customary factor of 1/2.) The first factor in the pressure is the permittivity of the material, which is proportional to its dielectric constant. The second factor is the electric field strength. These two parameters are all that is needed to estimate the pressures that an electric field can exert on a fluid.

The permittivity can be written as

$$\epsilon = \kappa\epsilon_0 \tag{2}$$

where ϵ_0 is the permittivity of free space. This constant depends on the choice of units and is needed to reconcile the electrical and mechanical units. In the SI system, its value is

$$\epsilon_0 \approx 8.854 \times 10^{-12} \quad \text{farads/m} \tag{3}$$

All other materials are referred to free space through the dielectric constant κ. Gases have dielectric constants close to unity. Most liquids lie in the range from 2 to 80, increasing with conductivity.

We normally try to make the electric field as large as possible, to enhance the desired effect. Practically, the field is limited either by the ability of the power supply to furnish current (for conductive liquids) or by the occurrence of electrical breakdown (for insulating fluids). Breakdown usually occurs when the field is in the range

$$1 \text{ MV/m} < E_{bk} < 20 \text{ MV/m} \tag{4}$$

The field can be higher for very small gaps ($\ll$100 μm) and for some insulators, but the range given here is usually appropriate for EHD.

Since both the dielectric constant and the electric field are limited in practice, there will clearly be a practical limit on the electric pressure available to work on the fluid. In macroscopic air gaps, for example, the breakdown field is approximate 3 MV/m, so the electric pressure is on the order of

$$p_e \sim \kappa\epsilon_0 E^2 = (1)(8.854 \times 10^{-12})(3 \times 10^6)^2 = 79.7 \text{ Pa} \tag{5}$$

This pressure is equivalent to that exerted by 8 mm of water. Since this is the highest pressure to be expected in air, the opportunities for electrically driven motion under normal conditions are clearly limited. If the air gaps are very small, however, the breakdown field can be much higher, due to the Paschen effect. Fields as high as 50 MV/m are commonly reached when the gaps are smaller than 5 μm, and worthwhile improvements are evident below 100 μm.

The situation is somewhat better in liquids. Dielectric constants are typically higher, and so are the breakdown fields. In a typical oil, for example, the dielectric constant might be on the order of 3 and the breakdown field as high as 20 MV/m. For this fluid, the electric pressure is on the order of

$$p_e \sim \kappa\epsilon_0 E^2 = (3)(8.854 \times 10^{-12})(20 \times 10^6)^2 = 10.6 \text{ kPa} \tag{6}$$

This is a substantial pressure, on the order of 0.1 atmosphere, and allows a wider range of applications.

Electrohydrodynamic motion is only practical when these limited pressures will be adequate for the intended motion. There are a variety of fluid mechanical situations of interest, however, depending on the mechanical nature of the fluid and its velocity. In addition, various fluids will have different electrical properties that influence the effect. To avoid a confusing mélange of results, the experimenter should have an approximate idea of the expected interaction between the field and the fluid. The simplest way to gain this perspective is to consider the relative magnitude of the effects by using dimensionless ratios.

III. ELECTROHYDROSTATICS

The simplest fluid situations are those with no motion. Normally gravity and surface tension will be the only forces opposing the electric pressure. Often, only one of these will be important, so the experimental design can be simplified by knowing which fluid force dominates. This can be determined by comparing the ratio of pressures generated by surface tension and gravity.

Surface tension generates a pressure difference only when an interface between two fluids is curved. This is commonly the case with jets and drops, but of less importance for large masses of fluids. The surface tension pressure is on the order of

$$p_c \approx \frac{T}{R} \tag{7}$$

where T is the surface tension coefficient and R is the radius of curvature of the surface. For most common liquids,

$$15 \quad \text{mN/m} < T < 80 \quad \text{mN/m} \tag{8}$$

Thus the surface tension pressure on a size scale of 1 mm is approximately

$$p_c \approx \frac{0.050}{0.001} = 50 \quad \text{Pa} \tag{9}$$

This pressure level is well below the limits on electric pressures, indicating that EHD effects can be more significant than surface tension.

The gravity pressure is given approximately by

$$p_g \approx \gamma g L \tag{10}$$

where γ is the mass density, g is the gravitational constant, and L is a typical height. For example, a column of water 10 mm high exerts a pressure of

$$p_g = (1000)(9.8)(0.01) = 98 \quad \text{Pa} \tag{11}$$

Again, this pressure is one that can be matched by electrostatic forces.

The relative importance of gravity and surface tension is expressed by the ratio of the two pressures, called the gravity-capillary number (or the Bond number):

$$N_{gc} = \frac{\gamma g h}{T/R} = \frac{\gamma g L^2}{T} \tag{12}$$

where the typical length L is used for both the height and the curvature of the liquid. When the two pressures are comparable, the gravity-capillary

number will be on the order of unity. This will occur when the surface deformation has a characteristic length given by

$$L \approx \sqrt{\frac{T}{\gamma g}} \tag{13}$$

For a typical liquid, with $\gamma = 1$ Mg/m^3 and $T = 50$ mN/m, the length is on the order of

$$L \approx \sqrt{\frac{(0.05)}{(1000)(9.8)}} = 2.26 \quad \text{mm} \tag{14}$$

For larger sizes, gravity dominates, while for much smaller sizes only surface tension will play a significant role in static situations. Of course, if there is no free interface, surface tension will always be negligible.

A. Gravity Dominated Electrohydrostatics

Now that the nature of the fluid force has been determined, the experimenter can turn to the effect of the electric pressure. The relative magnitude of this effect is expressed by the ratio of the electric to mechanical pressures. For the case where gravity is more important than surface tension, this ratio is given by the electrogravity number,

$$N_{eg} = \frac{\epsilon E^2}{\gamma g L} \tag{15}$$

In addition to indicating the relative importance of the electric forces, this number can also serve to estimate the expected results. If gravity and electric forces are the only two effects present, the electrogravity number will normally be on the order of unity, and the expected change in liquid height can be estimated as

$$L \approx \frac{\epsilon E^2}{\gamma g} \tag{16}$$

As an example of using this relation to estimate the result expected in a particular experiment, consider one of the earlier examples of electrohydrostatic experimentation (Stuetzer, 1959). His apparatus consisted of a container for the liquid, with two electrodes, as sketched schematically in Fig. 1. When a voltage is applied to the needle electrode, the liquid rises in the manometer tube on the right. On the basis of the dimensionless number discussed above, we expect to see pressures in the liquids limited to approximately 10 kPa (1 m of water) and those in the air limited to

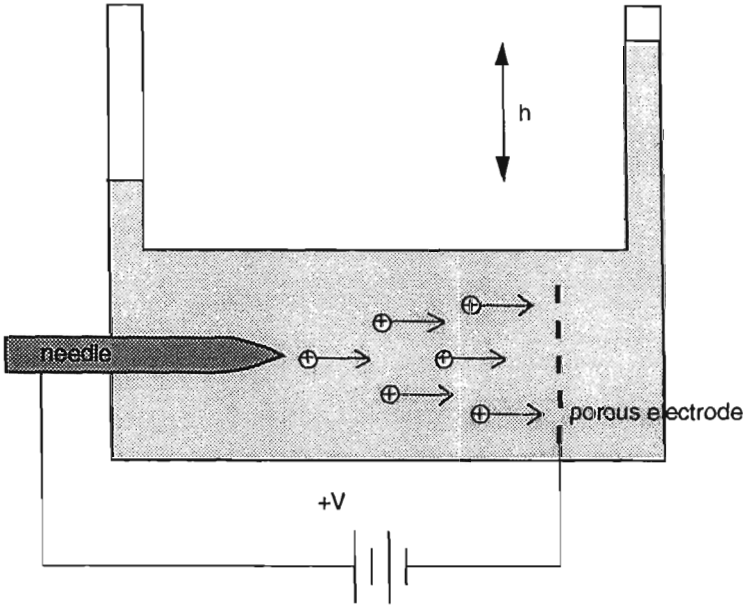


Figure 1 Apparatus for studying electrically induced hydrostatic pressures.

approximately 100 Pa (10 mm of water). These are substantially the results reported by Stuetzer.

Similar agreement is normally obtained for other experimental work including different geometries and field generation. For example, liquid will climb up a wire inserted vertically into the liquid surface (one of the so-called Sumoto effects). The height of liquid can be estimated by Eq. 16 as approximately 1 cm, since the wire is partially in air, and the electric field will be limited by air breakdown. This is approximately the height obtained experimentally (Pickard, 1961). Similar agreement is observed when the liquid rises between plate electrodes driven by ac voltages (Melcher, 1976). In fact, virtually all of the experimental work on electrohydrostatics gives results that can be estimated by Eq. 16 when gravity is the dominant fluid force.

Of course, there is more to the experiments than estimating the order of magnitude of the result. In the experiment shown in Fig. 1, for example, no pressure was generated at all if the electrodes consisted of two plates, instead of a needle and a plate. The needle serves to concentrate the electric field, raising it to values high enough to cause injection of charge directly into the liquid. These charges are then pulled through the fluid

to the other electrode. Their motion drags the fluid to set up the pressure gradient that is measured. If the charges are not injected into the fluid, the electric forces will be exerted on the electrodes alone, and since the electrodes are porous, this force will not be passed on to the liquid. Thus there is no guarantee that the estimated pressures will actually be realized in a given configuration. This will depend on the skill of the designer.

B. Capillary Electrohydrostatics

If the size scale is small enough, surface tension replaces gravity as the most significant hydrostatic force. In this case, the magnitude of the electric effect is related to the electrocapillary number

$$N_{ec} = \frac{\epsilon E^2 L}{T} \tag{17}$$

When this ratio is small, the electric field will have little effect on the fluid. As it reaches or exceeds unity, however, then the surface will respond with a noticeable deformation. Note that the ratio increases with the size scale, so the electric field is more effective in generating surface deformations with a large curvature. When the scale is large, however, gravity effects will dominate over surface tension, and the electrocapillary ratio becomes less significant.

Typical of electric forces overcoming surface tension is the appearance of small conical protrusions on liquid surfaces exposed to a field. The length scale for such cones can be estimated by setting the electrocapillary number equal to unity and is given by

$$L \approx \frac{T}{\epsilon E^2} \tag{18}$$

For a water surface exposed to air, the typical length will be

$$L \approx \frac{0.072}{(8.854 \times 10^{-12})(3 \times 10^6)^2} = 0.9 \quad \text{mm} \tag{19}$$

at the breakdown field.

In water, this EHD effect therefore appears only around or above 1 mm. The upper limit can be extended considerably if the gravitational pressure is reduced. This occurs normally in spacecraft and has led to numerous proposals for controlling fuel and other liquids under reduced gravity conditions (Blackmon, 1965; Kaldeich, 1992). Larger length scales are also possible if the mass associated with the surface is reduced. This approach was used in the classic experiment on the coning effect (Taylor, 1964). A sketch of the experiment is shown in Fig. 2.

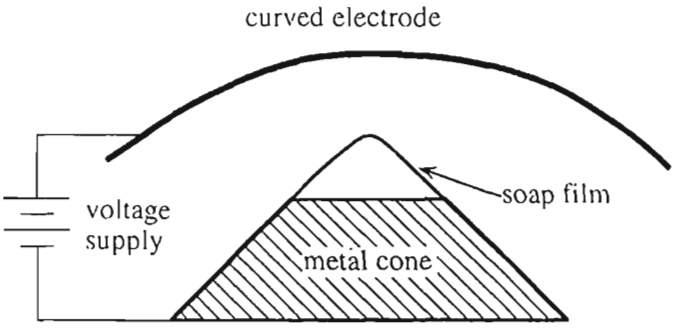


Figure 2 Apparatus for studying capillarity dominated EHD.

The central puzzle in the cone concerns its sharp tip. Its curvature is very large, so both the surface tension and the electric fields there approach infinity. To obtain a more convenient larger cone, Taylor used a soap film rather than a liquid. Since the mass of the soap film is so small, the interfering effects of gravity are removed. At the same time, a lower electric field can be used, since the electrocapillary number increases with size. With these changes, it was possible to produce a cone with a shape that agreed very closely with the one predicted by his theory.

IV. DYNAMICS

Most of the experimental work in electrohydrodynamics involves motion of the fluid, so dynamical pressures must normally be considered in experimental analysis. In addition, electric forces can often set the fluid into motion in unexpected ways, so it is necessary to consider whether the electric forces are strong enough to influence the dynamic behavior of the fluid. As in the electrohydrostatic examples discussed above, the nature of the fluid motion should be determined first, before the complication of electric forces is added.

A. Dynamic Fluid Forces

There are two types of fluid forces that arise in virtually all practical fluid flows. The first is the inertial (or Bernoulli) pressures, which have the magnitude

$$p_i \approx \gamma U^2 \tag{20}$$

where U is the velocity of the flow. It naturally increases with the speed and also with the density of the fluid. Thus air (and other gases) will have

low inertial pressures, while those of liquids will be much higher. As an example, consider air flowing at 1 m/s. With a density of 1.2 kg/m^3, its inertial pressure will be on the order of

$$p_i \approx (1.2)(1)^2 = 1.2 \quad \text{Pa} \tag{21}$$

This is less than the limiting values for electric pressures in air, so EHD effects could be important in such a flow. Because pressure depends on the square of the velocity, slower flows will be much more likely to respond to electrostatic pressures.

The other fluid force of universal importance in flow is the viscous pressure, given approximately by

$$p_v \approx \frac{\eta U}{L} \tag{22}$$

where η is the dynamic viscosity of the fluid. As an example, water has a viscosity of 1 mPa·s (1 centipoise), so the viscous pressure associated with a flow at 1 m/s in a channel of 1 mm is

$$p_v \approx \frac{(0.001)(1)}{0.001} = 1 \quad \text{Pa} \tag{23}$$

This pressure, like those in the previous examples, can be exceeded by the electric pressure, which is therefore likely to play a role in flows of this type.

Although both the inertial and the viscous pressures exist in a flowing fluid, one of them is likely to control the flow at any particular operating condition. The dominant fluid pressure is described by the inertial-viscous (or Reynolds) number, which is the ratio of the inertial to the viscous pressures

$$N_{iv} = \frac{\gamma U^2}{\eta U/L} = \frac{\gamma UL}{\eta} \tag{24}$$

If this ratio exceeds unity, inertial pressure predominates, while viscous pressures control the flow for lower Reynolds numbers. Note that the critical value is unity, not 2000. The value of 2000 is associated with the transition from laminar (inertial) flow to turbulent (inertial) flow.

B. Inertial Flow

If the inertial-viscous number exceeds unity, then the effectiveness of the electric pressure will depend on the ratio of the electric and inertial pressures (electroinertial number)

$$N_{ei} = \frac{\epsilon E^2}{\gamma U^2} \tag{25}$$

If the fluid motion is caused solely by the electric field, we expect this number to be on the order of unity, which leads to the approximate relation

$$U \approx \sqrt{\frac{\epsilon}{\gamma}}\, E \tag{26}$$

Note that there is a linear relation between the fluid velocity and the electric field. This relation has the same form as the mobility relation (see Chapter 1) leading to the description of the term in the radical as the electroconvective mobility

$$\mu_{ec} \equiv \sqrt{\frac{\epsilon}{\gamma}} \tag{27}$$

which gives the relation between the fluid velocity and the electric field that causes it. Note that this mobility depends only on the physical properties of the fluid. For a typical insulating liquid, with $\kappa = 3$ and $\gamma = 1$ Mg/m^3, the mobility is

$$\mu_{ec} = \sqrt{\frac{(3)(8.854 \times 10^{-12})}{1000}} = 1.6 \times 10^{-7} \quad \text{m}^2/(\text{V}\cdot\text{s}) \tag{28}$$

As an example, application of a typical field ($E = 1$ MV/m) could lead to fluid motion with a velocity on the order of

$$U \approx (1.6 \times 10^{-7})(1 \times 10^{6}) = 0.16 \quad \text{m/s} \tag{29}$$

Electroconvection is often observed in practical situations involving electric fields and insulating liquids, but not in gases (Felici, 1972). It is an important source of error in measurements of ionic mobility in liquids.

In using dimensionless numbers, care should be taken to ensure that all relevant effects are included. An example of the need to consider additional variables arose in the use of EHD to cause uniform breakup of an aqueous jet into drops (Crowley, 1983). In this experiment, electrodes surrounding the jet produced electric pressure variation along the jet, which acted to expand or contract the jet in synchronism with the ac excitation, as shown in Fig. 3. The jet had a diameter of approximately 100 μm, and was moving at approximately 10 m/s. For a liquid jet, inertial pressures are normally larger than capillary pressures, since a jet cannot form unless it overcomes the capillary forces that hold it in the nozzle. Thus the dominant mechanical pressure will be inertial. For the intended

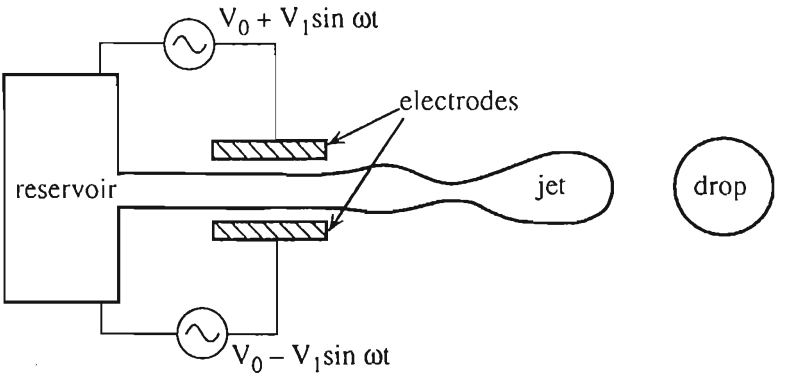


Figure 3 Apparatus for exciting jet breakup.

application (an ink-jet printer), the inertial pressure is on the order of

$$p_i \approx (1000)(10)^2 = 100 \quad \text{kPa} \tag{30}$$

The device operates in air, so the electric pressure will be on the order of 0.1 kPa. At first glance, this appears to be too weak to influence the jet motion, since the pressure ratio is

$$N_{ei} = \frac{p_e}{p_i} = \frac{1}{1000} \tag{31}$$

A closer look, however, reveals other considerations. The jet is inherently unstable, so any perturbations are exponentially amplified as they are carried along, leading to the production of drops. To be effective, the exciter does not need to generate pressures equivalent to the inertial pressure of the jet. Instead, it need only overcome the naturally occurring perturbations. In this application, therefore, the low value of the electro-inertial number is not disqualifying.

C. Viscous Flow

For slow flows of thick fluids through small channels, viscous effects are likely to control the fluid motion, and the appropriate gauge of the electrical effect is the ratio of electric to viscous pressures (the electroviscous number):

$$N_{ev} = \frac{\epsilon E^2}{\mu U/L} = \frac{\epsilon E^2 L}{\mu U} \tag{32}$$

If the fluid motion is solely due to the electric field, we expect this number to be on the order of unity, and the fluid velocity will therefore be on the order of

$$U = \frac{\epsilon L}{\mu} E^2 \tag{33}$$

Note that the velocity increases with the square of the field, so it is not possible to define a mobility here.

A number of EHD pumps have been reported in the literature, some of them with parameters that suggest that viscosity provides the predominant mechanical pressure. A typical example (Melcher, 1966) uses a traveling electric field both to induce charges in a viscous liquid and then to pull it in the direction of the field, as sketched in Fig. 4. This experiment used Aroclor 1232, with a dielectric constant of 5.7 and a viscosity of 15 centipoise. The liquid flowed along a channel with a depth of 25 mm. The electrodes were closely spaced along the direction of flow, which caused problems with local breakdown near the adjacent edges. As a result, the average electric field over the bulk of the fluid was on the order of 0.02 MV/m. With these parameters, we would estimate the peak velocities as

$$U = \frac{(5.7)(8.854 \times 10^{-12})(0.025)}{(0.015)} (0.02 \times 10^6)^2 = 3.3 \quad \text{cm/s} \tag{34}$$

This is very close to the velocity reported in the experiments (3 cm/s). Similar agreement is obtained for other experiments with viscous EHD flows (Crowley et al., 1990).

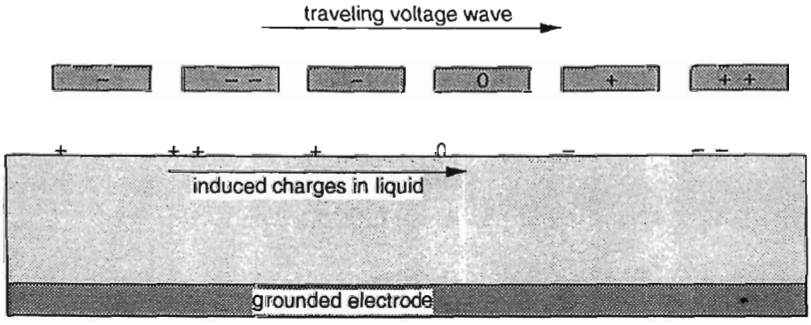


Figure 4 Apparatus for inducing EHD pumping.

V. CONVECTION AND CHARGE DECAY

In many experiments, the fields can be maintained by external power supplies connected to electrodes in the liquid. In other cases, however, the fields are generated by charges that are either inside or on the surface of the fluids. These charges can move through the fluid, which normally leads to a loss of field strength. If charges of the same sign exist inside the fluid, for example, they will spread out under the effect of their mutual repulsion. If a fluid is conductive, the charge carriers in the fluid can neutralize the excess charge, which again weakens the field. In many fluids, this charge decay represents an important practical consideration in experimental work.

A. Charge Decay

The importance of charge decay is determined primarily by how long it takes to lose the charge and thus the field. There are several mechanisms for charge loss, depending on the electrical nature of the fluid and the amount of charge present. The most common situation involves a fluid that has a measurable electrical conductivity. In practice this corresponds to a conductivity greater than 10^{-12} S/m (10^{-14} mhos/cm). A charge placed in such a fluid will be neutralized in a time on the order of

$$\tau_e = \frac{\kappa\epsilon_0}{\sigma} \tag{35}$$

where σ is the conductivity of the fluid. In ethanol, for example, the conductivity is approximately 1.4×10^{-7} S/m, and the dielectric constant is 25.8. The charge decay time is therefore on the order of

$$\tau_e = \frac{(25.8)(8.854 \times 10^{-12})}{1.4 \times 10^{-7}} = 1.6 \quad \text{ms} \tag{36}$$

Thus any charges placed in ethanol will be gone in a few milliseconds.

Many fluids, however, are insulators in the practical sense. Air, like most gases, does not have an appreciable conductivity, and neither does a highly insulating liquid like hexane. In such cases, charge does not decay by neutralization but by spreading out in response to its self-repulsion. The time constant for this space charge decay is given by (Crowley, 1986)

$$\tau_e = \frac{\kappa\epsilon_0}{\rho\mu} \tag{37}$$

where ρ is the density of the charge (in C/m^3) and μ is its mobility. The charge decays faster for fluids with high mobilities. Generally, gases have

the highest mobilities, and viscous liquids have the lowest. Thus charge will decay fastest in gases, and much more slowly in thick liquids like heavy oil.

The decay rate also depends on the charge density, so a very concentrated charge will decay faster. In effect, this sets a practical limit on the amount of charge that can be put in a fluid, since the charge must usually exist for a finite amount of time to have an effect. If the charge must persist for a time t, then we can anticipate that its density can be no greater than

$$\rho \sim \frac{\kappa \epsilon_0}{\mu t} \tag{38}$$

over most of this time. As an example, if the electric force on air must last for a time interval of 1 ms, then the greatest charge density that can be expected is

$$\rho \sim \frac{(1.0)(8.854 \times 10^{-12})}{(1.5 \times 10^{-4})(0.001)} = 59 \quad \mu C/m^3 \tag{39}$$

using the mobility of ions in air (1.5×10^{-4} m^2/Vs).

The experimenter can determine whether conduction or repulsion plays the dominant role in charge decay by taking the ratio of the two decay times,

$$N_{\sigma\rho} = \frac{\sigma}{\rho\mu} \tag{40}$$

If this conduction-repulsion number is large, conduction dominates, while if it is small, space charge effects will control the decay.

B. Convection

The charge decay time should always be compared to another time interval associated with the system to determine the effect of charge decay. In an electrohydrodynamic experiment, this second time is most often related to the motion of the fluid. If the fluid moves with a velocity U and the experiment has a typical size of L, then the mechanical time constant will be given approximately by

$$\tau_m = \frac{L}{U} \tag{41}$$

The ratio of the two times is the electroconvective number (sometimes called the electric Reynolds number), which can take two forms. If the

conduction process is more important than space charge repulsion, the appropriate ratio is the convection-conduction number

$$N_{U\sigma} = \frac{\tau_\sigma}{\tau_U} = \frac{\epsilon U}{\sigma L} \tag{42}$$

On the other hand, if charge repulsion dominates, the electroconvective number should be written as a convection-repulsion number

$$N_{U\rho} = \frac{\tau_\rho}{\tau_U} = \frac{\epsilon U}{\rho \mu L} \tag{43}$$

This ratio indicates whether the fluid should be considered as an insulator or a conductor for the particular experiment. If the number is smaller than unity, the charge decays before the motion is completed, and the fluid acts as a conductor. This will naturally occur when the conductivity is large, but also when the velocity is slow, and the sizes large. Thus a fluid mass slowly moving across a long distance is more likely to lose its charge, and hence its electric pressure. Conversely, a small mass that rapidly traverses a short distance is likely to behave as an insulator, losing little of its charge.

C. Example of the Use of the Electroconvective Number

An example of an EHD device that relies on an insulating fluid is the flowmeter shown in Fig. 5. A pulse of charge is injected into the liquid by the needle electrode and is carried downstream by the flow. As it passes the sensing electrode, it induces a current through the meter. The time delay between the original pulse and the induced pulse in the sensing electrode is related to the velocity of the flow. Obviously, the device depends on the preservation of the charge during the time it takes to reach the sensing electrode. To achieve good sensing, the electroconvective number must be large. As an example, consider a moderately conductive fluid like the Aroclor discussed earlier, with a conductivity on the order of 1 nS/m, flowing with a velocity of 1 m/s. Substantial charge decay will occur when the electroconvective number approaches unity, so the distance between the injecting and sensing electrodes should be

$$L < \frac{\epsilon U}{\sigma} = \frac{(5.7)(8.854 \times 10^{-12})(1.0)}{1.0 \times 10^{-9}} = 50 \quad \text{mm} \tag{44}$$

For water with a conductivity of 10 μS/m, the distance will be shorter by a factor of 10,000, which makes the device impractical. For highly insulating fluids and for all gases, the conductivity σ is replaced by the product $\rho\epsilon$, which depends on the amount of charge injected.

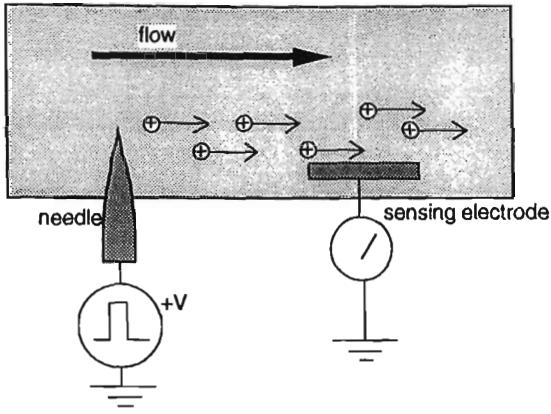


Figure 5 EHD flowmeter.

NOMENCLATURE

E	electric field, V/m
g	gravitational acceleration, 9.8 m/s^2
L	length, m
N	dimensionless ratio
p	pressure, Pa
R	radius of curvature, m
T	surface tension, N/m
U	velocity, m/s
ϵ	permittivity, F/m
ϵ_0	permittivity of free space, 8.854×10^{-12} F/m
γ	mass density, kg/m^3
η	(dynamic) viscosity, Pa s
κ	dielectric constant
τ	time constant, s
μ	mobility, m^2/Vs
ρ	charge density, C/m^3

Subscripts

c	capillary
e	electric
g	gravity

i	inertial
ρ	space charge repulsion
σ	conductive
U	convective
v	viscous
bk	breakdown

REFERENCES

Blackmon, J. B. (1965). Collection of liquid propellants in zero gravity with electric fields. *J. Spacecraft*, 2(3), 391–398.

Crowley, J. M. (1983). Electrohydrodynamic droplet generators. *Journal of Electrostatics*, 14, 121–134.

Crowley, J. M. (1986). *Fundamentals of Applied Electrostatics*. Wiley, New York.

Crowley, J. M., G. S. Wright et al. (1990). Selecting a working fluid to increase the efficiency and flow rate of an EHD pump. *IEEE Transactions of Industry Applications*, 26(1), 42–49.

Felici, N. J. (1972). D. C. conduction in liquid dielectrics. Part II, Electrohydrodynamic phenomena. *Direct Current*, 2(4), 147–165.

Kaldeich, B. (1992). First European Symposium. Fluids in Space (ESA SP-353). Ajaccio, France; ESA, Noordwijk, The Netherlands, p. 615.

Melcher, J. R. (1966). Traveling-wave induced electroconvection. *Physics of Fluids*, 9, 1548–1555.

Melcher, J. R. (1976). Electric fields and forces in semi-insulating liquids. *Journal of Electrostatics*, 2, 121–132.

Pickard, W. F. (1961). Experimental investigation of the Sumoto effect. *Journal of Applied Physics*, 32(10), 1888–1893.

Stuetzer, O. M. (1959). Ion drag pressure generation. *Journal of Applied Physics*, 30(7), 984–994.

Taylor, G. I. (1964). Disintegration of water drops in an electric field. *Proceedings of the Royal Society of London*, A280, 383–397.

BIBLIOGRAPHY

This chapter has presented the general ideas behind the application of electrohydrodynamics, but few of the details. This bibliography contains a representative sample of papers describing details of experimental work in the major areas described above. They are arranged by the primary mechanical effects that control the fluid response.

A. General

Chang, J.-S. (1989). Stratified gas-liquid two-phase electrohydrodynamics in horizontal pipe flow. *IEEE Transactions on Industry Applications*, 25(2), 241–247.

Crowley, J. M. (1986). *Fundamentals of Applied Electrostatics*. Wiley, New York.
Crowley, J. M. (1994). *Electrohydrodynamics*. In press.
Crowley, J. M., G. S. Wright and J. C. Chato (1990). Selecting a working fluid to increase the efficiency and flow rate of an EHD pump. *IEEE Transactions of Industry Applications*, 26(1), 42–49.
Melcher, J. R. (1972). Electrohydrodynamics. Applied Mechanics. Proc. 13th Internat. Conf. Theo. and Applied Mechanics, Moscow. Springer Verlag, New York, pp. 240–263.
Melcher, J. R. (1976). Electric fields and forces in semi-insulating liquids. *Journal of Electrostatics*, 2, 121–132.
Pickard, W. F. (1963). Ion drag pumping. II, Experiment. *Journal of Applied Physics*, 34(2), 251–258.
Stuetzer, O. M. (1966). Ion drag pumps. *Journal of Applied Physics*, 31(1), 136–146.

B. Gravity

Blackmon, J. B. (1965). Collection of liquid propellants in zero gravity with electric fields. *J. Spacecraft*, 2(3), 391–398.
Melcher, J. R., and M. Hurwitz (1967). Gradient stabilization of electrohydrodynamically oriented liquids. *Journal of Spacecraft*, 864–871.
Pickard, W. F. (1961). Experimental investigation of the Sumoto effect. *Journal of Applied Physics*, 32(10), 1888–1893.
Schnurmann, R., and M. G. C. Lardge (1972). Electric climbing of dielectric liquids. *Proceedings of the Royal Society of London*, A327, 393–402.
Stuetzer, O. M. (1959). Ion drag pressure generation. *Journal of Applied Physics*, 30(7), 984–994.
Stuetzer, O. M. (1963). Pressure analysis of conduction in liquids. *Physics of Fluids*, 6(2), 190–194.

C. Surface Tension

Hoburg, J. F. (1980). Viscous dominated interfacial electrohydrodynamic instability in polar geometry. *Physics of Fluids*, 23(1), 22–30.
Inculet, I. I., K. J. Hodgson and J. G. Millward (1986). Cross current dual aerodynamically shaped atomizer electrostatic spray nozzle. *IEEE Transactions on Industry Applications*, IA-22(6), 977–981.
Joffre, G., B. Prunet-Foch, S. Berthomme and M. Cloupeau (1982). Deformation of liquid menisci under the action of an electric field. *Journal of Electrostatics*, 13, 151–165.
Joffre, G., and M. Cloupeau (1986). Characteristic forms of electrified menisci emitting charges. *Journal of Electrostatics*, 18, 147–161.
Mahoney, J. F., J. Perel et al. (1987). Mechanism for high-mass sample ion desolvation in electrohydrodynamic mass spectrometry. *International Journal of Mass Spectrometry and Ion Processes*, 79(3), 249–266.

Roth, D. G., and A. J. Kelly (1980). Analysis of the disruption of evaporating charged droplets. IAS Annual Meeting, Pt. II, Cincinnati, OH, USA. IEEE, New York, pp. 998–1004.

Schneider, J. M., C. D. Hendricks et al. (1967). Stability of an electrified jet. *Journal of Applied Physics*, 38, 2599–2605.

Taylor, G. I. (1964). Disintegration of water drops in an electric field. *Proceedings of the Royal Society of London*, A280, 383–397.

Wright, G. S., P. T. Krein et al. (1993). Factors affecting the dynamic electrical manipulation of menisci. *IEEE Transactions on Industry Applications*, 29(1), 103–112.

D. Inertial Flow

Brown, D. R. (1964). Swirling of a liquid under the influence of a uniform electric field. *Nature*, 202, 868–870.

Crowley, J. M. (1965). Growth and excitation of electrohydrodynamic surface waves. *Physics of Fluids*, 8(9), 1668–1676.

Crowley, J. M. (1983). Electrohydrodynamic droplet generators. *Journal of Electrostatics*, 14, 121–134.

Gerdt, R., J. M. Crowley et al. (1978). Electrohydrodynamic pumping of cable oil. *Journal of Electrostatics*, 8, 477–488.

Nguyen, H. D., and J. N. Chung (1990). Flows inside and around a vaporizing/condensing drop translating in an electric field. *Transactions of the ASME. Journal of Applied Mechanics*, 57(4), 1044–1055.

Sharbaugh, A. H., II, and G. W. Walker (1985). The design and evaluation of an ion-drag dielectric pump to enhance cooling in a small oil-filled transformer. *IEEE Transactions on Industry Applications*, IA-21(4), 950–955.

Weinberg, F. (1992). Electrically driven convection. First European Symposium. Fluids in Space (ESA SP-353), Ajaccio, France, ESA; Noordwijk, The Netherlands, pp. 123–129.

E. Viscous Flow

Atten, P., F. M. J. McCluskey et al. (1988). Electroconvection and its effect on heat transfer. *IEEE Transactions on Electrical Insulation*, EI-23(4), 659–667.

Fuhr, G., T. Muller et al. (1992). Microfabricated electrohydrodynamic (EHD) pumps for liquid of higher conductivity. *Journal of Microelectromechanical Systems*, 1(3), 141–146.

Melcher, J. R. (1966). Traveling-wave induced electroconvection. *Physics of Fluids*, 9, 1548–1555.

Melcher, J. R., and M. S. Firebaugh (1967). Traveling-wave bulk electroconvection induced across a temperature gradient. *Physics of Fluids*, 10(6), 1178–1185.

Melcher, J. R., and G. I. Taylor (1969). Electrohydrodynamics: a review of the role of interfacial shear stresses. *Annual Review of Fluid Mechanics*, pp. 111–146.

F. Convection and Charge Decay

Kim, K., and R. J. Turnbull (1976). Generation of charged drops of insulating liquids by electrostatic spraying. *Journal of Applied Physics*, 47(5), 1964–1969.

Lion, K. S. (1959). *Instrumentation in Scientific Research*. McGraw-Hill, New York, pp. 133–135.

Malaczynski, G. W., and T. Schroeder (1992). An ion-drag air mass-flow sensor for automotive applications. *IEEE Transactions on Industry Applications*, 28(2), 304–309.

Melcher, J. R. (1967). Charge relaxation on a moving liquid surface. *Physics of Fluids*, 10(2), 325–332.

Melcher, J. R. (1974). Electric fields and moving media. *IEEE Transactions on Education*, E-17(2), 100–110.

Tanaka, T., N. Yamada et al. (1985). Characteristics of streaming electrification in pressboard pipe and the influence of an external electric field. *Journal of Electrostatics*, 17(3), 215–234.

Zahn, M., and T. Takada (1983). High voltage electric field and space-charge distributions in highly purified water. *Journal of Applied Physics*, 54(9), 4762–4775.

Zheltukhin, V. A., Y. K. Solomatnikov et al. (1978). Effect of electric-field frequency on heat transfer. *Heat Transfer—Soviet Research*, 10(6), 10–13.

TABLES OF PRESSURES, TIMES, AND RATIOS

The pressures, time constants, and ratios described in this chapter are summarized here for reference.

Table 1 Pressures

Symbol	Expression	Name
p_i	γU^2	inertial
p_v	$\mu U/L$	viscous
p_g	$\gamma g L$	gravity
p_c	T/L	capillary (surface tension)
p_e	ϵE^2	electric

Table 2 EHD Pressure Ratios

Symbol	Expression	Name
N_{ei}	$\frac{\epsilon E^2}{\gamma U^2}$	electroinertial
N_{ev}	$\frac{\epsilon E^2 L}{\mu U}$	electroviscous
N_{eg}	$\frac{\epsilon E^2}{\gamma g L}$	electrogravitational
N_{ec}	$\frac{\epsilon E^2 L}{T}$	electrocapillary

Table 3 Times

Symbol	Expression	Name
τ_σ	ϵ/σ	conduction charge decay
τ_ρ	$\epsilon/\rho\mu$	space charge decay
τ_U	L/U	mechanical convection

Table 4 EHD Time Ratios

Symbol	Expression	Name
$N_{\sigma\rho}$	$\frac{\sigma}{\rho\mu}$	conduction-repulsion
$N_{U\sigma}$	$\frac{\epsilon U}{\sigma L}$	convection-conduction
$N_{U\rho}$	$\frac{\epsilon U}{\rho\mu L}$	convection-repulsion

This Page Intentionally Left Blank

8

Injection Induced Electrohydrodynamic Flows

P. Atten

Centre National de la Recherche Scientifique
Grenoble, France

A. Castellanos

University of Sevilla
Sevilla, Spain

I. INTRODUCTION

Electrohydrodynamics (EHD) is the study of the motion of liquids subjected to electric fields. The forces that are exerted by an electric field on free or polarization charges present in a liquid are transmitted by collisions on the neutral molecules. Typically, the liquid will be set in motion, thus changing the distribution of charges that in turn modify the electric field. This coupling makes EHD a difficult subject.

The liquid state is chemically very reactive compared to the gas or solid state. Trace impurities undergo chemical reactions giving as end products ionic pairs. Also at the liquid-electrode interfaces electrochemical reactions take place, injecting ions into the bulk of the liquid. Both processes make it impossible to have liquids free of ions, i.e., perfectly insulating liquids do not exist in nature. In practical situations what will be considered as a good liquid insulator will depend upon the restrictions imposed by the user.

Electrical forces may be used to control and handle liquids in a variety of ways. For example, charged liquid drops of a predetermined size may be originated from electrified jets or nozzles. The subsequent motion of these drops may be suitably controlled by electric fields, and applications

have arisen in such diverse fields as ink jet printers, electrostatic painting and coating, electrospray, chemical reactors, combustion chambers. Another large area of application is based on the enhancement of the bulk motions due to space charge injected from fine grids, blades, or metallic points or by means of a conductivity variation induced by thermal gradients. These techniques have been applied to build EHD pumps without mobile parts, to favor heat transfer exchange in large industrial transformers and cables. In biomedical sciences, the separation of proteins by means of electrical forces is an indispensable tool. In natural sciences, EHD is needed to understand atmospheric electricity. Finally, we should mention the growing importance of EHD in microgravity environments to handle and locate liquids at desired positions. Thus fuel management in spacecraft has already been attempted. Also, electrical forces may be used to stabilize strongly the melted zone of rods of different materials used to grow large crystals of ultrahigh purity in the containerless process known as the floating zone technique.

This chapter is organized as follows. In Secs. II and III the equations of electrohydrodynamics are deduced and then cast in nondimensional form to put in evidence the scales that appear frequently in EHD. Sections IV and V are dedicated to the problems of unipolar injection induced instability and convection and section VI to EHD flows in geometries of low and no symmetry.

II. ELECTRICAL EQUATIONS

A. Maxwell Equations: The Electroquasistatic Limit

A nonrelativistic treatment is enough for the vast majority of problems, since liquid velocities are quite small compared to the velocity of light c. The Galilean limit of relativistic mechanics is defined unambiguously, but some confusion seems to exist about this limit for the case of electromagnetism. It may be shown, using the Maxwell equations together with the relativistic transformation laws for the fields and the constitutive laws, that there are two well defined limits when $c \to \infty$. Thus two distinct Galilean electromagnetisms wholly consistent with our ordinary conceptions of space and time exist. These two limits are characterized by the fact that either $E > cB$ or else $E < cB$ and are usually called electroquasistatics and magnetoquasistatics respectively. A detailed derivation will not be presented here, but it suffices to say that in electrohydrodynamics the electric field is the dominant one.

Given a physical system, previous experience or an order of magnitude analysis is of help to decide between limits. To illustrate this point, con-

sider a liquid in which an electric field **E** is present. Suppose further that the liquid follows Ohm's law, $\mathbf{J} = \sigma\mathbf{E}$, with **J** the current density and σ the electrical conductivity. Denoting by ϵ and μ the permittivity and permeability of the liquid, the fourth Maxwell equation now reads,

$$\nabla \wedge \mathbf{B} = \sigma\mu\mathbf{E} + \epsilon\mu \frac{\partial \mathbf{E}}{\partial t} \tag{1}$$

If the magnetic field is determined by **J**, then $B \sim \sigma\mu El$, where l is a typical distance in the system. Hence $E/cB \sim \tau_e/\tau_{em} = \tau_{em}/\tau_m$, where $\tau_e = \epsilon/\sigma$, is the charge relaxation time, as we shall see below, $\tau_{em} = l/c$ the transit time for electromagnetic waves in the system, and $\tau_m = \sigma\mu l^2$ the magnetic diffusion time. For typical systems in the laboratory, $\epsilon \sim 10^{-11}$ farad/m, $\mu \sim 10^{-6}$ henry/m, $l \sim 10^{-2}$ m, and numerically we obtain $E/cB \sim 1/\sigma$. It is then clear that in dielectric liquids characterized by very low values of the conductivity, Maxwell equations reduce to the electroquasistatic limit, thus falling in the realm of EHD. On the contrary, in highly conductive liquids such as mercury or molten metals and semiconductors, magnetic effects will be dominant, and it is in the domain of magnetohydrodynamics (MHD).

In dielectric liquids, Maxwell equations may be nondimensionalized, taking l and τ as the scales for the length and time of mechanical processes; l_E and τ_E (l_H and τ_H) as the scales over which the electric field (magnetic field) changes appreciably; and E_0 as the scale for the electric field. Derived scales for q, the charge density, and **J** and **H**, the magnetic intensity field, are $q_0 = \epsilon E_0/l_E$, $J_0 = q_0 l/\tau$, and $H_0 = (l_H/l_E)(\epsilon E_0 l/\tau)$ (notice that $E_0/cB_0 = c/v \gg 1$ with $v = l/\tau$, and the scale for J_0 has been chosen to make both terms in the charge conservation equation of similar magnitude).

We have Maxwell equations in dimensionless form

$$\nabla\cdot\mathbf{D} = q \tag{2}$$

$$\nabla \wedge \mathbf{E} = -\left(\frac{v}{c}\right)^2 \left(\frac{l_H}{l}\right)\left(\frac{\tau}{\tau_H}\right) \frac{\partial \mathbf{B}}{\partial t} \tag{3}$$

$$\nabla\cdot\mathbf{B} = 0 \tag{4}$$

$$\nabla \wedge \mathbf{H} = \mathbf{J} + \left(\frac{l_E}{l}\right)\left(\frac{\tau}{\tau_E}\right) \frac{\partial \mathbf{E}}{\partial t} \tag{5}$$

together with the charge conservation law

$$\frac{\partial q}{\partial t} + \nabla\cdot\mathbf{J} = 0 \tag{7}$$

For steady fields, $l \sim l_E \sim l_H$ and $\tau \sim \tau_E \sim \tau_H$, while for an ac field of frequency ω, $\tau_E \sim \tau_H \sim \omega^{-1}$. It is then clear that unless the frequency is of order of $(c/v)^2$, the electric field equations together with the the charge conservation equation are decoupled, in the nonrelativistic limit, from the magnetic equations. The magnetic field is determined after solving for the electric field. To conclude, in electrohydrodynamics, the Maxwell equations reduce to

$$\nabla \cdot \mathbf{D} = q \qquad \nabla \wedge \mathbf{E} = 0 \qquad \frac{\partial q}{\partial t} + \nabla \cdot \mathbf{J} = 0 \tag{8}$$

B. Constitutive Law for the Current Density

According to the constitutive law for the current density, dielectric liquids are classified into two broad categories: liquids for which Ohm's law holds, which for brevity will be called Ohmic liquids, and the non-Ohmic liquids. This property does not refer to any intrinsic property of the liquids involved but rather depends on the preparation, the history, and above all on the electric field intensity. For low electric fields most of the liquids exhibit an ohmic behavior. But for high fields, injection phenomena are the main source of ions and electroneutrality, and Ohm's law fails to be valid.

1. Ohmic Regime

Putting $\mathbf{J} = \sigma \mathbf{E} + q\mathbf{v}$, with $\mathbf{v}$ the liquid velocity, in the charge conservation equation and using Gauss's law, this equation, in nondimensional form, becomes

$$\frac{dq}{dt} + \frac{\tau}{\tau_e} q = 0 \tag{9}$$

where dq/dt stands for $\partial q/\partial t + \mathbf{v} \cdot \nabla$, the material derivative, and σ has been assumed to be constant. For a medium at rest, $\tau = \tau_e$, and charge relaxes exponentially, $q(t) = q(0)e^{-t}$, with t measured in units of $\tau_e = \epsilon/\sigma$, the charge relaxation time. On the other hand, τ may be related to the period of an imposed ac field. Then, for high enough values of the frequency, $dq/dt \simeq 0$, and the presence of the charge density may be of no relevance to the dynamics of the system.

If τ is related to a mechanical time, the ratio τ_e/τ is usually called the electric Reynolds number R_E. For large values of R_E the charge appears as frozen, and if it is initially zero it will be always zero. In more general situations, τ will be a combination of electrical and mechanical times.

2. Unipolar Injection Regime

Suppose, for simplicity, that only one ionic species is injected into a perfectly insulating liquid, $\sigma = 0$. Then the constitutive law for the current density is

$$\mathbf{J} = qK\mathbf{E} - D\nabla q + q\mathbf{v} \tag{10}$$

The first term gives the contribution due to the drift of ions that move relative to the liquid with a velocity $K\mathbf{E}$, with K the ionic mobility. The second term accounts for molecular diffusion, with D the charge diffusion coefficient. The third term is due to convection of charge density by the velocity field.

If λ and l denote the spatial scales of variation for charge density and electric potential V, the dimensionless charge conservation equation becomes

$$\frac{dq}{dt} + \left(\frac{l}{\lambda}\right)\left(\frac{\tau}{\tau_T}\right)\mathbf{E}\cdot\nabla q - \left(\frac{\tau}{\tau_D}\right)\nabla^2 q + \left(\frac{\tau}{\tau_c}\right) q^2 = 0 \tag{11}$$

where $\tau_T = l^2/KV$ is the ionic transit time, $\tau_D = \lambda^2/D$ is the ionic diffusion time, and $\tau_c = \epsilon/Kq_0$ is the charge relaxation time associated with Coulomb repulsion. The ratio between diffusion and drift terms is $(D/KV)(l/\lambda) \sim (0.025/V)(l/\lambda)$, where Einstein's relation $D/K = k\Theta/e$ (k the Boltzmann constant and e the elementary charge) has been taken into account for ambient temperature, $\Theta \simeq 300$K. Thus diffusion will be negligible compared to drift unless the potential difference V is of the order of 0.025 V for $\lambda \sim l$, or else very high gradients are present ($\lambda \ll l$). Usually this will only happen in thin layers, either boundary layers or internal layers, where diffusion is needed to match the outer or mainstream solutions of the diffusion-free problem. In what follows $\lambda \sim l$ will be assumed and diffusion will be neglected.

The ratio between drift and Coulomb repulsion is given by the nondimensional number $C = q_0 l^2/\epsilon V$. For low (large) values of C the characteristic time that enters into the problem is the transit time τ_T (Coulomb repulsion time τ_c).

Notice that if diffusion is neglected the dimensional charge conservation equation has an exact solution $q = q_0/(1 + t/\tau_c)$ with τ_c the algebraic bulk relaxation time. This solution is valid on $d\mathbf{r}/dt = K\mathbf{E} + \mathbf{v}$, so that unless a given element of liquid can be traced via a particle line to a source of charge, it will support no bulk charge density. The algebraic charge relaxation time τ_c depends on the initial level of charge, but after several decay times the charge density reaches a limiting value ϵ/Kt independent of the initial conditions.

III. MECHANICAL EQUATIONS

The mechanical equations that govern the dynamics of liquids are the conservation of mass and momentum

$$\frac{d\rho}{dt} + \rho\nabla\cdot\mathbf{v} = 0 \qquad \rho\frac{d\mathbf{v}}{dt} = \nabla\cdot(\mathcal{T}^{\text{mech}} + \mathcal{T}^{\text{e}}) \tag{12}$$

with ρ the mass density and $\mathcal{T}^{\text{mech}}$, $\mathcal{T}^{\text{e}}$ the mechanical and electrostatic stress tensors.

For isentropic flows, pressure and density variations are related by $d\rho/dt = (\partial\rho/\partial p)_S(dp/dt) = (1/c_s^2)(dp/dt)$, where p is the pressure, S is the entropy, and c_s is the velocity of sound in the liquid. Taking $\rho(l/\tau)^2$ as the scale for the pressure, we have for real flows $\Delta\rho/\rho \sim (v/c_s)^2$. Then for liquid velocities much smaller than the velocity of sound, ρ may be taken as constant, and the mass conservation equation reduces to

$$\nabla\cdot\mathbf{v} = 0 \tag{13}$$

If in addition the liquid is Newtonian, and with scalar electrical permittivity,

$$\mathcal{T}_{ij}^{\text{mech}} = -p\delta_{ij} + \eta\left(\frac{\partial v_i}{\partial x_j} + \frac{\partial v_j}{\partial x_i}\right) \qquad \mathcal{T}_{ij}^{\text{e}} = \epsilon E_i E_j - \frac{1}{2}\delta_{ij}(1 - b)E_k E_k \tag{14}$$

with η the dynamic viscosity and $b = (\rho/\epsilon)(\partial\epsilon/\partial\rho)_\Theta$ the electrostriction parameter.

Substituting these expressions in the momentum conservation equation we obtain the Navier-Stokes equation, that together with the incompressibility condition gives

$$\rho\frac{d\mathbf{v}}{dt} = -\nabla p^* + \eta\nabla^2\mathbf{v} + q\mathbf{E} - \frac{1}{2}E^2\nabla\epsilon \qquad \nabla\cdot\mathbf{v} = 0 \tag{15}$$

with $p^* = p - (1/2)\rho(\partial\epsilon/\partial\rho)_\Theta E^2$, the modified pressure.

The term $q\mathbf{E}$, called the Coulomb force, is the force per unit volume on a medium containing free electric charge. It is the strongest EHD force term and usually dominates when dc electric fields are present. The next term, called the dielectric force, is due to the force exerted on a nonhomogeneous dielectric liquid by an electric field. It is usually weaker than the Coulomb force and only dominates when an ac electric field, with a period much shorter than the charge relaxation time and/or the ionic transit time, is imposed. The electrostrictive force, being the gradient of a scalar, is treated as a modification of the liquid pressure.

The Navier-Stokes equation, written in dimensionless form, is

$$\frac{d\mathbf{v}}{dt} = -\nabla p^* + \left(\frac{\tau}{\tau_\nu}\right)\nabla^2\mathbf{v} + \left(\frac{q_0 E_0 \tau^2}{\rho l}\right) q\mathbf{E} - \left(\frac{\epsilon E_0^2 \tau^2}{\rho l}\right)\frac{1}{2} E^2 \nabla\epsilon \tag{16}$$

where $\tau_\nu = l^2/\nu$ is the viscous relaxation time with the classical Reynolds number defined as $Re = \tau_\nu/\tau = lv/\nu$, with $\nu = \eta/\rho$ the kinematic viscosity. The two new nondimensional electromechanical parameters may be written in a variety of ways depending on the physical mechanisms that determine the velocity field, the charge density, and the gradient of permittivity.

Consider, for example, the motion of a liquid driven by Coulomb forces. The flow may be viscous or inertial dominated. In the viscous regime, the second term is of the same order as the third. Equating both terms, a natural time scale $\tau_{EV} = \eta/\epsilon E^2$, called the electroviscous scale, will appear to play a significant role. In the inertial regime, the most frequently encountered in nature or in industrial processes, the acceleration term should be comparable to the Coulomb force. This implies that the typical liquid velocity is given by $v \sim MKE$, that is, the liquid velocity is M times the own ionic velocity. The parameter $M = \sqrt{(\epsilon/\rho)}/K$ is the ratio of two mobilities, $K_h = \sqrt{(\epsilon/\rho)}$, called the hydrodynamic mobility, and K, the true ionic mobility. Taking into account *Walden's rule*, i.e., $K\eta \sim$ *constant*, we see that M is proportional to viscosity (see Secs. V and VI for a discussion of the important role played by M in Coulomb-driven flows).

The electrical forces may act in the bulk or concentrated at any possible interface between different liquids. The reader interested in interfacial effects is referred to the excellent review by Melcher and Taylor (1969) on the electrohydrodynamics of liquids in the Ohmic regime and subjected to Coulomb forces concentrated at interfaces. The role of dielectric forces acting in the bulk and/or at interfaces is analyzed by Pohl (1978). For those readers with a broad interest in electrohydrodynamics the book by Melcher (1981) is recommended. We shall be concerned here with the role of Coulomb forces acting at the bulk of the liquid.

IV. EHD INSTABILITY FOR UNIPOLAR INJECTION INTO AN INSULATING LIQUID

Charge injection is the phenomenon of creation, at the metal/liquid interface, of charge carriers, usually ions, of the electrode polarity. In "insulating" liquids this injection is generally of electrochemical nature and most often occurs at one electrode only (Felici, 1972a; Denat et al., 1979). Under very high fields, however ($E >$ a few MV/cm), as at a blade edge or a needle tip, the injection process in liquids is of electronic rather than

of electrochemical nature (Haidara and Denat, 1991). In liquids of high enough resistivity the injected current generally dominates over the residual conduction current due to ions created in the liquid bulk. The problem of unipolar injection into a perfectly insulating liquid is therefore typical of real situations and plays a central role in EHD. In this class of problems, the three particular electrode geometries of high symmetry (parallel plates, coaxial cylinders, and concentric spheres) are particularly interesting because the Coulomb force is irrotational in the absence of liquid motion when the injection is uniform. Therefore rest is a possible solution and it is necessary to examine in what conditions this solution destabilizes.

A. Linear Instability Problem

There is an analogy between the pure unipolar injection problem and the Rayleigh-Bénard problem of a horizontal fluid layer heated from below. In the latter case the unstable density gradient brings about fluid motion when the temperature difference is large enough for buoyancy to overcome the damping action of viscous forces. Above the critical value of the relevant parameter, the Rayleigh number, there occurs instability of the fluid, and heat is partially transferred by convection (Chandrasekhar, 1961).

For the unipolar injection case, the charge density q decreases from the injector to the collector in the motionless state; when accompanying the charge carriers during their movement, the charge density decreases according to the law $q = q_0/(1 + t/\tau_c)$, with $\tau_c = \epsilon/Kq_0$. Let us consider the action of a liquid motion. A positive velocity component w along the field line (as in zone 1 of Fig. 1a) results in a decrease of the time required

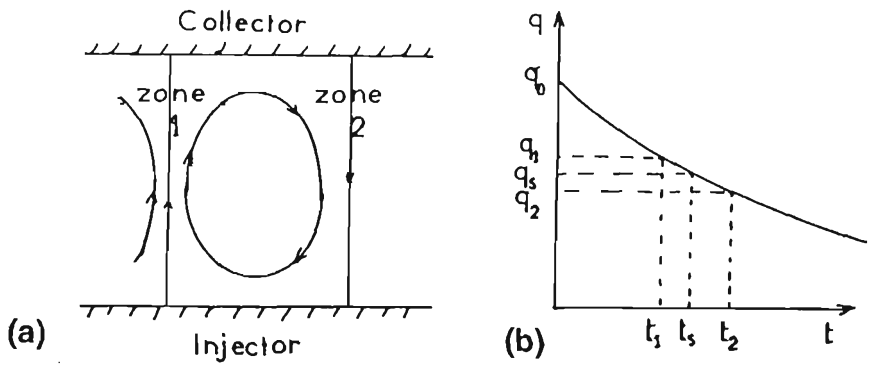


Figure 1 (a) Cross section of a roll-like flow perturbation and (b) values of the charge density as a function of the time of Coulombic repulsion.

by the ions to be at a given distance z from the injector: $t_1 = z/(KE + w)$. Coulomb repulsion therefore acts during a time smaller than $t_s = z/KE$, and the charge density q_1 is higher than the value q_s existing at rest (Fig. 1b). If we consider a convective motion in the form of two-dimensional rolls (Fig. 1a), in the return zone (No. 2) the liquid velocity diminishes the resulting ion velocity and we have $t_2 = z/(KE - w) > t_s$ and $q_2 < q_s$. Therefore the motion gives rise to a net torque that tends to accelerate it. Because of this positive coupling between velocity and charge perturbations the stationary charge distribution is unstable (for a detailed derivation see the Felici model (1969, 1972b)). The destabilizing force is proportional to $q_1 - q_2$ and consequently to the mean charge gradient. The stability parameter T formally represents the ratio of driving Coulomb force and damping viscous forces, so we write

$$T = \frac{\epsilon V}{K\eta} \tag{17}$$

where V stands for the applied voltage (for another derivation using the typical times see Castellanos (1991)). Note that according to Walden's rule ($K\eta \sim Cst$) the stability parameter is simply proportional to the applied voltage and in particular does not formally depend on any length.

The instability criteria have been obtained by using the standard mathematical technique of linear instability analysis (Schneider and Watson, 1970; Atten and Moreau, 1972). In the absence of precise laws concerning the injection rate, it is assumed that the injection is autonomous, i.e. the charge density q_0 does not depend on variables like fluid velocity or electric field (this assumption leads to lower bounds for the critical instability criteria). The critical values T_c depend on the parameter C (defined in II.B), which is a nondimensional measure of the charge volumic density at the injector. In the case of two plane parallel rigid electrodes, let us first consider the weak injection limit $C \ll 1$, which corresponds to a very small distortion of the electric field. It is easily seen that the charge gradient is proportional to C^2 and the criterion is $T_c C^2 = 220.7$. In the second asymptotic case of space charge limited (SCL) injection ($C \to \infty$), $T_c \to 161$. Critical values have also been determined for finite injection strengths (Atten and Moreau, 1972). The critical nondimensional wave number is close to 5 and only slightly depends on C; no information on the preferred convective planform can be gained from the linear analysis.

In the case of coaxial cylinders and concentric spheres, there are also the two limit cases of very weak and very strong injection strengths. Two facts however make the problem more intricate than that of plane parallel geometry: (i) there is an extra parameter α, which is the ratio of inner and outer radii, and (ii) the behavior depends on which electrode is injecting. In

particular, for weak injection and $\alpha > 0.3$, we obtain (Oliveri and Atten, 1986; Agrait and Castellanos, 1990)

$$(T_c)_{\text{inner}} > (T_c)_{\text{planes}} > (T_c)_{\text{outer}} \tag{18}$$

The converse is true for strong injection, and these behaviors have been qualitatively justified. Let us point out that due to curvature of the electrodes, there is no more degeneracy, and linear analysis gives the planform of the most unstable perturbation.

B. Nonlinear Instability

The analogy with the Rayleigh-Bénard problem fails when considering the nonlinear behavior just above the critical value of the stability parameter. The physical reason for that failure is the difference in the conduction mechanism of the scalar quantity in the motionless state: drift with a finite velocity for charge carriers, diffusion for heat. In the thermal problem, above the critical conditions there appears a well-defined convective pattern (two-dimensional rolls in the case of high Prandtl number liquids) and the amplitude of steady convective motion varies in a continuous way with the Rayleigh number. In the unipolar injection problem in two parallel plates geometry, the charge perturbation $q_1 - q_2 \propto w/(K^2E^2\text{-}w^2)$ increases more than linearly as a function of the amplitude w of the velocity perturbation. For a viscous liquid a stable steady solution cannot exist with liquid velocity lower than the ionic velocity KE (Felici, 1969). From a mathematical viewpoint, this occurs because the bifurcation is sub-critical: in an interval $[T_{nl}, T_c]$ below T_c there exist two finite amplitude solutions, one stable and the other unstable. This is related with a hysteresis loop and jumps of the steady values of both the velocity amplitude and the current at the linear T_c and nonlinear T_{nl} criteria (for a detailed study see Atten and Lacroix, 1979). For $C \ll 1$ the criterion is $T_{nl} \approx T_c C$, whereas for $C \gg 1$, $T_{nl} \approx 110$. Note that for a fluid of low viscosity, the inertial effects play an important role and can lead to a steady solution with a velocity amplitude less than KE.

An experimental study has only been performed in planar geometry with SCL injection into viscous liquids (Fig. 2). The theoretical description accounts for all aspects of the phenomenon except for critical values, which are lower than predicted: $(T_c)_{exp} \approx 100$ and $(T_{nl})_{exp} \approx 90$ instead of 161 and about 110 (Atten and Lacroix, 1979).

C. Instability in Transient Conditions

The transient current technique was first used in the unipolar injection problem to determine the mobility of charge carriers. By applying a step

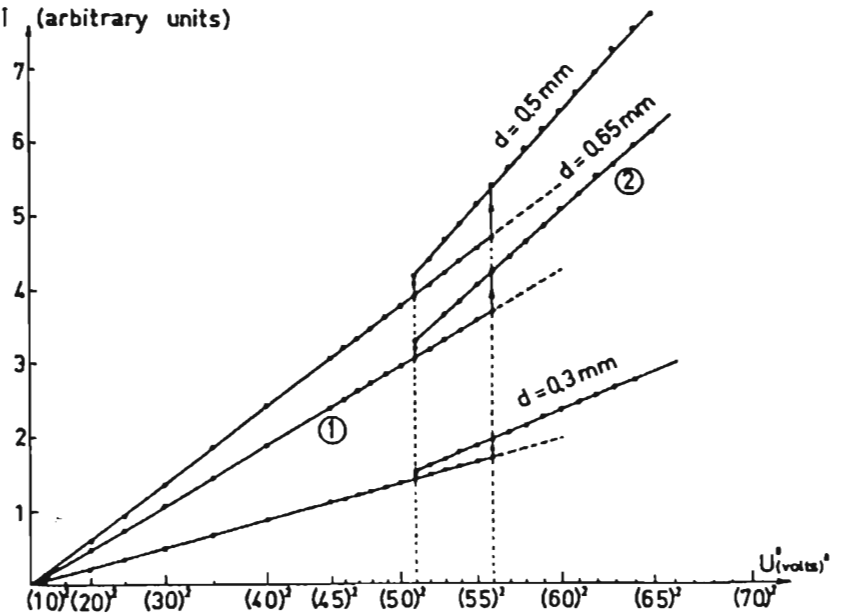


Figure 2 Space charge limited injection into a mildly polar liquid, "pyralene 1460," between plane parallel electrodes. Variations of the steady state current as a function of the square of the applied voltage. Branches 1 are relative to the motionless regime and 2 to steady convection of finite amplitude. Note the discontinuities at nonlinear (51 V) and linear (56 V) instability voltages. Current unit: 2 nA, 0.2 nA, and 0.1 nA for d = 0.3, 0.5, and 0.65 mm respectively. (After Atten and Lacroix, 1979.)

voltage, the current variation exhibits a transient regime of increase up to a maximum, which corresponds to the arrival of the first injected charges on the opposite electrode (Atten and Gosse, 1969; Denat et al., 1979). The transit time allows us to determine the ionic mobility, provided that the liquid is not put into motion. For large enough applied voltages V and/or strong enough injections, there appears a motion that accelerates the transit of charge carriers and leads to apparent mobility values K_a greater than the true one. Generally, K_a increases with V and further takes a saturation value in the case of SCL injection (for a detailed presentation of transient EHD instabilities and convection, see the review by Tobazéon (1984)).

At low enough voltages it is possible, in some cases, to recover the true mobility and also to determine an apparent instability voltage V_a as

the threshold above which K_a begins to increase (Watson et al., 1970). The transient conditions of such a determination, however, raise questions about the validity of this measurement technique (Atten, 1974). Indeed, the instability problem is here conceptually different. In steady conditions we have instability once a perturbation has a positive growth rate, whatever its magnitude may be. In transient conditions the instability is not strictly characterized; it is revealed by the effects of "manifest convection" and therefore depends on both the sensitivity of the detection technique of the motion and the magnitude of initial perturbations. For an injection induced by a step voltage, for instance, the space charge layer has a thickness λ that initially increases linearly with time: $\lambda \approx KEt$. In most liquids the transient current is the best variable to detect manifest convection: for times t lower than the "stability time" t_1, the current I follows the law for a motionless transient regime (Fig. 3); for $t > t_1$, I

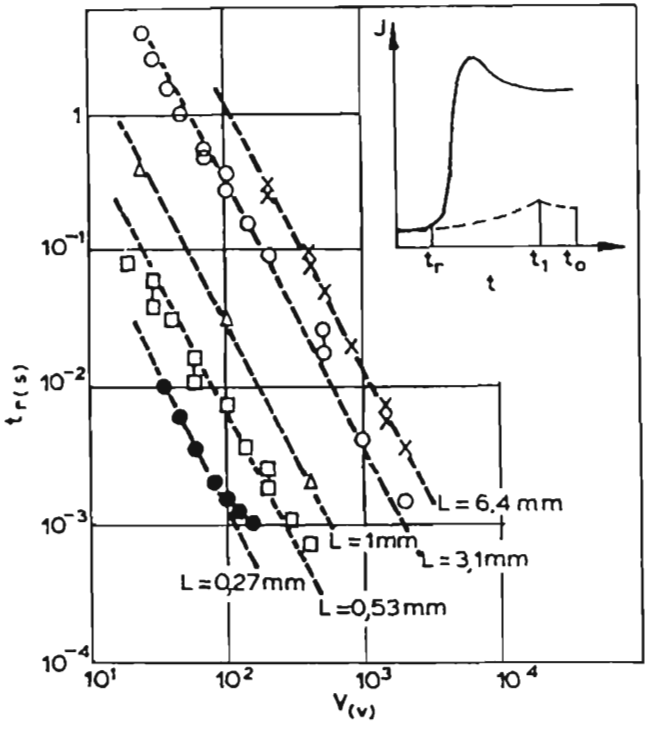


Figure 3 Transient space charge limited injection in deionized nitrobenzene: delay time for manifest convection versus step voltage value for different electrode spacings. Insert: typical measured current (full line) and theoretical current shape in the absence of motion (dashed line). (After Filippini et al., 1970.)

increases more steeply because of the contribution of convection to charge transport. An expression for t_1 can be obtained by assuming that manifest convection is detected for a well-defined value T_{a1} of the stability parameter: $T_{a1} = \epsilon V'_a/K\eta$, ($V'_a \approx E\lambda$) characterizing the space charge layer. We obtain

$$t_1 \approx T_{a1} \frac{\eta}{\epsilon E^2} \tag{19}$$

(note that $\eta/\epsilon E^2$ is the electroviscous time defined in Sec. III). Experiments fully confirm the variation law (19) for SCL injection (Fig. 3) and gives T_{a1} values ranging from 20 to 50 (Filippini et al., 1970; Tobazeon, 1984). In the case of SCL injection under ac fields, a similar derivation leads to a critical field $E_a \approx 2.2[T_{a2}(\eta/\epsilon)f]^{1/2}$ for frequency $f > f_c \sim 1/t_T$. Experiments confirm the $f^{1/2}$ dependence and give T_{a2} on the order of T_{a1} (Atten et al., 1982).

D. Influence of a Forced Flow

A flow with a mean velocity parallel to the electrodes interacts with the convection generated by unipolar injection. It is convenient to distinguish the case of applied voltages close to the instability voltage from conditions of more intense agitation. The linear instability of plane Couette and plane Poiseuille flows subjected to moderate unipolar injection has been examined by Castellanos and Agrait (1992). They found that for low values of the Reynolds number Re, longitudinal rolls are favored because the growth of transverse perturbations is greatly inhibited. The conclusions are reversed for values of Re above about $5 \cdot 10^4$ because the energy transfer from the primary to the secondary flow via Reynolds stresses then favors the transverse waves.

The analysis applies to the case of Couette flow between cylinders, for example. For a Poiseuille flow between two parallel plates there is an entrance region that makes the problem more intricate. Consider such a flow entering the region where an SCL injection occurs ($x > x_0$). For $V < V_c$, the ions injected at $x = x_0$ have two orthogonal velocity components, $U(z)$ due to the forced flow and KE due to Coulomb force. Their trajectories determine the separatrix between charged and charge free zones, and the ions reach the opposite electrode at the abscissa $x_0 + L_E$, L_E being the electric entrance length ($L_E \approx Ud/KE$). For $V > V_c$, the instability problem bears some similarity to the one in transient conditions, and manifest convection is detected for $x > x_0 + L_1$ with $L_1 < L_E$, L_1 corresponding to the instability time t_1 (Atten and Honda, 1982a). Moreover, the observed flow pattern is not that predicted by the linear instability analysis, because of the strong nonlinearity of the EHD unipolar injec-

tion problem. The pattern depends on the ratio of ionic and mean flow velocities: for U lower than a few times KE, the pattern is three-dimensional (modulated transverse rolls or hexagonal cells), whereas for higher U values, there appear first longitudinal rolls, which further destabilize (Atten and Malraison, 1981).

V. INJECTION INDUCED ELECTROCONVECTION

A. General Considerations

Let us consider now the convection state induced by the injected space charge and which contributes to the charge transfer. The mean current density $\bar{j}$ due to both the drift of charge carriers and their convection has the expression (deduced from Eq. 10)

$$\bar{j} = K\bar{q}\overline{E} + \overline{qw} \tag{20}$$

where $\overline{E}$ and $\bar{q}$ are the mean field and charge density and $\overline{qw}$ is the correlation between velocity and charge density fluctuations and represents the convective part of the current. From the point of view of transfer of the scalar quantity, the EHD problem bears an analogy with Rayleigh-Bénard convection where the advection of hot and cold blobs in the fluid increases the heat transfer. The first fact to point out here is the rather large magnitude of liquid velocities, which reflects the intensity of the Coulomb force. An order of magnitude can be obtained by balancing the kinetic and electrostatic energy densities (Felici, 1969, 1972b):

$$w' \sim \left(\frac{\epsilon}{\rho}\right)^{1/2} E \qquad \text{or} \qquad \frac{w'}{KE} \sim M = \frac{(\epsilon/\rho)^{1/2}}{K} \tag{21}$$

The hydrodynamic mobility $(\epsilon/\rho)^{1/2}$ is on the order of a few 10^{-7} m^2/Vs for the dielectric liquids, and the typical velocities are in the range 0.1–1 m/s.

The nondimensional number M is an important parameter that generally gives insight into the basic features of EHD flows. For M high enough, the fluid velocity fluctuations are greater than the velocity of charge carriers with respect to the fluid and can entrain these charges against the action of the electric field. The charge distribution then depends drastically on the motion it induces. This is the case of most liquids and also of gases (at atmospheric pressure) with small charged particles (Atten et al., 1987). For $M < 1$, conversely, the motion only slightly affects the trajectories of charge carriers, which are determined essentially by the electric field. This occurs in the case of air with ions or big particles as

charge carriers. In the example of the electric wind, the gas flow has no significant influence on the ion trajectories or on the passage of current.

In the following, we consider only the case of high M values. Electroconvection of course depends on the geometry and on the injection strength. Two regimes of convection must be distinguished, depending on which of the inertial or viscous effects are dominating. The regime of dominant viscous effects corresponds to low values of the Reynolds number Re characterizing the big eddies of length scale d, d being the reference length of the system. Although Re is low, the flow is not laminar and can be considered as turbulent if we take into account its mixing and transport properties. For high values of the Reynolds number, the inertial effects dominate, and there are eddies of scales ranging from large (a fraction of d) to small or very small values (Castellanos, 1991). This second regime, the fully turbulent one, is characterized by different properties of transport of scalar quantities. The transition between the two regimes corresponds to a Reynolds number $Re_t \sim 10$ (Lacroix et al., 1975).

B. Electroconvection Between Plane Parallel Electrodes

Convective motion induced by SCL injection was examined in detail by Lacroix et al. (1975). We give in this section an overview of the main results. In the case of viscous dissipation dominating at large scale, it is natural to expect the typical fluid velocities to vary in proportion to the force. Balancing the viscous and Coulomb terms in Eq. 15, and using for charge density the expression $q \sim \epsilon E/d$ as deduced from Poisson's equation, we obtain $\eta w'/d^2 \sim qE \sim \epsilon E^2/d$. This gives for the velocity

$$\frac{w'}{KE} \cong \frac{T}{T_c} \tag{22}$$

The dependence predicted by Eq. 22 was experimentally confirmed. An order of magnitude analysis was developed to estimate the current. It led to the nontrivial prediction of the mean current varying as $V^{5/2}/d^3$, as found experimentally (Lacroix et al., 1975). As for the thermal problem, it is convenient to define an electric Nusselt number Ne as the ratio of the effective current I and the current I_0 that would exist without liquid motion. This Ne obeys the law (see Fig. 4)

$$Ne \approx \left(\frac{T}{T_c}\right)^{1/2} \tag{23}$$

Let us remark that although the current is transported mainly by convection, there is no linear dependence between I and the typical liquid velocity w'.

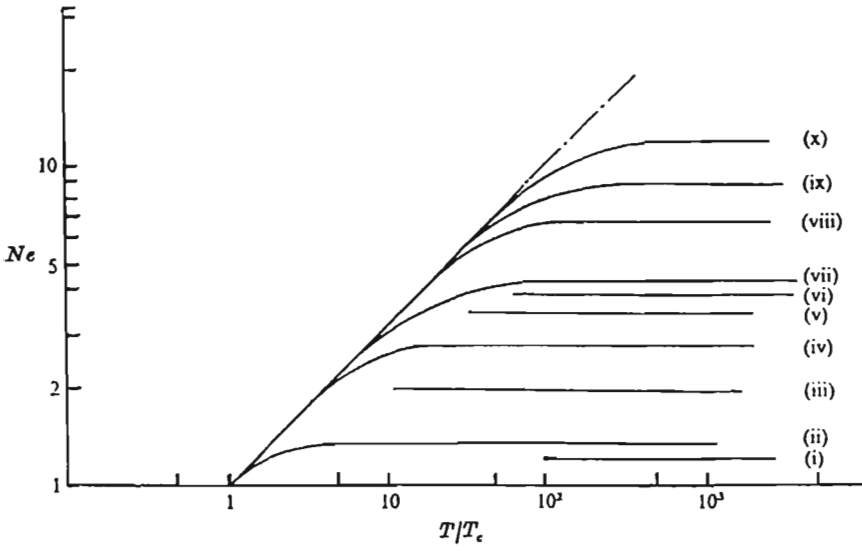


Figure 4 Electric Nusselt number Ne (space charge limited injection) versus the stability parameter $T/(T_c)_{exp}$ in various liquid/injected ion couples: (i) methanol/H^+; (ii) chlorobenzene/Cl^-; (iii) ethanol/H^+; (iv) nitrobenzene/Cl^-; (v) ethanol/Cl^-; (vi) propylene carbonate/Cl^-; (vii) pyralene 1460/Cl^-; (viii) pyralene 1500/Cl^-, 35°C; (ix) pyralene 1500/Cl^-, 20°C; (x) pyralene 1499/Cl^-. (After Lacroix et al., 1975.)

In the fully turbulent regime, Eq. 21 for the typical velocity can be obtained by using a more precise argument, which can be generalized. This states that the kinetic energy of a "blob" of fluid leaving the immediate vicinity of the injector is provided by the work of the Coulomb force; at mid-height $z = d/2$ we obtain

$$\frac{1}{2}\rho w'^2 \sim \frac{qEd}{2} \sim \frac{\epsilon E^2}{2} \tag{24}$$

which gives again Eqs. 21. Experiments confirmed this functional dependence for w' and gave the estimate of the numerical factor in Eq. 21 (Lacroix et al., 1975) as

$$w' \approx \frac{1}{3}\left(\frac{\epsilon}{\rho}\right)^{1/2} E = K_{ehd}E \quad \text{or} \quad \frac{w'}{KE} \approx \frac{M}{3} \tag{25}$$

The current was found to vary as usual in space charge limited conditions: $I \propto V^2/d^3$. Its values, however, are higher than those estimated with the

ionic mobility in the case of liquids. Indeed, an order of magnitude analysis gave for the electric Nusselt number (see Fig. 4)

$$Ne = \frac{I}{I_0} \approx \left(\frac{M}{3}\right)^{1/2} \tag{26}$$

Again there is no proportionality between the current and the characteristic velocity: the apparent steady state mobility defined by $j \approx (9/8)K_{app}\epsilon V^2/d^3$ takes the expression $K_{app} \approx (KK_{ehd})^{1/2}$. It appears that the more viscous the liquid, the greater will be the magnification of space charge limited current due to electroconvection. Finally, let us mention that the strong turbulent mixing results in a constant mean charge density in the liquid bulk (Lacroix et al., 1975).

In the other asymptotic case ($C \ll 1$), the injection is physically "electrode limited" and the current density takes the value $j = Kq_0E(0)$ where q_0 and $E(0)$ are respectively the charge density and the field at the injector (generally q_0 is a function of $E(0)$). In the weak injection case $C \ll 1$, the electric field is very slightly distorted, and the induced liquid motion has only a weak influence on total charge transfer, because it can only very slightly modify $E(0)$. Indeed assuming that q_0 is not affected by the movement, it is easily shown that (Atten et al., 1988)

$$1 \leq Ne < \frac{1}{1 - C/2} \approx 1 + \frac{C}{2} \tag{27}$$

(note the strong difference with the SCL injection case). To a very good approximation, the current can be assumed to remain independent of the state of motion. The problem is therefore restricted to the examination of the functional dependence of the typical liquid velocity.

In the viscous dominating regime ($Re < 1$), by balancing the viscous and Coulomb terms in Eq. 15 we deduce (Atten et al., 1988)

$$w' \sim \left(\frac{jVd}{\eta}\right)^{1/2} = KE\left(\frac{q_0d^2}{K\eta}\right)^{1/2} = KE(TC)^{1/2} \tag{28}$$

The numerical factor can be estimated from the comparison with the finite amplitude convection in the vicinity of the critical conditions. From the asymptotic behavior of an approximate analytical solution (Castellanos et al., 1987), we deduce

$$\frac{w'}{KE} \approx 3\left(\frac{TC}{T_{n1}C}\right)^{1/2} \approx 0.2(TC)^{1/2} \tag{29}$$

In the fully turbulent regime ($Re \gg 1$), the energy argument and further approximations lead to (Atten et al., 1988)

$$w' \sim \left(\frac{jd}{\rho K}\right)^{1/2} \approx \left(\frac{q_0 V}{\rho}\right)^{1/2} = C^{1/2}\left(\frac{\epsilon}{\rho}\right)^{1/2} E \tag{30}$$

For a constant q_0, w' increases as $V^{1/2}$. Note that the $C^{1/2}$ dependence implies a rather vigorous motion in the case of weak injection.

C. Electroconvection in Cylindrical Geometry

The case of an annular region between coaxial cylinders (wire/cylinder for example) is interesting because of the diverging character of the electric field. Electroconvection should then exhibit an intermediate convective regime between the viscous dominated convection and the fully developed turbulent convection. In this complex intermediate regime, one expects the convective flow to be fully turbulent in an outer annular zone and dominated by viscous effects in the axial zone around the injecting wire. An experimental study performed in a coaxial wire/cylinder cell showed two regimes of current variation (Perez et al., 1988). However, there arises in this case the difficulty of deriving precise laws, because injection occurs naturally from the action of the high electric field at the wire liquid interface and the current is lower than the space charge limited one. For high applied voltages (the transition voltage is about 10 times that relative to planar geometry), I approximately varies as V^2, and the apparent steady mobility is between 2 and 3 times greater than the one relative to the planar case (Perez et al., 1988). For moderate V values, the current dependence on voltage is determined by both the injection law and the convection properties.

In fully turbulent conditions, the agitation is more vigourous than it is in planar geometry. This can be justified using again the energy argument, which gives for the radial velocity component

$$u \cong \frac{1}{3}\left[2 \ln\left(\frac{R_2}{R_1}\right)\right]^{1/2}\left(\frac{\epsilon}{\rho}\right)^{1/2} E \tag{31}$$

This relation fairly well accounts for the values determined through transient experiments (Perez et al., 1988).

D. Electroconvection in Transient Conditions

Transient electroconvection has been studied experimentally for SCL injection in planar geometry via measurement of current and apparent mobil-

ity K_a (see Sec. IV.C). For high enough applied voltages, the convection is fully turbulent during the major part of the transient regime, and K_a is found to be close to K_{ehd} (Hopfinger and Gosse, 1971; Tobazeon, 1984). This implies that the transient typical turbulent velocity w' is not significantly higher than the one characterizing the steady state. Such a result is not surprising, because considerations of conversion of electric energy into kinetic energy lead to an upper bound for K_a that is a fraction of $(\epsilon/\rho)^{1/2}$ (Felici, 1972b; Castellanos, 1991).

The transient current, however, is more intense than the steady state one, and it exhibits a well-marked maximum I_m at time $t = t_T$ (Fig. 3). In the case of viscous effects dominating over the inertial effects, I_m varies as V^3, which gives a transient electric Nusselt number $Ne_t \sim T$. In the fully turbulent regime, I_m varies as V^2, and $Ne_t \sim M$ (Atten et al., 1982b; Tobazeon, 1984). The reason for such a high efficiency of transient convection in transporting charge (when compared with steady state) is that in transient conditions, the expansion of the charged convective zone occurs via "filaments" of charged liquid that invade the quasimotionless zone, the "return filaments" being charge free (Felici, 1972b). In steady conditions the strong mixing due to convection results in a mean charge in the liquid bulk so that forward and backward filaments have only slightly differing charge densities (Lacroix et al., 1975).

E. Interaction with a Forced Flow

For high enough applied voltages under strong injection, the injected space charge fully destabilizes a laminar forced flow orthogonal to the electric field direction (for example, Poiseuille flow between plane parallel electrodes or in an annular duct). This electrically induced (or reinforced) agitation increases the friction on the walls, and the pressure drop in a pipe or a rectangular duct can be increased by more than one order of magnitude. Thus the injection induced convection is the basic phenomenon that explains the improperly named "electroviscous effect" observed by numerous authors (Atten and Honda, 1982).

On the other hand, the forced flow modifies the turbulence structure of electroconvection existing without forced flow. Schematically the "filaments" transporting charge are inclined with respect to the electric field direction due to the mean flow velocity parallel to the electrodes. Therefore the efficiency of convection in transferring charge decreases as a function of the Reynolds number Re of the forced flow. For instance, a decrease of the current of more than 50% of its value for $Re = 0$ was observed in the case of electroconvection between coaxial wire and cylinder (Perez et al., 1988).

VI. INJECTION INDUCED FLOWS IN ASYMMETRIC ELECTRODE GEOMETRY

Although there is quite a large variety of asymmetric electrode geometries, we mainly consider here the case of one sharp electrode with a low radius of curvature at some place where the electric field takes large values. Typical examples are the assemblies known as blade-plane, point-plane, wire-plane, wire-two-plate (wire midway between two parallel plates), etc., but we can also consider more intricate cases like electrostatic precipitators. In dielectric liquids there arise moderate or strong injections at the high field locations, and in gases "injection" occurs via the corona effect. Thus the injected space charge has a strongly nonuniform distribution on the injector, which results in highly nonuniform charge density distribution in the bulk.

A. General Properties

The first point to mention is that the fluid cannot remain at rest in such geometries. Putting $\mathbf{v} = 0$ in the Navier-Stokes equation (Eq. 16) implies that the pressure gradient is compensated for by the electric force, and therefore that this force is irrotational: $\nabla \wedge \mathbf{F} = \nabla \wedge (q\mathbf{E}) = 0$. The distribution of Coulomb force is rotational in low symmetry configurations, and there appear large-scale eddies the structure of which is primarily determined by the geometry. For example, in blade-plate and wire-plate geometries, there are two roll-like large eddies (Atten and Haidara, 1985). The driving force of these eddies is a plume of charged fluid going from the blade (or the wire) to the plate (Fig. 5). In a wire-two-plate geometry, there are two wire-plate charged plumes driving four large eddies (McCluskey and Atten, 1985), and in a point-plane electrode assembly, the axial plume induces a large vortex ring. For high enough applied voltages a smaller scale turbulence is superposed on the large scale structures.

For asymmetric geometries, the two fundamental parameters are still T and M. As an illustration let us compare the behavior of gas and liquid in blade-plate geometry (Fig. 5 depicts the corresponding flow structures and the charge distributions). In the case of air, for instance, we have $M \ll 1$, and the electric wind has but a negligible influence on the trajectories of ions that do not significantly differ from the field lines. Then the EHD problem is greatly simplified: gas motion is neglected to determine the charge distribution (through Eqs. 8 and 10, and then Eq. 16 is solved to obtain the flow field (Yamamoto and Velkoff, 1981). For a liquid with high enough M value, conversely, the ionic drift velocity is lower than the liquid velocity, and the ions are entrained by the flow they induce.

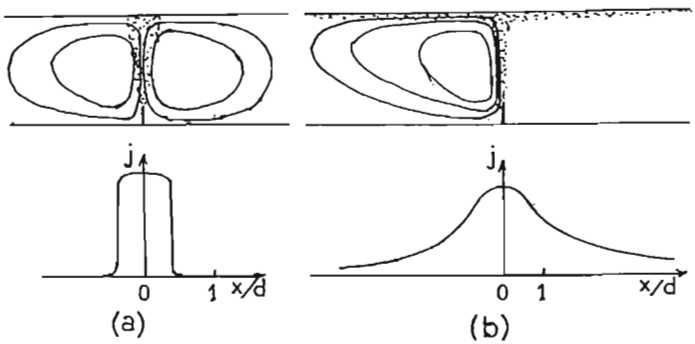


Figure 5 Blade/plane configuration with the blade inserted in a conducting plate. Cross sections showing schematically the streamlines and the space charge distribution (top figures) and the distribution of current density on the collecting plate (bottom figures). (a) Ionic wind in gases; (b) ion injection in liquids.

The charged plume has a width much lower than in gas, and this plume divides into wall jets, which convect the charge far away along the plate (McCluskey and Atten, 1985); the current density on the plate is very different from the previous case (Fig. 5). Solving this EHD problem is a very difficult task that has not yet been performed theoretically.

Let us consider the particular problem of electrostatic precipitators where corona discharges occur on wires located midway between the two collecting plates. These corona created ions are charging the particles to be removed from the gas. The important fact to point out here is the low mobility values for small particles (diameter $\leq$ 10 μm), which lead to rather high M values: $M > 3$ (Atten et al., 1987). The problem of resulting flow is here very intricate; the forced flow is affected by the approximately periodic charge distribution of ions, which induces large scale secondary flow. The charged small particles that are entrained and dispersed by the turbulent diffusion also contribute to the generation of turbulence through the mechanism prevailing in electroconvection. An experimental simulation using liquids confirmed a simplified analysis (based on the concept of turbulent diffusion) of the electroaerodynamic functioning of electrostatic precipitators (Lahjomri and Atten, 1987).

B. Charged Plumes

We consider here the case of fluid/charge carrier systems such that $M \gg 1$, i.e., the fluid velocity is much higher than the carrier drift velocity. With injection by a blade or a needle, the charge distribution in the bulk

is schematized in Fig. 5b, and by no means can the charge carrier mobility be deduced from the current-voltage characteristic $I(V)$ using approximate formulae valid only when the fluid motion is fully negligible. A prediction of $I(V)$ was made by Takashima et al. (1988) with the assumptions of "jets" of charge of constant width or radius and of SCL injection. This work is of rather limited interest because the width or radius of the charge jet is not constant and the system is not space charge limited (in practice, the field is always maximum on the tip of the sharp electrode). In the following we examine the charged plumes on the basis of the analogy with classical plumes, the typical example of which is the rising of hot gases above a chimney. At steady state the Coulomb force induces the motion, which convects the charge. The analogy applies fully in the limit case of the drift velocity KE being very small compared with the plume velocity.

For laminar plumes generated by injection from very restricted areas, the charge is confined in a core much narrower than the plume of characteristic width δ (Fig. 6a), and the current I (or the current per unit length J) is $I = Q(z)w_0(z)$, where $Q(z)$ is the convenient integral of charge density in a cross section and $w_0(z)$ is the maximum velocity in the plume. By making some approximations when solving the Navier-Stokes equations, it is easy to obtain the asymptotic laws of variation of w_0 and δ. Assuming

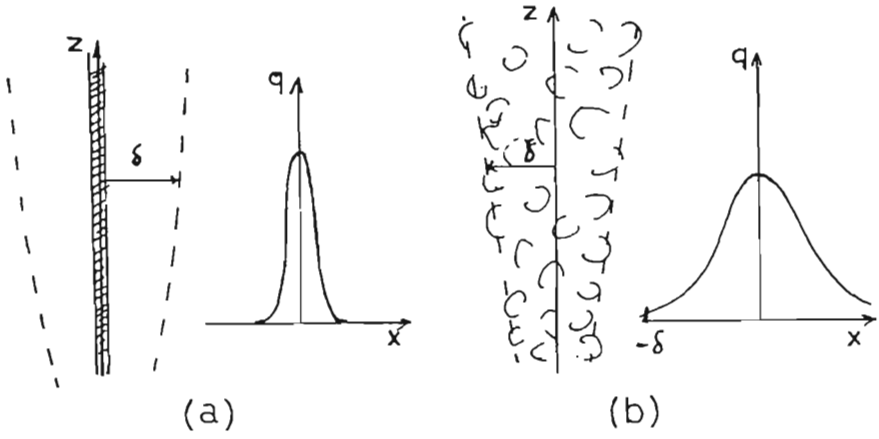


Figure 6 Schematic view of charged plumes and typical profiles of charge density. (a) Laminar charged plume with the charge core; (b) turbulent charged plume. (After Malraison et al., 1994.)

further that the applied field E is constant along the plume, we find in the two-dimensional case (McCluskey and Perez, 1992)

$$w_0(z) \propto \left(\frac{JE}{\rho\nu^{1/2}}\right)^{2/5} z^{1/5} \qquad \delta(z) \propto \left(\frac{\rho\nu^3}{JE}\right)^{1/5} z^{2/5} \tag{32}$$

the proportionality constants being close to 1. For an axisymmetric plume we have similarly (Malraison et al., 1994)

$$w_0(z) \propto \left(\frac{IE}{\rho\nu}\right)^{1/2} = Cst \qquad \delta(z) \propto \left(\frac{\rho\nu^3}{IE}\right)^{1/4} z^{1/2} \tag{33}$$

the proportionality constants also being on the order of 1.

For turbulent plumes, the velocity fluctuations convect the charge and act roughly like a very strong diffusion. Charge is now distributed in the whole plume volume (Fig. 6b). As for buoyant plumes (see for instance Turner, 1973), it is assumed that the velocity fluctuations u' and w' (in the directions normal and parallel to the electric field respectively) have similar amplitude and are proportional to the mean velocity $w_0(z)$: $u' \approx w' = \alpha w_0(z)$, and that some surrounding fluid is entrained into the plume. By expressing conservation of mass, electricity, and momentum, one obtains the laws (Malraison et al., 1994) for two-dimensional turbulent plumes

$$w_0(z) = \left(\frac{JE}{2\alpha\rho}\right)^{1/3} = Cst \qquad \delta(z) = 2\alpha z \tag{34}$$

$$q(z) = \left(\frac{J\rho^{1/2}}{2\alpha E^{1/2}}\right)^{2/3} z^{-1} \tag{34'}$$

and for axisymmetric turbulent plumes

$$w_0(z) = \left[\frac{25}{48\pi\alpha^2}\frac{IE}{\rho}\right]^{1/3} z^{-1/3} \qquad \delta(z) = (6/5)\alpha z \tag{35}$$

$$q(z) = \left[\frac{25}{18\pi 3^{1/2}\alpha^2}\frac{I\rho^{1/2}}{E^{1/2}}\right]^{2/3} z^{-5/3} \tag{35'}$$

Equations 32 to 35 characterize the asymptotic behavior of the plumes far from the injecting and collecting electrodes and must be matched with approximate solutions in the vicinity of both electrodes in order to obtain solutions in real electrode assemblies. Note finally that the above expressions give the typical fluid velocities once the current is known. Prediction

of both currents and velocities is a much more intricate problem that requires knowledge of the injection laws.

C. Forced Flow Effect

The effect of a cross flow on a convective flow generated by a very localized injection has been examined in the wire-two-plate geometry already mentioned in Sec. VI.A. In the absence of forced flow, there are two wire-plate charged plumes driving four large eddies. With a cross flow, we may distinguish two resulting flow structures depending on the Reynolds number Re of the forced channel flow. For relatively low values of Re, the two wire-plate plumelike structures resist strongly the oncoming flow: the space charge is distributed in two oblique wire-to-plate jets of charge, and the motion is extremely turbulent. Note that a significant proportion of charge carriers is convected downstream along the plates by two wall jets (McCluskey and Atten, 1985). For high enough Re value, the two wire-plate structures break up and the entire injected space charge is convected downstream in a thin wake behind the injecting wire. The mean velocity of the oncoming flow necessary to break the jetlike structure is at least four times the transverse mean velocity in these wire-plate jets (McCluskey and Atten, 1985).

The effect of a flow parallel to the force acting on the space charge has been studied only in the case of a wake behind a wire in a developed Poiseuille flow. In that case the injected charge is entrained by the flow, and the Coulomb force, which is important only over a limited distance downstream, partly compensates the deficit velocity of the wake (McCluskey and Atten, 1988). Note that the charge zone is thinner than the wake itself in the first zone where the wake expands.

REFERENCES

Agrait, N., and A. Castellanos (1990). Linear convective patterns in cylindrical geometry for unipolar injection. *Phys. Fluids A*, 2, 37.

Atten, P. (1974). Electrohydrodynamic stability of dielectric liquids during transient regime of space-charge-limited injection. *Phys. Fluids*, 17, 1822.

Atten, P., and J. P. Gosse (1969). Transient of one-carrier injections in polar liquids. *J. Chem. Physics*, 51, 2804.

Atten, P., and M. Haidara (1985). Electrical conduction and EHD motion of dielectric liquids in a blade/plane electrode assembly. *IEEE Trans. Electr. Ins.*, EI-20, 187.

Atten, P., and T. Honda (1982). The electroviscous effect and its explanation. I, The electrohydrodynamic origin; study under unipolar D.C. injection. *J. Electrostatics*, 11, 225.

Atten, P., and J. C. Lacroix (1979). Nonlinear hydrodynamic stability of liquids subjected to unipolar injection. *J. Mécanique*, 18, 469.

Atten, P., and B. Malraison (1981). Superposition d'une injection unipolaire et d'un écoulement de Poiseuille. In *Symmetries and Broken Symmetries in Condensed Matter Physics* (N. Boccara, ed.). IDSET, Paris, p. 503.

Atten, P., and R. Moreau (1972). Stabilité électrohydrodynamique des liquides isolants soumis à une injection unipolaire. *J. Mécanique*, 11, 471.

Atten, P., B. Malraison, and S. Ali Kani (1982). Electrohydrodynamic stability of dielectric liquids subjected to A. C. fields. *J. Electrostatics*, 12, 477.

Atten, P., F. M. J. McCluskey, and A. C. Lahjomri (1987). The electrohydrodynamic origin of turbulence in electrostatic precipitators. *IEEE Trans. Ind. Appl.*, IA-23, 705.

Atten, P., F. M. J. McCluskey, and A. T. Perez (1988). Electroconvection and its effect on heat transfer. *IEEE Trans. Electr. Ins.*, EI23, 659.

Castellanos, A. (1991). Coulomb driven convection in electrohydrodynamics. *IEEE Trans. Electr. Ins.*, IE26, 1201.

Castellanos, A., and N. Agrait (1992). Unipolar injection induced instabilities in plane parallel flows. *IEEE Trans. Ind. Appl.*, IA23, 513.

Castellanos, A., P. Atten, and A. T. Perez (1987). Finite amplitude electroconvection in liquids in the case of weak unipolar injection. *J. Physico-Chem. Hydrodyn.*, 9, 443.

Chandrasekhar, S. (1961). *Hydrodynamic and Hydromagnetic Stability*, Oxford University Press, Chap. 2.

Denat, A., B. Gosse, and J. P. Gosse (1979). Ion injections in hydrocarbons. *J. Electrostatics*, 7, 205.

Felici, N. (1969). Phénomènes hydro- et aéro-dynamiques dans la conduction des diélectriques fluides. *Rev. Gén. Electr.*, 78, 717.

Felici, N. (1972a). D.C. conduction in liquid dielectrics (part I). *Dir. Current*, 2, 90.

Felici, N. (1972b). D.C. conduction in liquid dielectrics (part II): electrohydrodynamic phenomena. *Dir. Current*, 2, 147.

Filippini, J. C., J. C. Lacroix, and R. Tobazéon (1970). Mise en évidence de l'apparition d'une instabilité pendant l'état transitoire en régime d'injection unipolaire dans les diélectriques liquides. *C. R. Acad. Sci. (Paris)*, B271, 936.

Haidara, M., and A. Denat (1991). Electron multiplication in liquid cyclohexane and propane. *IEEE Trans. Electr. Ins.*, EI26, 592.

Hopfinger, E. J., and J. P. Gosse (1971). Charge transport by self-generated turbulence in insulating liquids submitted to unipolar injection. *Phys. Fluids*, 14, 1671.

Lacroix, J. C., P. Atten, and E. J. Hopfinger (1975). Electroconvection in a dielectric liquid layer subjected to unipolar injection. *J. Fluid Mech.*, 69, 539.

Lahjomri, A. C., and P. Atten (1987). Simulation EHD des precipitateurs électrostatiques. *Rev. Phys. Appl.*, 22, 693.

McCluskey, F. M. J., and P. Atten (1985). Velocity profiles in the injection zone of an EHD generator and efficiency considerations. *IEEE Trans. Electr. Ins.*, EI-20, 405.

McCluskey, F. M. J., and P. Atten (1988). Modifications to the wake of a wire across Poiseuille flow due to a unipolar space charge. *J. Fluid Mech.*, 197, 81.

McCluskey, F. M. J., and A. T. Perez (1992). The electrohydrodynamic plume between a line source of ions and a flat plate. *IEEE Trans. Electr. Ins.*, EI-27, 334.

Malraison, B., P. Atten, A. T. Perez (1994). Panaches chargés résultant de l'injection d'ions dans un liquide isolant par une lame ou une pointe placée en face d'un plan, *J. Phys. III* (France), 4, 75.

Melcher, J. R. (1981). *Continuum Electromechanics*. MIT Press, Cambridge, Mass.

Melcher, J. R., and G. I. Taylor (1969). Electrohydrodynamics: a review of the role of interfacial shear stresses. *Annual Review of Fluid Mechanics*, 1, 111.

Oliveri, S., and P. Atten (1986). The linear stability of a spherical liquid layer subjected to unipolar charge injection. *Phys. Fluids*, 29, 1378.

Perez, A. T., P. Atten, B. Malraison, L. Elouadie, and F. M. J. McCluskey (1988). Heat transfer augmentation induced by electrically generated convection in liquids. In *Experimental Heat Transfer, Fluid Mechanics and Thermodynamics* (R. K. Shah, E. N. Ganic, and K. T. Yang, eds.). Elsevier, p. 941.

Pohl, H. A. (1978). *Dielectrophoresis*, Cambridge University Press.

Schneider, J. M., and P. K. Watson (1970). Electrohydrodynamic stability of space-charge-limited currents in dielectric liquids. I. Theoretical study. *Phys. Fluids*, 19, 1948.

Takashima, T., R. Hanaoka, R. Ishibashi, and A. Ohtsubo (1988). I-V characteristics and liquid motion in needle-to-plane and razor blade-to-plane configurations in transformer oil and liquid nitrogen. *IEEE Trans. Electr. Ins.*, EI23, 645.

Tobazéon, R. (1984). Electrohydrodynamic instabilities and electroconvection in the transient and A.C. regimes of unipolar injection in insulating liquids: a review. *J. Electrostatics*, 15, 359.

Turner, J. S. (1973). *Buoyancy Effects in Fluids*. Cambridge Monographs on Mechanics and Applied Mathematics. Cambridge University Press, p. 165.

Watson, P. K., J. M. Schneider, and H. R. Till (1970). Electrohydrodynamic stability of space charge limited currents in dielectric liquids. II. Experimental study. *Phys. Fluids*, 13, 1955.

Yamamoto, T., and H. R. Velkoff (1981). Electrohydrodynamics in an electrostatic precipitator. *J. Fluid Mech.*, 108, 1.

9

Gas Discharge Phenomena

T.G. Beuthe and Jen-Shih Chang

McMaster University
Hamilton, Ontario, Canada

I. TYPES OF GAS DISCHARGES

Crookes (1879) first suggested that the ionized state of gases should be considered a fourth state of matter, and the term "plasma" was first used in the open literature by Langmuir (1929) to describe the state of ionized gases in discharge tubes. Since then, plasmas have become increasingly important for various industrial applications, since they represent the source of highest continuously maintainable temperature.

A plasma is defined as the ionized state of matter, consisting of a quasi-neutral mixture of neutral particles, positive ions, negative ions, and electrons with an average thermal energy typically exceeding 0.5 eV (1 eV = 11,500K). Plasmas may be in a state of thermal equilibrium in which the gas temperature T_g is equal to the electron temperature T_e, but in the plasmas generated via corona and spark and glow discharges, the electron temperature is greater than the gas temperature ($T_e \gg T_g$).

The object of this chapter is to provide a brief overview of the fundamental aspects governing plasmas found in gas discharges, with particular emphasis on glow, arc, corona, and spark discharges. Gas discharge phenomena can generally be divided into those that occur at low pressures ($\leq$100 torr) such as glow discharges and those that occur at high pressure ($\geq$760 torr) such as corona or spark discharges. Although arc discharges can occur under both low and high pressure conditions, they have been included under discharges that occur at high pressure in this case.

A. Low Pressure Gas Discharge

1. Glow Discharges

Glow discharges typically occur under low to medium gas pressure conditions (typically 10^{-3}–75 torr) and distinguish themselves primarily by their relatively small discharge currents (0.1–100 mA) and high applied voltages (typically 0.5–20 kV).

Glow discharges can be produced by high voltage dc, RF, or microwave applied electric fields. The electric field applies a force to the electrons in the gas (which are either emitted by the cathode in the case of the dc discharge or can be initially injected by a starter electrode typically through the use of a Tesla coil in an RF discharge), and if the ratio of the electric field to the pressure in the system E/p is high enough, the electrons will be able to gain enough energy between collisions to ionize the gas molecules.

A typical dc glow discharge in a tube with plane electrodes, a large electrode gap, and a relatively small diameter is shown in Fig. 1. As indicated, the dc glow discharge is characterized by several diffuse luminous zones. The relative sizes of these zones varies with pressure and interelectrode distance. Increasing the pressure tends to decrease the length of the

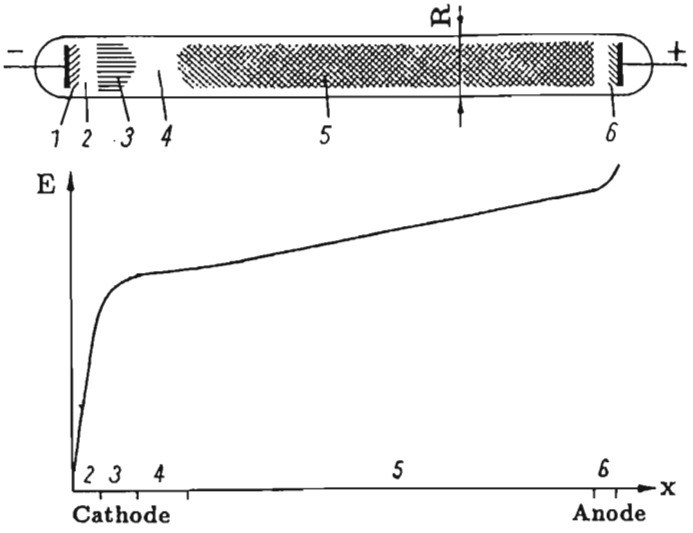


Figure 1 Typical glow discharge. 1, cathode sheath; 2, crookes or cathode dark space; 3, negative glow; 4, Faraday dark space; 5, positive column; 6, anode sheath.

negative glow and the Faraday dark space and increase the size of the positive column. Increasing the interelectrode distance tends to increase the length of the positive column but does not significantly affect the length of the negative glow or the Faraday dark space. The potential drop across the region immediately adjacent to the cathode often makes up the major part of the applied voltage as shown. Aside from the cathode region, the space charge is essentially zero over the entire length of the discharge, and the gas is in the form of a plasma.

When a high frequency RF or microwave electric field is used to produce a glow discharge, the electrons tend to oscillate in the applied field and ionize the gas molecules via electron impact ionization. In this case, the high frequency applied electric field can only penetrate to a certain depth into the plasma gas. As a result, the temperature profiles of an RF or microwave discharge can exhibit off-axis maxima, as shown in Fig. 2.

Glow discharges typically have high electron temperatures (1–5 eV) and low gas temperatures (300–500K). The generated electrons tend to cause a relatively low degree of ionization ($\sim 10^{-6}$ is typical) in the gas, and the charged particle density is typically of the order of 10^{6}–10^{13} cm^{-3}, as summarized in Figs. 6 and 7.

B. High Pressure Gas Discharge

1. Arc Plasmas

Arc plasmas represent a continuous source of high temperature thermal plasma (Davy, 1809) and constitute by far the most important industrial source of high temperature thermal plasmas today. As the name implies, arc plasmas are generated in an electrical arc struck between two electrodes. It is generally agreed that the arc should be defined only in terms of its current and voltage drops. Arc currents typically extend from a lower limit on the order of 0.1 to 1 A to a very large ($\geq$10,000 A) but unspecified upper limit. The voltage drop between the electrodes is typically in the range of a few volts to a few tens of volts. The applied voltage can be direct, alternating (typically 50–60 Hz), or transient.

The electrons emitted from the cathode region of the arc are accelerated toward the anode under the influence of the applied electric field. In the process, they transfer their kinetic energy through collisions with the intervening gaseous atoms and molecules. The arc plasma is formed primarily through electron impact ionizations and through thermal impact ionization reactions of the gaseous atoms and molecules with each other.

Although arcs can be struck at high pressures ($p \geq 7600$ torr or 10 atm), low pressures ($p \leq 10$ torr), or even under vacuum conditions ($p \leq 10^{-3}$ torr), most practical applications utilize arcs operated under atmo-

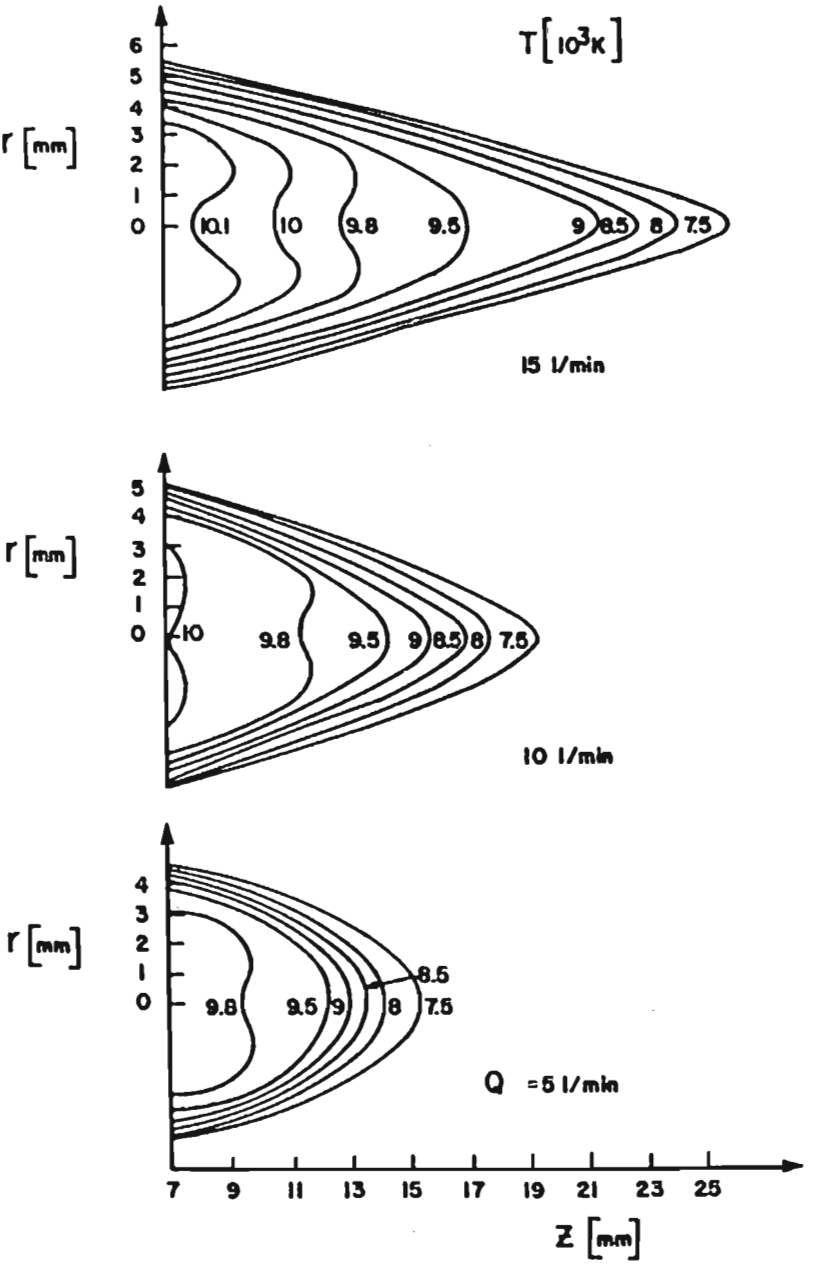


Figure 2 Temperature map in the exit jet of an induction plasma at different total plasma gas flow rates (gas, argon; diam., 14 mm; f = 17 MHz; power = 6 to 8 kW). (From Donskoi, 1977.)

spheric or reduced pressure conditions (p = 10–760 torr). In many cases, the arc plasma is assumed to be at close to local thermodynamic equilibrium conditions ($T_e = T_i = T_g$). Although there may be some validity to this assumption in the case of high pressure (Eddy and Sedghinasab, 1988) or high current (Uhlenbusch and Fischer, 1971) arcs, recent studies seem to indicate that thermal arc plasmas are not in thermal equilibrium under reduced pressures and low currents (Shindo, Inaba, and Imazu, 1980) or even at atmospheric pressure conditions (Gleizes et al., 1982). Typical temperature profiles observed in a free-burning arc are shown in Fig. 3. As can be seen from this figure, the hottest temperature occurs at the center of the discharge, close to the cathode tip. The point-to-plane geometry shown in Fig. 3 is typically used in welding applications and metallurgi-

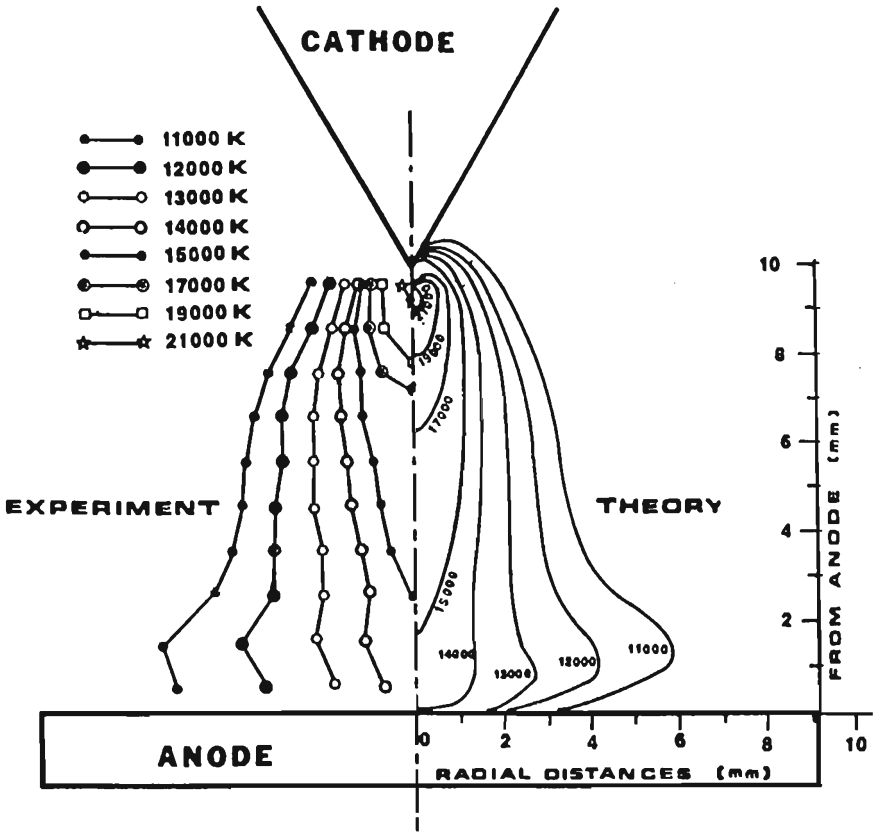


Figure 3 Calculated and measured isotherms of a free-burning argon arc (I = 200 A; p = 760 torr). (From Hsu, Etemadi, and Pfender, 1983.)

cal furnaces. It is referred to as a transferred arc since the anode is also the piece that is heated by the action of the arc. Gas and electron temperatures in a plasma arc can be as high as 25,000K, and electron densities are typically in the range of 10^{15}–10^{17} cm^{-3}, as summarized in Figs. 6 and 7.

2. Corona Discharges

Corona discharges are relatively low power electrical discharges that take place at or near atmospheric pressure. The corona is invariably generated by strong electric fields using small diameter wires, needles, or sharp edges on an electrode. Corona takes its name ("crown") from mariners' observations of discharges from their ships' masts during electrical storms. The corona appears as a faint filamentary discharge radiating outward from the discharge electrode.

Corona discharges exist in several forms, depending on the polarity of the field and the geometrical configuration of the electrodes. For positive corona in the needle-plate electrode configuration, discharges start with the burst pulse corona and proceed to the streamer corona, glow corona, and spark discharge as the applied voltage increases as shown in Fig. 4. For negative corona in the same geometry, the initial form of discharge will be the Trichel pulse corona, followed by the pulseless corona and spark discharge as the applied voltage increases. For wire-pipe or wire-plate electrode configurations, the corona generated at a positive wire electrode may appear as a tight sheath around the electrode or as a streamer moving away from the electrode. Corona generated at negative electrodes may take the form of a general rapidly moving glow, or it may be concentrated into small active spots called "tufts" or "beads."

The positive sheath form of corona discharge is known as Hermstein's glow (Hermstein, 1960) and is similar to the discharge (at lower pressures) found in a Geiger tube. It is characterized by a steady current at a fixed voltage, quiet operation, and almost no sparking. In the streamer corona, the discharge is confined to a narrow channel that originates at the electrode. It produces an unsteady current (because the streamer is repetitive), is quite noisy, and is the direct precursor to a spark. Once streamers form at an electrode, the sparking potential has almost been reached.

A negative glow usually requires clean, smooth electrodes to form. The glow is made up of individual electron avalanches that trigger successive avalanches at nearby locations. The total current from the electrode is steady, but it is composed of many tiny pulses. The discharge is noisy and the sparking potential is high compared with the positive streamer corona. The glow often changes with time into the tuft form, a process associated with the formation of more efficient mechanisms of generating

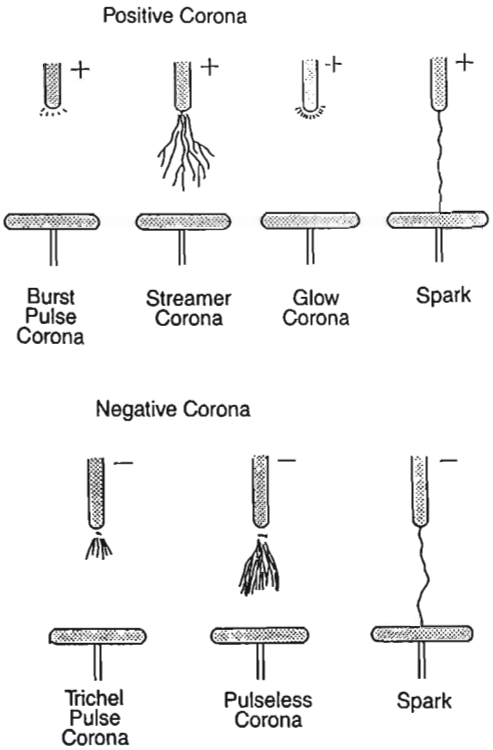


Figure 4 Schematic of type of corona discharges.

successive avalanches. The tuft corona is also noisy and has a similar sparking potential to the glow form. The average current is steady but is composed of tiny pulses like the glow corona. The tuft corona is more spatially inhomogeneous than the glow corona. Differences between negative tuft and glow coronas have been investigated recently (Lawless et al., 1986; McLean et al., 1986).

A corona discharge is usually space charge limited in magnitude, since the plasma emits ions of one polarity that accumulate in the interelectrode space. This gives the corona a positive resistance characteristic: increases in current require higher voltages to drive them. If the current in the discharge is raised sufficiently, additional current-carrying species will be produced and spark discharges will result. A spark is usually characterized by a negative resistance characteristic, but the transition from corona discharge to spark discharge is not sharply defined.

The corona is sustained by the electron energies gained from the high electric fields near the electrode over the short mean free path in the gas of about 10^{-7} m. The threshold for corona generation is determined by the criterion that each avalanche must generate enough secondary electrons from the process to ensure the development of later generations. Once the corona is started, the accumulation of positive ions near the electrode increases the space charge component of the field greatly, to the point that the generation is dominated by the space charge.

A positive streamer forms when the positive ion density is large enough to extend the region of corona initiation into the interelectrode gap. The process then builds by photoionization, with the positive ion head moving in front of a nearly neutral column. This process results in a positive streamer corona in an active volume much greater than the other forms, which are confined by their generation mechanisms to the near-electrode regions.

A schematic of the single streamer charge distribution is shown in Fig. 5 for a point-to-plane corona in dry atmospheric air. The time and size scales of the streamer corona are listed in Table 1. As shown in Fig. 5, the size of the plasma is approximately 10 cm long and 20μm wide and is relatively dense (up to 10^9 cm^{-3}). A streamer corona is a relatively low temperature plasma, with ion/neutral temperatures on the order of 1000K (Chang and Maezono, 1988) Therefore once the streamer corona is formed in a closed chamber, a low temperature dense plasma environment can be generated over a large volume. It is, however, transient in nature.

3. Spark Discharges

The continuity of arc or glow discharges is guaranteed by the presence of an adequate source of current or high voltage. If the total energy available for a discharge is limited, for example by the presence of a large capacitor, the electrical discharge tends to manifest itself in the form of rapid impulse type filament discharges known as sparks, as shown in Fig. 4, at pressures above atmospheric pressure. The time and space dependent development of such a discharge represents a complex physical phenomena that depends on numerous parameters such as pressure (if above atmospheric), electrode geometry, and electrode gap. As explained in the previous section, sparks can be regarded as a natural extension of the corona discharge state, but a spark discharge propagates ions more intensely than does the streamer corona discharge. The core of the spark channel consists of a dense, high temperature plasma, and the total propagation of spark discharges usually changes with time. Therefore a spark

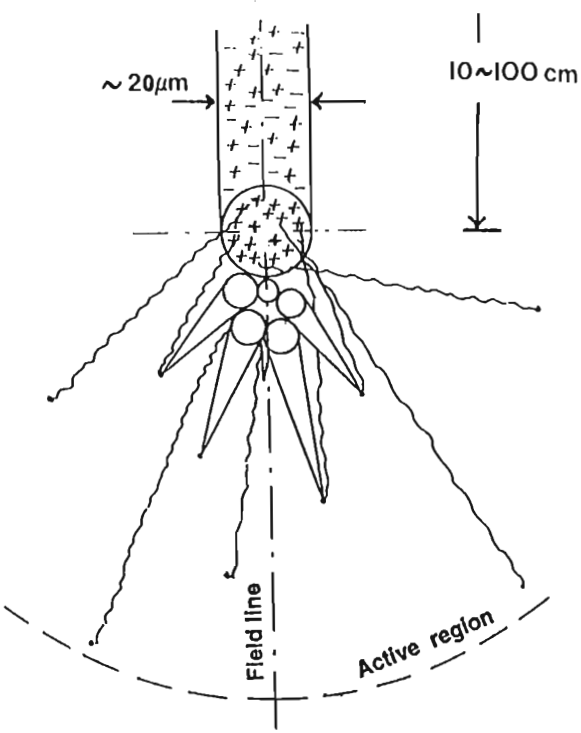


Figure 5 Schematic of streamer corona charge distributions.

Table 1 Time and Space Scales of Streamer Corona for a Gap from 1 to 100 cm

Streamer rise time	$\simeq$ 1 nsec
Streamer duration	$\simeq$ 1 μsec
Repetition period	$\simeq$ 1 nsec
Streamer diameter	$\simeq$ 20 μm
Electric field	$10^{-19} < E/N < 10^{-17}$ Vm^2
Ion temperature	$\simeq 10^3$ K

discharge induced plasma will occupy a smaller fraction of the total volume than that of a streamer corona induced plasma.

Sparks tend to generate nonlocal thermodynamic equilibrium plasmas in which the gas temperatures can be as high as 1000K, but the electron temperatures can be orders of magnitude larger. The electron density is estimated to be 10^{10}–10^{13} cm^{-3} (see Chapter 10).

C. Partial Discharges, or Silent Discharges

A silent discharge is generally used where the implementation of silent discharge corresponds to a capacitor that has two dielectrics between its plates: (1) the insulator and, connected in series with it, (2) air or oxygen. In a silent discharge, the discharge generated ions traverse the space in a pulse and are stored in the surface of the dielectric materials. Since these accumulated space charges generate a reverse electric field, the corona discharge will be terminated. Therefore it is possible to produce a sparkless high electron temperature/low gas temperature reactive plasma to enhance chemical reactions. A detailed discussion of this type of discharge will be give in Chapter 24.

D. Plasma Parameters in Gas Discharges

A summary of the typical gas and electron temperatures that can be expected in the plasmas discussed above has been outlined in Fig. 6. As shown here, arc and jet plasmas cover approximately the same electron and gas temperature region. Although arc plasmas and plasma jets can be generated intermittently, they are generally used as a continuous discharge. Spark plasmas are intermittent by nature, however. Glow discharges tend to have gas temperatures that range from room temperature to no more than a few hundred degrees above room temperature. Their electron temperatures are generally much higher then those generated by the other plasma generation mechanisms shown here.

Fig. 7 illustrates the observed electron density as a function of electron temperature for plasmas generated by various discharges. As shown in Fig. 7, arc and jet plasmas have the highest electron density. These discharges normally operate at atmospheric or reduced pressures, and the degree of ionization (charged particle density/total particle density) that can occur in arc generated plasmas can approach unity. Glow discharges operate under reduced pressure conditions that cause the electron density to be lower than that seen under arc or plasma jet conditions. The degree of ionization is also much lower.

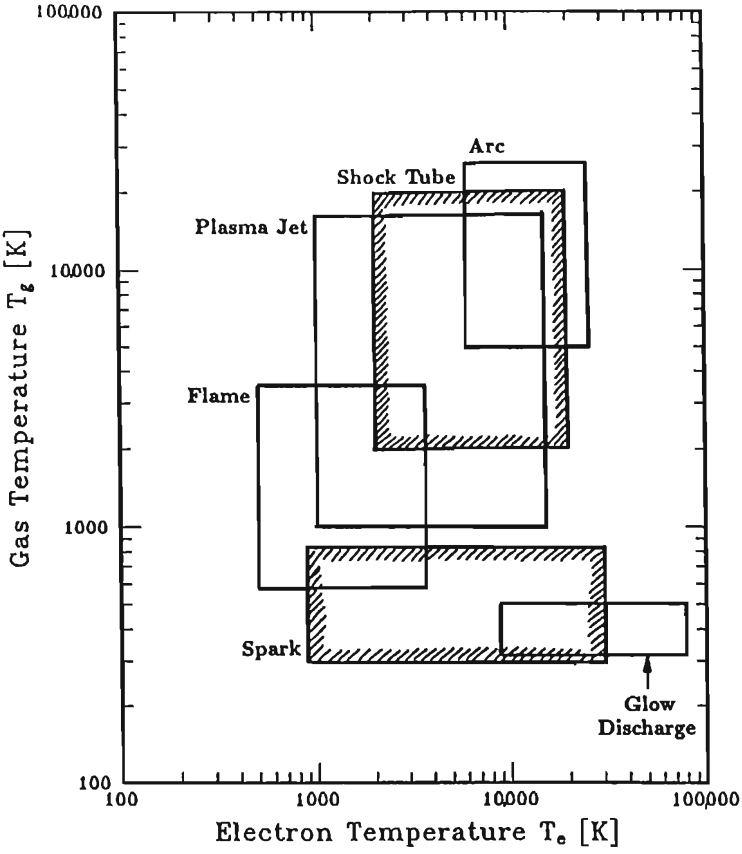


Figure 6 Range of electron and gas temperatures occurring in thermal plasmas.

II. ELEMENTARY PHENOMENA AND CONCEPTS

A. Atom Structure and Energy Levels

An atom is made up of two major parts: its nucleus, consisting of positively charged protons and neutral neutrons, and its electrons, which occupy the space surrounding the nucleus, much as the planets of the solar system are located relative to the sun. In the plasmas encountered in the electrical discharges discussed above, the behavior of the atom is essentially determined by the behavior of its electrons to various stimuli. The electrons have an energy that is a function of the temperature of the aggregate plasma in which the atom is located through the inelastic collisions occur-

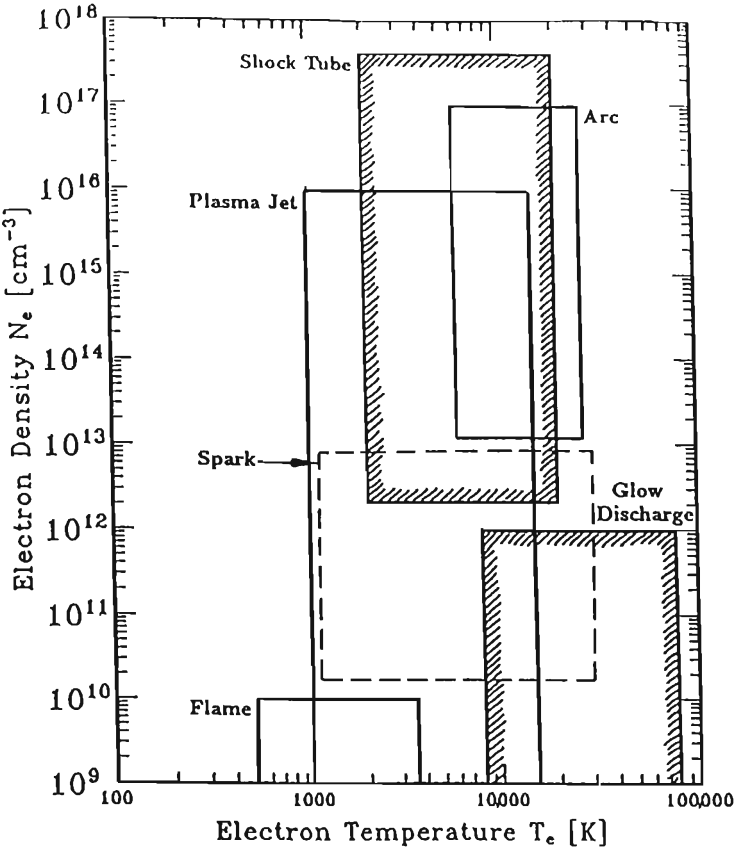


Figure 7 Range of electron densities as a function of electron temperatures occurring in thermal plasmas.

ring within the plasma, as well as a function of the energy of the photons $E = h\nu$ impinging on the atom.

Quantum mechanical principles require that the electrons surrounding the atomic core exist only at discrete energy levels as shown in Fig. 8 for a hydrogen atom. Only a finite number of electrons can exist at a given energy level, and each electron must have a unique state or set of quantum numbers in accordance with the Pauli exclusion principle.

As the energy level of an electron increases, the individual levels tend to be spaced closer together, until they reach the $n = \infty$ level. Here the energy of the electron is sufficiently large to liberate it from the atom.

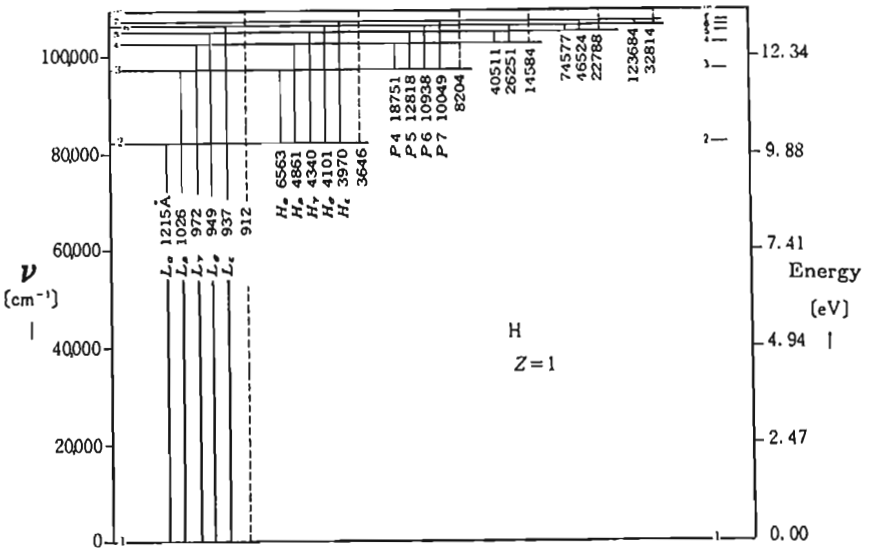


Figure 8 Electron energy levels in the hydrogen atom. (From Chang et al., 1984.)

Once free from the influence of the atom, the electron enters an energy continuum and is free to exist at any energy level.

The energy values $E_{Z,n}$ that an electron bound to a hydrogen nucleus may take can be written in the relatively simple form:

$$E_{Z,n} = hcZ^2R_H\left(1 - \frac{1}{n^2}\right) \tag{1}$$

where h is Planck's constant, c is the speed of light, Z represents the nuclear charge number, R_H is Rydberg's constant ($R_H = 109678\ \text{cm}^{-1}$), and n represents the principal quantum number. In addition to the principal quantum number, each electron also has a spin quantum number S associated with it, since the electron has the freedom to spin about its own axis. There are only two spin quantum numbers for a bound electron: $S = +\frac{1}{2}$ or spin up, and $S = -\frac{1}{2}$ or spin down.

B. Molecular Structure and Energy Levels

When atoms combine to form molecules or molecular ions, both the electrons and the behavior of the individual nuclei in the molecules influence

the energy levels that the molecules can attain. In general, the following modes of excitation are possible in molecules:

1. As in atoms, the individual electrons can be excited.
2. The nuclei of the molecules can vibrate with respect to each other.
3. The molecules can rotate about their own axes.
4. There may be energy levels caused by the torsional motion of the molecule.

As with the electron energy levels, all of these molecular energy levels occur at discrete levels, and there may be more than one axis of vibration, rotation, or torsion, as shown in Fig. 9.

C. Collision Phenomena and Gas Kinetics

Collisions between species are the most important aspect governing the behavior of a plasma. The neutral and ionic molecules and atoms within the plasma undergo various interactions with photons, electrons, or other neutral or charged atoms or molecules. In order to understand these interactions, it is necessary briefly to examine the laws that govern these processes. The usual concepts used to describe these interactions are based on the theory of gas kinetics. Although the results calculated using these concepts may not always agree well with experimental results, because the principles of quantum mechanics have not been rigorously applied, they are nonetheless helpful in providing a general picture of the nature and behavior of plasmas.

To begin with, a number of general and very simple conservation principles that govern all collisions can be applied. These are (a) the conservation of energy (kinetic, internal, photon), (b) the conservation of momentum, (c) the conservation of angular momentum, (d) the conservation of charge, and (e) the conservation of mass.

Over and above these conservation laws, it is useful to introduce the concepts of cross section and collision frequencies, mean free path, and total cross section.

1. Cross Section and Collision Frequencies

When a test particle is injected with velocity $\mathbf{v}$ into a gas, the probability that it will undergo a collision with one of the gas molecules $d\mathbf{w}$ can be expressed as

$$d\mathbf{w} = n \cdot \sigma(\mathbf{v}) \cdot dx \tag{2}$$

where n is the density of gas molecules, dx represents the distance the injected particle travels in the gas, and $\sigma(\mathbf{v})$ is known as the collision cross section, also known as the coefficient of proportionality. In general, $\sigma(\mathbf{v})$

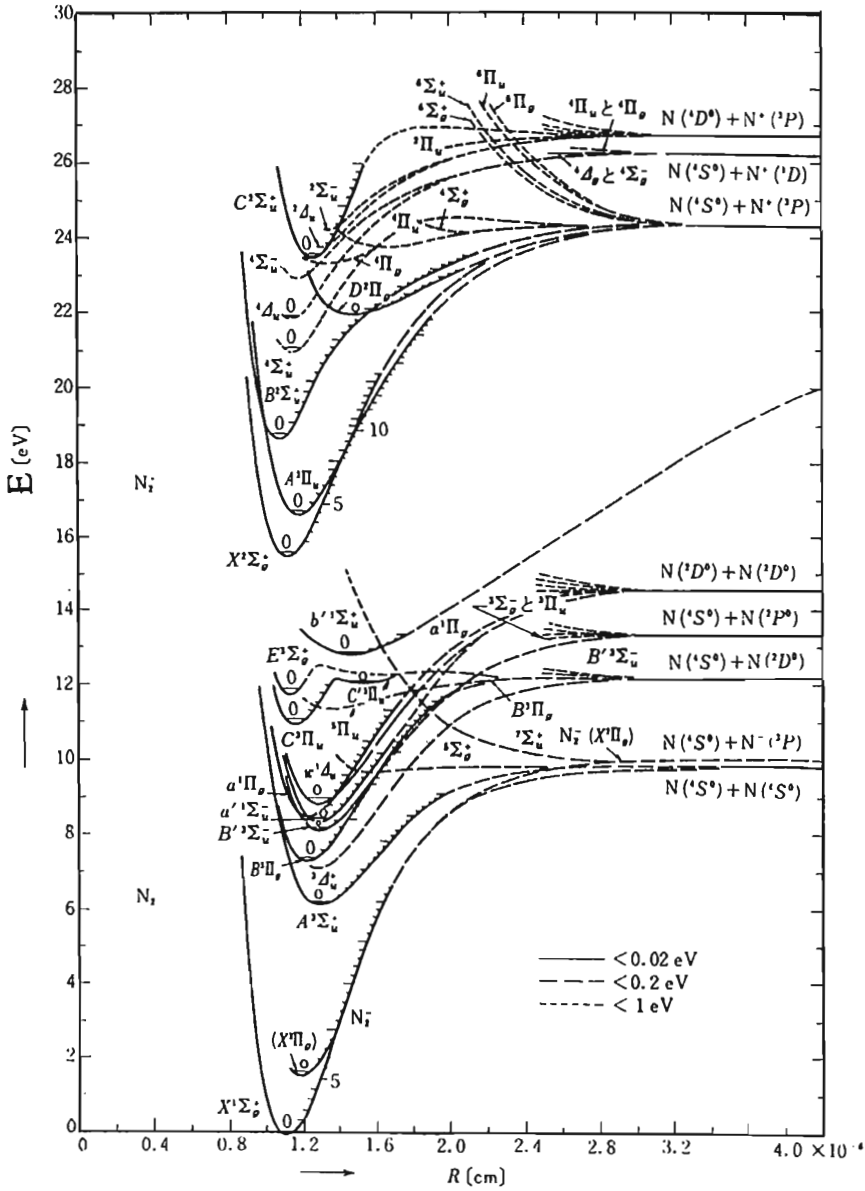


Figure 9 Energy levels in the nitrogen molecule. (From Chang et al., 1984.)

depends on the velocity, or, in other words, the temperature of the particle. Since the value of $\sigma(\mathbf{v})$ does not depend on the direction in which the particle is travelling within the gas, the collision probability remains constant the entire time the particle is travelling in the gas. As a consequence, if the velocity of the particle is constant, the number of collisions that the test particle will undergo in a time interval dt can be expressed as

$$n \cdot \sigma(\mathbf{v}) \cdot dx = n \cdot \sigma(\mathbf{v}) \cdot \mathbf{v} \cdot dt \tag{3}$$

Thus the collision frequency of the test particle per unit time ν becomes

$$\nu = n \cdot \mathbf{v} \cdot \sigma(\mathbf{v}) \tag{4}$$

if dt is large. It should be noted, however, that Eq. 4 is strictly valid only if σ is independent of $\mathbf{v}$.

2. Mean Free Path

The mean free path λ is defined as the average path a test particle travels between collisions. Assuming a constant velocity of the test particle of $\mathbf{v}$, it covers a distance of $\mathbf{v}\tau$ in time τ. During this time the particle undergoes $\nu\tau$ collisions, and therefore the average distance between collisions can be written as

$$\lambda = \frac{\mathbf{v}\tau}{\nu\tau} = \frac{1}{n \cdot \sigma(\mathbf{v})} \tag{5}$$

If the distribution of free paths is desired, consider a beam of N_0 test particles moving through a gas with a velocity $\mathbf{v}$. If $N(x)$ is defined as the number of particles that travel a distance x without undergoing a collision, then the number of particles that will undergo a collision between x and $x + dx$ and must consequently be removed from the beam is

$$dN = N(x) n \cdot \sigma \cdot dx \tag{6}$$

Hence

$$\frac{N(x)}{N_0} = e^{-n\sigma x} = e^{-x/\lambda} = P(x) \tag{7}$$

where $P(x)$ is defined as the probability of a free path exceeding the length of x. Different types of collisions that can occur in a discharge plasma include elastic as well as inelastic collisions.

3. Elastic Collisions

Elastic collisions are defined as collisions in which the total kinetic energy of the particles, and as a consequence also their internal energy, remains

unchanged. In a neutral gas at ambient temperature, almost all collisions are of this type, and in a plasma, a still significant fraction of the total number of collisions are elastic.

In elastic collisions, the fraction K of the energy transferred from a particle of mass m to a particle of mass M can be expressed as

$$K = \frac{2mM}{(m + M)^2} \tag{8}$$

In the case where $m \ll M$, such as an electron-atom collision,

$$K \simeq \frac{2m}{M} \tag{9}$$

The value of K reaches a maximum of $K \simeq \frac{1}{2}$ when $m \simeq M$, as would be the case when two atoms or molecules of the same species collide.

4. Inelastic Collisions

If two particles collide, and their internal energy as well as their kinetic energy changes, this is known as an inelastic collision. Inelastic collisions are of particular interest in plasmas and include processes such as vibrational, rotational, and electronic excitation, ionization, recombination, charge transfer, attachment, detachment, and dissociation. These will be discussed in more detail in Sec. IV below.

5. Total Cross Section

A collision between an incoming test particle and a gas molecule can cause any one of a number of different types of collisions as outlined above. For this reason, the total probability σ that any one of these collisions will occur is the sum of all the individual probabilities σ_i:

$$\sigma = \sigma_1 + \sigma_2 + \cdots + \sigma_n \tag{10}$$

Thus the probability of a particular collision p_i occurring is

$$p_i = \frac{\sigma_i}{\sigma} \tag{11}$$

The yield of a reaction Q_i is defined as the number of reactions that occur per unit length of flight of the test particle and can be expressed as

$$Q_i = n\sigma_i = \frac{1}{\lambda_i} \tag{12}$$

Q_i is also the effective cross section per unit volume at a fixed pressure and is usually quoted at a pressure of 1 torr (133 Pa).

The total cross section Q is defined as the sum of all cross sections for all types of reactions and thus can be written

$$Q = \sum Q_i \tag{13}$$

It should be noted that individual cross sections normally have a maximum at a certain relative velocity between the two interacting particles. If the relative velocity is smaller, the energy available is not enough to allow the reaction to occur. If the velocity is too great, the interaction time between particles is too short for a reaction to go forward. In general, two particles must approach within a few atomic radii of each other to react.

D. Maxwell-Boltzmann Distribution Function

The continuous movement of plasma particles and their collisions with each other lead to a most probable distribution of their random velocities v and translational kinetic energies $E = \frac{1}{2}mv^2$. The density dN of particles of any kind with velocities ranging from v to $v + dv$ can be written as

$$dN = Nf(v)dv \tag{14}$$

where N is the density of particles under consideration, and $f(v)$ is known as the Maxwell-Boltzmann distribution function. For particles in complete thermodynamic equilibrium, the principles of statistical mechanics lead to the following expression for $f(v)$:

$$f(v) = 4\pi v^2 \left(\frac{m}{2\pi kT}\right)^{3/2} \exp\left(-\frac{mv^2}{2kT}\right) \tag{15}$$

Here k is the Boltzmann constant, and m represents the particle mass.

Although the peak of the Maxwell-Boltzmann energy distribution function is normally much lower than the energies needed to cause inelastic collision reactions to take place in a plasma, the long, high energy tail of this function plays an important role, as will be seen in Sec. IV.

III. TRANSPORT EQUATIONS

A. Plasma and Sheath

As mentioned earlier, an idealized plasma consists of a quasineutral mixture of neutral particles, positive ions, negative ions, and electrons, that can be described by a single temperature. Such an idealized complete thermodynamic equilibrium plasma can only exist in an infinitely large space of uniform temperature in which there are no applied electric fields.

In reality, plasmas created via electrical discharges are maintained in relatively small volumes with cold walls, containing potentially large electric fields. The presence of an electric field tends to accelerate the charged particles, and the presence of the walls tends to create a plasma sheath.

The plasma sheath is a region near the containing walls in which charged particles recombine by collision with the walls. Since the electrons have a much larger mobility than the ions due to their relatively small mass in comparison with the heavy ions, they tend to recombine much faster at the walls. This creates a sheath region in which the plasma is no longer quasineutral due to the overabundance of positively charged ions near the wall. A further consequence of this sheath is appearance of a potential **V** due to Poisson's equation:

$$\nabla^2 \mathbf{V} = \frac{-e(N_i - N_e)}{\epsilon_0} \tag{16}$$

since $N_i \neq N_e$.

B. Transport Equations

In order to model a nonequilibrium plasma, it is necessary to solve the continuity equation in conjunction with the charged particle transport equation (Chang et al., 1984; McDaniel, 1969; Chang and Beuthe, 1992). The continuity equation states

$$\nabla \cdot \mathbf{J}_i = -\frac{d[N_i]}{dt} + source - sink \tag{17}$$

and the charged particle transport equation can be written

$$\mathbf{J}_i = N_i \mathbf{U}_g \pm \mu_i N_i \mathbf{E} - D_i \nabla N_i - G_i N_i \nabla T_g \tag{18}$$

where **J** is the particle flux density, N is the particle density, **E** is the electric field, D is the diffusion coefficient, **U** is the velocity, μ is the mobility, G is the thermophoresis coefficient, and T is the temperature. The subscripts i, and g refer to ions, and gas respectively. The sign of the mobility term is determined by the charge of the particle in question, + for positively charged particles and − for negatively charged particles.

In Eq. 17, $\nabla \cdot \mathbf{J}$ represents the net flow across a control volume, and $d[N]/dt$ represents the accumulation of the species within the control volume. The source and sink terms occur as a result of the chemical reactions occurring within the control volume. In Eq. 18, $N\mathbf{U}$ represents the particle flux due to charged particles transported by the convection of gas, $\mu N\mathbf{E}$ represents the flux due to the drift motion of charged particles under the

influence of an electric field, $D\nabla N$ represents the flux caused by diffusion, and $GN\nabla T$ represents the thermophoresis flux caused by spatial temperature inhomogeneities (Waldman and Schmitt, 1966).

Taking the scalar product $\nabla\cdot$ of each side of Eq. 18, the transport equation becomes

$$\nabla\cdot\mathbf{J}_i = \nabla\cdot(N_i\mathbf{U}_g) \pm \mu_i\nabla\cdot(N_i\mathbf{E}) - D_i\nabla^2 N_i - G_i\nabla\cdot(N_i\nabla T) \tag{19}$$

which can be substituted into Eq. 17 to yield

$$\frac{d[N_i]}{dt} = \text{source} - \text{sink} + \nabla\cdot(N_i\mathbf{U}_g) \pm \mu_i\nabla\cdot(N_i\mathbf{E}) - D_i\nabla^2 N_i - G_i\nabla\cdot(N_i\nabla T) \tag{20}$$

The overall species density can be calculated via the ideal gas law, and the concentration of electrons in the system can be calculated via the assumption of quasineutrality, which states that

$$[e] = [\text{positive ions}] - [\text{negative ions}] \tag{21}$$

where [] denotes the concentration of species in cm^{-3}.

C. Mobility

When subjected to an electric field E, the charged particles in a plasma acquire a constant drift velocity U in the direction of the field. The fact that this velocity is constant tends to indicate that the acceleration force provided by the electric field is being counterbalanced by the collisions that the charged particles undergo in the plasma. The mobility of a charged particle is defined as

$$\mu = \frac{\mathbf{U}}{\mathbf{E}} \tag{22}$$

Considering a heavy ion of mass m_i and charge e, the velocity U of the ion can be written as

$$\mathbf{U} = \frac{e\lambda}{m_i\bar{v}\cdot\sigma n}\mathbf{E} \tag{23}$$

$$= \text{const.}\frac{\mathbf{E}}{P} \tag{24}$$

where λ and $\bar{v}$ are the mean free path and the mean thermal velocity of the ion respectively. Of particular note in Eq. 24 is the parameter $\mathbf{E}/P$, which represents a measure of the energy gained by a charged particle between collisions. In general, this expression holds for a wide range of pressures and electric fields for ions. However, for electrons, the range is much narrower, as shown in Fig. 10.

At low pressures and/or high electric fields, Eq. 24 tends to show the limitations implicit in the assumptions used to derive it. In spite of these limitations, the value of $\mathbf{E}/P$ is often quoted in connection with electrical discharges, and a significant effort has been expended to explain the experimental results of mobility measurements in terms of the $\mathbf{E}/P$ parameter.

For gas mixtures, Blanc's law can be applied as follows:

$$\frac{1}{\mu_{AB}} = \frac{f_A}{\mu_A} + \frac{f_B}{\mu_B} \tag{25}$$

where μ_A, μ_B, and μ_{AB} represent the mobility of ion A, ion B, and the equivalent ion AB respectively, and N_A, N_B are the density of gases A and B respectively. The terms f_A and f_B are defined as

$$f_A = \frac{N_A}{N_A + N_B} \qquad f_B = \frac{N_B}{N_A + N_B} \tag{26}$$

D. Diffusion

Diffusion refers to the movement in a gas caused by an uneven spatial density distribution of the neutral and charged species making up the gas. This motion is purely thermal in origin and causes a flux of particles from points of high concentration to points of low concentration due to the collisions between the species. The velocity of diffusion can be expressed as

$$\mathbf{U} = -\frac{D}{N}\nabla N \tag{27}$$

where D is the diffusion coefficient in $\text{cm}^2\text{sec}^{-1}$ and N is the concentration of particles in cm^{-3}.

1. Diffusion of Charged Particles

Although the basic physical principles underlying the diffusion of charged particles in a plasma are essentially the same as those of the neutral species, there is an additional factor to consider due to the electrostatic interaction between charged and neutral particles.

In general, it can be stated that the diffusion of ions in their own gas is roughly four to five times smaller than neutral particles owing to the long-range electrostatic interactions between the ions and the neutral particles through induced electric dipoles. In the presence of a weak electric field, the diffusion coefficient D is related to mobility μ by Einstein's relationship:

$$\frac{D}{\mu} = \frac{kT}{e} \tag{28}$$

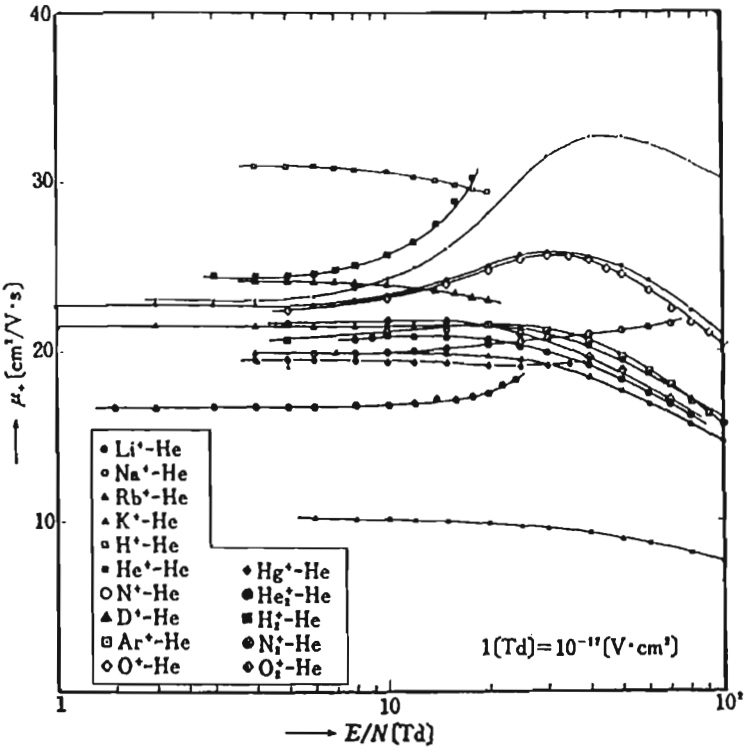


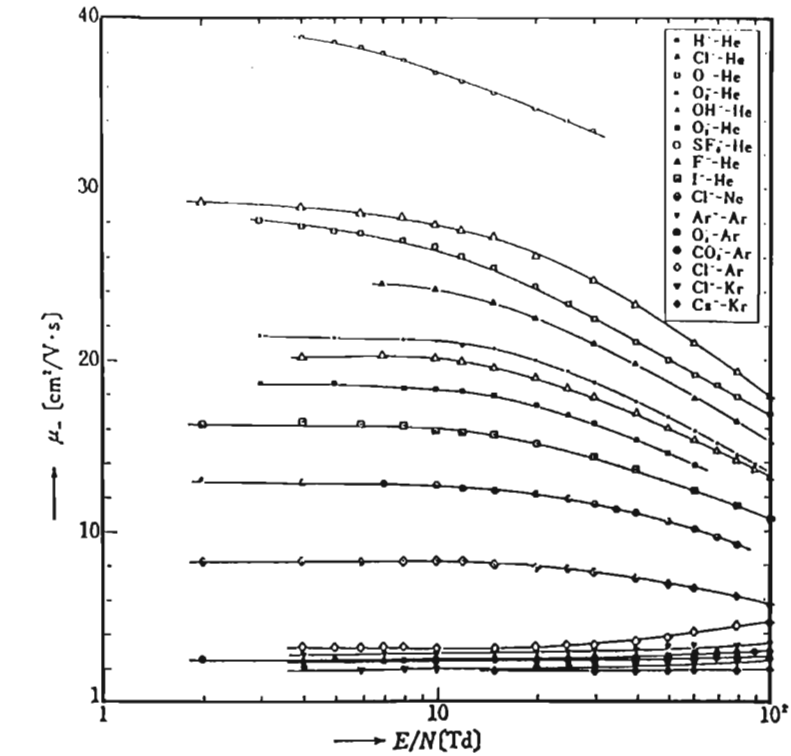
Figure 10 Ion mobilities and electron drift velocity. (From Chang et al., 1984.)

It should be noted, however, that Eq. 28 only holds as long as the field is not large enough to impart a velocity comparable to the thermal velocity of the plasma, and the tacit assumptions have been made that μ is independent of E and that the distribution of velocities is Maxwellian.

The diffusion coefficient of electrons in a neutral gas is several orders of magnitude greater than that of ions. Due to their light mass they have a greater velocity and mean free path.

2. Ambipolar Diffusion

In a plasma, where the concentration of positively and negatively charged species is roughly equal, if there were no interaction between the electrons and the ions, the electrons would rapidly diffuse away owing to their larger diffusion coefficient, leaving the ions and neutral species behind. This



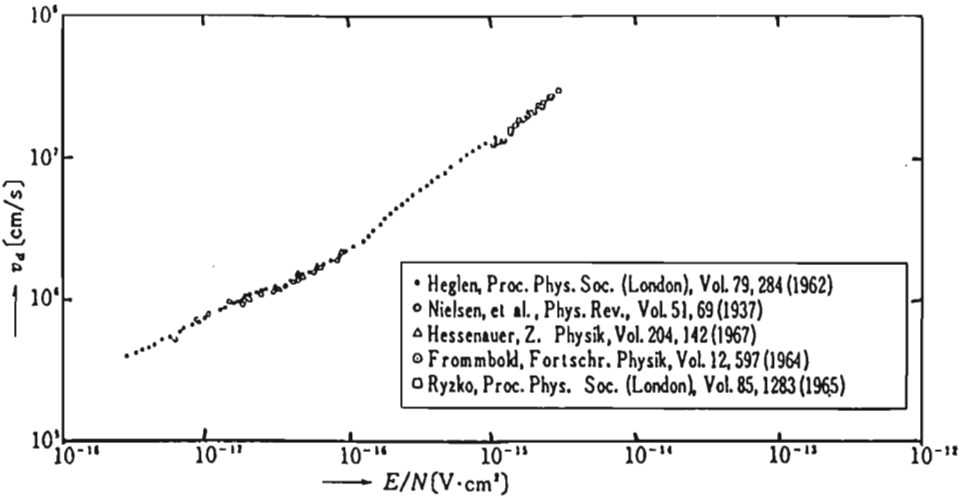


Figure 10 Continued.

does not occur, however, since the rapid diffusion of the electrons is counteracted by the electrostatic field $\mathbf{E}_s$ created between the electrons and their positively charged ionic counterparts. This field tends to retard the electrons and accelerate the ions, causing both eventually to move at the same speed. As a result, the flow $\mathbf{J} = N\mathbf{U}$ of both species is the same, and yields (von Engel, 1955)

$$\mathbf{J} = -D_a \nabla N \tag{29}$$

where D_a is called the ambipolar diffusion coefficient:

$$D_a = \frac{D_+\mu_- + D_-\mu_+}{\mu_- + \mu_+} \tag{30}$$

$$= \left(\frac{k}{e}\right)(T_e + T_i)\mu_+ \qquad \text{for} \quad \mu_- \gg \mu_+ \tag{31}$$

$$= \left(\frac{kT_e}{e}\right)\mu_+ \qquad \text{for} \quad T_e \gg T_i \tag{32}$$

$$= \left(\frac{kT_i}{e}\right)\mu_+ = 2D_+ \qquad \text{for} \quad T_e \simeq T_i \tag{33}$$

where T_e and T_i are the electron and ion temperatures respectively. It should be noted that Eq. 30 is valid only if the densities of charged particles are large enough that small movements of ionized species create a sufficiently large electric field that the quasineutrality condition $N_+ = N_- = N$ is not significantly disturbed. Typical observed ambipolar diffusion coefficients have been listed in Table 2.

E. Chemical Reactions and Reaction Rates

As mentioned earlier, the source and sink terms of species referred to in Eq. 20 are determined by the rate of the chemical reactions occurring within the thermal plasma. In general, such reactions can take the form of two- or three-body collision reactions. In the case of two-body collision reactions,

$$\mathrm{A} + \mathrm{B} \xrightarrow{k_2} \mathrm{C} + \mathrm{D}(+\mathrm{E} + \mathrm{F}) \tag{34}$$

the rate of decrease of concentration of species A or B can be expressed as

$$\frac{d[\mathrm{X}]}{dt} = -k_2[\mathrm{A}][\mathrm{B}] \tag{35}$$

Table 2 Ambipolar Diffusion Coefficients

Species	$D_a p$[cm²/s·torr]
He—He^+	560
He—Ar^+	905
He—Hg^+	790
He—He_2^+	697 ± 9
He—N_2^+	900
Ne—Ne^+	115
Ne—Ne_2^+	450
Ne—O_2^+	450
Ar—Ar^+	150
Ar—Ar_2^+	69
H_2—H^+	700
H_2—H_2^+	600
N_2—N_2^+	150
N_2—N_4^+	150 ± 5
Hg—Hg^+	10.8
O_2—O_2^+	110 ± 10
O_2—O_3^+	216 ± 20

and the rate of increase of species C or D (as well as E and F) can be expressed as

$$\frac{d[X]}{dt} = k_2[A][B] \tag{36}$$

where [X] represents the concentration of A or B in Eq. 35 and the concentration of C, D, E, or F in Eq. 36, and k_2 represents the two-body reaction rate coefficient with units of cm³/s.

In the case of three-body collision reactions,

$$A + B + M \xrightarrow{k_3} C + D(+E + F) + M \tag{37}$$

M acts as an intermediary to facilitate the reaction. The rate of decrease of concentration of species A or B can be expressed as

$$\frac{d[X]}{dt} = -k_3[A][B][M] \tag{38}$$

and the rate of increase of species C or D (as well as E and F) can be expressed as

$$\frac{d[X]}{dt} = k_3[A][B][M] \tag{39}$$

where [X] has the same meaning as in Eqs. 35 and 36 and k_3 represents the three-body reaction rate coefficient with units of cm^6/s.

Plasmas represent a system in which a large number of elementary processes involving the exchange and transmission of energy and particles between electrons, ions (both positive and negative), atoms, and molecules (including radicals) take place. The chemical reactions leading to the source and sink terms in Eq. 20 represent one of the most interesting and at the same time most complex areas of plasmas. Listed below are some of the more important collision processes that take place under corona discharge conditions.

As indicated earlier, the values of the reaction rate coefficients k are normally tabulated directly in units of cm^3/s for two-body reactions and in units of cm^6/s for three-body reactions. In some cases, however, only the collision cross sections are available. In this case, the value of the reaction rate coefficients can be derived from the collision cross sections via the relationship (Chang et al., 1984)

$$k = \int_0^\infty \sigma(v) v f(v)\, dv \tag{40}$$

where v represents the velocity or energy of the colliding species, N the density, σ the collision cross section, and $f(v)$ the energy distribution.

In cases where the mean energy of the colliding species is large, Eq. 40 would have to be solved by integrating over the entire cross section. However, in cases where the mean energy of the colliding species is small (a few eV), the solution of Eq. 40 can be greatly simplified. Assuming a Maxwellian energy distribution in the plasma particles (see Eq. 15) and assuming that the reaction cross section σ can be approximated by a linear function $C(E - E_{th})$ as shown in Fig. 11, Eq. 40 simplifies to (Chang et al., 1984)

$$k = 100C\left(\frac{8e}{\pi m_{coll}}\right)^{1/2} E_{th}^{3/2}\left(\frac{kT_{coll}}{eE_{th}}\right)^{1/2}\left(\frac{1 + 2kT_{coll}}{eE_{th}}\right)\exp\left(\frac{-eE_{th}}{kT_{coll}}\right) \tag{41}$$

where C is the linear slope of the collision cross section in the threshold region as shown in Fig. 11 in cm^2/eV, E_{th} is the threshold energy of the collision cross section as shown in Fig. 11 in eV, e is the electron charge ($1.602 \times 10^{-19}\ C$), k is Boltzmann's constant ($8.6184 \times 10^{-5}\ eV/K$), m_{coll} is the mass of the colliding species in kg, and T_{coll} is the temperature of the colliding species in eV.

IV. TYPES OF CHEMICAL REACTIONS

A large variety of chemical reactions can occur within an ionized gas involving atomic species, radical species, complex molecular species, as

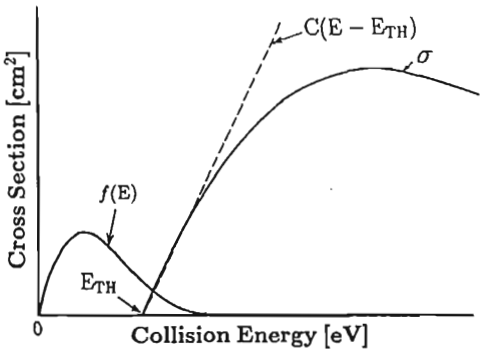


Figure 11 Typical collision cross section σ and Maxwellian energy distribution $f(E)$ of particles in an ionized gas.

well as electrons and ions. Radical species and more complex molecules may be generated through ionic or electronic processes. Since two-body reactions involving electrons or ions can be 10 to 10^8 times larger than reactions involving purely neutral species, as shown in Table 3, the effective production or loss rate of species caused by these ionic reactions can become comparable with neutral reactions even though the density of ions is much less than the density of neutral species (Chang et al., 1991). As shown below, the typical rate equations for neutral and ionic reactions can be written as

$$\frac{dN}{dt} = k_1[A][B] + k_2[C^+][B] - \cdots \tag{42}$$

where

$$A + B \xrightarrow{k_1} N + M \tag{43}$$

and

$$C^+ + B \xrightarrow{k_2} N + L \tag{44}$$

However,

$$[A] \gg [C^+]; \qquad k_1 \ll k_2 \tag{45}$$

Thus

$$k_1[A] \approx k_2[C^+] \tag{46}$$

Table 3 Typical Order of Magnitude of Various Chemical Reaction Rates (20°C)

Reactions	k(cm^3/s)
Ion molecule	$10^{-12} \sim 10^{-9}$
$H_2^+ + H_2 \rightarrow H_3^+ + H$	2.0×10^{-9}
$H_2O^+ + H_2O \rightarrow H_3O^+ + OH$	1.3×10^{-9}
$Ar^+ + H_2 \rightarrow ArH^+ + H$	3.5×10^{-10}
$NH_3^+ + H_2 \rightarrow NH_4^+ + H$	4.0×10^{-13}
$O^+ + O_2 \rightarrow O_2^+ + O$	4.0×10^{-11}
Atomic or radical	$10^{-23} \sim 10^{-11}$
$C_2H_5 + C_2H_5 \rightarrow C_4H_{10}$	2.7×10^{-11}
$O + NO_2 \rightarrow NO + O_2$	2.5×10^{-12}
$O + O_3 \rightarrow 2O_2$	2.5×10^{-14}
$H + H_2 \rightarrow H_2 + H$	7×10^{-17}
$CH_3 + C_2H_6 \rightarrow CH_4 + C_2H_5$	8×10^{-22}
$Br + H_2 \rightarrow HBr + H$	8×10^{-24}
Molecule	$10^{-31} \sim 10^{-14}$
$NO + O_3 \rightarrow NO_2 + O_2$	2×10^{-14}
$HI + C_2H_5I \rightarrow C_2H_6 + I_2$	1.6×10^{-23}
$2NO_2 \rightarrow 2NO + O_2$	1.6×10^{-31}
Ions in liquids	$10^{-22} \sim 10^{-11}$
$e^-(aq) + H^+ \rightarrow H$	4×10^{-11}
$CO_2 + OH^- \rightarrow HCO_3^-$	7×10^{-19}
$CH_3COOC_2H_5 + CH^- \rightarrow CH_3COO^- + C_2H_5CH$	1.6×10^{-22}
Ion-electron	$10^{-7} \sim 10^{-6}$
$e + NH_4^+ \rightarrow H_2 + NH_2$	1.5×10^{-6}
$e + H_3^+ \rightarrow H_2 + H$	2.3×10^{-7}
Electron-molecule	$10^{-11} \sim 10^{-7}$
$e + O_3 \rightarrow O^- + O_2$	1×10^{-11}
$e + HI \rightarrow I^- + H$	9.6×10^{-8}
Positive-negative ion	$10^{-7} \sim 10^{-5}$
$H^+ + H^- \rightarrow H_2 + \phi$	4×10^{-7}
$NO^+ + NO_2^- \rightarrow$ products	6.4×10^{-6}

Therefore ionic reactions may play an important role in discharge chemistry. The following discussion will confine itself to the discussion of the chemical reactions caused by inelastic collisions.

A. Neutral Reactions

Neutral reactions between atomic and molecular species play an important role in the determination of neutral species density. Atomic and molecular

collisions tend to dominate the behavior of the ionized gas in the lower gas temperature ranges. The neutral reactions of interest in ionized gases created via electrical discharges have been outlined in Table 4. These include:

1. Excitation reactions in which one of the colliding species is excited to another vibrational, rotational, or electronic state
2. Dissociation reactions in which a diatomic or polyatomic molecule is split into atoms or molecules
3. Recombination reactions in which atomic and/or molecular species combine to form more complex molecular species
4. Exchange reactions in which components of molecules are exchanged between reactants
5. Deexcitation reactions in which molecules or the walls of the vessel containing the plasma remove the excitation energy of atoms or molecules

B. Ionic Reactions

Ionic reactions tend to dominate the chemical kinetics of a thermal plasma at higher temperatures. However, significant concentrations of ionic species can also occur in the lower temperature regions.

Table 4 Neutral Reactions

(1) Excitation	
$A + B \rightarrow A^* + B$	thermal
$A^* + B \rightarrow A + B^*$	collision of the second kind
$h\nu + A \rightarrow A^*$	photon
(2) Dissociation	
$AB + h\nu \rightarrow A + B$	photon
$AB + M \rightarrow A + B + M$	diatomic thermal
$ABC + M \rightarrow AB + C + M$	triatomic thermal
(3) Recombination	
$A + B \rightarrow AB + h\nu$	radiative
$A + B + M \rightarrow AB + M$	diatomic molecular
$A + BC + M \rightarrow ABC + M$	triatomic molecular
(4) Exchange Reactions	
$A + BC \rightarrow AB + C$	
(5) Deexcitation by collision with wall	
$A^* + \text{wall} \rightarrow A + \text{wall}$	atomic
$A^{**} + \text{wall} \rightarrow AB + \text{wall}$	molecular

In general, the charged species can consist of atomic ions A^+, A^-, molecular ions AB^+, AB^-, ABC^+, ABC^-, etc., and electrons e. Ionic chemical reactions can be broadly classified into:

1. Those that act as sources of ions
2. Those that convert ions from one form into another
3. Those in which electrons act as intermediaries
4. Those that act as sinks of ions

1 Sources of Ions

As shown in Table 5, reactions that act as sources of ions can be classified into two general categories: (a) ionization reactions, which act as sources of positive ions, and (b) attachment reactions, which act as sources of negative ions.

Ionization. When an atom or molecule has absorbed enough energy (ionization energy) to allow one of its electrons to escape, the atom (or molecule) is said to have been ionized. Typical ionization energies of gaseous

Table 5 Sources of Ions

(a) Ionization	
(i) *Photoionization*	
$h\nu + A \rightarrow A^+ + e$	atomic
$h\nu + A^* \rightarrow A^+ + e$	from excited state
$h\nu + A^+ \rightarrow A^{2+} + e$	second ionization
$h\nu + AB \rightarrow AB^+ + e$	molecular
$\rightarrow A^+ + B + e$	dissociative
$h\nu + AB^* \rightarrow A^+ + B + e$	dissociative, from excited state
(ii) *Electron impact ionization*	
$e + A \rightarrow A^+ + e + e$	direct, atomic
$e + A^* \rightarrow A^+ + e + e$	from excited state
$e + A^{**} \rightarrow A^+ + e + e$	from metastable excited state
$e + A^+ \rightarrow A^{2+} + e + e$	second ionization
$e + AB \rightarrow AB^+ + e + e$	direct, molecular
$\rightarrow A^+ + B + e + e$	dissociative
$\rightarrow A^+ + B^- + e$	ion-pair formation
$e + AB \rightarrow A^+ + B^+ + e + e$	
$e + AB^* \rightarrow A^+ + B + e + e$	dissociative, from excited state
(iii) *Ion impact ionization*	
$A^+ + B \rightarrow A^+ + B^+ + e$	

(*continues*)

Table 5 (Continued)

(iv) *Thermal impact ionization*	
$A + B \rightarrow A^+ + B + e$	from the ground state
$\rightarrow A^+ + B^-$	by electron capture
$A^* + B \rightarrow A^+ + B + e$	from an excited state
$\rightarrow A^{2+} + B + e + e$	
$A^+ + B^+ \rightarrow A^{2+} + B^+ + e$	
$\rightarrow A^{2+} + B^+$	charge transfer
$A + B + C \rightarrow AB + C^+ + e$	
(v) *Ionization by excited or metastable particles*	
$A^* + B \rightarrow A + B^+ + e$	via excited state
$A^{**} + B \rightarrow A + B^+ + e$	Penning ionization
$\rightarrow (AB^*) \rightarrow AB^+ + e$	associative ionization
$A^{**} + B^{**} \rightarrow (AB^*) \rightarrow A^+ + B + e$	metastable-metastable
$\rightarrow (AB^*) \rightarrow AB^+ + e$	
(vi) *Autoionization*	
$A^* \rightarrow A^+ + e$	
(b) Attachment	
$e + A \rightarrow A^- + h\nu$	radiative, atomic
$e + A \rightarrow (A^{-*}) \rightarrow A^- + h\nu$	dielectronic
$e + AB \rightarrow AB^- + h\nu$	radiative, molecular
$\rightarrow A^- + B$	dissociative
$\rightarrow (AB^-)^* \xrightarrow{M} AB^-$	collisional stabilization
$e + A + M \rightarrow A^- + M$	three body, atomic
$e + A + e \rightarrow A^- + e$	three body, atomic, via electron
$e + AB + M \rightarrow AB^- + M$	three body, molecular
$A^+ + B \rightarrow A^{2+} + B^-$	electron exchange

atoms are listed in Table 6. In the process of ionization, the internal energy of the particle has increased by the energy required to remove an electron. Ionization can occur by (i) photoionization, (ii) electron impact ionization, (iii) ion impact ionization, (iv) thermal impact ionization, or it can occur (v) via excited or metastable particles or (vi) via autoionization, as summarized in Table 5.

Photoionization. Here, the energy needed to cause ionization is provided by a photon of energy $E = h\nu$ via the photoelectric effect, where h is Planck's constant and ν is the frequency of incoming light. High

Table 6 Ionization Energy E_i[eV] of Gaseous Atomic Species. The Numbers 1, 2, 3, . . . indicate the Number of Electrons that Can Be Ionized by This Energy

	1	2	3	4	5	6	7	8
H	13.598							
He	24.587	54.416						
N	14.534	29.601	47.448	77.472	97.888	552.057	667.029	
O	13.618	35.116	54.934	54.934	77.412	113.896	138.116	739.315
Ne	21.564	40.962	63.45	97.11	126.21	157.93	207.27	239.09
Ar	15.759	27.629	40.74	59.81	75.02	91.007	124.319	143.456
Kr	13.999	24.359	36.95	52.5	64.7	78.5	111.0	126.
Xe	12.130	21.21	32.1					

energies are required to eject an electron, and thus the frequencies lie in the UV or x-ray regions of the electromagnetic spectrum. Photon interaction with a molecule can result in simple ionization or simultaneous ionization and dissociation of the molecule. Ionization can take place directly, or stepwise via excited states. The cross section for photoionization σ_i increases sharply from zero at the ionization energy of the atom or molecule to peak at a finite value on the order of $\sigma \approx 10^{-17}$ cm^2. Each successive ionization causes an additional peak in the cross section. At high energies, σ_i is very small.

Electron Impact Ionization. Electron impact ionization takes place in much the same way as photoionization. In this case, the incoming electron provides the energy needed to eject an electron from the target atom or molecule. The resulting reactions are generally analogous to those caused by photoionization, as shown in Table 5. The electron impact ionization cross section σ_i also increases rapidly once the ionization energy of the target atom or molecule has been exceeded. Typical ionization cross sections for atoms and molecules are shown in Figs. 12 and 13 respectively. For molecules, both direct and dissociative ionizations are possible:

$$AB + e \rightarrow AB^+ + 2e$$
$$\rightarrow A + B^+ + 2e$$

If the target atom or molecule has long-lived metastable excited states, the ionization efficiency is generally greater via a two-step process in which the particle is first excited and subsequently ionized:

$$A + e \rightarrow A^{**} + e$$
$$A^{**} + e \rightarrow A^+ + e + e$$

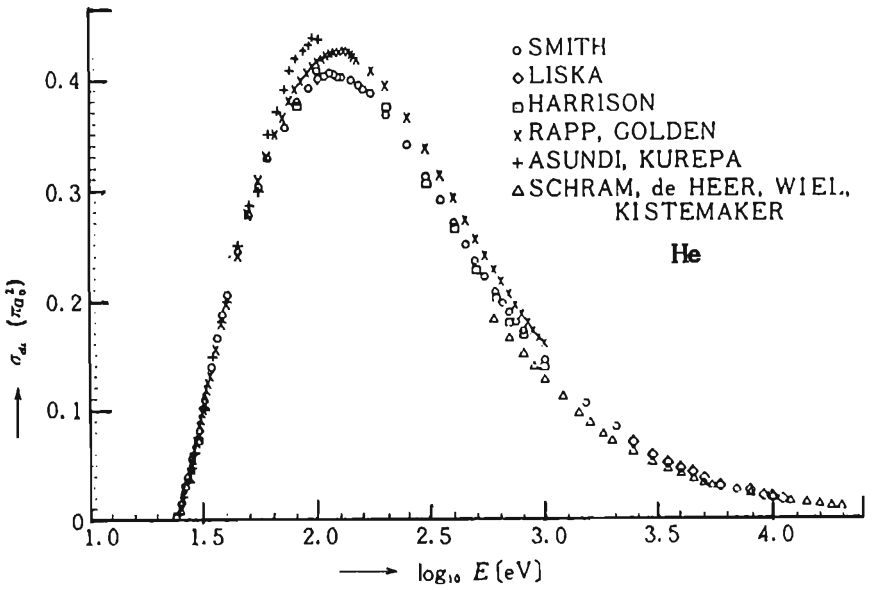


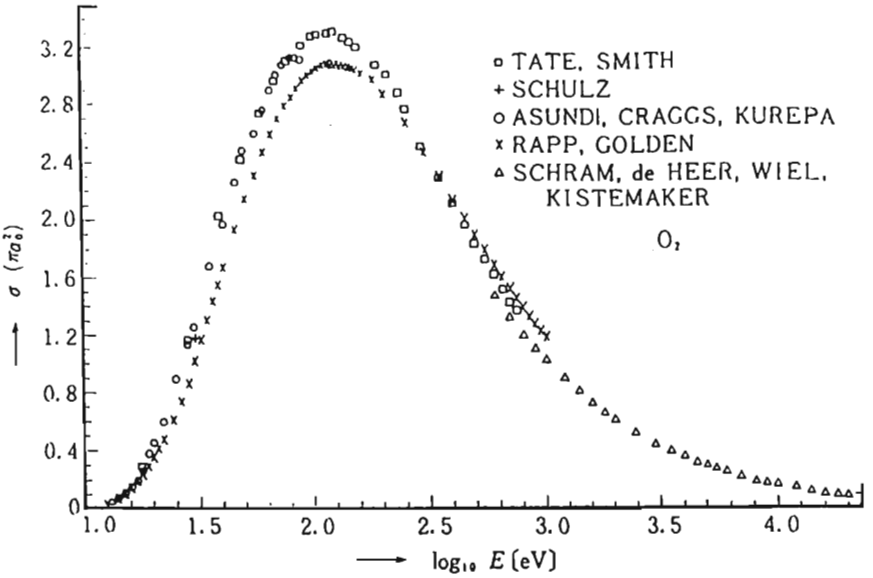
Figure 12 Electron impact ionization cross section for He. (From Chang et al., 1984.)

Ion Impact Ionization. It is possible to ionize an atom via impact with an ion. This type of reaction normally requires a great deal of energy on the part of the incoming ion and therefore occurs relatively infrequently in discharge plasmas.

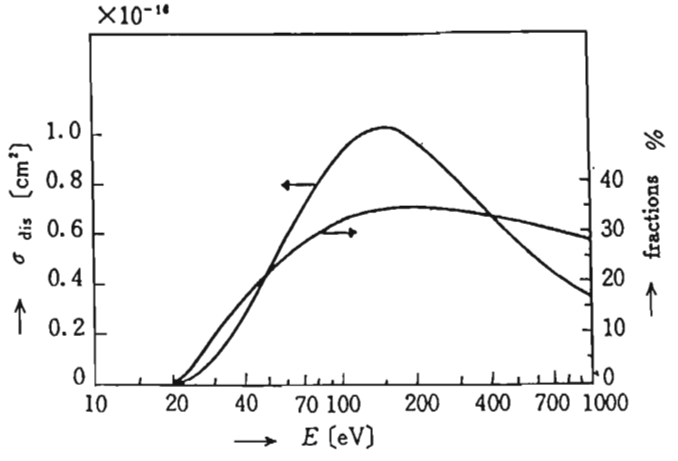
Thermal Impact Ionization. Since it is relatively difficult to accelerate a neutral atom or molecule to the energies needed to ionize other atoms or molecules, studies generally tend to concentrate more closely on the effects of photoionization or electron impact ionization. Thermal impact ionization reactions are of particular importance when describing the behavior of plasmas created via electric discharges such as arc discharges in which atomic, molecular, and ionic temperatures are large. Of the reactions shown in Table 5, McLaren and Hobson (1968) suggest that thermal ionization occurs most probably via the first excited state in a two-step process:

$$A + A \rightarrow A^* + A$$
$$A^* + A \rightarrow A^+ + A + e$$

Ionization by Excited or Metastable Particles. This class of ionization reactions is often also known as collisions of the second kind, or, in the



(a)



(b)

Figure 13 Electron impact ionization cross section for O_2. (a) Total ionization cross section; (b) dissociative ionization cross section and fractions. (From Chang et al., 1984.)

case where the excited state is metastable, as the Penning effect. Here the excitation energy of one particle is transferred to another. The excitation energy of the impacting particle can appear as kinetic energy, excitation energy, or it can cause the target particle to ionize. If ionization occurs, a large fraction of the excess energy is carried off by the ejected electron. In general, the largest cross sections for this class of reactions occur when the energy difference is small and the impact velocity is large. Typical metastable atoms and molecules are listed in Tables 7 and 8 respectively.

Table 7 Metastable Atoms

Atoms	Ground state	Metastable state	Potential energy [eV]	Life-time [s]
He	1^1S_0	2^3S_1	19.82	6×10^5
		2^1S_0	20.61	2×10^{-2}
Ne	2^1S_0	3^3P_2	16.62	> 0.8
		3^3P_0	16.72	> 0.8
Ar	3^1S_0	4^3P_2	11.55	> 1.3
		4^3P_0	11.72	> 1.3
Kr	4^1S_0	5^3P_2	9.92	> 1
		5^3P_0	10.56	> 1
Xe	5^1S_0	6^3P_2	8.32	?
		6^3P_0	9.45	?
H	$1^2S_{1/2}$	$2^2S_{1/2}$	10.20	1/7
Hg	6^1S_0	6^3P_0	4.66	?
		6^3P_2	5.43	?
N	$2^4S_{3/2}$	$2^2D_{5/2}$	2.38	6.3×10^4
		$2^2D_{3/2}$	2.38	1.4×10^5
		$2^2P_{3/2}$	3.58	13
		$2^2P_{1/2}$	3.58	13
O	$2^3P_{2,1,0}$	2^1D_2	1.96	1.1×10^2
		2^1S_0	4.17	7.8×10^{-1}
		3^5S_2	9.13	?

Table 8 Metastable Molecules

Molecules	Ground state	Metastable state	Potential energy [eV]	Life-time [s]
H_2	$^1\Sigma_g^+$	$c^3\prod_u$	11.75	$v = 0$; $\sim 10^{-3}$ $v > 0$; $\sim 10^{-4}$
O_2	$^3\Sigma_g^-$	$a\Delta_g$	0.98	2.7×10^3
		$b^1\Sigma_g^+$	1.63	7
		$C^3\Delta_u$	4.2	?
		$A^3\Sigma_u^+$	4.43	$\sim 10^3$
		$c^1\Sigma_u^-$	4.5	?
N_2	$^1\Sigma_g^+$	$A^3\Sigma_u^+$	6.17	1.3 ~ 2.6
		$W^3\Delta_u$ ($v = 0$)	7.32	?
		$a'^1\Sigma_u^-$	8.52	1.4
		$a^1\prod_g$	8.67	$\sim 10^{-4}$
		$w^1\Delta_u$	9.02	$\sim 10^{-4}$
		$E^3\Sigma_g^+$	11.88	1.9×10^{-4}

Autoionization. Autoionization occurs when an excited particle goes through a radiationless decay transition and ejects an electron as a consequence.

Attachment. Collisions of electrons with certain atoms and molecules can result in the creation of negatively charged heavy ions. As a general rule, atomic hydrogen, atomic oxygen, molecular oxygen, the halogens (fluorine, bromine, iodine, etc.), nitrous oxides, and large organic molecules readily form negative ions. The negative ions of nitrogen and rare gases (helium, neon, argon, krypton, xenon, etc.) have very short lifetimes, and thus these gases do not readily form negative ions. The bonding energy of the electron to the particle is known as the electron affinity. It can vary between 0.43 *e*V for oxygen to several electron volts for halogens.

Radiative Attachment. In the case of atoms or molecules, electron attachment can occur directly, with the excess energy of attachment being given off as a photon. This is known as radiative attachment. The reaction rate for such reactions is normally small ($k < 10^{-14}$ cm^3/s).

Dissociative Attachment. For molecules, electron attachment can occur in conjunction with the dissociation of the molecule, the excess energy being carried off as kinetic energy by one of the particles. Typical cross sections and rate constants at 300K are shown in Fig. 14 and Table 9 respectively. As illustrated in Fig. 14, the gas temperature has been shown to have a significant effect on dissociative attachment reactions due to vibrational excitation within the target molecule.

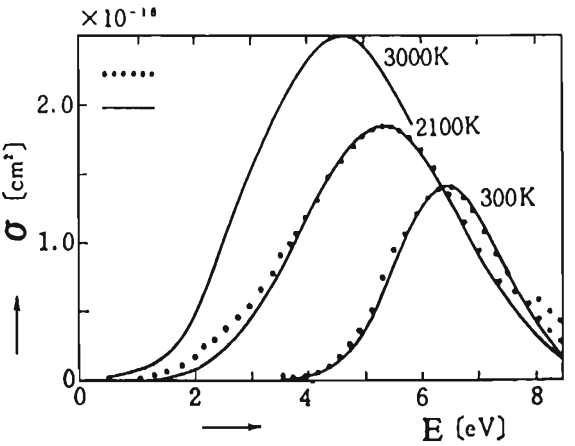


Figure 14 Dissociative attachment cross section for O_2 at various temperatures. (From Chang et al., 1984.)

Three-Body Attachment. At higher gas pressures, three-body attachment is the main source of negative ions. Reaction rates depend significantly on gas and electron temperatures as shown in Table 10.

2. Ion Interconversion Processes

Ion interconversion processes are reactions in which new ions are created via collisions involving other ions, but no free electrons are involved in the process. These processes can involve (a) ion-molecule reactions as well as (b) photodissociation reactions. As indicated in Table 12 by the ± sign, these reactions can involve either positive or negatively charged ions.

Ion-Molecule Reactions. Ion molecule reactions are very important to the behavior of plasmas created via electrical discharges. Ion-molecule reactions can include such reactions as (i) charge transfer, (ii) clustering, (iii) ion-atom interchange, and (iv) switching reactions. The reaction rate constants of these reactions are normally fairly independent of temperature, as shown in Fig. 15. This tends to indicate that ion-molecule reactions depend less on the relative collision speed of the reactants and more on the polarizability of the neutral target species by the impacting ion. Typical reaction rates are listed in Table 11.

Photodissociation. In photodissociation reactions, an incoming photon injects its energy into a molecular ion. The ion subsequently breaks apart into an ionic and a neutral component, as shown in Table 12.

Table 9 Typical Rate Constants for Dissociative Attachment

Reactions	T[K]	k[cm^3/s]
$e + Br_2 \rightarrow Br^- + Br$	298	$(3.2 \pm 0.8) \times 10^{-13}$
$e + DBr \rightarrow Br^- + D$	300	2.2×10^{-11}
$e + DI \rightarrow I^- + D$	300	9.6×10^{-8}
$e + F_2 \rightarrow F^- + F$	3600 ~ 6000	$2 \sim 0.2 \times 10^{-7}$
$e + HBr \rightarrow Br^- + H$	300	3×10^{-11}
$e + HI \rightarrow I^- + H$	300	2.0×10^{-7}
$e + I_2 \rightarrow I^- + I$	300	4.1×10^{-9}
	250 ~ 520	$8.4 \times 10^{-9}\left(\frac{300}{T}\right)\exp\left(-\frac{1150}{T}\right)$
$e + H_2O \rightarrow O^- + H_2$	400 ~ 1040	$10^{-11} \sim 10^{-7}$
	278 ~ 355	$7.3 \times 10^{-8}\exp\left(-\frac{4800}{T}\right)$
	300	4×10^{-15}
	2800	2.5×10^{-10}
$e + O_2 \rightarrow O^- + O_2$	300	$< 1 \times 10^{-11}$
	112 ~ 361	$2 \sim 3 \times 10^{-11}$
	200 ~ 300	$8.9 \times 10^{-12}\left(\frac{T}{300}\right)^{3/2}$
$e + HBO_2 \rightarrow BO_2^- + H$ $\rightarrow OH^- + OH$	1700 ~ 2450	$(3.2 \pm 1.6) \times 10^{-10}\exp\left(-\frac{10600}{T}\right)$

Table 10 Typical Rate Constants for Three-Body Attachment

Reactions	M	T[K]	k[cm^6/s]
$e + O + M \rightarrow O^- + M$	Ar		$1.0 \times 10^{-30}(300/T)$
$e + O_2 + M \rightarrow O_2^- + M$	N_2	300	3.5×10^{-32}
	O_2	195–600	$1.4 \times 10^{-29}(300/T)\exp(-600/T)$
$e + CO_2 + M \rightarrow CO_2^- + M$	CO_2	300	$< 6 \times 10^{-36}$
$e + H + M \rightarrow H^- + M$	H	7500	3×10^{-32}
$e + NO + M \rightarrow NO^- + M$	CO_2	200–500	$1.0 \times 10^{-29}(300/T)^{3/2}\exp(-940/T)$

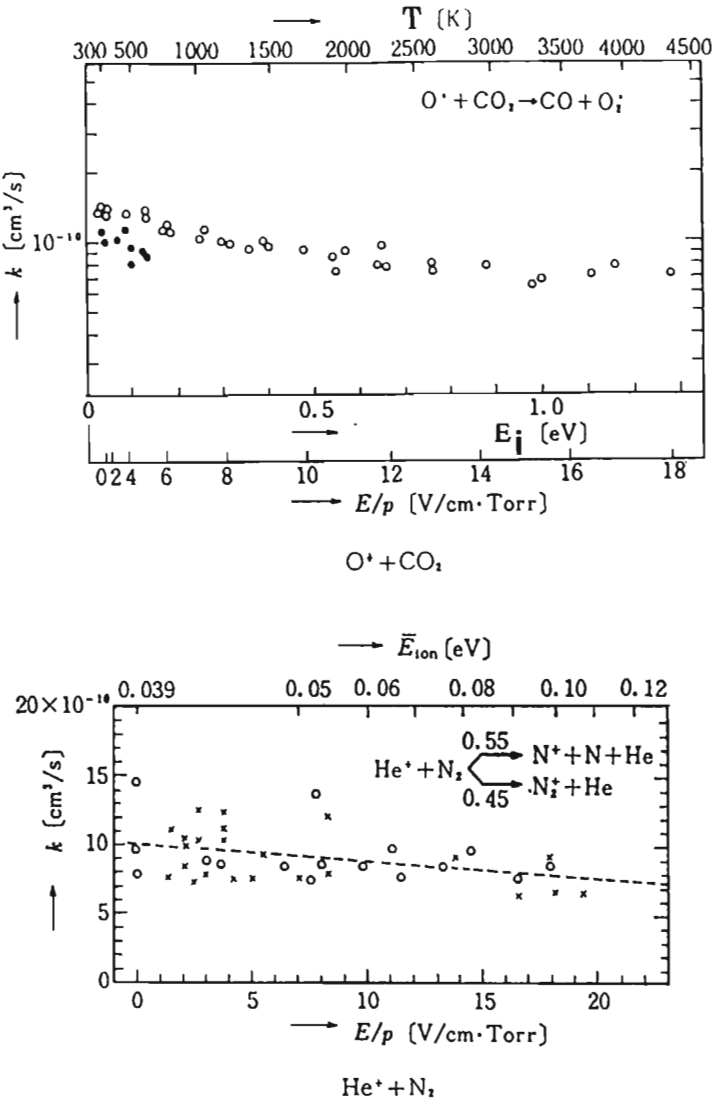


Figure 15 Ion-molecule reaction rate constants as a function of temperature. (From Chang et al., 1984.)

Table 11 Ion-Molecule Reaction Rates

Reactions	$k_c \times 10^9$[cm^6/s]
$He^+ + O_2 \rightarrow O^+ + O + He$	1.5
$He^+ + N_2 \rightarrow N^+ + N + He$	1.7
$\rightarrow N_2^+ + He$	1.5
$O^+ + H_2 \rightarrow OH^+ + H$	2.0
$O^+ + O_2 \rightarrow O_2^+ + O$	0.04
$H_2^+ + H_2 \rightarrow H_3^+ + H$	0.59
$N_2^+ + H_2 \rightarrow N_2H^+ + H$	2.0
$N_2^+ + O \rightarrow NO^+ + N$	0.25
$\rightarrow O^+ + N_2$	$<10^{-2}$
$N_2^+ + O_2^+ \rightarrow O_2^+ + N_2$	0.1
$O_2^+ + N \rightarrow NO^+ + O$	0.18
$NH_3^+ + NH_3 \rightarrow NH_4^+ + NH_2$	0.52
$H_2O^+ + H_2O \rightarrow H_3O^+ + OH$	0.49
$OH^+ + H_2O \rightarrow H_3O^+ + O$	0.47
$CH_4^+ + CH_4 \rightarrow CH_5^+ + CH_3$	0.61
$CH_3^+ + CH_4 \rightarrow C_2H_5^+ + H_2$	0.86

Table 12 Ion Interconversion Processes

(i) *Ion-molecule reactions*	
(a) Charge transfer	
$A^{\pm} + B \rightarrow B^{\pm} + A$	atom-atom
$A^{\pm} + B^* \rightarrow B^{\pm} + A$	atom-atom, via excited state
$A^{\pm} + BC \rightarrow BC^{\pm} + A$	atom-molecule
$A^{\pm} + BC \rightarrow B^{\pm} + A + C$	dissociative
$AB^{\pm} + C \rightarrow C^{\pm} + A + B$	dissociative
(b) Clustering	
$A^{\pm} + B + M \rightarrow AB^{\pm} + M$	
(c) Ion-atom interchange	
$A^{\pm} + BC \rightarrow AB^{\pm} + C$	
$A^{\pm} + BC \rightarrow AB + C^{\pm}$	
(d) Switching	
$A^{\pm}\cdot B + C \rightarrow A^{\pm}\cdot C + B$	
(ii) *Photodissociation*	
$h\nu + AB^{\pm} \rightarrow A^{\pm} + B$	

3. Electrons as Intermediaries

When electrons collide inelastically with neutral atoms or molecules without ionizing them, the resulting reaction can cause excitation or dissociation in the target atoms or molecules, as shown in Table 13. A typical cross section of an electron impact dissociation reaction is shown in Fig. 16.

4. Sinks of Ions

Reactions that act as sinks of ions can be classified into (a) volume recombination reactions, which act as sinks of positively charged ions and sometimes also negatively charged ions, (b) detachment reactions, which act as sinks of negatively charged ions, and (c) reactions in which a collision of an ion with the walls of the container causes it to be neutralized.

Volume Recombination. Volume recombination refers to reactions in which an attachment of particles takes place in the course of an encounter between a positive ion and an electron or a positive ion and a negative ion.

There are many different recombination processes, as shown in Table 17, and the coefficient of recombination α depends strongly on both the nature of the reactants and the products involved in the process.

Three-Body Ion-Ion Recombination. At low pressures, recombination by two-body collisions is relatively unlikely for most ions due to the large relative velocity of both the reactants. If a third body is present however, the reaction goes forward much more rapidly. The reaction rate constant for three-body recombination increases with increasing pressure to reach a maximum of $\alpha \approx 10^{-6}$ cm^{6}sec^{-1} at atmospheric pressure and decreases with increases in pressure above atmospheric.

Mutual Neutralization. For two-body ion-ion recombination, mutual neutralization reactions tend to form excited species. Typical recombination rates are listed in Table 14. These reactions act as sinks for both positive and negative ions simultaneously.

Radiative Recombination. Electron-ion recombination coefficients are generally smaller than those of ion-ion recombination reactions due to the relatively higher velocity of electrons. For example, radiative re-

Table 13 Electrons as Intermediaries

$e + A \rightarrow A^* + e$	electron impact excitation
$\rightarrow A^{**} + e$	electron impact (metastable) excitation
$e + AB \rightarrow e + A + B$	electron impact dissociation
$e + ABC \rightarrow e + AB + C$	electron impact dissociation

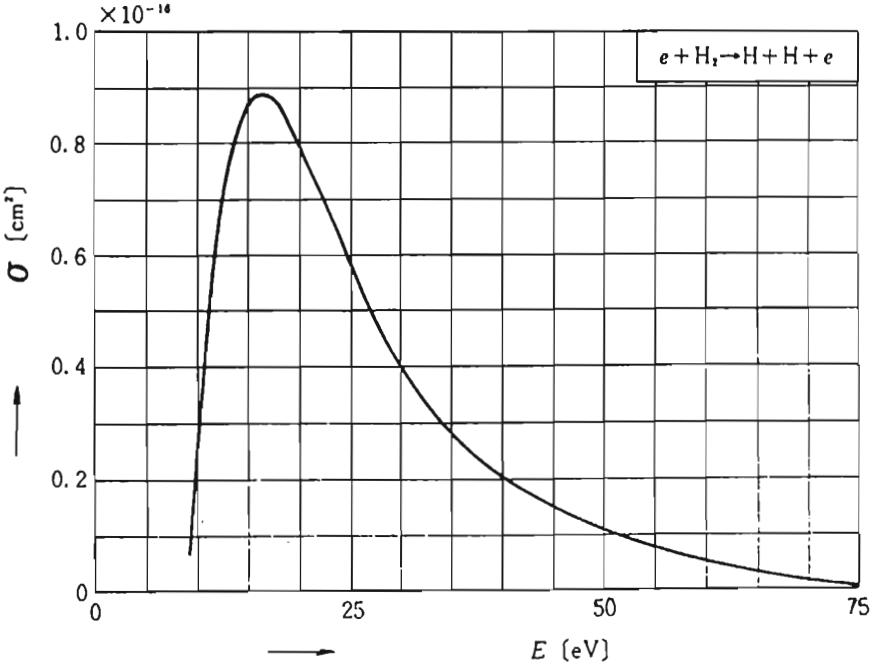


Figure 16 Electron impact dissociation of hydrogen. (From Chang et al., 1984.)

combination, which results when an electron falls into an atomic level of a positive ion and releases a photon as a result, has a reaction rate constant of $\alpha = 10^{-12} - 10^{-14}$ cm^{3}sec^{-1}. This process is important to explain the luminous emissions of certain electrical discharges.

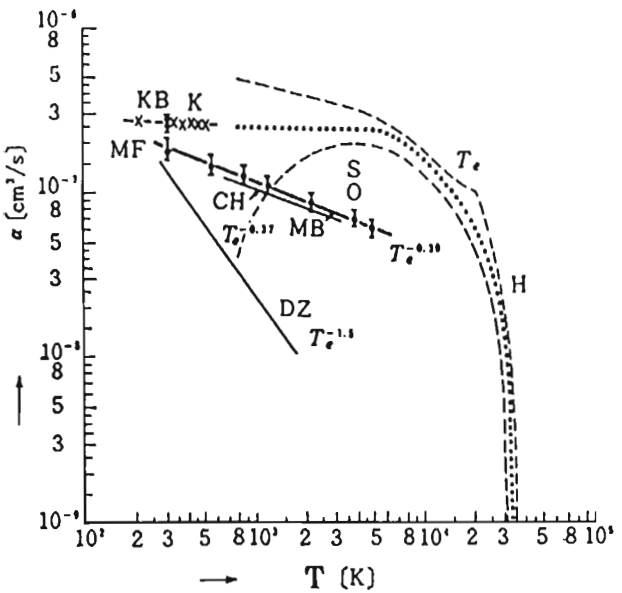
Dissociative Recombination. Dissociative recombination, on the other hand, which results from a recombination of electrons with molecular ions, has a much larger reaction rate constant of $\rho \approx 10^{-7}$ cm^{3}sec^{-1}. Typical recombination rates and temperature dependencies are shown in Table 15 and Fig. 17 respectively.

Table 14 Mutual Neutralization Reaction Rates

Reactions	$\alpha \times 10^7$[cm^3/s]
$N^+ + O^- \rightarrow$	2.9 ± 1
$O^+ + O^- \rightarrow$	2.8 ± 1
$NO^+ + NO_2^- \rightarrow$	64 ± 7
$NO^+ + NO_3^- \rightarrow$	57 ± 6

Table 15 Dissociative Recombination Rates

Reactions	ρ[cm³/s]
CO^+	$6.8 \pm 1.2 \times 10^{-7}$
F_2^+	$2.3 \pm 0.3 \times 10^{-9}$
CO_2^+	8×10^{-6}
	$3.4 \pm 1.2 \times 10^{-6}$
CH_4^+	3.9×10^{-6}
$C_3H_8^+$	$5.3 \pm 5 \times 10^{-6}$
NH_3^+	9.2×10^{-6}
O_3^+	$T^{-0.4}$
H_3^+	$2.3 \pm 0.3 \times 10^{-7}$
H_5^+	$3.6 \pm 1.0 \times 10^{-6}$
HCO^+	$2.0 \pm 0.3 \times 10^{-7}$
$N_2 \cdot N_2^+$	2.0×10^{-6}
$O_2 \cdot O_2^+$	2.3×10^{-6}
$NO \cdot NO^+$	$1.7 \pm 0.4 \times 10^{-7}$
NO_2^+	4×10^{-7}
NH_4^+	$1.5 \pm 0.3 \times 10^{-6}$
$NH_4^+ \cdot (NH_3)$	$2.52 \times 10^{-6}\ T_e^{0.197}$
$NH_4^+ \cdot (NH_3)_2$	$2.68 \times 10^{-6}\ T_e^{0.050}$
$NH_4^+ \cdot (NH_3)_3$	$3 \pm 1 \times 10^{-6}$
$H_3O^+ \cdot H_2O$	2.7×10^{-6}



N₂
K: Kasner
MB: Mehr and Biondi
H: Hagen
S: Sayers
CH: Cunningham and Hobson (1972)
DZ: Dunn et al. (1970)
MF: Maier and Fessenden
KB: Kasven and Biondi (1965)

Figure 17 Dissociative recombination of nitrogen. (From Chang et al., 1984.)

Detachment. The detachment of electrons from negatively charged atoms and ions can proceed via collisions with neutral atoms, positively charged atoms or ions, negatively charged atoms, or electrons, or via interaction with photons as shown in Table 17. The most likely detachment process in a discharge is associative detachment, which leads to the formation of complex molecules, as shown in Table 16.

Neutralization by Collision with Wall. In this process, a positive ion recombines via an interaction with the walls of the container. This class of reactions is intimately connected with the process of ambipolar diffusion outlined in Sec. III.D.

Table 16 Typical Associative Detachment Coefficients

Reactions	k[cm^3/s]
$H^- + H \rightarrow H_2 + e$	1.3×10^{-9}
$O^- + O \rightarrow O_2 + e$	1.4×10^{-10}
$O^- + N \rightarrow NO + e$	2.0×10^{-10}
$O^- + H_2 \rightarrow H_2O + e$	6.0×10^{-10}
$O^- + NO \rightarrow NO_2 + e$	1.6×10^{-10}
$O^- + CO \rightarrow CO_2 + e$	4.4×10^{-10}
$Cl^- + H \rightarrow HCl + e$	9.0×10^{-10}
$O_2^- + O \rightarrow O_2 + e$	3.0×10^{-10}
$O_2^- + N \rightarrow NO_2 + e$	5.0×10^{-10}
$OH^- + O \rightarrow HO_2 + e$	2.0×10^{-10}
$H^- + O_2 \rightarrow HO_2 + e$	1.2×10^{-9}
$OH^- + H \rightarrow H_2O + e$	1.0×10^{-9}
$CN^- + H \rightarrow HCN + e$	8.0×10^{-10}
$O^- + N_2 \rightarrow N_2O + e$	$< 1 \times 10^{-14}$
$OH^- + N \rightarrow HNO + e$	$< 1 \times 10^{-11}$
$O^- + SO_2 \rightarrow SO_2 + e$	7×10^{-10}
$S^- + H_2 \rightarrow H_2S + e$	$< 1 \times 10^{-15}$
$S^- + O_2 \rightarrow SO_2 + e$	3×10^{-11}
$O^- + C_2H_4 \rightarrow C_2H_4O + e$	7.7×10^{-10}
$O^- + O_2(^1\Delta_g) \rightarrow O_3 + e$	$\sim 3 \times 10^{-10}$
$S^- + CO \rightarrow COS + e$	3.1×10^{-10}
$C^- + CO \rightarrow C_2O + e$	4.1×10^{-10}
$C^- + CO_2 \rightarrow 2CO + e$	4.7×10^{-11}
$C^- + N_2O \rightarrow CO + N_2 + e$	9.0×10^{-10}

Table 17 Sinks of Ions

(a) Volume recombination	
$A^+ + e \rightarrow A + h\nu$	radiative
$\rightarrow (A^{**}) \rightarrow A^* + h\nu$	dielectronic
$A^+ + e + M \rightarrow A + M$	three-body, atomic
$A^+ + e + e \rightarrow A + e$	three-body, electronic
$AB^+ + e \rightarrow A^* + B$	dissociative
$AB^+ + e + M \rightarrow A + B + M$	dissociative, three-body
$AB^+ + e + e \rightarrow A + B + e$	dissociative, three-body
$A^+ + B^- \rightarrow A + B^*$	mutual neutralization
$A^+ + B^- \rightarrow AB + h\nu$	mutual neutralization, radiative
$A^+ + B^- + M \rightarrow AB + M$	mutual neutralization, three-body
$AB^+ + C^- \rightarrow A + B + C$	dissociative neutralization
$A^+ + BC^- \rightarrow A + B + C$	dissociative neutralization
$A^+ + B^- \rightarrow C + D$	neutralization, switching
$A^+ + B^- + M \rightarrow C + D + M$	neutralization, switching, three-body
(b) Detachment	
$A^- + B \rightarrow A + B + e$	collisional
$\rightarrow AB + e$	associative
$A^- + h\nu \rightarrow A + e$	photodetachment
$AB^- + h\nu \rightarrow A + B + e$	dissociative photodetachment
$AB^- + M \rightarrow AB + e + M$	molecular
$A^- + e \rightarrow A + e + e$	electron
$A^- + B^* \rightarrow A + B + e$	via metastable
$A^+ + B^- \rightarrow A^+ + B + e$	
$A^- + B^- \rightarrow A + B^- + e$	
(c) Neutralization by collision with wall	
$A^+ + \text{wall} \rightarrow A + \text{wall}$	positive atomic ion
$AB^+ + e + \text{wall} \rightarrow AB + \text{wall}$	
$AB^+ + CD^- + \text{wall} \rightarrow AB + CD + \text{wall}$	

REFERENCES

Chang, J. S., and T. G. Beuthe (1992). Modelling of Ar-CO_2 thermal plasma. *J. High Temp. Chem. Proc.*, 1, 333–1341.

Chang, J. S., and I. Maezono (1988). Electrode surface temperature profiles in corona discharges. *J. Phys. D: Appl. Phys.*, 21, 1023–1024.

Chang, J. S., R. M. Hobson, Y. Ichikawa, and T. Kaneda (1984). *Atomic and Molecular Processes in an Ionized Gas*. Tokyo Denki University Press, Tokyo.

Chang, J. S., P. A. Lawless, and T. Yamamoto (1991). Corona discharge processes. *IEEE Trans. Plasma Sci.*, 19, 1152–1166.

Crookes, W. (1879). On the illumination of lines of molecular pressure, and the trajectory of molecules. *Phil. Mag.*, 7, 57.

Davy, H. (1809). An account of some new analytical researches on the nature of certain bodies, particularly the alkalies, phosphorous, sulphur, carbonaceous matter, and the acids hitherto uncompounded; with some observations on chemical theory. *Phil. Trans. Roy. Soc.*, 97, 71.

Donskoi, A. V., V. M. Goldfarb, and V. S. Klubnikin (1972). *Physics and Technology of Low-Temperature Plasmas* (S. V. Dresvin, ed.; English edition translated by T. Cheron and edited by H. U. Eckert). Iowa State University Press.

Eddy, T. L., and A. Sedghinasab (1988). The type and extent of non-LTE in argon arcs at 0.1–10 bar. *IEEE Transactions on Plasma Science*, 16:4, 444–452.

von Engel, A. (1955). *Ionized Gases*. Oxford University Press, London.

Gleizes, A., H. Kafrouni, H. Dang Duc, and C. Maury (1982). The difference between the electron temperature and the gas temperature in a stationary arc plasma at atmospheric pressure. *J. Phys. D: Appl. Phys.*, 15, 1031–1045.

Hermstein, W. (1960). *Archiv für Elektrotech.*, 45, 209–279.

Hoyaux, M. F. (1968). *Arc Physics*. Springer-Verlag, New York.

Hsu, K. C., K. Etemadi, and E. Pfender (1983). Study of the free-burning high-intensity argon arc. *J. Appl. Phys.*, 54, 1293–1301.

Langmuir, I. (1929). The interaction of electron and positive ion space charges in cathode sheaths. *Phys. Rev.*, 33, 954, 1929.

Lawless, P. A., K. J. McLean, L. E. Sparks, and G. H. Ramsey (1986). Negative corona in wire-plate electrostatic precipitators. Part I, Characteristics of individual tuft-corona discharge. *J. Electrostatics*, 18, 199–217.

McDaniel, E. W. (1969). *Collision Phenomena in Ionized Gases*. John Wiley, New York.

McLaren, T. I., and R. M. Hobson (1968). Initial ionization rates and collision cross sections in shock-heated argon. *Phys. of Fluids*, 11:10, 2162–2172.

McLean, K. J., P. A. Lawless, L. E. Sparks, and G. H. Ramsey (1986). Negative corona in wire-plate electrostatic precipitators. Part II, Calculation of electrical characteristics of contaminated discharge electrodes. *J. Electrostatics*, 18, 219–231.

Shindo, H., T. Inaba, and S. Imazu (1980). An experimental investigation of non-equilibrium effects in wall-confined argon plasma arcs. *J. Phys. D: Appl. Phys.*, 13, 805–815.

Uhlenbusch, J. F., and E. Fischer (1971). Influence of diffusion and nonequilibrium populations on noble-gas plasmas in electric arcs. *Proceedings of the IEEE*, 59:4, 578–587.

Waldman, L., and K. H. Schmitt (1966). Thermophoresis and diffusophoresis of aerosols. In *Aerosol Science* (C. N. Davies, ed.). Academic Press, New York.

This Page Intentionally Left Blank

10

Generation of High Voltages

A. Chakrabarti
McMaster University
Hamilton, Ontario, Canada

S. Jayaram
University of Waterloo
Waterloo, Ontario, Canada

I. INTRODUCTION

High voltage is widely used in equipment and in the testing of power apparatus. The types of high voltage in use can be classified as (a) ac (b) dc and (c) pulse voltages. Some examples of equipment in which high voltage dc is employed are

Gas lasers (several kV)
Electron microscopes and x-ray units (~100 kV)
Electrostatic precipitators, accelerators (MV)

ac high voltages are used in the testing of power apparatus insulation, in the generation of high dc voltages, in air pollution control in discharges, and elsewhere.

High pulse voltages are used in pulse lasers, insulation testing, flue gas cleaning, and the like. All three classes of voltages are used in research and testing laboratories, where they find numerous applications.

II. GENERATION OF HIGH ALTERNATING VOLTAGES

Usually, the following means are used in the generation of high alternating voltages:

Single transformers

Cascaded transformers
Series resonance circuit
Tesla coil

A. Single Transformers

Power frequency single transformers are the most common and simple means of generating high ac voltages. A single transformer unit is generally used to generate voltages up to several hundred kilovolts. Figure 1 shows two basic circuits for test transformers (Kind, 1978). Considerable economy is achieved if the center point rather than one terminal of the high voltage winding is grounded. Each terminal of the high voltage winding needs to be insulated for half the output voltage. These transformers are made like any other power transformers with regard to the design of the

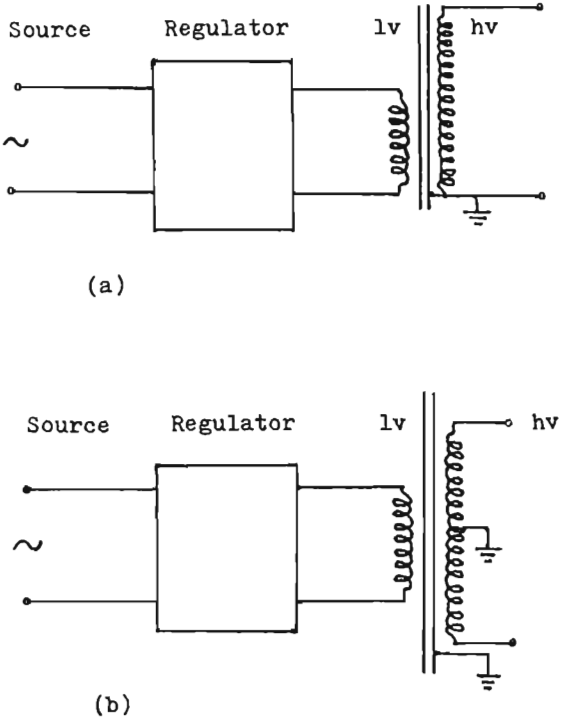


Figure 1 Single stage high voltage transformer. lv: low voltage winding; hv: high voltage winding. (a) Single isolated terminal at the output. (b) Both terminals isolated at the output.

core and windings in relation to power ratings. However, because of the nature of the application (breakdown tests), heavier insulation is used on high voltage windings to protect against transient overvoltages. Also, low magnetizing current is employed for minimum distortion of the output voltage waveform. The high voltage winding should be partial discharge free for partial discharge tests.

B. Cascaded Transformers

Single unit transformers have been used for voltages up to 750 kV (Kuffel and Abdullah, 1970). However, because of cost, transport, and erection problems, several units are usually cascaded so that high voltage windings of all units are connected in series. The low voltage winding of the second stage is fed from the secondary side of the first stage, and the low voltage winding of the third stage is fed from the secondary winding of the second stage, as shown in the schematic circuit diagram in Fig. 2. So the second

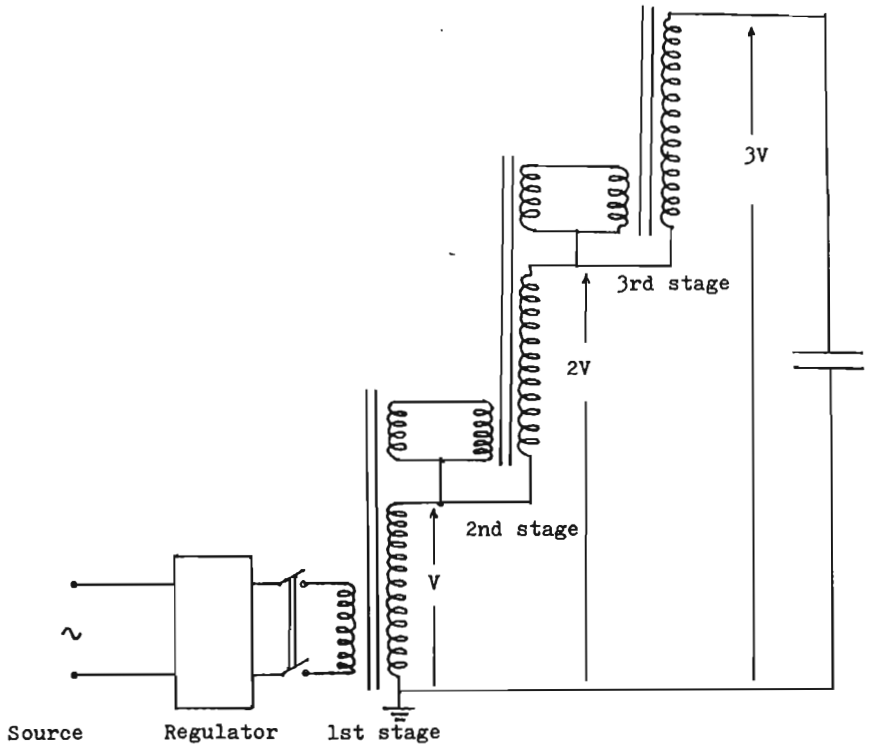


Figure 2 Three transformers connected in cascade.

transformer should carry part of the output power plus the excitation power for the third transformer, and the first transformer should carry its part of the output power plus the excitation power for the second and the third transformers. If the power carried by the third stage is P, then the power by the second and the first stage will be $2P$ and $3P$ respectively. Test transformers in cascade have produced voltages >2 MV. The voltage difference between the first and the second stage is V, and that between the first and the third stage is $2V$. Therefore the second and third stages should be placed on insulating bases rated for the corresponding voltage difference. Center tapping may be used for economy, in which case the first, second, and third stages are to be insulated for $V/2$, $3V/2$, and $5V/2$, respectively. Usually the load or the test object to these high voltage sources is capacitive. Sometimes, a variable reactor for power factor correction is used when the load capacitance is high. This is shown in Fig. 3. Such a reactor can reduce the current drawn from the supply by a factor of 10 or more, thus reducing the cost of the supply regulator, circuit breakers, etc.

C. Series Resonance Circuit

In a series resonance circuit, a finely variable reactor is connected in series with the high voltage transformer and a capacitive load so as to resonate at 60 Hz or any desired frequency. This circuit is shown in Fig. 4. On resonance, current is limited only by the resistance in the circuit. Very high voltage may be produced across the test object. A practical figure of voltage amplification is V/v = 20–50 when V = voltage across

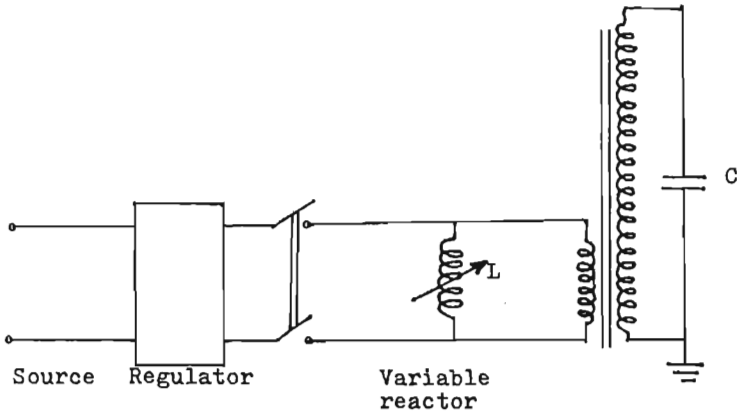


Figure 3 Variable reactor for power factor correction.

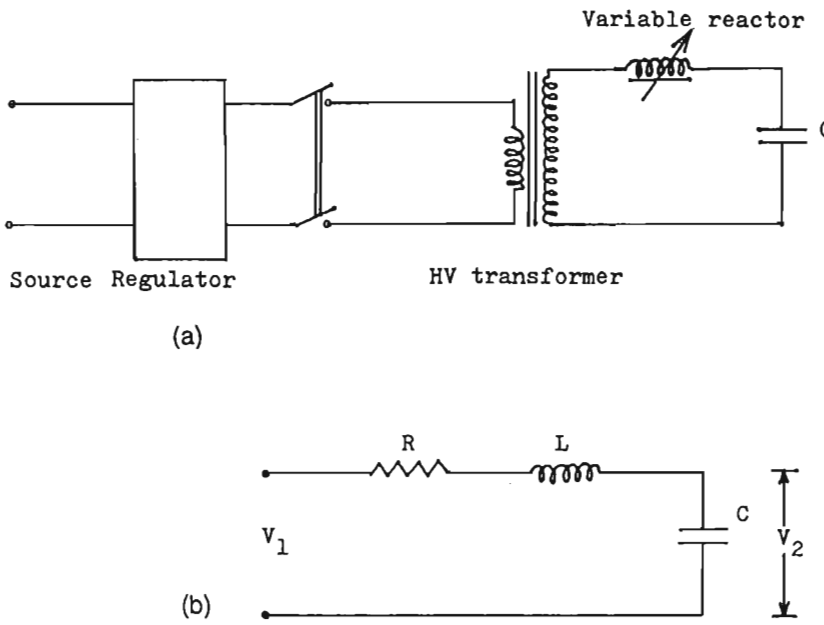


Figure 4 Series resonance circuit (a) and its equivalent representation (b).

load, v = transformer secondary voltage. With this circuit a pure sine wave can be obtained, whereas using a transformer, a distorted voltage waveshape may be produced because of the nonlinear magnetization curve. In case of a failure of the test object, a short circuit is automatically controlled. There is no power arc formation, so that multiple breakdowns can be harmless. All these are important in cable testing. However, this arrangement works only for capacitive loads. Pollution testing and wet tests cannot be done, as a pure capacitive load is absent. In a series circuit, for $R \ll \omega L$, R being the effective circuit resistance,

$$V_2 = \frac{V_1}{1 - \omega^2 LC} \tag{1}$$

V_2 and V_1 are as shown in Fig. 4.

D. Tesla Transformer

The circuit comprises a series LC primary circuit and a secondary circuit in loose magnetic coupling due to the use of an air core. A discharge in the primary circuit initiated by a spark gap (or, more recently, by a triac,

for better control of the firing instant) will excite high frequency oscillations in the typical range of 10^4 to 10^5 Hz. The frequency of oscillations in the secondary will be the same as that in the primary when $L_1C_1 = L_2C_2$ (Fig. 5).

$$\frac{V_2}{V_1} = \left(n\frac{C_1}{C_2}\right)^{0.5} \tag{2}$$

where V_1 = maximum voltage to which C_1 is charged, V_2 = maximum voltage on C_2, and n = efficiency of energy transfer from the primary capacitance to the secondary circuit (Kuffel and Abdullah, 1970). Voltages of more than 1 M*V* have been generated with Tesla transformers. Tests at high frequency voltages are mainly carried out on equipment used in communication engineering.

III. GENERATION OF HIGH DIRECT VOLTAGES

The following means are usually used to produce high direct voltages:

Half- and full-wave rectifier
Voltage doubler circuit
Voltage multiplier circuit
Deltatron circuit
Van de Graaff generator

A. Half-Wave Rectifier

This is the simplest circuit for the generation of high direct voltages. The rectifier conducts current only in one direction and so it conducts for one half cycle of 60 Hz to charge the capacitor *C* (Fig. 6). During the next half cycle *C* discharges through the load *R*.

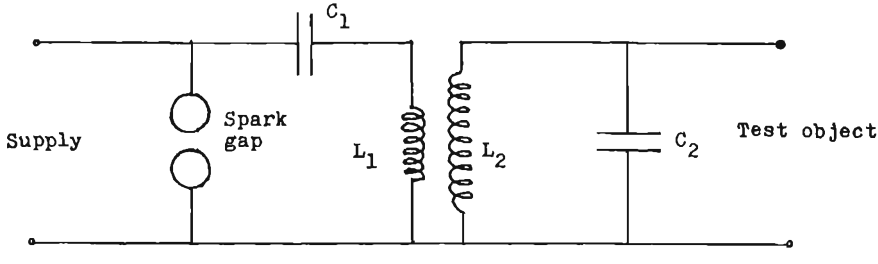


Figure 5 Tesla transformer.

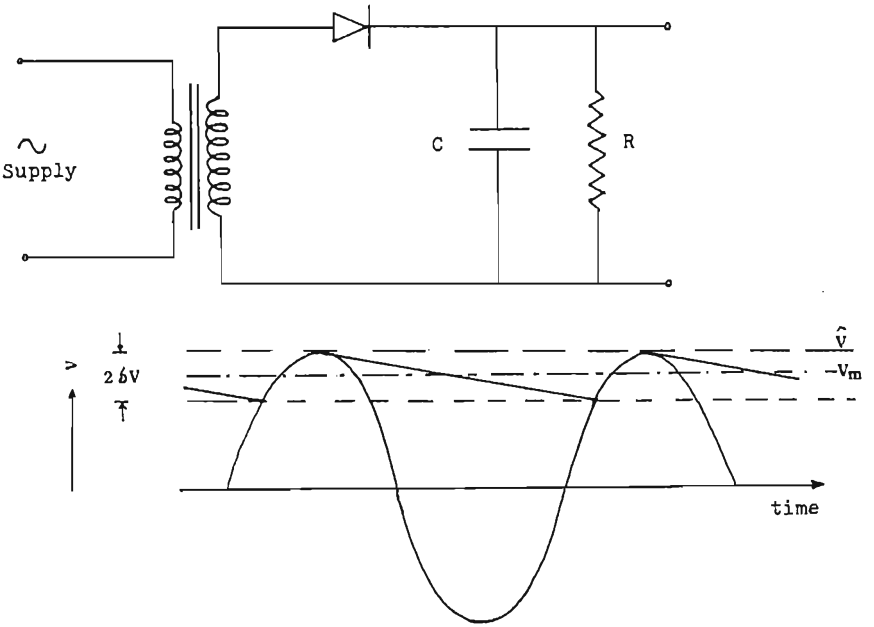


Figure 6 Single-phase half-wave rectifier.

The variation of the dc voltage around an average value of V_m is called a ripple. For very small ripples, the ripple factor is given by

$$\frac{\delta v}{V_m} = \frac{1}{2fRC} \tag{3}$$

where $V_m + \delta v = V_p$ and f = ripple frequency. During the negative half cycle, the voltage across the rectifier may be $2V_p$. Therefore the rectifier should be designed to withstand this voltage. Because of the unidirectional current, there is a possibility of the saturation of the transformer core.

B. Full-Wave Rectifiers

Full-wave rectification can be obtained with two or four rectifiers as shown in Fig. 7(a) and (b). Charging of the capacitor can involve a time constant because of the internal resistance of the rectifiers and protective resistance in series. The ripple factor is half that for the half-wave rectifier. Thus $\delta v/V_m = 1/4fRC$. As the current flows in both directions, there is no core saturation problem in the transformer.

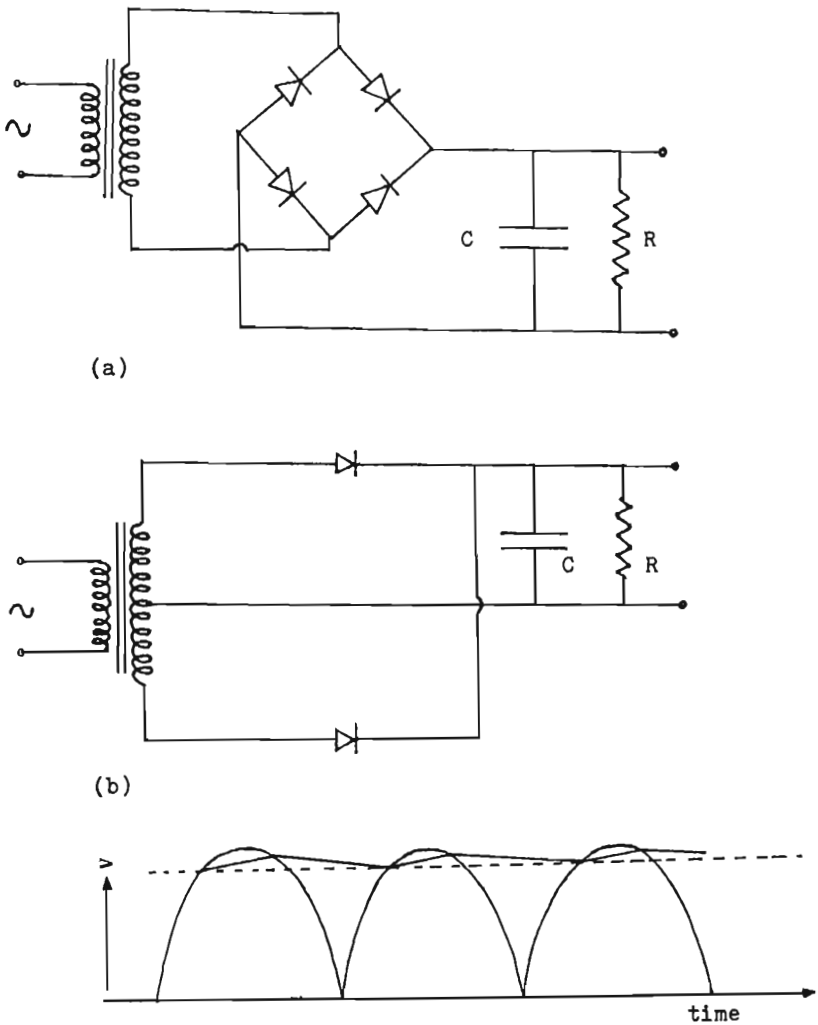


Figure 7 Full-wave rectifiers. (a) Full-wave bridge-connected rectifiers. (b) Bi-phase connection of rectifiers.

C. Voltage Doubler Circuit

Figure 8 shows a voltage doubler circuit. When point B is positive with respect to A, the capacitor C_1 is charged, with point C being positive with respect to A to a voltage V_p, where V_p is the peak voltage of the secondary

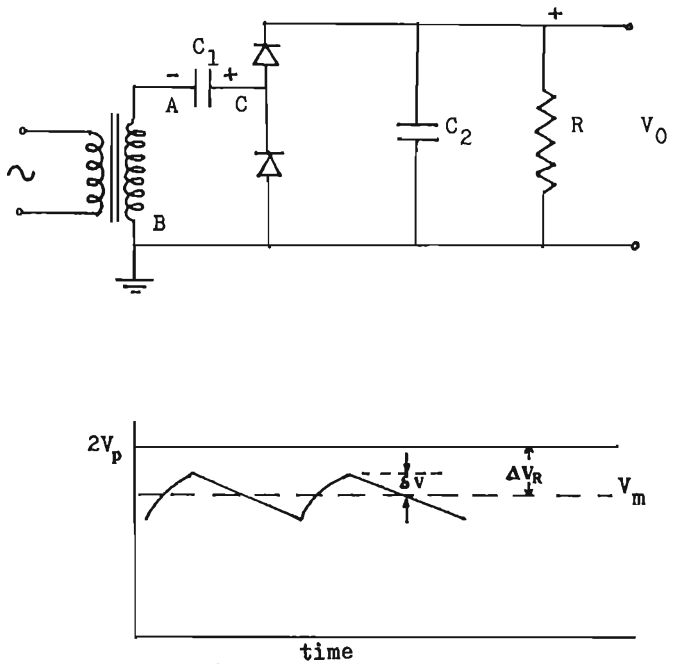


Figure 8 Voltage doubler circuit used for impulse generator charging (Cockroft-Walton circuit).

of the transformer. During the next half cycle, A is positive and rises to a peak value V_p; the voltage at point C rises with it to $2V_p$. Thus the maximum charging voltage to C_2 is $2V_p$. Because of a load connected across the output, the output voltage is going to be smaller than $2V_p$ by ΔV_R, called the "regulation." If V_m is the mean value of the output voltage, the ripple factor is given by

$$\frac{\delta v}{V_m} = \frac{1}{2fRC_2} \tag{4}$$

and the average output voltage is

$$V_m = \frac{2V_p}{1 + \dfrac{1}{fR}\left(\dfrac{1}{C_1} + \dfrac{1}{C_2}\right)} \tag{5}$$

The peak inverse voltage on C_2 is $2V_p$, and there is no transformer core saturation. This type of circuit is used to charge impulse generators. This is also known as a Cockroft-Walton circuit. Another voltage doubler circuit

where the voltage $2V_p$ is distributed equally across two capacitors is shown in Fig. 9.

D. Voltage Multiplier Circuits

Figure 10 shows a voltage multiplier circuit using the Cockroft-Walton principle. The basic stage comprises a voltage doubler circuit with a supply transformer as shown in Fig. 8. For higher output voltages of 4, 6, $8V_p$, etc., the circuit is repeated with a cascade connection. If the crest value of the supply voltage is V_p, then under no load conditions C_3' is charged to V_p, C_3 is charged to $2V_p$, and at the output it is $2NV_p$ if there are N stages. The ripple voltage is given by

$$\delta v = I_m \frac{N(N+1)}{4fC} \tag{6}$$

for $C_1 = C_2 = C_3 = \cdots = C$.
In general,

$$\delta v = \frac{I_m}{f} \frac{1}{2} \sum_{1}^{N} \frac{k}{C_k} \qquad \text{for } C_1 \neq C_2 \neq C_3 \neq \cdots \tag{7}$$

For $C_1' = C_2' = \cdots = C' \neq C$, the voltage drop ΔV_R is

$$\Delta V_R = \frac{I_m}{f}\left[\frac{1}{3C}\left(N^3 - \frac{3N^2}{4} - \frac{N}{4}\right) + \frac{1}{3C'}\left(N^3 + \frac{3N^2}{4} + \frac{N}{4}\right)\right] \tag{8}$$

If $C = C'$, then

$$\Delta V_R = \frac{2I_m}{3fC}\left(N^3 + \frac{3N^2}{8} + \frac{N}{8}\right) \tag{9}$$

where I_m = average load current.

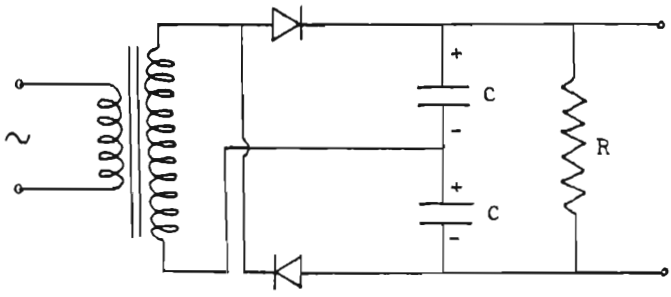


Figure 9 Voltage doubler circuit where $2V$ is distributed across two capacitors.

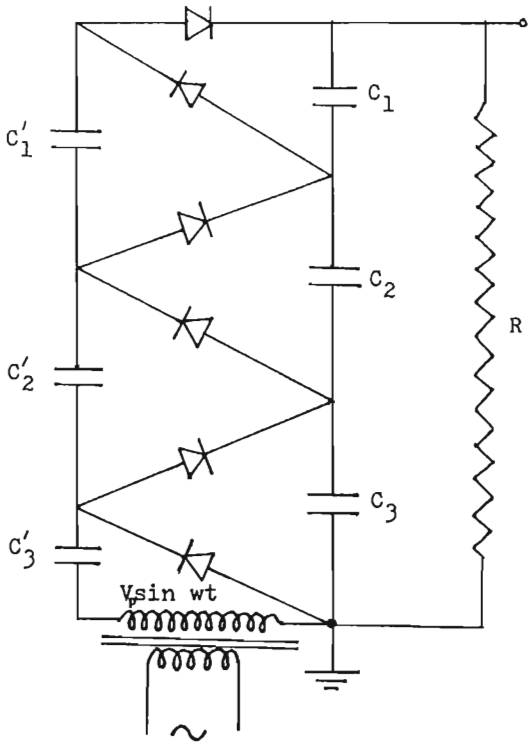


Figure 10 Cascaded rectifier voltage multiplier circuit.

A few variations of this circuit are possible. There can be cascade rectifiers connected in parallel at every stage or in parallel only at the top of the column to provide for better voltage regulation. The supply frequency may be as high as 500 Hz. This enables a smaller value of stage capacitance to be used without affecting the efficiency of charge transfer from one stage capacitor to the next. The typical ratings are a few MVs and ~30 mA. The permitted ripple factor is ~5%.

E. Deltatron Circuit

This circuit (Enge, 1971) has the advantage of small ripple factor, stability, and small stored energy. Voltage output is limited to ~1 MV and current to a few mA. The circuit consists of a cascade connection of transformers without iron cores. These are supplied from a high frequency source (50–100 kHz). Fig. 11 shows the circuit (Khalifa, 1990). C_p and C_s are compensating capacitors for magnetizing and leakage inductances, respec-

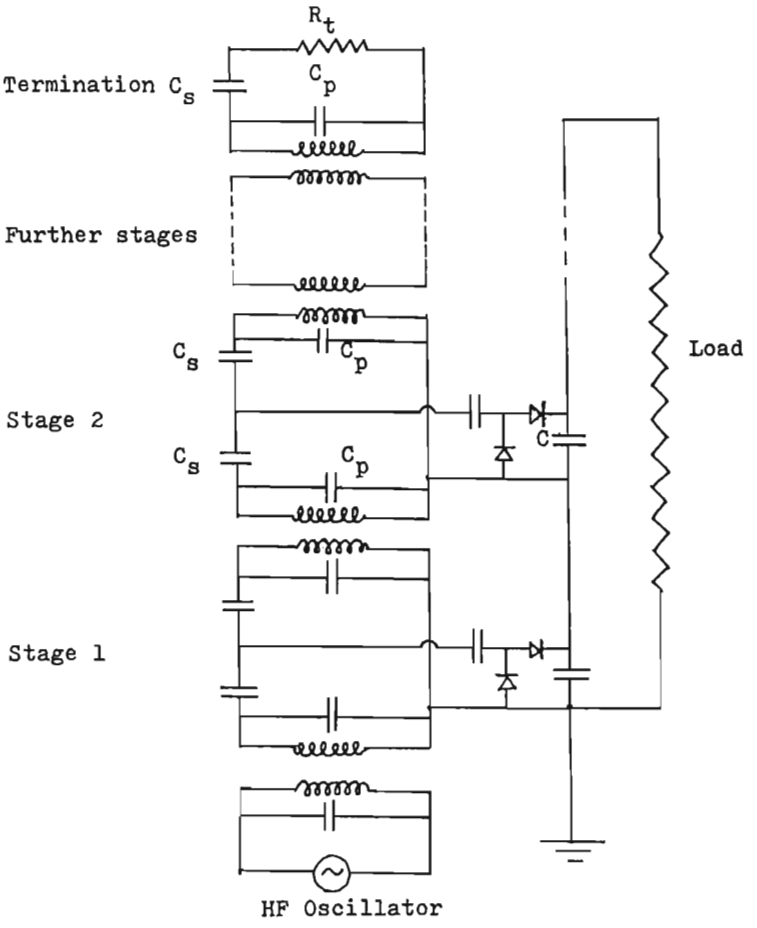


Figure 11 Deltatron circuit.

tively. R_t is the terminating resistor. The circuit behaves like a terminated line along which voltage remains nearly constant, but there will be a phase shift between input and output. A Cockroft-Walton circuit is connected to each stage. As the frequency is high, the capacitors C can be made very low, with correspondingly low energy stored and fast response to load changes or supply variations. The phase shift between the input voltages of different stages provided by their transformers helps reduce ripples from the output.

F. Electrostatic Generators

1. Van de Graaff Generators

The main advantages of these generators are (1) that output is ripple free and (2) that voltages of up to 5 to 6 MV are available. (Tandem accelerators up to 25 MV have been built.) Figure 12 shows the principle of operation of these generators. Charge is spread onto an insulating moving belt by means of corona discharge points at high voltage (10–100 kV). The belt is motor driven, the speed being a few m/s. The deposited charge is conveyed to the upper end where it is removed from the belt by discharging points, which are connected to the inside of an insulated metal sphere. This sphere forms the high voltage electrode. The potential of the high voltage terminal is $V = Q/C$ above ground, where Q is the charge on the high voltage electrode and C is its capacitance with respect to ground.

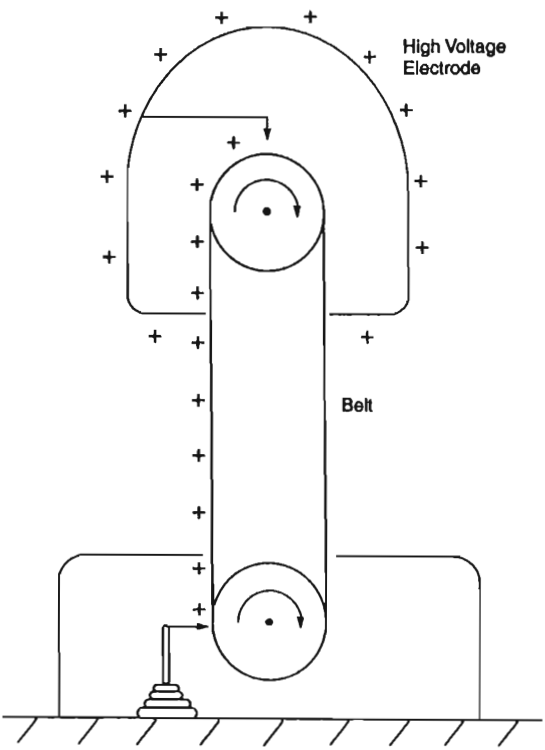


Figure 12 Van de Graaff electrostatic generator.

The equilibrium voltage is attained by input charges to the high voltage electrode and charges removed by load and by corona. The high voltage electrode is shaped to eliminate the possibility of corona discharge on the electrode; also, grading rings are used to get uniform distribution of the electric field between the high voltage electrode and ground.

The difficulties with Van de Graaff generators are low current rating (hundreds of μA), local discharges due to high voltage close to the belt, and movement of the belt due to vibrations interfering with the clearance.

Felici's generator is an improvement upon these difficulties. The belt is replaced by an insulating cylinder surrounding a gas discharge chamber. The chamber is subjected to a high *dc* field and ions of both polarities are drawn by a pair of electrodes connected to the load. Typical operating range is a few hundred kilovolts at a few mA.

2. Variable Capacitance Generator

A variable capacitor constant potential electrostatic generator consists of a stator with interleaved rotor vanes. The combination constitutes a variable capacitor and operates in vacuum. The current equation at any instant is given by (Khalifa, 1990)

$$i = c\frac{de}{dt} + e\frac{dc}{dt} \tag{10}$$

where c is the capacitance being charged to a voltage, e and the instantaneous power input is

$$p = ce\frac{de}{dt} + e^2\frac{dc}{dt} \tag{11}$$

For a capacitor charged with direct voltage, $de/dt = 0$. Thus

$$p = e^2\frac{dc}{dt} \tag{12}$$

When dc/dt is negative, mechanical energy is converted into electrical energy and vice versa. For the position of maximum capacitance C_m, charge $Q_m = C_m e$. As the rotor rotates, the capacitance decreases, and so voltage across the capacitor increases and thus current flows from the generator to load.

IV. IMPULSE VOLTAGES

Transient or impulse voltages are generated in power systems by lightning or switching operations. The former are short duration waves, of only a few microseconds, whilst the later are complex waves lasting for several hundred microseconds, often accompanied by oscillations (Wagner and

Clayton, 1964; Gallagher, and Pearmain, 1982). Both lightning and switching impulses consist of steep wave fronts. The amplitudes of these voltages may exceed the normal operating ac or dc voltages by a factor of two or more (Greenwood, 1991). Because of the nature of these overvoltages they can cause unequal stress distribution along the windings of transformers and generators, or the length of string insulators, and can lead to breakdown of the insulation system (Franklin and Franklin, 1983). It is therefore imperative that the power system component or equipment be tested for its withstand capability under impulse voltage conditions.

An impulse voltage is a unidirectional voltage that rises rapidly to a maximum value and then decays slowly to zero. The waveshape is generally defined in terms of the times T_1 and T_2 in microseconds (μs), where T_1 is the time taken by the voltage wave to reach its peak value and T_2 is the total time from the start of the wave to the instant when it has declined to one-half of the peak value (Gallagher and Pearmain, 1982; Kuffel and Zaengl, 1984). Impulses are normally referred to as T_1/T_2 waves.

A. Lightning Impulses

The magnitudes of overvoltages on transmission lines produced by lightning strokes are determined by the stroke current and the surge impedance of the network. The surge impedance Z is composed of the distributed inductance L and capacitance to ground C. In its simplest form, Z is defined as $Z = (L/C)^{1/2}$. For an overhead transmission line, surge impedance is of the order of 400 Ω. A lightning stroke of 20 kA through 400 Ω surge impedance can generate a surge voltage with a crest value of 8000 kV (Gallagher and Pearmain, 1982). Lightning protection systems, surge arresters, and the different kinds of losses in the network will damp and distort the traveling waves that are produced by the lightning strokes. The actual voltage that reaches the line end equipment is of a magnitude much less than the 8000 kV that would have been caused by the direct lightning hit. Normally the voltage amplitudes are clipped to ~400 kV by the lightning arresters. If the system voltages are of order greater than 300 kV, switching overvoltages of magnitudes greater than 400 kV are easily produced during switching operations. Switching transients have also become a major consideration with the advent of extra high voltage (EHV) systems (Gallagher and Pearmain, 1982; Kuffel and Zaengl, 1984; Khalifa, 1990; Greenwood, 1991). The International Electrotechnical Commission (IEC) recommends that all equipment designed for operating above 300 kV be tested for both lightning and switching withstand capabilities (IEC Publication, 1973).

Although surges due to lightning have a wide variety of shapes, in most high voltage laboratories worldwide it has become standard to use 1.2/50 μs impulse as a standard lightning impulse voltage for testing purposes.

Following the lightning stroke, the time required for the overvoltage to reach the peak value is relatively small (~1 μs); hence the true shape of the front of the lightning impulse voltage is often difficult to measure. Referring to Fig. 13, the points A and B on the impulse are marked corresponding to 30% and 90% of the peak voltage V_p. The virtual origin is defined as the point O_1 on the x-axis where the line O_1S drawn through the points A and B cuts the x-axis at O_1. The virtual front time T_1 and the virtual time to half value T_2 are then defined as marked on the full lightning impulse wave in Fig. 13.

For those impulses chopped at the crest or on the tail, T_c is defined as the time to chopping, Fig. 14(a). If the lightning is chopped in the front, the time to front is defined as indicated on Fig. 14(b), by T_{fc}. International standards stipulate a 1.2/50 μs waveshape for lightning impulse voltage tests with the following permissible tolerances:

Front time T_1: = 1.2 μs ± 30%

Time to half value T_2: = 50 μs ± 20%

Overshoot V_{os}: < 5%.

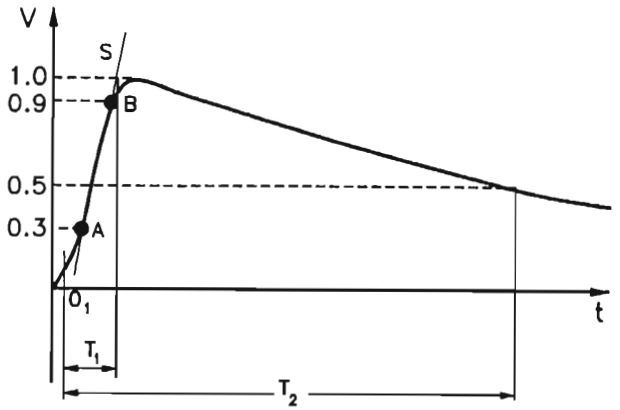


Figure 13 Full-wave lightning impulse voltage showing front and tail times T_1 and T_2.

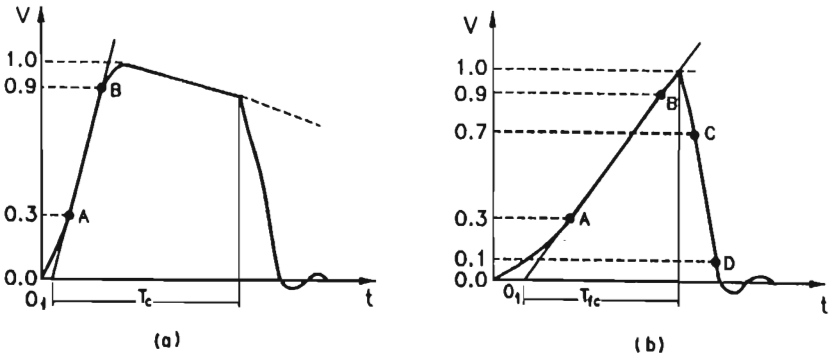


Figure 14 Chopped lightning impulse voltage. (a) Impulse chopped at tail. (b) Impulse chopped at front.

B. Switching Overvoltages

Origin of Switching Overvoltages. Switching overvoltages are generated within the system and are produced during any of the following operations (Greenwood, 1991; IEC Publication, 1973).

Energization of transmission lines and cables
Deenergization or load rejection of transmission lines or cable
Switching ON and OFF of equipment like transformers and reactors
Fault initiation and clearing in the system

The waveshapes of switching overvoltages vary widely; however, based on experience, surges with front times between 100 and 300 μs have been

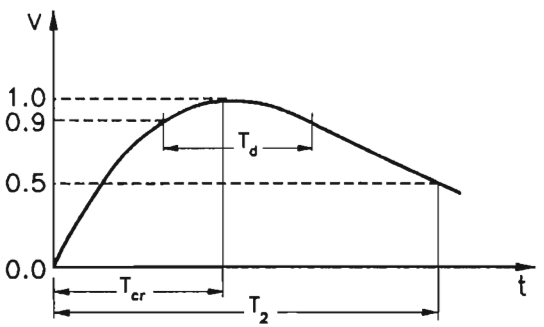


Figure 15 Switching impulse voltage.

considered to be the most dangerous, as the flashover distances of practical interest are lowest for this range of front times (Kuffel and Zaengl, 1984; IEC Publication, 1973). The recommended standard switching surge has a front time of about 250 μs and tail (half value) time of 2500 μs. Fig. 15 shows internationally accepted switching transients for power equipment and component testing purposes (Khalifa, 1990; IEC Publication, 1973). In defining switching transients it is difficult to establish the actual crest value with high accuracy because of the slow nature of these transients. In addition to specifying T_c, an additional time parameter T_d, the time during which the impulse voltage lies above 90% of its peak V_p, is often used in defining the switching transients (Kuffel and Zaengl, 1984; Kind, 1978). The tolerances on switching surges are

$$T_{cr} = 250\ \mu s \pm 20\%$$

$$T_2 = 2500\ \mu s \pm 60\%$$

The simulation of both lightning and switching impulse voltages in laboratories for testing purposes is determined based on the time parameters T_1 and T_2 for the front and tail times, as the impulse shape is described uniquely by T_1 and T_2.

V. GENERATION OF HIGH VOLTAGE IMPULSES

A. Single-Stage Impulse Generators

The two most important basic circuits used for the generation of impulse voltages are shown in Fig. 16(a) and (b). A high voltage dc source is used to charge the generator capacitor C_1 until the spark gap G breaks down. For better reproducibility, sphere gaps are commonly used as ignition spark gaps. The capacitance C_2 represents the capacitance of the test object and other capacitive elements in parallel with the load. The resistors R_1 and R_2, together with the load capacitor C_2, form the wave shaping

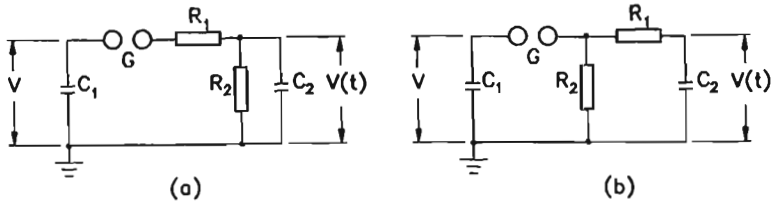


Figure 16 Basic single-stage impulse generator circuit.

network. The equivalent circuits shown in Fig. 16(a) and (b) differ from one another by the respective position of the discharge resistor R_1 to that of the damping resistor R_2. In both circuits R_1 controls the front time and R_2 that of the tail time. Inductances of the circuit elements have been ignored in the equivalent circuit representation, as their presence would make the analysis more complex.

The ignition of the spark gap results in a sudden discharge of the capacitor C_1 into the load circuit capacitance C_2 through R_1. The smaller the time constant R_1C_2, the faster the voltage approaches the peak value on C_1. The peak value V_p on the output side cannot be greater than the voltage determined by the redistribution of the initial charge C_1V onto $(C_1 + C_2)\,V_p$ in the parallel combination. The voltage efficiency of the generator is therefore defined as

$$\text{Voltage efficiency } \eta = \frac{V_p}{V} \leq \frac{C_1}{C_1 + C_2} \tag{13}$$

For a given charging voltage V, the generator output voltage V_p should be as high as possible, hence, $C_1 \gg C_2$. The exponential decay of the impulse voltage on the tail would then occur with the time constants $C_1(R_1 + R_2)$ in circuit (a) and C_1R_2 in circuit (b), respectively.

The maximum transferred energy from the capacitor C_1 to the output circuit is

$$W = \frac{1}{2} C_1 V_p^2 \tag{14}$$

It is recommended that the value of C_1 be at least five times that of C_2, thereby giving a typical value of η above 75% (Gallagher and Pearmain, 1982). Higher amplitude impulses are obtained by increasing the spacing of the spark gap G for a given generator capacitor and the charging dc source.

B. Analysis of Single-Stage Impulse Generator Circuit

Although in theory both circuits, Fig. 16(a) and (b), can be used for generation of impulse voltages, in the design of practical impulse generators the circuit of Fig. 16(b) is preferred because of its higher utilization factor. In Fig. 16(a), the resistors R_1 and R_2 form the voltage divider arms of the input voltage V, and hence the generator voltage efficiency is lower for the circuit configuration (a) than for (b). For the same reason the analysis below refers to the circuit (b).

The capacitor C_1 is charged for time $t < 0$ to a voltage V. The capacitor discharges directly into the wave shaping circuit for $t > 0$. For the circuit

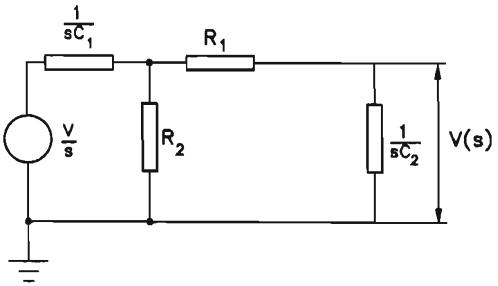


Figure 17 Laplace transform circuit for Fig. 16(b).

of Fig. 16(b), with the ignition of the spark gap G, the equivalent Laplace transform is as shown in Fig. 17

$$V(s) = \frac{V}{R_1C_2}\frac{1}{s^2 + as + b} \tag{15}$$

with

$$a = \frac{1}{R_1C_1} + \frac{1}{R_1C_2} + \frac{1}{R_2C_1} \quad \text{and} \quad b = \frac{1}{R_1R_2C_1C_2} \tag{16}$$

$$V(s) = \frac{V}{R_1C_2}\frac{1}{\alpha_2 - \alpha_1}\left(\frac{1}{s + \alpha_1} - \frac{1}{s + \alpha_2}\right) \tag{17}$$

$$s^2 + (\alpha_2 + \alpha_1)s + \alpha_1\alpha_2 = s^2 + \frac{R_2C_2 + R_2C_1 + R_1C_2}{R_1R_2C_1C_2}s + \frac{1}{R_1R_2C_1C_2} \tag{18}$$

The roots of the quadratic equation $s^2 + as + b = 0$ are

$$\alpha_1, \alpha_2 = \frac{a}{2} \mp \sqrt{\left(\frac{a}{2}\right)^2 - b} \tag{19}$$

For the output voltage to be positive, $\alpha_1 > \alpha_2$, and the two roots are

$$\alpha_1 = \frac{1}{2}\frac{R_2C_2 + R_2C_1 + R_1C_2}{R_1R_2C_1C_2} - \sqrt{\left(\frac{R_2C_2 + R_2C_1 + R_1C_2}{R_1R_2C_1C_2}\right)^2 - \frac{4}{R_1R_2C_1C_2}} \tag{20}$$

$$\alpha_2 = \frac{1}{2}\frac{R_2C_2 + R_2C_1 + R_1C_2}{R_1R_2C_1C_2} + \sqrt{\left(\frac{R_2C_2 + R_2C_1 + R_1C_2}{R_1R_2C_1C_2}\right)^2 - \frac{4}{R_1R_2C_1C_2}} \tag{21}$$

Inverse transformation of Eq. (17) into the time domain gives

$$V(t) = \frac{V}{R_1C_2}\frac{1}{\alpha_2 - \alpha_1}[\exp(-\alpha_1 t) - \exp(-\alpha_2 t)] \tag{22}$$

From Eq. 21,

$$\alpha_2 = \frac{1}{2}\frac{1}{R_1C_1} + \frac{1}{R_1C_2} + \frac{1}{R_2C_1} + \sqrt{\left(\frac{1}{R_1C_1} + \frac{1}{R_1C_2} + \frac{1}{R_2C_1}\right)^2 - \frac{4}{R_1R_2C_1C_2}} \tag{23}$$

In practice, $R_2 \gg R_1$, and $C_1 \gg C_2$, so Eq. 23 reduces to

$$\alpha_2 \cong \frac{1}{2}\frac{1}{R_1C_2} + \sqrt{\left(\frac{1}{R_1C_2}\right)^2 - \frac{4}{R_1R_2C_1C_2}} \tag{24}$$

$$\alpha_2 = \frac{1}{2}\frac{1}{R_1C_2} + \frac{1}{R_1C_2}\sqrt{1 - \frac{4R_1C_2}{R_2C_1}} \cong \frac{1}{R_1C_2} \tag{25}$$

From Eq. 18,

$$\alpha_1\alpha_2 = b = \frac{1}{R_1R_2C_1C_2} \tag{26}$$

hence

$$\alpha_1 \cong \frac{1}{R_2C_1} \tag{27}$$

The equation for the output voltage then becomes

$$V(t) = V\exp\left(-\frac{t}{R_2C_1}\right) - \exp\left(-\frac{t}{R_1C_2}\right) \tag{28}$$

From Eq. (28) it is seen that the impulse voltage is the difference of two exponential functions and is graphically represented as shown in Fig. 18.

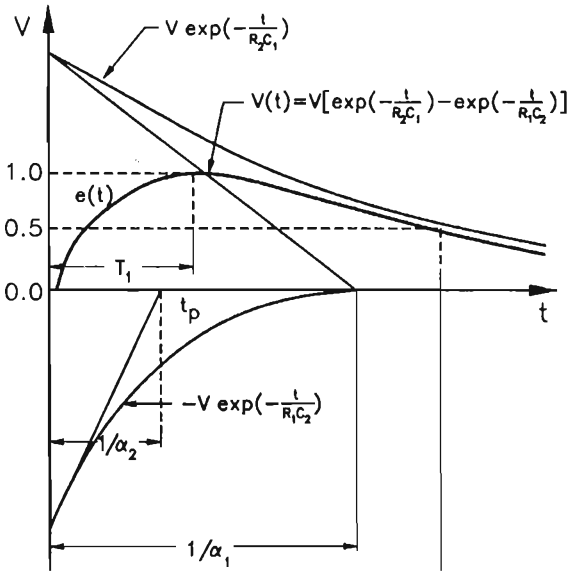


Figure 18 The two components of double exponential impulse voltage.

Time to the peak value t_p can be found by differentiating Eq. (28) with respect to time and equating the differential to zero; hence

$$\frac{dV(t)}{dt} = 0 \qquad \text{at} \qquad t = t_p \tag{29}$$

$$\frac{dV(t)}{dt}\Big|_{t=t_p} = 0 = kV - \alpha_1 \exp(-\alpha_1 t_p) + \alpha_2 \exp(-\alpha_2 t_p) \tag{30}$$

$$\text{Where} \qquad k = \frac{1}{R_1 C_2(\alpha_2 - \alpha_1)} \tag{31}$$

$$\text{or} \qquad \alpha_1 \exp(-\alpha_1 t_p) = \alpha_2 \exp(-\alpha_2 t_p) \tag{32}$$

$$\ln \alpha_1 - \ln \alpha_2 = t_p(\alpha_1 - \alpha_2) \tag{33}$$

$$t_p = \frac{1}{\alpha_1 - \alpha_2} \ln\left(\frac{\alpha_1}{\alpha_2}\right) \tag{34}$$

For impulses of very high amplitudes, it becomes necessary to use voltage multiplier circuits because of the following limitations with single stage impulse generators:

Construction cost and the size of the single capacitor of voltage ratings above 100 kV are very large.

The increase of the physical size, and hence the cost of other circuit elements such as charging and wave shaping resistors, increases the cost of the impulse generator further.

It becomes difficult to use spark gaps as a means of switching devices for very high voltages.

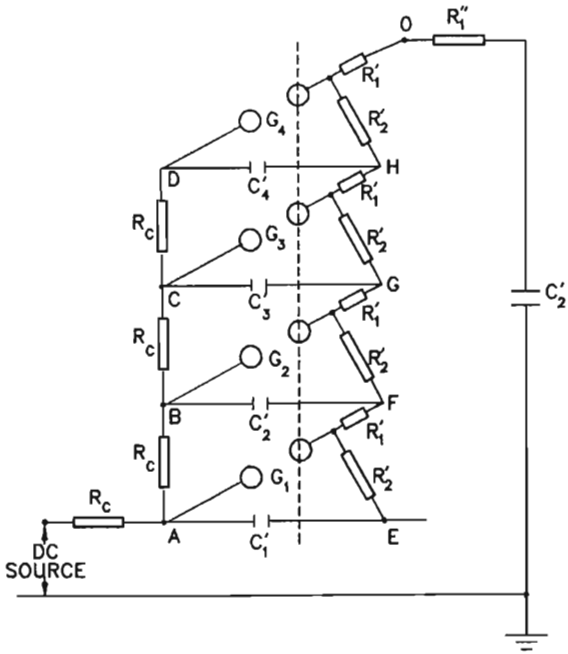
During the charging period, corona from high voltage charging resistors and the dc source are difficult to suppress.

C. Multi-Stage Impulse Generator

To generate impulse voltages of high peak values of order greater than several hundred kilovolts, it becomes necessary to cascade several single-stage units to form a multi-stage impulse generator. The voltage multiplier circuit proposed by Marx is the basis for a multi-stage impulse generator (Marx, 1924). The principle is based on charging a number of capacitors in parallel and then discharging them in series using spark gaps as switching elements. A typical configuration for a Marx generator utilizing the circuit connection of Fig. 16(b) is shown in Fig. 19 for a four-stage multiplier.

The generator capacitor C_1 is formed of four different stage capacitors, C_1' to C_4'. The front and discharge resistors R_1 and R_2 of the basic impulse circuit (Fig. 16) are also divided as several stage resistors nR_1' and nR_2' in order to improve the efficiency of the generator; where n is the number of stages. The dc source voltage charges the capacitors C_1' to C_4' through the charging resistors R_c and the wave shaping resistors R_1' and R_2'. At the end of the charging period, when all the capacitors are fully charged, the points A, B, C, and D are all at a potential V equal to the dc source voltage. The points E, F, G, and H remain at ground potential as the voltage drop across the resistors R_2' is negligible. The gap spacing is set so that the breakdown voltage of the gaps G_1 to G_4 is slightly higher than the charging voltage V.

The discharge of the generator capacitors is initiated by the breakdown of the first stage gap, G_1. With the sparkover of the gap G_1, the remaining gaps break in a quick succession, immediately discharging the capacitors C_1' to C_4' in series. With the breakdown of the gap G_1, the potential of point A changes from V to zero, causing a voltage swing of $-V$ at point A. Because the capacitor C_1' has been charged previously to a voltage V, the potential at point C must instantaneously swing to $-V$ from zero. This voltage swing at point C makes the potential difference across the gap G_2 to be $2V$. The gap breaks down, causing the point D to change by $-2V$. The potential at point E jumps from zero to $-2V$, placing a voltage



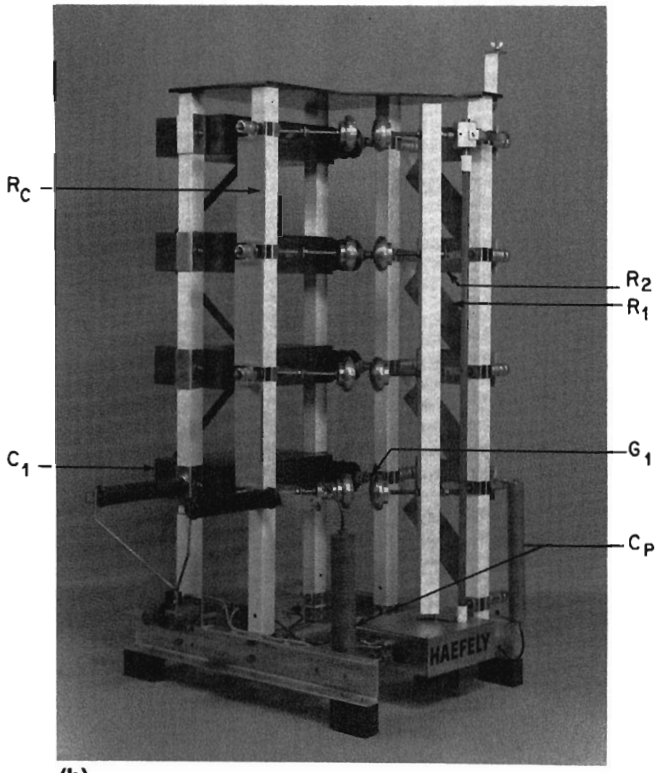
(a)

Figure 19 Four-stage impulse generator. (a) Schematic diagram; (b) 800 kV, 24 kJ SGS-type Haefeley's impulse generator. (Courtesy of Haefeley, Inc., Basel, Switzerland.)

difference of $3V$ across the gap G_3 and causing it to break down. The sequence continues until the output point O is at a potential of $-4V$ with respect to ground. The discharge of capacitors in series provides a cumulative output voltage equal to the sum of all the individual stage voltages. The polarity of the output voltage $V(t)$ is opposite to that of the charging dc source voltage V.

D. Tripping or Triggering of Impulse Generator

For a smooth operation of the multi-stage impulse generator it is essential that all the switching gaps G_1 to G_4 break down simultaneously. Self tripping of the impulse generator can be achieved by setting the bottommost gap to a slightly smaller spacing. Once the charging dc voltage reaches a high enough voltage to break the first gap, overvoltages appear across the



(b)

Figure 19 (*Continued*)

gaps at the higher stages causing the generator as a whole to operate in sequence, and the impulse is produced. Controlled tripping is however established by providing an external trigger pulse to the bottommost ignition spark gap G.

Trigger gaps are generally based on the trigatron spark gap, given in Fig. 20. The two spheres are the two electrodes of the first gap. The grounded left side sphere is provided with a small hole in the center, through which an insulated metal rod is mounted with an annular clearance of about 1 mm. The trigger sequence consists of

1. Applying a trigger pulse of the order of 10 kV to the rod, to cause a discharge between the rod and the grounded sphere.

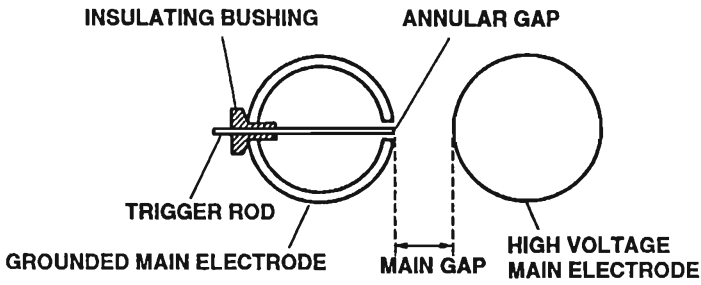


Figure 20 Trigatron spark gap for impulse generator tripping.

2. This initial discharge creates copious amounts of charge at the surface of the grounded sphere, which causes the main gap between the two spheres to break. The enhancement of field in the main gap by the trigger pulse further assists in breakdown of the main gap.
3. Gaps in the higher stages break because of the potential swing owing to the charge on the capacitors C_1 to C_4. Since the trigatron is sensitive to the polarity of the charging dc voltage, it is recommended that the trigger pulse polarity be changed along with the dc source polarity when the impulse polarity is reversed (Kind, 1978; Humphries, 1986).

VI. PULSE APPLICATION IN ELECTROSTATIC INDUSTRIES

Pulse energization for various applications is not a new concept; but only with the recent development of reliable pulsar hardware has it become a viable option for many industrial applications. The pulse generators of the types that were discussed in previous sections are mainly built for use in high voltage testing. The application of pulse power technology to industries other than power equipment testing includes

Methods of improving the particle collection efficiency of high resistivity dust using pulse energized electrostatic precipitators (Hall, 1990; Lloyd, 1988; Masuda and Hosokawa, 1984)

Pulse corona discharge for ozone production (Masuda and Hosokawa, 1984; Longlais et al., 1991)

Pulsed power application for food processing and preservation (Cross, 1988; Jayaram et al., 1992)

Applications for electroporation and electrofusion in cell biology (Jayaram et al., 1993; Neumann et al., 1989)

The requirements for generation of these special pulses vary with their applications. Compared to conventional (1.2/50 μs lightning or 250/2500 μs switching) impulses, which are mainly used in testing, these special pulses differ in their (1) rise time (subnanoseconds to microseconds); (2) durations (nanoseconds to hundreds of microseconds), and (3) repetition rate (frequency varying from 1 Hz to several kHz). Based on the type of switching used, high voltage pulse power supplies are classified into three principal circuits: rotating spark gap (Hall, 1990; Masuda and Hosokawa, 1984), thyristor switched (Milde, 1992; Jacoby and York, 1980), and thyratron switched (Hall, 1990; Jayaram et al., 1993) pulse power supplies.

A. Rotating Spark-Gap (RSG) Power Supplies

RSG power supplies consist of a pulse forming capacitor bank C_p, consisting of parallel and series connected capacitors, and a rotating spark gap; see Fig. 21. Charging of C_p is carried through the rectifier circuit during one-half of the cycle and discharges into the load in the next half cycle.

The spark gaps provide a low inductance path for charging and discharging the pulse forming capacitor C_p. Pulse repetition rate depends on the speed of the rotating switch, which in a standard design (Masuda and Hosokawa, 1984) is synchronized with the ac power supply. Because of the low inductance of the spark gap, the RSG generator is capable of

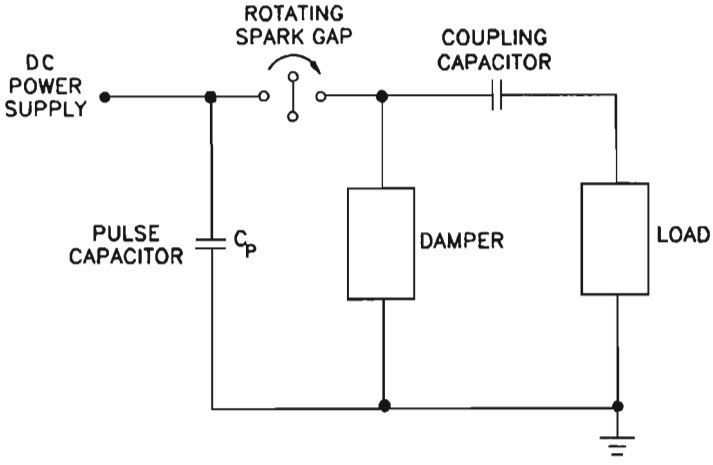


Figure 21 Rotating spark-gap pulse power supply.

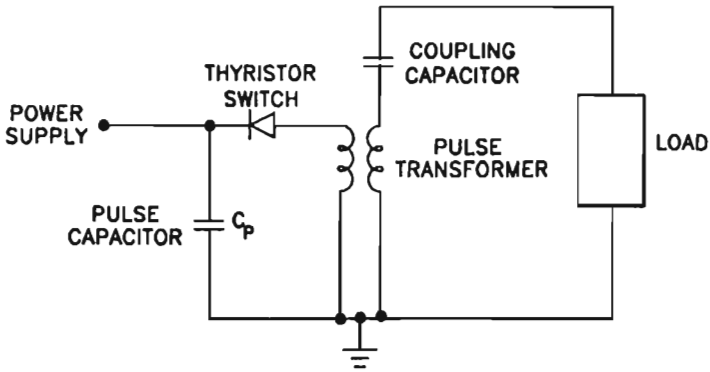


Figure 22 Thyristor switched pulse power supply.

producing pulses of very narrow duration (~1 μs). The reliability of the pulse production depends on the material and the surface irregularities of the spark-gap electrodes. The RSG generator has its limitation in recovering the holdoff electrical strength quickly compared to thyratron switched power supplies.

B. Thyristor Switched Power Supplies

The second system that uses a pulse transformer and thyristors as switching devices is shown in Fig. 22. The pulse capacitor C_p is charged to a relatively low voltage and then transferred onto the load via a thyristor (silicon controlled rectifier, SCR) switch and a pulse transformer. The voltage multiplication is carried out through the pulse transformer. Because of the pulse transformer, the circuit has a limited *di/dt* capability and hence limitation on generation of narrow pulses. Only pulses of the order of >100 μs can be produced using this method.

C. Thyratron Switched Power Supplies

Thyratron switched power supplies are capable of generating narrow pulses using a gas-filled thyratron as a switch. The schematic of the pulse power supply is shown in Fig. 23. The pulse forming capacitor C_p is charged through the resistor R_1 and diode D_1 from a dc source S_1. The low inductance and low resistance path for the discharge of the stored energy is provided through the thyratron itself, which can recover the holdoff electric strength quickly. The pulse repetition rate could be varied by varying the frequency of the trigger pulse generator, which is on the

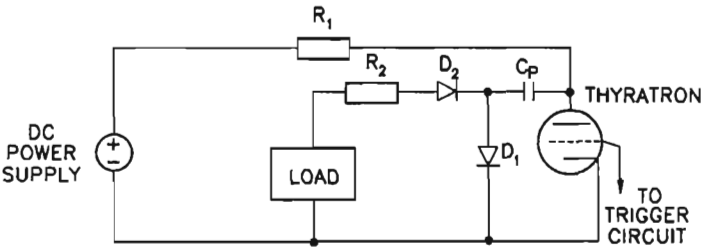


Figure 23 Thyratron switched pulse power supply.

low voltage side (800 V). Thyratron switched power supplies have many advantages over the other two types of pulse power supplies discussed above because of high *di/dt*.

REFERENCES

Allibone, T. E., A. Beetlestone, and G. S. Innes (1934). *Brit. J. Radiol.*, 7, 83.

Charlton, E. E., W. F. Westendrop, L. E., Dempster, and G. Hotaling (1939). *J. Appl. Phys.*, 10, 374.

Charlton, E. E., and W. F. Westendrop (1941). *G.E. Rev.*, 44, 654.

Cornic, K. J., and T. R. Thompson (1982). Steep-fronted switching voltage transients and their distribution in motor windings, Part 2. IEE Proc., 129, 56–63.

Craggs, J. D., and J. M. Meek (1954). *High Voltage Laboratory Technique*. Butterworths, London.

Cross, J. D. (1988). Perforation of synthetic plastic films. U.S. Patent No. 4,777,338.

Enge, H. A. (1971). Cascade transformer high voltage generator. U.S. Patent No. 3596, 167 (July).

Felici, N. J. (1953). *Direct Current*, 1, 122.

Felici, N. J. (1965). *J.I.E.E.*, 1969.

Franklin, A. C., and D. P. Franklin (1983). *The J&P Transformer Book*. Butterworths, London.

Gallagher, T. J., and A. J. Pearmain (1982). *High Voltage: Measurement, Testing and Design*. John Wiley, New York.

Goodlet, B. L. (1929). *J.I.E.E.*, 67, 1177.

Greenwood, A. (1991). *Electrical Transients in Power Systems*. Wiley Interscience, New York.

Hall, H. J. (1990). History of pulse energization in electrostatic precipitation. *J. Electrostatics*, 25, 1–22.

Humphries, S., Jr. (1986). *Principles of Charged Particle Acceleration*. John Wiley, New York.

IEC Publication 60-2 (1973). *High Voltage Test Techniques, Test Procedures*.

Jacoby, B. A., and T. M. York (1980). High voltage SCR trigger circuit utilizing disc capacitors in a Marx array. *Rev. Sci. Instrum.*, 51, 885–887.

Jayaram, S., G. S. P. Castle and A. Margaritis (1992). Kinetics of sterilization of Lactobacillus brevis cells by the application of high voltage pulses. *Biotechnology and Bioengineering*, 40, 1412–1420.

Jayaram, S., G. S. P. Castle, J. S. Chang, A. A. Berezin, P. Looy, R. Mangal, and M. Mozes (1993). Pulse power energization effects on ESP efficiency in collection of high resistivity flyash particles. Proc. IEEE—IAS 1993 Annual Conf., 1882–1886.

Kind, Dieter (1978). *An Introduction to High-Voltage Experimental Technique*. Friedrich Vieweg & Sohn Verlagsgesellschaft mbH, Braunschweig, Germany.

Khalifa, M. (1990). *High-Voltage Engineering: Theory and Practice*. Marcel Dekker, New York.

Kuffel, E., and M. Abdullah (1970). *High Voltage Engineering*. Pergamon Press, Oxford.

Kuffel, E., and W. S. Zaengl (1984). *High Voltage Engineering Fundamentals*. Pergamon Press, Oxford.

Lloyd, D. A. (1988). *Electrostatic Precipitator Handbook*. Adam Hilger, Bristol.

Longlais, B., D. A. Reckhow, and R. Brink (1991). *Ozone in Water Treatment Application and Engineering*. Lewvs Publishers, New York.

Marx, E. (1924). Investigations in the testing of insulators with impact voltage. *Elektrotech. Zeits.*, 45, 652–654.

Masuda, S., and S. Hosokawa (1984). Pulse energization system of electrostatic precipitator for retrofitting application, Proc. IEEE—IAS 1984 Annual Conf., 1177–1184.

Milde, H. I. (1992). Pulse corona discharge in electrostatic precipitators. *IEEE Trans. on Electr. Insul.*, 17, 179–186.

Mitchell, R. G. (1943). *Wireless Eng.*, 20, 414.

Mitchell, R. G. (1945). *Wireless Eng.*, 22, 474.

Naidu, M. S., and V. Kamaraju (1982). *High Voltage Engineering*. Tata McGraw-Hill, New Delhi.

Neumann, E., A. E. Sowers, and C. A. Jordan (1989). *Electroporation and Electrofusion in Cell Biology*. Plenum Press, New York.

Philips, S. F. (1977). *IEEE Trans.*, EI 12, 130.

Sandhaus, S. (1976). Nouveaux aspects de l'ergonomité. *Revue mensuelle suisse d'odontostomatologie*, 86, 1312

Trump, J. G. (1947). *Elect. Eng.*, 66, 525.

Van Dorsten, A. C. (1955). *Phil. Tech. Rev.*, 17, 109.

Wagner and Clayton (1964). Lightning phenomena. In *Electrical Transmission and Distribution Reference Book*. Westinghouse Electric Corporation, East Pittsburg, Pennsylvania, pp. 543–577.

11

Measurement of Electrostatic Fields, Voltages, and Charges

Mark N. Horenstein

Boston University
Boston, Massachusetts

I. INTRODUCTION

The design of an electrostatic system, experiment, process, or device often requires the measurement of electric fields, potential, or charge. Examples of electrostatic environments in which measurements are important include electrostatic precipitators, static control systems for manufacturing, electrophotography, electrostatic flow systems, electrostatic spraying, atmospheric studies, and EOS/ESD hazard identification. This chapter outlines the basic principles and techniques of electrostatic measurement. The reader is assumed to have a working knowledge of field theory fundamentals as outlined in Chapter 1. The references cited at the end of this chapter are not an exhaustive list but are meant to provide the reader with an introductory sampling of works that address the subject of electrostatic measurements.

II. BASIC TECHNIQUES FOR ELECTROSTATIC MEASUREMENT

Electrostatic measuring instruments require sensors that can respond to the related quantities of electric field, potential, and charge. In this section, several commonly used electrostatic sensors are introduced and the basic techniques of electrostatic measurement are explored.

A. Force Sensors

The most fundamental electrostatic sensors are those that respond directly to the force exerted by an electric field on a charged conductor. Electromechanical force sensors of this type were used by the early experimenters who discovered the laws of electrostatics. Force sensors are still used in certain types of electrostatic voltmeters (Schwab, 1972) in which the voltage to be measured deflects a pivoting capacitor plate tied to a torsion spring. At one time, these mechanically based electrostatic voltmeters were the principal measuring instruments of electrostatics and high-voltage engineering. Though largely surpassed by more modern instruments based on solid-state electronics, instruments based on electromechanical sensors are worthy of mention and are still used occasionally in special applications and in ultra-high-voltage work (e.g., Nyberg et al., 1979).

B. Conventional Voltmeters

A conventional voltmeter measures the potential difference between its terminals while drawing minimal current from the measured source. Common examples of this type of instrument include digital multimeters, electrometers, and oscilloscopes set to dc coupling. In an electrostatic system, a voltmeter can be used to measure the potential of a conductor held at a fixed voltage if the input resistance of the meter is much larger than the resistance connecting the conductor to its source of voltage. The meter capacitance must be charged through the latter resistance but will not affect the final meter reading, since a limitless supply of charge is available from the source of conductor voltage. A voltmeter can also be used to measure the potential of a floating, charge-bearing conductor if the meter's input resistance is suitably large and if its internal capacitance is much smaller than the conductor's capacitance to ground. In the system of Fig. 1, for example, a voltmeter with internal input resistance R_M and capacitance C_M is used to measure the potential of floating conductor carrying charge Q. Before the application of the voltmeter, the conductor potential equals Q/C_G, where C_G is the conductor capacitance to ground. Upon application and immediate removal of the voltmeter, the conductor potential falls to the value

$$V_C = \frac{Q}{C_G + C_M} \tag{1}$$

as some of the conductor charge is transferred to C_M. For the parameters $Q = 0.1\ \mu C$, $C_G = 100$ pF (typical of a bench top experiment in air), and $C_M = 10$ pF, the initial conductor potential will equal 1 kV. After application of the voltmeter, the conductor potential will drop to the value $V_C = Q/(C_G + C_M) = 0.1\ \mu C/110$ pF $= 909$ V. Note that the conductor

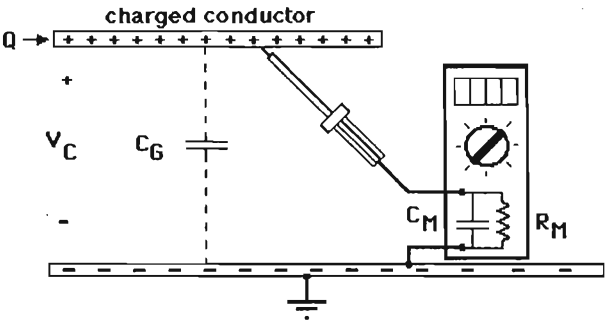


Figure 1 Voltmeter with internal resistance R_M and capacitance C_M discharges charged conductor with decay time constant $\tau = R_M(C_G + C_M)$, where C_G is the net conductor capacitance to ground.

potential will remain at the reduced value of 909 V, corresponding to a conductor charge of 0.091 μC, when the voltmeter is removed. The charge transferred to C_M during the measurement operation is permanently removed from the charged conductor when the meter is taken away.

If the voltmeter is not immediately removed, but instead allowed to remain in contact with the conductor, the internal resistance of the meter will discharge the conductor exponentially over time according to the decay law:

$$V_C(t) = V_C(t = 0) \exp[-t/R_M(C_G + C_M)] \tag{2}$$

In this equation, the internal meter resistance R_M, which includes leakage, is presumed to be ohmic. Time $t = 0$ defines the moment when the voltmeter is first applied, with $V_C(t = 0)$ given by Eq. 1. For an R_M of 1 GΩ (typical of an electrometer of reasonable quality) and a total capacitance $C_G + C_M$ of 100 pF (typical for a bench top experiment in air), the decay time constant becomes 0.1 s. This decay time constant is too short to make manual measurements feasible. In order to make such a measurement, an electrometer impedance approaching 10^{12} Ω (1 TΩ) would be required.

A conventional voltmeter cannot be used to measure the potential of a charged, insulating surface, because the current required to charge the meter capacitance or supply its internal resistance has no conducting path over which to flow. More fundamentally, the potential of an insulating surface is not fixed but is influenced by geometry and the proximity of other conducting surfaces and objects, including the meter probe. In general, noncontacting methods must be used under controlled geometries in order to obtain meaningful measurements of insulator surface potentials. This issue is discussed in more detail in Sec. II.E.

C. Electrostatic Field Mill

In many applications, electrostatic measurement methods that require no contact with the source of field provide welcome relief from the capacitive and resistive loading effects of conventional voltmeters. In noncontact methods, an electric field sensor is placed near, but not touching, a conductor or surface to be measured. Values of surface potential or charge are inferred by monitoring the electric field measured by the sensor.

A quasistatic periodic or transient field made to be incident on a nearby grounded electrode can be measured using a flush-mounted segment such as the one illustrated in Fig. 2. Such a segment will introduce negligible distortion to the field if its voltage is kept close to that of the host electrode, i.e., near ground potential. The charge induced on the segment will be given by $Q = \epsilon AE(t)$, where ϵ is the permittivity of the medium and A the segment area, and where $E(t)$ is assumed to be spatially constant over the area of the segment. Integrating the segment current $i(t) = dQ/dt$ over time yields a value for Q, and thus for the incident field $E(t)$.

If the field is truly electrostatic (no variation in time), the current to an isolated sampling segment of the type shown in Fig. 2 will be zero. Under such conditions, other types of noncontacting sensors are required. One sensor, called the electrostatic field mill, or sometimes the vibrating capacitor electrometer or field chopper, measures electric fields by perturbing the capacitance of the sampling segment relative to the field source. The capacitance perturbation induces a current in the sampling segment that is proportional to the electric field strength incident on the field mill.

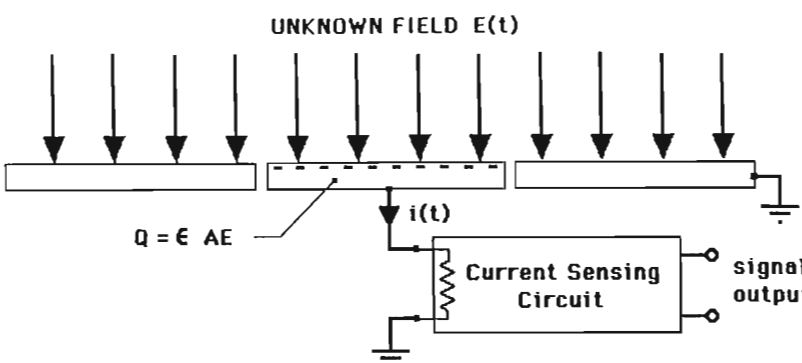


Figure 2 Measuring the field at a conductor surface using an isolated sampling electrode.

A complete field mill system consists of a sensing electrode, a chopping electrode or shutter that alternately shields and exposes the sensing electrode to the incident field, and a current-to-voltage converter. One type of field mill based on a rotating chopper (Trump et al., 1980; McKnight et al., 1983) is depicted in Fig. 3. A second popular configuration, based on a "tuning-fork" shutter (Vosteen and Bartnikas, 1987; Secker, 1984), is depicted in Fig. 4. Other types of capacitance-perturbing "shutters" include rotating perforated disks, rotating split cylinders, and longitudinally vibrating plates.

Under normal operating conditions, the shutter and field mill body are connected directly to ground, and the sensing electrode is connected to ground via the low input impedance of a current-sensing circuit. A low impedance connection ensures that the electrode will lie near ground potential even when induced currents flow to and from the sensor. The current detector may be as simple as a single low-valued resistor; alternatively, a sophisticated electronic circuit may be employed.

Field detection is enabled when the shutter is set into mechanical motion. The measured field must vary slowly in time compared to the period of shutter opening and closing. When the shutter is closed, as in Fig. 3(a) or 4(a), a minimum of field flux terminates on the sensing electrode. Conversely, when the shutter is fully opened, as in Fig. 3(b) or 4(b), the field flux terminating on the sensing electrode reaches a maximum. At any given intermediate shutter position, a charge proportional to the net field flux will be induced on the sensing electrode. As the shutter opens and closes, a periodic current equal to the time rate of change of the induced charge will thus flow to the sensing electrode via the current sensing circuit. This capacitive, or displacement, current will be 90° out of phase with the exposed sensor area, as indicated in Fig. 5, and its magnitude will be directly proportional to the field incident on the field mill. Neglecting fringe fields around the shutter, the instantaneous charge induced on the sensing electrode will be given by

$$Q = \epsilon_0 \int_A E \, dA = Q\epsilon_0 A(t) E \tag{3}$$

where $A(t)$ is the area of the sensing electrode. (If the field mill operates in a medium other than air or vacuum, an appropriate permittivity must be substituted for ϵ_0.)

The current $i(t)$ flowing to the sensing electrode will be equal to dQ/dt. If E is essentially constant over the aperture area, this derivative can be expressed as

$$i(t) = \frac{dQ}{dt} = \frac{d}{dt} \epsilon_0 A(t) E = \epsilon_0 E \frac{dA(t)}{dt} \tag{4}$$

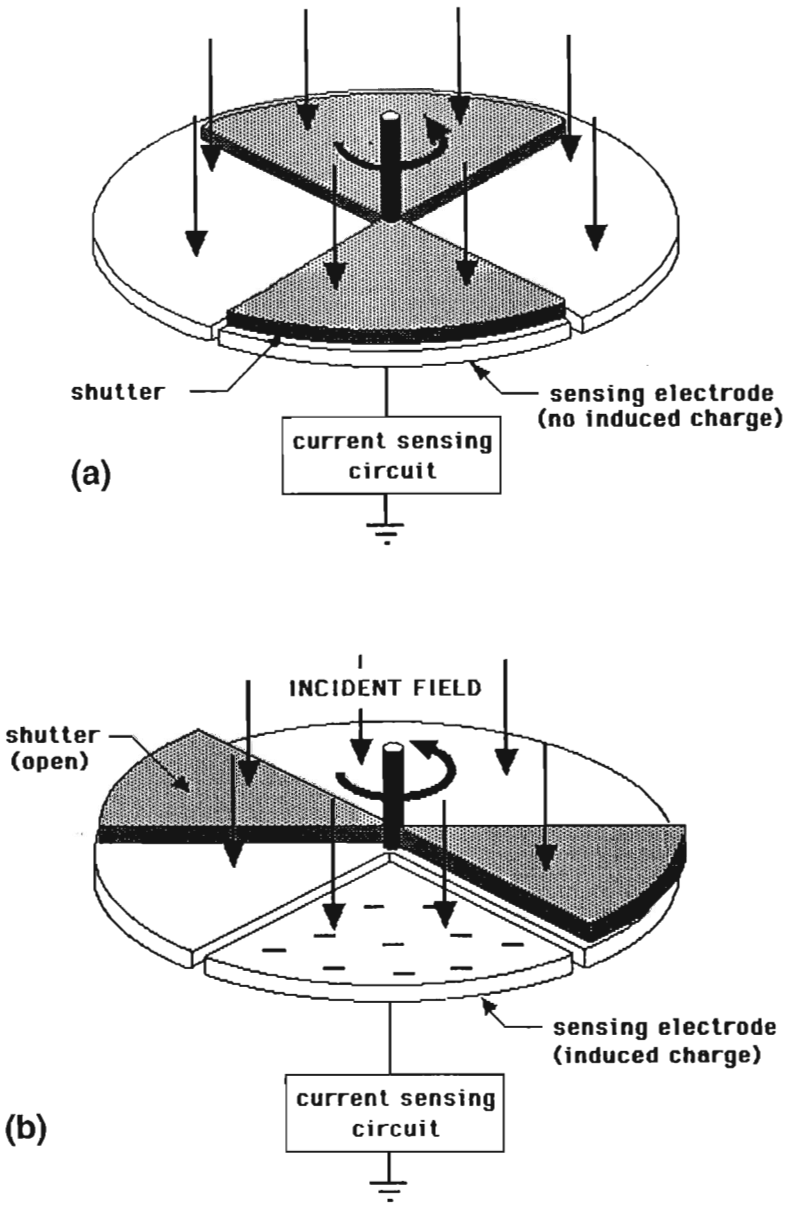


Figure 3 Basic components of a rotating electrostatic field mill. (a) Shutter closed; charge induced on the sensing electrode is minimum. (b) Shutter open; charge induced on the sensing electrode is maximum.

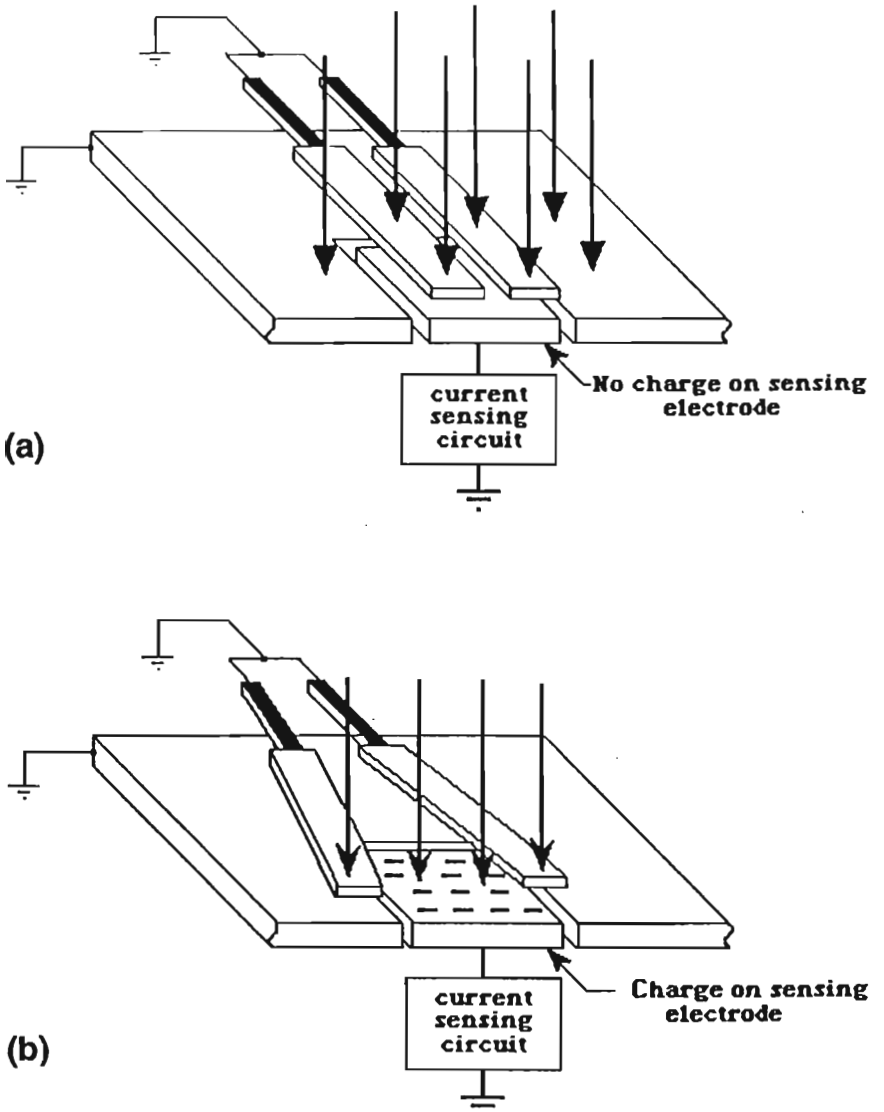


Figure 4 Electrostatic field mill based on tuning-fork shutter.

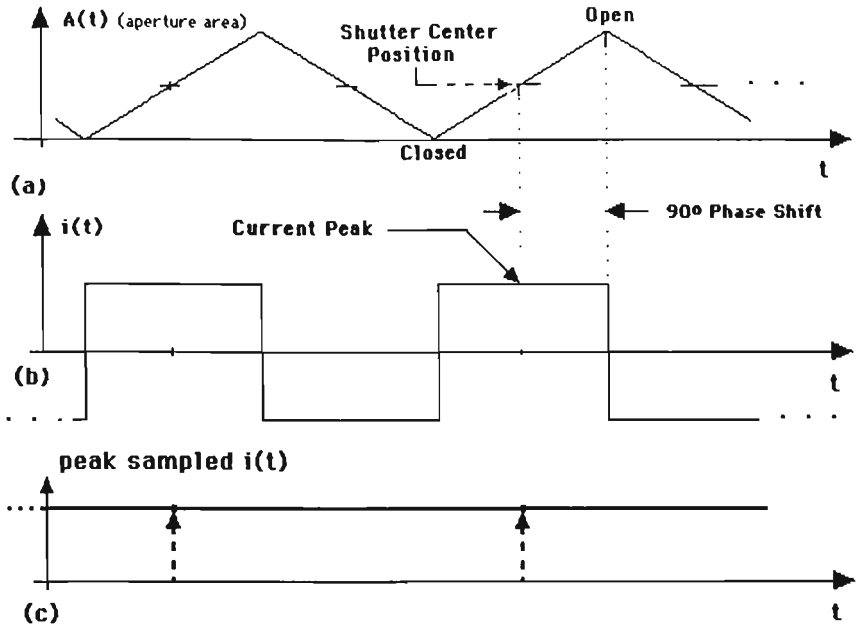


Figure 5 Waveforms associated with field mill operation. (a) Exposed sensor aperture area versus time; this waveform could also represent the charge induced on the sensing electrode. (b) Current flow to the sensing electrode. (c) Output of the current sensing circuit after sample-and-hold is performed at regular intervals (arrows).

By sampling $i(t)$ at its peak, when dA/dt is maximum, a value for the incident field E, including polarity, can be obtained. The sampling can be synchronized to the peak of $i(t)$ by a signal derived from the shutter driving mechanism.

An alternative method of current monitoring, illustrated in Fig. 6, involves a sampling technique called synchronous detection (Haykin, 1983; Lathi, 1989), also known as coherent detection or lock-in amplification. In a field mill with synchronous detection, the current signal $i(t)$ from the sampling electrode is fed to a low-pass filter only over one half of its periodic cycle. During the other half period, the input to the low-pass filter is set to zero. The electronic gating is synchronized, using a signal derived from the shutter driving mechanism, to the shutter driving frequency f_S. The phase of the gate signal is adjusted to have its time window centered around the peak of the current signal, i.e., at the point of maxi-

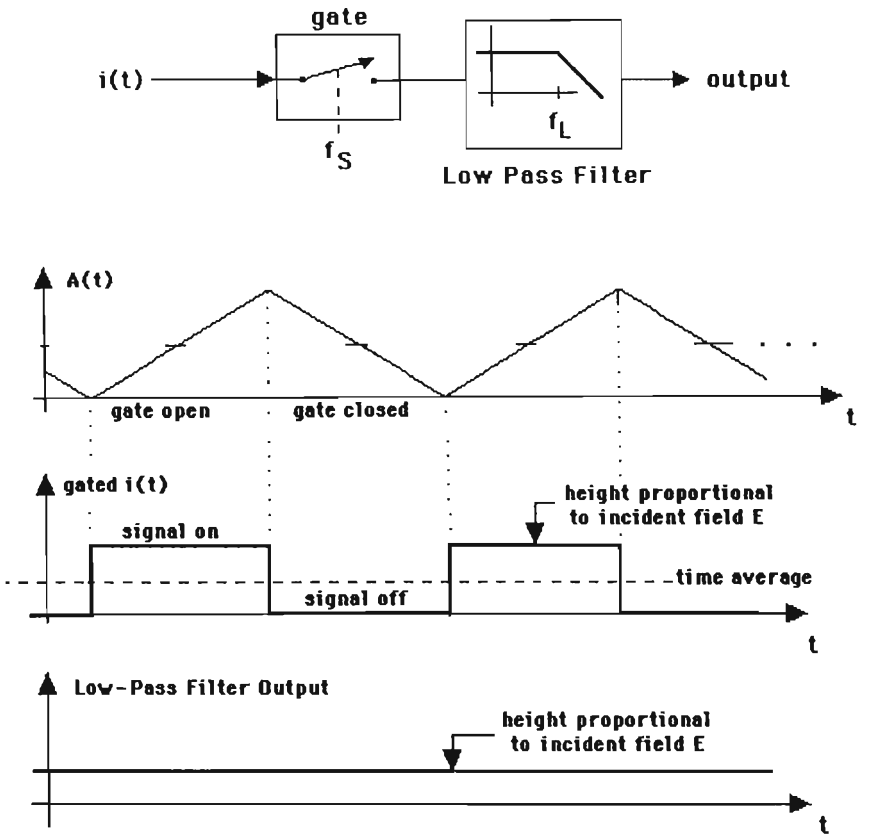


Figure 6 Synchronous detection signal processing technique. The current signal $i(t)$ from the sensing electrode is gated over one half the aperture window and sent to a low-pass filter. The output is proportional to the incident electric field intensity.

mum dA/dt. The cutoff frequency f_L of the low-pass filter is set well below the shutter frequency f_S, allowing the low-pass filter to extract the time average of the gated signal. The latter will be proportional to the incident field E. The synchronous detection technique allows any noise components that lie above f_L to be attenuated by the low-pass filter, thereby greatly improving the signal-to-noise ratio of the field mill system. A second advantage of synchronous detection is realized when ions or other space charges impact on the field mill. This application of the field mill is discussed in Sec. III.

A field mill is best calibrated using a method that relates its output to a known applied E-field. Calibration methods based on design formulas or field solutions are useful for initially estimating field mill performance, but the presence of field distortion at the shutter, imprecise sampling synchronization, and circuit variations make direct calibration of field mill output in the presence of a known field preferable.

D. Noncontacting Voltmeters

Synchronous field mills play an important role in a class of instruments known as feedback-null surface potential monitors (Vosteen and Bartnikas, 1987; Vosteen, 1988), also known as noncontacting voltmeters. Commercial versions of these instruments are now standard equipment in most electrostatics laboratories. The basic operating principle is illustrated by the block diagram of Fig. 7. A miniature probe-mounted field mill feeds a synchronous detection circuit and high-voltage amplifier. The output of the high-voltage amplifier drives the potential of the field mill body, thus forming a negative feedback loop. When the probe is exposed to a surface of nonzero potential, the detected field signal, amplified by the high-voltage amplifier, raises the probe potential toward that of the measured surface, thereby reducing the net field magnitude seen by the probe. The feedback loop reaches equilibrium when the voltage of the probe body lies nearly at the potential of the measured surface, causing only a residual field signal to be present at the probe. The residual signal in this "null"

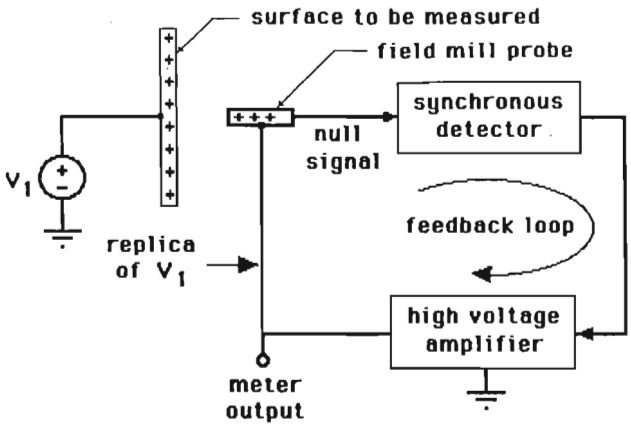


Figure 7 Feedback-null surface potential monitoring technique, also known as the noncontacting voltmeter technique. The feedback loop replicates the measured potential V_1 and applies it to the body of the field-mill probe, forcing the field measured by the latter to be zero.

condition can be made arbitrarily small by increasing the gain of the high-voltage amplifier. The potential of the measured surface is determined by monitoring the voltage applied to the probe by the feedback loop. The range limits of such a measuring system are generally determined by the saturation levels of the high-voltage amplifier. If the probe views a surface with spatially varying potential, the probe body will attain some average voltage at which its net field signal reaches a null. This voltage will reflect spatial averaging of the actual surface potential, tempered by the probe-to-surface spacing.

E. Measurement Conditions for Noncontacting Voltmeters

Noncontacting voltmeters can be useful in innumerable electrostatic situations. The readings from these instruments, however, must always be interpreted with a full understanding of system conditions. In this section, voltmeter behavior under three commonly found sets of conditions is examined.

1. Probe Exposed to Conducting Surface at Fixed Potential

When the probe of a noncontacting voltmeter is held close to a conductor constrained to a fixed potential by a voltage source, the conductor potential will not be affected by the proximity of the probe. Under these conditions, the null-field condition will be reached when the probe potential approaches that of the conductor, and the reading obtained will be unambiguous.

2. Probe Exposed to Floating Conductor with Fixed Charge

If a noncontacting voltmeter is used to measure the potential of a charge-bearing, floating conductor, the conductor potential, and hence the meter reading, will be affected by the proximity and position of the probe. The situation can be modeled by the two-body capacitance problem of Fig. 8, where C_1 and C_2 denote the capacitances to ground of the conductor and probe, respectively, and C_M the mutual capacitance between them. The relationship between the various quantities in this system can be expressed by the matrix equation

$$\begin{bmatrix} Q_1 \\ Q_2 \end{bmatrix} = \begin{bmatrix} C_1 & C_M \\ C_M & C_2 \end{bmatrix} \begin{bmatrix} V_1 \\ V_2 \end{bmatrix} \tag{5}$$

For constant Q_1 on the conductor, and for the condition $V_2 = V_1$ (null-field condition in which the probe is raised to the potential of the conductor), Eq. 5 yields

$$V_1 = V_2 = \frac{Q_1}{C_1 + C_M} \tag{6}$$

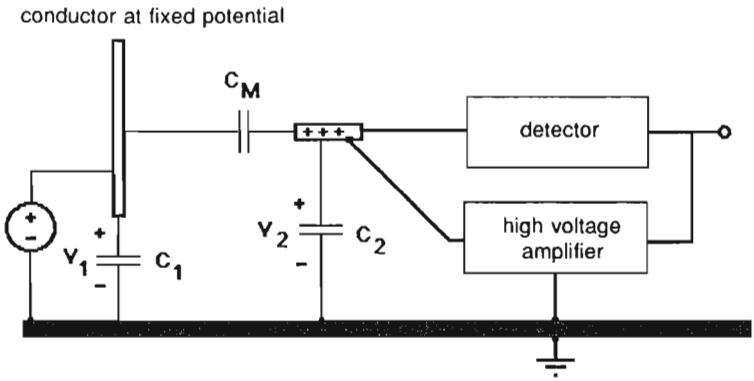


Figure 8 Two-body capacitance representation of field mill probe, measured conductor, and ground plane.

Since C_M will be a function of probe position, the meter reading becomes position dependent. In the limit $C_M \ll C_1$ (large conductor-to-ground capacitance), Eq. 6 yields the unambiguous result $V_1 = V_2 = Q_1/C_1$, which is the potential of the floating conductor with the probe absent. If C_1 is known, the value of Q_1 can be determined from this simplified relationship.

3. Probe Exposed to Insulating Surface with Accumulated Surface Charge

One of the most common uses of noncontacting voltmeters involves the measurement of charge on insulating surfaces. Measurements under these conditions are the most obscure and require careful interpretation if they are to be unambiguous. In the absence of a measured conductor, the two-body capacitance description of Fig. 8 cannot be used to analyze the system. In the special case where the surface charge resides on an insulating layer that is tightly coupled to an underlying ground plane, however, noncontacting voltmeters can provide meaningful measurements. The scenario described is illustrated in Fig. 9. Under the conditions shown, the surface potential of the charge layer becomes well defined and determined primarily by its coupling to the ground plane. Specifically, the surface potential Φ of the charge layer can be computed by taking the line integral $-\int E \cdot ds$ vertically through the insulating layer, where $E = -\sigma_s/\epsilon$. This integral leads to the result $\Phi = \sigma_s d/\epsilon$, where d is the thickness of the insulator and ϵ its permittivity. If the lateral dimensions of the insulating layer are large compared to its thickness, the region above the charge

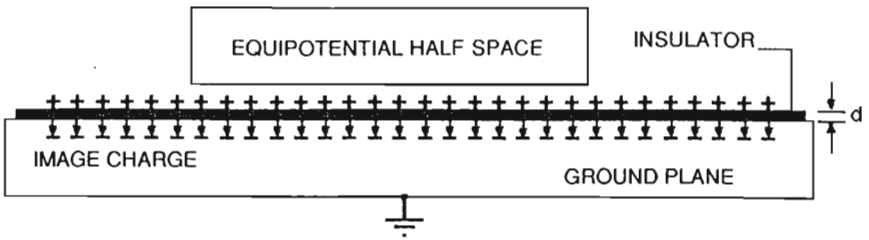


Figure 9 Uniform charge on an insulating layer tightly coupled to a ground plane. If the layer is infinite in the horizontal plane, the half space above the charge layer becomes a region of constant potential.

layer can be modeled as a half space of zero electric field and constant potential Φ. In essence, the surface charge and its ground-plane image function as a double layer that introduces a potential jump between the zero potential of the ground plane and the region above the charge layer.

If the probe of a noncontacting voltmeter is placed in the half space above the charge layer, the uniformity of the system will initially be perturbed, causing a component of electric field to terminate on the probe. The noncontacting voltmeter will respond by raising its probe potential until the null-field condition is reached. Null field will occur when the probe is raised to the potential $\sigma_s d/\epsilon$ of the region above the charge layer. The voltmeter reading can thus be used to determine the density of the charge layer using the equation

$$\sigma_s = \epsilon E = \frac{\epsilon V_P}{d} \tag{7}$$

where V_P is the probe potential (i.e., the meter reading), σ_s is in C/m^2, and d is in meters.

If the charged insulator does not rest over a tightly coupled, dominant ground plane, its surface potential will be strongly influenced by the position of the probe as well as by the insulator position relative to other conductors and dielectrics. Under these conditions, the meter reading becomes extremely sensitive to probe position and cannot be determined without detailed analysis (often numerical) of the fields in the system. In general, the field incident on the probe will consist of two superimposed components, one equal to the field produced by the measured charge with the probe grounded, and the other created by the probe itself with the measured charge absent and the probe raised to the potential V_P. The voltmeter will raise the probe potential V_P until the latter field component

cancels the former. The relationship between the resulting field-nulling V_P and the unknown surface charge is difficult to determine and requires a detailed field solution that takes into account the probe shape, probe position, and insulator geometry. Because of the difficulty in translating voltmeter readings into actual charge values, noncontacting voltmeter measurements of isolated charge distributions that are not tightly coupled to ground planes are best used for relative measurement purposes only. A noncontacting voltmeter used in this way becomes particularly useful when measuring the relative decay of charge over time.

F. Capacitively Coupled Sensors

The widespread availability of metal-oxide-semiconductor field effect transistors (MOSFETs) has made possible a class of field measuring instruments based on capacitive coupling. MOSFET sensors are found in a number of commonly available hand-held instruments as well as in numerous custom installations. A MOSFET field sensor has the advantage of no moving parts, but it can exhibit drift and introduce unwanted dc offsets.

The basic operating principle of the capacitively coupled MOSFET field sensor is illustrated in Fig. 10. The MOSFET gate is connected to a sampling segment (b) of area A that is exposed to the field to be measured. The MOSFET must be a depletion-mode type that can pass current at zero gate voltage and respond to gate voltages of either polarity. Enhancement-mode MOSFETs, which respond to one polarity of gate voltage only and have large threshold voltages, are generally unsuitable for electrostatic applications.

A sensing electrode exposed to an incident electric field will develop a surface charge density equal to $-\epsilon E$, where E is positive into the electrode and ϵ the permittivity of the medium above the sampling segment. The total charge $-\epsilon AE$ induced on the sampling segment will induce an equal and opposite charge ϵAE on the gate of the MOSFET, in turn charging the MOSFET capacitance C_{GS} to the voltage $v_{GS} = \epsilon AE/C_{GS}$. If a drain-to-source voltage v_{DS} is applied to the MOSFET, a drain current of magnitude

$$i_D = K(v_{GS} - V_t)^2 \qquad \text{for } v_{DS} > v_{GS} - V_t \tag{8}$$

or

$$i_D = 2K\left[(v_{GS} - V_t)v_{DS} - \frac{{v_{DS}}^2}{2}\right] \qquad \text{for } v_{DS} < v_{GS} - V_t \tag{9}$$

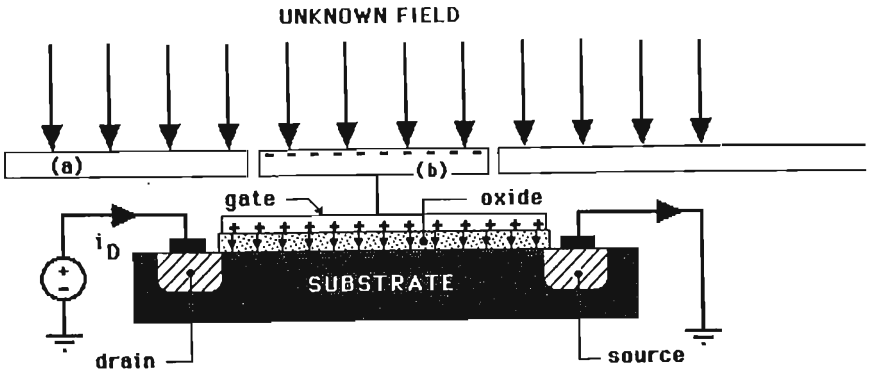


Figure 10 Operating principle of the capacitively coupled MOSFET field sensor. (a) Host electrode; (b) isolated sampling segment. The incident unknown field E induces a charge $-\epsilon AE$ on the sampling segment. An equal and opposite charge ϵAE is induced on the MOSFET gate, thereby charging the MOSFET gate capacitance C_{GS} to the voltage $\epsilon AE/C_{GS}$.

will flow in response, where V_t is the MOSFET threshold voltage. Equation 8 defines the MOSFET's "constant-current" region (i_D independent of v_{DS}), and Eq. 9 the MOSFET's triode region (Horenstein, 1990). The threshold voltage V_t and the conductance parameter K are fixed parameters of the MOSFET; V_t will be negative and typically in the range -0.5 V to -5 V for an n-channel depletion-mode MOSFET. The parameter K, typically in the range 0.5 to 4 mA/V^2, will be positive.

The nonlinear relationship between i_D and the field-induced v_{GS} can be compensated for via active-load compensation using the circuit configuration of Fig. 11. In this circuit, the current of the sensing MOSFET is drawn through a second enhancement-mode device that has its gate connected to its drain. The square-law behavior of the devices cancel, leading to an output of

$$v_{OUT} = V_{DD} - \sqrt{K_R}\, v_{GS1} + V_{t2} + \sqrt{K_R}\, V_{t1} \tag{10}$$

where $K_R = K_1/K_2$, V_{t1} is negative, and V_{t2} is positive. This equation has a constant slope with respect to v_{GS1} and is valid as long as Q_1 operates in its constant-current region.

Another MOSFET field sensing technique, shown in Fig. 12 (Garverick and Senturia, 1982; Horenstein, 1985), uses a feedback loop to replicate the field-induced gate voltage and drain current of the sensing MOSFET

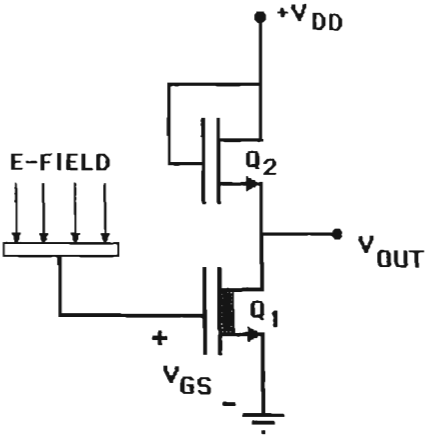


Figure 11 Active load field-measuring circuit that compensates for the square-law behavior of the MOSFET. Both MOSFETs must operate in their constant-current regions.

in a second matched depletion-mode MOSFET. The gate voltage applied by the feedback loop to Q_2 becomes the output of the circuit. The circuit can operate with Q_1 in either the constant-current or the triode region.

The square-law behavior of MOSFETs can also be compensated for using digital processing methods. In one scheme, the MOSFET current is sampled, digitized, and converted to its corresponding V_{GS} using a software algorithm.

MOSFET sensors are not very well suited for applications in which stable dc measurements are required over long periods of time. After initial charging by field induction, the capacitance C_{GS} will be discharged over time by any currents that flow over gate-to-ground leakage paths. The latter are inevitably introduced by the device packaging and mounting arrangements. Gate-to-substrate leakage paths on the MOSFET surface may also contribute to the discharge current. The user has little control over internal leakage paths, but current flow over external gate-to-ground leakage paths can be minimized if the insulators supporting the gate lead and sensing electrode are kept meticulously clean and moisture free. With care, stable measurements over time intervals as long as several minutes are possible using MOSFET sensors. Additionally, the installation of a guard ring around the MOSFET gate lead can dramatically reduce the flow of current over external leakage paths (Negro et al., 1967). As depicted in Fig. 13, the guard ring is driven by an active circuit to the same potential

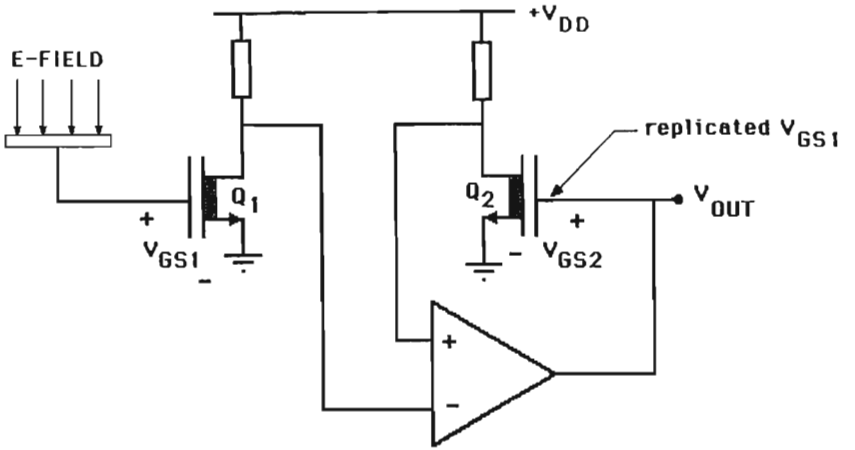


Figure 12 Feedback circuit replicates the field-induced gate voltage v_{GS1} in the matched MOSFET Q_2. The MOSFETs can operate in their constant-current or triode regions.

as the floating MOSFET gate. Any leakage paths that surround the gate will be fed primarily from the source of guard ring voltage, rather than by the gate itself.

MOSFET sensors are not very well suited for applications in which significant space charge is present. The flow of space charge to the gate electrode quickly charges the gate capacitance C_{GS}, saturating the MOSFET circuit and obscuring its ability to measure field-induced voltages. Field monitors based on MOSFETs are also affected by the offsets and drifts common to all dc coupled signal processing circuits. These latter undesirable features can be reduced by proper instrument design and component selection, but MOSFET field-sensing circuits are the still best left to applications involving short duration space charge–free measurements (less than one minute or so) in which zero field conditions can be established prior to measurement.

Instruments involving MOSFET sensors, including a variety of handheld "electrostatic locating meters" available commercially, are generally calibrated in fixed-field geometries. Typically, a large energized conducting plate is held a known distance from the MOSFET's sensing electrode and the instrument output adjusted to coincide with the applied plate potential. Because this calibration procedure is most often used, many handheld MOSFET-based meters are calibrated in voltage units at some fixed

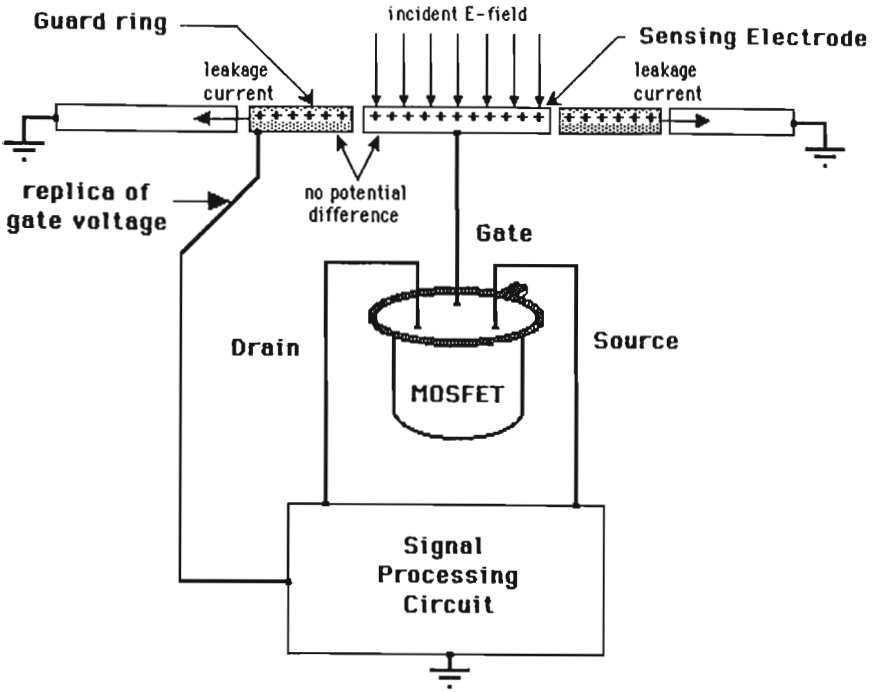


Figure 13 Use of a guard ring to reduce leakage current from an isolated gate-sensing electrode. The guard ring is maintained at the same potential as the MOSFET gate.

distance to the measured surface, even though the meter fundamentally measures electrostatic field strength. When measuring small conducting objects, floating conductors, or insulating surfaces, potential readings obtained with these instruments must be interpreted with care. If absolute quantities are desired, the details of the field geometry and distortion created by the proximity of the instrument itself must be considered (Blitshteyn, 1984). More realistically, hand-held instruments are best suited for rough relative measurements made under known, fixed geometries.

III. ELECTROSTATIC MEASUREMENTS WITH SPACE CHARGE PRESENT

The various electrostatic measuring techniques described thus far are all affected by the presence of space charge. In an electrostatic system, volume space charge usually takes the form of ions produced by corona

or other discharge processes. Charged particulates may also contribute significantly to the space charge density.

The presence of space charge will affect measured fields and potentials and may also contribute current flow to sensing electrodes of field mills and MOSFET sensors. One method for measuring electric fields with small quantities of space charge present, called the field filter (Waters and Selim, 1980), involves the use of an auxiliary repelling field to shield the sensing electrode from incident ions. Readings must be adjusted to include the contribution of the applied repelling field to the sensor output.

Another method for measuring fields with space charge present involves the use of the synchronously detected field mill of Sec. II.C. If a charge-carrying field is incident on the field mill, current will flow to the sensing electrode, producing a conduction component to the sensor current $i(t)$ that will be superimposed on the field-induced displacement current signal. The modification to the field magnitude produced by the space charge will be reflected in the displacement current component of $i(t)$. The conduction component produced by the space charge will peak when the shutter is fully open and will thus lie 90° out of phase with the field-induced displacement current component. As illustrated in Fig. 14, synchronous detection can be used to extract the desired displacement current signal from the total current signal $i(t)$. The total signal is first fed to a high-pass filter to remove the dc portion of the unwanted space charge

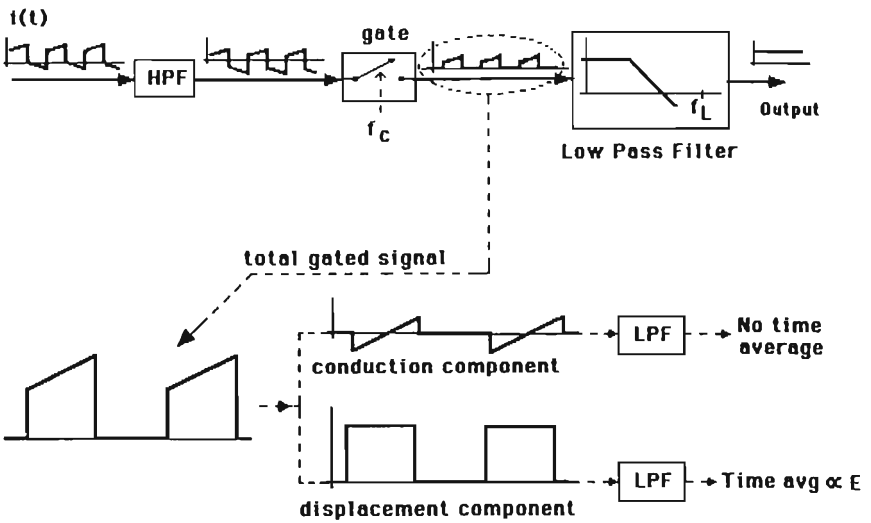


Figure 14 Use of synchronous detection to extract the desired field-induced displacement current component of $i(t)$.

conduction current. The ac version of $i(t)$ is then electronically gated over a time window centered on the mid-position of the shutter and fed to a low-pass filter. The conduction component of $i(t)$, which peaks when the shutter area is a maximum, will be 90° out of phase with this electronic window and will contribute no time-average value to the output of the low-pass filter. The desired even-harmonic displacement current signal, on the other hand, will contribute a net time average proportional to the incident electric field.

A third measuring technique, called the floating plate method, can provide indirect information about ambient space charge density. As depicted in Fig. 15, an isolated, electrically floating conductor is precharged to some known voltage and then left exposed to the ambient space charge. In most electrostatic systems, the latter typically consists of positive and/or negative ions of air, but it could consist of charged particulates or even ions within an insulating liquid. The potential of the plate is monitored by a noncontacting electrostatic voltmeter of the type described in Sec. II.D. A relative measure of the space charge density can be obtained by observing how quickly the plate-to-ground capacitance is discharged by the resulting space charge conduction current. For a fixed geometry relative to surrounding grounded surfaces, the current flowing from plate to ground, which will have contributions from both positive and negative carriers, becomes

$$i_g = \int_{\text{area of plate}} (\rho_+ \mu_+ + \rho_- \mu_-) E(x, y) dA \tag{11}$$

where $E(x, y)$ is the electric field incident at the surface of the plate (defined as positive out). This equation assumes that the ion flow can be described by a mobility limit in which ion velocity is given by $v = \mu E$ (Crowley, 1989). This limit is generally valid for ions in air at atmospheric pressure.

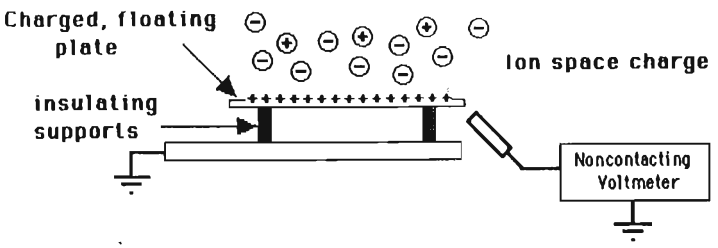


Figure 15 Floating plate method of measuring relative space charge densities.

For small space charge densities, E will be approximately proportional to the plate potential V, independent of ρ_+ and ρ_- (Melcher, 1981). Under these conditions, the plate current to ground becomes

$$i_g = aV(\rho_+\mu_+ + \rho_-\mu_-) = GV \tag{12}$$

where a is a geometry-related constant having the units of area/length that results from integrating $E(x, y)$ over the plate surface. The quantity $G = a(\rho_+\mu_+ + \rho_-\mu_-)$ describes the net conductance connecting the plate to ground. The plate capacitance to ground C_P will be discharged exponentially at the rate $\tau = C_P/G$. If $\rho_+ = \rho_- = \rho$, measurements of τ can provide estimates of ρ if μ_+ and μ_- are known. Alternatively, relative ratios of space charge densities under the same geometrical conditions can be determined by comparing measured decay time constants, e.g.,

$$\frac{\tau_1}{\tau_2} = \frac{C_P a\rho_2(\mu_+ + \mu_-)}{C_P a\rho_1(\mu_+ + \mu_-)} = \frac{\rho_2}{\rho_1} \tag{13}$$

This latter technique is commonly used to evaluate the "effectiveness" of ionizing air generators found in static-controlled workstations and ESD-protected environments.

REFERENCES

Blitshteyn, M. (1984). Measuring the electric field of flat surfaces with electrostatic fieldmeters. *Eval. Eng.*, 23(10), 70–86.

Chubb, J. N. (1989). Instrumentation and standards for testing static control materials. IEEE Industry Application Society, 1989 Annual Meeting, IAS-89(2), 1948–1951.

Crowley, J. M. (1989). *Fundamentals of Applied Electrostatics*. John Wiley, New York.

Garverick, S. L., and S. D. Senturia (1982). An MOS device for AC measurement of surface impedance with application to moisture monitoring. *IEEE Trans. Electron Dev.*, ED-29(1), 90–94.

Haykin, S. (1983). *Communication Systems*. John Wiley, New York, pp. 130–132.

Horenstein, M. N. (1985). A direct gate field effect transistor for the measurement of DC electric fields. *IEEE Trans. Electr. Dev.*, ED-32 (3), 716.

Horenstein, M. N. (1990). *Microelectronic Circuits and Devices*. Prentice-Hall, Englewood Cliffs, New Jersey, pp. 175–190.

Lathi, B. D. (1989). *Modern Digital and Analog Communication Systems*. Holt, Reinhart and Winston, Philadelphia, p. 225.

McCaslin, J. B. (1964). Electrometer for ionization chambers using metal-oxide-semiconductor field-effect transistors. *Rev. Sci. Instrum.*, 35(11), 1587.

McKnight, R. H., F. R. Kotter, and M. Misakian (1983). Measurement of ion current density at ground level in the vicinity of high voltage DC transmission lines. *IEEE Trans. Pow. App. Sys.*, PAS-102(4), 934.

Maruvada, P. S., R. D. Dallaire, and R. Pedneault (1983). Development of field-mill instruments for ground level and above-ground electric field measurement under HVDC transmission lines. *IEEE Trans. Pow. App. Sys.*, PAS-102(3), 738.

Melcher, J. R. (1981). *Continuum Electromechanics*. MIT Press, Cambridge, Massachusetts.

Negro, V. C., M. E. Cassidy, and R. T. Graves (1967). A guarded insulating gate field effect electrometer. *IEEE Trans. Nucl. Sci.*, NS-14, 135.

Nyberg, B. R., K. Herstad, K. B. Larsen, and T. Hansen (1979). Measuring electric fields by using pressure sensitive elements. *IEEE Trans. Elec. Ins.*, EI-14, 250–255.

Schwab, A. C. (1972). *High Voltage Measurement Techniques*. MIT Press, Cambridge, Massachusetts, pp. 97–101.

Secker, P. E. (1984). Instruments for electrostatic measurements. *J. Electrostat.*, 16(1), 1–19.

Trump, J. G., F. S. Safford, and R. T. Van deGraff (1980). Generating voltmeter for pressure insulated high voltage source. *Rev. Sci. Instr.*, 11, 549.

Vosteen, R. E., and R. Bartnikas (1987). Electrostatic charge measurement. *Engineering Dielectrics*. Vol. IIB, Electr. Prop. of Sol. Insul. Matls., ASTM Spec. Tech. Publ. 926, pp. 440–489.

Vosteen, W. (1988). A high speed electrostatic voltmeter technique. IEEE Industry Applications Society, 1988 Annual Meeting, IAS-88(2), 1617–1619.

Waters, R. T., and E. O. Selim (1980). Field filters—new static probes for field measurement at electrodes. *IEEE Trans. Ind. Appl.*, IA-16(3), 464.

Zahn, M. (1979). *Electromagnetic Field Theory: A Problem Solving Approach*. John Wiley, New York.

12

Electrostatic Flow Measurement Techniques

Kazutoshi Asano

Yamagata University
Yonezawa, Japan

I. INTRODUCTION TO ELECTROSTATIC SINGLE PHASE FLOW MEASUREMENT

The measurement of wind velocity is one of the classical tasks in meteorology, but in recent days too, even in industrial, office, and public environments, the measurement of air flow is important in order to create a comfortable indoor climate.

In such circumstances, a conventional rotating anemometer cannot be used because of its noise and improper functioning at low speeds. A new type of equipment without moving parts is required. A further requirement is to detect three components of the air stream to be able to detect the wind direction. Possible candidates for such measurements are a laser Doppler method and an ultrasonic method. However, both are quite expensive and massive systems. An ion flow anemometer is another candidate, although it is not as well known.

The principle of the ion flow anemometer has been known for a long time, especially in the field of stratospheric measurement. There have been many different kinds of ion flow anemometers developed. The principle of ion flow anemometry has been applied to quite wide fields in different circumstances, from a low velocity indoor (Lovelock and Wasiliewska, 1949; Franzen et al., 1961; Nygaard, 1965; Kurz and Olin, 1971; Janka, 1984; Asano and Kinukawa, 1986; Higashiyama and Enomoto,

1987; Asano et al., 1988, Higashiyama and Asano, 1990) or in a pipe flow (Jones et al., 1968) to a supersonic velocity in a pipe (Cooley and Stever, 1952; Desai and Johnston, 1971), or from normal air pressure to low pressure at a high altitude (Lilienfeld et al., 1967; Good et al., 1978; Barat 1982a, 1982b; Yamanaka et al., 1985). Moreover, an ion flowmeter has been applied to air flow measurements in an automobile injection system (Cops and Moore, 1977; Cockshott et al., 1983; Barriol et al., 1984) and has been used as a speed meter of an aircraft (Durbin and McGeer, 1982).

There are three different ways to detect wind velocity. One is to detect the change of the ion drift velocity. A second is to detect the deflected ions flowing into a collector. A third is to detect an ion transit time over a known distance. There are, of course, modifications of these types; for example, Durbin and McGeer (1982) developed the air speed vector sensor by combining the first and second method.

II. PARALLEL GRID TYPE

Figure 1 shows the simplest model that explains the fundamental behavior of flow measurement by ion based techniques. Although in this figure, a duct, which confines the air stream, is indicated, it is not necessary, as long as the model can be considered to be one-dimensional. In this model,

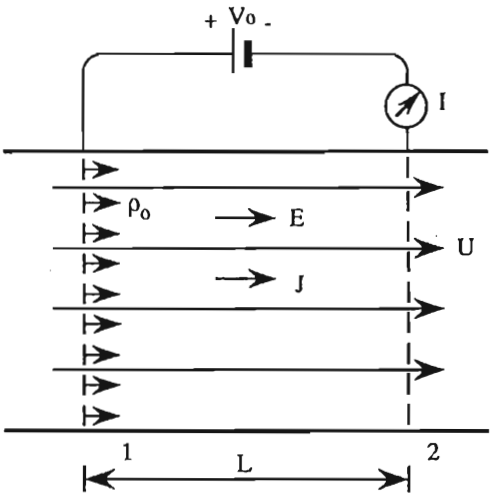


Figure 1 Principle of parallel grid type wind velocity sensor.

charges are emitted by some means at electrode 1. The uniform electric field is developed between two electrodes by applying an external dc voltage. Due to this electric field, the emitted charges are forced to move toward electrode 2. The motion of emitted charges is retarded by friction, and momentum is imparted to the fluid. If this ion drag effect is used to pump or to accelerate fluid, this system is called an ion drag pump (Woodson and Melcher, 1968).

In this type of anemometer, the amount of emitted ion is negligibly small; thus the ion drag effect can be regarded as unimportant.

The current density within the duct is written as (Melcher, 1981a; Asano and Kinukawa, 1986)

$$\vec{J} = \rho(\mu\vec{E} + \vec{U}) \tag{1}$$

where ρ = charge density, μ = mobility of the ion, $\vec{E}$ = electric field, and $\vec{U}$ = velocity of moving fluid (air velocity).

From this electrode configuration, two different types of wind measuring systems are possible. If a cloud of charge density ρ_0 is instantaneously emitted at the emitting electrode, and assuming no moving fluid, $U = 0$, the flowing current becomes a constant under the condition of

$$0 \leq t \leq T_0,$$

where T_0 = arrival time at electrode 2. The current is expressed as

$$I = A\rho_0\mu E = \frac{A\rho_0\mu V}{L} \tag{2}$$

where V = applied voltage and A = cross section of a duct. When the cloud reaches electrode 2, the current disappears. This time interval T_0, without moving air, is

$$T_0 = \frac{L}{\mu E} = \frac{L^2}{\mu V} \tag{3}$$

When there is a wind with velocity U, the arriving time will be changed. Thus the new arriving time T' is

$$T' = \frac{L}{\mu E + U} \tag{4}$$

By taking the difference of both time intervals, we can measure the wind velocity U:

$$\Delta T = T_0 - T' = \frac{LU}{(\mu E)^2} = \frac{LU}{(\mu V/L)^2} = \frac{L^3 U}{\mu^2 V^2} \tag{5}$$

Another method is to use the current density itself. If the ions are continuously emitted at the emitting electrode, there will be a continuous current:

$$I_0 = A\rho\mu E = \frac{A\rho\mu V}{L} \qquad \text{without wind} \tag{6}$$

The current will be increased by an external wind U:

$$I_w = A\rho\left(\mu\frac{V}{L} + U\right) \qquad \text{with wind} \tag{7}$$

By taking the difference of the currents, the wind velocity U can be measured.

$$\Delta I = I_w - I_0 = A\rho U \tag{8}$$

Although these methods are theoretically possible for the measurement of wind velocity, practically there are difficulties. For example, to measure ΔT of Eq. 5, the shape of the current pulse must be rectangular, but the actual shape is a distorted trapezoid. Thus the accurate measurement of ΔT is not as simple as imagined. Other methods to be discussed below are much more practical.

III. DIFFERENTIAL TYPE

In the previous section, the one-dimensional motion of ions is assumed. If we take into account their two-dimensional motion, more complicated, or sophisticated, systems can be constructed.

A. Flat Collectors

The basic configuration of this anemometer is shown in Fig. 2 (Nygaard, 1965). The discharge current and wind direction are approximately perpendicular. Without wind, the discharge current will be divided to both collecting electrodes. It is obvious that the current downstream will increase with increased external wind. Thus the current difference $I_2 - I_1$ is a direct measure of the air velocity U_∞. Nygaard has shown that if the position of the wire is moved toward the windward direction to obtain the condition $I_2 = I_1$, the displacement position Δy is a direct measure of the wind velocity.

$$\Delta y = y_0 - y = \gamma U_\infty \tag{9}$$

Experimental results are shown in Fig. 3.

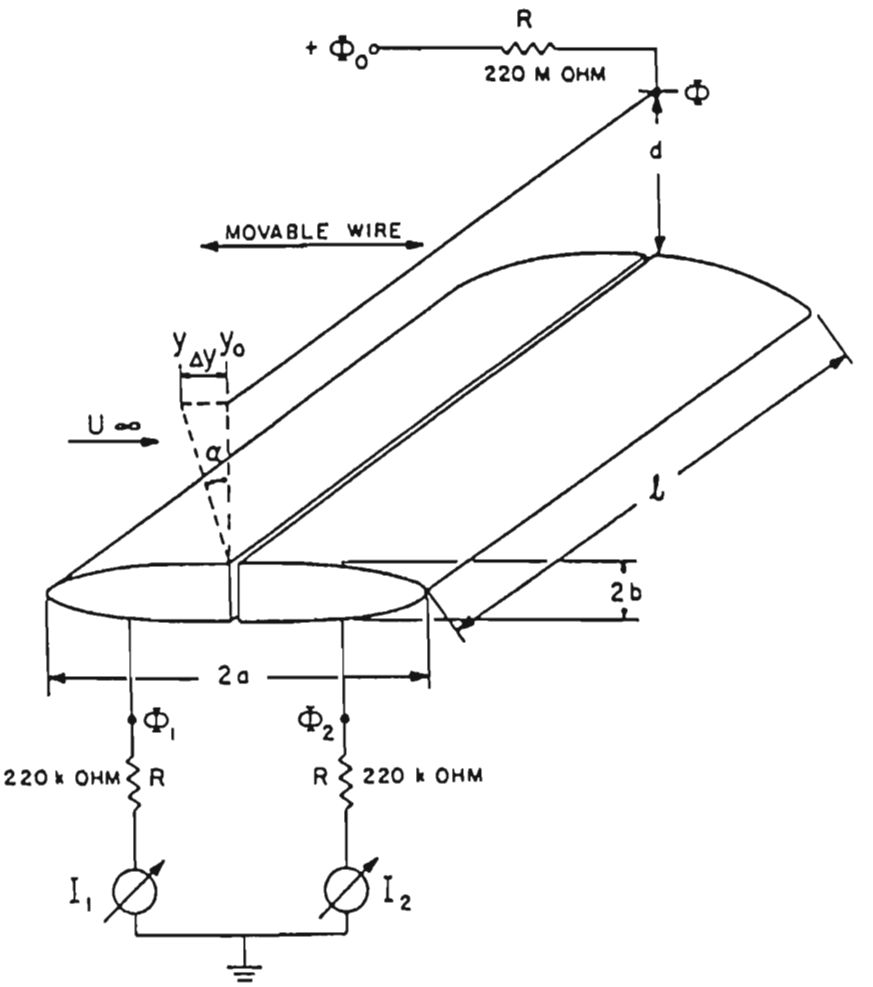


Figure 2 Schematic of the gas discharge anemometer (all electric potentials are with respect to ground).

The two-dimensional motion of charged particles is important in various applications, not only for anemometry but for many other fields in electrostatics. Melcher has shown the solution of such problems analytically by using the characteristic line method (Melcher 1981b). The simplified model of Fig. 2 is shown in Fig. 4. Electrodes embedded in a smooth wall have the potential difference V. Ions entering from the left are entrained in the

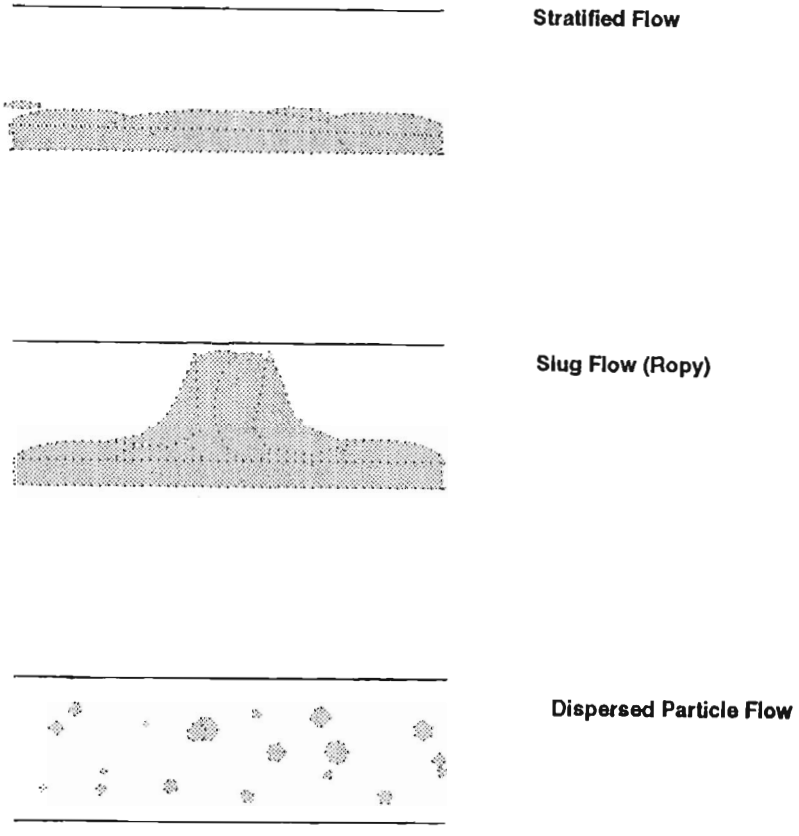


Figure 3 The relationship between the displacement Δy that gives $\Phi_1 = \Phi_2$ and wind velocity U_∞.

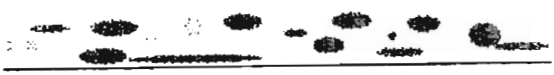
uniform velocity U. With a positive V, the left electrode intercepts some of the ions from the flow. His solution for the linear region is

$$i = (\rho U c w)\nu \ln\left(\frac{c}{a}\right) \tag{10}$$

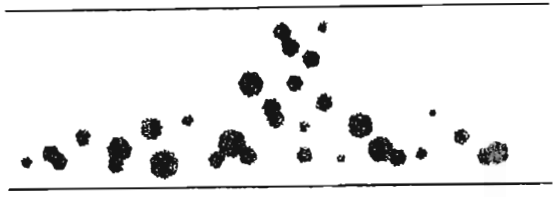
where $\nu = bV/\pi Uc$. Other dimensions are shown in Fig. 4. The normalized current as a function of the normalized voltage is shown in Fig. 5.

B. Wire Collectors

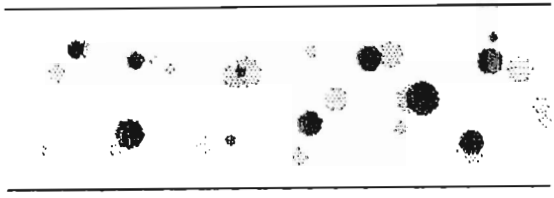
Another type of differential anemometer uses wire collectors; one wire collector is placed windward and the other leeward, as shown in Fig. 6.



Stratified Flow



Slug Flow



Dispersed Flow

Figure 4 The simplified model of the gas discharge anemometer.

The ion source is placed between two electrodes, and the difference of the currents is measured (Barat, 1981; Asano and Kinukawa, 1986; Asano et al., 1988; Higashiyama and Asano, 1990). In this configuration, the electric field is not simple, and the actual path of the ions is very complicated. Thus the relation between the difference of the currents and the external wind velocity cannot be simply obtained.

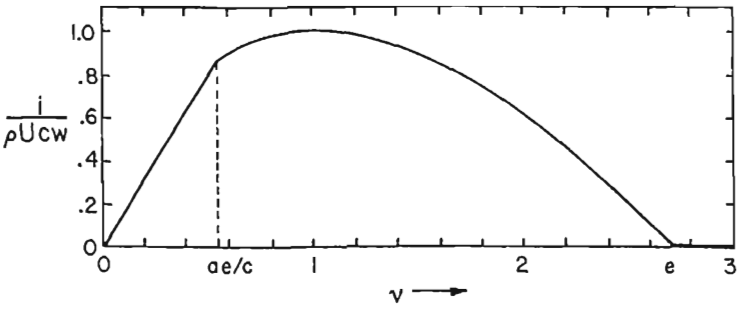


Figure 5 Normalized current to electrode in Fig. 4 as function of normalized voltage $\nu = bV/\pi Uc$.

Without a space charge, the Laplace solution of the apparatus shown in Fig. 6 can be obtained by using the conformal transformation technique. Computed results of this method are shown in Fig. 7, from which the trajectory of an emitted ion can be visualized. Although this electrode configuration has been patented by Barat (1981), the detailed characteristics of this anemometer have not been published. We have examined the characteristics of this electrode configuration carefully (Asano and Kinukawa, 1986; Asano et al 1988; Higashiyama and Asano, 1990).

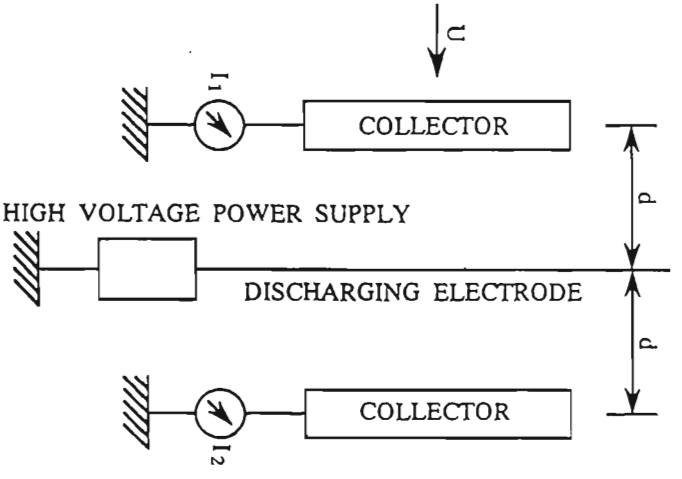


Figure 6 Differential type wind velocity sensor.

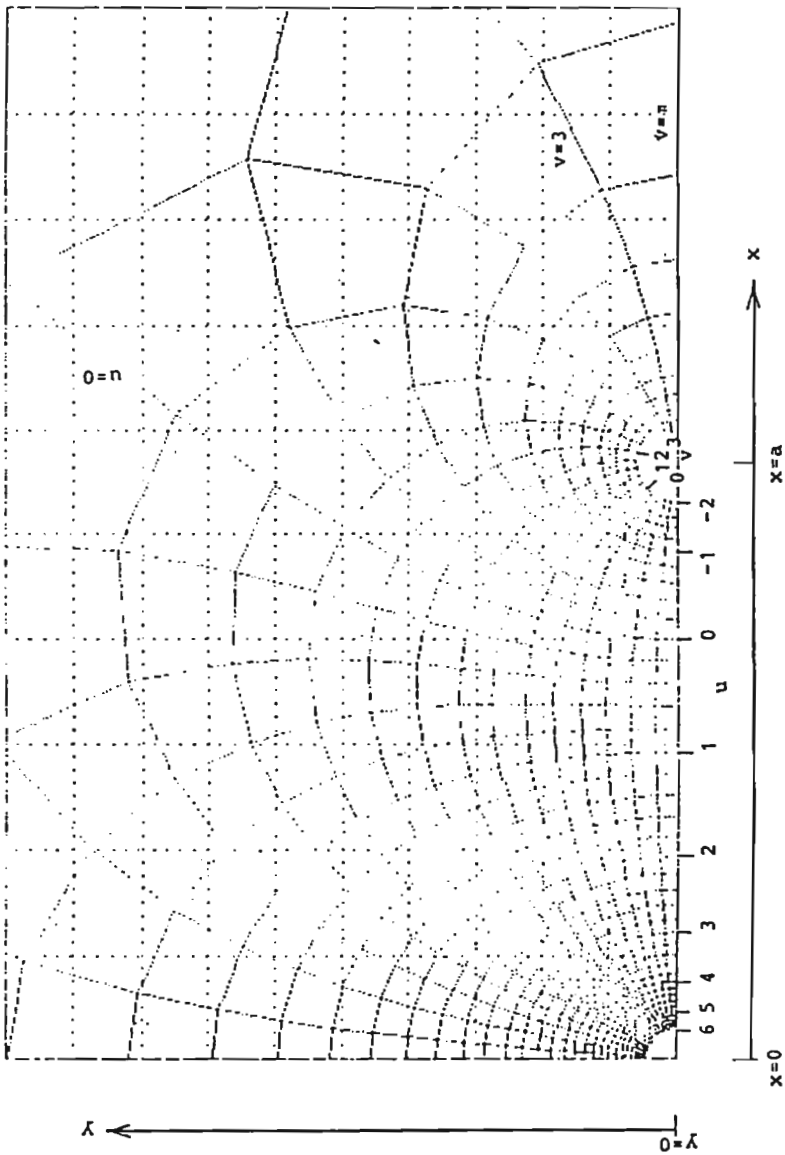


Figure 7 Potential distribution around wire electrodes.

We have examined electrodes of different sizes and different materials. It was found that the most suitable emitter wire is a tungsten wire 100–200 μm in diameter. Usually, 100 μm wire is used.

The requirements for collector wires are rather conflicting. In order to collect as many emitted ions as possible, the diameter of the collector must be large. On the other hand, if it is too large, the leeward air stream of a collector is no longer laminar, which affects the ion emission of the emitter wire; one such effect is shown in Fig. 8(a) and (b). Figure 8(a) indicates the effect of the collector wire, while Fig. 8(b) does not show such effect. Good results are observed with a 1 mm diameter nickel wire with a separation distance between the emitter and the collector of 12 mm.

The difference between the two currents is computed electronically. Since the emitting current fluctuates with time, it is necessary to compensate such a fluctuation by some means. The simplest way to reduce this effect was performed by dividing the current difference by the total current:

$$I_d = \frac{I_2 - I_1}{I_2 + I_1} \tag{11}$$

The electronic measurement system is shown in Fig. 9.

One of the interesting characteristics of Fig. 6 is the relation between the total current and the applied voltage. Even though we can calculate the Laplace field, the current field with this configuration cannot be computed. Only the analytical current field for coaxial cylinders is available. Figure 10 shows the comparison of experimental results with simple coaxial cylinders.

Although there are difficulties in understanding the characteristics of the experimental configuration, the output signal and the external wind show a good linear relation. Of course, much also depends on the configuration of the electrodes and the applied voltages. The most important factors that characterize this anemometer are the leeward turbulence of the collector electrode and the corona wind from the emitter. In order to overcome the former, the multicollector electrode method is adapted. The eight-collector electrode shows excellent performance; the four-collector electrode also shows satisfactory results. Fig. 11 shows the relation between the output signal and the external wind when the applied voltage is changed.

C. Two-Dimensional Measurements

Two-dimensional detection of wind direction and velocity is based on the measured signals of two orthogonal components of the wind: the x and y

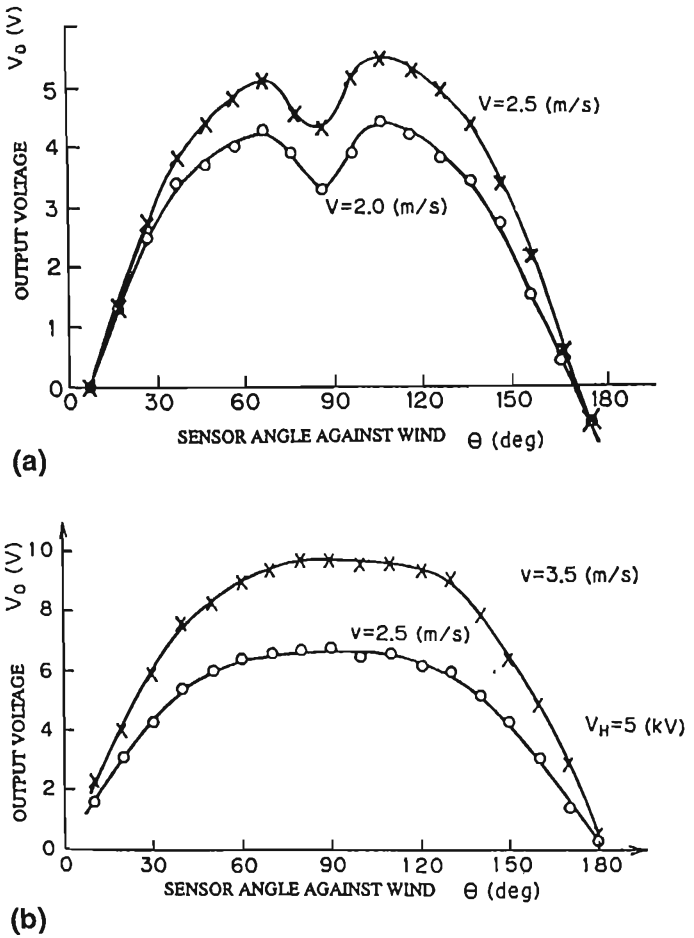


Figure 8 Angular dependency of the sensor (a) before modification, (b) after modification.

components in the horizontal plane (Higashiyama and Ksano, 1990). The principle of detecting wind direction and velocity is illustrated in Fig. 12. Two pairs of grounded collectors are placed at the same distance from an emitter. The planes formed by each pair of collectors are perpendicular to each other.

When ions are being produced continuously along a wire by corona discharge as before, it is reasonable to assume that the magnitude of ionic current flowing into each collector is equal under windless conditions.

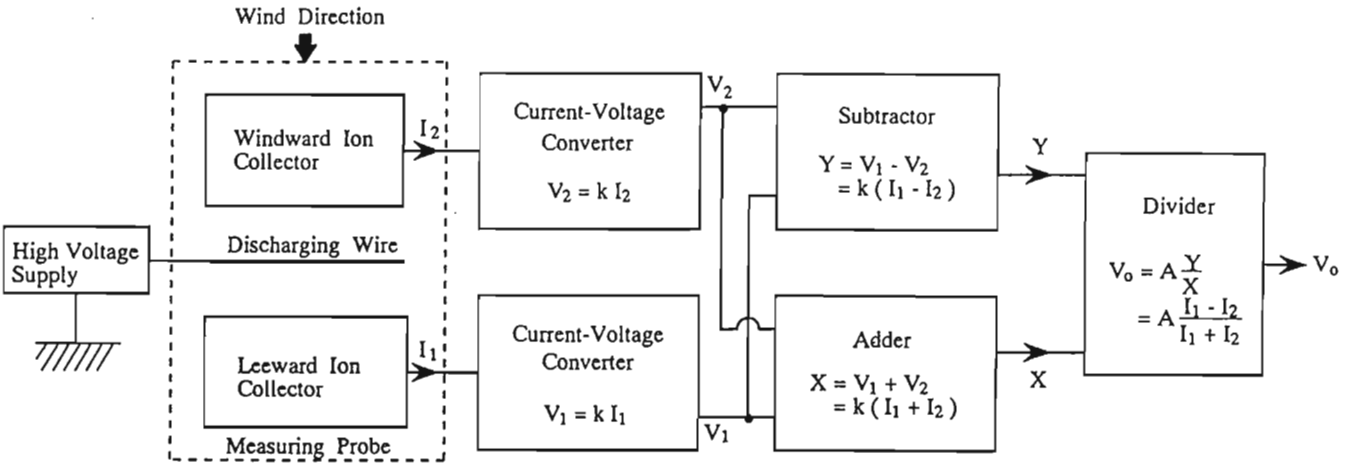


Figure 9 Schematic diagram of a differential ion flow anemometer.

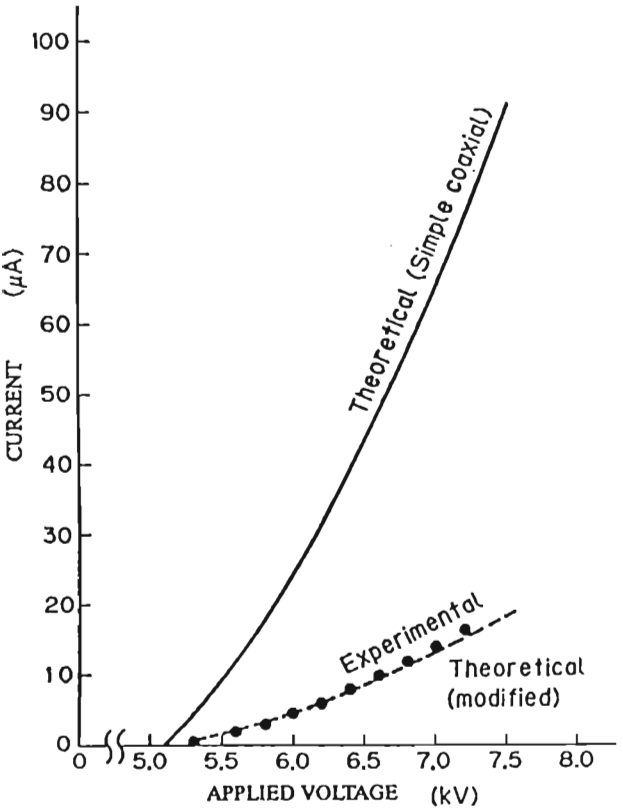
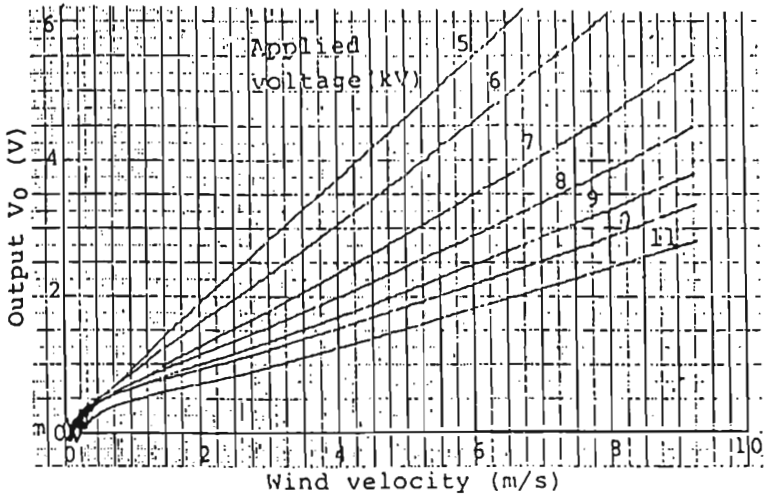


Figure 10 Voltage-current characteristics of the sensor.

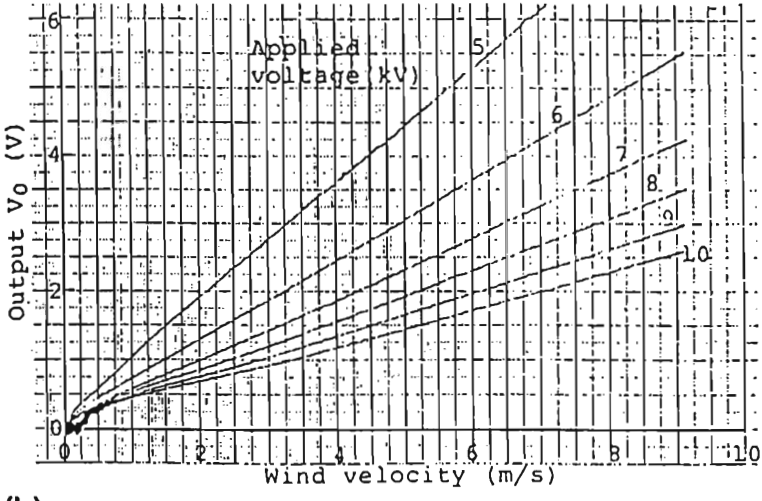
When the wind direction θ is changing, the x and y components of the wind are measured independently using each pair of collectors, provided the relative position of the collectors is fixed. Here, the wind direction must coincide with the direction from the collector plane from C_x to C'_x as shown in Fig. 12. Since each output signal defined by ionic current in the x and y directional collectors is a function of wind velocity and wind direction θ, the outputs $V_x(w, \theta)$ and $V_y(w, \theta)$ are independently determined from each pair of currents:

$$V_x(w, \theta) = A\left(\frac{I_x - I'_x}{I_x + I'_x}\right) \tag{12}$$

$$V_y(w, \theta) = A\left(\frac{I_y - I'_y}{I_y + I'_y}\right) \tag{13}$$

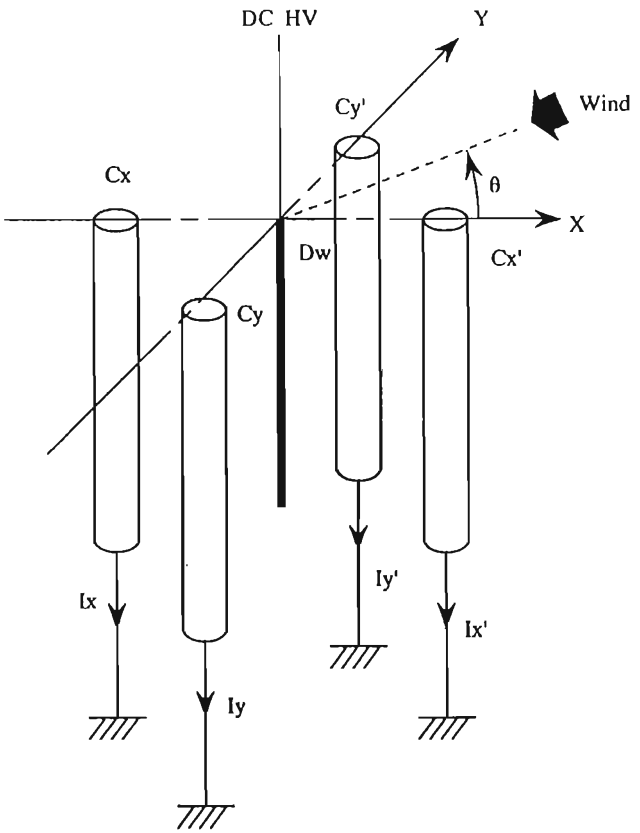


(a)



(b)

Figure 11 Influence of the applied voltage on anemometer output: (a) four-collector; (b) eight-collector.



Cx - Cx', Cy Cy' : collector pairs for detection of X-and Y-component of wind

Dw : discharging wire

Figure 12 Configuration of a cage type ion flow anemometer.

In order to obtain the wind velocity and direction simultaneously, a vectorial operation on $V_x(w, \theta)$ and $V_y(w, \theta)$ is necessary. For this operation, two critical conditions are required. The first is a linear response of the output to wind velocity. Assuming that the output is proportional to wind velocity for wind directions in both the x and the y directions, the following relation should hold:

$$V_x(\theta = 0) = V_y\left(\theta = \frac{\pi}{2}\right) = Kw \tag{14}$$

The second requirement is that the response to wind direction vary sinusoidally as

$$V_x(w, \theta) = V_x(w, 0) \cos \theta \tag{15}$$

$$V_y(w, \theta) = V_y\left(w, \frac{\pi}{2}\right) \sin \theta \tag{16}$$

For a wind of arbitrary direction, the wind velocity and direction are calculated by combining Eqs. 14–16:

$$w = \frac{[V_x^2(w, \theta) + V_y^2(w, \theta)]^{1/2}}{K} \tag{17}$$

$$\theta = \arctan \frac{V_y(w, \theta)}{V_x(w, \theta)} \tag{18}$$

The angle defined by Eq. 18 is effective only for the range from $-\pi/2$ to $\pi/2$. In order to obtain an angle ranging from $\pi/2$ to $3\pi/2$, the angle calculated by Eq. (18) needs to be added to or subtracted from π depending on the polarity of V_x and V_y.

As shown in the previous section, our eight-or four-collector electrode can be converted for this two-dimensional wind measurement. The probe actually used has four or eight tungsten collector electrodes 1 mm in diameter surrounding a discharging wire 0.1 mm in diameter and 30 mm in length. When eight collectors are used, they are divided into four groups and each pair of collector groups is arranged orthogonally to detect the x and y components.

The electronic circuitry to obtain output signals of the anemometer is composed of I/V converters, adder, subtracter, and divider as before, but now two sets of circuitry are needed. The schematic diagram of an experimental system detecting wind velocity and direction simultaneously is shown in Fig. 13. The measuring probe has eight collectors, two of which are connected together. Four different voltage signals converted from each ionic current are transmitted to a personal computer NEC PC-9801 through an A/D converter and an interface circuit. The wind direction and velocity are calculated by using Eqs. 12–18.

The output signal for changing wind direction is shown in Fig. 14(a) for a constant velocity of 5 m/s. The wind direction obtained experimentally agreed with the expected value within $\pi/60$ radian over the whole range. The wind velocity obtained experimentally also agreed with the applied value. Figure 14(b) shows output signals for changing wind velocity for a wind direction of $\pi/4$. Regardless of the variation of wind velocity, wind direction and velocity agree reasonably well with expected values.

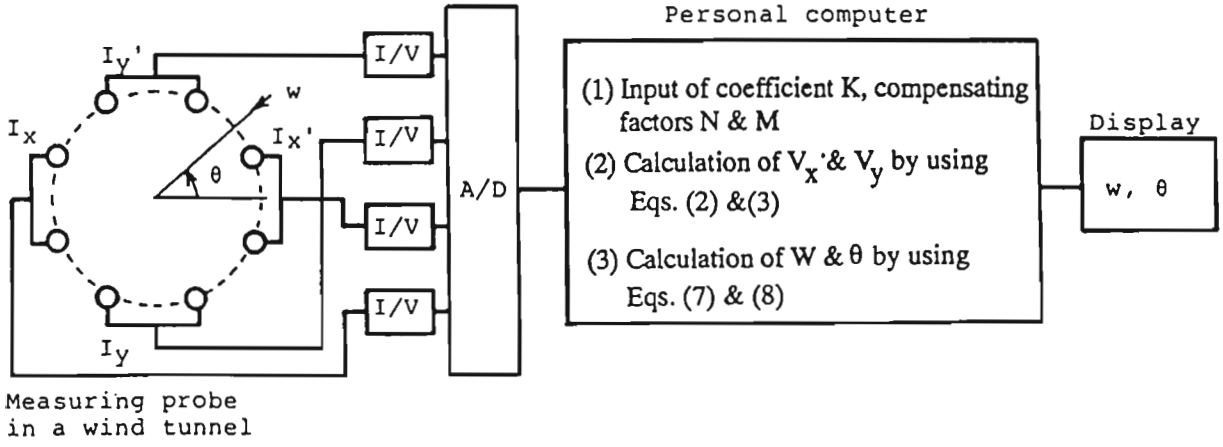


Figure 13 Schematic diagram of a cage type ion flow anemometer for two-dimensional anemometry.

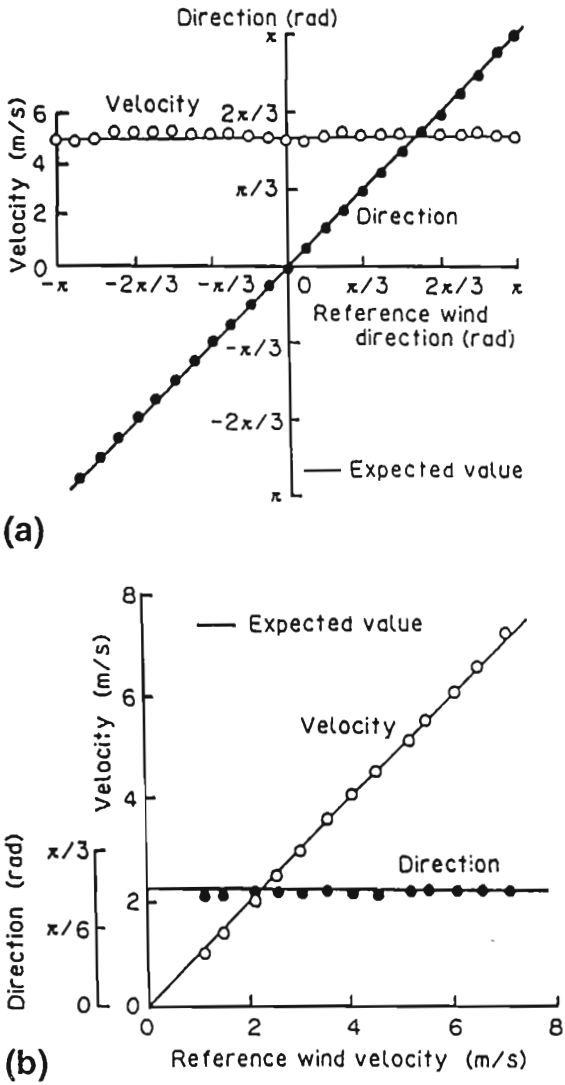


Figure 14 Comparison of output signals of the cage type ion flow anemometer with expected values. (a) Constant wind velocity of 5 m/s. (b) Constant wind direction of $\pi/4$.

IV. PULSED ION FLOW ANEMOMETER

The anemometers described in the previous sections used the total amount of ion current. However, the amount of ions produced varies in time due to discharge phenomena; it also varies due to the variation of ambient conditions such as temperature, pressure, humidity, and so on. The fluctuation of the current-produced ions should always be compensated for in an ion flow anemometer.

On the contrary, ion transit time is almost independent of such air conditions and of the amount of ions. The ion transit type anemometer employs ions directly flowing through a collector or ions passing near an induced electrode. Cooley and Stever (1952) measured a maximum point or a zero cross point of induced current due to a positive burst corona in a low pressure supersonic flow using an oscilloscope. Another advantage of this type is quick response; the information on an induced current could be converted directly to wind velocity in real time.

Figure 15 shows the basic setup of a probe of this type of anemometer (Asano et al., 1990). The probe electrode consists of an emitter assembly as an ion emitter, a ring collector, and a ring ion detector. The detector is placed between the emitter assembly and the collector. Negative ions are generated at the tip of the positive electrode of an emitter assembly during a period when a negative voltage pulse is applied to the point elec-

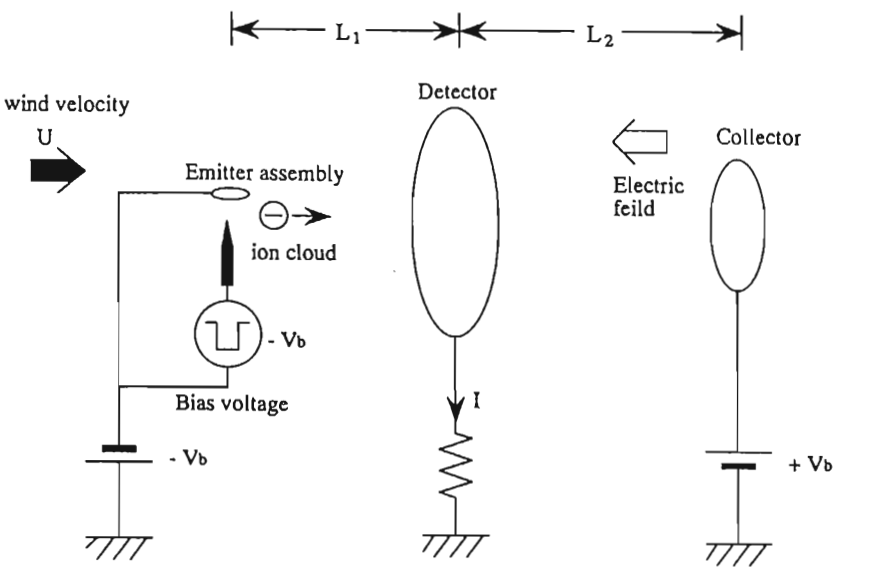


Figure 15 Arrangement of probe electrodes of the pulsed ion flow anemometer.

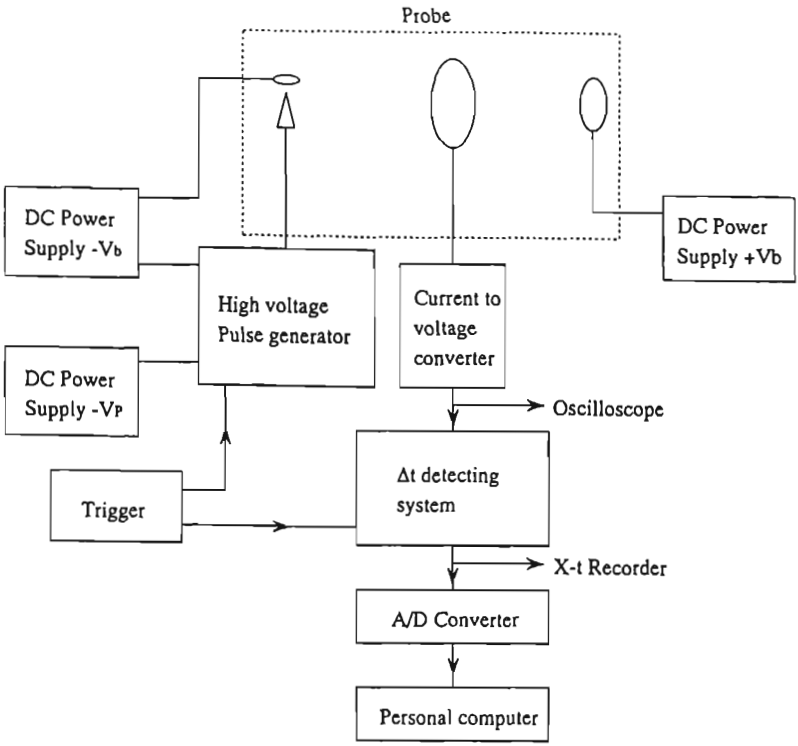


Figure 16 Block diagram of the pulsed ion flow anemometer.

trode. The ion cloud moves away under an electric field from the emitter assembly toward the collector. During the traveling period, induced current flows into the grounded detector.

When air flows from the emitter assembly to the collector as shown in Fig. 15, the ion velocity becomes faster than under calm conditions, and thereby the ion transit time diminishes. The pulse ion anemometer is based on the detection of the difference of the ion transit times. To make certain that the time of ion emission is obtained, ions should be generated within a negligibly short period relative to the ion transit time.

The zero cross time t_0 is expressed as Eq. (19) in terms of the distance L_1 between the emitter assembly and the detector and the average velocity u_0 of the ion cloud.

$$t_0 = \frac{L_1}{u_0} \tag{19}$$

cross time t_0 will be modified by an existing external wind U.

The difference in the zero cross time Δt is expressed as

$$\Delta t = t_0 - t_0' = \frac{L_1 U}{u_0(u_0 + U)} \tag{20}$$

Equation 20 indicates the simple but nonlinear relationship between the wind velocity U and the difference of the zero cross times Δt under calm and windy conditions.

Since the average velocity of ions u_0 is not a measurable variable in practice, the equation is rewritten by using measurable values.

$$\Delta t = \frac{t_0^2 U}{L_1 + t_0 U} \tag{21}$$

$$U = \frac{L_1 \Delta t}{t_0(t_0 - \Delta t)} \tag{22}$$

A block diagram of the anemometer is shown in Fig. 16. The anemometer consists of the electrodes, two dc high voltage power supplies, a high voltage pulse generator, a current-to-voltage converter, a t_0 and Δt measuring circuit, and a personal computer.

One of the experimental results of this system is shown in Fig. 17. This shows the nonlinear response of the anemometer to wind velocity. Using

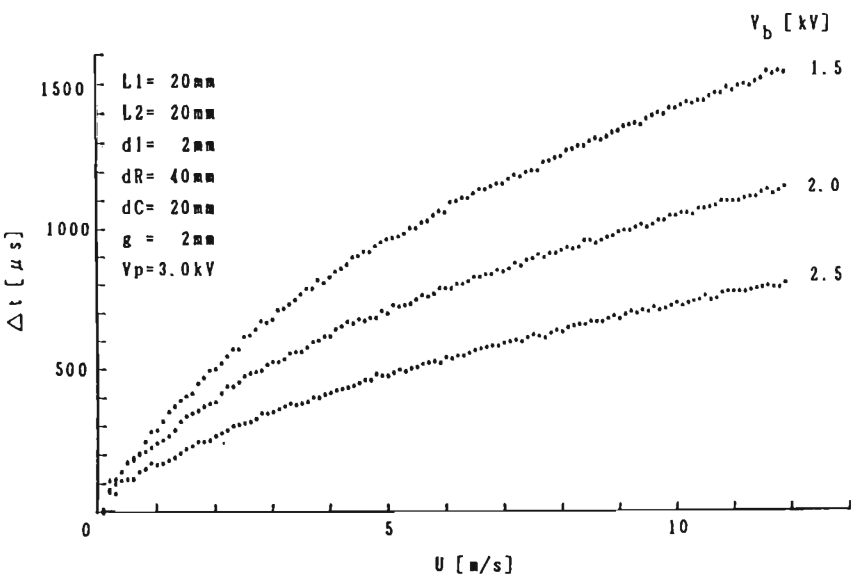


Figure 17 Dependency of time interval Δt on wind velocity U.

this characteristic curve, the wind velocity can be obtained by measuring the time difference Δt. The time difference Δt or the output of the anemometer is increased as the bias voltage decreases. This suggests that the sensitivity of the anemometer is adjustable with the bias voltage.

REFERENCES

Asano, K., and T. Kinukawa (1986). On the study of a differential type ion-flow anemometer. *Proc. Inst. Electrostatics Japan*, 10, 123–130 (in Japanese).

Asano, K., Y. Higashiyama, and H. Okuyama (1988). Fundamental characteristics of cage type ion-flow anemometer. *Proc. Inst. Electrostatics Japan*, 12, 441–449 (in Japanese).

Asano, K., Y. Higashiyama, K. Yatsuzuka, and K. Urayama (1990). Ion-flow anemometer using high-voltage pulse. *IEEE 1990 IAS Conf.* (Seattle) 802–808.

Barat, J. (1981). *Patent* J. (A) 1981–9304.

———. (1982a). A high-resolution ionic anemometer for boundary-layer measurements. *J. Appl. Meteorology*, 21, 1480–1488.

——— (1982b). Initial results from the use of ionic anemometers under stratospheric balloons: application to the high-resolution analysis of stratospheric motions. *J. Appl. Meteorology*, 21, 1489–1496.

Barriol, R., G. Hannoyer, and C. Rousseau (1984). A new approach for ionic air flow sensors: transit time. *SAE Technical Paper Series*, No. 840138.

Cockshott, C. P., J. P. Vernon, and P. Chambers (1983). An air mass flowmeter for test cell instrumentation. *Fourth International Conference on Automotive Electronics, IEE Conference Publication* (London), No. 229, pp. 20–26.

Cooley, W. C., and H. G. Stever (1952). Determination of air velocity by ion transit-time measurements. *Rev. Sci. Instrum.*, 23, 151–154.

Cops, M. H., and J. H. Moore (1977). Electronic fuel injection systems utilizing corona discharge air mass flow transducers. *SAE Technical Paper Series*, No. 770402.

Desai, P. V., and W. C. Johnston (1971). Corona discharge anemometer and its operational hypothesis. *Rev. Sci. Instrum.*, 42, 595–600.

Durbin, E. J., and T. McGeer (1982). An airspeed vector sensor for V/STOL aircraft. *J. Aircraft*, 19, 449–455.

Franzen, B., W. Fucks, and G. Schmitz (1961). Korona-anemometer zur Messung von Turbulenzkomponenten. *Z. Flugwiss.*, 9, 347–351.

Good, R. E., J. H. Brown, and G. Harpell (1978). *Development of a Corona Anemometer for Measurement of Stratospheric Turbulence*. AFGL-IP-265. Air Force Geophysics Lab. Hanscom AFB, Massachusetts.

Higashiyama, Y., and S. Enomoto (1987). α-ray ionization anemometer for measuring low wind velocity. *Radioisotopes*, 36, 325–331.

Higashiyama, Y., and K. Asano (1990). Two dimensional anemometry with an ion-flow anemometer. *J. Electrostatics*, 25, 245–254.

Janka, K. (1984). Ion deflection air flow meter with constant deflection. *Rev. Sci. Instrum.*, 55, 976–982.

Jones, W. M., D. Maidment, and D. V. Morgan (1968). A simple ionic flowmeter for measuring very small rates of flow of air. *J. Sci. Instrum.* (J. Phys. E) Ser. 2, 1, 623–627.

Kurz, J. L., and J. G. Olin (1971). *A New Instrument for Air Flow Measurements, Flow: Its Measurement and Control in Science and Industry*, Vol. 1, Pt. II. Instrument Society of America (Pittsburgh, Pa., USA), pp. 765–772.

Lilienfeld, P., Solon, L. R. and H. DiGiovanni (1967). Ion tracer anemometer for the measurement of low density air flow. *Rev. Sci. Instrum.*, 38, 405–409.

Lovelock, J. E., and E. M. Wasilewska (1949). An ionization anemometer. *J. Sci. Instrum. Phy. Ind.*, 26, 367–370.

Melcher, J. R., (1981a). *Continuum Electromechanics*. (MIT Press, Cambridge, Mass.) Sec. 5.7.

——— (1981b). *Continuum Electromechanics*. MIT Press, Cambridge, Mass., Sec. 5.5.

Nygaard, K. J. (1965). Anemometric characteristics of a wire-to-'plane' electrical discharge. *Rev. Sci. Instrum.* 36, 1771–1774.

Woodson, H. H., and J. R. Melcher (1968). *Electromechanical Dynamics, Part 3*. John Wiley, New York, pp. 776–783.

Yamanaka, M. D., H. Hirosawa, and Y. Matsuzaka (1985). 'Glow-discharge' ionic anemometer. *Rev. Sci. Instrum.*, 56, 617–622.

This Page Intentionally Left Blank

13

Electrostatic Multiphase Flow Measurement Techniques

Glenn Harvel and Jen-Shih Chang

McMaster University
Hamilton, Ontario, Canada

I. INTRODUCTION

A. Multiphase Flow Measurement

The study of multiphase gas-liquid-solid flow requires accurate measurement of each phase velocity and phase fraction. Most instrumentation available today provides this type of information but has various disadvantages ranging from poor sensitivity to geometrical limitations (Beck and Wainwrite, 1969; Hewitt, 1978; Banerjee and Lahey, 1981). Recent studies have developed several multiphase flowmeters based upon electrostatics principles. These flowmeters have found increased sensitivity to the measurement of the flow velocity and the void fraction; yet they have their own limitations. One important advantage of these devices is the fast time response that allows these devices to be used for analyzing fast transient phenomena. The following sections will discuss the basic physical principles behind electrostatic flowmeters, along with design considerations and potential applications.

Most electrostatic multiphase flow measurement techniques inherently measure the impedance of the flow or some aspect of it. The electrical impedance of the flow essentially falls into a conductance term or a capacitance term. Conductance is simply the inverse resistance of the two-phase flow and best applies where one phase has higher electrical conductivity and is fairly continuous, as is the case in most solid-liquid and gas-liquid

flow. Capacitance measurement is based upon the gas, liquid, and solid phases each having a different dielectric constant; hence this measurement applies to most multiphase flow systems.

Electrostatic principles are also used in the detectors of other multiphase flow measurement techniques. For example, piezoelectric transducers can be used to measure ultrasonic waveforms that have interacted with multiphase flow. Another example uses ionization (charge) chambers for the detection of radiation attenuation. Examples of these devices will be discussed later in the chapter.

The various techniques for measurement of two-phase flow parameters such as void fraction, phase distribution, and phase velocity will be discussed for gas-liquid and gas-solid two-phase flow applications. Several techniques are mentioned to ensure a fairly complete list with particular strengths and weaknesses addressed.

B. Multiphase Flow Parameters

The void and solid fractions or liquid holdup are the volume fraction of the test section occupied by a given phase. This value is expressed either as a percentage or as a value between 0 and 1. The sum of all volume fractions of each phase is 1, as expressed below, where α_k is the void fraction for phase k.

$$\sum_k \alpha_k = 1 \tag{1}$$

For example, the void fraction α_g and liquid holdup α_l of gas-liquid two-phase flow can be defined by

$$\alpha_g = \frac{V_g}{V_g + V_l} \tag{2}$$

$$\alpha_l = \frac{V_l}{V_g + V_l} = 1.0 - \alpha_g \tag{3}$$

for gas-liquid two-phase pipe flow as shown in Fig. 1.

Hence we can obtain phase velocities from gas and liquid volume flow rates Q_g and Q_l (m^3/s) as

$$U_g = \frac{Q_g}{\alpha_g A_{cs}} = \frac{U_{gs}}{\alpha_g} \quad \text{(m/s)} \tag{4}$$

$$U_l = \frac{Q_l}{\alpha_l A_{cs}} = \frac{U_{ls}}{\alpha_l} \quad \text{(m/s)} \tag{5}$$

where A_{cs} is the cross-sectional area in m^2 of the flow channel; U_{gs} and U_{ls} are the superficial velocities of the gas and liquid phases. These phase

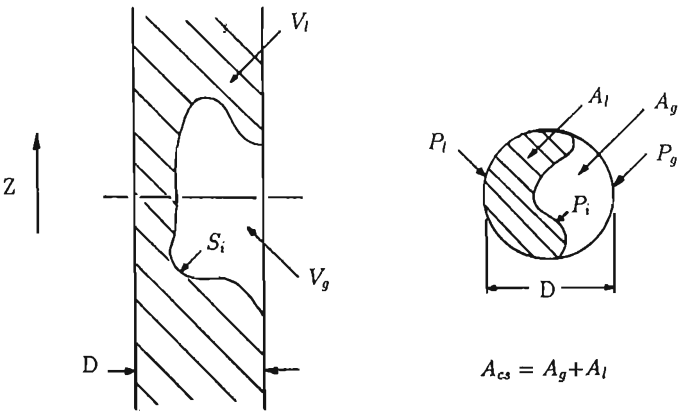


Figure 1 Two-phase pipe flow and definitions: A is the area, V is the volume, P is the Perimeter, l denotes liquid, g denotes gas, i denotes interface, S_i is the interfacial area, D is the diameter, and Z is the axial position.

velocities are local cross-sectional or volume averaged phase velocities, since the void fraction is not always constant along the flow tubes.

The phases may or may not distribute themselves evenly throughout the test volume. Different patterns of distribution may occur as shown in Figs. 2 and 3 for gas-liquid and gas-solid two-phase flow systems, respectively. These distribution patterns are known as flow regimes. The flow regimes that can occur depend primarily on the phase velocities, test geometry, and orientation with respect to gravity. For example, in horizontal gas-liquid two-phase flow, we observe stratified smooth (SS), stratified wavy (SW), annular (A), dispersed bubble (DB), slug (SL), and plug (PL) flow depending on the gas and liquid superficial velocities.

Stratified smooth flow occurs when the liquid is at the bottom of the pipe and the gas flows along the top. The surface of the liquid is smooth; however, the gas-liquid interface is wavy. Both plug flow and slug flow are what Taitel and Dukler (1976) call intermittent flow (I) and are characterized by the liquid bridging the gap between the gas-liquid interface and the top of the pipe. The difference between slug and plug flow depends on the degree of agitation of the bridge. Plug flow is considered the limiting case of slug flow where no entrained bubbles exist in the liquid slug.

Annular flow occurs when the walls are wetted by a thin film of liquid, while the gas flows at high velocity through the center of the pipe. Liquid droplets are usually entrained in this gas. When the upper walls are wetted periodically by large aerated waves, it is neither slug flow requiring a

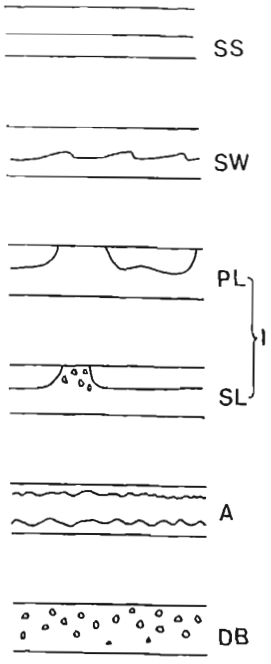


Figure 2 Typical gas-liquid flow regime patterns: SS is stratified smooth flow, SW is stratified wavy flow, PL is plug flow, SL is slug flow, I is intermittent flow, A is annular flow, and DB is dispersed bubble.

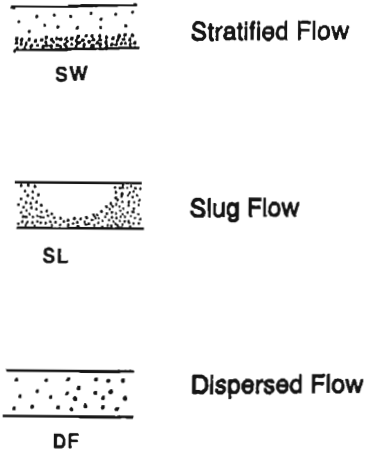


Figure 3 Typical gas-solid flow regime patterns.

complete fluid bridge nor annular flow requiring a stable film. Taitel and Dukler (1976) designated this flow pattern as wavy annular flow. This region, however, was not recognized by Mandhane et al. (1974) and was considered slug flow.

In the dispersed bubble or bubbly regime, small gas bubbles are distributed throughout the liquid phase that otherwise completely fills the pipe. The transition to this regime is characterized by the gas bubbles losing contact with the top of the tube. At first, the bubbles are near the upper portion of the pipe, but at higher liquid flow rates they become uniformly distributed throughout the system.

Typical flow regime maps based upon the superficial velocities are shown in Figs. 4 and 5 for gas-liquid and gas-solid two-phase flow, respectively.

Different flow regimes have a significant effect on the momentum, heat, and mass transfer behavior and can also influence most of the two-phase

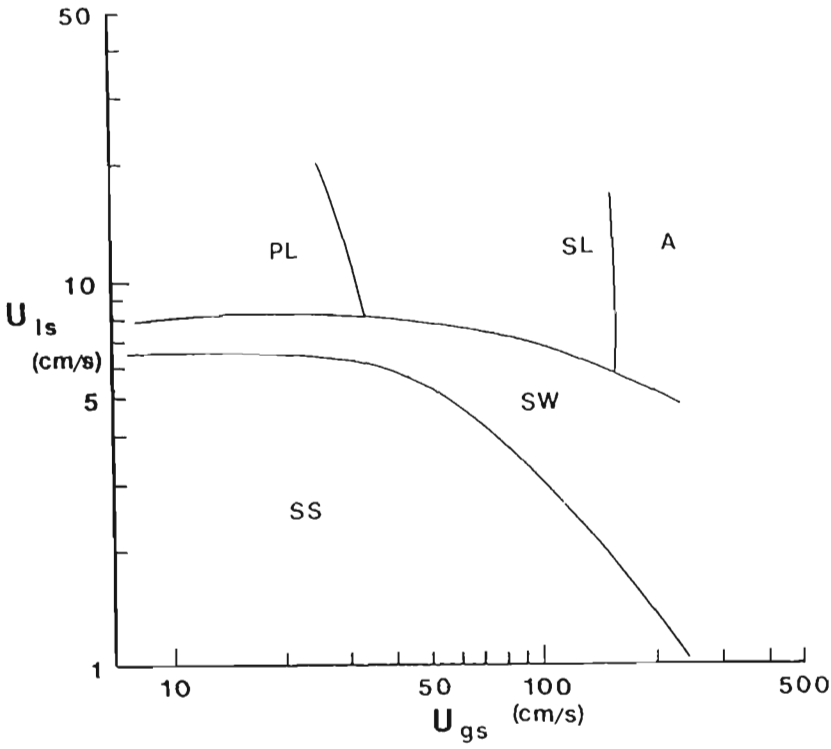


Figure 4 Typical gas-liquid flow regime map for horizontal flow.

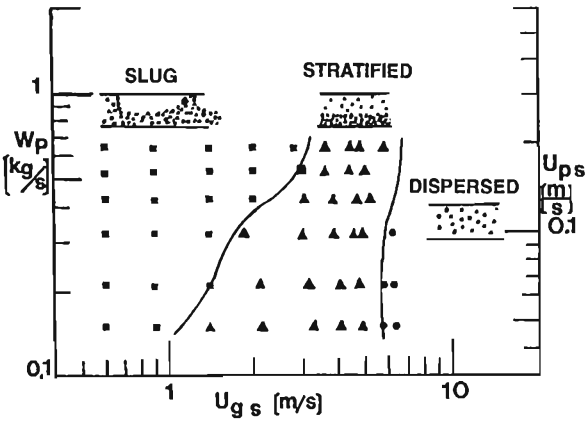


Figure 5 Typical gas-solid flow regime map for horizontal flow. (After Brodowicz et al., 1988.)

flow instrumentation, since the response time and the phase fraction ranges significantly vary. Identification of these flow regimes is important both for understanding the influence on the flow and for thermal design of the system.

II. MEASUREMENT OF PHASE FRACTION

Both ac and dc devices exist that can measure the volume fraction or void fraction occupied by either phase in a two-phase system. The dc based devices rely mainly on the principle of conduction of electricity through the phases, and the ac based techniques rely mainly on the principle of capacitance or inductance of the phases depending on the operating frequency.

A. Gas-Liquid Flow

A conductance transducer has also been used to determine the local phase fraction in pipe flow (Sekoguchi et al., 1975a; Kataoka et al., 1986; Ishii and Revankar, 1991). The transducer is influenced by the conductivity of each phase. For a constant applied voltage, the variation in conductance between the probe tip and the sheath will alter the current measured. From the time response in the current signal, information can be obtained for the interfacial frequency and void fraction of each phase that passes the tip of the transducer.

Cross-sectional or volume averaged type conductance transducers have been examined by Andreussi et al. (1988) and Tsochatzidis et al. (1992). This technique uses ring type sensors that are in contact with the fluid flow and embedded in the walls of the pipe. The ring type device is somewhat superior to the probe type device (Brunner and Chang, 1980), since the sensors are flush mounted and will not have as strong an influence to the flow. However, the technique provides volume averaged information regarding void fraction.

Andreussi et al. (1988) utilize a three-ring sensor in which the first two rings act as a fast response meter for detecting sudden changes in the void fraction. The third ring is used with one of the first two rings to obtain volume averaged void fraction information. Andreussi et al. (1988) clearly state that the separation of the second and third rings should be large. This improves the linearity of the device but inherently averages the flow.

Although Andreussi et al. (1988) name their technique an impedance technique, they operate the device in a conductance mode by applying a frequency of $\approx$100 kHz. At frequencies $\leq$0.5 MHz, capacitance and inductance effects are small and the conductance term is dominant, and for frequencies $\geq$0.5 MHz the capacitance term is dominant (Brunner and Chang, 1980). However, the conductivity of the liquid often changes as a function of time and applied voltages.

Tsochatzidis et al. (1992) provide a more detailed theory of this device and have applied the technique to two-phase gas-liquid flow in a packed bed.

Several authors have examined capacitance techniques for the measurement of void fraction in gas-liquid flow as shown in Fig. 6 (Chang et al., 1984, Cimorelli and Evangelisti, 1967). Chang et al. (1984) used ring type sensors around the periphery of a nonconducting pipe. Cimorelli and Evangelisti (1967) used a shell and tube annulus test section with the shell and the tube as the electrodes. Although the fluids are able to contact the sensors, appropriate instrumentation is used to separate the capacitive and conductive components.

The capacitance transducer uses a dielectric constant difference of the gas and liquid, where the specific dielectric constants ϵ_s of gases, which include steam and other liquid vapors, are close to 1; the specific dielectric constants of liquids range from 2 to 100; and those of nonconducting solids range between 2 and 12. The electrodes can be placed inside or outside the flow tubes depending on sensitivity and response time requirements.

The primary advantage of the capacitance transducer lies in its ability to capture fast transient phenomena (1 ms) nonintrusively and at low cost. This is an improvement over other techniques, which either have difficulty in responding to rapidly changing input or intrusively disturb the flow

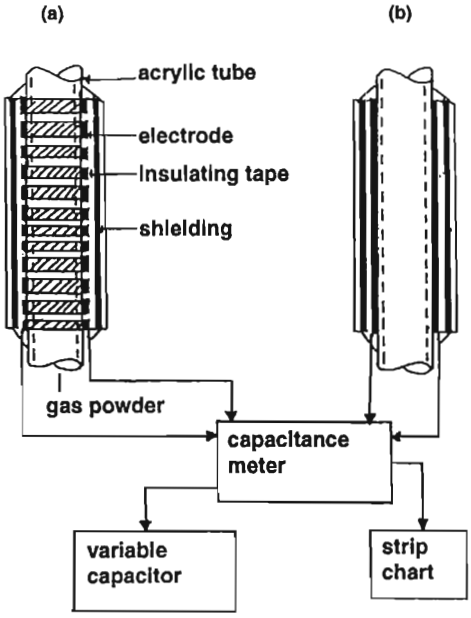
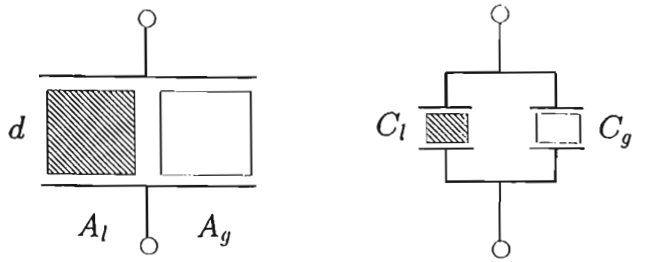


Figure 6 Capacitance transducer concept: (a) strip type; (b) ring type.

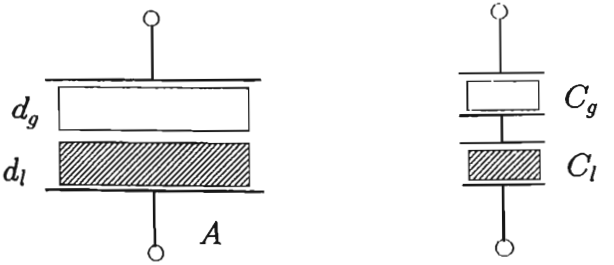
measurement. In addition, the transducer is easy to manufacture and can be configured to any geometrical shape.

The capacitance measured by a transducer for two-phase fluids can be treated as an approximation of a parallel plate capacitor. Typical equivalent plate capacitance circuits for gas-liquid two-phase flow for various flow regimes are shown in Fig. 7 (Chang et al., 1984). The capacitance is related to the charge Q_E on the plates and is inversely related to the electric potential V_E between them. This relationship is equivalent to the dependence on the dielectric nature of the material ϵ, the cross-sectional

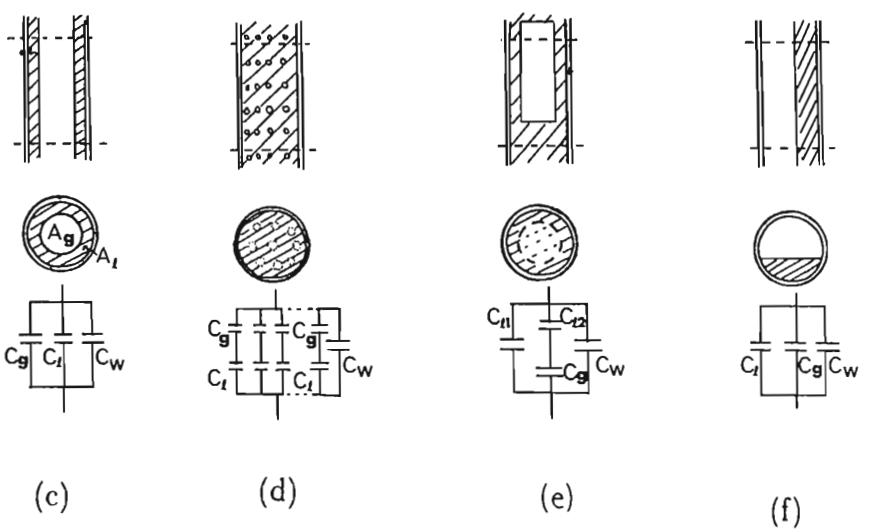
Figure 7 Equivalent circuits for capacitance transducers: (a) parallel arrangement, (b) series arrangement, (c) annular flow, (d) bubbly flow, (e) slug flow, and (f) stratified smooth flow; where A_l is the flow area occupied by the liquid, A_g is the flow area occupied by the gas, C_l is the capacitance of the liquid, C_g is the capacitance of the gas, C_W is the capacitance of the wall, d_l is the separation distance between electrodes occupied by the liquid, and d_g is the separation distance occupied by the gas. (After Chang et al., 1985.)



(a)



(b)



(c) (d) (e) (f)

area between the plates A, and the inverse relationship to the separation distance d. The two or more phases present in an experimental system will have different dielectric constants and will occupy different regions in the control volume. The equivalent circuit for the capacitance transducer in two-phase flow is then a selection of series and parallel capacitors of different dielectric constants.

$$C_p = \frac{Q_E}{V_E} = \frac{\epsilon_s \epsilon_0 A}{d} \tag{6}$$

The void fraction will affect either the cross-sectional area or the separation distance depending on the orientation with respect to the capacitance transducer. This orientation will reveal two general and distinct relationships between the void fraction and the capacitance of the transducer.

For the parallel and series circuits, the void fraction and capacitance are related by Eqs. 7 and 8 respectively:

$$C_p = \frac{\epsilon_1 A_1}{d} + \frac{\epsilon_2 A_2}{d} = \frac{A}{d}[\epsilon_1 \alpha_1 + \epsilon_2(1 - \alpha_1)] \tag{7}$$

$$C_p = \frac{1}{d_1/\epsilon_1 A + d_2/\epsilon_2 A} = \frac{A\epsilon_1\epsilon_2}{d[\epsilon_2\alpha_1 + \epsilon_1(1 - \alpha_1)]} \tag{8}$$

where α_1 is the void fraction of phase 1.

Detailed theoretical considerations for a capacitance transducer have been developed by Chang et al. (1984) for various gas-liquid flow regimes. Chang et al. (1984) use a linear difference theory as a first-order approximation to calculate the void fraction based upon a nondimensional capacitance value:

$$\alpha = C_p' = \frac{C_{TP} - C_l}{C_g - C_l} \tag{9}$$

where this relationship may change with geometry and transducer design.

A Faraday shield is used to reduce the influence of the external environment, namely the local electromagnetic fields and the electronic equipment (Irons and Chang, 1983a). Guard rings are used to suppress the electric field along the axial length of the test section. This ensures that the capacitance transducer is sensing a local measurement. The dielectric insulator isolates the Faraday shield from the sensing ring electrodes.

Capacitance and impedance probes are also recommended to use together with a temperature sensor, since the dielectric constant and conductivity of the fluid are functions of the temperature. (A detailed discussion can be found in Chang et al., 1984).

B. Gas-Solid Flow

The capacitance transducer is more often used for gas-solid two-phase flow as the solid flow is discontinuous. Conductance techniques do not work well in this type of flow due to the discontinuity of charge transfer and the sticking of particles to the electrodes due to electrostatic forces.

Two different electrode arrangements have been used for this measurement (Irons and Chang, 1983a and 1983b; Sugaya et al., 1990). The single ring type electrode was previously discussed for gas-liquid flows; however, under certain conditions, the solid material may not contain a significant dielectric constant difference, and a more sensitive arrangement of the multiple ring electrode system may be necessary. The strip type arrangement uses two long electrodes along the length of the pipe. A considerably larger control volume is used and a better sensitivity to the solid particles can be achieved. Due to the improved sensitivity, the strip type capacitance transducer is also more sensitive to different flow regimes (Irons and Chang, 1983b).

Essentially, the capacitance transducer follows a similar theory for both the strip type and the ring type transducer arrangements. In both arrangements, shielding from stray capacitance and electric fields is important, and with proper calibration these devices will provide accurate information. Disadvantages of the capacitance method are sensitivity to moisture and electrostatic discharge as discussed in detail by Sugaya et al. (1990).

III. MEASUREMENT OF PHASE DISTRIBUTION

Phase distribution is an important consideration both spatially and temporally. The void fraction transducers previously discussed can be used to obtain temporal variations in the void fraction signal as shown in Figs. 8 and 9 (Chang et al., 1985) for gas-liquid and gas-solid flow regimes, respectively. Capacitance waveforms show that the flow regime can be well characterized for these void fraction waveforms. The waveform produced by such a signal is unique for each flow regime or phase distribution that can occur.

Huang et al. (1989) and Xie et al. (1989) have developed a tomographic approach to imaging the phase distribution by use of a capacitance technique as shown in Fig. 10, which shows an eight-electrode sensor placed peripherally around a nonconducting region of the pipe. The capacitance is measured between any two plates, and a linear back-projection algorithm is used to reconstruct the phase distribution. The measurement area is interpreted by the eight-electrode system as a collection of pixel regions each sensed by several capacitance electrodes. The pixel regions will have

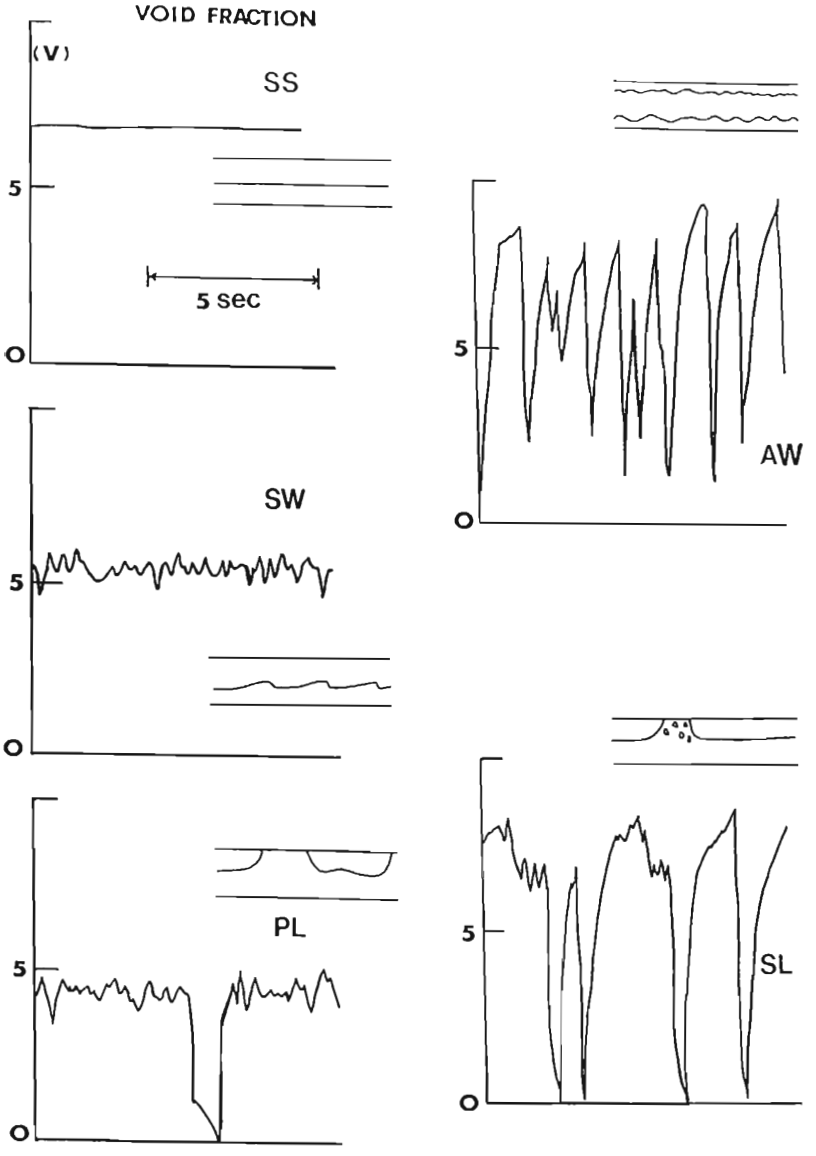


Figure 8 Typical transient response of capacitance transducers for various gas-liquid flow regimes.

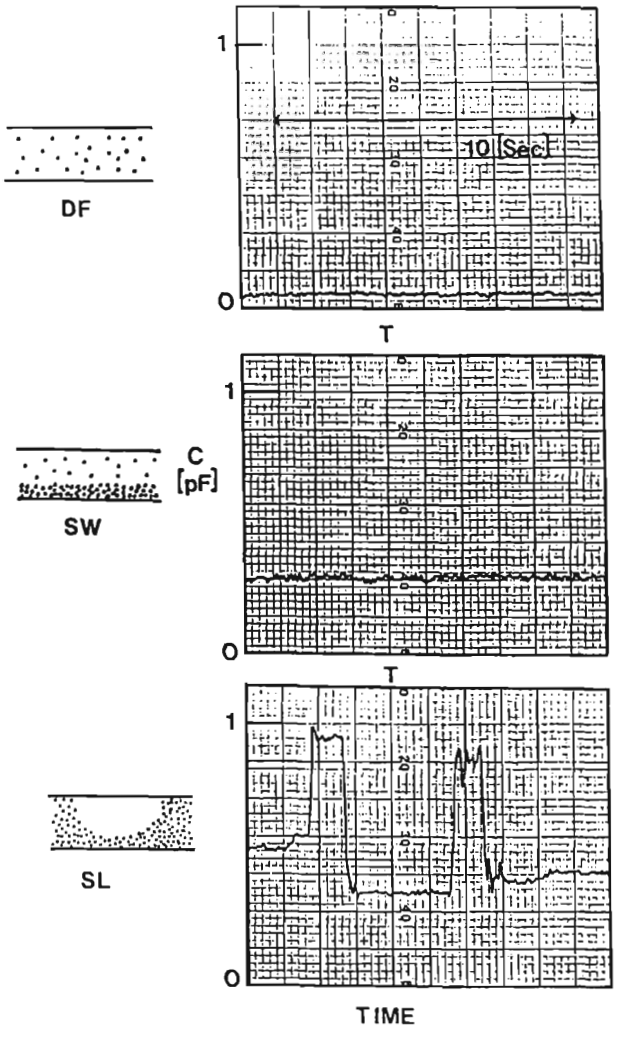


Figure 9 Typical transient response of capacitance transducers for various gas-solid flow regimes: DF, dispersed particle flow; SL, slug flow; and SW, stratified wavy flow. (After Chang et al., 1988.)

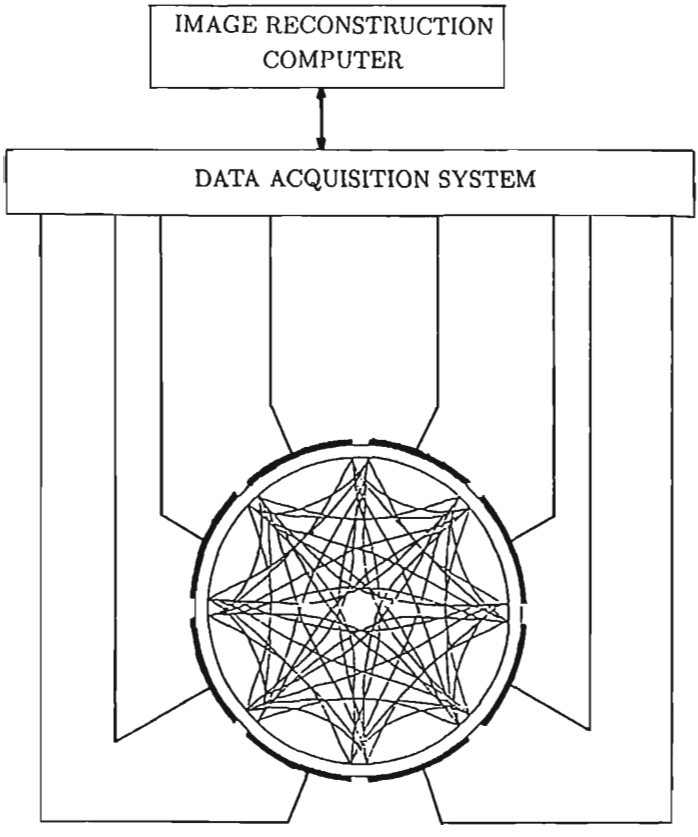


Figure 10 Eight-electrode capacitance tomographic technique. (After Xie et al., 1989.)

different sizes due to the arrangement of the electrodes in a ring. This will influence the local accuracy of the measurement. However, since the transducer concept is considered as measuring the presence or absence of each phase, and not relative quantity, the influence of pixel size will not be significant. However, due to the signal processing, time and space resolutions of the transducer are poor at this moment (a few seconds and a few centimeters).

Other researchers have been investigating a similar concept based upon the conductance between the electrodes as opposed to the capacitance. Seagar et al. (1987) have examined electrical impedance imaging on the

human body to illustrate the phase differences that can be imaged. Lin et al. (1991) have performed similar work in gas-liquid two-phase flow. The results are similar to the capacitance tomography system but possibly with better accuracy. However, the essential difference is due to the stage of development of the two techniques and the number of electrodes used.

IV. MEASUREMENT OF PHASE VELOCITY

There are several electrostatic techniques that can be used for the measurement of phase velocity. The most common technique is the double resistivity probe or conductance transducer as shown in Fig. 11 and as discussed by Sekoguchi et al. (1975a). Capacitance techniques can be used in two approaches to measure phase velocity. The waveforms from two transducers separated along the pipe can be cross-correlated to determine the phase velocity. The other method is to calculate directly the phase velocity from the measured void fraction and knowledge of the entrance mass flow rate (Irons and Chang, 1983a, 1983b). Brodowicz et al. (1988) and Gajewski et al. (1991) developed a two-phase velocity meter for the measurement of average flow velocity and mass flow rate based upon capacitive and inductive techniques, respectively. Ighodaro and O'Neill (1991) have examined powder flow rate measurements using a charge injection technique.

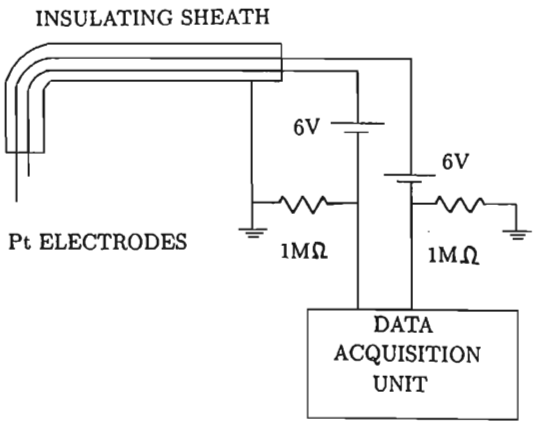


Figure 11 Double resistivity probe for phase velocity measurement. (After Sekoguchi et al., 1975a.)

A. Gas-Liquid Flow

Sekoguchi et al. (1983) discuss two techniques and several analysis methods for the measurement of a liquid slug in a gas-liquid system. Both techniques are electrical double sensing devices that respond to the liquid void fraction in the test section.

The first technique uses a double resistivity probe and employs a direct time delay measuring method as shown in Fig. 11. Sekoguchi et al. (1975a) provide more detail about the operation and fundamentals of this instrument. Other work has been done on this technique by Ishii and Revankar (1991) and Sekoguchi et al. (1975b). This device measures the local resistivity of the probe volume that corresponds to the type of material present. Use of two probes in one device provides the time of flight information required to measure bubble or wave velocity parallel to the probe. This technique has demonstrated good local measurements for forward flow but is intrusive to the flow. Also, measurement of the wave velocity in annular flow is difficult by this technique since position of the probe is very important and the film thickness does vary with time.

The second technique uses two terminals to inject a current through the test section as shown in Fig. 12. Between these terminals, two double ring electrode sensors are placed that receive an induced voltage proportional to the water content in their sensing region. Both cross-correlation and cross-spectrum coherence methods are discussed. This system allows for the measurement of the transit time of the liquid slugs as they pass the sensors for both forward and reverse flows depending on the correlation method used. Sekoguchi et al. (1983) showed excellent agreement of liquid slug or wave velocity for slug to annular flow regimes.

B. Gas-Solid Flow

Irons and Chang (1983a, 1983b) discuss the use of capacitance transducers for the measurement of a pneumatically driven powder flow. The particle velocities are determined by measuring the particle fraction as discussed previously. From this measurement, and knowledge of the gas flow rate, the particle velocities can be calculated. The mathematical expressions are given in Eqs. 10 and 11, where U_{ps} is the superficial particle velocity and U_p is the particle phase velocity.

$$\alpha_p = \frac{U_{ps}}{U_{ps} + U_{gs}} \tag{10}$$

$$U_p = \frac{U_{gs}}{\alpha_p} \tag{11}$$

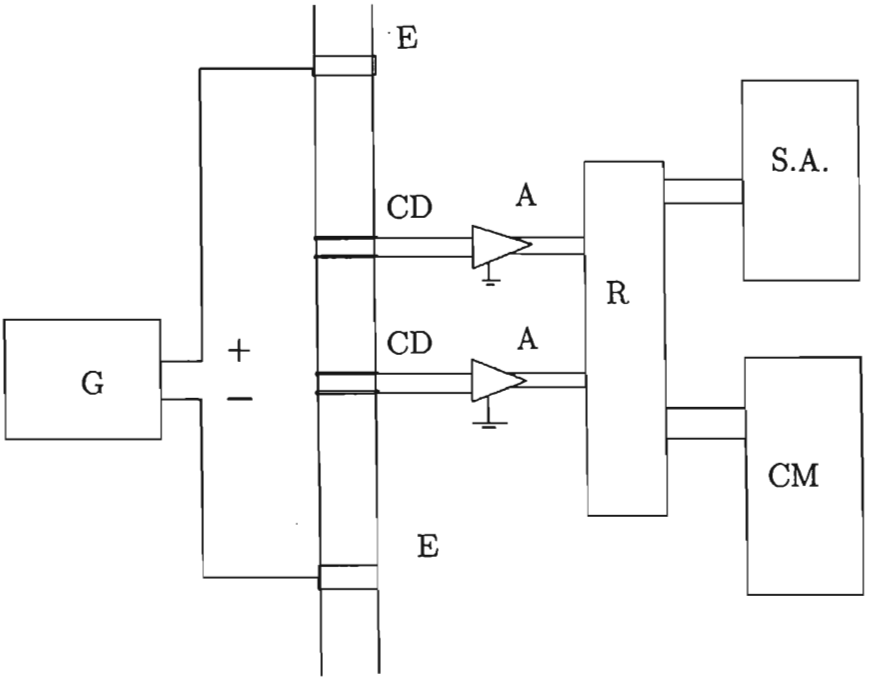


Figure 12 Conductance method for phase velocity measurement: E is an electrode, CD is the conductance detector electrode, A is an amplifier, G is a dc constant current generator, R is the data recorder, S.A. is a spectrum analyzer, and CM is a computer. (After Sekoguchi et al., 1983.)

In this case the measurement of the particle velocity is still inferred from the measurement of the particle fraction. This suggests that any influence to the void fraction such as flow regime effects could affect the accuracy of the particle velocity measurement. If two capacitance transducers were used at a specified separation, the particle fraction waveforms could be cross-correlated to identify easily the particle velocity without actual knowledge of either the particle fraction or the gas flow rate. This approach requires that the particle fraction not change in time or space at the two measuring locations. Under these conditions, the analysis of the particle fraction would be necessary to determine the particle velocity.

The inductive technique developed by Gajewski et al. (1991) uses two electrodes to sense the natural charging of solid particles due to flow. The theoretical basis for their technique is described by Gajewski and Kala (1990). The Gajewski et al. (1991) technique is nonintrusive and can mea-

sure the mass flow rate, but there is a strong nonlinear dependence on the average flow velocity that may be due to stronger charging effects at higher velocities. The results presented by Gajewski et al. (1991) also indicate a dependence on the two materials used. It was not explained whether this difference was due to the different particle sizes or material content, although Gajewski and Kala (1990) did model a dependence for both particle size and material type. This technique requires careful calibration before application to ensure that these effects are properly included.

The charge injection technique employs a series of electrodes and a corona needle that apply an electrostatic charge and sense the charge motion (Ighodaro and O'Neill, 1991). As a powder passes the corona needle, an electrostatic charge will be applied to the powder by a high voltage pulse between the corona needle and the first electrode or collecting electrode. The following electrodes will act as transducers and will respond to the motion of the charged particles. Use of more than one sensor allows for time of flight analysis. The last sensor is grounded to remove residual charge from the powder. Each sensing electrode measures the total quantity of charge. The magnitude of the charge is related to the powder density. The mass flow rate is simply determined from the powder density and time of flight measurement.

Ighodaro and O'Neill (1991) state that the technique could not be used at low flow velocities due to unacceptable pulsations in the flow. These pulsations may reflect a flow regime influence on the charge injection technique. Reasonable results were obtained between 0.2 and 6.0 g/s mass flow rate. Although Ighodaro and O'Neill (1991) have demonstrated the technique, some concern must be raised over the use of this method for continuous flow monitoring, as charged particles will tend to remain attached to the electrode walls. This could result in a significant loss of particle fraction from the flow and may reduce the sensitivity of the device after long periods of time.

V. MEASUREMENT OF FILM THICKNESS AND INTERFACIAL AREA

Other two-phase flow parameters are possible to measure using electrostatic techniques. Applications to film thickness and interfacial area will be mentioned here but not discussed in detail, as many of the techniques already discussed have been used by various authors to examine these two parameters.

Keska and Fernando (1992) and Ozgu and Chen (1973) have examined the application of a capacitance technique for the measurement of liquid

film thickness in gas-liquid flow. Although both authors used the impedance type probes that contact the liquid, their devices were set into a capacitance mode. Ring type noncontact transducers could also be used with similar results. The authors have demonstrated remarkable accuracy for the measurement of film thickness, but this type of device inherently averages the film thickness across the separation length of the ring sensors. For smooth and constant film thicknesses, such as liquid levels, this technique is satisfactory, but the inherent averaging is a serious disadvantage when film thickness varies either with time or with axial length. The use of film thickness to calculate the interfacial area would lead to significant errors for certain flow regimes, such as stratified wavy or annular ones, as the wavy interface would have an interfacial area significantly greater than the averaged value measured in this manner. It is possible that some merit could be achieved for heat conduction models of thin films, but the lack of accurate dynamic information at the interface would not allow for an accurate heat convection model to be ascertained, seriously weakening the results. The film thickness measurement by this technique is only considered valid for application to liquid level measurements.

The ring and strip type capacitance transducer has been demonstrated for the measurement of interfacial area (Chang et al., 1985). The results were noted to agree well with the theory.

Kataoka et al. (1986) and Ishii and Revankar (1991) examined the use of a double resistivity (conductance) probe for applications to interfacial area in gas-liquid flow. In their work, a double sensor is necessary to obtain not only the gas bubble frequency but also the interfacial velocity as well. This technique is based on the assumption that the bubble intersects the probe along the normal to the bubble surface and in the direction of flow.

Kang and Kim (1992) demonstrated a flush-wire probe for the measurement of liquid film thickness. This device is simply a conductance transducer with one electrode flush mounted on the wall of the test section

Table 1 Electrostatic Techniques and Devices for Multiphase Flow Measurement

Electrostatic techniques	Electrostatic devices
Ring capacitance transducer	Ionization chamber
Strip capacitance transducer	Proportional counter
Conductance transducer	Geiger-Mueller tube
Double resistivity probe	Vidicon tube
Flush-wire probe	Photomultiplier tube
Charge injection	Piezoelectric transducer

and the other electrode as a wire some known distance normal to the wall. The authors suggest that the flush-wire probe enhances spatial resolution over other conductance transducers, but the device remains an intrusive technique.

A list of the multiphase flow measurement techniques based on the electrostatic nature of the phase is given in Table 1.

VI. ELECTROSTATIC DETECTORS FOR MULTIPHASE FLOW APPLICATIONS

Several techniques exist for the measurement of multiphase flow parameters that do not sense the electrostatic nature of the flow medium but instead use electrostatic principles in a detector. These techniques utilize another principle for determination of the multiphase flow parameters such as neutron attenuation (Chang and Harvel, 1992), ultrasonic propagation (Matikainen et al., 1986; Chang and Morala, 1990), or gamma densitometry (Chan and Banerjee, 1981). These techniques fall essentially into two categories: sound wave measurement and radiation measurement.

A. Sound Wave Measurement

Ultrasonic techniques using a piezoelectric type transducer are often used for multiphase flow measurements. An ac pulsed signal is applied to the piezoelectric material causing a vibration in the crystal lattice. The transmitted sound pulse interacts differently with each phase. The interfaces between phases with different acoustic impedances reflect the sound pulses back toward the transducer. Vibration in the crystal induces an electrical pulse in the transducer detecting the sound wave.

Two methods are possible with ultrasonic devices for multiphase flow measurement. The pulse echo method is used primarily for film thickness measurements, and the transmission method is used for phase fraction measurements. Chang and Morala (1990) used these methods to determine the void fraction, phase distribution, interfacial areas, and bubble diameter in a gas-liquid two-phase flow. Matikainen et al. (1986) used the pulse echo technique for the detection of gas-liquid interface locations in two-phase flow. Ultrasonic techniques have indicated an excellent time response and excellent spatial accuracy.

B. Radiation Measurement

Radiation interacts with matter usually in the forms of absorption or scattering. This interaction can be useful for determining the phase fraction.

For example, a gamma densitometer uses a beam of gamma radiation and a gamma sensitive detector (Chan and Banerjee, 1981). In gas-liquid two-phase flow, the gamma beam is significantly reduced by the mass of the liquid in the test section exponentially. The void fraction is determined by measuring the amount of liquid in the test section.

Another possibility is to use a radioactive tracer for the determination of phase velocity (Kehler, 1979). In this case, detectors are placed axially along the flow channel and the signal strength of the tracer is recorded. Velocity is measured by knowledge of time of flight between detectors.

For both these applications, measurement of the radiation flux is achieved by an electrostatic type detector. Examples of these detectors are ionization chambers and photomultiplier tubes (Knoll, 1989). Each of these detectors relies on an interaction between the radiation and some medium to produce electrons or charged particles. For example, the ionization chamber uses a pressurized gas that is ionized by the radiation flux. The ions are collected at the cathode or anode. Each collection of ions produces a voltage pulse. Counting electronics are used to determine the number of pulses, which is directly proportional to the radiation field.

Another example is the vidicon tube used in a neutron camera (Dance and Corollo, 1986; Chang and Harvel, 1992). A neutron-to-photon converter screen transforms the neutron radiation flux into a light beam. The photons strike the vidicon target, changing the local electrical conductivity. The target is scanned by an electron beam, which produces a charge on a collecting electrode proportional to the light intensity (Bryant and McIntire, 1985).

Several other electrostatic devices exist, such as the proportional counter and the Geiger-Mueller tubes, which perform similarly to the ionization chamber, or the photomultiplier tube, which performs similarly to the vidicon tube (Knoll, 1989). Table 1 provides a partial list of electrostatic devices currently in use for multiphase flow measurement.

NOMENCLATURE

α	Void fraction
ϵ	Dielectric constant
A	Area
C_p	Capacitance
d	Separation distance
Q	Volumetric flow rate
Q_E	Electric charge
U	Velocity

V Volume
V_E Electric potential

Subscripts

cs Cross-section
g Gas
gs Superficial gas
k Phase number
l Liquid
ls Superficial liquid
p Particle
ps Superficial particle

REFERENCES

Andreussi, P., A. Di Donfrancesco, and M. Messia. (1988). An impedance method for the measurement of liquid hold-up in two-phase flow. *Int. J. Multiphase Flow*, 14(6), 777–785.

Banerjee, S., and R. T. Lahey, Jr. (1981). Advances in two-phase flow instrumentation. *Advances in Nuclear Science and Technology*, 13, 227–414.

Beck, M. S., and N. Wainwrite (1969). Current industrial methods of solid flow detection and measurement. *Powder Tech.*, 2, 189.

Brodowicz, K., J. S. Chang, B. Donevski, I. Sekovanic, and W. Tofiluk (1988). Gas-solid two-phase flow patterns, pressure drop and void distributions in an inclined flow tube. In *Experimental Heat Transfer, Fluid Mechanics, and Thermodynamics* (R. K. Shah, E. N. Ganic, and K. T. Yang, eds.). Elsevier, New York, pp. 1338–1342.

Brunner, K., and J. S. Chang (1980). Flow regime transitions under strong electric fields in a horizontal two-phase flow. Conference Record of 1980 IEEE Industrial Applications Society, pp. 1042–1047.

Bryant, L. E., and P. McIntire (1985). *Nondestructive Testing Handbook, 2nd ed., Vol. 3: Radiography and Radiation Testing*. American Society for Nondestructive Testing.

Chan, A. M. C., and S. Banerjee (1981). Design aspects of gamma densitometers for void fraction measurement in small scale two-phase flow. *Nuclear Instruments and Methods* 190, 135–148.

Chang, J. S., and G. D. Harvel (1992). Determination of gas-liquid bubble column instantaneous interfacial area and void fraction by a real-time neutron radiography method. *Chemical Engineering Science*, 47(13/14), 3639–3646.

Chang, J. S., and E. C. Morala (1990). Determination of two-phase interfacial areas by an ultrasonic technique. *Nuclear Engineering and Design*, 122, 143–156.

Chang, J. S., R. Girard, R. Raman, and F. B. P. Tran (1984). Measurement of void fraction in vertical gas-liquid two-phase flow by ring type capacitance transducers. *Mass Flow Measurements-1984*, ASME Press, New York, pp. 93–99.

Chang, J. S., T. A. Myint, B. Donevski, A. A. Berezin, G. A. Irons, and W. K. Lu (1985). Determination of the interfacial parameters in gas-solid two-phase pipe flow by capacitance transducers. In *Particulate and Multiphase Processes—Colloidal and Interfacial Phenomena* (T. Ariman and T. Nejat Veziroglu, eds.). Hemisphere Publishing Corporation, Springer-Verlag, pp. 173–187.

Chang, J. S., T. A. Myint, N. Hayashi, W. Tofiluk, and K. Brodowicz (1988). Time averaged particle fraction and flow patterns in gas-powder two-phase horizontal flow. In *Particulate Phenomena and Multiphase Transport* (T. Nejat Veziroglu, ed.). Hemisphere Publishing Corporation, pp. 47–56.

Cimorelli, L., and R. Evangelisti (1967). Capacitance method for void fraction measurement in bulk boiling conditions. *Int. J. Heat and Mass Transfer, 10,* 277–288.

Dance, W. E., and S. F. Corollo (1986). High sensitivity electronic imaging system for reactor or non-reactor neutron radiography. *Neutron Radiography* 2: 415–422.

Gajewski, J. B., and W. Kala (1990). How to measure the velocity and mass flow rate of a two-phase flow of solid particles in pipelines. *Materials Science*, 16 (1–3), 113–120.

Gajewski, J. B., B. Glod, and W. Kala (1991). An electrostatic flow meter for measuring the two-phase flow parameters in pneumatic transport; results of preliminary tests. In *Electrostatics 1991* (B. C. O'Neill ed.). Inst. Phys. Press, Bristol, pp. 159–164.

Hewitt, G. (1978). *Measurements of Two-Phase Flow Parameters*. Academic Press, New York.

Huang, S. M., A. B. Plaskowski, C. G. Xie, and M. S. Beck (1989). Tomographic imaging of two-component flow using capacitance sensors. *Journal of Physics E, Scientific Instruments*, 22(3), 173–177.

Ighodaro, D. A., and B. C. O'Neill (1991). Powder flow-rate measurements by means of a pulse charge injection technique. *Electrostatics 1991* (B. C. O'Neill, ed.). Inst. Phys. Press, Bristol, pp. 135–140.

Irons, G. A., and J. S. Chang (1983a). Dispersed powder flow through vertical pipes. *Powder Technology*, 34, 233–242.

Irons, G. A., and J. S. Chang (1983b). Particle fraction and velocity measurement in gas-powder streams by capacitance transducers. *Int. J. Multiphase Flow*, 9(3), 289–297.

Ishii M., and S. T. Revankar (1991). Measurement of local interfacial area and velocity in bubbly flow. ANS Proceedings 1991 National Heat Transfer Conference, pp. 181–189, July 28–31.

Kataoka, I., Ishii, M., and A. Serizawa (1986). Local formulation and measurement of interfacial area concentration in two-phase flow. *Int. J. Multiphase Flow, 12*(4), 505–529.

Kang, H. C., and M. H. Kim (1992). The development of a flush-wire probe and calibration method for measuring liquid film thickness. *Int. J. Multiphase Flow*, 18(2), 423–437.

Kehler, P. (1979). Pulsed neutron measurement of single and two-phase liquid flow. *IEEE Transactions on Nuclear Science*, NS-26(1), 1627–1631.

Keska, J. K., and R. D. Fernando (1992). An experimental study of liquid film

thickness measurements in a two-phase flow. *AICHE Symposium Series: Heat Transfer, San Diego*, 88(288), 34–43.

Knoll, G. F. (1989). *Radiation Detection and Measurement*. John Wiley, New York.

Lin, J. T., L. Ovacik, O. C. Jones, J. C. Newell, M. Cheney, and H. Suzuki (1991). Use of electrical impedance imaging in two-phase gas-liquid flows. ANS Proceedings 1991 National Heat Transfer Conference, pp. 190–198, July 28–31.

Mandhane J. M., G. A. Gregory, and K. Aziz (1974). A flow pattern map for gas-liquid flow in horizontal pipes. *Int. J. Multiphase Flow*, 1, 537–553.

Matikainen, L., G. A. Irons, E. C. Morala, and J. S. Chang (1986). Ultrasonic system for detection of transient liquid-gas interfaces using the pulse-echo technique. *Rev. Sci. Instr.*, 57, 1661–1666.

Ozgu, M. R., and J. C. Chen (1973). A capacitance method for measurement of film thickness in two-phase flow. *Rev. Sci. Instr.*, 44(12), 1714–1716.

Seagar, A. D., D. C. Barber, and B. H. Brown (1987). Electrical impedance imaging. *IEE Proceedings Pt. A*, 134(2), 201–210.

Sekoguchi, K., H. Fukui, M. Tsutsui, and K. Nishikawa (1975a). Investigation into the statistical characteristics of bubbles in two-phase flow: fundamentals of the instrumentation using the electric resistivity probe technique. *Bulletin of the JSME*, 18, 391–396.

Sekoguchi, K., H. Fukui, M. Tsutsui, and K. Nishikawa (1975b). Investigation into the statistical characteristics of bubbles in two-phase flow: application and establishment of electric resistivity probe method. *Bulletin of the JSME*, 18, 397–404.

Sekoguchi, K., M. Takeishi, K. Hironaga, and T. Nishiura (1983). Velocity measurement with electrical double-sensing devices in two-phase flow. In *Measuring Techniques in Gas-Liquid-Solid Two-Phase Flows* (J. M. Delhaye and G. Cognet, eds.). Springer-Verlag, Berlin, pp. 455–477.

Serizawa, A., I. Kataoka, and I. Michiyoshi (1975). Turbulence structure of air-water bubbly flow—I: measuring techniques. *Intl. J. Multiphase Flow*, 2, 221–233.

Serizawa, A., K. Tsuda, and I. Michiyoshi (1983). Real-time measurement of two-phase flow turbulence using a dual-sensor anemometry. *Measuring Techniques in Gas-Liquid Solid Two-Phase Flows* (J. M. Delhaye and G. Cognet, eds.). Springer-Verlag, Berlin, pp. 495–523.

Sugaya, M., N. Hayashi, and J. S. Chang (1990). Effects of highly charged powder on solid fraction measurement by capacitance transducers in solid-gas two-phase flow. *Trans. IEE of Japan*, 110-A(3), 197–205.

Taitel Y., and A. E. Dukler (1976). A model for predicting flow regime transitions in horizontal and near horizontal gas-liquid flow. *AIChE Journal*, 22(1), 47–53.

Tsochatzidis, N. A., T. D. Karapantsios, M. V. Kostoglou, and A. J. Karabelas (1992). A conductance probe for measuring liquid fraction in pipes and packed beds. *Int. J. Multiphase Flow*, 18(5), 653–667.

Xie, C. G., A. B. Plaskowski, and M. S. Beck (1989). Eight-electrode capacitance system for two-component flow identification. *IEE Proceedings Pt. A*, 136, 184–190.

14

Printers

P. T. Krein

University of Illinois at Urbana–Champaign
Urbana, Illinois

K. S. Robinson

Eastman Kodak Company
Rochester, New York

I. SURVEY OF PRINTER TECHNOLOGY

A. Introduction

Modern printing systems for computer output and office applications are generally divided into impact and nonimpact technologies. Impact technologies, including the conventional typewriter and pin printers that form characters as matrixes of dots, tend to be configured for low-end needs, for inexpensive hardware where slow print speeds are acceptable. Because the dots or characters are formed mechanically, there are limits to opportunities for quality improvement. Concerns about noise, reliability, pictorial representation, print speed, and flexible operation have led to the evolution of nonimpact printing technologies. Most nonimpact printing technologies either were developed from the electrophotographic process (Chapter 15) or use one of many varieties of ink jet printing. Hence electrostatics plays an important role in modern nonimpact printing systems. Two other nonimpact printing techniques that rely on electrostatics are ionography and electrography. Thermally driven imaging is an important nonelectrostatic printing technology.

In this chapter, we shall review the fundamental performance issues in document and graphics printers. The two major electrostatic printing technologies, electrophotographic and continuous ink jet, will be de-

scribed. Some less common electrostatic technologies are discussed briefly. References provide a gateway to more detailed information in the literature.

B. Demands of Image Quality

Image quality is perhaps the most critical performance issue in any printer. At the low end, text and graphics must be rendered with adequate legibility, even when performance drifts. At the high end, the ultimate objective might be printed output of photographic quality. The implications of these needs are deeply linked to human perception. For printed output, terms such as "sharpness," "contrast," "color," and so on need to be defined and translated into a process.

1. Implications of Vision Characteristics

Human vision involves detection of light intensity, shapes and edges, and color. Light intensity, or luminance, is generally discussed in terms of gray scale for printing applications. The obvious boundary levels for gray scale range are white, for a blank sheet of paper, and black, for a fully printed document. It is well known that a certain minimum contrast (i.e., luminance difference) must be present before an observer can detect the change. The concept of minimum contrast leads naturally to intensity digitization, with a single digital level corresponding to the minimum gray level change. Recent reports in the literature (Murch and Weiman, 1991) find experimentally that the best-case human sensitivity corresponds to about a 10-bit representation of gray level, i.e., about 1000 distinct gray levels. In practice, the necessary number of levels is usually much lower. An older study (Graham, 1965) found that, for fixed illumination levels, brightness changes can be detected reliably over only two orders of magnitude. These can be encoded with six to seven bits.

The eye seems to process images through spatial Fourier analysis, extracting component frequencies of the intensity variation from a complex picture. Consider the familiar benchmark of 20/20 vision, in which an image change over a 1/4" distance can be discerned from 20 feet away. This displacement can be defined in terms of the angular resolution at the retina

$$\frac{0.25 \text{ in displacement}}{240 \text{ in radius}} \approx 1.0 \text{ mrad} \approx 0.06^\circ \tag{1}$$

At a typical reading distance of 20 cm, angular displacement of 1 mrad corresponds to feature size of about 20 μm (5 features/mm). This has been confirmed through experimental data (Lowry and DePalma, 1961), showing that visual sensitivity at reading distance drops off rapidly beyond

5 features/mm. Features much smaller than this tend to be merged by the eye—a useful effect in building color images or other pictures with fine details.

2. Color

The eye has long been known to be trichromatic, meaning that it processes color in terms of three primaries, three distinct bands of the visible spectrum. These are associated with spectral sensitivities of three pigments (Nathans, 1989), with sensitivity band peaking near a wavelength of 565 nm in the yellow (with good sensitivity extending into the red), a second peaking near 535 nm in the green, and a third peaking near 420 nm in the blue. A red-green-blue (RGB) primary system recognizes this human response for the design of computer displays and television monitors. Most individuals with some form of color blindness have one defective or missing pigment, and interpret colors according to a subset dichromatic system. Displays present an image by creating the necessary light signal, and so are based on additive or positive color systems. White light is created by adding all three colors.

A document, in contrast, creates an image by selectively absorbing light. A green printed area must absorb light except in the green portion of the spectrum, for example. Printed images are therefore formed with subtractive or negative color systems. The necessary primaries are "not red" (known as cyan), "not green" (known as magenta), and "not blue" (corresponding to yellow). This forms the CMY subtractive primary system. White represents the initial blank sheet, i.e., nothing has been subtracted, while black represents complete subtraction through the mixing of all three colors. Real cyan, magenta, and yellow must absorb the correct spectral bands. In a typical printer using easily manufacturable inks, dyes, or toners, the combination of all three will yield a muddy olive drab instead of a solid black, because the spectral absorptions are imperfect. As a result, a separate black is usually used in subtractive systems to form the CMYB four-color printing system.

3. Digital Images

Just as in the case of gray level, visual acuity and color perception are often translated into a digitized quantitative framework. For example, the above discussion indicates that features smaller than 200 μm are unlikely to be noticed on a document at normal reading distance. A natural choice is to build up an image from dots of 100 μm diameter or less. Each such dot defines an image pixel. In a color printer, each pixel is formed from spots of cyan, magenta, or yellow. To produce gray scale or mixed colors, one must either control the size of each ink spot or form each 100 μm

pixel from combinations of smaller spots. A pixel formed from a controlled array of spots is termed a macropixel.

Figure 1 illustrates a macropixel process in a printer able to generate 260 dots/cm (660 dots/inch). The general process of building up a picture from spots is termed halftoning, while the process of arranging spots to approximate a desired gray scale is termed dithering. There are many ways to arrange dots for a halftone picture (Ulichney, 1987). The figure shows a hexagonal grid ordered dither approach, with which this printer can generate 10 levels of gray (including full black, not shown) at 100 pixel/cm resolution—very good, but not sufficient to match the full capabilities of human vision. An extremely high quality printer would need to provide 40 dB of gray level (a factor of 100 in relative reflectance) in a dot 100 μm across. The spot size is determined by the area to be covered, so spots about 100 μm/$\sqrt{100}$ = 10 μm across should work. This translates to 1000 dots/cm, or 2500 dots/inch.

The biggest drawbacks of small spots are the immense data needs and the time required to place an image on either paper or the photoconductor of a laser printer. If a printer's spot rate (the number of spots printed or exposed per unit time) is independent of spot size, then low quality modes with large spots will be needed for fast printing.

Example 1 Printer data rates.

Consider a color printer that uses the CMYB ink system and produces

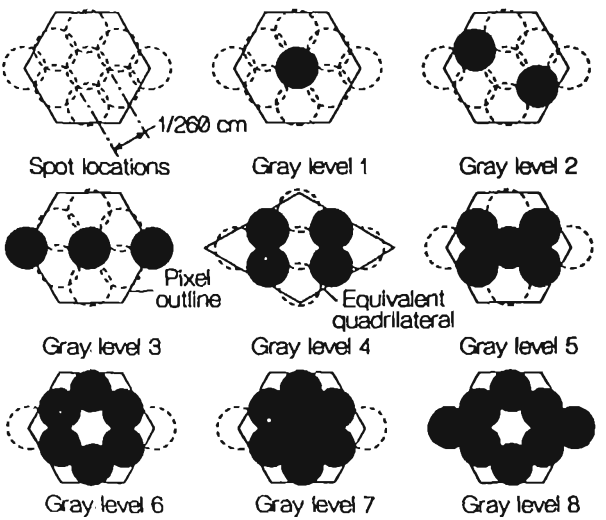


Figure 1 Gray scale based on macropixels.

240 dots/cm. How much data is represented by a 20 × 25 cm printed page?

> The page contains $20 \times 25 \times 240 \times 240 = 28.8 \times 10^6$ dot locations. Each location can have up to 8 different color arrangements (cyan, magenta, yellow, black, white, or combinations of any two colors) and therefore must be coded with three digital bits. The total bit count is at least 86.4×10^6, corresponding to just over 10 MByte.

If this page is to be printed in 6 s (a rate of 10 pages per minute), the data flow rate into the printer exceeds 1.5 MByte/s.

Example 2 Spot rate requirements.

To produce the 20 × 25 cm image of Example 1 in 6 s, how fast must dots by generated by the printer?

> There are 28.8×10^6 dot locations, each of which could be visited by one of four ink systems corresponding to the various colors. To complete the image in 6 s, the printer must create spots at the rate of 19.2×10^6 dots/s.

For ink jet systems, the dot rate translates immediately into ink droplet production. In an electrophotographic technology, the dot rate corresponds to exposure rates for the photoconductor. In practice, this means that ink jet printers are relatively slow unless they use large arrays of jet nozzles.

Example 3 Rates implied by external factors.

In many computing environments, the printer uses a serial data port. Assuming that all image processing is performed in the computer, and that the printer simply applies dots as requested, how long will it take to deliver a complete 20 × 25 cm image to the printer at 9600 baud?

> From Example 1, the image requires 86.4×10^6 bits for representation. At 9600 baud (9600 bits/s), it will take 9000 s, or 2½ hours, to transfer all this data to the printer.

This extreme time implies that either much faster communication links must be used, or that less data should be used and the printer should process image data internally. In a real printer, the data stream contains characters to be printed, rather than details of dots. The printer must translate the incoming characters into full dot-by-dot images. Part of the time savings can come from the fact that a typical printed page is mostly blank space.

4. Printing Terminology

In this section, a summary of terms often used to describe image quality and the capabilities of a printing system is given. There are few relevant standards at this writing, and the terms are used in slightly different ways among various manufacturers.

Term	Definition
Addressability	The number of possible dot locations per unit length. This is determined primarily by the capability of the printing mechanism. Dot-matrix printers sometimes move in half steps, so that their addressability can be double the resolution. Electrostatic printing methods usually have extremely high possible addressability.
Aliasing	Artifacts in an image resulting from regularity in dither patterns or drop placement. As in digital communications and filtering, aliasing is related to unwanted spatial frequencies produced in the printing process. Examples are jaggies, referring to jagged edges when addressability is low, staircasing, a regular stepping pattern when lines are printed at unfavorable angles, and various moiré patterns produced by interaction of images with dither patterns.
CMY and CMYB	The subtractive cyan-magenta-yellow or cyan-magenta-yellow-black color systems. A color printer normally provides these primaries.
Dithering	The process of representing gray levels with various patterns of spots. The term normally refers to digital printing, in which only one spot size is available. Dithering also refers to the process of perturbing the dot location or gray scale pattern to help avoid aliasing.
Gray scale	Contrast expressed as the range of reproducible intensity values at each pixel.
Gray level	A single intensity level on a gray scale. Usually expressed independent of the illumination conditions.
Halftoning	The process of converting a continuous image to binary form, which can then be represented digitally as a collection of spots. The term often refers to the printer's classical screening process.
Luminance	Light intensity (units are candelas per square meter).
Optical density	A measure of the fraction of light of a specified spectrum that is absorbed by a printed image.

Term	Definition
Pixel *or* pel (picture element)	The smallest region of an image for which complete information is defined, sometimes used interchangeably with *spot* when describing printer output.
Macropixel	An image element deliberately made larger than the smallest possible region, in order better to reproduce color or gray scale. Many ink spots will be present in a single macropixel. The term superpixel is sometimes used.
Registration	Reproducibility of position in systems that print at a given location multiple times. An example is any color process with multiple passes. Registration is said to be perfect if multiple passes print at the same place. Registration is critical in most color printers, since colors cannot be mixed consistently if the spot location varies.
Resolution	Usually expressed as 1/(spot size). The number of printer output elements that can be formed distinctly or resolved per unit length. *Addressability* typically exceeds *resolution* so that spots overlap as illustrated in Fig. 1 so that maximum densities can be printed.
Spot *or* subpixel	The smallest element from which an image is built up. When describing printer output, spot refers to the actual ink dots.
Spot rate	The number of spots that can be printed per unit time.

C. Laser and LED Electrophotographic Printers

Shown in Fig. 2 is a block diagram of the information flow in a typical laser or light-emitting-diode (LED) printer. Illustrated are the major subsystems and the transformation that each makes on the information. For example, the exposure system together with the "front-end" electronics receives an electronic signal and transforms the information into a light signal. The photoreceptor receives the light signal and transforms it into an electrostatic latent image. The final output of the system is a permanent visual image on a receiver sheet, such as a piece of paper or a transparency sheet.

Laser and LED printers have much in common with xerographic copiers (see Chapter 15). The focus here is on the exposure system and photoreceptor, since these system components distinguish printers from copiers. Copiers have an exposure system designed to illuminate a paper

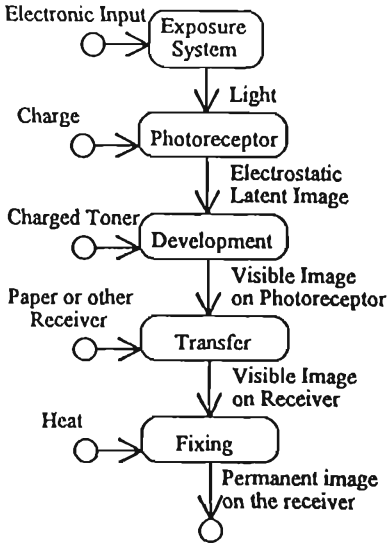


Figure 2 Block diagram of information flow in a laser or LED printer.

original placed on a platen and focus the reflected light onto the photoreceptor. The exposure system in printers is more complicated than that in copiers because it is designed to illuminate the photoreceptor directly, writing the image dot by dot. Copiers require a panchromatic photoreceptor for color reproduction. Black-and-white copiers typically have a panchromatic photoreceptor since the originals to be copied may have a variety of colors. The photoreceptor in printers could be made simpler than those designed for copiers because lasers and LEDs are nearly monochromatic. Sensitivity of a printer photoreceptor is needed only at the wavelengths emitted by the laser or LED's.

1. Exposure System Overview

The electronic information sent to the printer is converted into a light signal by the exposure system. A laser or a linear array of light-emitting-diodes (LEDs) is the light source. The light beam writes a two-dimensional image to form an electrostatic latent image on the photoreceptor. In laser printers, the beam is scanned across the image, typically using a rotating polygon mirror to write in one dimension. Analogously, the linear diode array spans the image in an LED printer. As the photoreceptor moves at a constant speed, the light beam is modulated to write in the second dimension. The laser beam must be modulated. The drive current is gated

to modulate the light output of the LEDs or laser diodes. For gas lasers, the modulation is performed externally to the laser, often by employing an acoustooptical Bragg cell interaction.

2. Photoreceptor Overview

Light from the exposure system is converted into an electrostatic latent image by the photoreceptor, as illustrated in Fig. 3. The unexposed photoconductive layer is highly insulating. It is sensitized or made photosensitive by depositing electric charge on its surface using a corona ionizer (see Chapter 21). A portion of the incident light from the exposure system is absorbed by the photoreceptor and produces charge carriers in the photoconductive layer. In regions exposed to light, the photoconductive layer becomes conductive and dissipates the surface charge, forming an imagewise charge pattern on the photoreceptor surface.

D. Ink Jet Printing

In an ink jet printer, liquid droplets are propelled toward the printing target. An image is painted from this spray. There are two major categories of ink jet technology (see Table 1):

Drop-on-demand ink jets. These are usually mechanical devices that eject droplets one at a time from a small orifice. The commercially available devices use either a pressure pulse (often generated with a piezoelectric crystal) or a thermal pulse that creates a bubble and forces out a drop.

Continuous ink jets. In this arrangement, a jet of ink is forced through an opening at high pressure. As the jet breaks up into drops, the drops are given an electric charge. A deflection system analogous to the plates in a cathode-ray tube directs the droplets to the desired print locations.

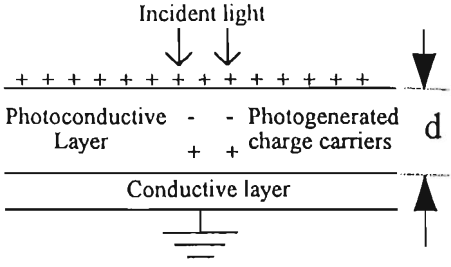


Figure 3 Electrostatic latent image formed by imagewise exposure of the photoreceptor.

Table 1

Drop-on-Demand Process Steps	Continuous Process Steps
1. Apply electrical or pressure pulse to eject surface drop.	1. Liquid jet flows continuously under high pressure.
2. Direct drop toward print target. Electric fields can be used if drops are charged.	2. Jet breakup into droplets is tightly controlled by a small ultrasonic vibration.
3. Wait for capillary refill, and allow meniscus to return to quiescent state.	3. Drops charge by induction as they break off. Charge is adjustable.
4. Apply pulses when drops are needed.	4. Drops move through a fixed deflection field to the target.
	5. Unused drops are recovered, filtered, and returned to the ink supply.

While there have been a few prototype electrostatic drop-on-demand ink jets (Winston, 1962; Miura and Naito, 1984; Oda and Miura, 1992), these are not yet in full production. Electrostatic ink jet technology is thus normally associated with continuous systems. Most commercial continuous systems use the deflection technology introduced by Sweet (1965), and this technology will serve as the focus for the discussion here.

Hertz and Samuelsson (1989) have developed alternative continuous methods. A more complete list of electrostatic ink jet methods can be found in Carnahan and Hou (1977). Basic block diagrams and a simple depiction of an electrostatic drop-on-demand process and the continuous process are given in Fig. 4.

In the drop-on-demand process, an ink drop must be drawn from the nozzle, as in Fig. 4a. The drop will carry a charge if the electrode at the right is used to extract it. The charged droplet can be deflected, if desired, or allowed to fly to the print target. The nozzle refills by capillary action prior to the command for the next drop. A mechanical drop-on-demand ink jet (Zoltan, 1972) substitutes a fast pressure pulse for the electric pulse in this process.

In any drop-on-demand system, the "off" condition of the ink jet has a static liquid surface in a small opening. Evaporation at this surface, or environmental contamination, can clog the opening with dye crystals or dust when the printer is idle. A recent development is the use of waxy solid ink systems for these printers. The ink is heated to liquid form only when printing is in progress.

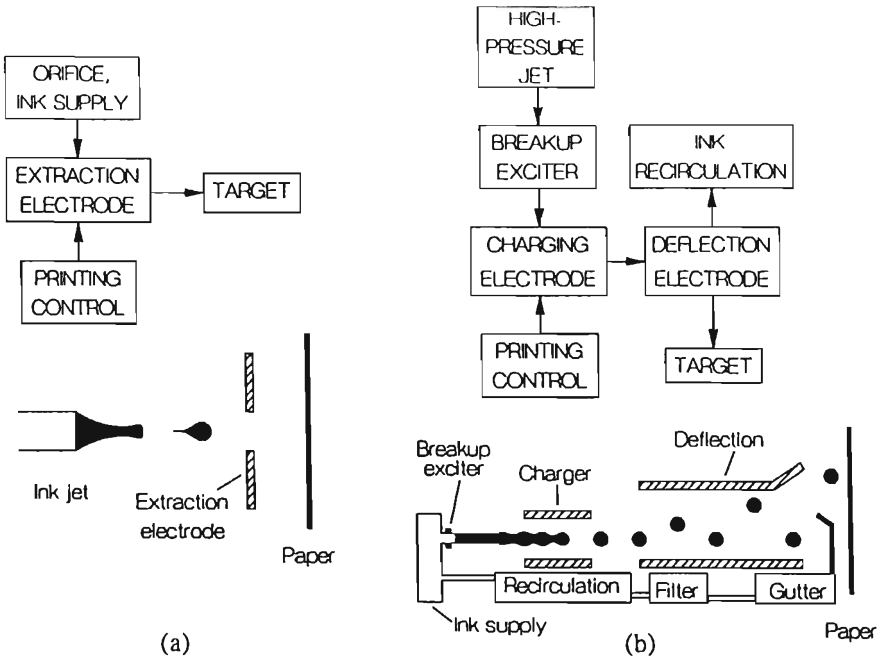


Figure 4 Block diagrams of major ink jet technologies. (a) Drop-on-demand; (b) continuous.

In the basic continuous process, the liquid emerges from the nozzle under high pressure as a jet. The nozzle is vibrated at a controlled rate to synchronize jet breakup into drops. As the drops break off, a cylindrical or parallel-plate electrode induces a controlled charge on each. The drops move through deflection electrodes. Those with a charge move toward the printing target in a controlled direction. Uncharged drops are caught in a gutter. Since most space on a page is normally blank, uncharged drops represent a large fraction of the total. The high flow rates require this unused ink to be recirculated. However, the nozzle openings are normally quite small (diameters below 50 μm are typical), and the ink must be thoroughly filtered to remove debris that might clog the openings.

Continuous ink jets provide very high drop rates. A recent example (Morita, 1989) produces drops at 230 kHz for each nozzle. Many systems use multiple nozzles. For example, Morita reports a printer with a full-width nozzle array, capable of producing color output with 120 dot/cm

resolution at 1.5 pages/s. Table 2 compares some of the basic performance and properties of the two major ink jet technologies.

E. Ionography and Electrography

Common to each of the electrostatic printing technologies is the process of transferring charge to a surface in an imagewise fashion to make an image. In laser or LED printers, charge is uniformly deposited onto the surface of the photoreceptor, and the exposure system writes the image. In ink jet printing, droplets are charged and electrostatically deflected to form the image. Two other techniques for creating an electrostatic latent image, ionography and electrography, rely on different means to transfer charge to write the image.

1. Ionography

Corona ions can be used to write an image directly on an insulating surface (Swatik, 1973; Schein, 1992) using a gating electrode as illustrated in Fig. 5. Ions are generated by air ionization in a variety of geometries. Illustrated is a conceptual pin or needle ion source. Other, more efficient, geometries are used commercially (Rumsey and Bennewitz, 1986). The flow of ions is controlled by a gating electrode. When the gating voltage is positive, ions are accelerated through the aperture toward the dielectric layer. When the gating voltage is negative, the flow of ions is stopped.

Ionographic printing by a linear array of apertures is analogous to an LED printer. One advantage over laser or LED printers is that ionography

Table 2

Characteristic	Drop-on-demand	Continuous
Steady applied pressure	Low (≈100 Pa)	High (≈200 kPa)
Transient control	Fast, large, pressure pulse	Adjustment of charging electrode
Spot rate per orifice	Typically 5 kHz or less	Typically more than 100 kHz
Orifice diameter	Determines printer resolution. 50 to 100 μm range is typical	Determines resolution and characteristic speed. 35 μm is typical
Ink concerns	Orifice protection when idle	Orifice protection and recycling of unused drops
Application trends	Low- to moderate-speed color printers	High-speed industrial marking systems or printers for mass mailing

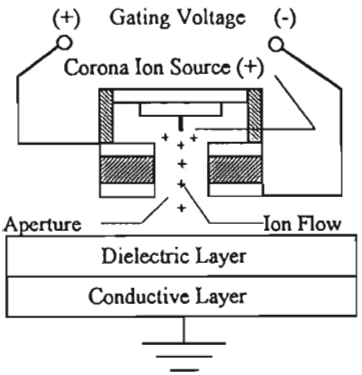


Figure 5 A stream of ions can be controlled to write an image on the surface of a dielectric layer.

does not require a photoreceptor. High-resolution printing requires a small printing aperture. High speed printing requires high ion output (ion current). This inherent trade-off between print quality (i.e., aperture size) and speed has limited the commercialization of ionographic printers.

2. Electrography

Air breakdown at the tip of a metal stylus can be used to write images (Swatik, 1977; Schaffert, 1980), as illustrated in Fig. 6. Ion are generated by air ionization at the tip of the metal stylus when V_{write} exceeds the Paschen breakdown voltage—about 320 volts in air. Charge is deposited on the surface of the dielectric layer forming the electrostatic latent image.

Images are written by gating V_{write} between low voltage (off—no ionization) and high voltage. Electrographic printing using a linear array of styli

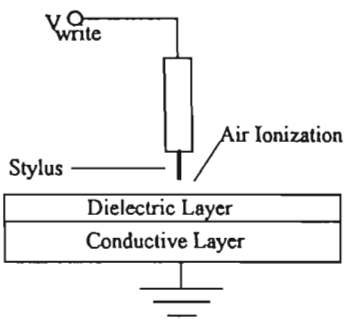


Figure 6 Electrography or electrostatic stylus printing.

is analogous to LED printing. As in ionography, the photoreceptor is not needed. High resolution printing requires that the styli be very small and spaced closely together. The minimum effective spacing between styli is limited by the thickness of the dielectric layer. Ions must be deposited on the dielectric layer to make the image. A neighboring stylus that is too close would attract some ions, leaving fewer available for writing. Printing resolution and reliability have limited commercialization of electrography.

II. BASIC PHYSICS OF OPERATION

A. Lasers and LED Electrophotographic Printers

Laser and LED printers have much in common with xerographic copiers. Their complex exposure system (Williams, 1984) and lesser demands on photoreceptor sensitivity distinguish laser and LED printers from copiers. Since lasers and LEDs are nearly monochromatic, photoreceptors designed for printers can be simpler than those in copiers, where panchromatic photosensitivity is needed. The technical literature on photoreceptors is extensive (Borsenberger and Weiss, 1993). The simple analysis here illustrates five basic performance criteria of photoreceptors summarized in Table 3.

1. Charging to the Initial Voltage (Charge Acceptance)

Initial voltage V_0 is determined by the capacitance per unit area C and the surface charge density Q_{surface}:

$$V_0 = \frac{Q_{\text{surface}}}{C} = \frac{Q_{\text{surface}} d}{k\epsilon_0} \tag{2}$$

where d is the photoconductor thickness, k is the dielectric constant, and ϵ_0 is the permittivity of free space. A corona ionizer is typically used to charge the photoreceptor to an initial voltage of several hundred volts. For example, assuming a 20 μm thick photoreceptor with a dielectric constant of 3, a corona ionizer must be able to deposit a surface charge density of

$$Q_{\text{surface}} = CV_0 = \frac{k\epsilon_0 V_0}{d} = \frac{3(8.85e^{-12}\text{F/m})(500\text{V})}{20\mu\text{m}} \approx 660\ \frac{\mu\text{C}}{\text{m}^2} \tag{3}$$

to reach an initial voltage of 500 volts. If the charger is not capable of depositing this much charge, the photoconductive layer could be made thicker.

Equation 2 is an upper limit on the voltage, assuming that the photoconductive layer has no volume charge density. Volume charge is typically

Table 3

Five basic photoreceptor performance criteria
1. Charging to the initial voltage (charge acceptance)
2. Dark decay (dark discharge)
3. Image formation time (photoinduced discharge)
4. Image stability (lateral conductivity)
5. Residual image (trapped charge)

present (Borsenberger and Weiss, 1993); it reduces the voltage and places additional demands on the charger.

2. Dark Decay (Dark Discharge)

Once the photoreceptor receives the initial uniform charge, it is critical for this charge to remain essentially constant during the printing cycle. Dark discharge is typically dominated by thermally generated charge carriers—free electron-hole pairs in the bulk, and charge injection from either the free surface or the interface with the conductive layer. Mobilities are sufficiently high to sweep quickly the charge from the bulk. The dark decay time is characterized by the depletion time $\tau_{\text{depletion}}$—the time when the thermally generated bulk space charge is equal to one-half of the initial surface charge Q_{surface}. Assuming that typical print cycles are characterized by times on the order of seconds, the depletion time must be much longer than 1 second:

$$\tau_{\text{depletion}} = \left(\frac{k\epsilon_0 V_0}{ad^2}\right)^{1/p} \gg T_{\text{cycle}} \approx 1 \text{ s} \tag{4}$$

where k is the relative dielectric constant, V_0 is the initial voltage, d is the photoconductive layer thickness, a is an empirical constant characterizing the material, and $p \leq 1$ is also an empirical constant (Borsenberger and Weiss, 1993). For example, the thickness of a photoreceptor needed to achieve a depletion time $\tau_{\text{depletion}}$ of 1 s assuming that the initial voltage V_0 is 500 volts using a material with a dielectric constant of 3 characterized by

$$p = 1[\text{dimensionless}] \qquad a = 30 \frac{\text{C}}{\text{m}^3 - \text{s}} \tag{5}$$

is

$$d = \sqrt{\frac{k\epsilon_0 V_0}{a\tau^p_{\text{depletion}}}} = \sqrt{\frac{(3)(8.85e^{-12}\text{F/m})(500\text{V})}{(30\text{C}/(\text{m}^3 - \text{s}))(1\text{s})^1}} = 21 \ \mu\text{m} \tag{6}$$

Dark decay may be reduced by making the photoreceptor thinner and, from Eq. 2, charge acceptance is improved by making the photoreceptor thicker. This is one of many design constraints in photoreceptor development and design.

3. Image Formation Time (Photoinduced Discharge)

Once the charged photoreceptor is exposed, the latent image must form before the image can be rendered visible by the development subsystem. Typically, the exposure time for any point on the photoreceptor is short compared with the transit time of charge carriers, so that the discharge is emission limited. The electrostatic latent image forms in a time characterized by the transit time τ_{Transit} of the mobile charge carriers created by exposure:

$$\tau_{\text{Transit}} = \frac{d^2}{\mu V_0} \tag{7}$$

where d is the photoconductor thickness illustrated in Fig. 3, μ is the mobility, and V_0 is the initial voltage. Assume that typical print cycles are characterized by times on the order of a second and that the time between exposure and development is a fraction of a cycle. From Eq. 7, the maximum thickness for the candidate photoreceptor with a mobility of $\mu = 10^{-6}$ cm^2/V $-$ s, charged to an initial voltage V_0 of 500 volts to achieve a 100 ms discharge time is

$$d = \sqrt{\mu V_0 \tau_{\text{Transit}}} = \sqrt{\left(10^{-6}\,\frac{\text{cm}^2}{\text{V} - \text{s}}\right)(500\ \text{V})(0.1\ \text{s})} \approx 70\ \mu\text{m} \tag{8}$$

Equations 7 and 8 assume that the mobility is constant and independent of the electric field. In reality, mobilities are field dependent, and more complete models take this into account (Borsenberger and Weiss, 1993). Nonetheless, the image formation time typically does not seriously constrain system performance.

The data throughput rate (see Example 1) places demands on the exposure system and photoreceptor. Dots are generated by modulating the light source (see Example 2). Sufficient light energy must illuminate the photoreceptor to provide sufficient photoinduced discharge. For example, at 240 dots/cm and 19.2 Mbit/s, each 42 μm diameter dot must be written within about 50 ns. This is a flash exposure, since the exposure time is very short compared with the charge carrier transit time. The discharge voltage as a function of exposure for flash exposure is (Borsenberger and Weiss, 1993)

$$V(\mathscr{E}) = V_0\left(1 - \frac{q_e \eta_0 \mathscr{E} d}{k \epsilon_0 V_0}\right) \tag{9}$$

where q_e is the electronic charge, η_0 is the photogeneration efficiency (number of charge carriers per absorbed photon), $\mathscr{E}$ is the exposure in photons per cm^2, d is the photoconductor thickness, k is the dielectric constant, ϵ_0 is the permittivity of free space, and V_0 is the initial voltage. For example, the exposure needed to discharge the photoreceptor to half of the initial voltage is

$$\mathscr{E} = \frac{k\epsilon_0 V_0}{q_e \eta_0 d}\left(1 - \frac{V(\mathscr{E})}{V_0}\right) = \frac{3(8.85e^{-12}\ \text{F/m})(500\ \text{V})}{(1.6e^{-19}\text{C})(1.0)(20\ \mu\text{m})}\left(1 - \frac{250}{500}\right)$$

$$\approx 2e^{+15}\frac{\text{photons}}{\text{m}^2} = 2e^{+11}\frac{\text{photons}}{\text{cm}^2} \tag{10}$$

This exposure can be written in terms of absorbed energy using the energy per photon:

$$E = \mathscr{E}\left(\frac{hc}{\lambda}\right) \approx \left(2e^{+15}\frac{\text{photons}}{\text{m}^2}\right)\left(\frac{(6.6e^{-34}\text{J} - \text{s})(3e^{+8}\text{m/s})}{500\ \text{nm}}\right)$$

$$\approx 8e^{-4}\frac{\text{J}}{\text{m}^2} = 0.8\frac{\text{erg}}{\text{cm}^2} \tag{11}$$

Ideally, each 42 μm diameter dot in the image requires about 1.4 pJ of absorbed light energy with a power of about 30 μW. Three idealizations are inherent in Eqs. 9, 10, and 11:

1. The mobility of charge carriers is independent of the electric field.
2. The photogeneration efficiency, the number of charge carriers produced per absorbed photon, is 1.0.
3. All incident light is absorbed.

Practically, lasers with a rated power of 3 to 30 mW are typically used (Schein, 1992).

4. Image Stability (Surface Conductivity)

Once the imagewise charge pattern exists on the photoreceptor surface, it must remain substantially unaltered for a time on the order of the printer cycle time. Moisture and other contaminants on the photoreceptor surface contribute to conductivity resulting in image blur. For the geometry of a dielectric layer on a ground plane, the charge relaxation time τ depends on the spatial wavelength λ charge pattern (Robinson, 1986):

$$\tau = \frac{\epsilon_0 \lambda}{\pi\sigma_s}\left(1 + \frac{k\lambda}{\pi d}\right) \gg \tau_{\text{cycle}} \approx 1\ \text{s} \tag{12}$$

where σ_s is the surface conductivity, k is the dielectric constant, and d is the layer thickness. Charge relaxation is faster for higher surface conductivity σ_s, shorter spatial wavelength λ (finer detail), and thicker photoreceptors. The shortest spatial wavelength is approximately twice the spot diameter for the gray scale shown in Fig. 1. Assuming a 240 dot per cm resolution and a 20 μm photoconductor thickness, the surface conductivity must be

$$\sigma_s = \frac{\epsilon_0 \lambda}{\pi \tau}\left(1 + \frac{k\lambda}{\pi d}\right)$$
$$= \frac{(8.85e^{-12}\text{F/m})(83\ \mu\text{m})}{\pi(1.0\text{s})}\left(1 + \frac{3(83\ \mu\text{m})}{\pi(20\ \mu\text{m})}\right) \approx 1.2e^{-15}\text{S} - \square \tag{13}$$

(surface resistivity must exceed about 9×10^{14} ohm/□) to avoid image blur due to lateral conductivity.

5. Residual Image

The idealized photoreceptor illustrated in Fig. 3 shows the charges on the surface of the photoconductive layer. If both the photogenerated electrons and holes were mobile, all charges would relax to the surfaces of the photoreceptor. In reality, charge is trapped in the bulk of the photoconductive layer, resulting in an undesirable residual voltage that cannot be discharged by exposure to light. Assuming that incident light is strongly absorbed and that trapped charge is confined to a thin layer thickness x_0 near the surface of the photoconductor, the residual voltage is

$$V_{\text{residual}} = \frac{n_{\text{trapped}}\, q_e x_0^2}{2k\epsilon_0} \tag{14}$$

For example, to keep the residual voltage less than 20 V, the number density of trapped charge confined to a thin 5 μm layer is

$$n_{\text{trapped}} = \frac{2k\epsilon_0 V_{\text{residual}}}{q_e x_0^2}$$
$$= \frac{2(3)(8.85e^{-12}\ \text{F/m})(20\ \text{V})}{(1.6e^{-19}\text{C})(5\ \mu\text{m})^2} \approx 2.7e^{+20}\text{m}^{-3} = 2.7e^{+14}\text{cm}^{-3} \tag{15}$$

B. Ink Jet

Since the continuous method is the most important commercial electrostatic ink jet process, it will serve as the focus for the physical discussion. Here we discuss the important effects in the various process steps. Figure 7 provides a geometric framework.

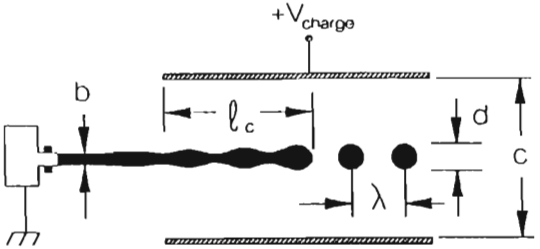


Figure 7 Continuous ink jet geometry.

1. The Jet and Its Breakup

The objective is to produce a stable stream of fine drops. The drop rate should be as high as possible, given a useful spot size. Drops should be spaced sufficiently to avoid drop-to-drop interactions. A linearized perturbation analysis (Lee, 1974) shows that, when a jet breaks into drops under resonant conditions, the jet surface wavelength λ (i.e., the drop separation) will be approximately 4.5 times the jet diameter. By equating the fluid volume in the jet cylinder of length λ with the volume in the drop, the drop diameter d can be found in terms of the orifice diameter b as

$$\pi\left(\frac{b}{2}\right)^2 \lambda = \frac{4}{3}\pi\left(\frac{d}{2}\right)^2 \qquad \lambda = 4.5b \qquad d = 1.89b \tag{16}$$

If the spot size at the paper target is to be less than 100 μm in diameter, the orifice diameter must be less than about 50 μm (not accounting for ink spread once the drop strikes the paper).

The orifice size is also constrained by speed. The jet must have time to break up in a controlled manner, and the droplets themselves must be in a stable state before they reach the target. Lee (1974) shows that the time required for jet breakup when $\lambda = 4.5b$ is

$$t_{\text{breakup}} = \sqrt{\frac{\rho b^3}{\gamma}} \cosh^{-1}\left(1 + \frac{\gamma}{b\,\Delta p}\right) \tag{17}$$

where γ is the surface tension, ρ is the mass density, and Δp is the disturbance pressure. For water from a 35 μm orifice, with $\Delta p \approx 100$ Pa, the time is 92 μs. If drops are formed every 10 μs, as is typical, a formation time of 92 μs gives plenty of room for the jet to emerge and break up. If the orifice is much larger than this, the jet will not have time to form

before reaching the target. Bogy (1979) presents a more detailed analysis of the breakup dynamics.

Another important aspect of jet breakup is the formation of small satellite droplets. It is known that satellite formation cannot be predicted with a linearized theory (Pimbley and Lee, 1977). Often, even if satellites form, their velocity will differ from that of the main drops enough so that the drops coalesce before striking the target. Of special concern is the infinite satellite condition, in which satellite velocities match those of the main drops, and the satellites will reach the target. Figure 8 shows experimentally determined operating regimes for a water-based jet. The usual objective is to avoid satellite formation completely (it will affect drop charging even if satellites coalesce). More recently (Tokunaga et al., 1984; Morita, 1989), attempts have been made to generate satellites deliberately and use these tiny droplets for printing. In this case, the infinite satellite boundary would be of interest. Extreme resolutions are possible with satellite techniques, although almost all the jetted ink must be recirculated.

For best operation, the jet velocity should allow matching of the optimum wavelength. One wavelength must flow through the orifice for each drop. If the time between drops is to be t_{drop}, the jet velocity U must be

$$U = \frac{\lambda}{t_{drop}} = \frac{4.5b}{t_{drop}} \tag{18}$$

For $t_{drop} = 10$ μs and $b = 35$ μm, this gives a velocity of 15.75 m/s. Considerable pressure must be exerted to force liquid through a small opening with this velocity. Morita (1989) quotes a static pressure of 470 kPa (4.8 kg/cm^2).

2. Drop Charging

Figure 7 shows a side view of a cylindrical charging arrangement. In a printer, the charger must surround the jet breakup region. The electrode induces a potential difference between the jet tip and the nozzle, and charge will flow to the end of the jet. As a drop breaks off, the charge is retained on the free drop. The electrode voltage is adjusted rapidly, so as to control the charge on each and every drop as it forms. Two critical parameters in this process are the time required to charge the jet tip and the charge per unit area induced on each drop. In many printers, only every second or third drop is given a charge. Uncharged drops in effect shield those with charge. This minimizes interaction between drops and ensures that the deflection field will dominate motion later on.

Charging time is governed by an RC time constant between the capacitive structure of the charger and the resistive liquid. Mechanical transport of charge also takes place because of fluid motion. The relative importance

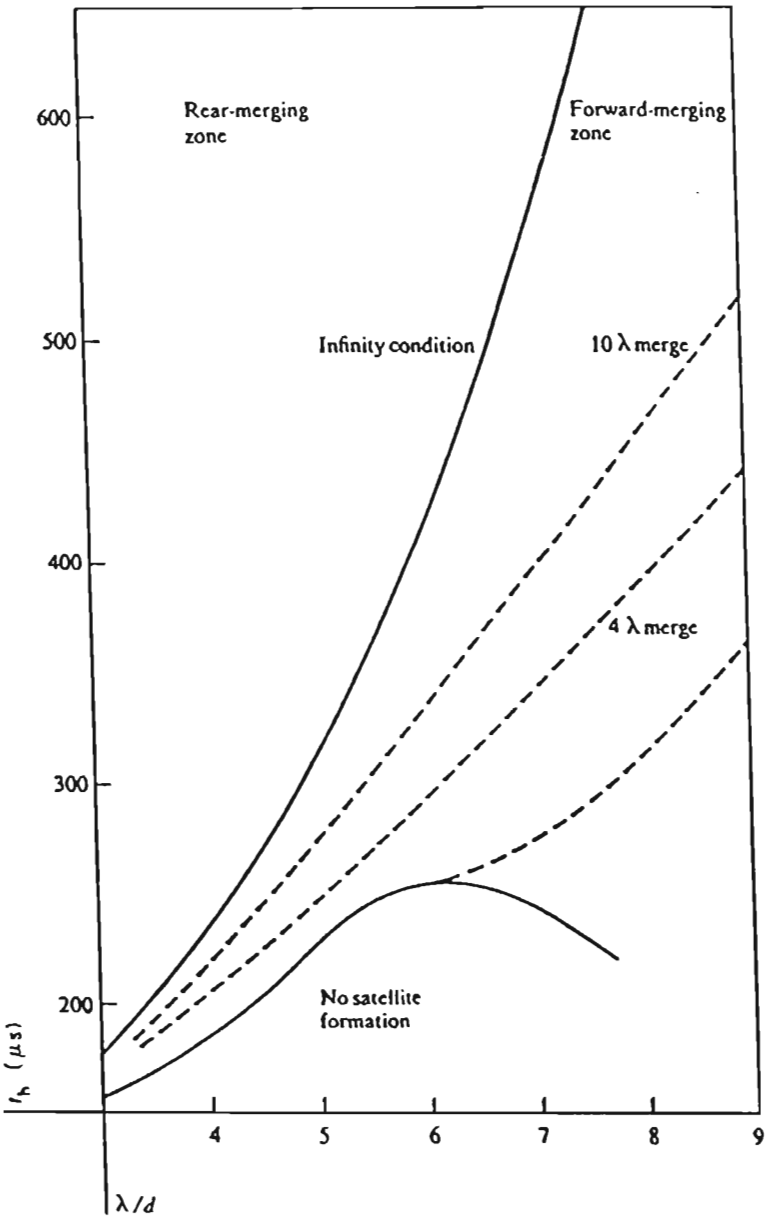


Figure 8 Satellite formation regimes. (From Pimbley and Lee, 1977, copyright 1977 by International Business Machines Corporation, reprinted with permission.)

of electrical and mechanical rates can be represented with the electric Reynolds number Re_e, the ratio

$$Re_e = \frac{\tau_{elec}}{\tau_{mech}} = \frac{\epsilon U}{\sigma l} \tag{19}$$

For the drop breakoff region, the ink's electrical permittivity ϵ and conductivity σ determine τ_{elec}. The velocity is U, and the characteristic length l corresponds to the jet diameter. For the charger, the electrical rate is the RC product of the electrode capacitance and the jet resistance. In a continuous jet, Re_e should be small, so that the electrical effects are very fast. If $Re_e \ll 1$, the charging process can be controlled rapidly, independent of velocity or jet variations. In a drop-on-demand system, Re_e would normally be of order 1 to create strong interaction between electrical forces and mechanical motion.

The shape of a spherical drop is, of course, maintained by surface tension. Charge on the drop surface will produce a mutual repulsion that offsets surface tension. If too much charge is imposed, the drop will be disrupted into small droplets. This balance between surface tension and surface charge density is the basis of the Rayleigh limit (Hendricks and Schneider, 1963)

$$q \leq \sqrt{8\gamma\epsilon_0\pi^2 d^3} \tag{20}$$

where γ is the surface tension of the liquid. The charging process in a continuous jet must stay below the Rayleigh limit. For a water drop 100 μm in diameter, the limit is 7.1 pC.

The drop charging process itself has been described by several authors (Sweet, 1965; Fillmore et al., 1977; Hendricks, 1973). A simple approach is to model Fig. 7 as a coaxial capacitor. The capacitance of the structure per unit length is

$$\frac{C}{l} = \frac{2\pi\epsilon_0}{\ln(c/b)} \tag{21}$$

where ϵ_0 is the permittivity of the air gap and c is the diameter of the electrode cylinder. If the interaction length between the jet and the electrode, l_c, is greater than λ, each drop will carry a charge $q = (C/l)\lambda V_{charge}$, where V_{charge} is the electrode voltage. When the optimum spacing $\lambda = 4.5b$ is used,

$$q_{drop} = \frac{9V_{charge}\pi\epsilon_0 b}{\ln(c/b)} = \frac{4.75V_{charge}\pi\epsilon_0 d}{\ln(c/b)} \tag{22}$$

The charging voltage is constrained by dielectric breakdown in the air gap to keep the electric field below about 3 MV/m. This requires

$$V < (3 \times 10^6 \text{ V/m}) b \ln (c/b) \tag{23}$$

For a ratio $c/b = 10$, and $b = 50$ μm, the voltage limit will be 345 V. Consider drops 100 μm in diameter. The charge per drop will be $(5.74 \times 10^{-15}$ F)(345 V) = 1.98 pC. In this case, the field breakdown limit is reached before the Rayleigh limit. For better accuracy, the capacitance between adjacent drops needs to be included as well. Detail is provided by Crowley (1986) and by Pimbley and Lee (1977). For deflection, the charge-to-mass ratio is of merit:

$$\frac{q_{\text{drop}}}{m_{\text{drop}}} = \frac{28.5 V_{\text{charge}} \epsilon_0}{d^2 \rho \ln(c/b)} \tag{24}$$

In the case of a 100 μm water drop with 1.98 pC of charge, the charge-to-mass ratio is 3.78 mC/kg.

3. Drop Deflection

The drop charging process induces a controlled charge, dependent on the desired location at the target. The drops are then deflected in a static electric field. The acceleration in the intended direction can be found from the force on a small charged object, $F = qE$, where q is the charge and E is the electric field vector. Force per unit mass gives the acceleration:

$$a_{\text{drop}} = \frac{28.5 V_{\text{charge}} \epsilon_0}{d^2 \rho \ln(c/b)} E_{\text{deflection}} \tag{25}$$

For the 100 μm water drop with 1.98 pC of charge, a strong field of 3 MV/m would produce acceleration of more than 11,000 m/s^2! Effects of gravity will be negligible compared to this, so that orientation of the ink jet system should not affect performance. Notice that, if the jet formation and breakup process does not vary over time, Eq. 25 consists of a few geometric parameters and two control inputs. This simplicity, combined with the separate charging and deflection control, is a major advantage of ink jet technology.

III. SOLVENT PROPERTIES

Table 4 shows the properties of some solvents for ink jet systems.

Table 4 Properties of Some Solvents for Ink Jet Systems

Liquid	(kg/m^3) Mass density	(Pa·s) Viscosity	(N/m) Surface tension	Dielectric constant
Water	1000	0.0010	0.072	80.0
Methanol	796	0.00055	0.022	31.2
Ethanol	794	0.0012	0.022	25.8
t-Butanol	787	0.0029	0.021	17.7
Ethylene glycol	1116	0.0162	0.048	41.2
Glycerol	1260	0.9500	0.059	15.3

Source: Wright et al., 1993.

IV. WORKED EXAMPLES

A. Ink Drop Charging

A continuous ink jet system uses an ethanol-based ink and nozzle diameter of 40 μm. The charging electrode is a cylinder 250 μm in diameter, spaced so that jet breakup takes place within it. The charger voltage is 50 V, maximum. What is the highest induced charge possible? Assume conductive ink.

If the breakup process is near its optimum, the wavelength λ will be 180 μm. Drop size will be 76 μm. The capacitance of the electrode over one wavelength will be $2\pi\epsilon_0/\ln(6.25) = 5.5$ fF. Maximum drop charge is expected to be just under 275 fC. The Rayleigh limit for the drop should be $\sqrt{6.99 \times 10^{-10}\gamma d^3} = 2.6$ pC. The maximum is almost a factor of ten below this limit.

B. Deflection Electrode Spacing

A continuous ink jet system is to be built with a full-width array of nozzles for very fast printing. The emerging droplets are expected to be 100 μm in diameter. Cylindrical charging electrodes 200 μm in diameter are proposed. Find the maximum charging electrode voltage to avoid air breakdown. Then estimate how far apart adjacent charging electrodes must be to avoid breakdown between them.

The maximum field is limited by air breakdown to about 3 MV/m. If the drops are 100 μm in diameter, then the jet must be about 53 μm in diameter. The voltage limit from Eq. 23 is $(3 \times 10^6)(53\ \mu m)\ \ln(200/53)$

= 211 V. The electrode-to-electrode field can be estimated based on a parallel line geometry. The electric field between parallel cylinders (Johnk, 1975, p. 536) is maximum at the surface of the cylinder at the point where the two electrodes are closest. At that location, the field strength is

$$|E| = \frac{V}{2 \ln[(h + \sqrt{h^2 - R^2})/R]} \cdot \left[\frac{1}{h - R - \sqrt{h^2 - R^2}} - \frac{1}{h - R + \sqrt{h^2 - R^2}}\right] \tag{26}$$

where $2h$ is the electrode center-to-center spacing and R is the electrode radius. To keep $|E| < 3$ MV/m when V = 211 V, we need center-to-center spacing $2h > 280$ μm (found by iterative solution of Eq. 26).

REFERENCES

Ashley, C. T., K. E. Edds, and D. L. Elbert (1977). Development and characterization of ink for an electrostatic ink jet printer. *IBM J. Research Devel.*, 21, 69–74.

Bogy, D. B. (1979). Drop formation in a circular liquid jet. *Ann. Rev. Fluid Mech.*, 11, 207–228.

Borsenberger, P. M., and D. S. Weiss (1993). *Organic Photoreceptors for Imaging Systems*. Marcel Dekker, New York.

Buehner, W. L., J. D. Hill, T. H. Williams, and J. W. Woods (1977). Application of ink jet technology to a word processing output printer. *IBM J. Research Develop.*, 21(1), 2–9.

Carnahan, R. D., and S. L. Hou (1977). Ink jet technology. *IEEE Trans. Industry Applications*, IA-13(1), 95–105.

Crowley, J. M. (1986). *Fundamentals of Applied Electrostatics*. John Wiley, New York.

Doane, T. G. (1981). A review of ink-jet printing. *J. App. Photo. Eng.*, 7, 121–125.

Fillmore, G. L., W. L. Buehner, and D. L. West (1977). Drop charging and deflection in an electrostatic ink jet printer. *IBM J. Research Devel.*, 21, 37–47.

Graham, C. H., ed. (1965). *Vision and Visual Perception*. John Wiley, New York, p. 69.

Hendricks, C. D. (1973). Charging macroscopic particles. In *Electrostatics and Its Applications* (A. D. Moore, ed.). John Wiley, New York, pp. 72–73.

Hendricks, C. D., and J. M. Schneider (1963). Stability of a conducting droplet under the influence of surface tension and electrostatic forces. *Amer. J. Phys.*, 31, 450–453.

Hertz, C. H., and B. A. Samuelsson (1989). Ink jet printing of high quality color images. *J. Imaging Tech.*, 15(3), 141–148.

Johnk, C. T. A. (1975). *Engineering Electromagnetic Fields and Waves*. John Wiley, New York, p. 536.

Lee, H. C. (1974). Drop formation in a liquid jet. *IBM J. Research Devel.*, 18, 364–369.

Lowry, E. M., and J. J. DePalma (1961). Sine-wave response of the visual system. *J. Opt. Soc. Amer.*, 51, 740–746.

Miura, M., and H. Naito (1984). Ink jet printing head utilizing air flow and electrostatic field. Proc. 2nd Cong. Advances in Non-Impact Printing, Arlington, pp. 154–156.

Morita, N. (1989). Multinozzle drop generator for continuous ink jet printing. *Electronics Communications in Japan*, Part 2, 72(7), 78–85.

Murch, G., and N. Weiman (1991). Gray-scale sensitivity of the human eye for different spatial frequencies and display luminance levels. *Proc. SID*, 32(1), 13–17.

Nathans, J. (1989). The genes for color vision. *Sci. American*, 260(2), 42–49.

Oda, G., and M. Miura (1992). The fundamental printing characteristics of a new electrostatic ink jet head. Proc. 8th Int'l. Cng. on Advances in Non-Impact Printing Tech., Williamsburg, pp. 343–345.

Pimbley, W. T., and H. C. Lee (1977). Satellite droplet formation in a liquid jet. *IBM J. Research Devel.*, 21, 21–30.

Robinson K. S. (1987). Unpublished data.

Robinson, K. S., R. J. Turnbull, and K. Kim (1980). Electrostatic spraying of liquid insulators. *IEEE Trans. Indus. Applications*, IA-16, 308–317.

Rumsey, J. R., and D. Bennewitz (1986). Ion Printing Technology. *J. of Imaging Tech.*, 12(3), 144–151.

Schaffert, R. M. (1980). *Electrophotography*. Focal/Hastings House, New York.

Schein, L. B. (1992). *Electrophotography and Development Physics*. Springer-Verlag, New York.

Swatik, D. S. (1973). Nonimpact printing. In *Electrostatics and Its Applications* (A. D. Moore, ed.). John Wiley, New York.

Sweet, R. G. (1965). High frequency recording with electrostatically deflected ink jets. *Rev. Sci. Instrum.*, 36(2), 131–136.

Tokunaga, K., T. Doi, M. Tobita, T. Yamada, and Y. Matsuda (1984). Full color printers with microdot (ink jet) technology. Proc. 2nd Cong. Advances in Non-Impact Printing, Arlington, pp. 163–164.

Ulichney, R. (1987). *Digital Halftoning*. MIT Press, Cambridge, Massachusetts.

Williams, E. M. (1984). *The Physics and Technology of Xerographic Processes*. John Wiley, New York.

Winston, C. H. (1962). Method of and apparatus for transferring ink. U.S. Patent 3,060,429.

Woodson, H. H., and J. R. Melcher (1968). *Electromechanical Dynamics*. John Wiley, New York.

Wright, G. S., P. T. Krein, and J. C. Chato (1993). Factors affecting dynamic manipulation of menisci. *IEEE Trans. Industry Applications*, 29(1), 103–112.

Zoltan, S. (1972). Pulsed droplet ejecting system. U.S. Patent 3,683,212.

15

Electrophotography

L. B. Schein

IBM Research Division
San Jose, California

I. INTRODUCTION

Copiers and laser printers, which use the electrophotographic technology, represent one of the most successful commercial applications of electrostatic phenomena. These devices, unknown to the general public before 1959, have become indispensable office equipment today. The design, manufacturing, and sales of electrophotographic equipment involves many of the world's largest corporations with total annual revenues approaching $50 billion worldwide.

The six process steps required in any electrophotographic device are easily understood (Schein, 1992) and are shown schematically in Fig. 1. They are

1. Charge — A corona discharge, caused by air breakdown, uniformly charges the surface of the photoreceptor, which, in the absence of light, is an insulator.
2. Expose — Light, reflected from a document (in a copier) or produced by a laser (in a printer), discharges the normally insulating photoreceptor, producing a latent image, i.e., a charge pattern on the photoreceptor that mirrors the information to be transformed into the real image.

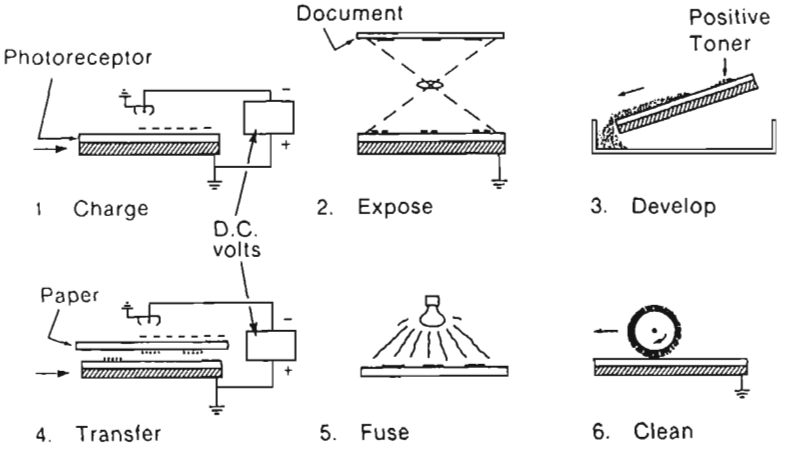


Figure 1 Schematic diagram of the six steps of the electrophotographic process: charge, expose, develop, transfer, fuse, and clean.

3. Develop	Electrostatically charged and pigmented polymer particles called toner, ≈10 μm in diameter, are brought into the vicinity of the latent image. By virtue of the electric field created by the charges on the photoreceptor, the toner particles adhere to the latent image, transforming it into a real image.
4. Transfer	The developed toner on the photoreceptor is transferred to paper by an electric field created by corona charging the back of the paper with a charge opposite to that of the toner particles.
5. Fuse	The image is permanently fixed to the paper by melting the toner into the paper surface.
6. Clean	The photoreceptor is discharged and cleaned of any excess toner using coronas, lamps, brushes and/or scraper blades.

This process involves a myriad of physical, chemical, and engineering challenges. For example, the corona discharge involves gas discharge phenomena. The gas discharge creates chemically active molecules that can destroy the photoreceptor surface. Furthermore, keeping the corona wire free of toner contamination is required to eliminate nonuniform charging, which can lead to streaks in the process direction in the copy. Another

example: during the expose step, light photogenerates charge carriers in the photoreceptor, which then must move through this normally highly insulating material without being trapped (or ghost images will be created in the copy). The physics of photogeneration and charge transport phenomena in photoconducting materials remains an active area of research. The choice of photoconducting materials continues to keep armies of chemists busy. And engineers must decide whether the photoreceptor should be in the form of a drum or a belt, based on the overall architecture of the copying or printing device. A third example: powder toner particles must be selected to charge correctly, fuse readily to the paper, not stick below fuse temperatures, flow properly, and yet not contaminate parts in the copier or printer. Many more examples of such physical, chemical, and engineering challenges are easily identified.

Electrostatic phenomena contribute to almost all of the process steps shown in Fig. 1. Discussed in detail in the remainder of this chapter are four key roles of electrostatics in electrophotography:

1. As already mentioned, corona charging resulting from a gas discharge is used in both charge and transfer steps.
2. During exposure, a charge pattern is created on the photoreceptor surface that mirrors the information to be transformed into a real image. Charged toner particles only respond to electric fields in air above the photoreceptor. Therefore the actual driving force for the development of toner is the electric fields immediately above the photoreceptor due the charge pattern on the insulating, photoreceptor surface. Calculation of these electric fields is a classic problem in electrostatics.
3. The toner particles, which are polymeric insulators, must be charged so that the electric fields of latent images can attract them. The explanation of the physics of insulator charging remains on the forefront of science.
4. During development, the charged toner particles are attracted to the latent image. Electrostatic phenomena determine the amount of toner that develops and therefore are at the very heart of the electrophotographic process, determining the best image quality that can be produced by electrophotography.

Other electrostatic phenomena also are important in the electrophotographic process. For example, during both transfer and clean the electrostatic force of adhesion of toner particles to the photoreceptor must be overcome. After fuse, the paper must be discharged, especially at low relative humidity. The interested reader is referred to the literature (Schein, 1992; Schaffert, 1980).

II. CHARGING

During the charge and transfer steps, the photoreceptor and the back of the paper are uniformly charged by extracting ions from an air breakdown. The air is caused to break down electrostatically by applying a high potential to a thin wire, creating a gas discharge, as discussed in detail in Chapter 9.

The voltage necessary to create the ionized air is determined (Cobine, 1958) by the electric field required to accelerate electrons to sufficient velocities to ionize air molecules (Paschen's breakdown), and by the distance from the wire at which the average electric field equals the Paschen sparking breakdown voltage. This voltage depends primarily on the wire diameter. Typically, a 50 μm diameter wire spaced 1 cm from the ground plane, operating at a potential of 8000 V, is sufficient to charge a photoreceptor moving at a speed of 5 cm/s (Vyverberg, 1965).

A device used to place this charge on the photoreceptor, called a corotron (Vyverberg, 1965), is shown in Fig. 2(a). Ions of the same polarity as the wire will be swept by the electric field toward the photoreceptor (and the shield). While the shield current is a source of inefficiency, it provides stability to the corona by forcing the operating condition to be far from threshold. The nature of the ionized molecules resulting from the corona discharge has been shown (Shahin, 1971) to be primarily CO_3^- and $(H_2O)_nH^+$ with $n = 4$ to 8.

The corona, as the discharge is called (Vyverberg, 1965; Cobine, 1958), appears as a uniform blue-white sheath around the wire for a positive polarity; for a negative wire there are glowing bluish points spaced at regular intervals along the wire. These nonuniformities are due to current avalanches caused by the slow velocity positive ion cloud as it moves toward the wire (Gallo, 1975, 1977). They represent a significant source of nonuniformity for negative charging. Another important source of nonuniform charging (for both polarities) is wire contamination due to toner and paper dust. To produce more uniform photoreceptor charging, a screen is sometimes added between the corona wire and the photoreceptor to produce a charging device known as a scorotron (Fig. 2(b)). The screen potential determines the approximate maximum potential to which the photoreceptor will be charged (Vyverberg, 1965).

III. ELECTRIC FIELDS OF LATENT IMAGES

Toner particles are attracted to the latent image by the Coulomb force F:

$$F = QE \tag{1}$$

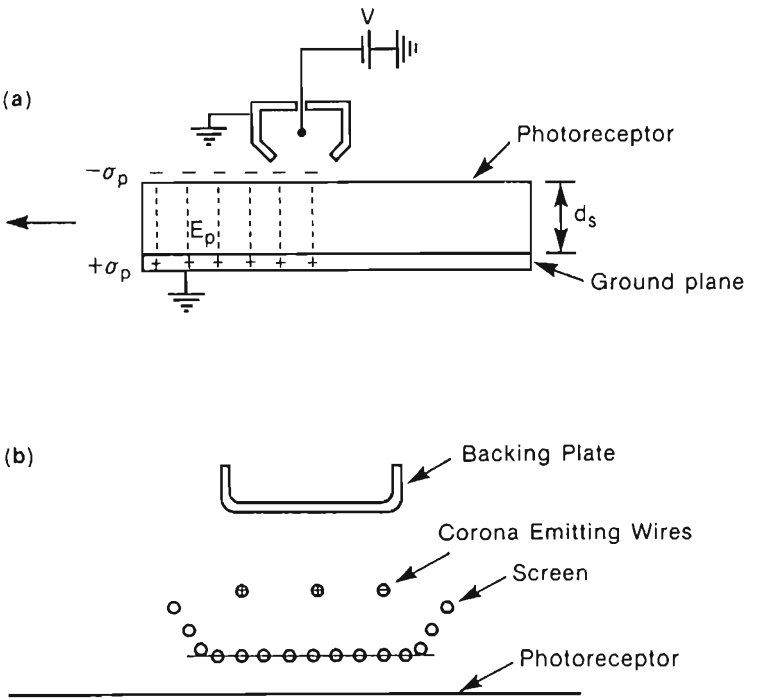


Figure 2 Schematic of devices used for charging a photoreceptor. In (a) a corotron is shown; in (b) a scorotron is shown in which a screen is placed between the corona wires and the photoreceptor. The potential of the screen determines the approximate maximum potential to which the photoreceptor will be charged.

where Q is the charge on the toner particles and E is the electric field associated with the latent image.

The calculation of the electric fields associated with charge patterns on a dielectric (the photoreceptor) is discussed in Chapters 1, 6, and 11 (see also Crowley, 1986). A few examples are given below to allow the reader to became familiar with the electric fields that occur in electrophotography. These examples include the electric field due to the latent images of a solid area, a single line, and parallel lines.

A solid area latent image is a uniformly charged photoreceptor surface. As shown in Fig. 2(a), the counter charges flow into the ground plane under the photoreceptor. Electric field lines connect the uniform charge on the photoreceptor surface and the counter charges in the photoreceptor ground plane, resulting in zero electric field in air above the photoreceptor

surface (far from the edges of the latent image). Therefore solid area latent images will not attract toner (except at edges). To create an electric field above a solid area latent image, a grounded electrode must be added (as part of the development system) that capacitively couples electric field into the air gap above the photoreceptor (Fig. 3). The uniform field E in the air gap above the photoreceptor is then (using Gauss's law)

$$E = \frac{\dfrac{\sigma_p}{\epsilon_0}\dfrac{d_s}{K_s}}{\dfrac{d_s}{K_s} + \dfrac{L}{K_E}} = \frac{V}{\dfrac{d_s}{K_s} + \dfrac{L}{K_E}} \tag{2}$$

where σ_p is charge per unit area associated with the latent image, d_s is the photoreceptor thickness, L is the electrode-photoreceptor distance, K_s and K_E are the photoreceptor and electrode-photoreceptor dielectric constants, respectively, and ϵ_0 is the permittivity of free space. The quantity $\sigma_p d_s/K_s\epsilon_0$ is the electrostatic potential V at the top surface of the photoreceptor with respect to the ground plane on the bottom surface (in the absence of the electrode), which is a useful, measurable parameter. Electric fields internal to the photoreceptor are chosen to be approximately 50% of dielectric breakdown. Typical values for an inorganic photoreceptor are $V = 1000$ volts and $d_s = 60$ μm, giving internal fields of 17 V/μm. For $L = 1200$ μm, $K_E = 6$ (e.g., see below), and $K_s = 6.6$, $E \simeq 5$ V/μm.

The electric fields associated with a line have been studied, and a qualitative understanding is useful for grasping the complicated nature of this problem. Neugebauer (1965) solved the electrostatic problem of a line of charges on a dielectric, i.e., a photoreceptor surface, by means of a series expansion using the method of images. He showed that the electric field

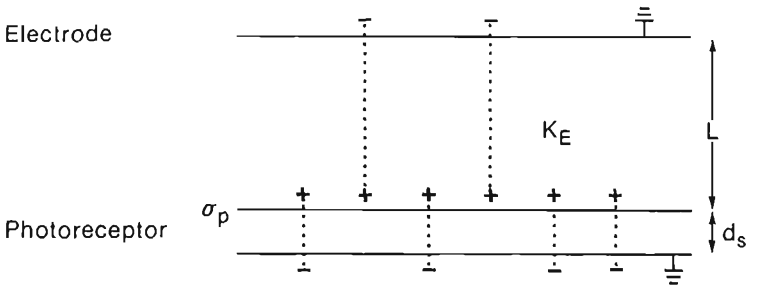


Figure 3 The electric field lines associated with a solid area latent image in the presence of an electrode.

depends on the thickness of the dielectric and the width of the line, and varies rapidly in space above the line. Variations of the perpendicular electric field as a function of distance above a 25 μm thick dielectric with dielectric constant 6.6 (an inorganic photoreceptor based on Se alloys) charged to 1000 V for a line of 10 μm half width are shown in Fig. 4(a). The sensitivity to line width, 1 μm above the photoreceptor surface, is shown in Fig. 4(b). Note the rapid spatial variations of the electric field, and that at large line width, i.e., solid areas, the electric field goes to zero.

An estimate of the ratio of line to solid area toner development can be made by estimating the respective electric fields. If an electrode is added (Fig. 3), a uniform field (Eq. 2) is added to the above fringe fields. This was shown above to be approximately 5 V/μm, slightly less than half the fringe field value shown in Fig. 4(a) (at 1 μm above the photoreceptor surface). These numbers suggest that the electric fields due to lines are approximately twice as strong as the electric fields due to solids, and a 2:1 ratio of line to solid area toner mass per unit area is to be expected.

However, in an actual development system, the electrostatic fields can become considerably more complicated. Some development systems use ≈200 μm diameter polymer coated metal balls to carry the toner to the latent image (Fig. 5). Such balls must maintain an equal potential across their surfaces. This will obviously change the electric field both spatially and with time (as the balls move across the latent image). The value of $K_E = 6$, assumed above, results from a recent experimental and theoretical solution (Schein et al., 1990) to the electrostatic problem of determining the appropriate electric field enhancement as seen by toner particles due to these metal balls. It is just the dielectric constant of a mixture of air ($K = 1$) and metal spheres ($K = \infty$) at high packing fraction (approximately 0.6). Further, as toner develops and neutralizes some of the charges of the latent image, the electric field changes. If that were not complicated enough, it is unclear where in space to evaluate the electric field when calculating toner development. Some workers have evaluated the field at 1 μm above the photoreceptor surface (as done above) or at a toner radius above the photoreceptor, but the correct value probably depends on the development system and the physics of development.

A series of parallel lines ideally would create a square wave charge pattern, but optical system imaging generally adds some rounding to the corners. If the electrostatic latent image can be approximated by the sinusoidal charge pattern

$$\sigma_p = \sigma_0 + \sigma_k \cos ky \tag{3}$$

where k is the spatial frequency, then the electric field can be obtained in closed form using Fourier analysis. In the absence of an electrode, the

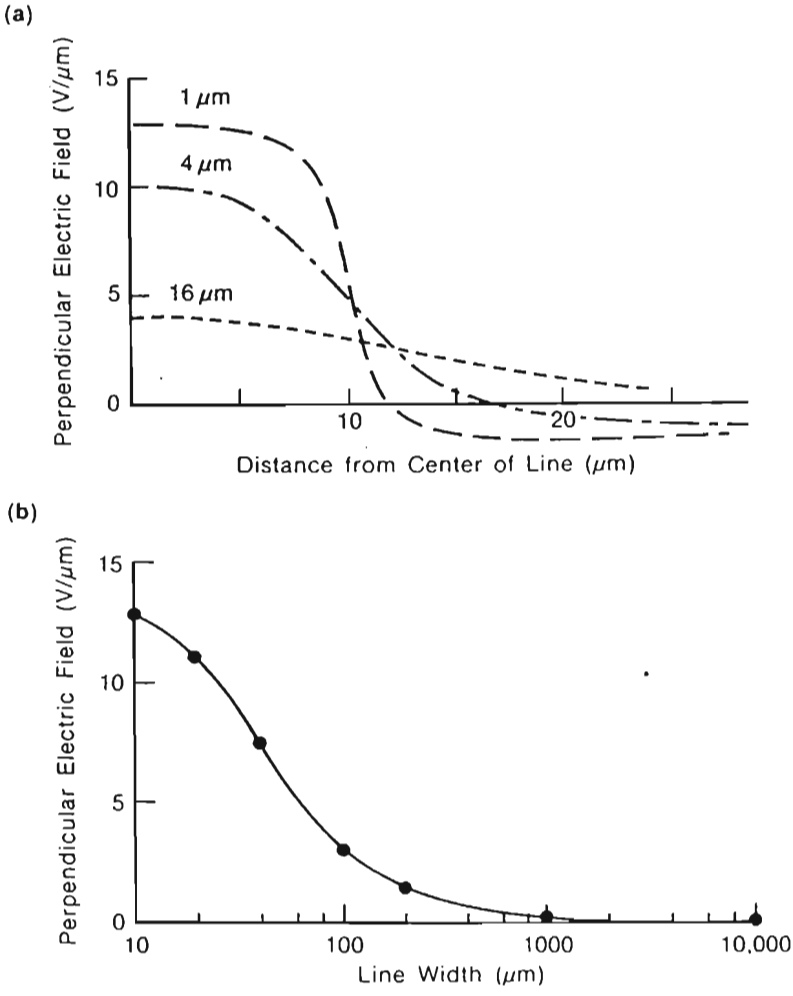
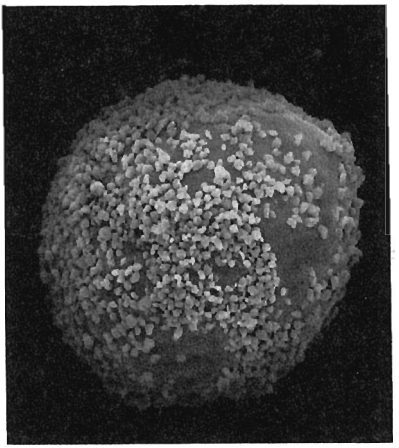


Figure 4 (a) Perpendicular electric field plotted versus the distance (1, 4, 16 μm) above a 25 μm thick photoreceptor of dielectric constant 6.6 for a line charge half width of 10 μm charged to 1000 volts (calculated as if the charging were uniform). (b) Perpendicular electric field component at the center of a line charged to 1000 volts plotted versus the width of line. (From Neugebauer, 1965.)



(a)



(b)

Figure 5 Scanning electron microscopic pictures of (a) 10 ± 2 μm size-classified toner and (b) toner adhering to a carrier particle.

perpendicular electric field is (Kao, 1973)

$$E_{\perp} = \frac{\sigma_k \tanh(kd_s)e^{-k(z-d)}}{\epsilon_0(K_E \tanh(kd_s) + K_s)} \cos ky \tag{4}$$

showing the exponential falloff with distance above the photoreceptor (z), similar to the results shown in Fig. 4, and the periodic variations with distance across the photoreceptor (y). For sharp latent images such as sharp boundaries, the electric field can be found by performing a Fourier expansion of the latent image and summing the values of $E_{\perp}$ for each k.

IV. TONER CHARGING

In electrophotography, the proper charge properties of the toner particles are crucial requirements for a good development system. The average charge-to-mass ratio Q/M determines the amount of toner developed onto solid area and character latent images: the lower the Q/M, the darker the images on the page. Wrong sign toner is "developed," i.e., attracted to the photoreceptor, onto nonimaged areas, giving an objectionable gray color to the white paper. Zero charged toner becomes dust in the machine, leading to reliability problems.

The charging of the insulating toner particles is almost always achieved by contact electrification: the toner particles are brought into contact with another material. At the interface of the surfaces, charge is exchanged. This method of insulator charging is a pervasive but not-well-understood solid-state physics problem (Schein, 1992; Lowell and Rose-Innes, 1980). One merely has to walk across a rug under low relative humidity conditions and experience the shock on touching grounded metal for a demonstration of the pervasiveness of charge exchange phenomena (between shoes and rugs). It occurs between all materials (metals and insulators, organic and inorganic) and remains one of the few solid-state physics problems that is at such a rudimentary level of understanding.

There are two primary types of development systems (Schein, 1992). In the magnetic brush dual component development system, used in most high speed machines, toner particles are charged by mixing them with a second powder called carrier (Fig. 5). Toner particles have diameters of approximately 10 μm and are blends of polymers and carbon black pigment. Carrier particles have diameters of approximately 200 μm and are composed of magnetically soft, conductive, metallic balls coated with a thin polymer layer. Contact between the toner and carrier surfaces causes charge to be exchanged. Depending on the materials chosen for the toner and carrier coating, the resulting charge on the toner may be positive or negative. This mixture, which has zero net charge, is introduced into the magnetic brush development system (Fig. 6) where toner particles are attracted to the latent image on the photoreceptor.

The second type of development system, monocomponent, eliminates the carrier particles and is therefore lighter and more compact, ideal for low speed machines. An example is shown in Fig. 7, which is a schematic diagram of a development system in a Canon personal copier. In this case the toner particles, which have magnetic material dispersed within the polymer, reside in a reservoir in which a roller rotates about stationary magnets. The toner is charged by contact with the rotating roller and is carried out of the reservoir past a magnetic doctor blade to the development zone.

The toner charge obtained is known to be determined by the materials chosen, but the appropriate physical and chemical properties remain unknown. Toners are usually made from polymers such as polystyrene, polyacrylics, polymethyl methacrylates, etc., blended with about 10% by weight of carbon black. Additives called charge control agents are usually added at the 1% level to toner to control toner charging. Examples are metal complex dyes and quaternary ammonium salts. A great deal of proprietary, empirical knowledge concerning charge control agents exists at each company making toners.

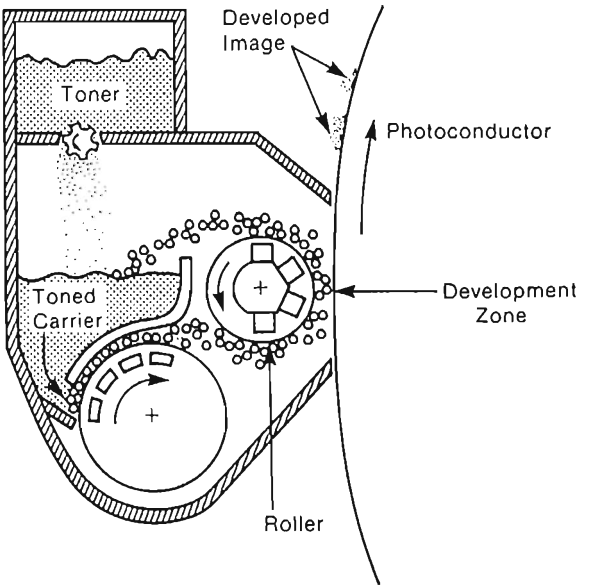


Figure 6 A schematic diagram of a magnetic brush development system. The carrier, which is polymer coated magnetically soft material, is attracted to the stationary magnets and, by a combination of magnetic and friction forces, is carried around the rotating roller into the development zone where the toner is attracted to the latent image. (From Williams, 1984 Copyright © 1984 by John Wiley and Sons, Inc.; reprinted by permission.)

The difficulties in bringing a scientific basis to toner, and therefore insulator, charging should not be underestimated and are well documented in prior reviews and books (Schein, 1992; Lowell and Rose-Innes, 1980). When the surfaces of two materials are brought into contact and separated, the actual area that made contact is difficult to determine. Whether pure contact or friction is required has not been determined. In fact, the terms contact electrification and triboelectrification, i.e., frictional electrification, are often used interchangeably. The precise natures of the surfaces are usually not well defined: dust particles, surface contaminants, and even water layers may be the "surface." Even for "clean" surfaces the nature of intrinsic and extrinsic surface states on insulators is not well understood. The magnitude of return currents during separation remains controversial. Finally, the number of surface molecules involved in the charging process is extremely small, on the order of one molecule in 10^4 or 10^5.

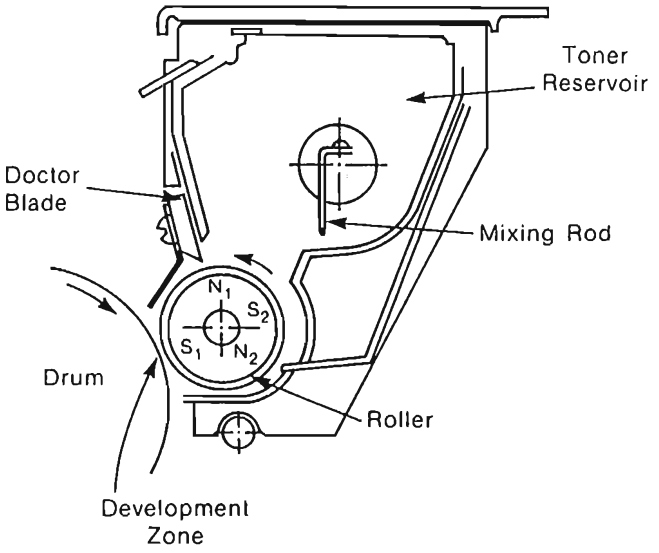


Figure 7 In the Canon monocomponent development system the magnets are stationary and the toner, containing magnetically soft material, is carried by the roller past a magnetic doctor blade into the development zone. (From Takahashi et al., 1982.)

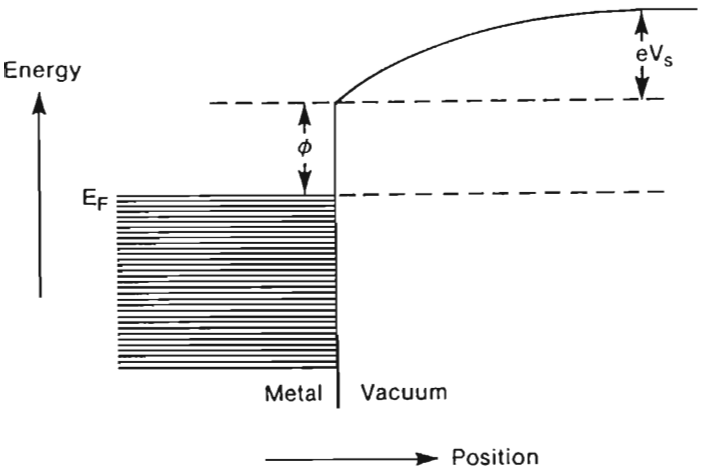
The construction of contact charge exchange models requires specification of the following items: the nature of the charge carrier (electrons, ions, or mass transfer), the driving force (difference in work function, concentration gradients), the mechanism (thermionic emission, tunneling), the energy states involved (bulk or surface, extrinsic or intrinsic), and the condition (whether the dynamic or equilibrium condition is being addressed).

These parameters are agreed upon only for metal-metal contacts (Lowell and Rose-Innes, 1980; Harper, 1967). In this case it has been shown that if two metals with different work functions ϕ_i are brought together (Fig. 8) and electrons are allowed to exchange by tunneling so that thermodynamic equilibrium is maintained, a contact potential difference V_c is created across the interface, given by

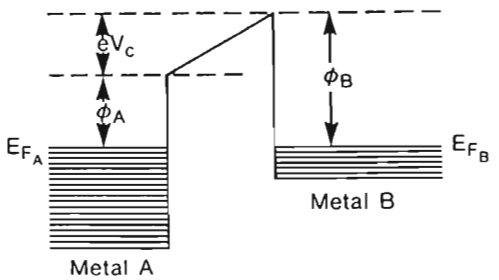
$$V_c = \frac{\phi_B - \phi_A}{e} \tag{5}$$

and the charge Q exchanged by electron tunneling is

$$Q = C_{AB} V_c \tag{6}$$



(a)



(b)

Figure 8 The average of an electron inside and outside of a metal is shown in (a) ignoring the image potential. Here ϕ is the work function, V_s is the surface potential, and E_F is the Fermi level. Two metals in close proximity (b) exchange charge until, in equilibrium, their Fermi levels are coincident. The transferred charge is such as to cause a difference in surface potential V_c equal to $(\phi_B - \phi_A)/e$. (From Harper, 1967.)

where C_{AB} is the capacitance between the two adjacent bodies. As the two bodies are separated, C_{AB} decreases (and consequently Q decreases) until charge exchange by tunneling stops. Harper (1967) showed that the cutoff of tunneling currents with distance is at about 10 Å.

When insulators are involved, serious experimental and theoretical difficulties abound. For example, there have been experiments on insulating polymers (Harper, 1967) and rare gas solids (Cottrell et al., 1984) in which no charge exchange was observed when contact was made with metals. On the other hand, several authors, beginning with the classic experiments of Davies (1969), have shown that, after many contacts are made to reach an equilibrium charge exchange, the charging of polymers in metal-insulator contact charging experiments depends linearly on the metal work function. Such results have been taken as evidence that electrons are being exchanged, driven by the work function difference between the metal and the insulator. There is also good evidence for an ion exchange mechanism (Shaw and Jex, 1928). Charge exchange experiments on glasses and polymers can be correlated with the basic and acidic nature of the surfaces. A possible mechanism could involve water adsorption from the atmosphere promoted by the acidic or basic groups, with OH^- and H^+ ions exchanged (Medley, 1953). Insulating materials have been ordered in lists (Schein, 1992; Lowell and Rose-Innes, 1980) called triboelectric series, with the property that a material higher on the list always charges positive when contacted by a material lower on the list. This empirical result suggests that a single charging mechanism is operative.

Charge characterization of mixtures of powders in electrophotography has been carried out for many years using a "cage blowoff" technique (Schein and Cranch, 1975). In this measurement, shown in Fig. 9, a mixture of two powders is put into a metal Faraday cage (also called a blowoff cage) with metal screens on both ends. The holes in the screens are chosen to be larger than the diameter of the smaller powder (toner) but smaller than the diameter of the larger powder (carrier). After sufficient blowing through the Faraday cage with an air gun, the toner particles leave. By measuring the change in mass M and charge Q, the average Q/M ratio of the toner particles can be obtained. It is generally observed that $M/Q \propto C_t^{-1}$, where the toner concentration C_t is the ratio of toner to carrier mass (Schein 1992).

That the surfaces of insulators are involved in insulator charging is suggested by the experiments of Hays (1974), Bauser et al. (1970), and Kittaka and Murata (1979), who altered the surfaces of organic films with exposure to ozone, oxygen, and UV irradiation, respectively, and observed changed charging behavior. These and other results have lead to the suggestion of the surface state theory of electrostatic charging (Krupp,

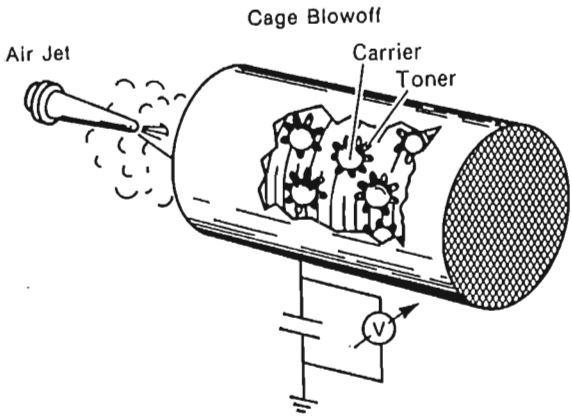


Figure 9 Apparatus used in the cage blowoff measurement. The stainless steel cage has screens on both ends with holes intermediate in size between the diameters of the carrier and toner. An air jet forces smaller diameter particles called toner out of the cage. Measurements of the charge and the mass left gives the Q/M ratio of the toner.

1971; Bauser et al., 1970; Bauser, 1974; Schein 1992; Lowell and Rose-Innes, 1980). In this theory, charge is exchanged between surface states of the two materials, driven by the "surface work function" difference between the materials. The theory has two limits, schematically indicated for insulator-insulator contacts in Fig. 10. In the high surface state density limit (Fig. 10(b)) charge exchange is large enough to raise the insulator with the larger work function (before charging) to the energy level of the insulator with the smaller work function (on the left in Fig. 10(b)). This limit requires the charge exchanged per unit area to be orders of magnitude larger than is experimentally observed and is therefore usually dismissed. In the low surface state density limit, charge is exchanged to fill the states between the two work functions (Fig. 10(a)), from the surface of the material with the lower work function to the surface of the material with the higher work function. Such a theory can account for the observation that $M/Q \propto C_t^{-1}$ in toner-carrier charging experiments. It can also explain the observed linear dependence of insulator charging on metal work function (Schein 1992, Lowell and Rose-Innes 1980, Davies 1969), but only if the density of surface states per unit energy is constant. It also implies electron exchange, which is difficult to reconcile with the evidence for ion transfer (Schein, 1992; Lowell and Rose-Innes, 1980). It assumes that a "surface work function" can be defined for an insulator, which requires

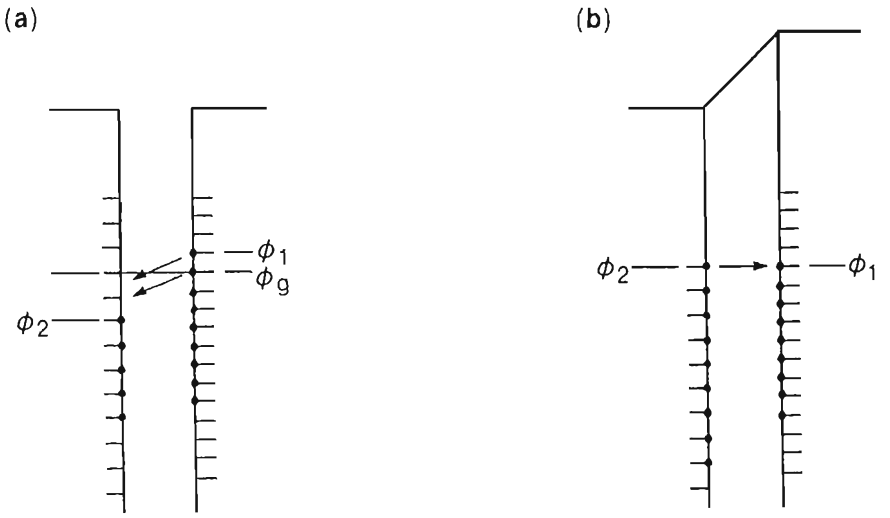


Figure 10 Schematic diagram of the insulator-insulator contact for the low (a) and high (b) density limits of the surface state theory. ϕ_1 and ϕ_2 are the surface work functions (energy difference from highest occupied level to vacuum) of the insulators, and ϕ_g is the final common work function after charge is exchanged. A dash at the interface represents a surface state; a dot on the dash indicates a filled surface state before contact; and an arrow indicates the movement of charges during charging.

thermodynamic equilibrium. However, these materials have virtually zero conductivity, making it difficult to understand how charges can move to establish an equilibrium condition. Further, the nature of the "surface states," which correspond to 1 molecule in 10^4–10^5 being charged, has never been identified.

Application of the surface state theory to toner-carrier mixtures requires calculation of the measurable parameter Q/M. Lee (Schein, 1992; Lee 1978) suggested applying the low density limit of the surface state theory to toner-carrier charging. He showed that M/Q is given by

$$\frac{M}{Q} = RC_t\left[\frac{\rho_c}{3N_c\Delta\phi e}\right] + r\left[\frac{\rho_t}{3N_t\Delta\phi e}\right] \tag{7}$$

where N_c (N_t) is the number of surface states per unit area per unit energy on the carrier (toner), $\Delta\phi$ is the difference in work function, R (r) is the carrier (toner) radius, and ρ_c (ρ_t) is the carrier (toner) density. Schein

(Schein et al 1992) suggested applying the high density limit of the surface states theory to toner-carrier charging and showed that

$$\frac{M}{Q} = RC_t\left[\frac{\rho_c}{3\epsilon_0 E_e}\right] + r\left[\frac{\rho_t}{3\epsilon_0 E_e}\right] \tag{8}$$

where E_e is an electric field created during the contact by the charge exchange. Note that Eq. 8 (the high density limit) is identical to Eq. 7 (the low density limit) with $N_c\Delta\phi e$ and $N_t\Delta\phi e$ replaced with $\epsilon_0 E_e$. There is an important difference between Eqs. 7 and 8: the slope-to-intercept ratio of M_t/Q_t versus C_t is determined entirely by known parameters, $R\rho_c/(r\rho_t)$, in Eq. 8; it is determined by the product of this parameter and N_t/N_c in Eq. 7. This result has obvious experimental implications.

These predictions can be compared with experimental measurements of M/Q versus C_t by Lee (1978) and Anderson (1989) and data shown in Fig. 11 (Schein et al., 1992). In the experiment of Schein et al. (1992) the concentration of charge control agent, toner additives at the 1% level that improve toner charging, was also varied, as summarized in Table 1. The

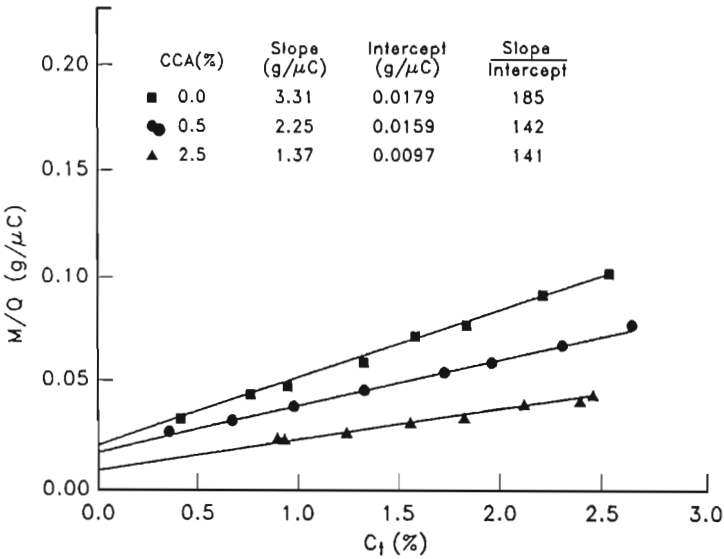


Figure 11 The graph shows the mass-to-charge ratio M/Q versus the toner concentration C_t for the same carrier and three toners with the percent charge control agent of 0, 0.5, and 2.5%. The least squares determined slope and intercept, and their ratio are given in the figure. (From Schein et al., 1992.)

Table 1 Analysis of Published M/Q vs. C_t Experiments

Data	Material parameters				Slope/intercept	
	R (μm)	r (μm)	ρ_c (g/cm^3)	ρ_t (g/cm^3)	Observed	$\frac{R\rho_c}{r\rho_t}$
Lee[a]						
Fig. 2	50	7.1	5.5	1	50	38
Fig. 3	50	7.1	5.5	1	29	38
Fig. 4	50	7.1	5.5	1	18	38
Fig. 5	125	7.1	5.5	1	236	96
Anderson[b]	50	5	4	1	32	40
	15	6	5.5	1	3.7	14
Fig. 11 (this paper)						
0% CCA	100	5	7.7	1	185	154
0.5%	100	5	7.7	1	142	154
2.5%	100	5	7.7	1	141	154

[a] From Lee (1978).
[b] From Anderson (1979).

interesting result is that the observed slope-to-intercept ratio (next to last column) agrees with the prediction of the high density limit of the theory (last column) within a factor of two for almost all the experiments, with no adjustable parameters. One must therefore argue that $N_c = N_t$ within a factor of two, for all of the different toner-carrier systems characterized by these sets of data, taken with different toners and carriers at different laboratories, which seems unlikely or that the high density limit is the correct description of the data.

The analysis of the data in Fig. 11 in Table 1 is also independent evidence for the validity of the high density limit. In this experiment, only the percentage of charge control agent was changed; the carrier remained unchanged. The increased charging due to the addition of charge control agent in the toner can be ascribed to a change in N_t in the low density limit of the theory. This predicts only a change in intercept. Nonetheless, experimentally both the slope and the intercept changed, maintaining the ratio constant, inconsistent with the low density limit but consistent with the high density limit of the theory. Clearly E_e, the field being created in the high density limit of the theory, changes as the amount of charge control agent is changed (E_e = 8.8 V/μm at 0% CCA and E_e = 21.3 V/μm at 2.5% CCA), indicating that E_e is determined by some material

properties. This is the first experiment that can distinguish between the low and the high density limit of the surface state theory. The experimental results indicate that only the high density limit describes the experimental data. Verification that the high density limit describes toner, and presumably all insulator, charging resolves one of the central questions in insulator charging: whether electrons, ions, or molecules are the charges exchanged. The resolution is that whatever charges are available will be exchanged to create E_e. A corollary is that if no free charges are present, it is predicted that no charge is exchanged, as has been observed in several insulator charging experiments (Harper, 1967; Cottrell et al., 1984).

Association of E_c with material properties is the next step required for a microscopic theory of insulator charging. Unfortunately, simple theory suggests that E_e equals the difference in work functions divided by the distance between the surface where charging ceases. Reasonable values for these parameters (1 eV, 10 Å) cannot account for the observed magnitudes of E_e.

V. TONER DEVELOPMENT

During the development step, toner particles are brought into the vicinity of the latent image; they are attracted by the Coulomb force. The goal of a development theory is to predict how much toner develops and to identify relevant hardware and material parameters. "How much" is usually quantified by predicting and measuring the developed toner mass per unit area (M/A). However, attempts to identify the relevant parameters lead to a difficulty: for any development system there are many potential parameters, as shown in Table 2 for the magnetic brush development system. This difficulty suggests that one might consider constructing a theory of development that would hopefully identify the most important parameters. That consideration leads to a second difficulty: there any many possible physical mechanisms to explain why toner leaves a carrier and goes to the latent image. Estimates of the magnitude of forces are confounded by the wide distribution of toner particle diameters and charges. Further, "back" development is possible from the latent image on the photoreceptor to the carrier beads in the magnetic brush development system. As one might guess, early attempts at a development theory involved first-order differential equations with empirically determined rate coefficients. Later, comprehensive experiments indicated regularities in the data, which led to the suggestion of theories based on electrostatic principles that have been verified experimentally.

The simplest possible development theory, which is almost never observed experimentally, is based on the concept of charge neutralization.

Table 2 Typical Hardware Parameter of the Magnetic Brush Development System

Hardware parameter	Typical values	Symbol
Photoreceptor velocity	5–50 cm/s	
Roller velocity	7.5–100 cm/s	
Flow rate	10 g/cm s at v_r = 25 cm/s	
Photoreceptor-to-roller spacing	1350 μm	L
Photoreceptor potential	800 volts	V
Roller voltage	100 volts	
Toner type		
Radii	2–30 μm	r
Concentration	0.5–3%	C
Charge-to-mass ratio	10–30 μC/g	Q/M
Carrier		
Radius	50–250 μm	R
Shape	Spherical, rough shape	
Coating	2 μm polymer coating	
Magnets: strength and configuration	(see Fig. 6)	
Roller: number and size, surface	1–5, 1–4 cm diameter, rough texture	
Mode: velocity of photoreceptor, with or against the roller		
Photoreceptor		
Type	a–Se, organic	d_s
Thickness	60 μm, 20 μm	K_s
Dielectric constant	6.3, 3	
Angle with respect to gravity	0–90°	

The concept is that toner develops until the toner charge per unit area σ_t equals the photoreceptor charge per unit area σ_p. Since $\sigma_t = (M/A)\cdot(Q/M)$, where Q/M is the toner charge-to-mass ratio, this predicts

$$\frac{M}{A} = \frac{V\epsilon_0}{(Q/M)(d_s/K_s)} \tag{9}$$

using the relationship between σ_p and V given below Eq. 2. As this much M/A is almost never observed experimentally, other phenomena must limit development.

We discuss theories of magnetic brush development and monocomponent development separately.

A. Magnetic Brush Development

Fig. 12 shows a magnified view of the development zone in a magnetic brush development system, and Fig. 13 illustrates the three theories of solid area development that have been proposed to describe the mechanism by which toner leaves the carrier particles and ends up on the photoreceptor surface (Schein, 1992): the field stripping theory, the powder cloud theory, and the equilibrium theory. Three measurements shown in the lower half of Fig. 13 can be used to distinguish among these three theories. Two of these involve measurement of the developed mass per unit area M/A as a function of roller velocity and development voltage V across the gap. The third involves measurements of the toner charge-to-mass ratio as a function of V.

In the field stripping theory, theory A in Fig. 13, the Coulomb force QE due to the latent image on the photoreceptor overcomes the forces (the electrostatic image force and the van der Waals force) that attract the toner to the carrier beads F_a. All particles whose adhesion force is less than QE are developed from the carrier beads onto the latent image. Because all toner particles have a finite adhesion force to carrier particles,

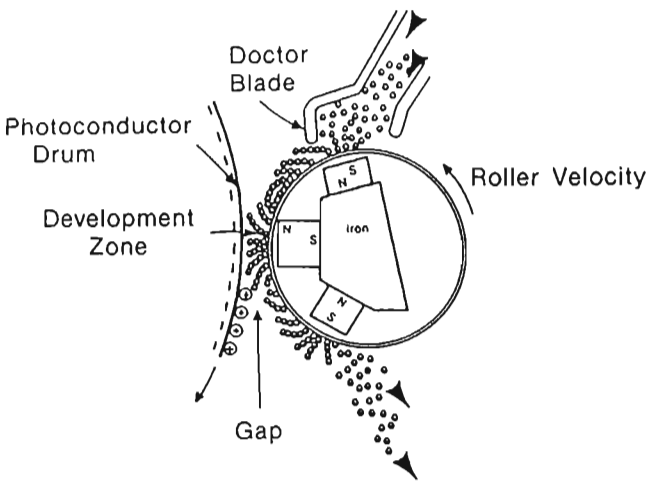


Figure 12 An expanded schematic view of the development zone of a magnetic brush development system (Fig. 6). In the development zone, forces acting on the toner particles cause them to leave the carrier particles and "develop" on the photoreceptor surface.

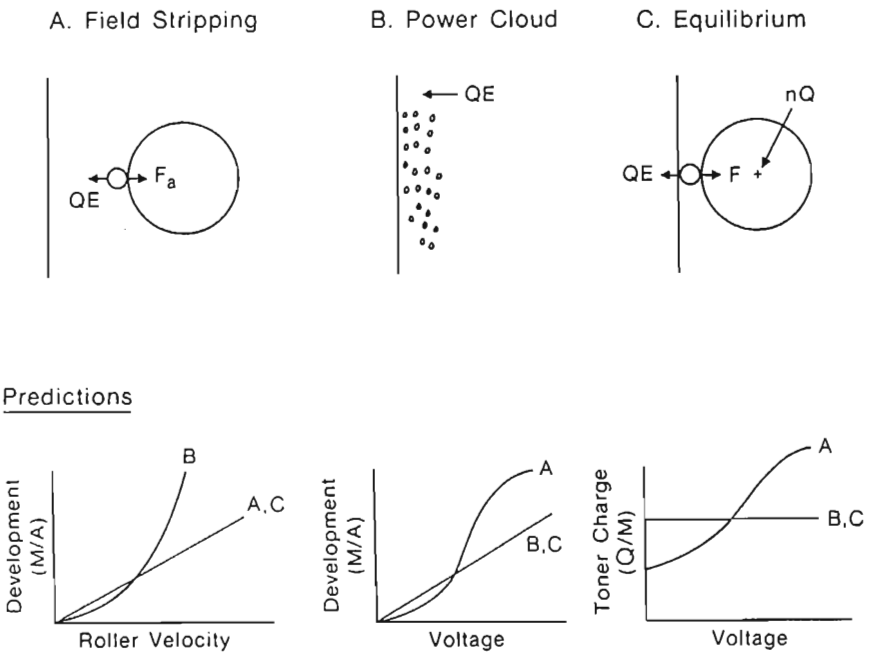


Figure 13 The field stripping theory (theory A), the powder cloud theory (theory B), and the equilibrium theory (theory C) are schematically indicated at the top of the figure, and their predictions are indicated on the bottom three graphs. Only the powder cloud theory (B) predicts nonlinear mass per unit area versus roller velocity; the equilibrium and field stripping theories can be distinguished by the other measurements.

it takes a minimum field to strip toner from the carrier particles, and consequently there should be no development at low voltages. Development curves, i.e., mass per unit area versus voltage, are proportional to integrals over the toner adhesion distribution function. Because the adhesion distribution is not expected to be rectangular, the development versus voltage curve should be nonlinear, usually S shaped. Toner particles with lower adhesion or lower charge develop first, so the developed toner charge-to-mass ratio Q/M should increase with applied voltage (see predictions in lower half of Fig. 13). The developed mass per unit area should be linear in roller velocity because development should increase as the amount of available toner increases.

In the powder cloud theory, theory B in Fig. 13, toner is freed from the carrier by inertial forces during carrier-carrier and carrier-photoreceptor collisions. The electric field associated with the latent image then attracts the free toner to the photoreceptor. If this theory describes the development mechanism, the developed toner mass per unit area should be proportional to the product of the carrier flow and a function of the inertial forces on the carrier beads. The flow of carrier particles is proportional to the roller velocity, and the inertial forces on the carrier beads increase with increasing roller velocity. As a result, the developed mass per unit area should exhibit a superlinear dependence on roller velocity, as indicated in the predictions in Fig. 13. This prediction distinguishes the powder cloud theory from the other theories and can be used to test for the presence or absence of this development mechanism. Predicting the outcome of the other measurements requires additional assumptions about the forces exerted on the toner particles. If development of toner depends only on the force exerted by the electric field on the toner, then developed mass per unit area should be linear in the applied voltage. If the amount of toner freed from the carrier depends on the inertial forces alone, the developed toner charge-to-mass ratio should be independent of the electric field. On the other hand, if the release of toner from the carrier depends on both inertial forces and toner charge (for example, via toner adhesion), one expects more complicated behavior.

The equilibrium theory, theory C in Fig. 13, assumes that toner continues to come off each of the carrier beads until the Coulomb force of the latent image balances the force of attraction of the toner to the carrier beads, i.e., until a force equilibrium is reached. In this theory the usual forces of attraction of toner to carrier beads (due to image and van der Waals forces) are ignored, because it is assumed that development only occurs in three body contact events between carrier, toner and photoreceptor. In this case, such forces are cancelled to first order by similar forces between the toner and photoreceptor. The predominant force of attraction between toner and carrier is assumed to be due to the carrier building up a net charge as a result of toner particle depletion from the carrier particle. If n toner particles develop from a carrier bead, a net charge of nQ builds up on the carrier, which attracts the next toner particle considering whether to develop. When this force equals the Coulomb force QE, toner particles cease coming off the carrier bead. Therefore n, the number of toner particles developed per carrier bead, is linear in E, or the applied voltage. This leads to the prediction that M/A, which is proportional to n, is linear in V. The developed mass per unit area depends linearly on roller velocity because development increases linearly with the number of carrier beads brought into contact with a point on the photo-

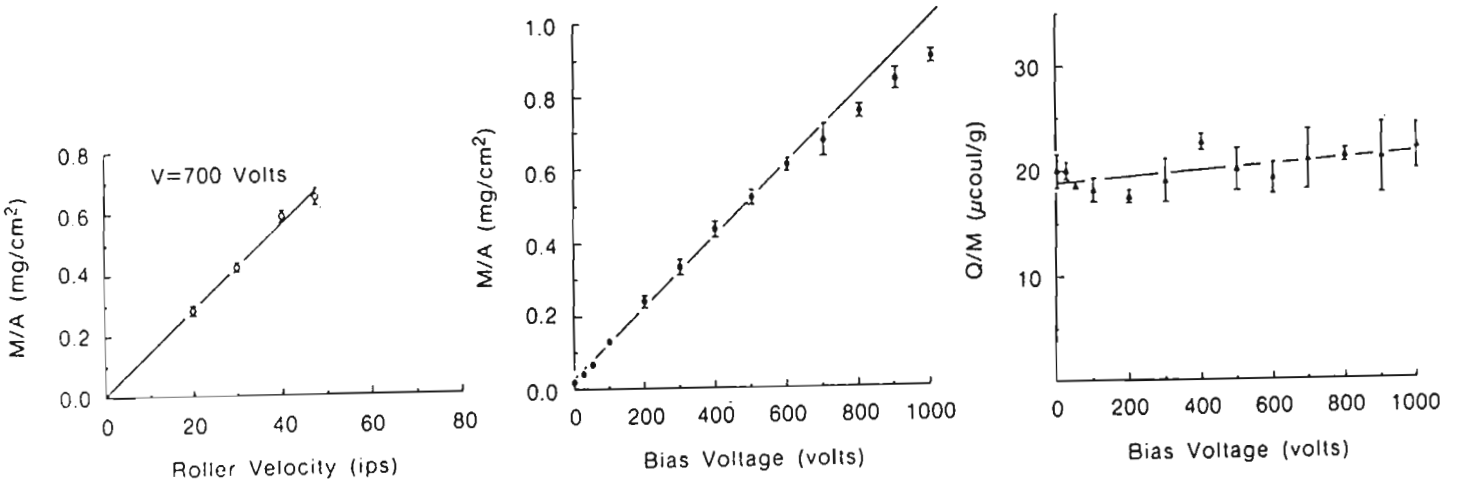


Figure 14 Solid area development experiments are consistent with only the equilibrium theory of magnetic brush development. (From Schein and Fowler, 1985.)

receptor. Because toner continues to develop until a force equilibrium is reached, i.e., the "average" toner particle develops, the developed toner charge-to-mass ratio should be independent of electric field or the voltage across the development gap.

Typical solid area development data are shown in Fig. 14 (Schein and Fowler, 1985). It can be seen that M/A is linear in the roller velocity, eliminating the powder cloud mechanism. M/A is linear in applied voltage, suggesting that the equilibrium model is a better description that the field stripping model. Finally the observation that Q/M is independent of V confirms the equilibrium model as the best description of solid area development.

This theory has been quantified theoretically three different ways, by considering the forces on the particles, by considering electric fields in the development zone, and by considering the behavior of all charges. They all lead to the same result (as one would expect)

$$\frac{M}{A} = \frac{V\epsilon_0}{\frac{Q}{M}\left(\frac{d_s}{K_s} + \frac{L}{K_E \nu}\right)} \tag{10}$$

where K_E is the dielectric constant of the mixture of metal balls and air in the development gap (about 6) and ν is the ratio of the roller speed to the photoreceptor speed.

Further consideration of this result leads one to the conclusion that elimination of the bead charge can enhance development, i.e., M/A. By making the carrier beads rough-shaped and uncoated at the corners, a conductive path can be made to occur through the bead chains. This provides a path for the bead charge to drain off, significantly increasing the electric fields in the development zone and enhancing M/A. This idea was first suggested by workers at Eastman Kodak Company and is now called the conductive magnetic brush development system (Schein, 1992).

B. Monocomponent Development

Figure 15(a) illustrates the development zone in a monocomponent development system in which carrier beads are not used. A toner chain (in the magnetic toner case) or a monolayer (in the nonmagnetic toner case) experiences both the electric field due to the latent image and various adhesion forces to the roller (electrostatic F_{es}, magnetic F_M). This situation suggests that a field stripping type of theory is appropriate (Schein et al., 1989).

Using a field stripping concept it becomes clear that M/A should have a threshold voltage V_{th} below which development is zero (Fig. 15(b)). This

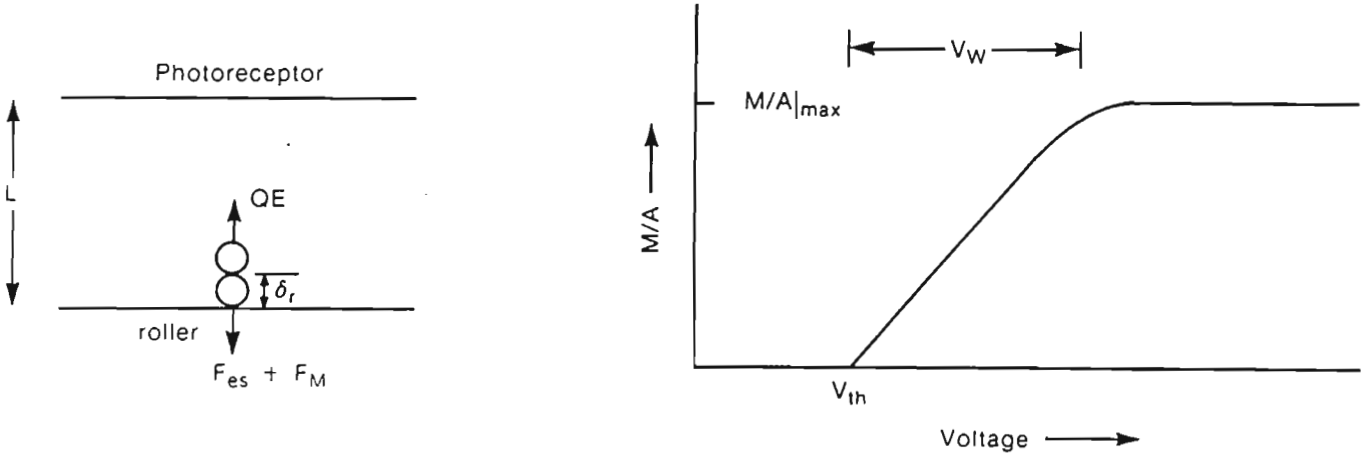


Figure 15 (a) A theory of monocomponent development based on the forces experienced by toner. (b) This theory predicts a voltage threshold and a maximum mass per unit area. The voltage width V_W of the rising portion of the curve is determined by the distribution of toner adhesion forces and toner space charge.

occurs when the Coulomb force of development QE exceeds the adhesion force. The maximum M/A is given by the M/A on the roller times the speed ratio v. Finally the voltage width V_w is determined by the toner space charge and the distribution of adhesion forces on the toner particles, i.e., there actually exists a distribution of threshold voltages. This model describes development for many extant monocomponent systems. In some systems, a high ac voltage ($\pm$ 1000 Vp-p) is applied across the development zone, which creates a cloud of toner in the development zone. In other systems, especially the nonmagnetic types, the monolayer of toner on the roller is directly contacted against the photoreceptor. In both cases the adhesion force of the toner to the roller goes to zero and the threshold goes to zero volts (or even negative values, due to space charge effects).

VI. SUMMARY

Electrophotography is one of the most successful commercial applications of electrostatic phenomena. In most embodiments it requires six process steps to produce a copy: charge, expose, develop, transfer, fuse and clean. Electrostatics plays key roles in almost all of these steps. Discussed in this chapter are the role of electrostatics in the charge, expose, develop, and transfer steps.

During charge and transfer, the photoreceptor and the back of the paper, respectively, are uniformly charged by extracting ions with an electric field from a gas breakdown, initiated by applying a high potential on a thin wire.

During exposure, the photoreceptor is exposed to the light, creating a charge pattern, called a latent image, on the photoreceptor surface. The latent image creates an electric field above the photoreceptor that attracts toner to the photoreceptor surface. The calculation of an electric field due to an arbitrary charge pattern is a classic problem in electrostatics. The electric fields due to three latent images are discussed, a solid area, a single line, and a series of parallel lines.

The proper charging of toner particles is an essential requirement of a good development system. Yet the contact charging of insulators, i.e., toner, remains a poorly understood phenomenon. It appears that the high density limit of the surface state model, which postulates that charge is exchanged to create an electric field during the contact, can explain the data. But identification of the physical significance of the electric field remains an unsolved problem. Therefore toner material choices are generally made by empirical means.

Finally, toner development, the process step that determines the best image quality that electrophotography can produce, has been shown to

be dominated by electrostatic considerations. In the dual component insulative magnetic brush development system, the buildup of charge on carrier beads, as toner develops onto the photoreceptor, limits toner development. In monocomponent development systems, a field stripping model, in which the Coulomb force due to the latent image overcomes the adhesion force of toner to the roller, appears to account for the data.

REFERENCES

Anderson, J. H. (1989). An electronic model of triboelectrification of two-component electrophotographic developers. *J. Imag. Sci.*, 33, 200.

Bauser, H. (1974). Static electrification of organic solids. *Dechema A-Monogr.*, 72, 11.

Bauser, H., W. Klopffer, and H. Rabenhorst (1970). On the charging mechanism of insulating solids. *Proc. 1st Int. Conf. on Static Electricity*, Vienna, Austria, May 4–6, in *Adv. Stat. Electrification*, 1, 2 (1971).

Cobine, J. D. (1958). *Gaseous Conductors*. Dover, New York.

Cottrell, G. A., C. E. Hatto, C. Reed, and A. C. Rose-Innes (1984). Contact charging of ideal insulators: experiments on solidified rare gases. *J. Phys. D: Appl. Physics*, 17, 989

Crowley, Joseph M. (1986). *Fundamentals of Applied Electrostatics*. John Wiley, New York.

Davies, D. K. (1969). Charge generation of dielectric surfaces. *J. Phys.*, D2, 1533.

Gallo, C. F. (1975). Coronas and gas discharges in electrophotography: a review. *IEEE Trans.*, IA-11, 739.

Gallo, C. F. (1977). Corona—a brief status report. *IEEE Trans.*, IA-13, 550.

Harper, V. R. (1967). *Contact and Frictional Electrification*. Oxford University Press, Oxford.

Hays, D. A. (1974). Contact electrification between mercury and polyethylene: effect of surface oxidation. *J. Chem. Phys.*, 61, 1455.

Kao, C. C. (1973). Electric field, transfer, and spread function in xerographic image studies. *J. Appl. Phys.*, 44, 1543.

Kittaka, S. and Y. Murata (1979). Photoelectric emission and contact charging of vacuum irradiated polymers. *Jpn. J. Appl. Phys.*, 18, 515.

Krupp, H. (1971). Physical models of static electrification of solids. *Static Electrification. Inst. Phys. Conf. Ser.*, 11, 1.

Lee, I.-H. (1978). A surface interaction model of triboelectrification of toner-carrier pairs. *Photogr. Sci. Eng.*, 22, 228.

Lowell, J., and A. C. Rose-Innes (1980). Contact electrification. *Advances in Phys.*, 29, 947.

Medley, J. A. (1953). The electrostatic charging of some polymers by mercury. *Nature*, 171, 1077.

Neugebauer, H. E. J. (1965). Electrostatics fields of xerographic images. In *Xerography and Related Processes* (J. Dessauer and H. Clark, eds.). Focal Press, New York, Chap. 8.

Schaffert, R. (1980). *Electrophotography*. Focal Press, New York.

Schein, L. B. (1992). *Electrophotography and Development Physics*. 2d ed. Springer Verlag, New York.

Schein, L. B., and J. Cranch (1975). The static electrification of mixtures of insulating powders. *J. Appl. Phys.*, 46, 5140.

Schein, L. B., and K. J. Fowler (1985). Physics of development in the IBM 6670 electrophotographic printer. *J. of Imaging Technology*, 11, 295.

Schein, L. B., G. S. P. Castle, and A. Dean (1989). Theory of monocomponent development. *J. Imag. Technol.*, 15, 9.

Schein, L. B., G. Beardsley, and M. Moore (1990). Development efficiency in electrophotography. *J. Imag. Technol.*, 16, 129.

Schein, L. B., M. LaHa, and D. Novotny (1992). Theory of insulator charging. *Phys. Lett. A*, 167, 79.

Shahin, M. M. (1971). Characteristics of corona discharge and their application to electrophotography. *Photogr. Sci Eng.*, 15, 322.

Shaw, P. E., and C. S. Jex (1928). Tribo-electrocity and friction III—solid elements and textiles. *Proc. R. Soc. London*, 118, 108.

Takahashi, T., N. Hosono, J. Kanbe, and T. Toyono (1982). Mechanism of canon toner projection development. *Photogr. Sci. Eng.*, 26, 254.

Vyverberg, R. G. (1965). Charging photoconductive surfaces. In *Xerography and Related Processors* (J. Dessauer and H. Clark, eds.). Focal Press, New York, Chap. 7.

Williams, E. M. (1984). *The Physics and Technology of Xerographic Processes*. John Wiley, New York.

This Page Intentionally Left Blank

16

Electrostatics in Flat Panel Displays

A. Kitai

McMaster University
Hamilton, Ontario, Canada

I. INTRODUCTION

Electrostatics play a vital role in a variety of display technologies. These include the cathode ray tube (CRT), plasma displays (PD), liquid crystal displays (LCD), and high field electroluminescent displays (HFEL).

Displays are currently experiencing a revolutionary phase in their development, because new requirements call for flat panels that are capable of high resolution color display. The most important markets include computer monitors and high definition TV (HDTV), which is now the new standard for the next generation of television systems. Requiring ~1100 lines of vertical picture resolution and screen sizes of over 1 m^2, current CRT and flat panel technologies are not yet at the point of meeting the needs of HDTV, which will generate an enormous market for the successful color display.

This chapter will focus on display technologies that have application for flat panels, which are expected to make significant inroads into CRT dominated areas. The use of electric fields in PD, LCD, and HFEL will be described in conjunction with device operation and materials used in the active region of the device. However, another potential candidate for flat panels is a flat CRT, which will be examined first.

II. FLAT CRTs

The CRT, in retrospect, is a very elegant means of addressing many ($\sim 10^6$) discrete pixels by deflecting an electron beam that is accelerated to high energies (10–30 KeV), allowing it to impart considerable energy to phosphor material on the screen. In order to use this idea in a flat panel display, two basic approaches are possible. The first (Pankove, 1980) steers or guides an electron beam across the back of the panel and then deflects it toward the screen through a 90° angle by means of an array of closely spaced electrostatic deflection electrodes as shown in Fig. 1. Periodic focusing prevents the electron beam from expanding due to space charge repulsion between electrons. This is achieved using apertures held at high and low voltages alternately, allowing a low energy (100 eV) beam to remain intact. Disadvantages of this structure include the need for a vacuum envelope, complex electrode structures, and difficulty achieving high resolution color displays.

More recently, another approach has been taken, using field emission of electrons from a conducting needle to form a cold cathode (Stowell, 1984). If a dense array of such tips is placed behind the phosphor screen, electrons may be generated when and where they are needed. The field emission process (Spindt et al., 1976) permits electrons to overcome the work function of sharp needles by Fowler-Nordheim field emission. The structure of a typical device is shown in Fig. 2, and the means of fabrication is illustrated in Fig. 3. The calculated emitting area of a tip is only $\sim 1 \times 10^{-15}$ cm^2, which suggests that only a few atomic sites on the tip contribute to the emission, allowing the electrons to be collected by an anode, not shown in Fig. 2. The Fowler-Nordheim theory for a clean metal surface relates the field emission current density J to the electric

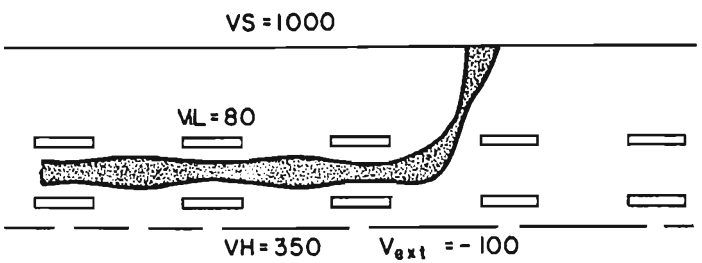


Figure 1 Guided-beam flat CRT construction showing deflection of electron beam toward screen.

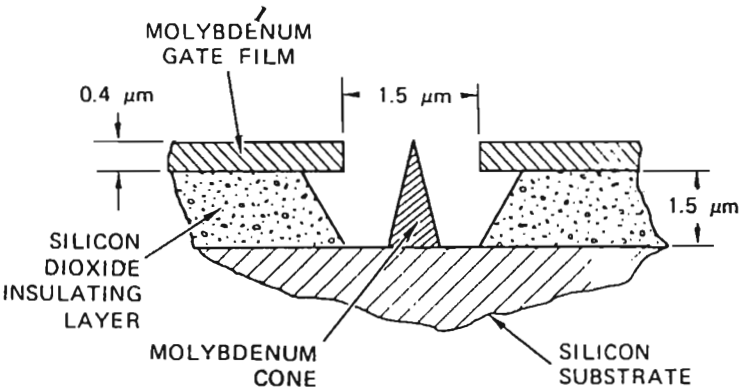


Figure 2 Cross section of cold cathode of the field emitter type.

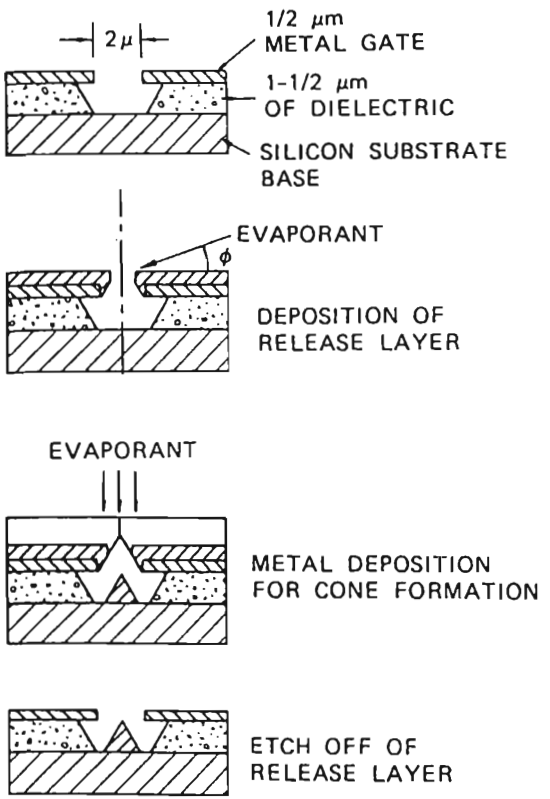


Figure 3 Fabrication sequence of field emitter device.

field at the surface E and the work function Φ by the equation

$$J = \frac{AE^2}{\Phi t^2(y)} \exp\left(-B \frac{\Phi^{3/2}}{E} v(Y)\right) \quad \text{A/cm}^2 \tag{1}$$

where A, B, y $v(y)$, and $t(y)$ are nonempirical parameters that may be calculated (Spindt et al., 1976).

By placing arrays of such tips behind a phosphor screen, over 200 foot lamberts of apparent brightness may be obtained with an anode voltage of under 1000 V. The glass envelope is supported by micropillars that remove the need for thick glass, and 300 color pixels per inch may be realized.

III. PLASMA DISPLAYS

The PD may be divided into two categories, ac and dc. In either case, field-excited ions collide with each other and give rise to visible light emission, or alternatively uv light generated by the plasma excites visible-emitting phosphors (Pankove, 1980). In a typical ac PD, two glass substrates are spaced to form a chamber containing a neon gas mixture. Each substrate holds a set of parallel conductors that are covered by a transparent dielectric. Selected intersections of the mutually orthogonal conductors emit localized neon-colored light when suitably driven.

A firing voltage V_f is necessary to initiate the discharge, and a lower sustain voltage V_s of alternating polarity follows. Typical values of V_f and V_s are 150 V and 90 V respectively. Fig. 4 shows a write, sustain, and erase waveform, with the wall voltage V_W that actually appears across the gas and is different from the electrode voltage due to charges on the

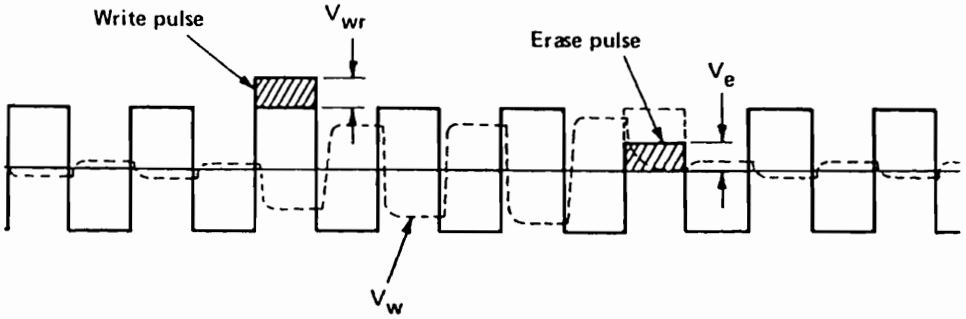


Figure 4 Write, sustain, and erase waveforms as function of time showing wall voltage V_W across plasma.

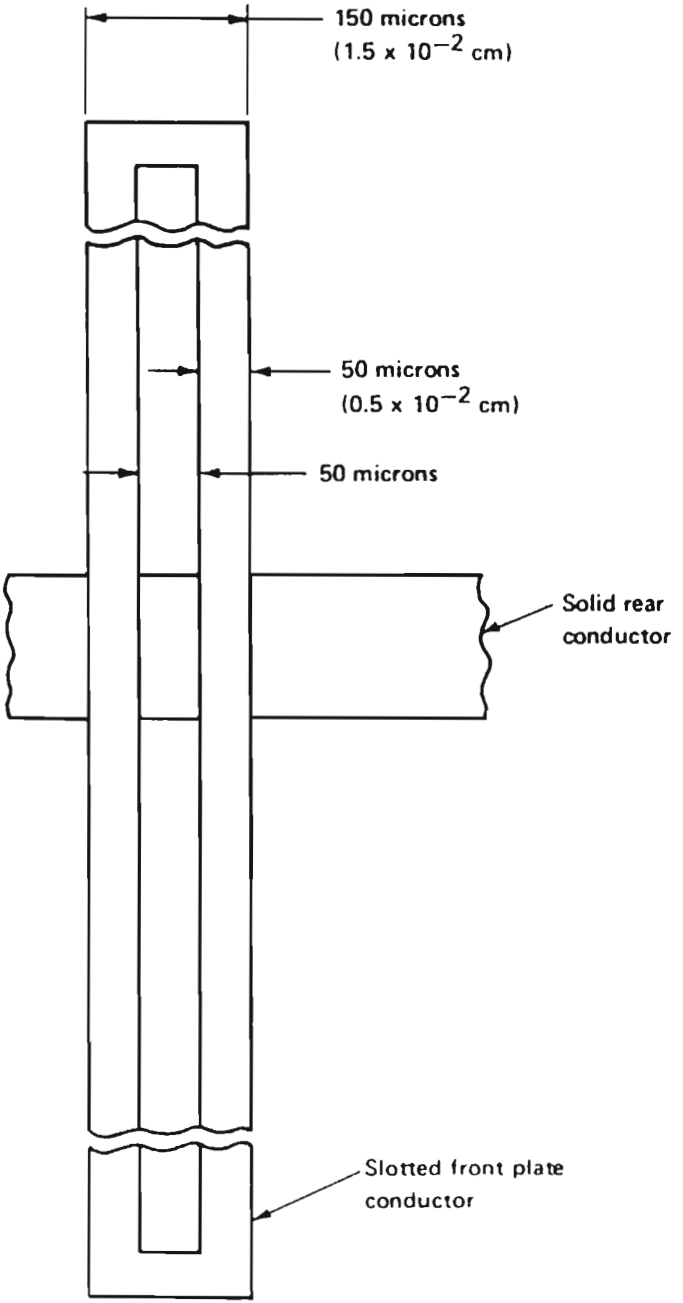


Figure 5 Plasma panel electrodes showing slotted geometry.

dielectric surface. A proper model of the device includes three capacitors in series, namely a wall capacitor, a gas capacitor, and another wall capacitor, which allows transient response to be determined if the gas discharge current is included. To improve optical efficiency, a slotted electrode may be used that avoids covering the plasma by the electrode, as shown in Fig. 5. A typical front-to-rear electrode separation is 100 μm. The gap

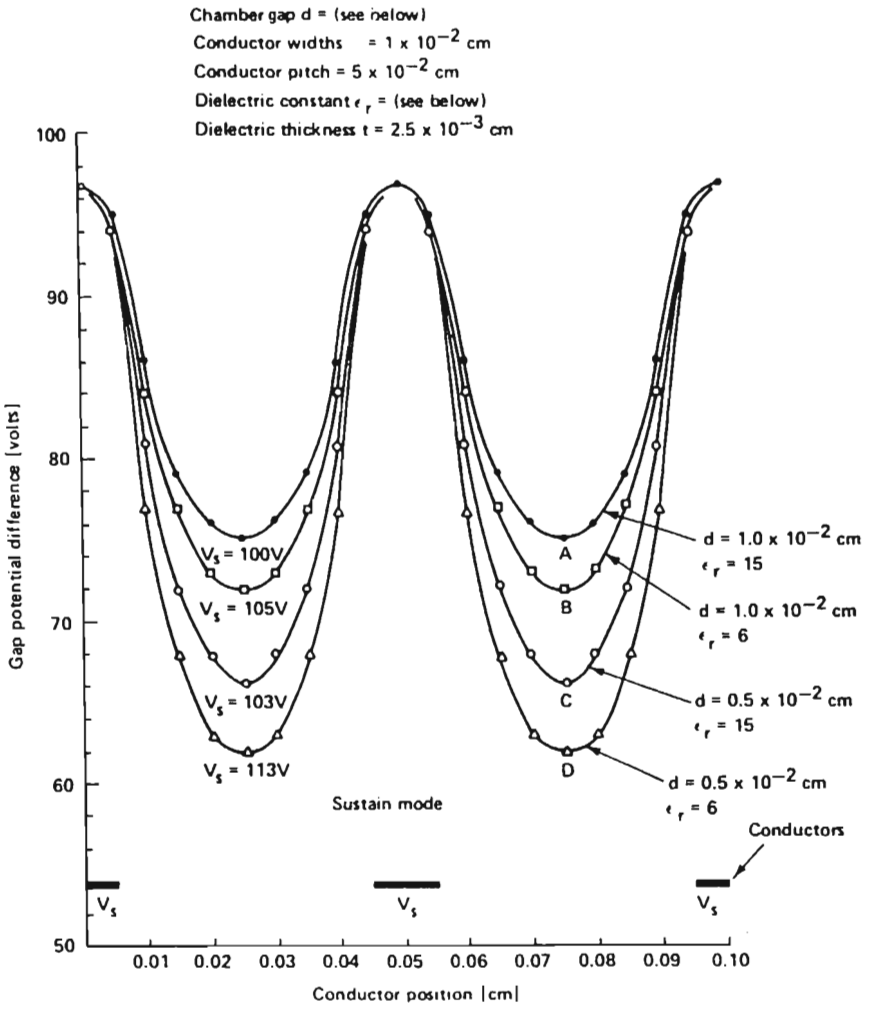


Figure 6 Computer simulation of potential across gap in plasma panel.

potentials are quite complex when multiple electrodes are considered, and Fig. 6 shows a computer simulation of such potentials.

Plasma panels are capable of displaying over 10^6 pixels, although resolution is inherently limited to below ~100 pixels per inch and color is hard to achieve. Nevertheless, plasma panels are mass produced for portable computers and banking terminals.

IV. ELECTROLUMINESCENT DISPLAYS

HFEL is not new (Destriau, 1936); however, significant technological changes have been made in device structures, and a much deeper understanding of the physics is now available.

In essence, HFEL devices initialize a strong electric field to generate hot electrons that are able to excite luminescence centers. Hence these electrons must have at least 2–3 eV of kinetic energy to allow them to excite visible luminescence. The most important material for achieving such luminescence is ZnS: Mn. ZnS has a large band gap (3.5 eV) that makes it transparent to visible light, and it efficiently generates hot electrons in electric fields of $\sim 2 \times 10^6$ V/cm. The means of applying such large fields has several variations. In the 1950s, powder devices were popular (Ivey, 1966). These contained 20–30 μm diameter grains of ZnS usually doped with copper. The copper acted as a luminescent center (although other metals such as Mn could also be used), but more importantly copper in the form of Cu_2S segregated at dislocations within such grains to yield tiny conductive needles buried within the grain. These needles were able to produce an enhanced electric field at their tips, which resulted in comet-shaped luminescent regions of the ZnS at the ends of the needles. See Fig. 7. A sandwich structure of a modern powder device

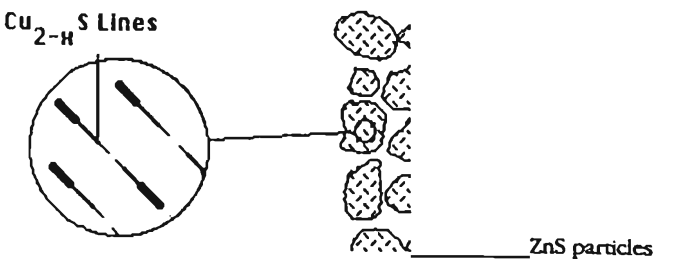


Figure 7 ZnS grains used in powder electroluminescent devices showing conducting $Cu_{2-x}S$ needles. The ZnS particles are typically 25 μm across. (From Chadha, 1992.)

is shown in Fig. 8. Such devices are used as backlights and touch-sensitive panels. The average electric field is only $\sim 10^5$/cm, which allows the use of low cost polymer dielectrics. This enables such devices to be flexible.

More recently (Inoguchi et al., 1974), thin film HFEL devices were developed. Here, as shown in Fig. 9, a thin film dielectric-semiconductor-dielectric sandwich is formed that is only ~ 1 μm thick in total. Preparation

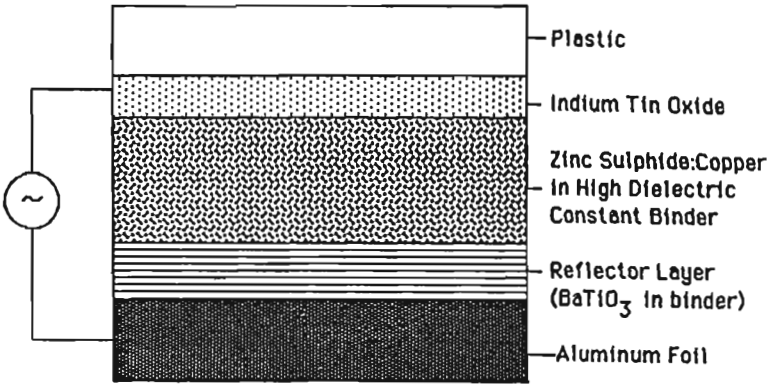


Figure 8 Powder electroluminescence device, used for backlighting. (From Chadha, 1992.)

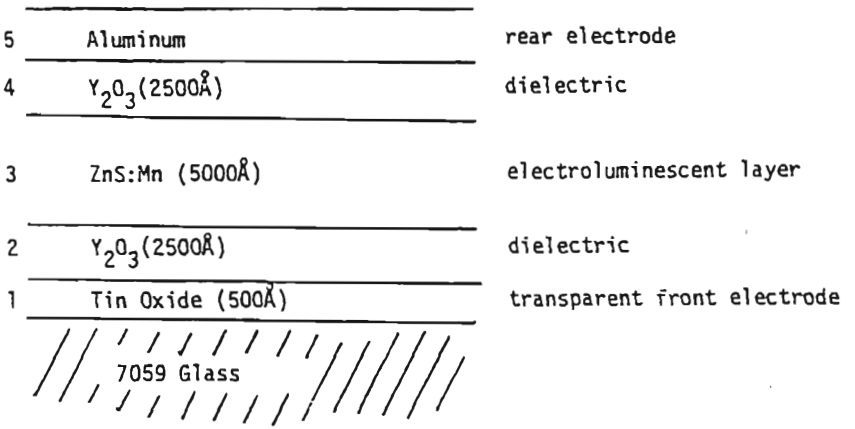


Figure 9 Thin film electroluminescent device.

is entirely by thin film vapor deposition, and a very steep brightness-voltage curve results, Fig. 10. The mechanism is a combination of tunneling, in which electrons trapped at surface states at the interfaces tunnel into the conduction band of ZnS and then gain kinetic energy, and avalanching, in which additional electrons are generated that increase the hot electron density. A band model is shown in Fig. 11.

Thin film HFEL devices have found application in matrix-addressed flat panel displays. They have the advantages of completely stable brightness with time and simple structure. Current difficulties include the lack of suitable phosphors for red, green, and blue color displays and the high cost of high voltage drivers for rows and columns. Nevertheless, HFEL is regarded as the ideal flat panel display because it is solid state, inherently light emitting, and rugged with respect to thermal and mechanical abuse.

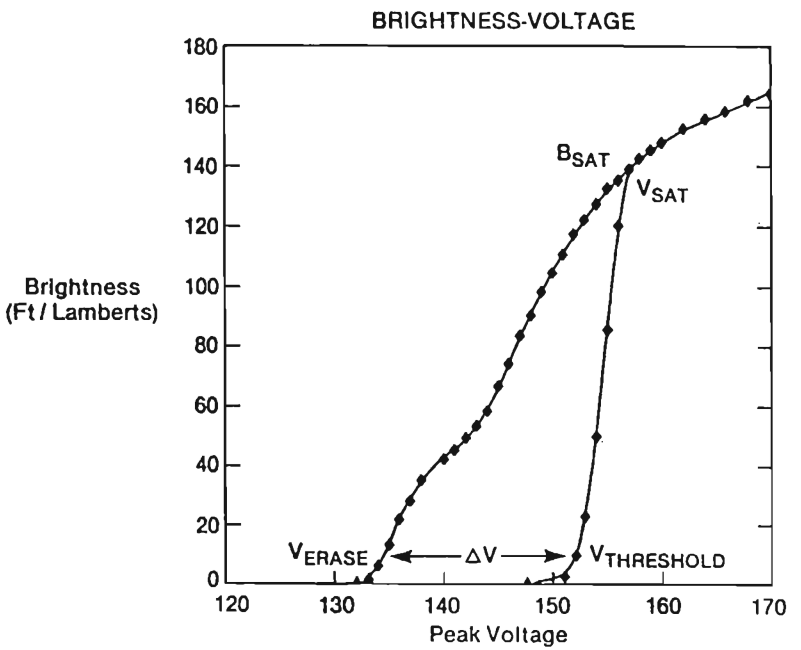


Figure 10 Brightness-voltage curve in thin film electroluminescent device showing steep brightness-voltage curve. This device also exhibits hysteresis. (From Hurd et al., 1979.)

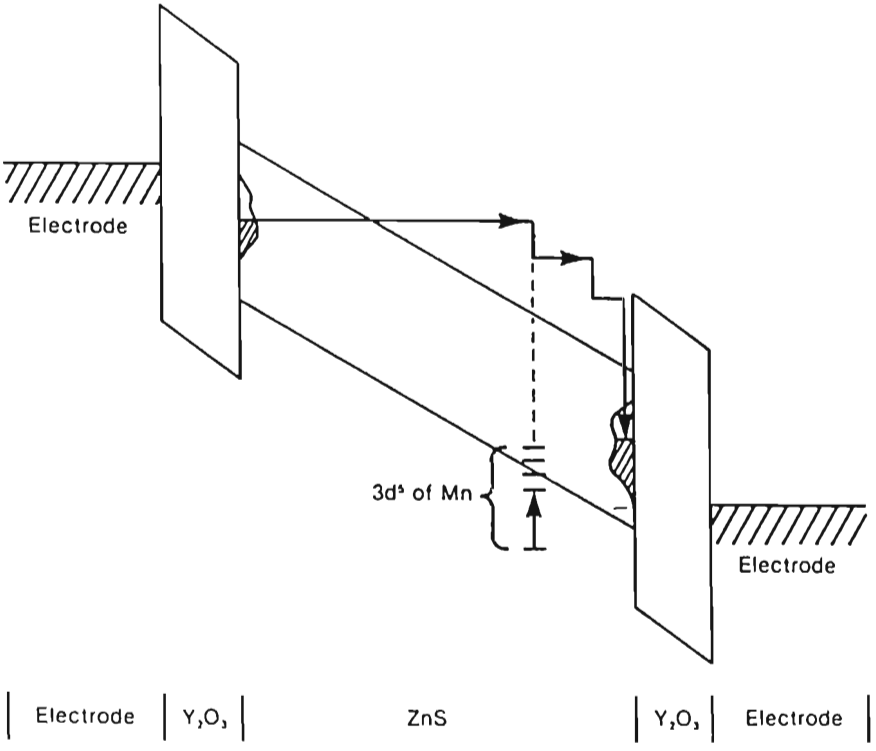


Figure 11 Band model of thin film EL device showing electron acceleration from interface states and impact excitation of Mn ions (the optically active center) in ZnS. (From Smith, 1981.)

V. LIQUID CRYSTAL DISPLAYS

The most important class of flat panel display now in large volume commercial production is the LCD. The near future will see widespread use of LCDs for color computer and data terminals, indicating the degree of development of this technology.

Under the application of an electric field, polar liquid crystal molecules will rotate or tilt so as to affect the polarization of the light shining through the medium, or alternatively so as to change the index of refraction of the medium along a particular axis. By suitable incorporation of the LC medium in an optical system, light may be efficiently modulated. Matrix addressing may be used to make high resolution displays of this type.

Two developments that now allow high resolution color LCDs to be achieved are thin film transistor arrays that individually address each pixel and color filters made in a dense three-color array to register with the LC cells.

Liquid crystal displays consist of a thin layer of liquid crystal material. Liquid crystals are organic materials that possess an intermediate phase between solid and isotropic liquid (Pankove, 1980), in which molecules interact with each other to produce various kinds of ordered states. The nematic phase has the molecules with major axes parallel to each other; the cholesteric phase has a helical structure of molecular ordering; and the smectic phases show layered structures with the major axes of molecules parallel within each layer. Since the materials are liquids, little energy is required to produce large changes in molecular ordering (see Fig. 12).

The ordering in a nematic phase in an electric field is dependent upon the elastic free energy density W_e, which is given in terms of a unit vector $d(x, y, z)$, known as the director, as

$$W_e = \frac{1}{2} K_{11}(\nabla \cdot d)^2 + \frac{1}{2} K_{22}(d \cdot \partial \times d)^2 + \frac{1}{2} K_{33}(d \times \nabla \times d)^2 \qquad (2)$$

Here, K_{11}, K_{22}, and K_{33} are the liquid crystal elastic constants and have typical values of $\sim 10^{-11}$ J/m.

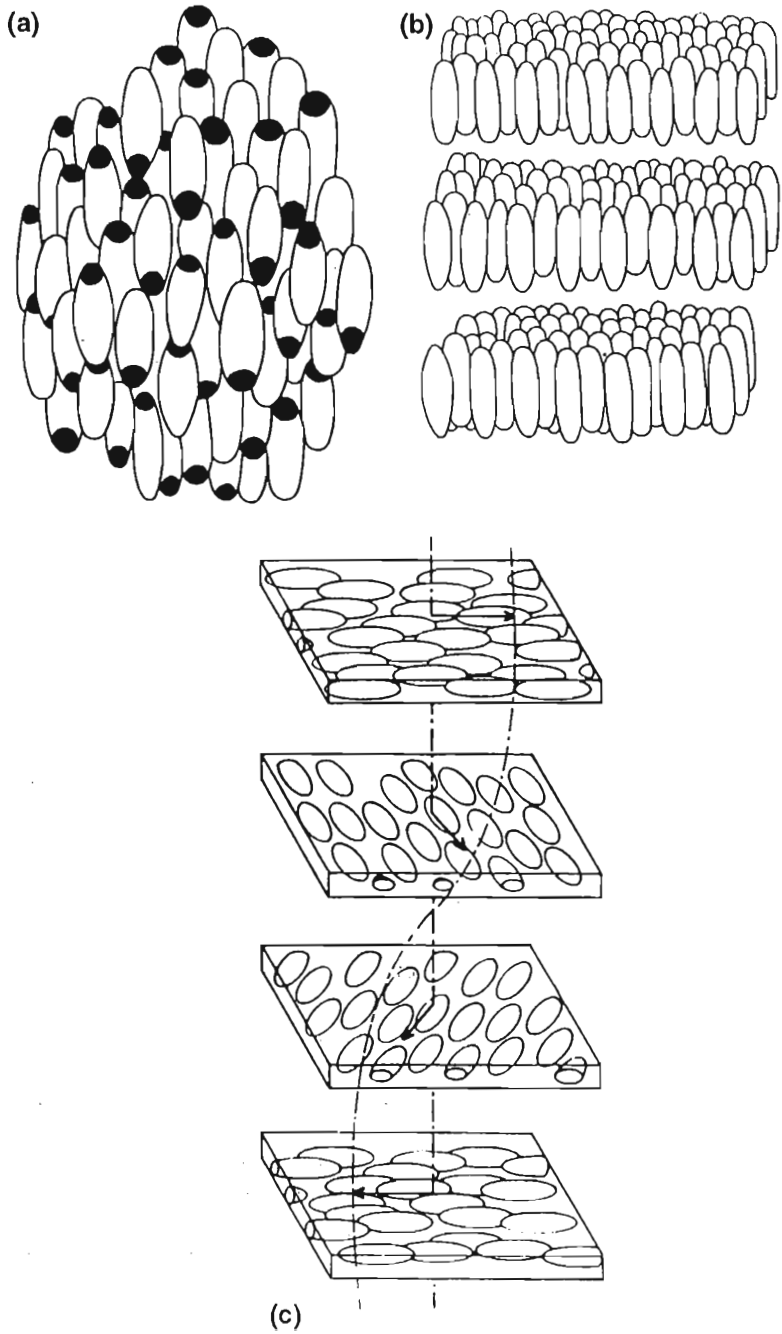
The electrostatic energy density due to the application of an electric field E is given by

$$W_d = -\frac{1}{2} \epsilon_\perp E^2 - \frac{1}{2} (\epsilon_\parallel - \epsilon_\perp)(d \cdot E)^2 \qquad (3)$$

where $\epsilon_\parallel$ and $\epsilon_\perp$ are the dielectric constants for E parallel and E perpendicular to d, respectively. Hence, if $\epsilon_\parallel - \epsilon_\perp > 0$, then W_d is minimized for $d \parallel E$, and if $\epsilon_\parallel - \epsilon_\perp > 0$, then W_d is minimized for $d \perp E$. Hence, a torque is exerted by E to rotate d to minimize W_d. Figure 13 shows a nematic material. Above a critical field, the molecules will align vertically as shown in Fig. 14.

Liquid crystals have two values of refractive index, n_0 for light polarized perpendicular to d and n_e for light polarized parallel to d. The optical birefringence $n_e - n_0$ may be as high as 0.3 in some nematics, far larger than solid state birefringement crystals with values like 10^{-4}.

There are three principal ways in which the director reorientation can be used to control light transmission. Most popular is through altering the polarization vector of light as it passes through the birefringement material. By placing polarizers on either side of the LC, light may be allowed to pass or may be blocked, depending upon the director orientations. A second method relies on random refraction of light passing through the LC


(a)
(b)
(c)

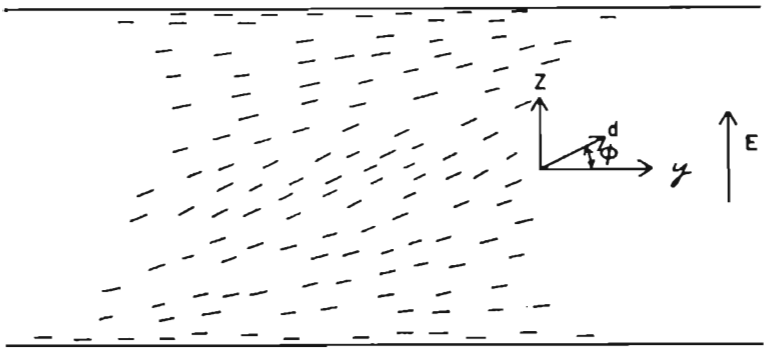


Figure 13 Orientation of nematic molecules with electric field perpendicular to glass surfaces.

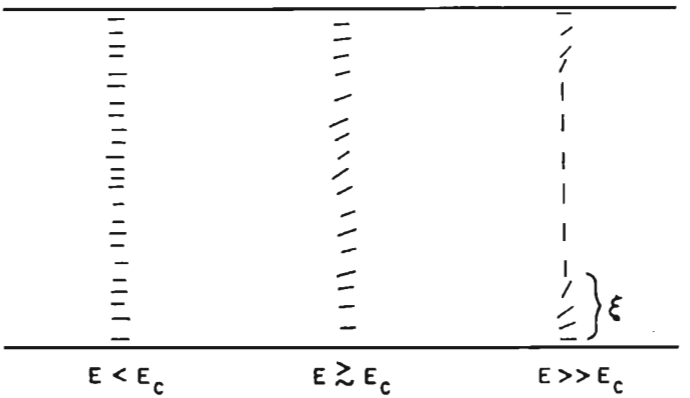


Figure 14 Response of nematic molecules showing the critical field E_c for molecular reorientation.

medium, which causes scattering. In a scattering state, light is reflected or scattered many times within the LC, and the device is opaque. Application of an electric field removes the random refraction, and light passes through. An important type of such an LCD is the polymer dispersed LCD. Here, rather than having a film of LC, a polymer that has micron sized pores filled with LC material is the active medium. When the refractive index of the LC is different from that of the polymer, light is scattered.

Figure 12 (a) Nematic, (b) smectic, and (c) cholesteric liquid crystal phases. (From Lerner, 1983.)

In an electric field, the LC refractive index changes to eliminate the scattering. Finally, it is possible to use the LC to orient molecules of dissolved dichroic dye, whose molecules reflect light with different spectral reflectivities depending upon the relative orientation of the molecule to the optical electric field. The advantage of the two latter techniques is that no polarizers are necessary.

More complex electric field effects also exist in liquid crystal materials (Helfrich, 1969). For example, in nematics, if the liquid is slightly conducting, the field E can induce an instability. First, the molecular alignment is slightly deformed by a thermal fluctuation. This reacts on the conduction-current pattern J and makes J inhomogeneous, resulting in a space charge Q, which results in liquid flow since force $F = QE$ acts on this space charge region.

REFERENCES

Chadha, S. (1993). Powder electroluminescence. In *Solid State Luminescence* (A. H. Kitai, ed.). Chapman and Hall, London, 159.

Destriau, G. (1936). Recherches sur les scintillations des sulfures de zinc aux rayons α". *J. Chim. Phys.*, 33, 587.

Helfrich, W. (1969). Conduction-induced alignment of nematic liquid crystals: basic model and stability considerations. *J. Chem. Phys.*, 51, 4092.

Hurd, J. M., and C. N. King (1979). Physical and electrical characterization of co-deposited ZnS:Mn electroluminescent thin film structures. *J. Electronic Materials*, 8, 879.

Inoguchi, T., Takeda, M., Kakihara, Y., Yashida, M., *Soc. for Information Display Int. Symp.* Digest of Technical Papers, 86, (1974).

Ivey, H. F. (1966). *Electroluminescence and Related Effects*. Advances in Electronics and Electron Physics. Academic Press, New York, Suppl. 1.

Lerner, R. G., and G. L. Trigg (1983). *Concise Encyclopedia of Solid State Physics*. Addison-Wesley, Reading, Mass. 144–147.

Pankove, J. I. (1980). *Display Devices*. Springer-Verlag, Berlin; New York. 1.

Smith, D. H. (1981). Modeling a.c. thin-film electroluminescence devices. *J. Luminescence*, 23, 209.

Spindt, C. A., I. Brodie, L. Humphrey, and E. R. Westerberg (1976). Physical properties of thin film field emission cathodes. *J. Appl. Phys.*, 47, 5248.

Stowell, R. D. (1984). Recent progress in low voltage field emission cathode development. *J. de Phys.*, 9, 269.

17

Applications of the Electrostatic Separation Technique

K. Haga

Fuji Electric CRD Company, Ltd.
Kanagawa, Japan

I. INTRODUCTION

Separation and classification are very important elemental manufacturing processes in many industries such as the mining and chemical industries. Equipment using many different methods of separation are applied in these processes.

Electrostatic separation (including electrostatic classification) is one separation method. This method, relying on the differences of electrostatic characteristics inherent in different materials, has an unexpectedly long history, with initial patents (to remove impurities from grain (Murata, 1982)) having been awarded 100 years ago. Since then the method has found application mainly in the separation of impurities in raw ore.

After an initial overview of the electrostatic technique, this paper will discuss a number of interesting applications of the technique in the fields of ore, coal, food, and scrap processing. Finally, a few new applications will be discussed.

II. OVERVIEW OF THE ELECTROSTATIC SEPARATION TECHNIQUE

Many methods (Murata, 1982; Haga, 1983; Haga, 1986) are used for the separation of a class of particles from a mixture based on size or some

other property. Some examples are particle size using sieves; density using wind, water or another liquid, or magnetic fluid force; surface phenomenon characteristics using float separation or oil agglomeration; and electromagnetic characteristics using electrostatics, magnetics, or eddy currents.

The electrostatic separation method utilizes inherent differences in friction charge characteristics, electric conductivity, and dielectric constants between substances. Since individual particles behave differently under the application of electrostatic, gravitational, and centrifugal forces, separation is possible. Electrostatic force is proportional to the surface area available for surface charge, while gravity is proportional to the mass of

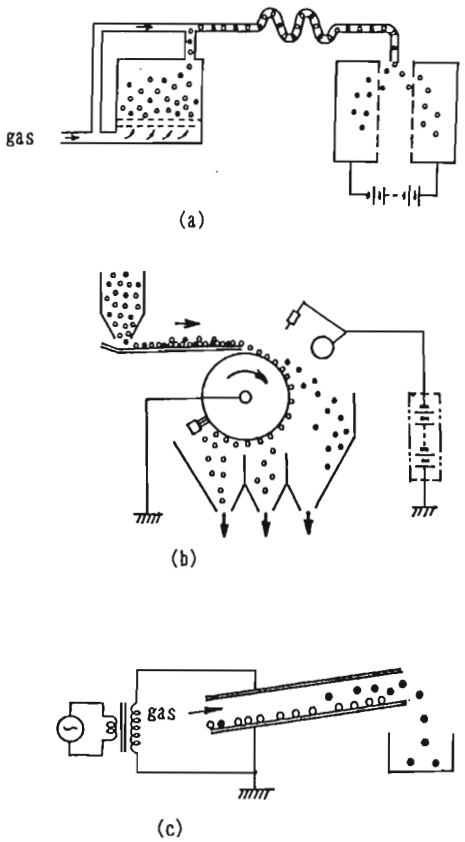


Figure 1 Representative methods of electrostatic separation. (a) Contact charge; (b) ion attachment; (c) induced charge. (From Kasai, 1981.)

the particle; so for objects with large surface areas relative to their masses (i.e., a small diameter particle, a thin sheet, a short fiber, or a light object) a small electrostatic force has a large effect, thus allowing efficient separation of the particles.

For electrostatic separation, particles must first be charged. A number of methods are currently used to charge the particles, including contact and collision friction charge; induced charge, electron or ion collision charge; pyroelectric effect; and field emission by light and radiation. An electrostatic force (Coulomb, image, or gradient) is then applied along with gravity, wind, or an alternating current. Three typical implementations of the technique are illustrated in Fig. 1 (Kasai, 1981).

III. INDUSTRIAL APPLICATIONS OF ELECTROSTATIC SEPARATION

A. Mining industry

Electrostatic separation has long been used to separate dry ore. Charging has primarily been by means of corona discharge, induced charge, or contact charge. Separation relies on the differences in conductivity between ores. For example, ilmenite (Fe, Mg, TiO_2), rutile (TiO_2), galena (PbS), and iron pyrite (FeS_2) exhibit good conductivity, while quartz (SiO_2), zircon ($ZrSiO_4$), monazite ($CePO_4$), and diamond exhibit poor conductivity. Various processes (depending on the composition of the ore) are utilized to create a large variation in surface resistance from particle to particle. A number of these processes are summarized in Table 1 (Beddow, 1981). In addition, the pyroelectric effect is used in the separation of feldspar from rock crystal, and gradient force acting of the polarized dielectric is used to separate rutile from vinyl chloride (Murata, 1982).

Recently, many researchers have been studying new methods of electrostatically classifying inorganic substances. Fig. 2 shows a classification apparatus utilizing a nonuniform electric field to investigate copper particles from 37 to 840 μm in diameter. The apparatus consists of two plate electrodes with some inclination angle to which are applied an alternating high voltage. As the electric field between the two electrodes is bent in an arc, moving particles experience a centrifugal force, being deflected toward the wide gap. As seen from the experimental results shown in Fig. 3 (Murata et al., 1982), the larger the particle size difference, the more effective the separation.

A classification method utilizing three-phase alternating current charging equipment using the principle of the boxer charger is illustrated in Fig. 4 (Ashizawa et al., 1983). The results of an experiment using this apparatus

Table 1 Typical Application Examples of Electrostatic Separator

Ore to be separated	Surface treatment	Charging method
Iron glance(Fe_2O_3) ~ quartz(SiO_2)	drying	corona discharge
Ilmenite (Fe, Mg, TiO_2) & rutile (TiO_2) ~ zircon ($ZrSiO_4$) & monazite ($CePO_4$) etc. after specific gravity separation	cleaning, drying for removing organic matter in raw ore at 650°C	corona discharge
Zircon ~ ilmenite	drying	corona discharge
Tin stone ~ anorthite	drying	corona discharge or induced charge
Feldspar ~ quartz	drying, HF vapor	contact charge
Rock salt (NaCl) ~ potash rock salt (KCl)	340°C heating & drying, annexed fatty acid 1 lb/t	contact charge
Iron pyrite(FeS_2) ~ coal	drying	corona discharge or induced charge
Coal ~ oil shale	humidity adjustment	corona discharge or induced charge
Diamond ~ silica	water cleaning & drying in muddy NaCl	induced charge

Source: Beddow (1981).

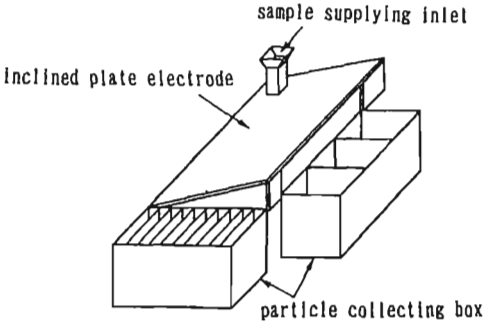


Figure 2 Classification apparatus using nonuniform electric field. (From Murata et al., 1982.)

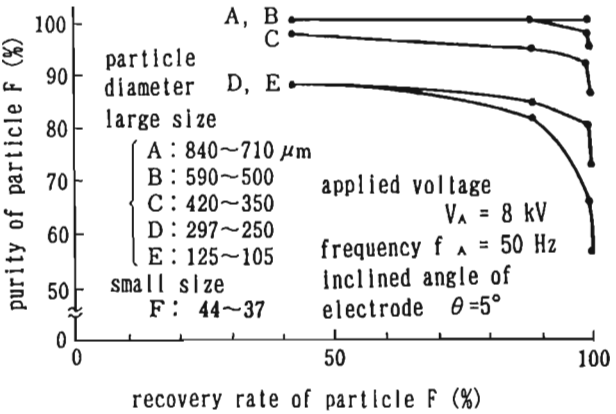


Figure 3 An example of experimental results. Separating characteristics of smaller particles F from bigger particles A to E with weight ratio 1 to 1. (From Murata et al., 1982.)

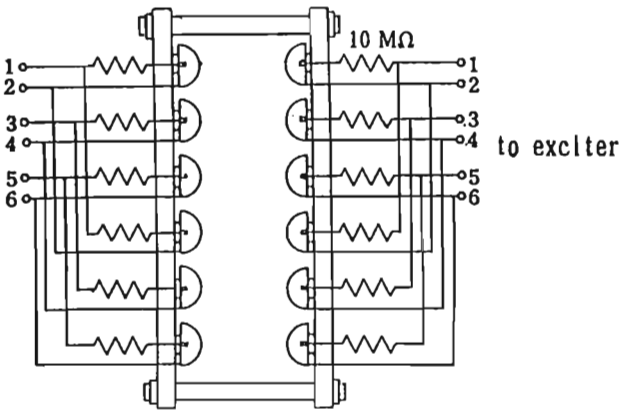


Figure 4 Three phase alternating current charging equipment using the boxer charger principle. (From Ashizawa et al., 1983.)

for the separation of 0.5 to 10 μm bridged polystyrene particles is shown in Fig. 5 (Ashizawa et al., 1983). In Fig. 6(a) (Tsuruta et al., 1985) a method utilizing a number of electrodes arranged as parallel cylinders is illustrated. When an alternating voltage is applied between adjacent electrodes, charged particles are forced to vibrate. Results relating to the

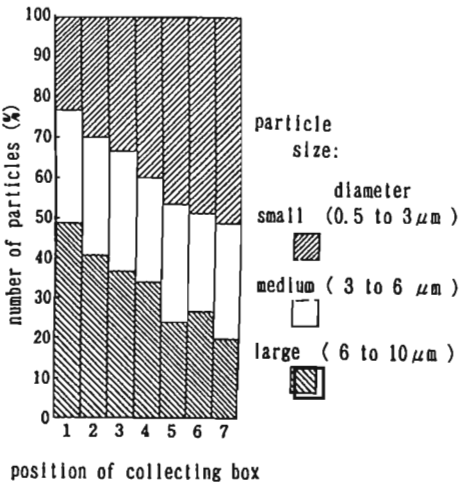


Figure 5 Sample results for the separation of bridged polystyrene particles. (From Ashizawa et al., 1983.)

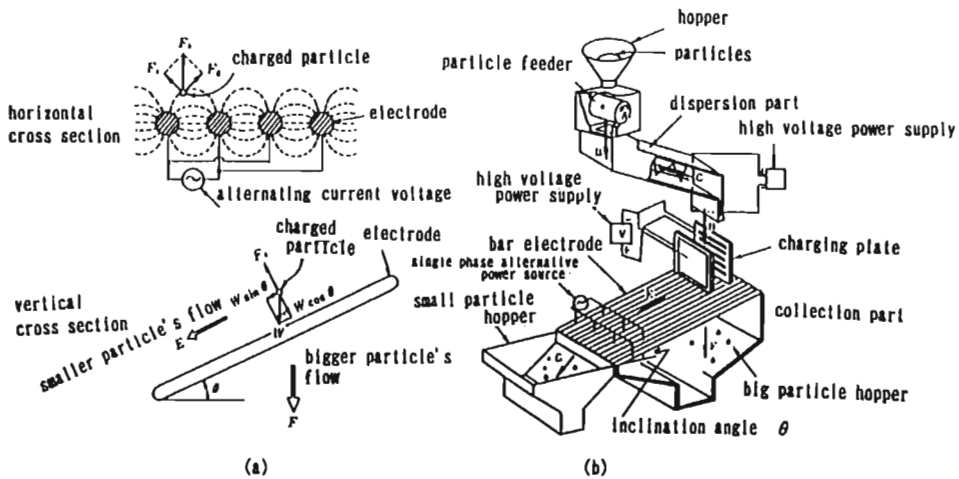


Figure 6 Electrostatic separator using single phase ac voltage. (a) Principle; (b) equipment. (From Tsuruta et al., 1985.)

separation of SiC particles using equipment based on this method (Fig. 6b) are shown in Fig. 7.

The apparatus shown in Fig. 8 (Dunn, 1977) is used for the separation and transportation of particles. Particles supplied from the feeder undergo oscillatory motion between the high voltage electrode and the earth ground. Separation is accomplished by the use of a 325 mesh sieve maintained at high voltage. Test results for the separation of molybdenum

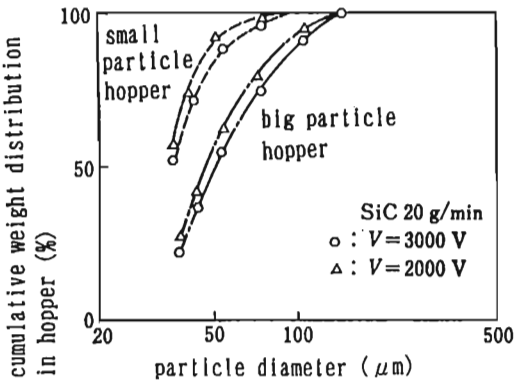


Figure 7 Sample result for the separation of SiC particles. (From Tsuruta et al., 1985.)

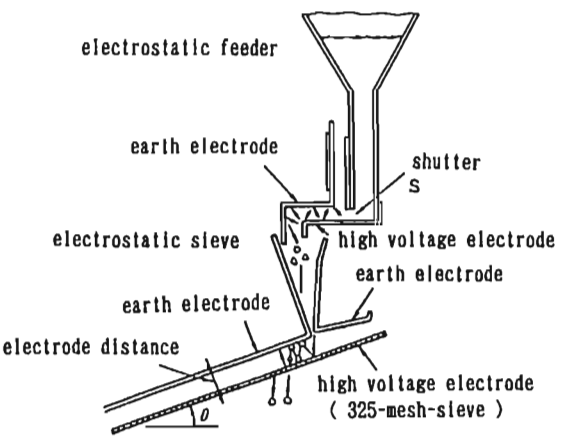


Figure 8 Electro/feeder/sieve equipment. (From Dunn, 1977.)

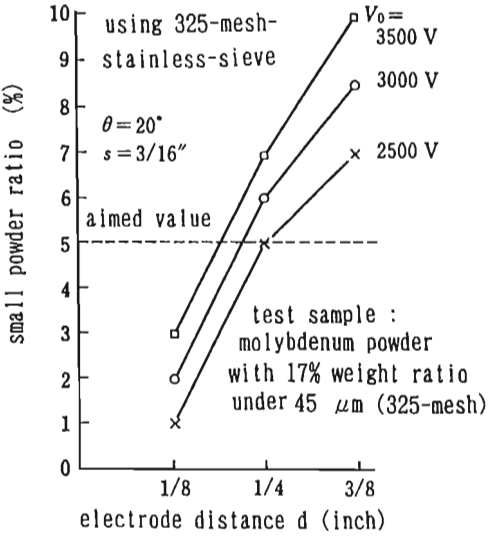


Figure 9 Separation efficiency for molybdenum powder. (From Dunn, 1977.)

powder are shown in Fig. 9. Adjustment of electrode voltage and gap width allow the distribution of particles on the sieve to be controlled.

B. Coal Industry

As coal remains a primary fuel in many countries around the world, the treatment of the ash and the reduction of emissions generated by combustion are serious problems. Separation techniques are researched and applied in all countries of the world. The scale of these techniques ranges from the simple techniques used by a peasant lady to create soap from the ashes in her fireplace to those utilized by large government projects. Technically, one speaks of separation principles such as gravity difference (heavy liquid, jigging separation), surface phenomena (floating, oil agglomeration), and electromagnetic (high gradient magnetic separation, electrostatic separation) (Toraguchi and Haga, 1982).

The equipment shown in Fig. 10 (Inculet et al., 1979) illustrates the application of the principle of collision charging between particles to effect separation. It consists of a vibrating feeder for feeding of fine coal powder, a floating layer bed made of copper in which collision charging takes place, parallel plate electrodes, and collecting boxes. High voltage dc is applied between the two electrodes. A mixture of coal particles and impurities

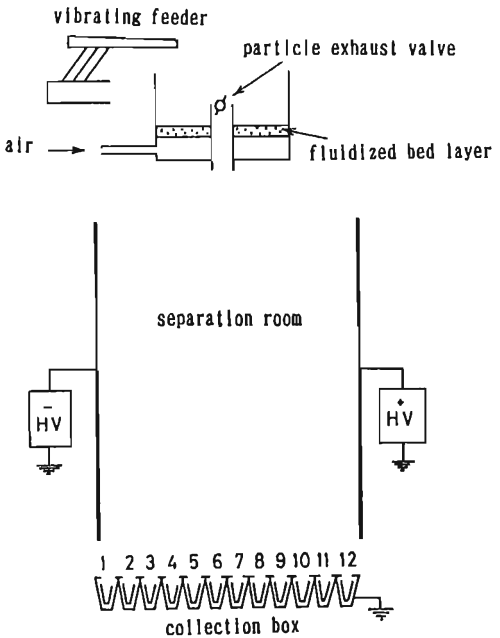


Figure 10 Fluidized bed charging type electrostatic separator. (From Inculet et al., 1979.)

(<150 μm diameter) is fed into the floating bed. As the particles collide with each other the coal particles become positively charged, and impurities, such as ash, become negatively charged. Under the influence of gravity, coal particles tend to fall into boxes closer to the negative electrode while impurities tend toward those boxes closer to the positive electrode. Sample results for a multistage separator are shown in Fig. 11 (Inculet et al., 1980). 100 g of 52.3% purity coal:ash mixture is input. After three stages, 58.7 g of 70.4% purity coal is successfully separated out of the coal:ash mixture. 85.4% of the coal is recovered.

Methods utilizing contact charging between particles and solid walls have also been studied. These methods include the cyclone (Fig. 12; Masuda et al., 1981; Masuda et al., 1983) and rotating cone (Fig. 13; Toraguchi and Nagasawa, 1982) type charger. As illustrated by the results shown in Table 2 (Toraguchi and Nagasawa, 1982), coal recovery efficiency for rotating cone type electrostatic separation (~50%) devices is much poorer than for gravity type separation devices (~90%).

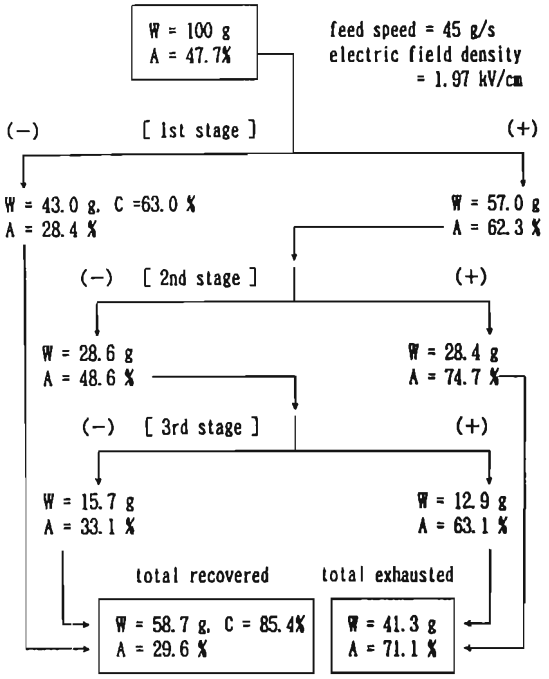


Figure 11 A test result using multistage separation. W, coal mixture weight (g); A, ash part (%); C, coal recovery factor (%). (From Inculet et al., 1980.)

Using ordinary mineral electrostatic separation techniques, equipment developed by Advanced Energy Dynamics, Inc., was able to reduce the ash ratio by 30 to 60% and the sulfur ratio by 60 to 90% (Toraguchi and Haga, 1982). In the electrostatic separation of fine coal powder for electric power generation, cyclone type separation has been reported to be more efficient than floating layer bed and drum type for removing of iron sulfide (Bouwma et al., 1984). Equipment combining an electrostatic floating layer bed and a separation room is shown in Fig. 14 (Ogata, 1985). Figure 15 shows sample results for equipment utilizing a coflow type electrostatic floating layer bed. The inner diameter is 27.9 cm. The spacing between the electrodes is 9.5 cm. The separation test result for a mixture of 25% coal and 75% sand shows that the separation efficiency is strongly dependent on the applied voltage.

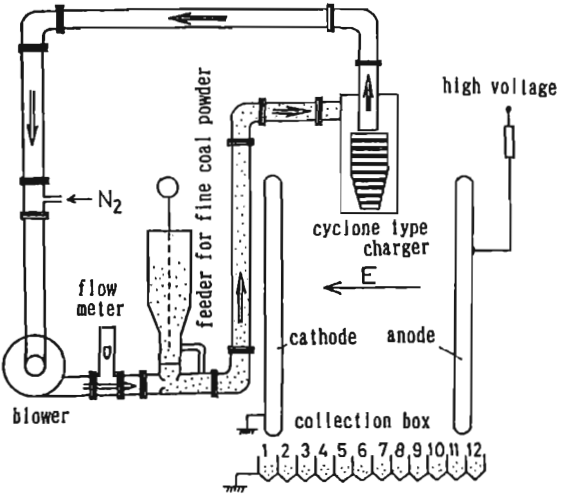


Figure 12 Cyclone charging type electrostatic separator. (From Masuda et al., 1983.)

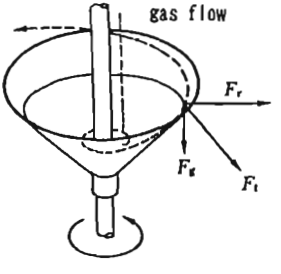


Figure 13 Rotating cone type charger. (From Toraguchi and Nagasawa, 1982.)

C. Food Industry

Electrostatic separation is also applied in the food processing industry. An interesting example is the equipment used for separating leaves and stems in the tea industry. The "Denkiboutoriki" (electric tea stem separator) was first put to practical use after 1953 and has now become standard equipment in this industry. As the physical characteristics of tea leaves (specific gravity, mass) are similar to those of the tea stem, separation schemes using sieves or wind power are very difficult to implement and,

Table 2 Comparison Between Electrostatic Separation and Gravity Separation (%)

		Electrostatic separation			Gravity separation			
Kind of coal	Ash part in raw coal	Ash part in refined coal	Ash removed ratio	Coal recovery ratio	Equi. specific gravity	Ash removed ratio	Coal recovery ratio	Comparison of recovery
A	17.4	9.4	50.8	85.0	1.72	54.5	90.5	94
B	13.4	7.4	67.3	63.3	1.66	58.5	79.2	80
C	20.2	9.3	75.0	61.6	1.68	59.0	91.4	67
D	15.5	10.7	64.9	53.7	2.0 <	33.3	98.1	55

Source: Toraguchi and Nagasawa (1982).

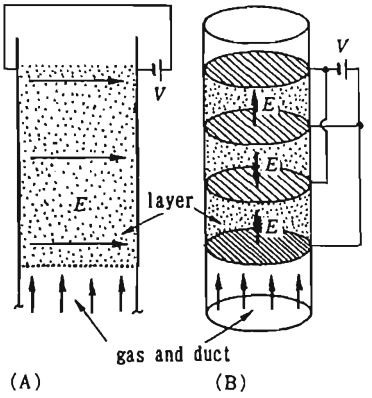


Figure 14 Electrode configuration for floating layer bed. (A) Cross flow; (B) coflow. (From Ogata, 1985.)

when implemented, operate at low efficiency. Electrostatic separation, however, can provide quite efficient separation. This is because a slight difference in water content ratio between the leaves and the stems results in a difference in dielectric constant and conductivity. Figure 16 illustrates equipment of the electrostatic induction type consisting of a two-stage rotating drum. The drum surface is roughened to prevent the adherence of tea leaves or stems (Fig. 17; Masui, 1982). By ensuring that the water content of the leaves and stems is about 7%, high separating efficiencies can be obtained.

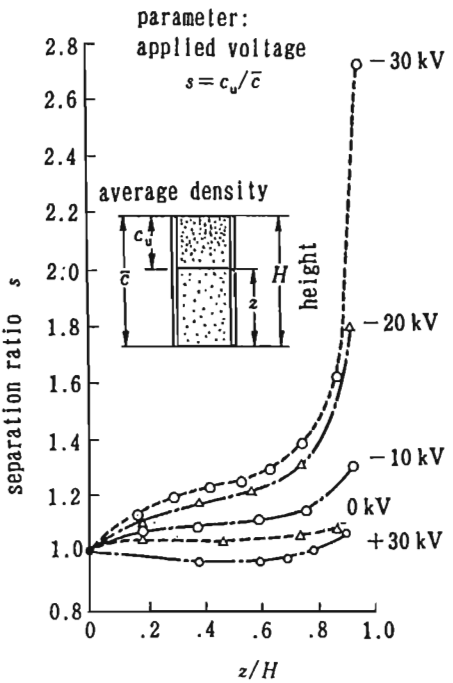


Figure 15 Sample result for the separation of coal from a coal-sand mixture. (From Ogata, 1985.)

Electrostatic separation has also been used in the removal from food of impurities such as hair, waste straw, scrap paper, plastics, and dead insects. Figure 18 (Masui, 1982) shows the main parts of an actual food separator. Foods are carried on a vibrating conveyer under high voltage electrodes. Impurities in the food are attracted to the electrodes and then carried away by suction pumps. A few examples of this type of equipment are listed in Table 3 (Masui, 1982).

D. Waste Processing Industry

Two applications of electrostatic separation are at the stage of practical application: the separation of copper electrical wire and the separation of compostable materials. Others, such as the separation of paper and plastic film (Kimura, 1981), and aluminum and organic substances (Cederholm, 1977) are documented in the literature.

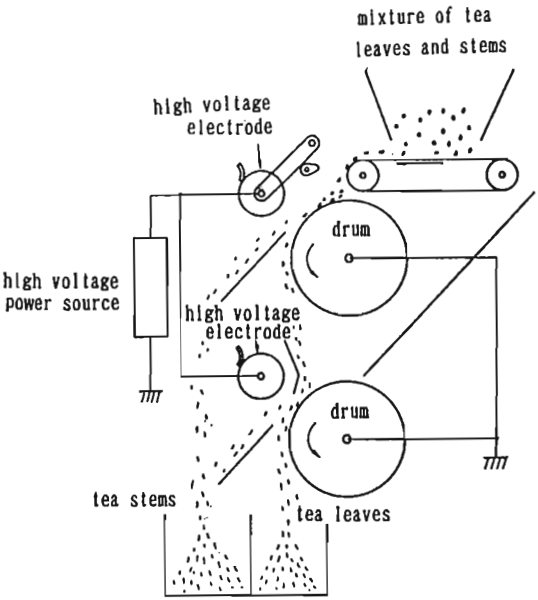


Figure 16 Electrostatic induction type separation of tea leaves and stems. (From Masui 1982.)

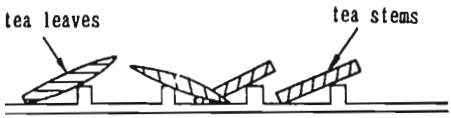


Figure 17 Rotating drum surface of electric tea stem separator. (From Masui, 1982.)

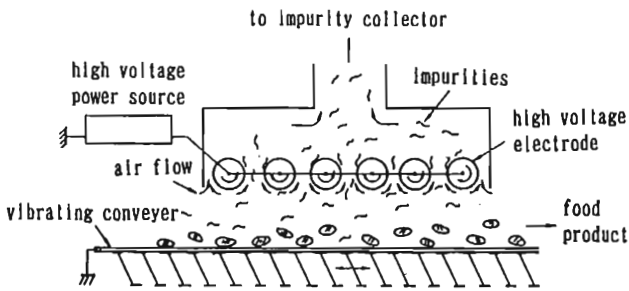


Figure 18 Main parts of electrostatic separator for removing impurities in foods. (From Masui, 1982.)

Table 3 Some Examples Using the Induction Type Electrostatic Separator

Raw material for general foods	Typical impurities for removing
1 Dried cuttlefish stick	hair
2 Chinese bamboo sprout	hair, thread chip, waste straw
3 Small fish	waste straw
4 Tangle	waste straw
5 Edible seaweed	waste straw
6 Dried laver	small shell
7 Dried mushroom chip (shiitake)	hair, waste straw
8 Dried vegetable	hair
9 Mushroom (enokitake)	hair
10 Drug	hair
11 Buckwheat	husks of buckwheat
12 Nut	husks of nut
13 Raw material for reclaimed plastics	hair, scrap of paper
14 Plastics molding	hair

Source: Masui, 1982.

There are a number of methods currently available for the separation out of copper in used electric wire such as burning, stripping, heavy liquid separation, dissolution, and electrostatic separation. Electrostatic separation has the advantages of high recovery efficiency, a high degree of purity, and freedom from pollution. An example of the type of equipment in current use is shown in Fig. 19 (Kojima, 1982). The electric wire and

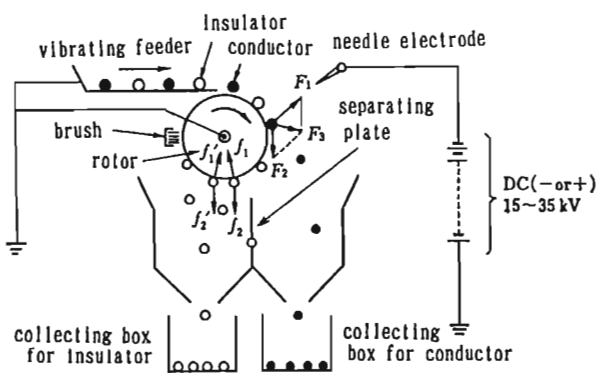


Figure 19 Principle of electrostatic separator for electric wire chips. (From Kojima, 1982.)

insulation is first crushed into millimeter long pieces. These pieces are then carried from a vibrating feeder to the rotor surface where they are given an electric charge from a needle electrode array. The rate of charge dissipation controls when the particles fall from the rotor. When used in a three stage configuration, copper can be extracted with over 99% efficiency. However, as this method relies on costly crushing and sieving equipment, it is only suitable for large scale processing.

An example of the application of electrostatic separation to the composting of garbage is shown in Fig. 20 (Takahashi et al., 1980). As compostable particles after fermentation are all under several millimeters in size, inert materials such as glass, plastics, and ceramics can be removed by means of electrostatic separation. In the equipment shown in Fig. 21 (Onuma and Suzuki, 1979), two cascade stages are employed, and separation is achieved due to differences in specific gravity and conductivity between the two type of particles. In practice, compostable materials with

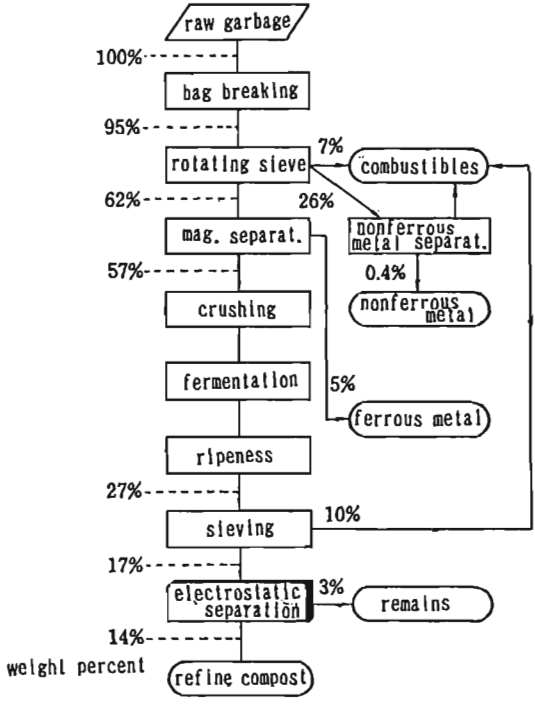


Figure 20 Flow sheet of compost plant for garbage. (From Takahashi et al., 1980.)

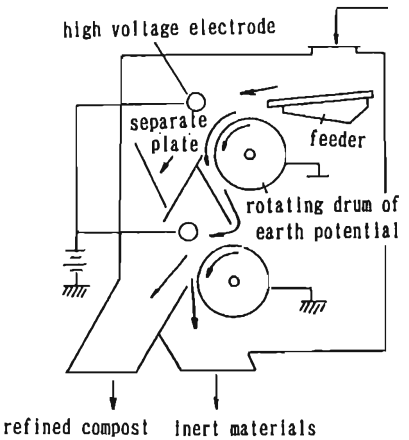


Figure 21 Rotating drum type electrostatic separator with two cascade stages. (From Onuma and Suzuki 1979.)

impurity rates between 8 and 25% have been reduced to under 0.5%. Highest efficiency is achieved when the water content is near 27%. The equipment in Fig. 21 employs a high voltage corona electrode to induce charge in the particles. The principle of operation of a similar piece of equipment in which the corona electrode has been replaced by a plate electrode is illustrated in Fig. 22. Compostable particles in predominately

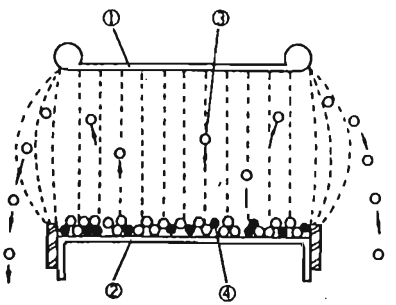


Figure 22 Principle of plate type electrostatic separator. 1, high voltage electrode; 2, earth electrode; 3, compost particles; 4, glass particles. (From Takahashi, 1982.)

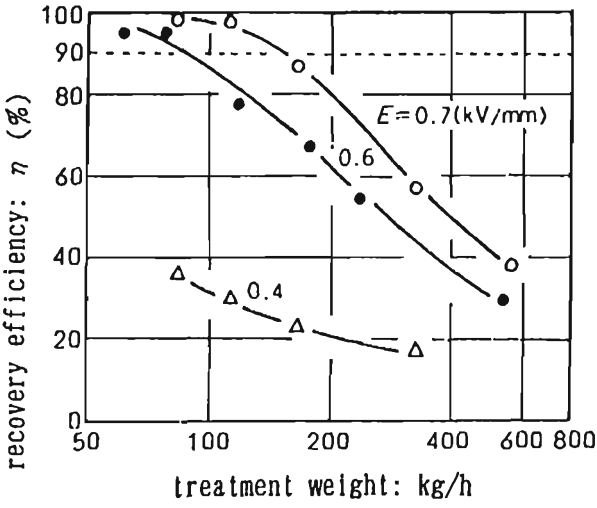


Figure 23 Recovery efficiency of plate type electrostatic separator. (From Takahashi, 1982.)

inert waste are fed in on the lower side of the toroidal electrodes, which rotate with constant intensity. Under the influence of the electric field, compostable particles oscillate in a vertical direction and eventually move out of the electrode. The results are illustrated in Fig. 23 (Takahashi, 1982) and show that compostable materials can be recovered with 99.5% purity. The rate of recovery of compostable material was found to be relatively independent of their water content in the range of 10 to 35%.

IV. APPLICATIONS TO SOLID-LIQUID SEPARATION AND ELECTROPHORESIS

In a wide sense, electrostatic separation may include the separation using static electricity of solid particles or colloidal liquid particles floating in liquid. In general, small particles in a liquid have a slight positive or negative charge on their surface. Fig. 24 (Murata, 1982) illustrates a plate electrode configuration for removing impurity particles in oil. The impurity particles are drawn and adhere to the plate electrodes and pleated dielectric. This apparatus can reduce impurities in oil by over two orders of magnitude for a wide range of particle sizes as seen in Fig. 25 (Murata, 1982).

This migration of electrically charged particles in solution or suspension under the influence of an externally applied electric field is known as

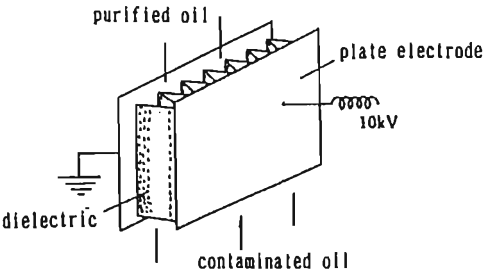


Figure 24 Electrode configuration for removing impurity particles in oil. (From Murata, 1982.)

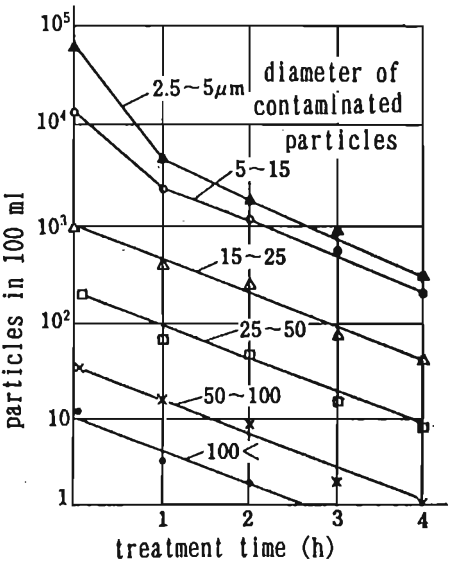


Figure 25 Sample result for the removal of impurity particles in oil. (From Murata, 1982.)

electrophoresis. Initially observed by the Russian physicist F. F. Reuss in 1807, electrophoresis has found wide application in the separation of polymers, starting around 1937 when Arne Tiselius separated blood into its three constituent parts, alpha, beta, and gamma globulin. Three main methods currently employ the principle of electrophoresis: the zone, the continuous, and the equipotential method (Freifelder, 1979; Ui and Horio, 1980). Figure 26 (Freifelder, 1979) illustrates an apparatus of the continuous free flow type. Buffer liquid is flowed continuously and uniformly in

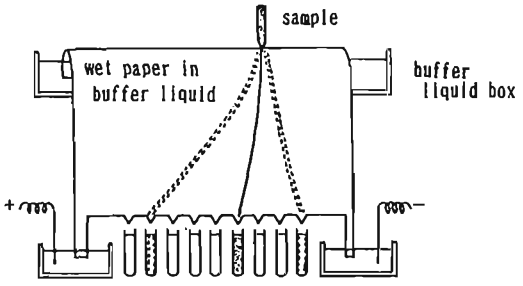


Figure 26 Continuous flow type electrophoresis equipment. (From Freifelder, 1979.)

the vertical direction, while an electric voltage is applied in the horizontal direction. The sample is injected at one point near the buffer reservoir and is carried by the buffer solution to the collection bins. Proteins, peptides, amino acids, and inorganic ions can be separated using this method. Figure 27 (Kaneko et al., 1984) shows similar equipment, along with sample results for the separation of X and Y spermatozoa.

Neutral particles in an electric field become polarized, and in the case of a nonuniform electric field migrate toward the region where the electric field is most dense. Application of this phenomenon, called dielectric cata-

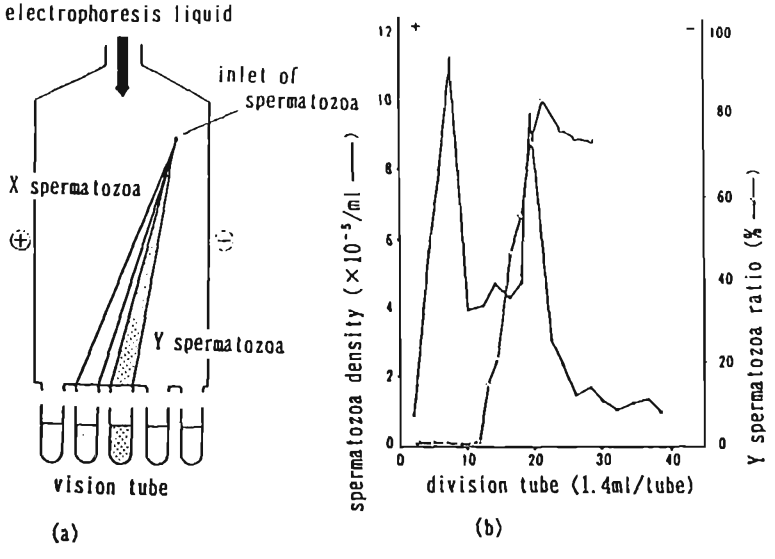


Figure 27 Separation of X and Y spermatozoa using free flow type electrophoresis equipment. (a) Principle; (b) sample result. (From Washizu, 1986.)

phoresis, to the manipulation of cells is currently being investigated (Washizu, 1986).

V. CONCLUSION

Electrostatic separation has the advantages of being more effective for small particles and less energy intensive than other methods. It also has a comparatively simple configuration. In order for electrostatic separation to gain a wider acceptance in industry, two main areas require further research.

The first area is related to the basic components of electrostatic separation—particle charging and electric field configuration. Further research is required into the methods of applying uniform electric charge to many particles. Research into the optimum electric field configuration for separation, taking into account other working forces such as gravity, must be continued.

The second area revolves around the equipment configuration and the efficient integration of electrostatic processing into the whole separation system. As the input to the separation process is natural materials having various dielectric and physical properties, the optimum equipment configuration will depend on its function. In addition, the cost-effective application of crushing, temperature, and humidity must be considered. In short, the trade-offs involved in setting up a complete separation system must be explored and analyzed.

In the future, it is expected that application of electrophoresis, dielectric cataphoresis, and electrostatic fluidized beds for solid-liquid separation will spread in the fields of polymer and biotechnology.

REFERENCES

Ashizawa, K., K. Fujibayashi, N. Murasaki, and M. Matsui (1983). Study on electrostatic powder classification by traveling-field-type charger. Conf. paper of the IEJ, Tokyo, pp. 83–85.

Beddow, J. K. (1981). Dry separation techniques. *Chem. Eng.*, 88, 16, pp. 70–84.

Bouwma, J., B. Kuypers, V. Vlasblom and A. Van der Waal (1984). Coal cleaning using electrostatic separation. *Electr. Magn. Sep. Filter Techn.*, 145–150.

Cederholm, C. (1977). Rohstoffe aus Haushaltsmüll. *TIZ Fachberichte*, 7/8, 182–186.

Dunn, J. P. (1977). The electro/powder separation process. *Int. Powder Metall Conf.*, 5, 9, 191–201.

Freifelder, D. (1979). *How to Research for Biochemistry (Mainly Physical Methods)—Electrophoresis* (H. Noda, tr.). Tokyo Kagaku Doujin, Tokyo, pp. 189–211.

Haga, K. (1983). Applications of electrostatic separation technique. Conf. paper of the IEJ, Tokyo, pp. 3–8.

Haga, K. (1986). Applications of the electrostatic separation technique. *Proceedings of the IEJ*, 10.6, 451–459.

Inculet, I. I., M. A. Bergougnou, R. M. Quigley, and J. D. Brown (1979). Fluidized electrostatic removal of mineral matter from coals mined at Hat Creek, British Columbia, Canada. *Conf. Rec. IEEE/IAS 1979 Annu. Meet.*, pp. 112–116.

Inculet, I. I., M. A. Bergougnou, R. M. Quigley, J. D. Brown, and D. K. Fraurshou (1980). The electrostatic separator with fluidized bed. *CIM Bull.*, p. 59.

Kaneko, T., R. Iizuka, S. Oshio, and H. Mouri (1984). Separation of X- and Y-bearing spermatozoa. *Proceedings of the IEJ*, 8, 3, 192–198.

Kasai, Y. (1981). Electrostatic separation. In *Handbook of Electrostatics* (Institute of Electrostatics of Japan, ed.). Ohm Press, Tokyo, pp. 586–591.

Kimura, K. (1981). Separation techniques for solid waste. *Chemical Engineering*, 26, 5, 68–74.

Kojima, J. (1982). Electrostatic separation for copper from crushed small chips of used electric wire material. *Proceedings of the IEJ*, 6, 3, 159–162.

Masuda, S., M. Toraguchi, T. Takahashi and K. Haga (1981). Electrostatic beneficiation of coal using a cyclonetribocharger. Conf. paper of the IEJ, Tokyo, pp. 77–80.

Masuda, S., M. Toraguchi, T. Takahashi, and K. Haga (1983). Electrostatic beneficiation of coal using a cyclonetribocharger. *IEEE Trans. Ind. Appl.*, IA-19, 5, 789–793.

Masui, N. (1982). Electrostatic separation for removal from green tea of stems and from food of impurities. *Proceedings of the IEJ*, 6, 3, 159–162.

Murata, Y. (1982). Electrostatic separation. *Proceedings of the IEJ*, 6, 3, 130–138.

Murata, Y., N. Masui, S. Miyazawa, and I. I. Inculet (1982). Non-uniform AC field electrostatic separator. Conf. paper of the IEJ, Tokyo, pp. 293–294.

Ogata, S. (1985). Application of electrostatic fluidized bed to separation technique. *Kagaku Kougaku*, 49, 2, 132–136.

Onuma, H., and S. Suzuki (1979). Rotating drum type electrostatic separator with two cascade stages. *Ebara Jihou*, 108, 18.

Takahashi, T. (1982). Electrostatic separator for compost. *Proceedings of the IEJ*, 6, 3, 148–151.

Takahashi, T., Y. Watabe, K. Tabei, and K. Haga (1980). New equipment for resource recovery: electrostatic separator and eddy current separator. *IEEE/IAS 15th Annu. Meet.*, pp. 1032–1037.

Toraguchi, M., and K. Haga (1982). Electrostatic separation of coal. *Proceedings of the IEJ*, 6, 3, 139–147.

Toraguchi, M., and M. Nagasawa (1982). Electrostatic beneficiation of coal using a cyclone-tribocharger. Conf. paper of the IEJ, Tokyo, pp. 289–292.

Tsuruta, K., M. Furuya, and T. Takahashi (1985). Single-phase AC electrostatic classifier. Conf. paper of the IEJ, Tokyo, pp. 331–334.

Ui, N., and T. Horio (1980). *Equipotential and Equivelocity Electrophoresis*. Kyoritsu Press, Tokyo, pp. 116 ff.

Washizu, M. (1986). Electrostatic cell handling—dielectrophoresis and electro cell fusion. *Proceedings of the IEJ*, 10, 3, 150–156.

18

Electrostatic Coalescence in Liquid-Liquid Systems

Wuhai He

McMaster University
Hamilton, Ontario, Canada

I. INTRODUCTION

A. Background

Phase coalescence may be defined as the aggregation of dispersed droplets that are suspended in another immiscible or partially miscible liquid, to form a heterogeneous dense packed zone at the main interface between the two bulk liquid phases. The coalescence phenomenon is associated with and important to some processing industrial operations, e.g., in the liquid-liquid extraction process. Indeed, liquid-liquid separation is not only restricted to extraction processes; it is also of considerable importance in effluent treatment plants and in any processes where liquid-liquid dispersions are present.

The rate of migration of droplets to the coalescing main interface depends on the type of dispersion and the properties and interfacial characteristics of the system. The coalescence is associated with the decrease in free energy of the liquid-liquid interface, and the actual mechanisms are very complex, involving the factors that govern the thinning of the continuous-phase film between the two coalescing interfaces. Depending on conditions, coalescence may occur either at the plane interface or at the drop-drop interface (Laddha and Degaleesan, 1983).

The entire emulsion-breaking process can be divided into three stages: (1) droplet coalescence and growth; (2) droplet settling; (3) coalescence

of the large water and oil droplets with their respective continuous phases in the coalescer. The throughput of the coalescer can be limited by any of these stages. The coalescence may be significantly enhanced under applied electric fields due to the increased rate of film thinning as the results of electrostatic attraction and enhancement of the electric field between the drops by induced charges. This chapter is mainly concerned with the phenomena related to the electrostatic coalescence process and its applications.

B. Coalescence Augmented by Electric Fields

The surfaces of droplets in a liquid-liquid emulsion develop an electrical double layer in the same way as solid particles in a suspension. This would tend to produce an electrostatic force of repulsion between the droplets. It is generally accepted that electrically enhanced separation rates result from the action of electric forces, which increase the rate of droplet coalescence. When an electric field is applied, coalescence of suspended droplets can occur in the continuous phase as droplets moving at different speeds collide. This process is enhanced by dielectrophoresis, which provides a force of attraction between two polarized droplets. Although several different models have been proposed for the electric forces at work in a suspension of droplets, the magnitude of the forces is always dependent on the magnitude of the applied electric field.

Practical evidence obtained with crude oil/water separations has shown that almost any type of high voltage field will promote to some extent the separation of water-in-oil emulsions. The mechanisms whereby this can occur are not clearly understood, except that if a large potential gradient can be established and maintained in the continuous phase of a liquid-liquid emulsion, it causes very fine drops to grow by coalescence with each other to a point where they fall out of the continuous phase under the action of gravity. The technique is specific for water-in-oil type emulsions, since it requires the continuous phase to be relatively insulating in character (Bailes, 1992).

C. Applications

The electrostatic coalescence technique can be used to separate dispersed droplets from another dielectric liquid. The petroleum industry has been using it to separate brine emulsified in crude oil; the chemical industry uses it to resolve water-in-oil (w/o) emulsions generated during liquid-liquid extraction processes. The technique can also be used to break w/o emulsions in liquid membrane separation process (Hsu and Li, 1985).

At present, the only large scale application of electrostatic coalescence occurs in the oil industry for resolving water-in-oil emulsions that arise either during production, when crude oil and water are coproduced, or during refining, when water is deliberately emulsified in the crude oil to aid the removal of hydrophilic impurities such as salt (Taylor, 1988).

II. PHENOMENA OF ELECTRICALLY AUGMENTED COALESCENCE

An applied electric field has several effects on aqueous droplets dispersed in oil. The insulative nature of the continuous oil phase allows the establishment of a high electric field across the emulsion. This field can polarize and elongate the aqueous droplets. It can cause unidirectional migration of the droplets in dilute emulsions by electrodynamic forces, i.e., by either an electrophoresis mechanism (space charge) or a dielectrophoresis mechanism (movement of dipoles in a nonuniform electric field). When the concentration of droplets becomes high it can also cause the coalescence of the droplets into large drops.

The mechanisms promoting droplet coalescence by electric fields are not clearly understood, although it is generally accepted that fields produce coalescing forces on the droplets in water-in-oil type emulsions. Some conflicting models propose to relate the force with field strength, and geometric and liquid properties. A number of different mechanisms have been proposed for the separation of liquid-liquid dispersions in an electric field. They may involve such effects as chain formation; dielectrophoresis; electrophoresis; formation of intermolecular bonds; dipole coalescence; electrofining; and random collisions (Bailes and Larkai, 1982).

A. Coalescence with Chain Formation

Pearce (1954) has suggested a two step mechanism of chain formation and coalescence for dispersions in which the water content is less than 10% by volume and the droplet size in the range of 5–30 μm in diameter based on observations with both dc and ac fields. The formation of chains is characterized by the following phenomena:

There is no general movement of droplets in the direction of maximum field strength.
Chains of droplets are formed by movements of single droplets in directions approximately perpendicular to the length of the chains.
The chains lie in the general direction of maximum field strength.
Chains do not always start or finish at an electrode; neither are they all complete.

According to Pearce (1954), the chains are formed by forces due to the potential differences between droplets as a result of their induced charges. The second step, coalescence, probably depends on two factors acting together or independently: (1) dielectric breakdown of the film of continuous phase between adjacent drops; and (2) the attractive force between droplets due to their potential difference. The effect is more directly determined by the resistivity difference between the two liquid phases.

B. Coalescence Enhanced by the Dielectric Component of EHD Forces

The mechanism proposed for enhanced electrostatic coalescence by the dielectrophoresis effect (the dielectric component of EHD forces; see also Chapters 7 and 8) is described as the movement of suspended droplets relative to the suspending medium as a result of polarization forces produced by an inhomogeneous electric field. The movement is toward regions of higher field intensity irrespective of polarity and is therefore observed with both ac and dc fields. The force is proportional to the field intensity, its divergence, the difference between the dielectric constants of the droplets and that of the surrounding medium, and the volume of the droplet. The dielectrophoretic force on a spherical droplet of diameter d suspended in another dielectric liquid and under a nonuniform electric field may be expressed as (Pohl, 1973)

$$\mathbf{F}_d = \frac{\pi d^3}{4} \epsilon_c \frac{(\epsilon_d - \epsilon_c)}{(\epsilon_d + 2\epsilon_c)} \nabla \mathbf{E}^2 \tag{1}$$

where ϵ_d and ϵ_c are the electrical permittivities of droplet (dispersed phase) and surrounding medium (continuous phase) respectively; $\mathbf{E}$ is the external electric field. It is noticed from this equation that if the droplet has a lower dielectric constant than the continuous phase, it will move to the lower field region. Even droplet with a higher dielectric constant may also move to the low-field region if it has a permanent dipole moment and is spinning.

It is noted also that the above equation was derived assuming that both dispersed and continuous phases were perfect dielectrics. For a real system with two liquid phases, the effect of conductivity must be taken into account by replacing the dielectric constant in the equation with the complex permittivity (Cross, 1987). Dielectrophoresis may enhance the coalescence through the force of attraction between two polarized droplets, which will also increase the rate of film thinning due to the reduced interfacial tension effect.

C. Coalescence Enhanced by the Space Charge Component of EHD Forces

Another mechanism proposed for enhanced electrostatic coalescence is the electrophoresis effect (the space charge component of EHD forces; see also Chapters 7 and 8) arising from the direct attraction of an electric field for charged droplets. The direction of motion for these charged droplets depends on the direction of the field. According to Waterman (1965), the electrophoresis phenomenon only appears very near the electrodes.

The electrophoresis phenomenon has the following properties (Pohl, 1973):

It produces motion of suspended particles in which the direction of motion depends on the sign of their charge and on the sign of the field. Occasionally the motion of charged droplets toward a sharp electrode occurs even when alternating high voltages are applied, due to the partial rectification and selective charge injection.

The effect is observed with particles of any size—atomic, molecular, colloidal, or even macroscopic.

Compared with dielectrophoresis, it requires relatively low electric fields.

It requires relatively small charges per unit volume of the particles.

D. Dipole Coalescence

Dipole coalescence is due to forces between droplets as a result of the droplets acquiring induced dipoles in the electric fields. Waterman (1965) suggested that dipole coalescence is the principal mechanism promoting separation of the dispersed droplets from a continuous phase, since it is effective throughout the bulk of the continuous medium in either ac or dc fields. The full expression for the force between two dipoles with a distance l between their centers has been given by Pohl (1973). For the case where the dielectric constant of the dispersed phase is much greater than that of the continuous phase, as in the case with a water-in-oil dispersion, this expression simplifies to (Cross, 1987):

$$\mathbf{F} = \left(\frac{3}{8}\right)\pi\epsilon_c\left(\frac{d}{l}\right)^4 d^2\mathbf{E}^2 \tag{2}$$

The dipole attraction is proportional to the square of the electric field; therefore one would expect that higher fields improve coalescence. In practice this is restricted by a critical electric field, which depends on the system involved and the electrode geometry, beyond which the droplet would break up and reemulsify due to the high droplet charge density.

E. Coalescence by Random Collision

Coalescence enhanced by increased rate of random collision was proposed by Hendricks and Sadek (1974, 1977). In this mechanism droplets are assumed to be propelled back and forth between the electrodes due to charges they acquire in the vicinity of the electrodes and in so doing they collide with one another and coalesce in the meantime. An analysis carried out by Hendricks and Sadek (1974) has demonstrated that if all the droplets attain a saturation charge by contacting with the electrodes, an exponential growth of the mean droplet diameter occurs. However, the model parameters are not readily measured, so correlation of experimental data is easily carried out. The collision frequency approach has also been investigated by Bailes and Larkai (1982). The intent of this work was to develop an expression that allowed straightforward correlation of coalescence efficiency versus the enhanced droplet collision rate. In this study the enhanced collision frequency was determined by taking into account the additional force imposed on the droplets by a pulsed electric field.

The electrofining mechanism proposed by Waterman (1965) essentially relies on the combined effects of electrophoresis, dc induced dipole coalescence, collision due to charged droplets moving in opposite directions, and collisions due to differentials in velocity of different sized droplets. It applies for a unidirectional electric field and dispersions containing a very low hold-up of dispersed phase.

III. FACTORS AFFECTING THE PERFORMANCE OF ELECTROSTATIC COALESCENCE

Although there are several nonelectrical factors affecting the coalescence performance, such as droplet size, density difference between phases, viscosity ratio of the phases, interfacial tension effect, temperature effect, etc. (Laddha and Degaleesan, 1983), this section is concerned mainly with electrical effect related factors. The dominant mechanism during the electrostatic coalescence process probably depends on such factors as fractional volumetric hold-up of dispersed phase, electrode geometry, and form and magnitude of imposed electric field as well as the electrical properties of the system. These factors have been investigated by Bailes and Larkai (1981, 1982, 1984a,b) based on the evaluation of overall performance with the coalescence parameter, which is defined as

$$P = \left(1 - \frac{\Delta H}{\Delta H_0}\right) \times 100\% \tag{3}$$

where ΔH is the dispersion band depth in the presence of the electric

field and ΔH_0 is the dispersion band depth in the absence of an electric field. Therefore P represents the percentage reduction in dispersion band depth in an electrostatic coalescer.

A. EFFECT OF PULSED FREQUENCY

According to Bailes and Larkai (1981), the coalescence performance under a pulsed electric field (pulse form: half wave or square wave) is much better than that under a dc electric field. They suggested that the mechanism of coalescence under a constant dc field is different from that under the pulsed field. Droplet chains are formed and disrupted repeatedly under pulsed fields, so the forces are created for random collisions leading to coalescence; while with constant dc fields, once steady state is attained, chains formed are perhaps relatively permanent, and low resistance paths are created for current leakage.

The experimental investigation conducted by Bailes and Larkai (1982) revealed that there is an optimum pulse frequency at which the best coalescence performance can be obtained, as seen in Fig. 1. It is noted that the mean conduction current also reaches the highest level at the optimum pulse frequency. They suggest that the mechanism of electrostatic coalescence involves the formation of chains of drops prior to actual coalescence, since chains of drops are primarily responsible for the conduction current.

B. Effect of Phase Ratio

The investigation of the effect of dispersed phase hold-up on electrostatic coalescence has been conducted experimentally by Bailes and Larkai (1984a). The study has revealed that there exists a hold-up at which best coalescence performance can be obtained, as shown in Fig. 2. They considered that when hold-up is reduced, the drops are relatively far apart and smaller, and it takes much longer to affect collision and coalescence of the drops to a size big enough to settle. Also it was found that for a given applied voltage the field strength decreases rapidly as the hold-up increases. Similar results were also reported by Hendricks and Sadek (1977). This leads to the conclusion that there may exist an optimum balance between electric field strength, droplet size, number of droplets per unit volume, and droplet separation for maximum electrostatic coalescence with minimum energy.

C. Effect of Electrode Coating

The influence of electrode coating (insulated electrode) is another important factor for the enhanced performance of electrostatic coalescence,

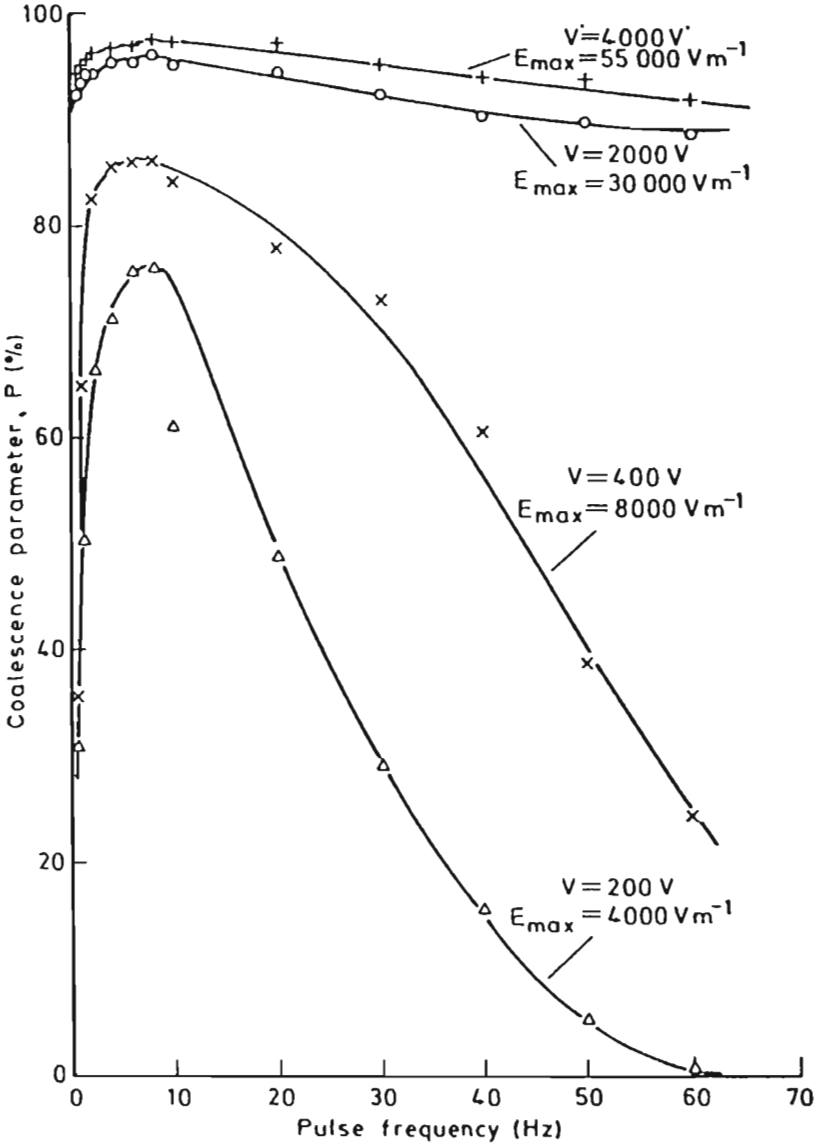


Figure 1 Effect of pulse frequency on coalescence performance. (Bailes and Larkai, 1982.)

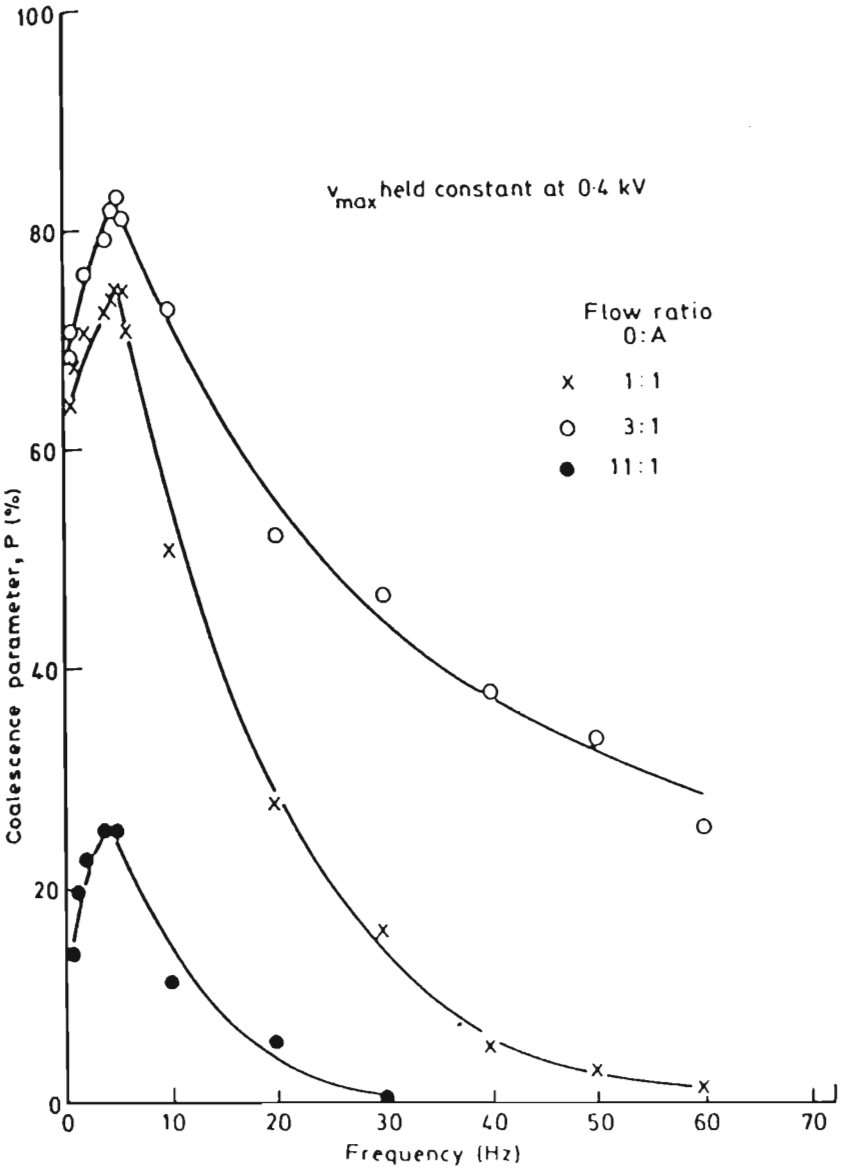


Figure 2 Effect of phase ratio on coalescence performance. (Bailes and Larkai, 1984a.)

especially for the applications in liquid-liquid extraction or recovery of the liquid membrane processes, where the liquid hold-up is usually high. As explained by Hsu and Li (1985) (Fig. 3), in a coalescer equipped with naked electrodes, if a single chain happens to extend from one electrode to the other, sparking will occur. On the other hand, in a coalescer equipped with insulated electrodes, the surface of the top electrode is coated with a layer of nonconductive, nonwetting insulating material. In this configuration, a conducting water chain formed is equivalent to a parallel array of tiny independent capacitors; therefore the current is also limited by the reactance of this tiny capacitor, and the sparking is suppressed.

Hsu and Li (1985) suggest that the insulating solid coating medium should be hydrophobic and have a dielectric constant at least above 4. Bailes and Larkai (1984b) also investigated the effect of electrode coating thickness on coalescence performance. The best coalescence performance is obtained by using only a thin coating, because of the substantial reduction in effective field strength at a given applied voltage. Also the interfa-

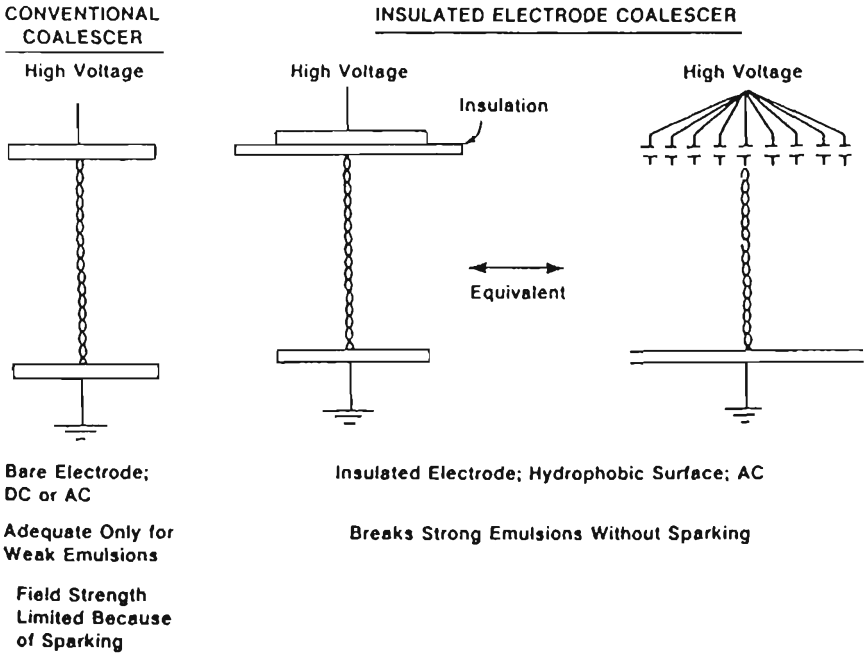


Figure 3 Comparison of conventional and insulated electrodes for an electrostatic coalescer. (Hsu and Li, 1985.)

cial relaxation time, which determines the optimum pulsed frequency, between the electrode coating and the layer of continuous phase diminishes with increased coating thickness.

REFERENCES

Bailes, P. J. (1992). Contacting and separation equipment—the electrical alternative. In *Proceedings of ISEC'90, Kyoto, Japan*. Elsevier Science Publishers, New York, pp. 1313–1325.

Bailes, P. J., and S. K. L. Larkai (1981). An experimental investigation into the use of high voltage D.C. fields for liquid phase separation. *Trans. I. Chem. Eng.*, 59, 229.

Bailes, P. J., and S. K. L. Larkai, (1982). Liquid phase separation in pulsed D.C. fields. *Trans. I. Chem. Eng.*, 60, 115.

Bailes, P. J., and S. K. L. Larkai (1984a). Influence of phase ratio on electrostatic coalescence of water-in-oil dispersions. *Chem. Eng. Res. Des.*, 62, 33.

Bailes, P. J., and S. K. L. Larkai (1984b). The application of electric fields to phase separation in a solvent extraction system. *AIChE Symp. Ser.*, 80, 170.

Cross, J. A. (1987). *Electrostatics: Principles, Problems and Applications*. Adam Hilger, Bristol, U.K.

Hendricks, C. D., and S. Sadek (1974). Electric field enhanced coalescence of water droplets in low-conductivity oils. *Ind. Eng. Chem. Fundam.*, 13, 139.

Hendricks, C. D., and S. Sadek (1977). Electric field enhanced coalescence of drops in liquid emulsions. *IEEE Trans. Ind. Appl.*, 1A-13 5, 489.

Hsu, E. C., and N. N. Li (1985). Membrane recovery in liquid membrane separation processes. *Sep. Sci. Tech.*, 20, 115.

Laddha, G. S., and T. E. Degaleesan (1983). Dispersion and coalescence. In *Handbook of Solvent Extraction* (T. C. Lo, M. H. I. Baird, and C. Hanson, eds.). John Wiley, New York, p. 125.

Pearce, C. A. R. (1954). The mechanism of the resolution of water-in-oil emulsions by electrical treatment. *Brit. J. Appl. Phys.*, 5, 136.

Pohl, H. A. (1973). Nonuniform field effects: dielectrophoresis. In *Electrostatics and Its Applications* (A. D. Moore, ed.). John Wiley, New York, p. 336.

Taylor, S. E. (1988). Investigations into the electrical and coalescence behavior of water-in-crude oil emulsions in high voltage gradients. *Colloids and Surfaces*, 29, 29.

Waterman, L. C. (1965). Electrical coalescers. *Chem. Eng. Prog.*, 61, 51.

This Page Intentionally Left Blank

19

Electrorheology

J. L. Sproston

University of Liverpool
Liverpool, England

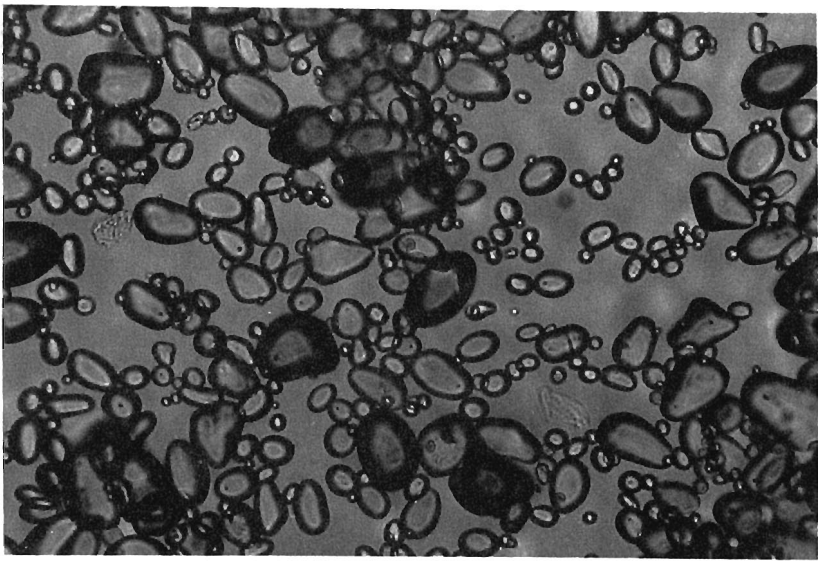
R. Stanway

University of Sheffield
Sheffield, England

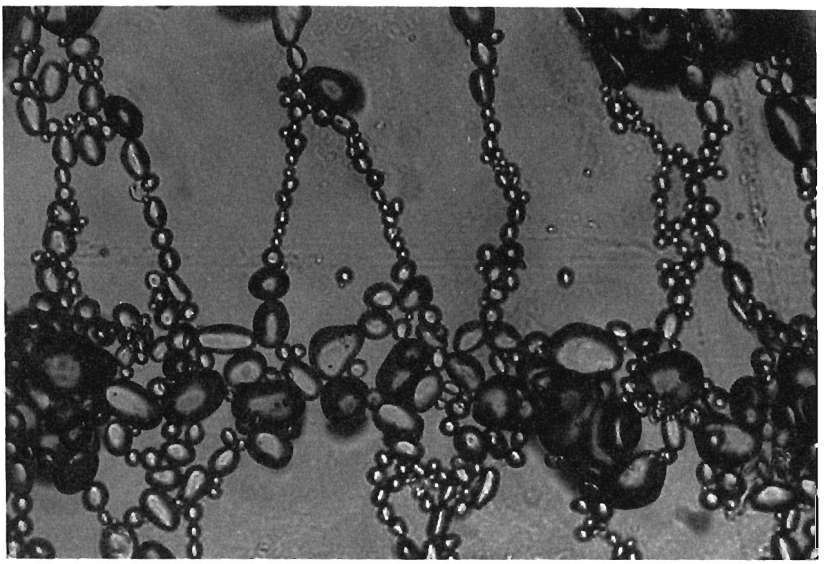
I. OUTLINE DESCRIPTION OF THE ELECTRORHEOLOGICAL EFFECT

The electrorheological (ER) effect, sometimes referred to as the Winslow effect after the person who first investigated it (Winslow, 1949), is a phenomenon in which the resistance to flow or to deformation of certain types of fluid can be changed by the application of an electric field. The fluids used by Winslow were nonaqueous silica suspensions that had been activated by a small amount of water. More recently there has been a large amount of work devoted to the development of other fluid types (e.g., Block and Kelly, 1988). All of these fluids are essentially comprised of a dielectric oil (such as a silicone oil) and some dispersed particulate. On application of an electric field, the solid phase forms a series of chainlike bridges in a direction roughly orthogonal to the electrodes (Fig. 1), thus producing a pronounced structural inhomogeneity. Under this condition, the liquid state of the unstressed fluid is replaced by that of a rigid gel, the transition occurring rapidly (typically in a millisecond).

The ER effect will occur for either ac or dc fields, typical field strengths being in the range of 2 to 6 kV/mm. Particulate sizes are in the range of 2 to 20 μm. Since any increase in fluid operating temperature will produce an increase in fluid electrical conductivity, the carrier liquid is specifically



(a)



(b)

Figure 1 Random orientation of starch particles (in the range of 5 to 50 μm) suspended in silicone oil. (a) No applied field; (b) applied field 2 kV/mm.

chosen to be one of small conductivity. A useful rule of thumb here is that the doubling temperature (that is, the temperature rise that produces a doubling of electrical conductivity) lies in the range 6 to 18°C.

Stangroom (1984) has listed other useful attributes of ER fluids, which include small base viscosity, low freezing point, high boiling point, hydrophobicity, and high dielectric strength. Also, if the fluid is to remain stable in either its rest or its working state, then density matching of the solid phase to the liquid is required.

II. FUNDAMENTAL PRINCIPLES

Electrorheological fluids can be used in a wide range of devices, but essentially they would be subject to mechanical forces to produce in the fluid a state of shear, tension, or compression (or combinations of these).

A. Fluids in Shear

In shear, where typically the fluid would be sandwiched between parallel plane electrodes and one electrode is moving while maintaining parallelism, the fluid behaves in a manner similar to that exhibited by a Bingham plastic (Fig. 2). Here flow occurs only after the imposition of a shear stress greater than the yield stress, the latter increasing with the applied field. Below the yield stress the ER fluid remains like a solid (although it may exhibit creep).

For cases in which the strain rate is small, it is possible to realize fluid yield stresses up to about 20 kPa for applied fields, just less than that at which electrical breakdown occurs. The fluids are pseudoplastic in that the apparent viscosity decreases with increasing shear rate (Uejima, 1972). The characteristic (stress/strain) curves for ER fluids can be generated by employing rotational viscometers such as the concentric cylinder type, the only modification needed being to facilitate the application of the electric field.

B. Fluids in Tension or Compression

Instead of the fluid being subject to shear forces, there are instances in which the fluid may experience tensile or compressive loads. Under these conditions, the fluid behaves rather as though it had a two-valued viscosity, one at small strain rates and another at higher rates. The static yield stress may then be as high as 50 kPa.

When (Fig. 3) the fluid is under a compressive load, the effect is rather complicated, in that the fluid is being forced out of the interelectrode space. Thus there will be a combined shear/compression mode. Also in

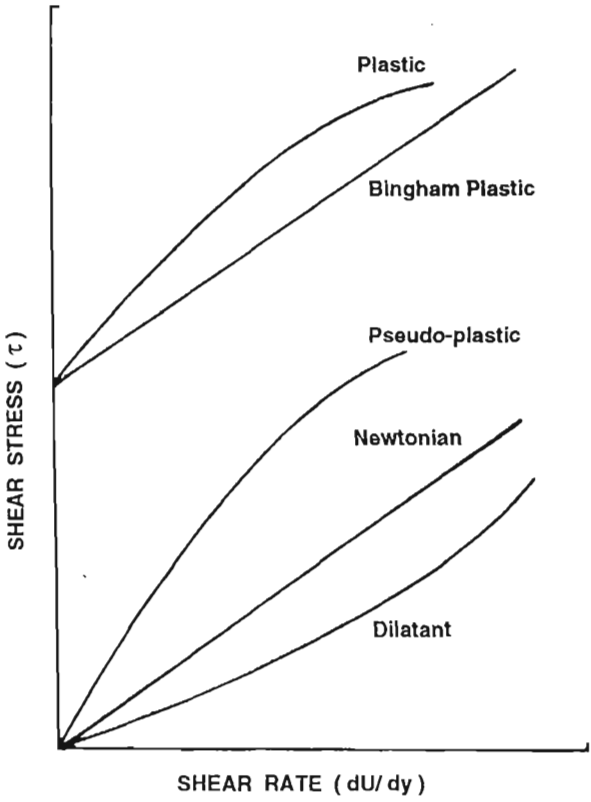


Figure 2 Shear stress/shear rate characteristics.

this case if the fluid is energized by a constant applied potential difference between the superimposed electrodes, then as the compressive load is increased the field will increase due to the diminishing gap. This can be easily compensated for (if required) by determining the instantaneous gap and providing a suitable control loop to the voltage source.

The characteristic curves in this situation can be generated by employing conventional plastometers, except again some arrangement must be found to apply the electrical field.

III. SPECIFIC AREAS OF APPLICATION

Industrial interest in the application of ER fluids has grown at a rapid pace during the last few years, and there is correspondingly an increase in commercial sensitivity. A recent review by Jordan and Shaw (1989)

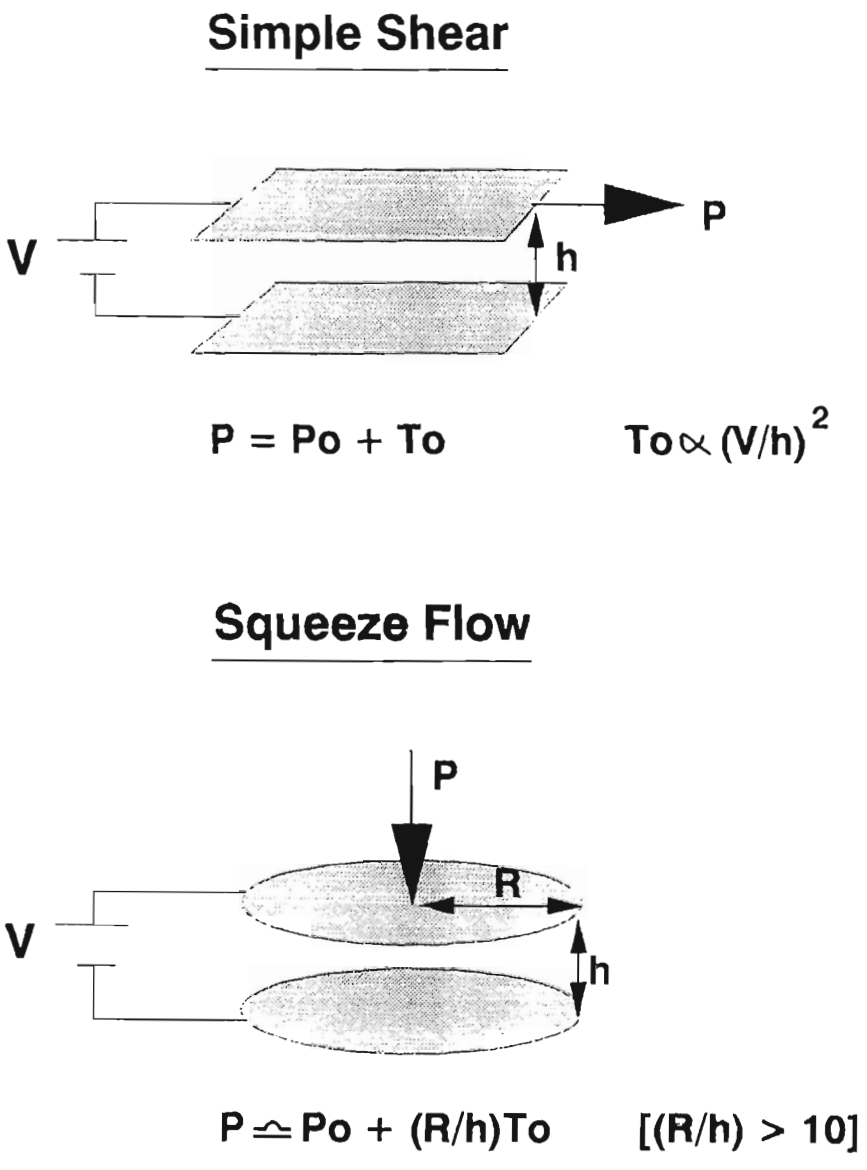


Figure 3 Electrorheological stress enhancement using squeeze flow instead of shear. P = total applied stress; P_0 = viscous stress; T_0 = electrorheological yield stress.

has not only outlined the advantages of employing ER fluids in mechanical devices but also highlighted the need for a closer understanding of the fundamental principles involved. It is relatively easy to produce a device that works, but it is much more difficult to produce a device that is reliable.

There are at present several major areas in which ER fluids are being applied; these are associated with torque transmission, vibration damping, and control of fluid flow. There are, however, many other areas that can benefit from the ER effect, as reviewed e.g., by Shulman et al. (1981); these include the expanding field of robotics, details of which are not included here.

A. Torque Transmission

A recent investigation by Sproston et al. (1990) was concerned with the transmission of torque across a multiplate ER fluid coupling (Fig. 4). The device consisted of a set of disc-shaped electrodes carried alternately by the shaft and casing. Energization of the fluid could be achieved easily by raising the casing to some high voltage and earthing the central shaft. Measurement of braking torque and input/output speed ratio was achieved for a range of field strengths and waveforms. Some of these results are shown in Fig. 5, where for example the difference between the characteristics of the device when electrically stressed and not can be easily seen.

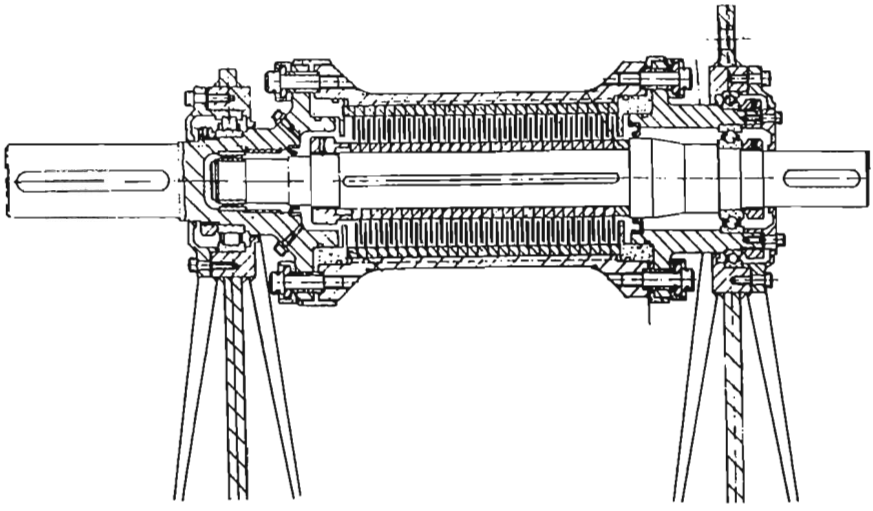


Figure 4 Multiplate torque transmitting device. Input shaft on right.

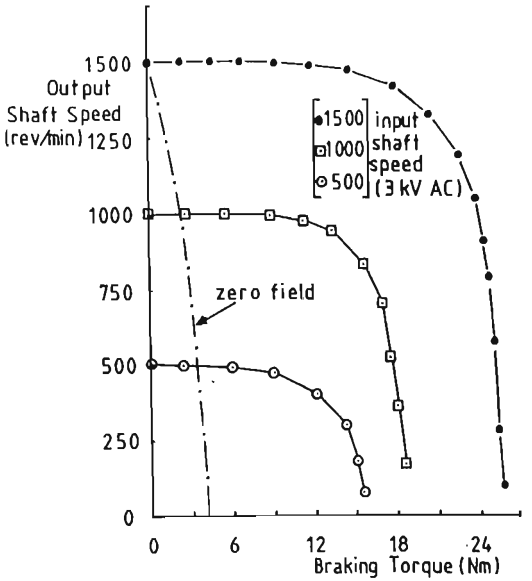


Figure 5 Output speed/braking torque characteristics for device in Fig. 4.

This particular device performs reliably over a wide range of input speeds and exhibits quite different characteristics for different electrical inputs. Further work is being carried out using various ER fluid types.

B. Vibration Damping

A recent investigation by Stanway et al. (1992) has been directed to the design and testing of a prototype automotive engine mount using ER fluids in tension and compression. Conventional mounts employ either a solid block of elastomeric material or a hydraulic fluid sandwiched between upper and lower members, the principle being that the transmission of engine vibration to the automotive body can be reduced. In the ER device the amount of vibration damping can be varied by altering the applied field across the fluid. One such mechanical arrangement is shown in Fig. 6 and some results in Fig. 7. Here it is seen that the resonant peak occurring at a vibration frequency of about 4.5 Hz can be reduced in amplitude by a factor of about five when the fluid is electrically stressed. From instantaneous measurements of engine vibration it is thus possible to control the amplitude/frequency response of the body by controlling the applied field.

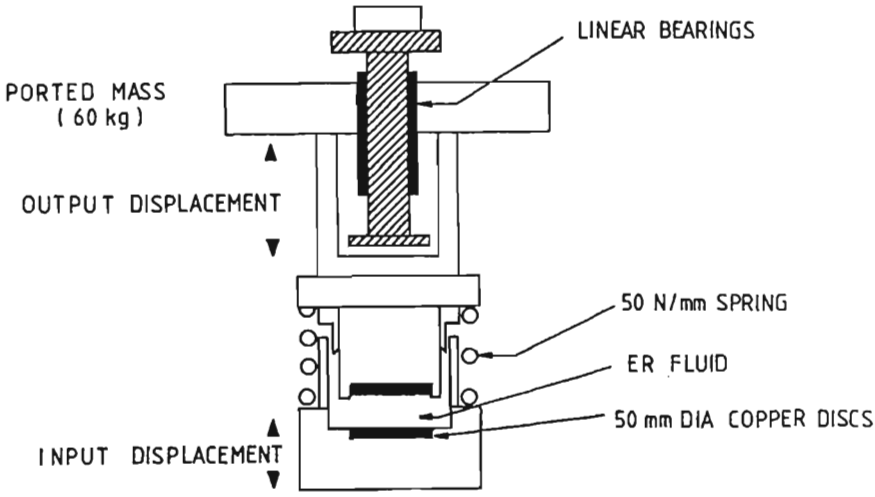


Figure 6 Prototype automotive engine mount.

This ER technique can be extended to other areas to include, for example, automotive shock absorbers and the control of vibration of rotating machinery.

C. Flow Control

The feasibility of controlling the flow rate of an ER fluid in a hydraulic circuit was demonstrated by Stanway et al. (1990) in a prototype valve. This consisted of a coaxial set of metal cylinders that were alternately raised to a high potential and earthed. As the ER fluid passed through the multiannular spaces, its flow rate could be controlled by the applied field (this in turn controlling the effective viscosity of the fluid). The resulting pressure drop as a function of flow rate and applied field strength can be seen in Fig. 8. Commercial valves are capable of performances much greater than this, however. Brooks (1982) quotes a maximum pressure drop of about 30 bar for a flow rate of 10 liter/min using a field strength of 3 kV/mm. A later study by Bullough (1990) shows a pressure drop of up to 70 bar for 2 liter/min at the same field strength.

The ER control valve could equally be used in a servomechanistic mode to control the flow of a second (main) flow, the advantage over conventional valves being that the ER valve has no moving parts.

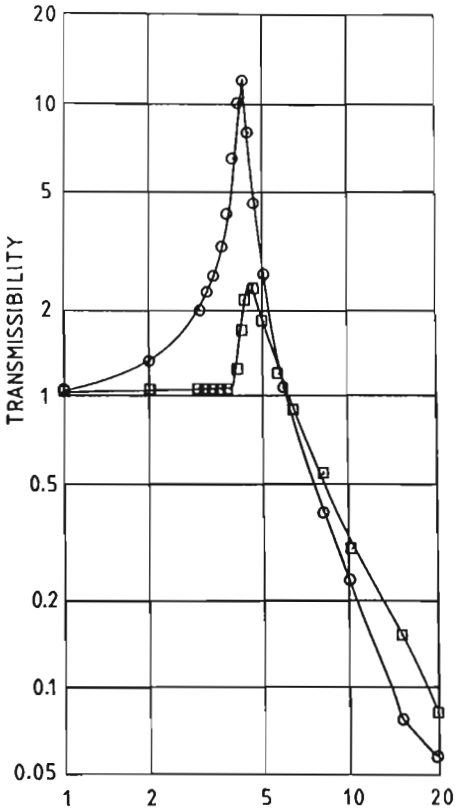


Figure 7 Transmissibility/vibration frequency characteristic for engine mount in Fig. 6. ⊙ No applied field; ⊡ 10 kV applied potential difference.

IV. USEFUL FORMULAE

As a means of providing the reader with the necessary background in order to facilitate determination of the size and scale of a proposed ER device, the following formulae are included.

A. Bingham Plastic Model

The equation governing the behavior of a Bingham plastic is of the form

$$\sigma = \sigma_0 + \eta\dot{\gamma} \tag{1}$$

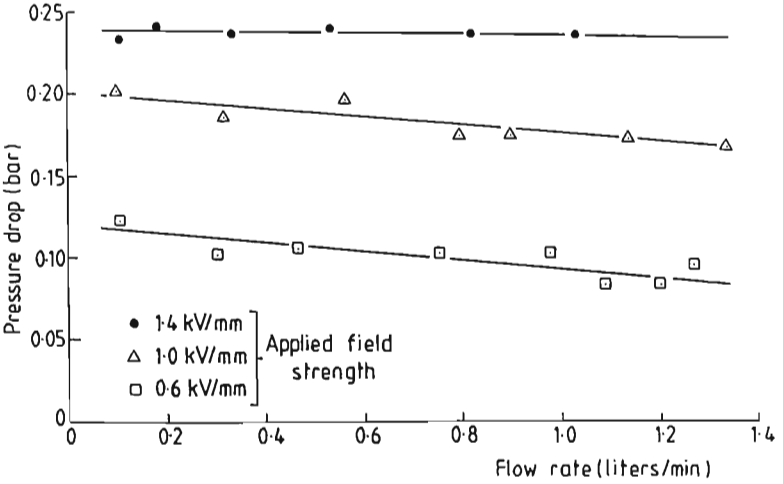


Figure 8 Pressure drop/flow rate characteristics for ER valve.

where σ is the shear stress, σ_0 is the static yield stress, η is the plastic viscosity, and γ is the shear rate. If the ER fluid in shear is assumed to follow this behavior, then when electrically stressed the yield stress increases dramatically, while the plastic viscosity remains fairly constant. It may be assumed that the yield stress increases approximately in proportion to the square of the applied field, i.e., that

$$\sigma_0 = CE^2 \tag{2}$$

where C is a constant.

For most commercially available fluids the value of σ_0 would not exceed 20 kPa.

B. Biviscosity Model

An alternative description of the behavior of an ER fluid, which reflects the thought that the fluid flows even for small shear forces (i.e., that the yield stress is fictitious), can be accommodated in equations of the form

$$\sigma = \eta_1 \dot{\gamma} \qquad (\sigma < \sigma_1)$$

and

$$\sigma = \sigma_0 + \eta_2 \dot{\gamma} \qquad (\sigma > \sigma_1)$$

where σ_0 and σ_1 are related by $\sigma_0 = \sigma_1 (1 - \eta_2/\eta_1)$.

Either σ_0 or σ_1 can be called the yield stress.

V. DESIGN EXAMPLES

The following two examples are chosen from work carried out at the University of Liverpool by the authors over the last few years. They do not represent optimal devices, merely ones that embrace the essential features of ER design.

A. Simple Torque Transmitter

The device shown in Fig. 9 consists of a single circular electrode (carried by the input shaft), which is immersed in ER fluid contained in the outer casing (carried by the output shaft), and which is earthed. Electrical energization of the fluid can be achieved by a suitable carbon brush in contact with the input shaft. Typically the gap between the electrode and the casing is in the range of 2 to 4 mm, with a larger gap near the perimeter so as to avoid unwanted field intensification and possible fluid breakdown. The choice of ER fluid is largely governed by the zero-field viscosity requirement; it may be for example that the output shaft speed is required to be very small when the field is absent, and this would necessitate an ER fluid of small viscosity.

If it is assumed that the total shear stress σ can be expressed as the sum of the static yield stress σ_0 and a Newtonian term $\mu du/dy$ (where μ is the dynamic viscosity and du/dy is the velocity gradient), then the torque T transmitted across the fluid is given approximately by

$$T = 2\int_{R_1}^{R_2} 2\pi r^2 \sigma \, dr \tag{3}$$

where R_1 and R_2 are the radii of the input shaft and the electrode, respectively. Here du/dy can be approximated by $r(\omega_i - \omega_o)/d$, where ω_i and ω_o are angular speeds of the input and output shafts and d is the gap between electrode and casing.

B. Simple Vibration Damper

The device shown in Fig. 10 consists of a piston rod carrying two rectangular plates that are constrained to move in a vertical mode by linear bearings. The outer casing, of rectangular cross-section, is fabricated from an insulating material (e.g., PTFE) but with the inner faces lined with copper sheet. With the casing filled with ER fluid, electrical energization of the fluid in the spaces between the casing and the plates can be achieved by raising the casing to some high potential and earthing the plates. In this way the shear stress on the plates can be controlled by the applied field, and hence the resisting force to an imposed movement of the rod can be

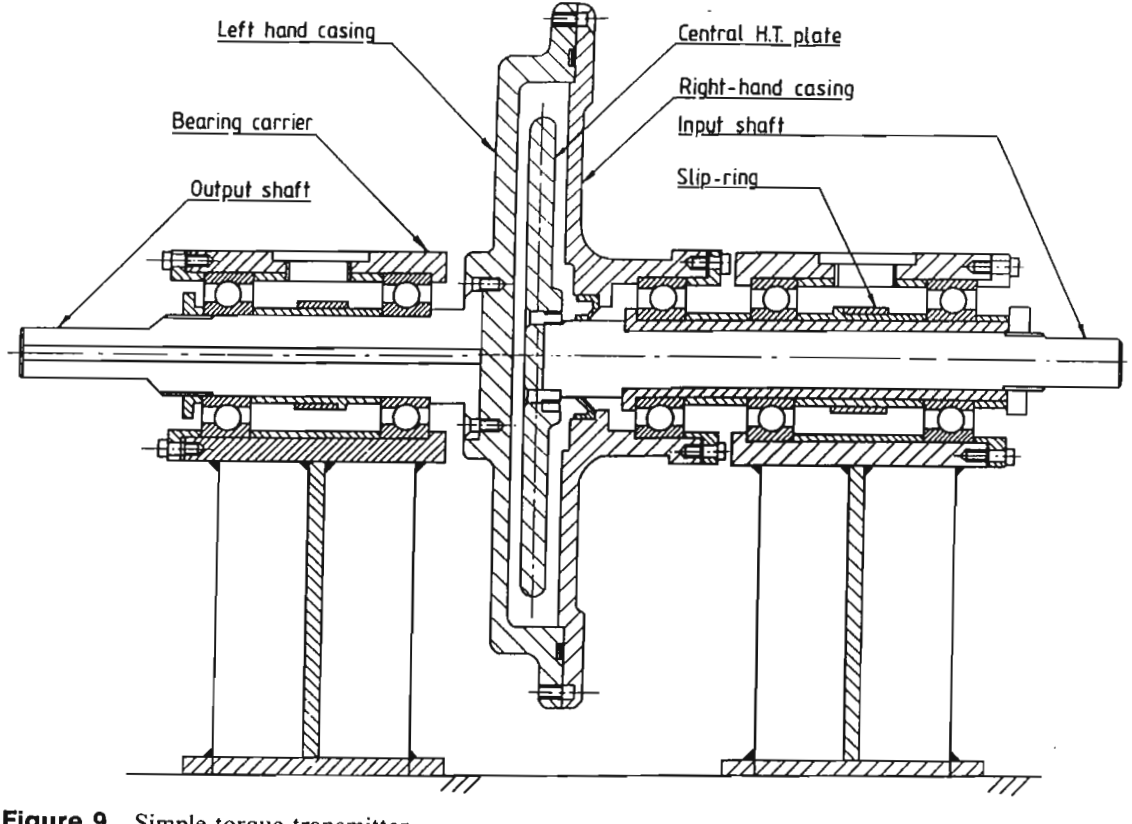


Figure 9 Simple torque transmitter.

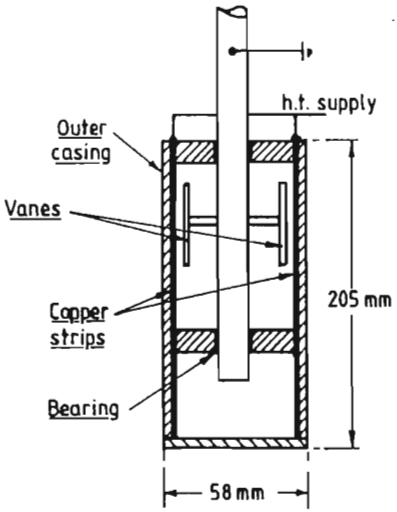


Figure 10 Simple vibration damper.

altered. Stanway et al. (1987) describe the evaluation of such a device and present an analysis of the digital processing of experimental records. In this simple example, if the edge effects at the plates and inertia terms are ignored, then the increase ΔF in the magnitude of the resisting force, due to the electrorheological influence, is given approximately by

$$\Delta F = 2\sigma_0 ab \tag{4}$$

where a and b are the dimensions of the plates. Under dynamic conditions, the value of σ_0 would be modified by an amount depending on the particular ER fluid employed. This value would require experimental determination.

VI. FUTURE PROSPECTS FOR ELECTRORHEOLOGICAL FLUIDS

The increasing interest being shown in the possible commercial exploitation of ER fluids stems mainly from the development of fluids that not only are chemically stable but also combine the attributes of low electrical conductivity and low moisture content. Combining this with an increasing range of operating temperatures, the future prospects for ER fluids look very good. There is, however, a continuing requirement for multidisciplinary effort aimed toward a fuller understanding of the ER effect.

The rapid response of an ER fluid to an electrical stimulus and the massive change in its fluid properties opens up a wide range of device possibilities, but the control strategies need careful analysis, and the significant nonlinearities need to be tackled.

REFERENCES

Block, H., and J. P. Kelly (1988). Electrorheology. *J. Appl. Phys.*, 21, 1661.

Brooks, D. A. (1982). Electro-rheological devices. *Chartered Mechanical Engineer*, Sept., 91.

Bullough, W. A. (1990). Innovative electron-hydraulic developments for the fluid power industry. Proceedings of 9th Int. Conf. on Fluid Power, BHRA, Cambridge, 55–56.

Jordan, T. C., and M. T. Shaw (1989). Electrorheology. *IEEE Trans. Elec. Ins.*, 24, 5, 849.

Shulman, Z. P., R. G. Gorodkin, E. V. Korobko, and V. K. Gleb (1981). Electrorheological effect and its possible uses. *J. Non-Newt. Fluid Mech.*, 8, 29.

Sproston, J. L., R. Stanway, and X. M. Wu (1990). The electrorheological effect and its application to torque transmission. Proceedings of 10th ICDL, Grenoble, France, 448–453.

Stangroom, J. E. (1984). U.S. Patent No. 4483788.

Stanway, R., J. L. Sproston, and N. G. Stevens (1987). Non-linear modelling of an electrorheological vibration damper. *J. Electrostatics*, 20, 167.

Stanway, R., J. L. Sproston, and R. Starkey (1990). On the design of force actuators and sensors using electrorheological fluids. Proceedings of 2nd Int. Tech-Transfer Cong., Actuator 90, Bremen, Germany, 138–143.

Stanway, R., J. L. Sproston, M. Prendergast, J. R. Case, and C. E. Wilne (1992). ER fluids in the squeeze-flow mode: an application to vibration isolation. *J. Electrostatics*, 28, 89.

Uejima, H. (1972). Dielectric mechanism and rheological properties of electrofluids. *Jpn. J. Appl. Phys.*, 11, 319.

Winslow, W. M. (1949). Induced fibration of suspensions. *J. Appl. Phys.*, 20, 1137.

20

Electrostatic Atomization and Spraying

S. Edward Law

The University of Georgia
Athens, Georgia

I. INTRODUCTION

Numerous operations in agricultural production and processing require efficient mass transfer of particulate matter generally smaller than several hundred micrometers in diameter. Management by electrostatic forces offers solutions having much present benefit and future potential in engineered as well as in naturally occurring processes. Even the most essential natural particulate transfer in agriculture, plant pollination by insects, appears electrostatics based (Corbet et al., 1982) and amenable to further electrostatic augmentation (Law, 1991). Nearer the consumer, milled solid products such as sugars, flours, spices, and flavoring additives are routinely surface applied as electrically charged sprays to alter favorably the processing and organoleptic properties of foodstuffs. Refinement and purification of such particulate ingredients is commonly achieved via the electrostatic separation methods of Chapter 17.

Presently, the most extensive incorporation of electric force field management for agricultural particulates is electrostatic crop spraying. It will likely provide significant societal benefits as the efficient and environmentally sound technology for application of the chemical and biological pesticide sprays necessary for expanding production of the world's food and fiber. Approximately 400 million kilograms of chemical pesticide active ingredients are dispensed annually at a cost of $6 billion for protection of U.S. crops against insects, disease, and weed pests (Pimentel and Levitan,

1986; Aspelin et al., 1991). Conventional spray application technology, which relies upon gravitational and inertial forces, often achieves less than 50% mass transfer of this pesticide onto the desired plant targets; the actual quantity reaching the insect or disease pest is estimated to be as low as ca. 0.01% (Graham-Bryce, 1975; Pimentel and Levitan, 1986). Full incorporation of just a twofold improved electrostatic methodology into crop spraying would thus offer potential annual savings of $3 billion in crop production costs, a 200×10^6 kg reduction in toxic active ingredients entering the ecosystem, and 6×10^{14} J savings in embodied energy associated with the pesticide itself. Worldwide savings would be threefold greater.

In development of an electrostatic crop spraying system, significant differences regarding both the theoretical basis and engineering design exist vis-à-vis industrial coating and painting systems. The following sections outline these differences, discuss basic phenomena encountered during interaction of charged sprays onto living plants, and establish the theoretical and engineering-design rationale for reliable electrostatic spray applications in agriculture. Finally, the current status of electrostatic crop-spraying technology is illustrated by examples of commercial systems including documentation of their operational and pest-control performance.

II. THEORETICAL CONSIDERATIONS

Electrostatic crop spraying rests upon a sound rationale. Entomological studies over the past several decades have established that in numerous cases the small droplets of a pesticide spray provide greater biological efficacy per unit mass of pesticide than do the larger droplets for achieving insect control (Himel, 1969; Lake and Taylor, 1974; Graham-Bryce, 1977). Felici (1965) recognized that the charge-to-mass ratio generally achievable on droplets, and hence the ratio of the electric-to-gravitational forces controlling motion in a given electric field, varies inversely with droplet radius. Thus it is for the biologically efficacious, finely atomized pesticide droplets (e.g., under 100 μm in diameter) that the incorporation of electrostatic deposition forces becomes most opportune. This is precisely the size domain that suffers much airborne drift and off-target deposition when only the mass dependent gravitational and inertial delivery forces are relied upon as in conventional crop spraying methods.

A. Force Field Options

The necessary conditions for effecting the desired electrostatic forces in pesticide spray applications are that (a) significant electric charge must

be imparted to each spray droplet and that (b) the charged droplet spray must be driven by an electric field, either externally applied or self-generated. Figure 1 depicts the electric force components that can be exploited either singly or superimposed, while Fig. 2 plots as a function of diameter the theoretical terminal velocities attainable by charged droplets acted upon by these force fields as well as by gravitation for comparison (Law, 1987).

In contrast to the continuous surface films applied for industrial coating, plant pest control requires thorough surface coverage by a vast array of discrete pesticide control sites deposited throughout the plant canopy. Thus a major challenge is penetration of charged sprays to the electrostatically shielded interior regions of agricultural crops typically ranging from ¼ to 2 m in extent. Seldom will a purely electrostatic approach suffice; a "hybrid" method of electrostatic crop spraying incorporating a proper balance of other spray-penetration forces (e.g., aerodynamic) will usually be appropriate, except in the few cases requiring preferential droplet depo-

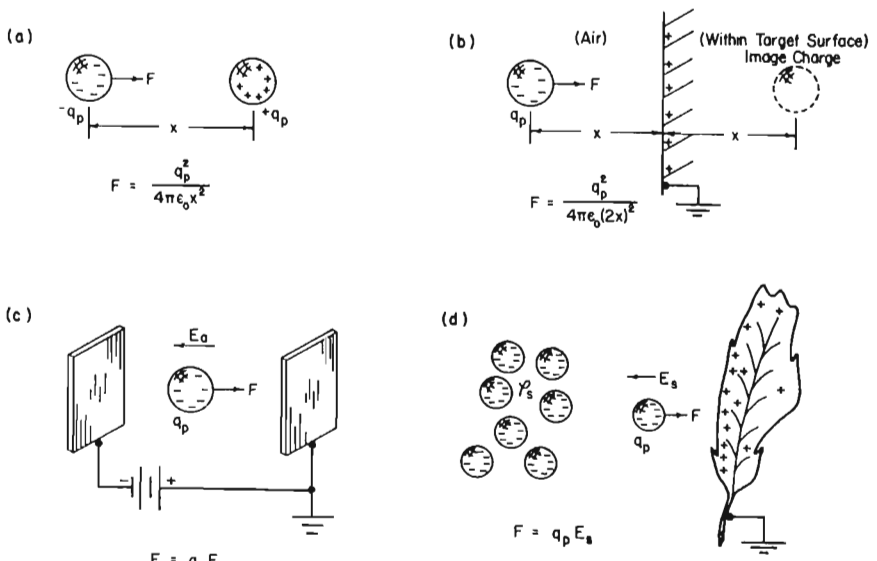


Figure 1 Electric force options for design of charged droplet crop spraying. (a) Inverse-square droplet-to-droplet force; (b) induced image-charge force; (c) externally applied electric field force; and (d) spray-cloud space charge force. (Reproduced with permission from Law, 1987. Copyright, Cambridge University Press.)

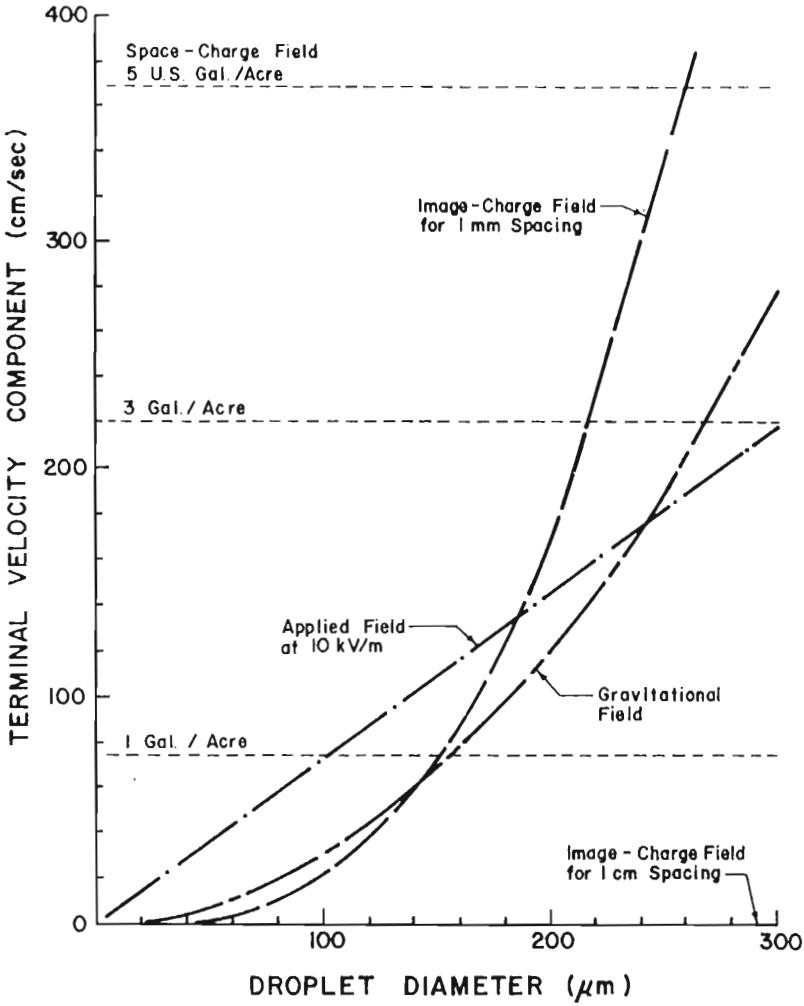


Figure 2 Terminal velocity components achieved by the electric force options driving an airborne charged pesticide-spray droplet. Space charge force calculated for 1 cm distance from leaf surface in 10 cm parallel leaf gap. (Reproduced with permission from Law, 1987. Copyright, Cambridge University Press.)

sition on the plant canopy's peripheral regions (e.g., hormonal sprays onto meristematic stem tips). Consequently, as compared with more conventional industrial electrostatic coating systems, agricultural crop spraying dictates a theoretical reassessment for optimally selecting the specific types of electric forces of Fig. 1 to be exploited (Law, 1987). For charged sprays dispensed from a mobile source such as a crop spraying machine traveling past target plants at 5–15 km/h, applied electric force fields imposed by 50–90 kV source electrodes become ineffective and would, in any case, deposit excessive pesticide spray onto the outer canopy. Once charged spray penetration into the deep canopy regions is achieved by nonelectrostatic means, electrostatic crop spraying, in contrast with industrial, then strongly relies upon the injected spray cloud's self-generated space charge field for deposition within the electrically shielded canopy. As charged droplets approach within several millimeters, image charges induced within plant surfaces also become significant for electrostatic attraction. Engineering designs should primarily exploit these two force fields for most agricultural crop spraying systems (Law, 1983).

Recent theoretical and experimental studies have established novel means for favorably manipulating the important charged-droplet-driving space charge electric field. Law and Bowen (1985) theoretically establish a dual particle-specie concept for improved deposition via space charge field enhancement, which is especially applicable for further supplementing electrostatic crop spraying forces within the plant canopy. Anantheswaran and Law (1981) provide an engineering design basis for properly incorporating a nonconductive wind barrier above a charged pesticide cloud for prevention of spray drift. Surface charge accumulated on the dielectric barrier generates an adequate repulsion field to ensure that the cloud's space charge force field is modified sufficiently to drive charged droplets away from the barrier and primarily down toward the grounded plants. As seen in Fig. 3, the safe self-charged dielectric barrier is equally effective as a 30 kV applied field for superimposing on the space charge field to maximize target deposition while eliminating deposition onto the wind shield. By dispensing an overlying like-polarity inert spray stratum, Inculet and Castle (1985) provide a convenient alternative method for favorably modifying a pesticide spray cloud's space charge field to ensure a downward electric droplet force. For earthed plants growing above a continuous plastic mulch film resting on the ground plane, Giles and Law (1990) verify that charge inadvertently captured on the underlying dielectric film deflects like-charged spray back upward to targets; as compared with uncharged spray, the electrodeposition benefit achieved with charged sprays was increased from a 2.7-fold value up to an enhanced 3.0-fold value due to the film's presence (i.e., an additional 10% deposition im-

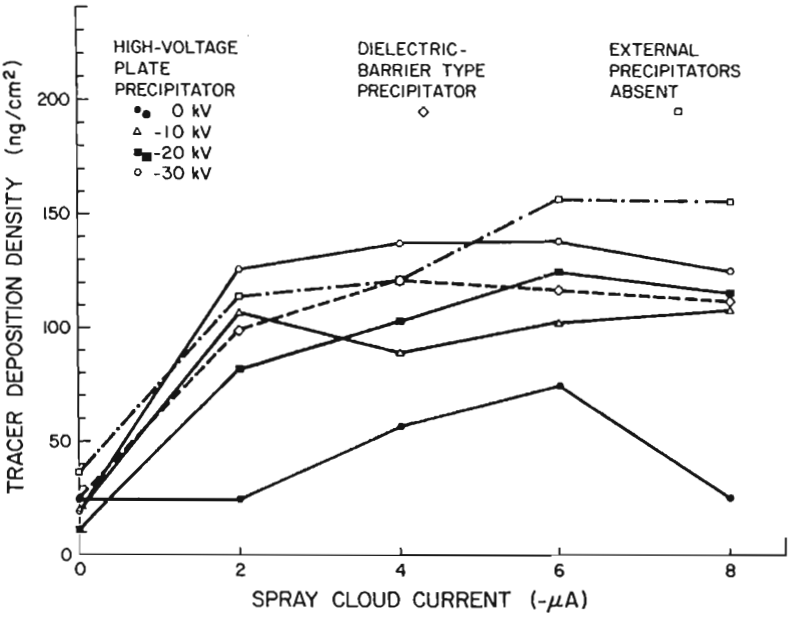


Figure 3 Spray deposition values achieved by different methods of electrostatic precipitation onto planar targets as functions of intensity of spray charging. (Reproduced with permission from Anantheswaran and Law, 1981. Copyright, American Society of Agricultural Engineers.)

provement). In contrast to these passive approaches for modifying the space charge field, active precharging of the dielectric mulch film to -15 $\mu C/m^2$ with air ions and elevating it 4 cm from earth has been shown to increase charged vs. uncharged spray deposition (i.e., electrodeposition benefit) onto target undersides where pests reside from a 1.9-fold value up to an enhanced 6.2-fold value (i.e., an additional 325% deposition improvement) while reducing environmentally abusive off-target deposition onto the underlying mulch film by 38% (Giles et al., 1991). Thus proper understanding and creative manipulating of space charge and boundary effects offer the designer of electrostatic pesticide sprayers means for optimizing application systems for specific crops and cultural practices.

B. Techniques for Agricultural Spray Charging

Most agricultural chemicals are dispensed as conductive aqueous solutions, emulsions, or wettable powder suspensions characterized by electrical resistivity values in the 10^{-1}–10^{4} Ωm range. Experience indicates

that electrification of such sprays to at least 1–2 mC/kg is generally required for initiating any significant degree of electrostatic control in outdoor pesticide applications. Of the various liquid charging methods described in Chapter 3, agricultural field tests have established the two most practical and reliable to be (a) ionized-field corona charging and (b) electrostatic induction charging. In addition, for application of certain specialized low-conductivity pesticide chemicals obeying narrowly defined constraints on electrical conductivity and permittivity, the direct electrostatic atomization and charging method based upon electrohydrodynamics becomes appropriate. Systems based upon this EHD method have been developed and extensively tested throughout the 1980s by Coffee (1980), especially as man-carried crop spraying devices. The recent work by Escallon and Tyner (1988) has further technically developed electrohydrodynamic spraying for agricultural applications of nonaqueous sprays of a 0.1–2000 centipoise viscosity range. Law (1984) critiques the relative advantages and disadvantages of the above spray charging methods and their applicability as dictated by the physical properties of the pesticide liquids to be electrified; dielectric constant and electrical conductivity (hence charge relaxation time constant) are primarily the relevant properties.

As seen in other chapters, the ionized-field particulate-charging method is routinely used in widespread industrial and commercial electrostatic processes such as particulate separation, coating, painting, and precipitation. In contrast, engineering the long-term reliability of this method for spraying conductive agricultural pesticides has proven difficult mainly due to the fragile nature of the exposed corona discharge electrode and personnel safety and charge leakage problems associated with the elevated ionizing voltages required (ca. 15–25 kV minimum) as well as the charge-limiting effects of reverse ionization from spray-fouled passive electrodes within charging devices (Law and Bowen, 1966; Splinter, 1968; Marchant, 1985). Energy-intensive means such as high velocity air curtains and heated insulators, respectively, remain less than satisfactory in a practical sense for maintaining passive-electrode cleanliness and the necessary high impedance path to earth across corona-electrode supports.

Figure 4 illustrates the engineering design features of an embedded-electrode, electrostatic-induction, spray-charging nozzle that has proven reliable for the severe operational conditions encountered in agricultural spraying (Law, 1978). In this pneumatic atomizing device, fine droplets (20–50 μm in diameter) are created via aerodynamic energy transferred by viscous drag to the axial jet of conductive spray liquid. For a relatively low positive potential (ca. 0.5–1.5 kV) applied to the miniature coaxial induction electrode positioned close by the liquid jet (e.g., 1.3 mm gap), an intense free electron surface density of ca. $10^8/mm^2$ is induced onto

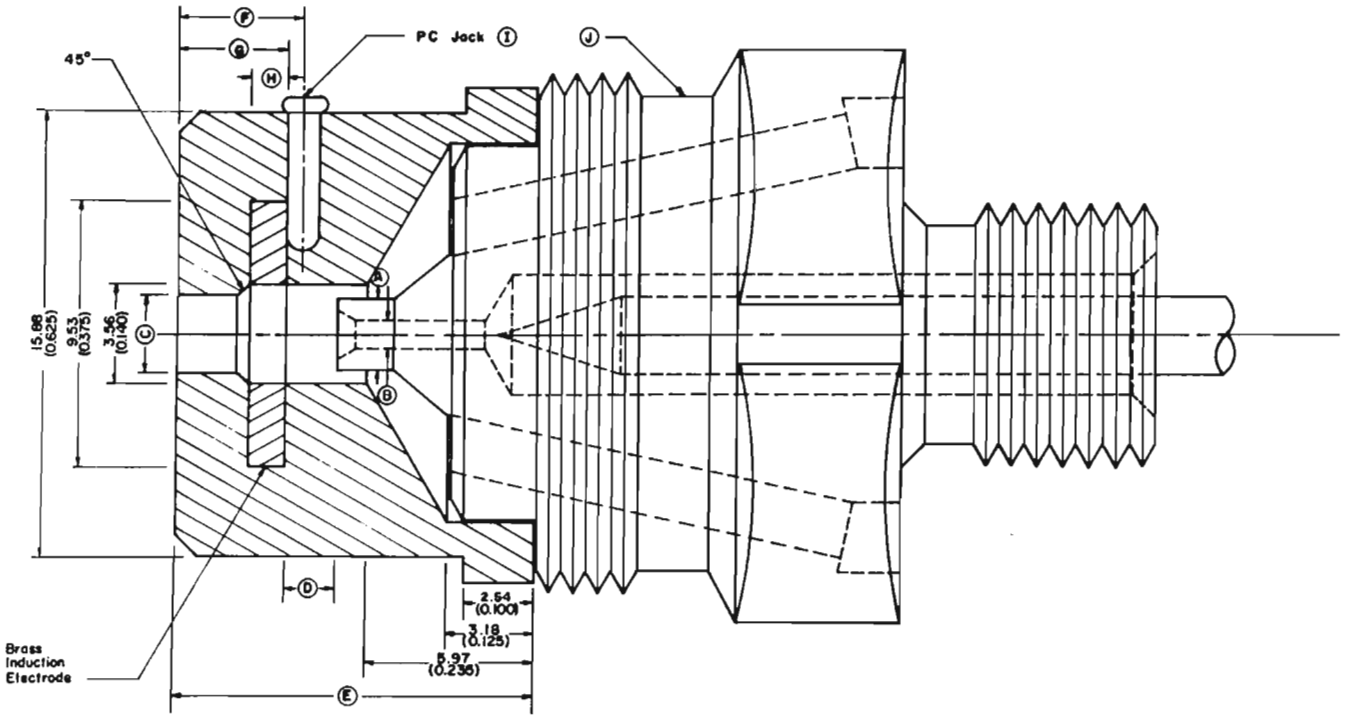


Figure 4 Engineering design features of electrostatic induction, pneumatic atomizing, spray charging nozzle showing sectioned view of the miniature induction electrode embedded within a dielectric channel. (Reproduced with permission from Law, 1978. Copyright, American Society of Agricultural Engineers.)

the earthed droplet formation zone by a 1.6×10^6 V/m field created by only a 1 kV electrode potential. Since charge must flow through the liquid jet to the droplet formation zone, the level of droplet charge imparted by induction will depend upon the time rate of charge transfer achievable through the liquid as compared to the time t_f required for droplet formation. Expressing the liquid's charge-transfer time constant τ as

$$\tau = K\rho\epsilon_0 \tag{1}$$

the appropriate design limits for induction spray charging are seen in Fig. 5 for the constraint $\tau < t_f/5$. Water based sprays are thus theoretically predicted as compatible for induction charging for $\rho < 4.5 \times 10^5$ Ωm. Law and Cooper (1987) have modified the resistivity of vegetable oil based pesticide sprays successfully to undergo induction charging. Once sheared

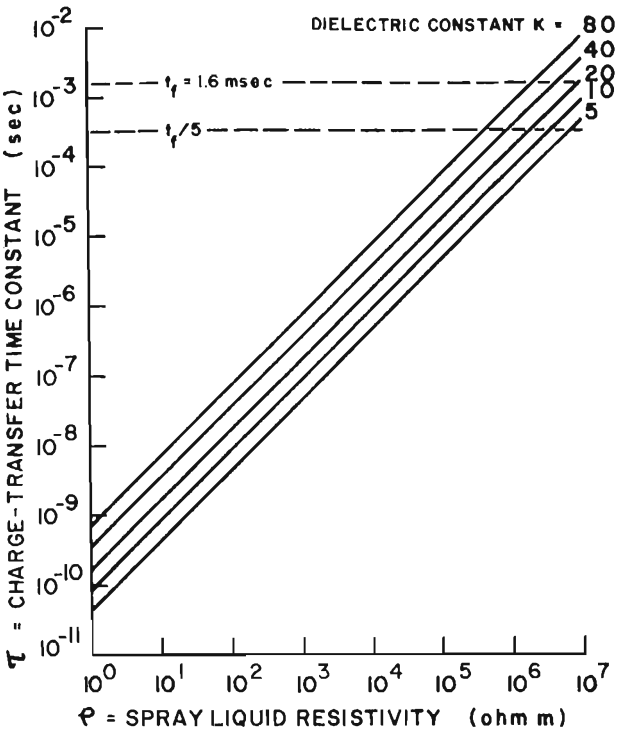


Figure 5 Charge-transfer time constants characterizing spray liquids as functions of liquid electrical resistivity and dielectric constant. (Reproduced with permission from Law, 1978. Copyright, American Society of Agricultural Engineers.)

from the jet, the nozzle's geometrical-electrical-aerodynamic design ensures that charged droplets have an axial exit velocity at least five-fold greater than the electrical migration velocity toward the oppositely charged induction electrode. Deposition of conductive droplets onto the smooth, passive electrode is prevented, thus precluding any "back corona" of positive air ions (Chapters 21 and 22) from water discharge peaks that would negate the induction charging process. The linear dependence of the induction charging process upon the potential applied to the embedded induction electrode is seen in Fig. 6 as well as the upper limit of induction charging as determined by the undesirable onset of gaseous discharge across the annular air gap at 1.9 kV as predicted by Peek's equation (1929) for this specific coaxial electrode design.

Compact induction nozzles offer electrostatic crop sprayer designers a simple and reliable means for imparting high ratios of droplet charge-to-mass ca. 5–15 mC/kg onto earthed sources of conductive pesticide sprays using relatively low values of charging voltage ca. 0.5–1.5 kVdc and electronic power ca. 10–50 mW. These low voltage and power requirements permit small (ca. 50 g) economical transistor-oscillator dc-to-dc battery-powered supplies dedicated to individual spray-charging nozzles, thus eliminating external high-voltage wiring harnesses to the nozzles and their associated current leakage and dielectric breakdown in the wet spray environment. The 200–400 W of aerodynamic power input per pneumatic atomizing nozzle, in addition to providing the small power needed for droplet creation and induction-electrode maintenance, may be exploited as an inherent air-carrier stream for charged droplet conveyance, plant canopy penetration, and turbulent dispersal therein.

C. Charged Droplet Interactions

Once dispensed from a spray charging nozzle, airborne pesticide droplets are subject to a number of important environmental and target-related phenomena that determine the degree of reliability and success for the electrostatic crop spraying process. Law (1987) mathematically analyzes these basic phenomena; a brief summary of the most significant aspects follows along with certain numerical and graphical results that provide basic guidance for engineering designs of electrostatic crop spraying systems.

1. Neutralization by Ambient Air Ions

Given adequate time, migration of naturally occurring air ions to charged droplets will tend to neutralize electrically a spray cloud. At typical ion-pair equilibrium concentrations n_i ca. $1–2 \times 10^3/cm^3$ and mobilities μ_i of

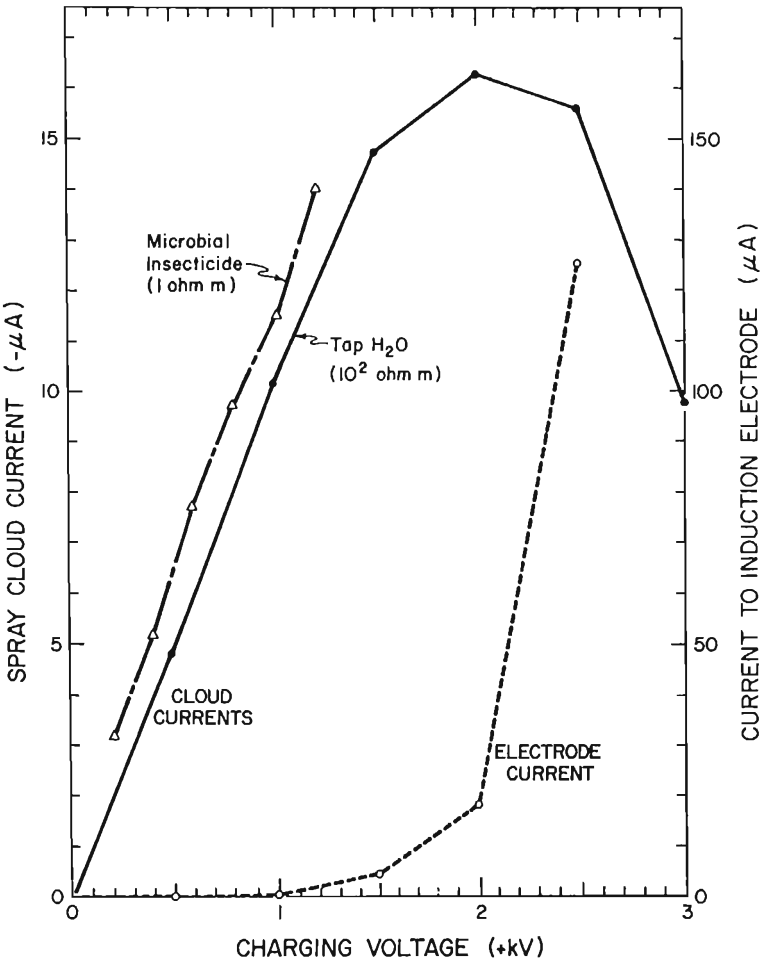


Figure 6 Spray-charging characteristics of embedded electrode, electrostatic induction nozzle as functions of input voltage when operating at 73 mL/min liquid flow and 276 kPa atomizing-air pressure. (Reproduced with permission from Law, 1983. Copyright, Institute of Electrical and Electronics Engineers.)

1.4 and 2.1 cm/s per V/cm field, respectively, for positive and negative singly charged air ions (Cobine, 1958), the cloud's charge-decay process is characterized by the time constant

$$\tau = \frac{\epsilon_0}{n_i q_i \mu_i} \tag{2}$$

For a typical 1 m diameter spray cloud charged to a moderate 5 $\mu C/m^3$ space charge density, opposite polarity air ions would comprise only ca. 60 ppm of the total free charge within the cloud confines; air ions from a 12½ m radius concentric zone would be required for complete neutralization of the cloud. In one elapsed time constant of $\tau \approx 200$ s, a 63% neutralization would occur; fortunately, only ca. 1% would occur in the 1–3 s period characterizing row crop or greenhouse spraying. Thus the designer need not be concerned with detrimental air-ion effects in electrostatic pesticide spraying except perhaps in the long airborne spray times associated with vector control.

2. Evaporation Effects

Aqueous based pesticide sprays are strongly subject to evaporative size reduction in many outdoor applications. Law and Bowen (1975) theoretically evaluate the interactions of surface charge and evaporation on such airborne agricultural sprays. It is experimentally and theoretically shown that no charge loss occurs via departing water vapor molecules and that only in the nonrelevant droplet size realm smaller than 0.1 μm does surface charge reduce the droplet's curvature-generated vapor pressure and hence the evaporation rate. As surface charge density increases on an evaporating pesticide droplet of fixed charge, the outward mechanical stress due to charge eventually grows to match the inward stress of surface tension Γ; the well known Rayleigh charge limit consistent with hydrodynamic stability is attained (Rayleigh, 1896) as

$$q_p = 8\pi\sqrt{\epsilon_0 \Gamma}\, r_p^{3/2} \tag{3}$$

and the unstable droplet will generally eject ca. 5–10% of its mass carrying away ca. 30% of its initial charge (Doyle et al., 1964). Roth and Kelly (1983) theoretically predict, on the basis of energy minimization principles, spontaneous creation of 6–8 sibling droplets of charge-to-mass greater than the parent droplet. Successive disruptions of the parent occur as long as other charge-loss modes (e.g., gaseous discharge) are not active. As a function of droplet radius, Fig. 7 plots the Rayleigh charge limit as well as charge-to-mass for the extreme surface tension values likely to be encountered in electrostatic spraying of water based pesticides. Theoretical analysis predicts for droplet sizes throughout the realm of agricultural sprays that the droplet charge limit causing hydrodynamic instability will be reached before that for ion emission as based upon the Felici (1964) equation for dielectric breakdown around small spheres. Therefore the charged droplet rupture process is likely prevalent in electrostatic crop spraying. While individual droplets suffer appreciable charge loss, conservation of charge is obeyed by the spray cloud. Clever process design

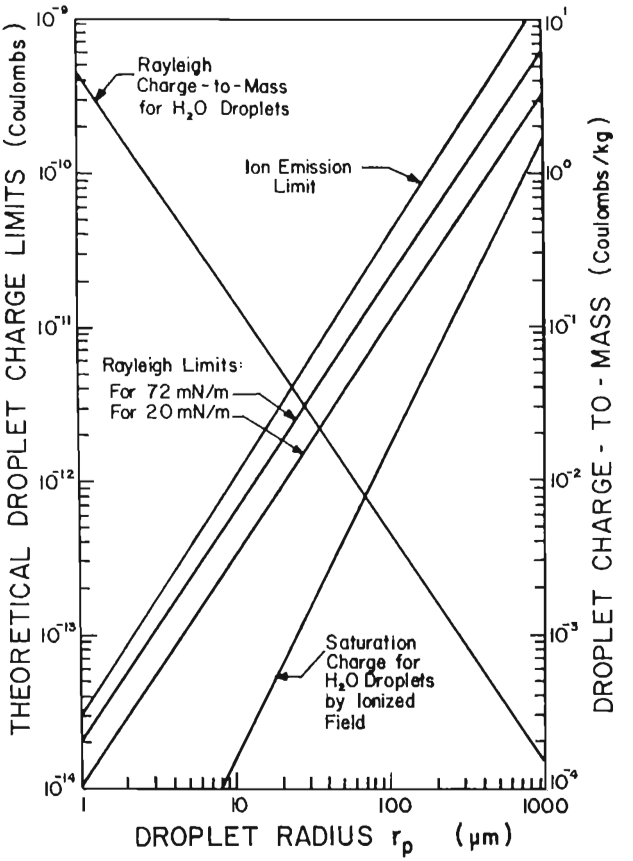


Figure 7 Rayleigh and other theoretical limits on charge carried by airborne pesticide droplets as determined by liquid surface tension and droplet radius. (Reproduced with permission from Law, 1987. Copyright, Cambridge University Press.)

should exploit the higher mobility sibling droplets for enhanced deposition characteristics in specific crop/pest complexes.

3. Target-Related Phenomena

Law (1989) summarizes electrical interactions occurring at targets undergoing electrostatic spraying and elucidates those possibly establishing inherent limitations in the electrodeposition process for charged sprays onto living plants.

Induced Corona. For an electrostatic crop sprayer passing at 5 km/h over a linear array of instrumented targets (7.6 cm diameter copper spheres) simulating a row of plants, Fig. 8 characterizes the interaction of the charged spray cloud's space charge field with a given target as the cloud is dispensed along the row. As seen, the interaction, exhibited here as electric field experienced at the surface of the earthed target, has a duration of ca. 600–1500 ms and a peak value ca. 2 kV/cm. For targets having sharp protrusions (e.g., certain leaf-tips), overly intense fields can induce corona discharge from the earthed tips, causing a self-limiting condition in the electrodeposition of the approaching charged sprays (Law and Lane, 1981, 1982); the severity of the limitation is seen in Fig. 9 to be a halving of the electrodeposition benefit for a single target. Under these

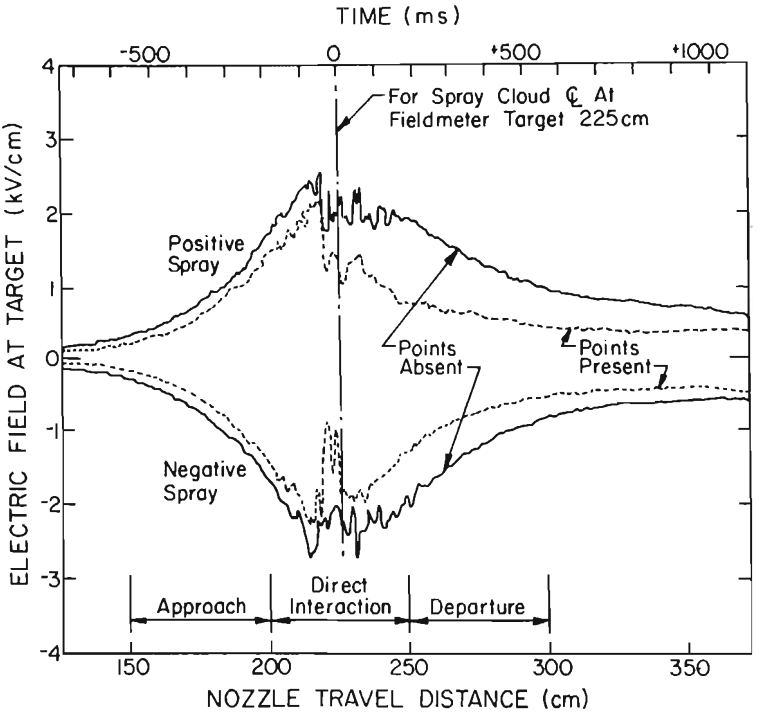


Figure 8 Transient characteristics of the space charge electric field imposed at a spherical earthed target being electrostatically sprayed by a nozzle passing by at 5 km/h while dispensing 4 mC/kg charged spray of indicated polarity. (Reproduced with permission from Cooper and Law, 1987. Copyright, British Institute of Physics.)

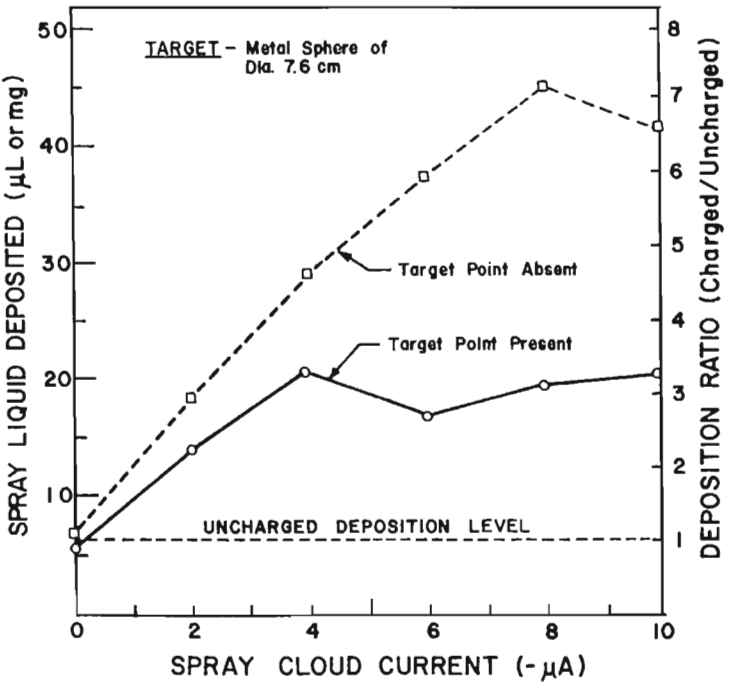


Figure 9 Effect that corona discharge induced from an earthed target point has upon the electrostatic deposition benefit for pesticide sprays as a function of spray-charging intensity. (Reproduced with permission from Law and Lane, 1982. Copyright, Institute of Electrical and Electronics Engineers.)

conditions, gaseous conduction induced from target points accounts for as much as 85% of the total charge exchanged between the incoming charged spray cloud and the target—useful charge transfer associated with electrodeposition is often as low as 15%. In addition to this negating of electrostatic attraction, Law and Bailey (1984) show that momentum and charge transfers of the induced air-ion flux from the earthed point actually repel charged droplets from the target, as documented in Fig. 10. This effect could have serious implications concerning achieving biologically important deposition onto certain plant components (Evans et al., 1992).

For a linear array of targets spaced 31 cm from each other, Cooper and Law (1987) show induced corona from a target point to cause ca. a 32% and a 44% collapse in the droplet driving space charge field of negatively and positively charged sprays, respectively, as compared with the field at a smooth target (Fig. 8). They also clearly document a corresponding

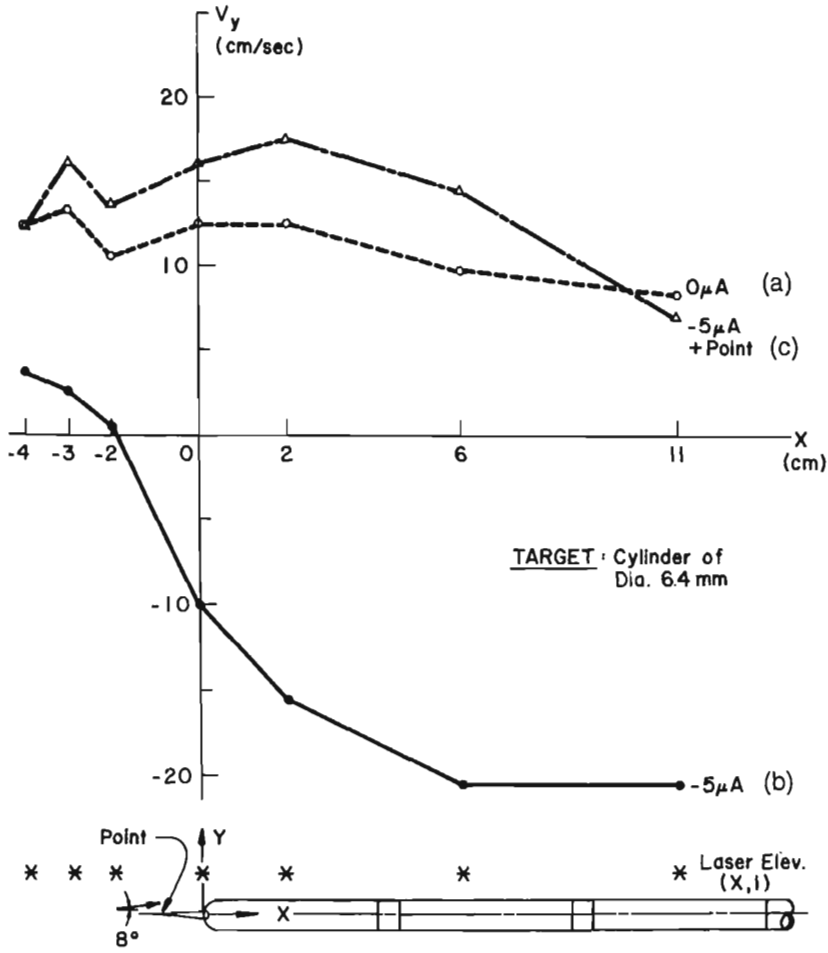


Figure 10 Droplet vertical velocity component v_y at laser-Doppler measurement locations along a cylindrical target 1 cm above its centerline for three spray and earthed-point conditions. (a) Uncharged spray = 0 μA spray-cloud current; (b) charged spray = 5 μA; and (c) charged spray onto target with point affixed = 5 μA + point. (Reproduced with permission from Law and Bailey, 1983. Copyright, Institute of Electrical and Electronics Engineers.)

statistically significant ($p < 0.01$) polarity dependent reduction in target electrodeposition benefit down to 1.80-fold and 1.50-fold for negatively and positively charged sprays, respectively, as compared with a polarity independent electrodeposition benefit of 4.02-fold for a smooth target. Thus when induced target corona is anticipated, the designer should judiciously select negative droplet charging.

Target RC Requirements. During the typical 600–1500 ms electrostatic crop spraying event, transient flow of current through the plant to earth is required if electrodeposition is to occur unimpeded. For targets having excessively resistive pathways to earth, the accumulation of charge on their boundaries during electrostatic spraying can elevate the electric potential of these regions toward that of the incoming charged cloud. This condition reduces the electric field that drives charged droplets to the target, and electrodeposition may consequently be diminished. The smaller the capacitance value C characterizing isolated targets, the greater will be the attained retarding voltage $V_0 = q/C$ resulting from impingement or deposition of droplets delivering a given charge q. For any finite value R of target leakage resistance to earth, this initial level of potential elevation will decay with time t as $V = V_0 e^{-t/RC}$ where RC is the target system's charge dissipation time constant. Theoretically it may be predicted that target RC time values that are short compared with the typical 1 s duration of electrostatic spraying processes (e.g., $RC < 0.1$ s) will allow such rapid leakage of the intercepted charge to earth that the target's potential will remain essentially grounded throughout most of the spraying event. This design criterion should preclude a detrimental target interaction by charge accumulation.

Models electrically simulating agricultural crops have been theoretically and experimentally analyzed to determine further target RC characteristics compatible with electrostatic crop spraying. Lane and Law (1982) studied transient displacement currents flowing through mature cotton plants in response to a rapidly changing imposed field (ca. 2×10^6 V/s rate of potential change) and found no attenuation of charge transfer for plants ranging in moisture content from field saturation to brittle, wilt-dried plants; thus electrostatic concerns regarding drought stress are eliminated. Franz et al. (1987) theoretically simulated the response of plants to charged-spray-imposed space charge fields; a 10 μs RC time constant was calculated for a simulated eight-leaf bean plant modeled as a number of paralleled leaf RC impedances in series with a stem resistance to earth.

In contrast to agronomic crops grown directly in the earth, Law and Cooper (1989) modeled plastic potted greenhouse and horticultural nursery plants by simple RC circuits and then experimentally varied target resistance and capacitance values over wide ranges in order to measure

their effects upon the target potential attained and the electrodeposition benefit achieved. For medium-size geranium and coleus plants growing in 18 cm diameter × 15 cm high plastic pots sitting on a conductive table as in a greenhouse, 90 pF characterized the capacitance of an individual potted plant system. A single Teflon supported 7.6 cm diameter metal sphere spray target, capacitively connected to an electrostatic fieldmeter via a 30 cm diameter parallel plate capacitator, provided an instrumented target system of 120 pF that adequately approximated plastic containerized plants on greenhouse benches. With the fieldmeter probe recessed into the grounded plate of the capacitor, transient values of target potential could thus be measured in a contactless manner and recorded on an oscillograph as a spray charging nozzle passed over at 5 km/h. For this plant capacitance, the theoretically imposed constraint $RC < 0.1$ s would be obeyed for a target leakage resistance to earth of $R \leq 10^9\ \Omega$, and negligible elevation in target potential would occur. As seen in Fig. 11, the increase in target potential due to charged spray application was indeed experimentally found to be only a negligible 160 V at $10^8\ \Omega$ leakage. At $10^{10}\ \Omega$ it had reached 3.3 kV as theoretically predicted from time constant considerations. It can be seen that even for the target's maximum voltage, which compares to only approximately 15% of the cloud's 32 kV space charge potential, there was no significant detriment to deposition; the fivefold electrodeposition benefit was statistically unchanged throughout the $0–10^{12}\ \Omega$ range of target leakage paths to earth. A survey of hanging and table supported plastic containerized living plants in commercial greenhouses indicated plant-to-earth resistances of $10^7–10^9\ \Omega$. Thus on both a theoretical and an experimental basis, it may be concluded that the electrical grounding of such plants should be adequate for satisfactory development of electrostatic crop spraying for greenhouse culture. Additional target capacitance effects are reported by Law (1989) for high impedance spray targets.

III. ELECTROSTATIC CROP SPRAYERS

Various prototype and commercial machines have been developed to practice, in a complementary manner, the afore-mentioned electrostatic spraying methodology for a number of agricultural pest control needs. These application areas broadly include ground equipment for spraying plants of row crops, orchards, and greenhouses, and aircraft spraying of large acreage crops such as cotton, corn, etc. Each crop-pest complex presents its distinct challenges and, correspondingly, electrostatic methods have found varying levels of appropriateness and success (Law and

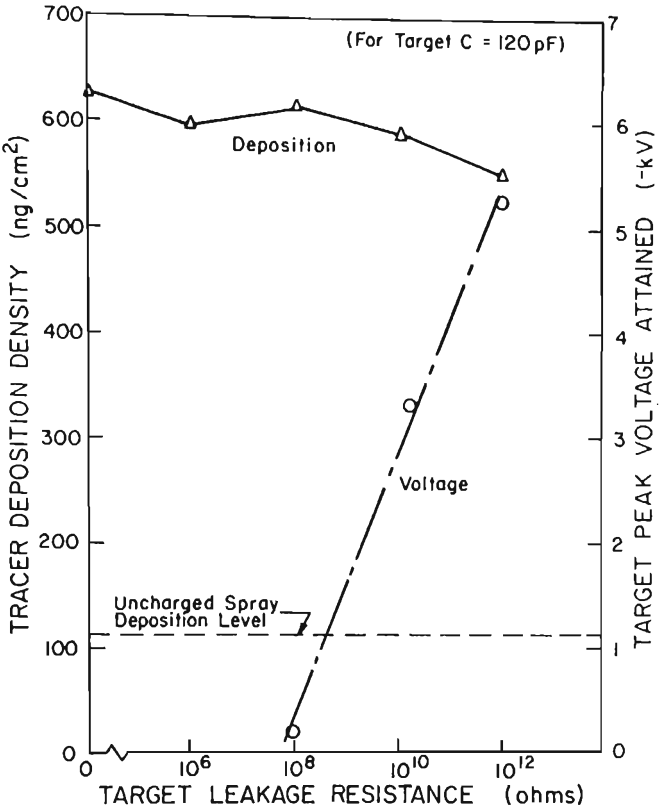


Figure 11 The effects that charge-leakage resistance to earth has upon the peak voltage attained and the deposition achieved on a 7.6 cm diameter metal-sphere target undergoing electrostatic spraying by a −4 mC/kg passing spray. (Reproduced with permission from Law and Cooper, 1989. Copyright, American Society of Agricultural Engineers.)

Mills, 1980; Herzog et al. 1983; Cooke et al., 1986; Franz et al., 1987; Hislop, 1988).

Figure 12 pictures a University of Georgia developed embedded electrode induction nozzle and associated electronics specifically designed for charging conductive water-borne pesticide sprays (Law, 1977). This is the key component facilitating the commercial development of greenhouse (Fig. 13) and row-crop (Fig. 14) electrostatic machines now in routine

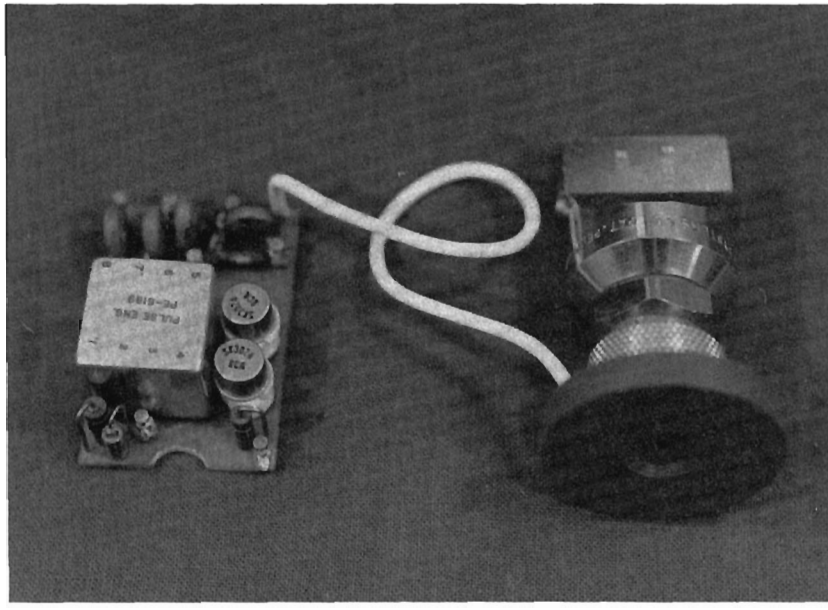


Figure 12 Embedded electrode, electrostatic induction, pneumatic atomizing, spray charging nozzle and electronic power supply for conductive pesticide applications. (Reproduced with permission from Law, 1983. Copyright, Institute of Electrical and Electronics Engineers.)

crop production use. Figure 15 documents the two-fold improvement in deposition efficiency of Captan fungicide applied to strawberry plants using this aerodynamic-electrostatic machine (Giles and Blewett, 1991). Electrostatic application of ½-rate pesticide active ingredient in only 8½ gal/acre (80 liters/hectare) of spray mix is seen to provide a leaf deposit (termed "dislodgeable foliar residue") statistically the same as did conventional hydraulic-pressure nozzles dispensing twice the active ingredient in 200 gal/acre (1870 liters/hectare) of spray mix. In addition, the persistence of the disease-preventing deposits was identical over the subsequent 21-day period (viz., exponential decay constant of 6.73 days for the foliar deposits).

Spraying of tree-size plants in orchards requires spray droplets to be dispensed in large volume, high velocity air carrier streams ca. 45,000 ft^3/min (21 m^3/s) at 100 mi/h (45 m/s) for achieving the appreciable travel



Figure 13 Hand-directed electrostatic sprayer for greenhouse pest control. (Photograph courtesy of Electrostatic Spraying Systems, Inc.)

distances and canopy depths required. While several prototype and commercial electrostatic orchard sprayer machines have been introduced over the past decade, limited success has been achieved mainly due to the great dominance of aerodynamic forces over electrostatic. Deposition improvements mainly within low air velocity regions hold promise (Inculet et al., 1981; Law and Cooper, 1988).

Electrostatic crop spraying from aircraft has also achieved only limited and generally inconsistent results in increasing the efficiency of pesticide deposition onto crops (Carlton, 1975; Carlton and Bouse, 1980). Technical difficulties relate to dissipation of the opposite residual charge buildup on the airframe as charged spray is disseminated, leading both to impaired charging ability and to neutralization of the descending spray by highly mobile air ions emitted by corona discharges from the airframe. This charge-management difficulty is likely solvable to a degree by pulsed laser ionization of a charge dissipation path to earth periodically, or by the method of polarity partitioning of right wing vs. left wing spray booms as theoretically developed by Inculet and Fischer (1989). Of more fundamen-



Figure 14 Tractor-mounted electrostatic crop sprayer incorporating thirty embedded electrode air assisted induction nozzles for row-crop pest control. (Photograph courtesy of Electrostatic Spraying Systems, Inc.)

tal concern is the question of the appropriateness of electrostatic spraying methodology for aerial crop spraying. Relatively large droplets of 200–500 μm diameter are not effectively controlled by electrostatic forces, but this size is normally used to ensure rapid settling of spray down the 2–4 m distance from the aircraft to the crop; slower settling, smaller pesticide droplets are severely subject to lateral drift from the treated area, causing environmental concerns. In order to resolve this difficulty, Law and Bowen (1988) have theoretically developed design equations that specify the initial charge-to-mass of larger droplets emitted from the aircraft, which will cause onset of Rayleigh instability and ejection of high charge-to-mass, biologically efficacious sibling droplets of small size at crop canopy elevation.

The electrohydrodynamic atomizing and charging nozzle of Fig. 16 (Escallon and Tyner, 1988) and the Electrodyne by Coffee (1980) provide elegant means for creating charged droplets by purely electrical energy. To a degree, droplet size may also be electrically controlled in conjunction with adjustments of liquid throughput. Though not applicable for widely used aqueous based pesticide sprays, EHD devices should provide design

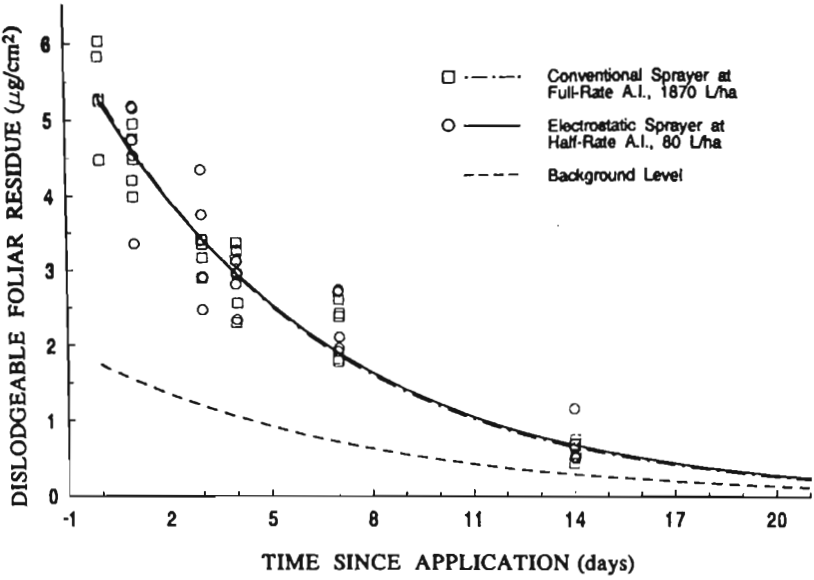


Figure 15 Comparison of the initial foliar deposits of Captan fungicide on strawberry plants and their subsequent exponential decay for conventional full-rate spray application of pesticide active ingredient (A.I.) vs. air-assisted electrostatic spray application of half-rate A.I. (Reproduced with permission from Giles and Blewett, 1991. Copyright, American Chemical Society.)

options for electrostatic applications of specialized oil based liquids generally within the 10^4–10^9 Ωm range of resistivity. For adequate crop canopy penetration and reduction of spray-drift susceptibility, however, the incorporation of appreciable nonelectrostatic droplet trajection forces (e.g., high velocity air carrier) is likely necessary for EHD nozzles (Parham, 1982; Hislop, 1988; Almekinders et al., 1991; Hislop, 1991).

IV. CONCLUSION

Electrostatic atomization and spraying in agriculture has found widest usage as the basis for incorporating electric force fields into the application of crop protection pesticides. Twofold improvements in droplet mass transfer efficiency onto plant surfaces are routinely achieved with corresponding environmental and economic benefits. Electrostatic induction has proven most satisfactory for charging water based sprays in the field, while electrohydrodynamic atomization serves well for charging low con-

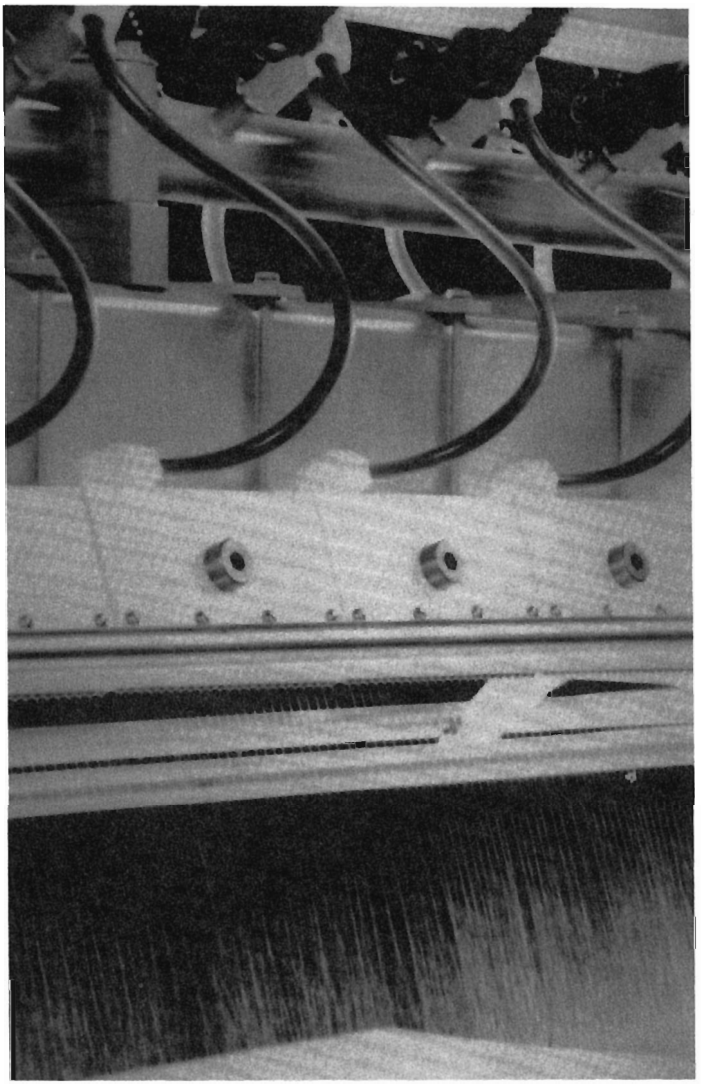


Figure 16 Electrohydrodynamic atomizing and charging nozzle of linear segmented design for spraying nonaqueous, low conductivity liquids. (Photograph courtesy of Terronics Development Corp.)

ductivity, nonaqueous liquids. Negative polarity sprays have been shown to be preferred for crop spraying. Once charged in excess of the necessary 1–2 mC/kg level, pesticide sprays usually require an auxiliary nonelectrostatic energy input to achieve adequate droplet trajection and penetration deeply into electrically shielded earthed plant canopies—hence hybrid designs such as the aerodynamic-electrostatic crop sprayer. Since source-applied fields using the 50–90 kV of industrial coating systems are generally hazardous on mobile equipment, are unmaintainable using conductive sprays, and tend to deposit pesticide only onto peripheral plant regions, electrostatic crop sprayer designs should best exploit and judiciously manage space charge field effects. Proper management must recognize that sprays highly charged to 20–25 $\mu C/m^3$ can impose fields as intense as $2–3 \times 10^5$ V/m at target surfaces, causing onset of induced corona from grounded leaf-tips. While the 200 s time constant characterizing ion neutralization of airborne charged spray clouds precludes any concern for charge loss by this phenomenon, both beneficial and detrimental effects of Rayleigh instability of evaporating charged pesticide droplets should be considered in process design. Having satisfactorily charged and dispersed spray droplets to pest infested regions within a living plant, electrodeposition should be reliably achieved even for plastic containerized plants having as great as 10^{10} Ω resistance in their grounding paths to earth. Thus crop conditions will likely never impede the electrodeposition process in electrostatic crop spraying.

NOMENCLATURE

C	capacitance of spray target, F
E	electric field, V/m
F	force acting on charged particulate, N
K	dielectric constant of spray liquid, unitless
n_i	air-ion numerical density, ion pairs/m^3
q_i	air-ion charge, C
q_p	particulate charge, C
r_p	particulate radius, m
R	target leakage resistance to earth, ohms
t_f	droplet-formation time, s
V	target potential, V
Γ	surface tension of spray liquid, N/m
ϵ_0	permittivity of free space ≈ air, C^2/Nm^2
μ_i	air-ion mobility, m^2/Vs
ρ	resistivity of spray liquid, ohm m
ρ_s	space-charge density, C/m^3
τ	charge-transfer time constant, s

REFERENCES

Almekinders, H., H. E. Ozkan, T. G. Carpenter, D. L. Reichard, and R. D. Brazee (1992). Spray deposit patterns of an electrostatic atomizer. *Trans. ASAE*, 35(5), 1361–1367.

Anantheswaran, R. C., and S. E. Law (1981). Electrostatic precipitation of pesticide sprays onto planar targets. *Trans. ASAE*, 24(2), 273–276, 280.

Aspelin, A., A. Grube, and V. Kibler (1991). Pesticide production and usage for 1989. Rpt. of Economic Analysis Div., Office of Pesticide Programs, U.S. Environmental Protection Agency, Washington, DC.

Carlton, J. B. (1975). Electrical capacitance determination and some implications for an electrostatic spray-charging aircraft. *Trans. ASAE*, 18(4), 641–644.

Carlton, J. B., and L. F. Bouse (1980). Electrostatic spinner-nozzle for charging aerial sprays. *Trans. ASAE*, 23(6), 1369–1373, 1378.

Cobine, J. D. (1958). *Gaseous Conductors: Theory and Engineering Applications*. Dover, New York.

Coffee, R. A. (1980). Electrodynamic spraying. In *Spraying Systems for the 1980's* (J. O. Walker, ed.). B.C.P.C. Monograph No. 24, London, pp. 95–107.

Cooke, B. K., E. C. Hislop, P. J. Herrington, N. M. Western, K. G. Jones, S. E. Woodley, and A. C. Chapple (1986). Physical, chemical and biological appraisal of alternative spray techniques in cereals. *Crop Protection*, 5, 155–164.

Cooper, S. C., and S. E. Law (1987). Transient characteristics of charged spray deposition occurring under action of induced target coronas: space-charge polarity effect. *Electrostatics 87*, IOP Press, Oxford, Brit. Inst. of Physics Conf. Ser. No. 85 (Sec. 1), 21–26.

Corbet, S. A., J. Beament and D. Eisikowitch (1982). Are electrostatic forces involved in pollen transfer? *Plant, Cell and Environ.*, 5, 125–129.

Doyle, A. D., R. Moffett, and B. Vonnegut (1964). Behavior of evaporating electrically charged droplets. *J. Colloid Sci.*, 19, 136–143.

Escallon, E. C., and A. E. Tyner (1988). Nozzle method and apparatus. U.S. Patent 4749125.

Evans, M. D., S. E. Law, and S. C. Cooper (1994). Image analysis of fluorescent spray deposits using light-intensified machine vision. *Applied Engineering in Agri.*, *10*(3), 441–447.

Felici, N. J. (1964). Contemporary electrostatics: physical background and applications. *Contemporary Physics*, 5(5), 377–390.

Felici, N. J. (1965). Electrostatic engineering. Science J., 1(9), 32–38.

Franz, E., R. D. Brazee, T. G. Carpenter, and D. L. Reichard (1987). Model of plant charge induction by charged sprays. *Trans. ASAE*, 30(2), 328–331.

Franz, E., D. L. Reichard, T. G. Carpenter, and R. D. Brazee (1987). Deposition and effectiveness of charged sprays for pest control. *Trans. ASAE*, 30(1), 50–55.

Giles, D. K., and T. C. Blewett (1991). Effects of conventional and reduced-volume, charged-spray application techniques on dislodgeable foliar residue of Captan on strawberries. *J. Agric. Food Chem.*, 39, 1646–1651.

Giles, D. K., and S. E. Law (1990). Dielectric boundary effects on electrostatic crop spraying. *Trans. ASAE*, 33(1), 2–7.

Giles, D. K., Y. Dai, and S. E. Law (1991). Enhancement of spray electrodeposition by active precharging of a dielectric boundary. *Electrostatics 91*, IOP Press, Oxford, Brit. Inst. of Physics Conf. Ser. No. 118(Sec. 1), 33–38.

Graham-Bryce, I. J. (1975). The future of pesticide technology: opportunities for research. *Proc. 8th Brit. Insecticides and Fungicides Conf.*, 3, 901–914.

Graham-Bryce, I. J. (1977). Crop protection: a consideration of the effectiveness and disadvantages of current methods and the scope for improvement. *Phil. Trans. Roy. Soc. London*, 281(B), 163–179.

Herzog, G. A., W. R. Lambert, S. E. Law, W. E. Seigler, and D. K. Giles (1983). Evaluation of an electrostatic spray application system for control of insect pests in cotton. *J. Econ. Entomol.*, 76(3), 637–640.

Himel, C. H. (1969). The optimum size for insecticide spray droplets. *J. Econ. Entomol.*, 62, 919–925.

Hislop, E. C. (1988). Electrostatic ground-rig spraying: an overview. *Weed Technology*, 2, 94–105.

Hislop, E. C. (1991). Air-assisted crop spraying: an introductory review. *Brit. Crop Protection Conf.* Monograph No. 46, pp. 3–13.

Inculet, I. I., and G. S. P. Castle (1985). Selective depositions using layered charged aerosols. *IEEE Trans.*, IA-21(2), 507–510.

Inculet, I. I., and J. K. Fisher (1989). Electrostatic aerial spraying. *IEEE Trans.*, 25(3), 558–562.

Inculet, I. I., G. S. P. Castle, D. R. Menzies, and R. Frank (1981). Deposition studies with a novel form of electrostatic crop sprayer. *Electrostat.*, 10, 65–72.

Lake, J. R., and W. A. Taylor (1974). Effect of the form of a deposit on the activity of barban applied to *Avena fatua* L. *Weed Res.*, 14, 13–18.

Lane, M. D., and S. E. Law (1982). Transient charge transfer in living plants undergoing electrostatic spraying. *Trans. ASAE*, 25(5), 1148–1153, 1159.

Law, S. E. (1977). Electrostatic spray nozzle system. U.S. Patent 4004733.

Law, S. E. (1978). Embedded electrode electrostatic-induction spray-charging nozzle: theoretical and engineering design. *Trans. ASAE*, 21(6), 1096–1104.

Law, S. E. (1983). Electrostatic pesticide spraying: concepts and practice. *IEEE Trans.*, IA-19(2), 160–168.

Law, S. E. (1984). Physical properties determining chargeability of pesticide sprays. *Advances in Pesticide Formulation Technology* (H. B. Scher, ed.). Amer. Chem. Soc. Monograph Ser. No. 254, Washington, D.C., pp. 219–230.

Law, S. E. (1987). Basic phenomena active in electrostatic pesticide spraying. In *Rational Pesticide Use* (K. J. Brent and R. K. Atkin, eds.). Cambridge University Press, Cambridge, pp. 81–105.

Law, S. E. (1989). Electrical interactions occurring at electrostatic spraying targets. *J. Electrostatics*, 23, 145–156.

Law, S. E. (1991). Electrostatic processes underlying natural and mechanized transfer of pollen. Technical Report, Biol. and Agric. Engineering Dept., Univ. of Georgia, Athens, Georgia, 46 pp.

Law, S. E., and A. G. Bailey (1984). Perturbations of charged-droplet trajectories caused by induced target corona: laser doppler analysis. *IEEE Trans.*, IA-20(6), 1613–1622.

Law, S. E., and H. D. Bowen (1966). Charging liquid spray by electrostatic induction. *Trans. ASAE*, 9(4), 501–506.

Law, S. E., and H. D. Bowen (1975). Theoretically predicted interactions of surface charge and evaporation on airborne pesticide droplets. *Trans. ASAE*, 18(1), 35–39, 45.

Law, S. E., and H. D. Bowen (1985). Dual particle-specie concept for improved electrostatic deposition through space-charge field enhancement. *IEEE Trans.*, IA-21(4), 694–698.

Law, S. E., and H. D. Bowen (1988). Hydrodynamic instability of charged pesticide droplets settling from crop-spraying aircraft: theoretical implications. *Trans. ASAE*, 31(6), 1689–1691.

Law, S. E., and S. C. Cooper (1987). Induction charging characteristics of conductivity enhanced vegetable-oil sprays. *Trans. ASAE*, 30(1), 75–79.

Law, S. E., and S. C. Cooper (1988). Depositional characteristics of charged and uncharged droplets applied by an orchard air-carrier sprayer. *Trans. ASAE*, 31(4), 984–989.

Law, S. E., and S. C. Cooper (1989). Target grounding requirements for electrostatic deposition of pesticide sprays. *Trans. ASAE*, 32(4), 1169–1172.

Law, S. E., and M. D. Lane (1981). Electrostatic deposition of spray onto foliar targets of varying morphology. *Trans. ASAE*, 24(6), 1441–1445, 1448.

Law, S. E., and M. D. Lane (1982). Electrostatic deposition of pesticide sprays onto ionizing targets: charge- and mass-transfer analysis. *IEEE Trans.*, IA-18(6), 673–679.

Law, S. E., and H. A. Mills (1980). Electrostatic applications of low-volume microbial insecticide spray onto broccoli plants. *J. Amer. Soc. Hort. Sci.*, 105(6), 774–777.

Marchant, J. A. (1985). An electrostatic spinning disc atomizer. *Trans. ASAE*, 28(2), 386–392.

Parham, M. R. (1982). Weed control in arable crops with Electrodyne© sprayer. *Proceedings Brit. Crop Protection Conf.-Weeds*, 3, 1017–1023.

Peek, F. W. (1929). *Dielectric Phenomena in High Voltage Engineering*. McGraw-Hill, New York.

Pimentel, D., and L. Levitan (1986). Pesticides: amounts applied and amounts reaching pests. *BioScience*, 36(2), 86–91.

Rayleigh, Lord (1896). *The Theory of Sound*, Vol. 11. MacMillan, New York.

Roth, D. G., and A. J. Kelly (1983). Analysis of the disruption of evaporating charged droplets. *IEEE Trans.*, IA-19(5), 771–775.

Splinter, W. E. (1968). Electrostatic charging of agricultural sprays. *Trans. ASAE*, 11(4), 491–495.

21

Electrostatic Precipitation

Senichi Masuda and Shunsuke Hosokawa

Masuda Research, Inc.
Tokyo, Japan

I. INTRODUCTION

The electrostatic precipitator (ESP) is a device for removing particulate pollutants in the form of either a solid (dust or fumes) or a liquid (mist) from a gas using an electrostatic force. Electrostatic precipitation has been widely used for cleaning gas from almost all industrial processes with a medium to large gas volume (>2,000 m^3/min), including utility boilers, blast furnaces, and cement kilns. ESP is also in wide use for air cleaning in living environments (homes, offices, hospitals, etc.) and work places (machine shops, food processing plants). ESP has large advantages over other particulate control devices: a lower operating cost, because of its low corona power and the low power needed in its blower due to a low pressure drop (<*ca* 10 mm H_2O); a high collection performance (99–99.9%) even for submicron particles (0.3 μm or smaller); and ease of maintenance. In particular, its low energy consumption has a great importance in view of the current concern in energy saving. An industrial precipitator represents one of the elements in an overall integrated pollution control system, including control devices for gaseous pollutants, so that its planning and design must be considered in this context.

Detailed introductions to ESP are given in the works of White (1962), Oglesby and Nichols (1978), and Boem (1982), and in the review article by White (1981).

II. WORKING PRINCIPLE

The working principle of ESP may be best understood by its simplest embodiment, cylinder type ESP (Fig. 1). It consists of a vertical grounded metal cylinder (the collecting electrode) and a wire (the discharge electrode) suspended along its center by an insulator bushing. The discharge

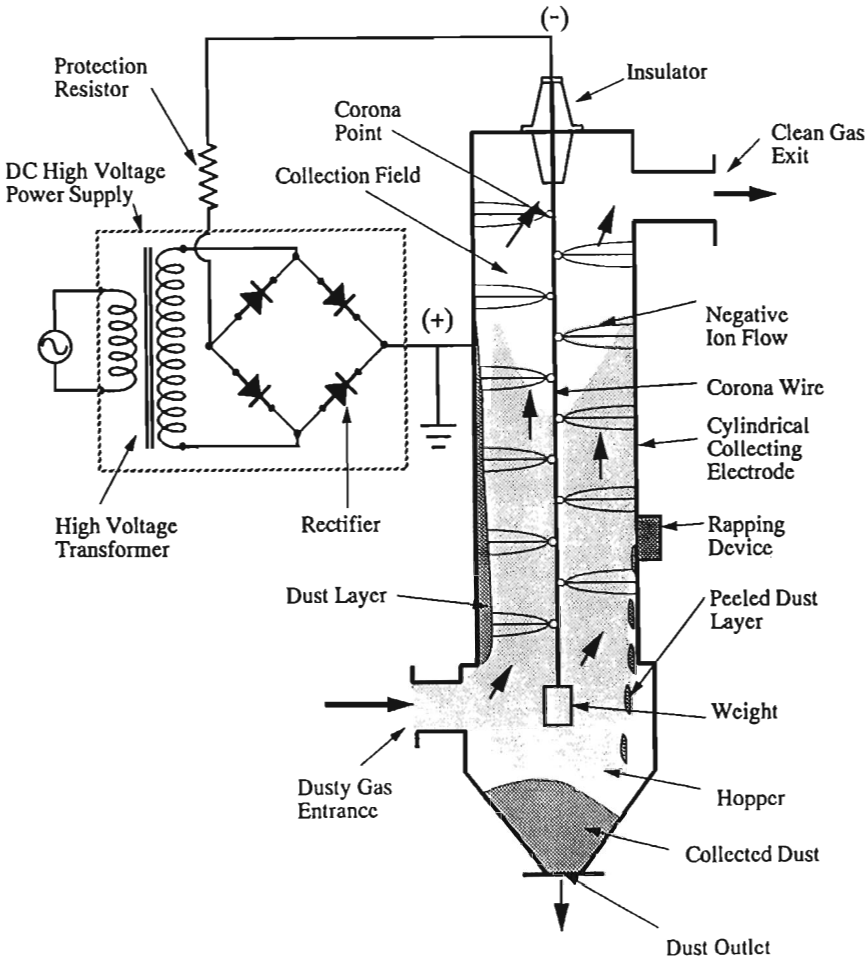


Figure 1 Basic construction of electrostatic precipitator (cylinder and vertical type).

electrode is connected to a dc high-voltage power supply, while the collecting electrode is grounded.

Increasing the voltage V beyond a certain threshold (the corona onset voltage) V_c, corona discharge begins to occur on the wire, accompanied by corona glow in the form of either spots (negative corona) or uniform glow (positive corona). These glows represent localized regions of gaseous ionization (partial breakdown), from which monopolar ions of the corona polarity are emitted toward the collecting electrode. These ions move across the interelectrode gap (collecting field), driven by a dc electric field, to arrive at the collecting electrode. The ionic current (corona current) flows through the interelectrode gas space, which is serving as a gas passageway.

When the voltage is further raised, the corona current I rises in a nonlinear fashion (Fig. 2) according to

$$I = AV(V - V_c) \tag{1}$$

where A represents a constant determined by electrode configurations, temperature, pressure, and composition of the gas. At a certain voltage Vs (the spark voltage), sparking occurs, which turns into arcing unless the voltage is interrupted. Thus the operation range of ESP is limited to the region between V_c and V_s. The higher the operating voltage, the better

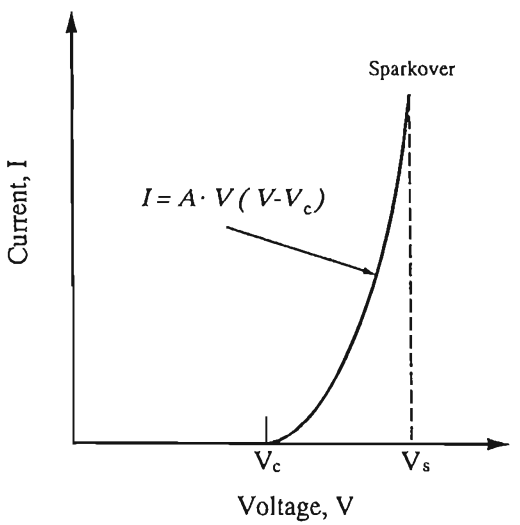


Figure 2 Voltage-current curve of corona discharge.

the collection performance under normal conditions, where no back corona is occurring. This range, $V_s - V_c$, is generally much broader in negative corona than in positive one, enabling stable operation of industrial ESPs under harsh conditions, so that the negative corona is used here. In ESP for air cleaning, however, use is commonly made of positive corona, since it generates much less ozone than the negative one (ca 10%; Penny, 1937).

In an integrated air purifier, where deodorization and disinfection of air are also done, a small quantity of the corona-induced ozone is used by using negative corona (Masuda et al., 1991).

Dirty gas containing particulate pollutants is introduced into ESP from a gas inlet at the bottom of the cylinder and flows upward in the cylinder through the interelectrode gap (collecting field). The particulates are bombarded by monopolar ions from the discharge electrode and are strongly charged; they are driven by Coulombic force toward the collecting electrode and are deposited on its inner surface. The cleaned gas is discharged to the stack from the gas outlet at the top, while the removed particles accumulate on the inner surface of the collecting electrode to form a dust layer there.

A mechanical rapping is given to the collecting electrode to dislodge the dust layer so that it falls down into the dust hopper. The dust held in the hopper is discharged to the outside from the dust outlet at the bottom of the hopper.

Within a small biionized region of the corona discharge, particles are bombarded by both positive and negative ions, so that they are given much less net charge, and the effect of the Coulombic force is greatly diminished. But they subject to another kind of electrostatic force, the gradient force, which acts on any dielectric body, with or without an electric charge, to drive them to a region of higher electric field, namely toward the surface of the discharge electrode. The gradient force becomes dominant in the strongly nonuniform field of this corona region. So the particles deposit on the surface of the discharge electrode to increase its apparent thickness with time, finally stopping the corona discharge. Hence, mechanical rapping must also be made on the discharge electrode.

Of course, no such rapping is necessary in wet ESPs, while the hard-to-remove dust layer requires a water jet or sand-blasting for cleaning both electrodes.

III. PHYSICS OF ESP

The electrostatic precipitator is a typical fuzzy system, where a large number of factors affect its performance in a complicated fashion. This

makes the design and performance prediction of ESP difficult, even though extensive investigations have been made so far to understand the physical background. However, without understanding the physics underlying ESP, a proper empirical approach in the engineering work of ESP is impossible.

A. Particle Charging in a Corona Field

Particles are suspended in a corona field, subjected to ion bombardment, and given ionic charge (see Chapters 3 and 22). In the negative corona a minute quantity of electrons also contributes to the charging (electron charging) in a region close to the discharge electrode. Electron charging enhances particle charging, especially when the voltage V is high and the gas mean free path λ is large (higher temperature).

In particle charging two different mechanisms exist in the transport of charge carriers (ions and electrons) to the particle surface: field-driven migration (field charging) and thermal diffusion (diffusion charging). Both mechanisms work together to give an overall charge to the particles.

Field charging becomes dominant for larger particles ($d > 2$ μm), and the quantity of charge q_f imparted to a spherical particle is given by Pauthenier's field charging equation (Pauthenier and Morean-Hanot, 1932, 1939):

$$q_f = \frac{q_{fs}(t/\tau_f)}{1 + (t/\tau_f)} \quad \text{(C)} \tag{2}$$

where

$$q_{fs} = \frac{12\pi\epsilon_0\epsilon_s a^2 E_{ch}}{\epsilon_s + 2} = \text{saturation charge of field charging} \quad \text{(C)} \tag{3}$$

$$\tau_f = \frac{4\epsilon_0}{\mu_i \rho_i} = \frac{4\epsilon_0 E_{ch}}{J_i} = \text{charging time constant of field charging} \quad \text{(s)} \tag{4}$$

where t = time(s), ϵ_0 = dielectric permitivity of free space = 8.85×10^{-12} (F/m), ϵ_s = specific dielectric constant of a particle, a = particle radius (m), μ_i = ion mobility (m^2/Vs), ρ_i = ion space charge density (C/m^3), E_{ch} = intensity of charging field (V/m), and J_i = ionic current density (A/m^2). Figure 3 shows the time-dependent rise of particle charge. It can be seen that the charge q_f arrives at 95% of its saturation charge q_s at $3\tau_f$. So we can assume for field charging

$$T_f = 3\tau_f = \text{effective charging time} \quad \text{(s)} \tag{5}$$

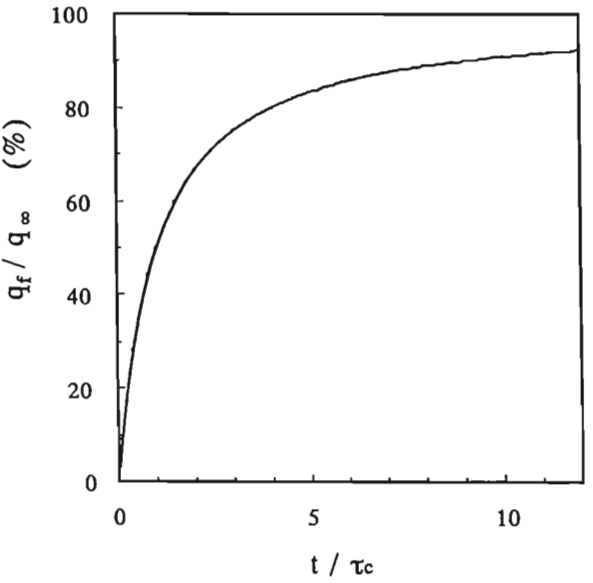


Figure 3 Time-dependent rise of particle charge by field charging.

It is obvious from Eqs. 2–4 and Fig. 3 that both electric field intensity E_{ch} and corona current density J_i play essential roles in field charging. The higher the value of E_{ch}, the greater the saturation charge q_{fs}, while the higher the value of J_i, the faster the charging speed.

Diffusion charging becomes dominant for submicron particles ($d < 0.2$ μm), and the charge q_d at time t (s) is given by (White, 1951)

$$q_d = q^* \ln\left(1 + \frac{t}{\tau_d}\right) \quad \text{(C)} \tag{6}$$

where

$$q^* = \frac{4\pi\epsilon_0 akT}{e} = \text{charge constant of diffusion charging} \quad \text{(C)} \tag{7}$$

$$\tau_d = \frac{4\pi\epsilon_0 kT}{aC_i n_i e^2} = \frac{4\pi\epsilon_0 kT\mu_i E_{ch}}{aC_i J_i e} \quad \text{(s)} \tag{8}$$

$$= \text{charging time constant of diffusion charging}$$

where k = Boltzmann's constant = 1.38×10^{-23} (J/K), e = elementary charge = 1.6×10^{-19} (C), $C_i = \sqrt{3kT/m_i}$ = root mean square value of ion thermal velocity (m/s), n_i = ion number density (m^{-3}), m_i = ion mass (kg), and μ_i = ion mobility (m^2/Vs). In diffusion charging there is no definite theoretical saturation charge. Furthermore, its charging speed is enhanced in a very small particle size region, where a is close to or smaller than the ion mean free path λ. This is due to the so-called slip motion of ions without colliding with molecules. The charging process in this region is governed by a/λ. Figure 4 indicates the time-dependent rise of particle charge by diffusion charging, calculated considering the slip motion.

It can be seen from Fig. 4 that we can take the following quantities for practical evaluation of diffusion charging:

$$q_{ds} = 6.2\, q^* = \text{effective saturation charge of diffusion charging} \quad \text{(C)} \tag{9}$$

$$T_d = 500\, \tau_d = \text{effective charging time of diffusion charging} \quad \text{(s)} \tag{10}$$

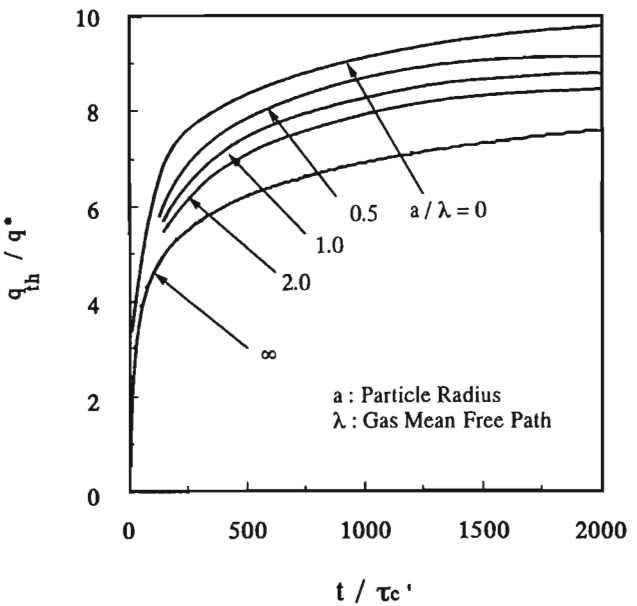


Figure 4 Time-dependent rise of particle charge by diffusion charging.

B. Theoretical Migration Velocity of a Charged Particle

The charging time in a corona field, T_f and T_d, estimated from Eqs. 5 and 10, lies in the range of 1 s or shorter under ordinary conditions. The transient time of acceleration for a particle to reach a steady migration velocity is in the range of 1 ms. Hence the migration velocity of a particle in an ESP is approximately

$$W_{th} = \frac{qE_{co}C_m}{6\pi\eta} = \text{theoretical migration velocity} \quad \text{(m/s)} \tag{11}$$

where

$$C_m = 1 + 2.514\frac{\lambda}{2a} + 0.80\frac{\lambda}{2a}\exp\left(-0.55\frac{2a}{\lambda}\right) \tag{12}$$

$$= \text{Cunningham's correction factor}$$

where q = overall saturation charge $q_{fs} + q_{ds}$, E_{co} = intensity of collection field, η = gas viscosity (Pa s), and λ = gas mean free path. In a very small size range, where a is comparable to or smaller than λ, so-called slip motion appears to reduce an effective value of η. The term C_m is to include this effect and is plotted against a (μm) in Fig. 5. It should be noted that $E_{co} = E_{ch}$ in the one-stage ESP, where the corona charging field and the electrostatic collection field are the same, while $E_{co} \neq E_{ch}$ in the two-stage ESP, where charging is made first in the corona precharg-

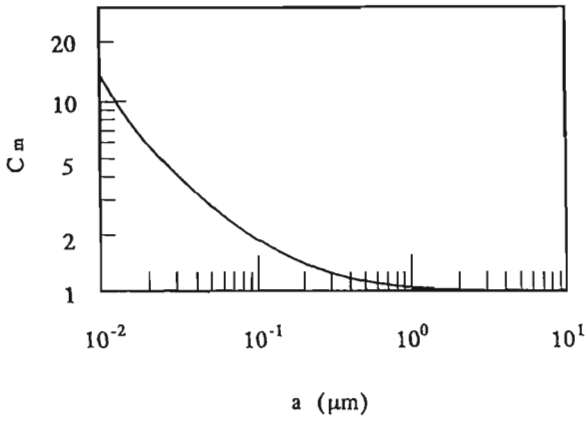


Figure 5 Cunningham's correction factor vs. particle radius (air: 20°C and 1 atm).

ing field and separation is made subsequently in the noncorona electrostatic field.

Figure 6 shows the theoretical migration velocity W_{th} calculated for one-stage ESP from Eqs. 3, 9, and 11 and plotted against a (μm). The curve takes a V shape, with a minimum in the range between 0.1 and 1.0 (μm). In the larger size range ($a > 1$ μm), the field charging is dominant, and W_{th} rises proportionally with a. In the smaller size range ($a < 0.1$ μm), diffusion charging and slip motion become dominant, and W_{th} rises with decreasing a.

It should be noted that W_{th} does not generally represent an actual collection velocity in practical ESPs where turbulent flow is prevailing. But in laminar flow it gives a true migration velocity (e.g., electrical mobility analyzer). Anyway, it helps us to get a clear understanding of the physical background of the electrostatic precipitation process.

C. Effective Migration Velocity

An essential factor affecting the collection process in a practical ESP (both one-stage and two-stage) is turbulence in a gas stream induced by both fluid dynamic instability and momentum transfer from ions to gas molecules (corona wind). The charged particles undergo a strong turbulence-induced random motion during the electrostatic migration toward the

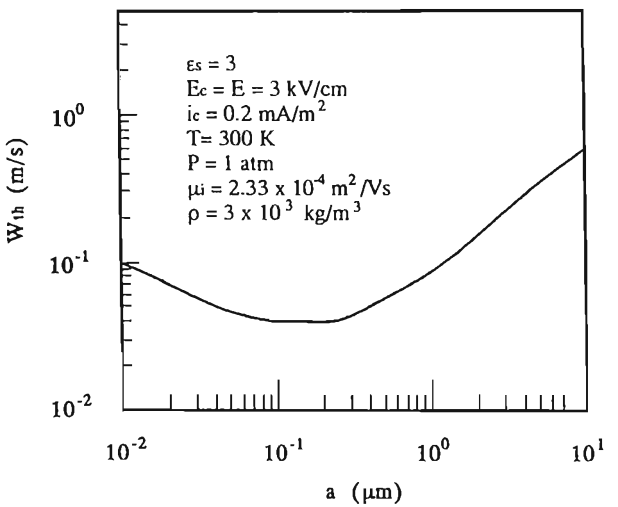


Figure 6 Theoretical migration velocity vs. particle radius.

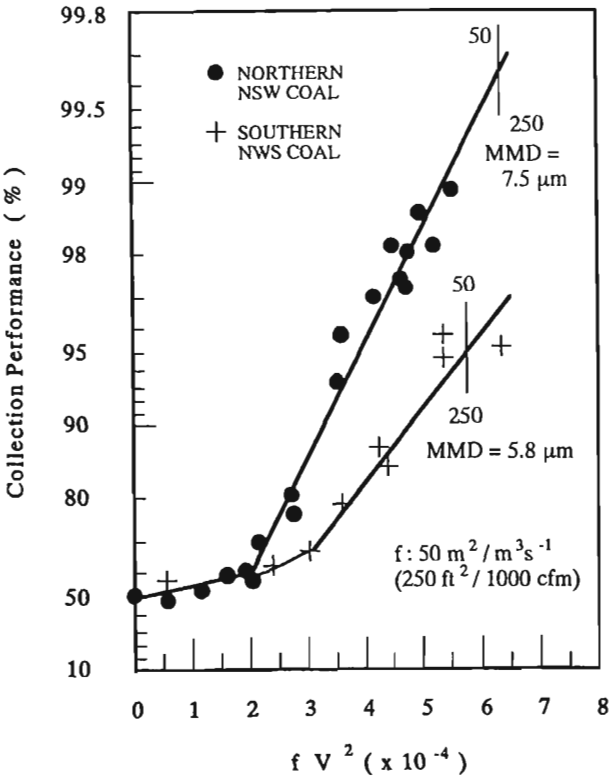


Figure 7 Performance line of electrostatic precipitator (f: SCA $m^2/m^3\ s^{-1}$; V in kV).

collecting electrode, as confirmed by observations using laser doppler anemometry (Masuda et al., 1979). This random motion equalizes more or less the number concentration of particles in the collection field, so that only the particles entering into a thin boundary layer near the collecting electrode are collected.

Based on this stochastic model of the particle collection process, the following Deutsch equation is derived to formulate the collection efficiency η of an ESP, using an effective migration velocity W_e (m/s) and a specific collection area f(1/m):

$$\eta = \frac{m_{iav} - m_{oav}}{m_{iav}} = 1 - \exp(-W_e f) \tag{13}$$

where

$$f = \frac{S_c}{Q_g} = \text{specific collection area (SCA)} \quad (m^2/m^3/s^{-1}) \tag{14}$$

where m_{iav} and m_{oav} = average dust mass loading at the inlet and outlet of the ESP (g/Nm^3), S_c = total collection area (m^2), and Q_g = total gas flow rate (m^3/s). W_e is a parameter having a dimension of velocity, including all the effects of many plant-specific factors, so that its magnitude can only be derived from the measured value of collection efficiency η using the design value of f and Eq. 14. Only a good data base of W_e enables a reliable estimation of its value in the design of a new ESP to be built.

The Deutsch equation has been modified by Allander and Matts (1957) in consideration of log normal distribution of particle size in most of the industrial dusts. It has been further modified (Matts and Ohnfeld, 1964; modified Deutsch equation) so as to give a better fit to the field test data:

$$\eta = 1 - \exp(-W_e f)^k \tag{15}$$

where k = a factor depending upon dust species and $k = 0.5$ for coal fly ash.

Another practical method of evaluating the performance of an ESP is to plot η or $1 - \eta$ as a function of fV^2, in consideration of the fact that $W_{th} \propto V^2$ (Potter and Paulson, 1974; Potter, 1977). Figure 7 indicates such plots, and the curves are called performance lines.

IV. PHENOMENA DETERIORATING COLLECTION PERFORMANCE

The originally very high performance of ESPs may be often deteriorated by various factors appearing in practical processes. Hence design and operation of an ESP must carefully consider these factors in advance to cope with the expected troubles.

A. Particle Size Factor

As described previously, the theoretical migration velocity W_{th} becomes minimum in a size range between 0.1 and 1.0 (μm) (Fig. 6), so that the fraction of particles in this size range tends to leak through ESP to be emitted to the environment. These particles (heavy metals, soot with absorbed VOCs, etc.) are mostly small in mass loading, but very large in number, and they are most hazardous to human health, as they easily penetrate into the depth of the human pulmonary system. The submicron particles (fume or mist) are generated by condensation from a gas phase,

while coarser particles are produced by material disintegration (crushing, grinding). When most of the particles are in the submicron range, a severe corona quenching is caused. Coarser particles, say larger than several tens of μm, are very easily collected by ESP, but they tend to undergo rapping reentrainment more easily.

Abatement

Preagglomerater. Use an electrostatic preagglomeration field in the form of a two-stage ESP in front of the ordinary collecting fields of the one-stage ESP. Or use a sonic preagglomerator comprising a powerful sonic generator (motor-siren; Hartmann whistle), so that very fine particles, having a larger amplitude of oscillation, collide on the larger particles.

Preduster. Use a cyclone for removal of coarser particles in front of the ESP.

Water Condensation. Use water spray in front of the ESP or inside it to raise the gas humidity and lower its temperature so as to saturate the gas with water vapor and generate water condensation around the fine particles (condensation nuclei). The effective size of the condensates grows very quickly to an easy-to-collect level, say up to several micrometers in a few milliseconds.

B. Corona Quenching

It is known in industrial ESPs that the corona current at the first field with the highest dust mass loading m (g/Nm^3) is the lowest, while it increases toward the downstream fields with decreasing m, and that this tendency is enhanced at a larger interelectrode gap lg (m). This is understandable, as the electric field in an ESP is a Poisson field determined by the space charge density ρ (C/m^3)($= \rho_i$ (ionic) $+ \rho_d$ (dust)) in the interelectrode space, its gap length lg (m), and the corona current I (A) (Pauthenier and Moreau-Hanot, 1932); and I shows a feature specific to the space charge limited current. The higher the magnitude of ρ_d, the smaller the magnitude of I, finally to become zero (corona quenching) and cause a great deterioration of collection performance. The corona quenching is enhanced by the magnitude of lg. It can be seen from Eq. 3 that the charge of an individual particle is proportional to its surface area, $4\pi a^2$(m^2), so that the total space charge density of dust ρ_d is proportional to the total surface area of dust per unit volume $S_d = \Sigma 4\pi a_i^2$ (m^2/m^3) (dust area loading). S_d can be estimated from the number concentration n_d (m^{-3}) and mass loading m of dust, and it can be measured (Masuda et al., 1987). The magnitude of S_d becomes excessively high for fine particles when n_d or m_d is large.

Increase in ρ_d also produces a local rise of electric field in the region near the collecting electrode, to trigger sparking easily and cause space charge-induced excessive sparking.

Abatement

Preduster. Use a suitable preduster (e.g., cyclone) for removing coarser dust before an ESP.

Preagglomerator. Use a suitable preagglomerator (electrostatic, sonic) to reduce S_d before an ESP.

Reduce Interelectrode Gap. Use a narrower gap, at least in the first collection field of the ESP.

C. Back Corona

The layer of dust deposited on the collecting electrode acts as insulating layer when its resistivity r_d (ohm-cm) exceeds a threshold comparable to that in gas space due to ionic flow. Then the voltage across the dust layer becomes excessively large to cause breakdowns at the local weak points in it. The breakdown points emit ions of opposite polarity toward the discharge electrode and deteriorate collection performance. This is called back corona and represents one of the most complicated abnormal phenomena in ESP (Masuda and Mizuno, 1976, 1977, 1978; Masuda, 1981).

In negative corona, widely used in industrial ESPs, back corona begins to manifest itself in a form of excessive sparking at $r_d = 5 \times 10^{10}$–10^{11} (ohm-cm). At this stage the breakdown points are limited in number, while the field intensity in gas space is adequately high (>5 kV/cm) to launch from the back corona points positive streamers toward the discharge electrode (space streamers). These space streamers easily bridge the interelectrode gap to turn into spark (excessive sparking), making a stable operation of ESP difficult without lowering the voltage. The result is a deterioration of the collection performance, if it is not completely lost. Back corona not only extends into gas space but also extends along the surface of the dust layer (surface streamers) as a result of negative surface charge accumulated by oncoming ionic current. Both are called streamer mode back coronas.

With a further increase in r_d, say beyond 10^{11}–10^{12} (ohm-cm), the number of breakdown points in the dust layer further grows to produce general glow on its entire surface (general glow mode back corona), while the streamers disappear. A large number of positive ions are emitted from the back corona region to the gas space, so that these positive ions and the original negative ions from the discharge electrode produce a biionized field in space. This not only deteriorates particle charging with a concur-

rent severe deterioration of collection performance (Masuda and Nonogaki, 1980, 1981; Masuda, 1981) but also diminishes the space charge density in gas space. Furthermore, a positive ion sheath is formed around the surface of the discharge electrode to enhance electron emission from it. As a result, once the general glow mode back corona occurs, a large over current also appears, and the current rating of the high-voltage power supply is exceeded.

As a result of the back coronas described above, the collection efficiency η plotted against the apparent dust resistivity r_d shows a sharp drop in the high-resistivity region, as shown in Fig. 8. As seen in the figure, a sharp drop also occurs in the low-resistivity region ($r_d < 10^4$ ohm-cm) owing to dust reetrainment resulting from the loss of an electrostatic cohesion force acting in the dust layer (Johnsen-Rahbeck effect).

When the polarity of the discharge electrode is reversed to positive, the mode of back corona shows a drastic change. Back corona consists of a number of separate negative glow spots not accompanied by diffuse glow or streamers. The corona current does not indicate an abnormal rise with increasing voltage, and the spark voltage V_s becomes substantially higher than that in the negative corona (*ca* 1.5 times; Masuda and Mizuno, 1977), possibly due to the onset of a very stable Hermstein's glow at the discharge electrode (Hermstein, 1960; Loeb, 1965).

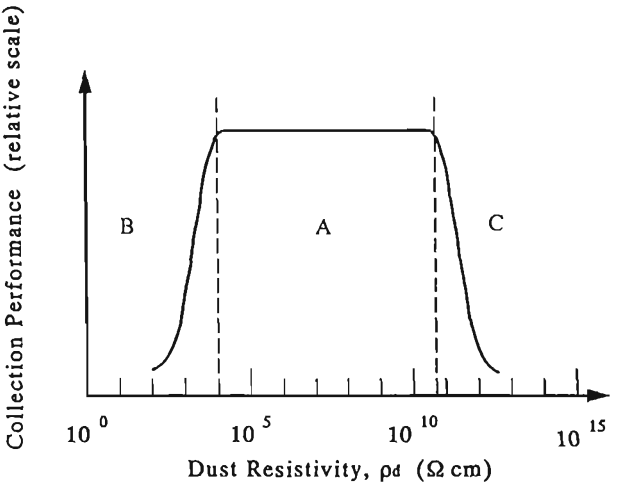


Figure 8 Collection efficiency vs. apparent resistivity of dust.

The initiation condition of back corona is given by the following equation, unless r_d is too high ($>10^{14}$ ohm-cm), as confirmed by experiment (Masuda and Mizunor, 1977):

$$J_d \times r_d \geqq E_{db} \tag{16}$$

where J_d = apparent current density in dust layer (A/cm2) and E_{db} = breakdown field strength of the dust layer (V/cm).

Based on Pauthenier's equation of field charging in the biionized field (Pauthenier, 1961), it is possible to estimate the deterioration of particle charging by back corona from the following ratio of the saturation charges with and without back corona (Masuda and Nonogaki, 1981, 1986):

$$\beta = \frac{q'_\infty}{q_\infty} = \delta \frac{1 + \gamma}{1 - \gamma} = \text{back corona severity} \tag{17}$$

where

$$\delta = \frac{V'}{V} \tag{18}$$

$$\gamma = \left(\frac{i_+}{i_-}\right)^{1/2} \tag{19}$$

where q'_∞ and q_∞ = saturation charge with and without back corona (C), V' and V = applicable corona voltage with and without back corona (V), and i_+ and i_- = density of positive and negative ionic current (A/m^2). It can be seen from these equations that the effect of back corona on the collection performance is determined by two factors: δ representing the drop of the applicable corona voltage caused either by excessive sparking or over current in the power supply, and γ representing the back corona severity in terms of bipolar ionic currents.

Figure 9 shows the effects of gas temperature T (°C) and its absolute humidity H (vol. %) on the apparent resistivity of dust r_d appearing in Eq. 16 (Sproul and Nakada, 1951; Masuda, 1962).

The inverse V curves suggest r_d to be resulted by two different conducting mechanisms working in parallel (Masuda, 1962).

One is the volume conduction through the dust particle body due to electronic conduction, and also ionic conduction, which works only in the presence of small ions in dust (Na^+, K^+, Li^+, etc.) and at an elevated temperature (>300°C) (Bickelhaupt, 1980).

Another is surface conduction through the conductive surface film of absorbed molecules (H_2O, OH, H_2SO_4, etc.), where the proton transfer and ionic conduction (H+, OH−, Na+, K+, Li+, etc.) play a major

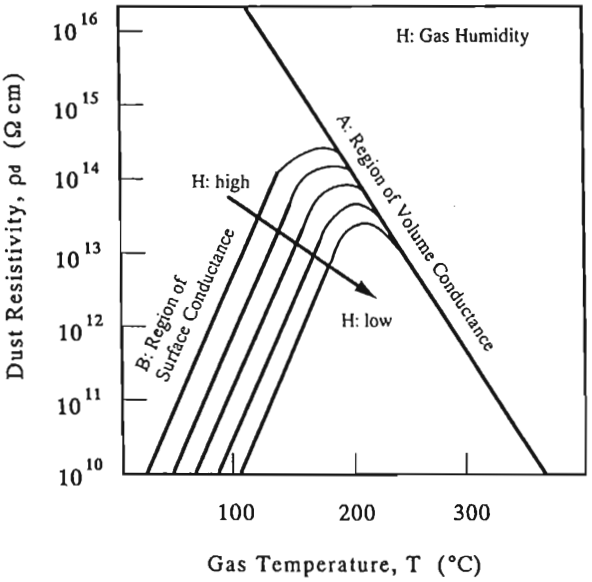


Figure 9 Apparent resistivity of dust vs. temperature and absolute humidity of gas.

role (Bickelhaupt, 1975). These two conduction mechanisms undergo the geometrical factor specific to the particle assembly of the dust, namely, the constriction of current paths at the particle-to-particle contacts (contact resistance; Masuda, 1962). The surface conductivity is greatly enhanced by the presence of special gaseous components, in particular SO_3, which are easily absorbed on the dust surface and have a strong tendency to attract water molecules to form a conductive film on them (Busby et al., 1963; Darby and Heinrich, 1966; Dismukes, 1975).

In a lower temperature region (<120–180°C), the surface conduction is dominant, and the abolute gas humidity H has a notable effect to lower r_d. Here, r_d rises with increasing T at a constant level of H, since the relative humidity concurrently drops to hamper water absorption to the dust surface and thereby lower surface conductivity. In a higher temperature region (>180–240°C), the volume conduction becomes dominant and r_d drops with increasing T, as a result of enhanced electronic and ionic conduction.

In addition, r_d also depends on the chemistry of the dust itself (Bickelhaupt, 1979, 1980), in particular its surface chemistry (e.g., SiO_2, CaO,

Al_2O_3; Paulson et al., 1978; Potter, 1980), crystallographic structure, and particle size.

In dust chemistry, catalytic elements, in particular V_2O_3, play an essential role to enhance the surface conductivity and thereby lower r_d by converting SO_2 adsorbed from gas to SO_3 and further to H_2SO_4.

The value of the dust breakdown strength E_{db} greatly depends on the dust chemistry, its crystallographic structure, gas composition, temperature, and pressure (mean free path, λ). E_{db} also critically depends on the thickness of the dust layer, decreasing greatly with increasing thickness (Masuda, 1960).

The mode of back corona, spark voltage V_s, particle charge q_p, and the overall collection performance are determined by all of these parameters. Furthermore, V_s is also determined by the existence of constituents having a lower ionization potential ϕ in either gas (e.g., NO; Masuda et al, 1979) or dust (e.g., Na, K; Masuda and Mizuno, 1978).

In a hot ESP operated on the upstream side of an air preheater of a boiler (300–400°C), the electrolytic conduction by alkali ions inside the dust (Na, K, Li) plays a dominant role in lowering r_d to abate back corona. However, these ions, positive in polarity, accumulate with time on the dust surface, leaving an ion depletion layer behind. This causes a time-dependent rise in dust resistivity, finally to cause back corona after a certain period of time, say 1 month (Bickelhaupt, 1974, 1980).

Abatement

Coal Mixing. Mix at a proper ratio high-sulfur coal with low-sulfur coal to lower the resultant fly ash resistivity below a proper threshold ($<10^{10}$ ohm-cm) to avoid back corona.

Coal Conditioning. Add a resistivity lowering agent (e.g., Na_2CO_3) to low-sulfur/low-alkali coal before burning (Bickelhaupt, 1975).

Gas Conditioning. Add a resistivity lowering agent into the gas stream before ESP, such as SO_3 and/or NH_3 (Busby and Darby, 1963; Darby and Heinrich, 1966; Dismukes, 1975; Altman et al., 1981; Gooch et al., 1984) or triethylamine (Potter and Paulson, 1974; Paulson et al., 1978).

Gas Humidification. Spray water into a gas stream before ESP to raise gas absolute humidity H and lower gas temperature T (Masuda et al., 1966). Injection of solvents in the spray dryer is also used (Mayer-Schwinning, 1990).

Two-Stage Type ESP. Use a two-Stage type ESP with a short corona precharging field followed by an electrostatic collecting field (Penny, 1951). Use of a precharger comprising water-cooled pipes for its counter

electrodes prevents back corona and deterioration in dust precharging (Rinard et al., 1981).

Gas Cooling. In an integrated pollution control system with an ESP, calcium scrubbing FGD and a gas-gas heat exchanger for reheating of gas after FGD, place the cooling side of the heat exchanger upstream of the ESP to cool its inlet gas from 130–140 to 90–100°C (Tanaka et al., 1933).

Wet ESP. Use a wet ESP with water spraying or water-irrigated collecting electrode (Fujishima and Tsuchiya, 1993). Use of the water-irrigated collecting electrode only in the final field lowers the cost for slurry treatment (hybrid ESP: Masuda et al., 1976). The slurry can be spray-dried before ESP, where the effect of gas humidification is also obtained.

Pulse Energization. Apply a high-voltage pulse (5–100 kV peak; 10–250 Hz; 100 ns–100 μs duration) with or without a dc high-voltage superimposed (White, 1962; Masuda et al., 1987; Milde and Feldman, 1978; Milde and Van Hoesen, 1979; Lausen et al., 1979; Kumar et al., 1979; Dinelli and Rea, 1984; Dubard et al., 1984; Porle, 1988; Fujishima and Tomimatsu, 1990). The corona current can be smoothly reduced by lowering the pulse frequency without reducing voltage to avoid the initiation of back corona (Eq. 16). Furthermore, a much higher voltage can be applied without sparking to increase particle charging (Eq. 3), especially with an enhanced electron charging. At the same time the distribution of ionic current becomes very uniform, and corona power can be greatly reduced (1/3–1/20). This advantage and performance enhancement become more pronounced at a lower cost by using a very narrow pulse high voltage generated by a rotary spark switch (duration time, 100 ns–10 μs) (Masuda and Hosokawa, 1988; Masuda et al, 1993; Paulson et al., 1993). Use of a long transmission line for the discharge electrode enables the pulse voltage to behave as a traveling wave, resulting in more energy savings in pulse energization (Masuda and Hosokawa, 1984; Masuda et al., 1985).

Intermittent Energization. Apply intermittently a rectified half-wave or full-wave out of a dc high-voltage power supply at a proper frequency (1–10 Hz) through a switching control of the primary circuit (Tachibana and Fujishima, 1988).

Automatic Voltage Control. Pick up the spark signal from an ESP, and control the voltage so as to keep the sparking rate at a proper value (Hall, 1954, 1981; Neulinger, 1990). At each sparking the voltage should be interrupted for a short period of time to avoid its transition into arc. When sparking occurs successively, the voltage should be finally interrupted.

D. Dust Reentrainment

The final stage of the electrostatic precipitation process is to remove the dust layer from the collecting electrode and to convey it to a dust hopper. In dry ESP, commonly used in industrial precipitators, the removal of the dust layer is made by mechanical rapping of the collecting electrode, and it is conveyed to the hopper by free fall. The ideal way of doing this is to let the entire dust layer slide along the electrode surface so that its bottom end gradually drops into the hopper.

However, a fraction of the dust layer is more or less disintegrated and dispersed into the gas stream by the normal component of rapping-induced electrode vibration (rapping reentrainment). The reentrained dust is collected again, and this collection/reentrainment process repeats itself during the course of electrostatic precipitation (Basset et al., 1977). At the final collection field, the reentrained dust is emitted from the outlet of the ESP to the stack. Hence a satisfactory performance can never be achieved without suppressing the rapping reentrainment of dust.

This phenomenon is essentially determined by the stability of the dust layer (dust cohesivity) and the magnitude of the normal component of the vibrating acceleration of the collecting electrode when rapped. The dust cohesivity is a function of dust composition and size, composition and temperature of gas, and the dust resistivity r_d. The dust cohesivity is caused not only by van der Waals force acting at the particle-to-particle contact points but also by the condensation of water molecules into those contact points (capillary condensation) to produce a larger effective contact area. So the dust cohesivity is diminished at an elevated temperature, while it is enhanced by the addition of proper chemical agents such as SO_3 (Dalmon et al., 1972; Dismukes, 1975; Patterson et al., 1979) enhancing water absorption onto the dust surface. The dust cohesivity is also very much dependent on the particle size. The rapping reentrainment generally becomes pronounced in the coarser dust. Furthermore, the dust layer in ESP is subject to ionic current to produce an apparent electric field $E_d = J_d \times r_d$ inside it. As a result, an electrostatic attraction force appears at each contact point, which acts as a kind of condenser, to produce an overall electrostatic cohesivity in the range $r_d > 10^{10}$ (ohm-cm) (Penny and Klinger, 1962; Simm, 1962; Dalmon and Tidy, 1972; Szirmai and Potter, 1974). This also is an essential factor affecting the dust reentrainment in ESP. The higher the values of r_d and J_d, the greater the electrostatic dust cohesivity.

The normal component of vibration of the collecting electrode is avoided by giving sufficient stiffness to the electrode, and by rapping it

in the tangential direction at its top or side end. The vibration is propagated as a traveling wave, which undergoes multiple reflection at the peripheries, so that the actual vibration at a point on the electrode is determined as the superposition of these waves.

In the case when r_d and/or J_d are too low, not only does the electrostatic cohesivity of dust completely disappear but also the particles arriving at the collecting electrode are immediately reverse-charged by electrostatic induction even in the presence of ion current, and they are pulled back by Coulombic force to jump into the gas stream again. Hence the particle motion takes the form of hopping, so that particles can never be collected by the ESP. This is called low resistivity reentrainment, and it generally occurs when $r_d < 10^4$ (ohm-cm) (e.g., carbon black; Fig. 8).

Dust reentrainment is also caused by an excessively high gas velocity, higher than 1–2 m/s in industrial ESPs operated at an elevated temperature (>100°C). This flow reentrainment is often enhanced by a nonuniform distribution of gas flow in an ESP to produce locally a higher than average gas velocity. Also, it is enhanced in gas leakage through a pass other than a collection field (hopper, canopy space, etc.).

Abatement

Proper Rapping Design. Rap collecting electrode in the tangential direction to avoid its vibration in the normal direction. Also, use an electrode having enough stiffness.

Proper Rapping Operation. Choose a proper rapping strength, adequately strong to dislodge the dust layer but not so excessively intense as to cause reentrainment. Also, choose a proper rapping cycle, more frequent at the upstream fields and much less frequent at the final field.

Gas Conditioning. Use a cohesivity enhancing agent (e.g., ammonia, trimethylamine, SO_3).

Wet ESP. Use wet ESP to avoid dust reentrainment, at least at its final field.

Bag Filter. Switch to the use of a bag filter for dust having an extremely high resistivity (e.g., CaO) or very low resistivity (e.g., carbon black). Here an ESP may be used as an electrostatic preagglomerator in case particle size is extremely small (e.g., carbon black).

Uniform Gas Distribution. Install proper guide vanes and perforated plates in the inlet and outlet spaces of the ESP. Make a careful test and adjustment of gas velocity distribution.

Gas Sealing. Install stopper plates in hoppers and canopy spaces to avoid gas leakage. Elongate the former into the inside of the hopper dust (dust seal).

E. Abnormal Dust Deposition

Abnormal deposition of dust occurs on the discharge electrode when corona discharge is hampered to produce coronaless regions on it. This is caused by either corona quenching or the operation of an ESP at a substandard voltage. The particles in the vicinity of the coronaless regions undergo the gradient force to be attracted to them without being driven back by Coulombic force, and deposit on them. Once this abnormal dust deposit happens, it further grows as a result of the dust-induced increase in the apparent radius of curvature of the discharge electrode, and it also extends along the surface of the discharge electrode in the tangential direction. The abnormal deposit also occurs when the rapping of the discharge electrode is not strong enough.

The abnormal dust deposit also occurs on the collecting electrode when the rapping is too weak, or when dust is either too fine or too sticky. When the dust includes lime (CaO or $Ca(OH)_2$) and the gas contains CO_2 and H_2O, calcite crystals grow in the voids of the dust deposits to cement the particles. This forms a very hard dust layer, firmly attached to the electrode, and it is hardly possible to remove it by rapping.

Abatement

Proper Rapping Intensity. Choose a proper intensity in the rapping of both discharge and corona electrodes.

Uniform Corona Distribution and Its Adequate Intensity. Apply always an adequately high voltage to produce uniform and active coronas on the discharge electrode, and not to produce the coronaless regions on it.

Mechanical Scraping. Use mechanical scraping of dust from collecting electrode, e.g., moving caterpillar type collecting electrodes comprising rotating wire brushes at the bottom area (Misaka and Yubata, 1993).

Water Jet or Sand Blast. Stop the operation of ESP periodically (e.g., once a month) and use either one of these methods for electrode cleaning.

V. INDUSTRIAL ESP

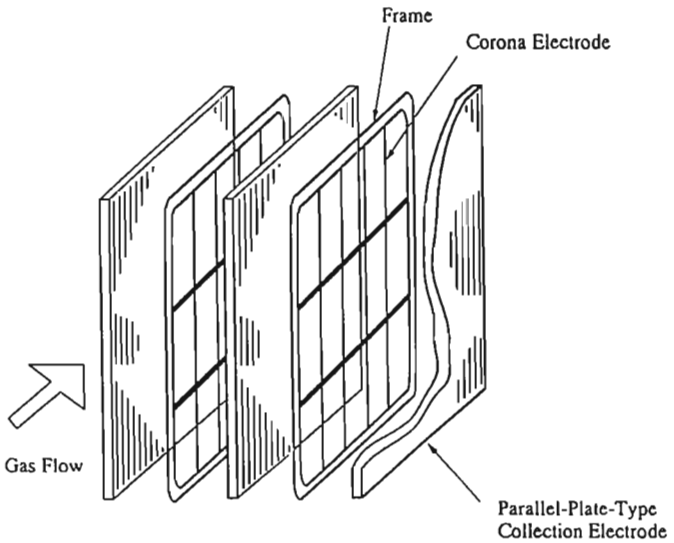
The largest application field of ESP is for controlling particulate pollutants in gas from industrial processes, mostly combustion gases at an elevated temperature (utility boilers; waste incineration plants; cement kilns; sinter machines and blast furnaces in steel mills; sintering and fuming furnaces in metallurgical plants). The gas flow direction in these ESPs is mostly horizontal, comprising a plurality of collection fields in series, each field equipped with grounded planar collecting electrodes, which are located parallel to the gas flow at an equal spacing to form gas passageways in

between. Discharge electrodes are located on the center plane of each passageway, as shown in Fig. 10. This ESP is called the horizontal type ESP, and it can better handle a large gas volume without deteriorating uniform gas distribution. The one-stage type is common in industrial ESPs to avoid an increase in dust reentrainment due to temperature-induced reduction in dust cohesion and adhesion with the aid of the ionic-current-induced electrostatic augmentation of these properties.

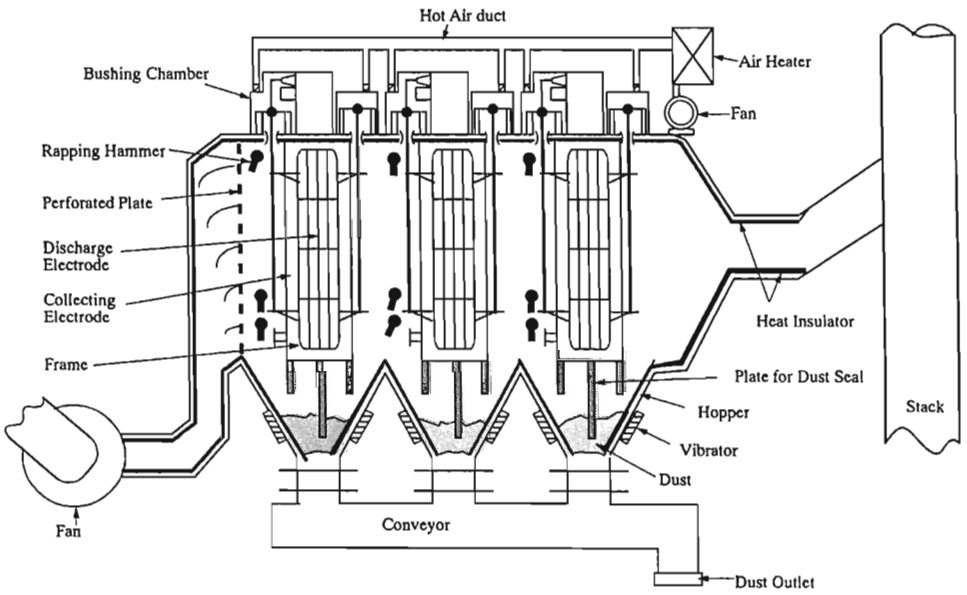
Figures 11 and 12 illustrate, respectively, the discharge and collecting electrodes widely used in industrial ESPs. The discharge electrodes are attached to the frame, which is supported by insulator bushings placed in a dust-free chamber (bushing chamber; Fig. 13) purged with clean air and heated electrically. This is to secure the insulation of bushings under any humid conditions, in particular in the startup period. The collecting electrodes are given an adequate stiffness in the vertical direction with a proper profile, or suitable stiffeners attached. ESP is operated at a pressure slightly lower than ambient air to avoid dust leakage to the outside. So dust is discharged from the hopper using a gas-tight outlet as shown in Fig. 14 in order to avoid air intake into the hopper. Otherwise a substantial reentrainment of hopper dust into the gas stream takes place.

The spacing between two adjacent collecting electrodes was traditionally D = 20–25 cm, but the wide ESP (Heinrich, 1978) having a larger spacing (40–60 cm) and a higher voltage (100–200 kV) is now widely used in large industrial ESPs. This is because of many practical advantages of wide ESP: (1) collection efficiency remains unchanged in spite of the increase in D, leading to a substantial cost down of ESP; (2) sparking rarely occurs, so that operation of the ESP is much more stable; (3) the effect of dust deposit on the collecting electrode is very much diminished, so that the high collection efficiency at the start of operation can be maintained during the entire period of operation (3–6 months); (4) the wide spacing enables an easy access of maintenance personnel into the gas passageway, making the maintenance work easy and cheap. Results of more detailed studies on wide ESP are given in Misaka, 1978; Matts, 1978; Ito and Takimoto, 1979; Itoh et al., 1979.

The wet ESP is used also in industrial ESPs where difficult dust is encountered, an extremely low emission is required, or simultaneous control of gaseous pollutants (NO, SO_2, air toxics, VOCs, odors, etc.) has to be made. Both vertical and horizontal types are used in wet ESP. Figure 15 shows an example of the vertical type multitube ESP. The particles are corona charged at an inlet of each vertical tube serving as the collection electrode by needle discharge electrodes attached to the high-voltage rod electrodes located along the centers of the tubes. Then the charged particles are collected at its upper region. Hence this ESP is a two-stage type.



(a)



(b)

Figure 10 Construction of industrial precipitator. (a) Collection field (one-stage, plate, horizontal type); (b) cross-section.

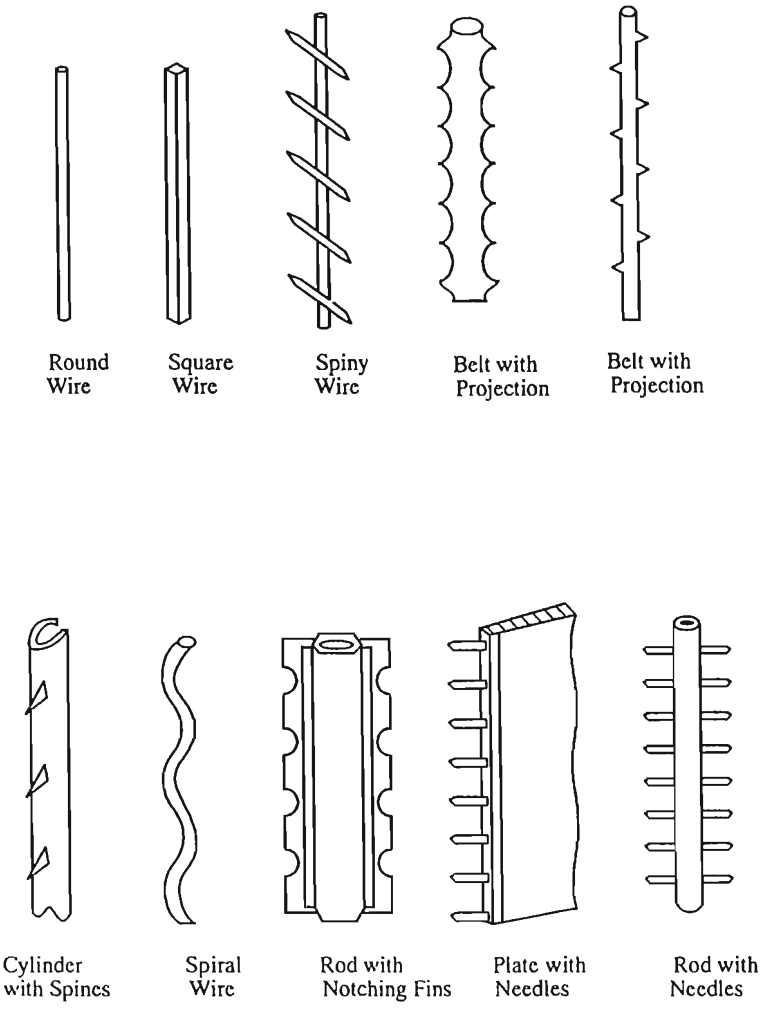


Figure 11 Construction of discharge electrodes.

The water irrigation in wet ESP is made by using spray nozzles in the horizontal or vertical direction, and dust collected on the water film on the collecting electrode is conveyed with water into to the hopper. The dense slurry is discharged from the hopper to the outside, while the top clear water in the hopper is reused after PH-conditioning to avoid electrode corrosion. A certain amount of the water must be continuously

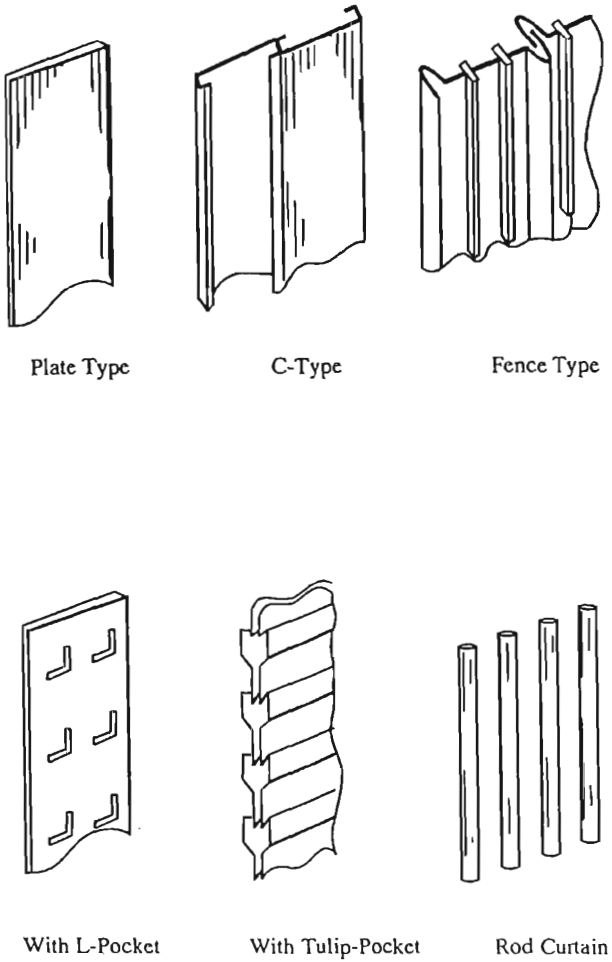


Figure 12 Construction of collecting electrodes.

replaced with fresh water to keep the level of dissolved mineral concentration (e.g., Ca) below a threshold, so as to avoid the growth of mineral crystals ($CaCO_3$) on the collecting electrode. Once it happens, the sharp edges of these crystals cause excessive sparking and make a stable operation of an ESP impossible. At the lower peripheries of the collection electrodes water tends to form water ligaments pulled by electric fields toward discharge electrodes, and they also cause excessive sparking. This must

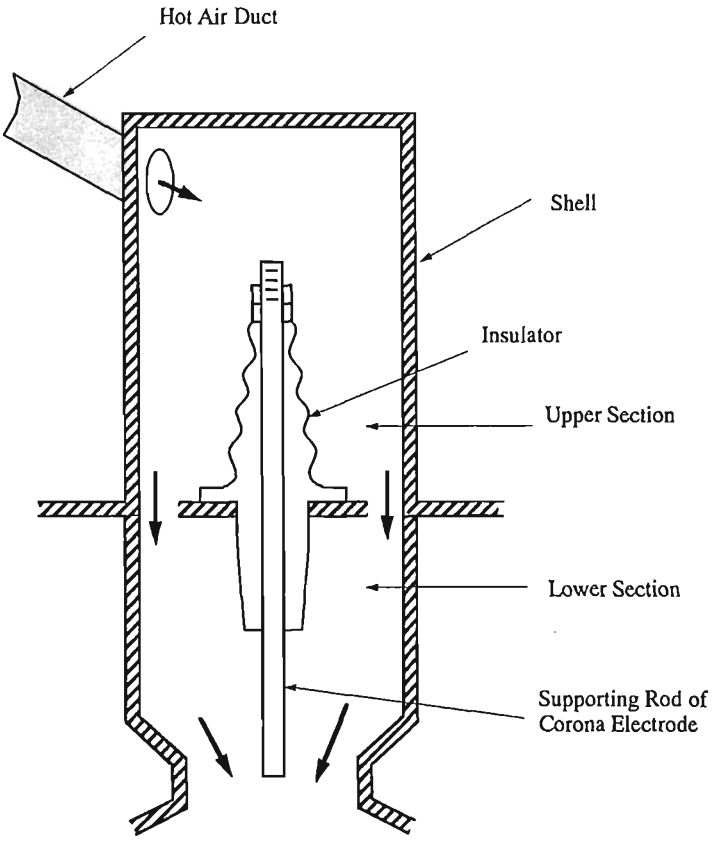
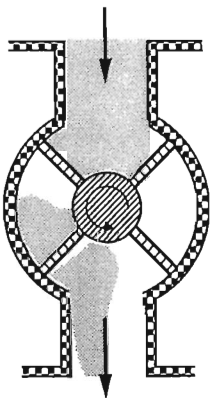


Figure 13 Bushing chamber.

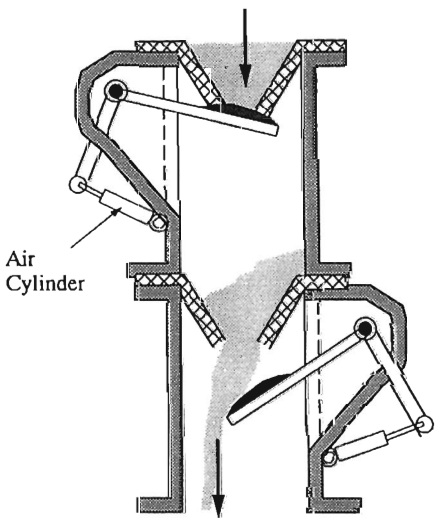
be avoided by a careful profile design of the bottom ends. The application fields of wet ESP are generally limited to a medium to smaller gas volume.

ESP is also used for particulate control in the process operated at an ordinary gas temperature. Dust cohesivity is great enough at this temperature to allow the use of two-stage type construction (Fig. 13) at a higher gas velocity (2–8 m/s). One example is an ESP for controlling carbon soot in automobile tunnels.

When explosive gas or inflammable dusts are encountered, a safety vent comprising a rapture disc must be attached to ESP to avoid explosion hazard.



(a)



(b)

Figure 14 Construction of dust outlet. (a) ESP is operated at a pressure slightly lower than ambient air to avoid dust leakage. (b) Dust is discharged using a gas-tight outlet.

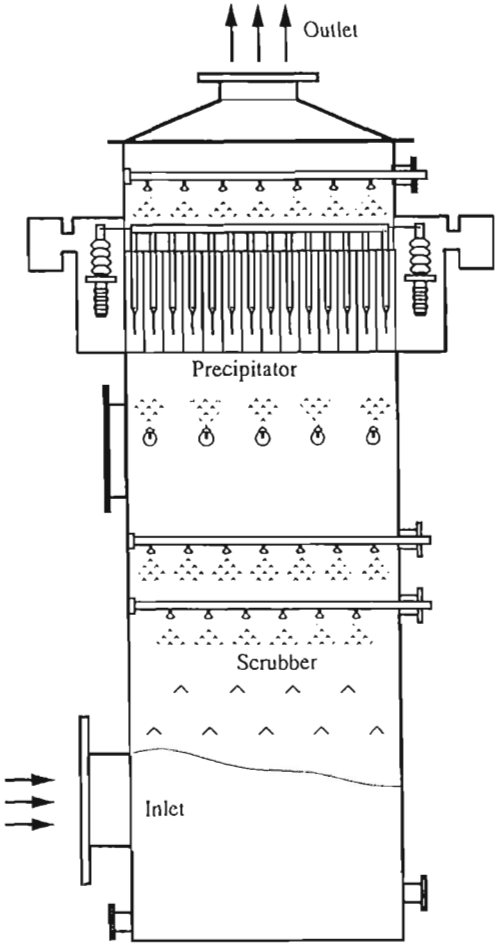


Figure 15 Multitube two-stage type wet ESP (vertical type).

VI. ESP FOR AIR CLEANING

ESP is used also for air cleaning in both living environments (homes, offices, air conditioning systems, hospitals, automobiles) and work places. The two-stage type, as shown in Fig. 16 (Penny type), is commonly used with positive corona at its charging field, as it generates substantially less ozone, hazardous for health, than negative corona (*ca* 10%; Penny, 1937).

Fig. 17 shows an example used in living environments, comprising plastic collecting electrodes (Masuda, 1986). Conductive paint is applied on

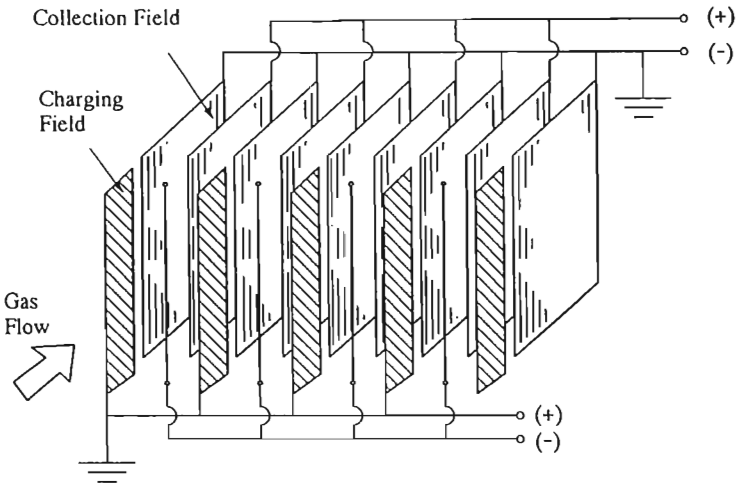
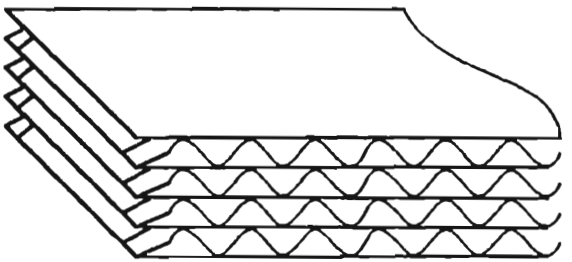


Figure 16 Multiplate two-stage type ESP (horizontal type).

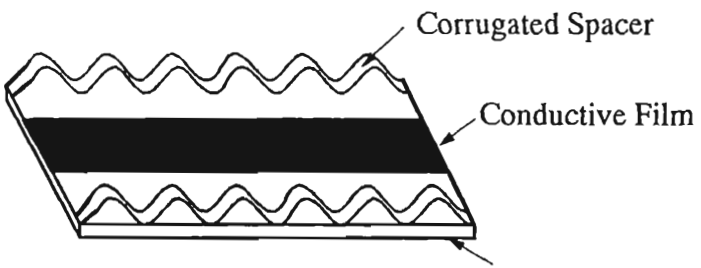
one side of each polypropylene film, with the opposite side not painted. These films are laminated in such a way that the painted surfaces face the unpainted ones, and a high dc voltage is applied between the neighboring films on their conductive layers. The opposite side surface also acts as an electrode because of its slight surface conduction due to the absorption layer of water molecules (electrostatic conductor). This leaks charges brought by oncoming collected particles and ions to the conducting paint electrode on the opposite side. This particular electrode design has great advantages: lower cost, very high safety, freedom from sparking, a very narrow interelectrode gap to produce a very high field intensity, and a high collection performance.

The electret fiber filter is also widely used for air cleaning of living environments (Turnhout et al., 1979; Turnhout et al., 1980). The electrostatically augmented membrane filter (Walkenhorst and Zebel, 1964; Castle and Inculet, 1970; Helfrich, 1977; Iinoya and Makino, 1974) and the electrostatic HEPA filter (Masuda and Sugita, 1981; Masuda, 1986) enable a higher performance for use in clean rooms.

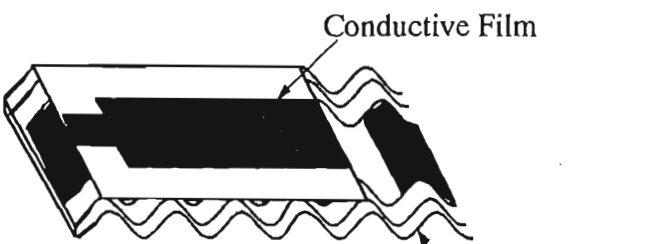
Figure 18 illustrates another example of ESP for air cleaning, which uses negative corona in its precharging field to generate a small amount of ozone at the same time. In the collecting field, use is made of an electrostatically augmented membrane filter (mini-pleats filter) for efficient aerosol collection, followed by a honeycomb type catalyzer stage for the



Construction



Element I



Element II

Figure 17 Plastic wafer collector of two-stage type ESP.

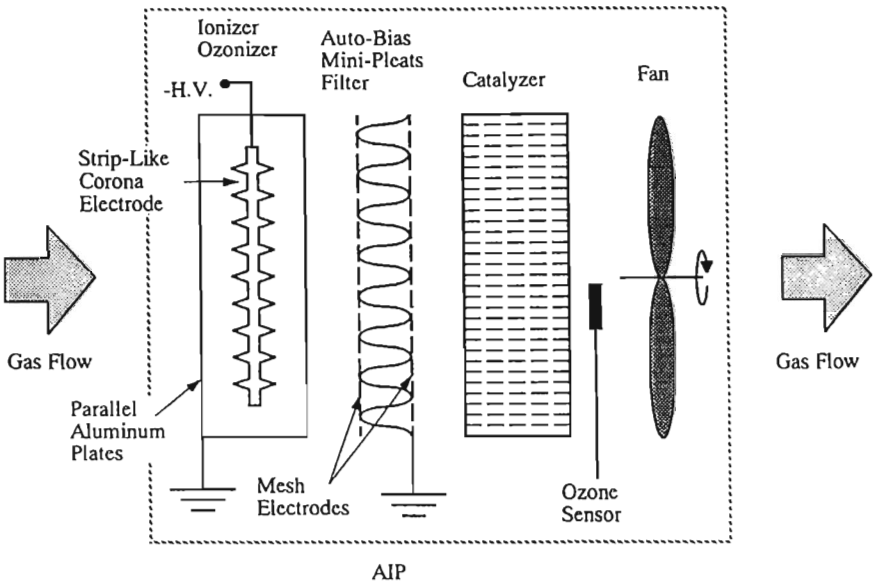


Figure 18 Integrated air purifier.

decomposition of the remaining ozone. This ESP, called an integrated air purifier (Masuda et al., 1993), collects aerosol particles, kills germs collected on the filter media through long-term exposure to a low concentration of ozone, and decomposes odors and indoor air toxics as well as ozone at the catalyzer stage.

VII. MEASUREMENTS FOR ESP

The following measurements are used for planning, design, and performance evaluation of an ESP, as well as the identification of the cause of its malfunction.

A. Collection Efficiency and Apparent Migration Velocity

Divide the cross-sections of inlet and outlet ducts of an ESP into a suitable number of subsections with equal areas. Insert the dust sampler head comprising a membrane filter to the center point of each subsection, and suction gas isokinetically to collect dust samples on the membrane filter. Then measure the weight of the sampled dust after drying. Measure also temperature and velocity at each center point, and calculate the inlet and outlet dust mass loadings m_i and m_o (g/Nm^3) at each point. From these

data, calculate the average inlet and outlet dust mass loadings m_{iav} and m_{oav} weighting the gas flow rate of each section. Then calculate the collection efficiency η and apparent migration velocity We using Eq. 13 or Eq. 15.

B. Apparent Dust Resistivity

1. Laboratory Measurement

Place the dust sample taken from either the inlet gas stream or the dust hopper into the resistivity measuring cell (resistivity cell) out of either parallel plate or concentric cylinder electrodes (Masuda, 1962), both comprising guard. Place the cell in a thermostat kept at a desired temperature T (°C) and absolute humidity H (gH_2O/m^3), and let the dust in the cell reach an equilibrium to T and H. Then measure the V-I curve of the dust sample. In general I rises proportionally with V up to a certain voltage, corresponding to the field strength in dust E_d = 1–3 kV/cm, above which it indicates a strongly higher than proportional rise up to the breakdown (Masuda, 1960). This is caused by partial breakdown occurring in voids within the dust (void discharge) and is accompanied by a number of random current spikes. Because of this phenomenon, the magnitude of r_d just before the total breakdown of dust is one order of magnitude lower than that measured in the proportional region. Furthermore, the breakdown field strength of dust, E_{ds}, lowers with decreasing dust thickness and humidity, and r_d shows a substantially lower value when measured directly in a corona field without using the resistivity cell (Masuda, 1960).

These phenomena raise a question in the use of the resistivity cell, as to the value of E_d at which r_d is measured. Even below E_{ds} the emission of false ions starts to occur from many partial breakdown points near the dust surface. In consideration of all these factors, the measurement of r_d at E_d = 5 (kV/cm) is recommended.

2. In Situ Measurement

Use an in situ resistivity cell of concentric cylinder electrodes, attached with a filter at one end, and connected to a suction pipe at another end. Insert the cell into the gas stream and suction the gas isokinetically. When dust fills the electrode gap, apply a dc voltage between the electrodes to measure the in situ dust resistivity.

C. Particle Charge and Space Charge Density

1. Suction Faraday Cage

Use a suction Faraday cage consisting of a grounded outer casing and an insulated inner cage holding a membrane filter inside it. The outer cell

has a sampling port at one end near the open end of the membrane filter, and a suction port at its opposite end connected to a suction pipe. Insert the suction Faraday cage into the inside of the ESP (conjunction between two collection fields), suction the gas, and measure the total charge Q (μC) brought by charged particles into the membrane filter by integrating the current from the inner cage. Then measure the total mass M (g) of the collected dust after drying and calculate the average charge-to-mass ratio of dust Q/M (μC/g). By measuring the total gas volume suctioned V (m^3) at the same time, the dust space charge density Q/V ($\mu C/m^3$) can also be derived. Furthermore, the dust area loading S_d can also be derived by attaching a boxer-charger in front of the Faraday cage (Masuda et al., 1987).

2. Millikan Cell

Sample the dust-laden gas from the ESP and introduce it into a Millikan cell (McDonald et al., 1980). Stop the gas flow and observe with a microscope the motion of individual charged particles in a space between two horizontal electrodes with the polarity of voltage positive and negative, and with the voltage off (free fall). Calculate charge and mass of individual particles from the velocities measured. Take at least 200 data to get a reliable result.

D. Back Corona

1. Direct Observation

Install an inspection hole comprising a glass window attached with a dust wiper and a shutter to the ceiling wall of the ESP and carry out the in situ direct observation of back corona either with the naked eye or using a portable image intensifier. Be careful, as a severe back corona of general glow mode occurring at an extremely high dust resistivity ($r_d > 10^{13}$ ohm-cm) may be dark enough not to be detected by the naked eye, even though emitting a large amount of false ions with a concurrently high value of J_i+/J_i- and a large drop in performance.

2. UHF Aerial

Insert a UHF parabola aerial inside the ESP and combine it with an amplifier having a 5–500 MHz bandwidth to detect the high-frequency pulse signals emitted from back corona of streamer mode (Masuda and Nonogaki, 1980). General glow mode cannot be detected.

3. Bipolar Current Probe

Insert into the interelectrode gap a bipolar current probe (Masuda and Nonogaki, 1980, 1981, 1984) to measure separately the negative ionic cur-

rent density J_{i-} from the discharge electrode and the positive ionic current density J_{i+} from the back corona. The ratio J_i+/J_i- is a parameter to determine the charge degradation in a back corona field (Masuda and Nonogaki, 1981; Masuda et al., 1984; Masuda and Nonogaki, 1986). This probe can be used also for measuring a local space potential in the interelectrode gap, filled with either monopolar or bipolar ions (Masuda et al., 1984; Dubard and Masuda, 1987).

E. Other Measurements

1. Cohesivity and Adhesivity of Dust

Use a centrifugal cell consisting of double coaxial cylinders and suspended by a flexible steel wire, with its inner cylinder electrostatically coated with dust and its outer cylinder serving as a protecting holder (Cross, 1975). An observation window and an illumination window (strobo-light) are attached on the outer cylinder of the rotating cell. Raise gradually the speed of rotation and observe the dust film to be disintegrated or detached at a certain speed. This gives the cohesivity and adhesivity of dust in terms of centrifugal acceleration, $\alpha = r\omega^2$.

Another method is to use a needle-to-plate corona cell, with its plate having a mesh at its center portion for providing pressurized air. Cover the plate with a dust layer, provide air pressure from the mesh under corona discharge, and measure the air pressure using a manometer, Δp (mm H_2O), at which the center part of the dust is fractured. The magnitude of Δp gives the electrostatically enhanced dust cohesivity (Simm, 1962).

2. Dust Reentrainment

Disperse into the inlet of an ESP the neutron labeled marker particles so that they are precipitated together with the dust in the ESP. Make the on-line measurement of the leakage of the marker particles at the outlet of the ESP using a neutron counter. This provides information of not only the rapping reentrainment but also the reentrainment occurring during the nonrapping period.

The load cells attached to the collecting electrodes also provide information on rapping reentrainment occurring in the operation of the ESP (Tasaicker, 1978).

REFERENCES

Altman, R. F., J. P. Gooch, R. E. Bickelhaupt, and E. B. Dismukes (1981). Flue gas conditioning studies, Proc. Int. Conf. on Electrostatic Precipitation, Monterey, California, pp. 107–144.

Basset, J. D., K. Akutsu, and S. Masuda (1977). A preliminary study of re-entrainment in an electrostatic precipitator. *J. Electrostatics*, 3, 311.

Bickelhaupt, R. E. (1974). Electrical volume conduction in fly ash. *J. Air Pollution Control Association*, 24, 3, 251.

Bickelhaupt, R. E. (1975). Surface resistivity and chemical composition of flyash. *J. Air Pollution Association*, 25, 2, 148.

Bickelhaupt, R. E. (1979). A technique for predicting fly ash resistivity. *EPA-Report 600-7-79-204*.

Bickelhaupt, R. E. (1980a). High resistivity behavior of hot-side electrostatic precipitators. *EPA-Report 600/7-80-076*.

Bickelhaupt, R. E. (1980b). An interpretation of deteriorative performance of hot-side precipitator. *J. Air Pollution Control Association*, 30, 8, 882–888.

Boem, J. (1982). *Electrostatic Precipitation*. Elsevier Scientific, Amsterdam.

Busby, T., and K. Darby (1963). Efficiency of electrostatic precipitators as affected by the properties and combustion of coal. *J. of Institute of Fuel*, 36 (May), 184.

Castle, P., and I. Inculet (1970). Proc. E.I.C. 1970 General Meeting, Paper No. 70-CSME-11.

Cross, J. (1975). Adhesion of electrostatic powder coatings. In *Static Electrification*. Institute of Physics Conf. Ser. No. 27, London, pp. 202–214.

Dalmon, J., and D. Tidy (1972a). The cohesive properties of fly ash in electrostatic precipitation. *Atmospheric Environment*, 6, 81.

Dalmon, J., and D. Tidy (1972b). A comparison of chemical additives as aids to the electrostatic precipitation of flyash. *Atmospheric Environment*, 6, 711.

Darby, K., and D. O. Heinrich (1966). Konditionierung der Rauchgasse von Kesselanlagen zur Verbesserung des Abscheidegrades von Elektrofiltern. *Staub-Reinhaltung der Luft*, 26, 11, 264.

Dinelli, G., and M. Rea (1984). Impulse energization of industrial ESPs, Proc. 2nd Int. Conf. on Electrostatic Precipitation, Kyoto, Japan, pp. 896–904.

Dismukes, E. B. (1975a). Conditioning of fly ash with ammonia. *J. Air Pollution Control Association*, 25, 2, 152.

Dismukes, E. B. (1975b). Conditioning of fly ash with sulfur trioxide and ammonia. EPA Report 600/2-75-015.

Dubard, J., and S. Masuda (1987). Measurement of the interelectrode space potential in electrostatic precipitators. *J. of Electrostatics*, 19, 243.

Dubard, J. L., W. Piulle, and L. E. Sparks (1984). Effects of pulse energization on electrical mechanism in fly ash Precipitator. Proc. Int. Conf. on Electrostatic Precipitation, Monterey, California, pp. 920–935.

Fujishima, H., and K. Tomimatsu (1990). Application of electrostatic precipitator with pulse energization system. Proc. 4th Int. Conf. Electrostatic Precipitation, Beijing, China, pp. 419–430.

Fujishima, H., and Y. Tsuchiya (1993). Application of wet type electrostatic precipitator for utilities' coal-fired boiler. Proc. 5th Int. Conf. on Electrostatic Precipitation, Washington D.C.

Gooch, J. P., E. B. Dismukes, R. E. Bickelhaupt, and R. F. Altman (1984). Flue

gas conditioning studies. Proc. 2nd Int. Conf. on Electrostatic Precipitation, Kyoto, Japan, pp. 194–209.

Hall, H. J. (1954). An automatic voltage control system for electrical precipitators. *AIEE Trans.*, 73 (May), 124.

Hall, H. J. (1981). High voltage power supplies and microprocessor controls for electrostatic precipitators. Proc. Int. Conf. on Electrostatic Precipitation, Monterey, California, pp. 668–699.

Heinrich, D. O. (1978). Der grosse Gassenabstand im Elektrofilter. *Staub-Reinhaltung der Luft*, 38, 11, 446.

Helfrich, D. J. (1977). Performance of an electrostatically aided fabric filtration. *Chemical Engineering Progress*, Aug. 1977, 45.

Hermstein, W. (1960). Untersuchungen über der Stromfaden-Durchschlag in Luft. *Archiv für Elektrotechnik*, XLV, 3, 209; XLV, 4, 279.

Iinoya, K., and T. Makino (1974). Application of electric field effects to dust collecting filters. *Aerosol Science*, 5, 357.

Ito, R., and K. Takimoto (1979). Wide spacing EP is available in cleaning exhaust gases from industrial sources. Proc. 1st EPA-Symposium on Transfer and Utilization of Particulate Control Technology, Denver, Colorado, EPA Report 600/7-79-004a.

Ito, S., S. Noso, M. Sakai, and K. Sakai (1979). Roof-mounted electrostatic precipitator. Proc. 1st EPA-Symposium on Transfer and Utilization of Particulate Control Technology, Denver, Colorado, EPA Report 600/7/79-044a, pp. 485--495.

Kumar, K. S., P. L. Feldman, H. I. Milde, and C. Schubert (1979). The results of first full-scale utility demonstration of pulsed precipitation. Rec. IEEE/IAS 1979 Annual Conf., Cleveland, Ohio, pp. 1333–1337.

Lausen, P., H. Henricksen, and H. H. Petersen (1979). Energy conserving pulse eneregization of precipitators. Rec. IEEE/IAS 1979 Annual Conf., Cleveland, Ohio, pp. 163–171.

Loeb, L. B. (1965). *Electrical Coronas*. University of California Press, Berkeley and Los Angeles.

McDonald, J. R., M. H. Anderson, P. B. Mosley, and L. E. Sparks (1980). Charge measurements on individual particles from existing laboratory precipitators with positive and negative corona at various temperatures. *J. Appl. Phys.*, 51, 3632.

Masuda, S. (1960). Reverse ionization phenomena in electrostatic precipitator. *J. Inst. Electr. Engrs. Japan*, 80, 865, 1482 (in Japanese).

Masuda, S. (1962). Effects of temperature and humidity on the apparent conductivity of high resistivity dust. *Electrotechnical Journal of Japan*, 7, 3, 108.

Masuda, S. (1981a). Resistivity and back corona. Proc. Int. Conf. on Electrostatic Precipitation, Monterey, California, pp. 131–161.

Masuda, S. (1981b). Bipolar current probe and its application in electrostatic precipitators for diagnosis of back discharge severity. Proc. 9th Conf. Association for Aerosol Research (GAF), Duisburg, Germany, pp. 207–216.

Masuda, S. (1986). Electrical precipitation of aerosols. Proc. 2nd Aerosol Int. Conf., Berlin, Germany, Pergamon Press, pp. 694–703.

Masuda, S., and S. Hosokawa (1984). Pulse energization of precipitators using long corona transmission lines. Proc. 2nd Int. Conf. on Electrostatic Precipitation, Kyoto, Japan, pp. 756–763.

Masuda, S., and S. Hosokawa (1988). Pulse energization system of electrostatic precipitator for retrofitting applications. *IEEE-IA Trans.*, 24, 4, 708.

Masuda, S., and A. Mizuno (1976). Light measurement of back discharge. *J. Electrostatics*, 2, 375.

Masuda, S. and A. Mizuno (1977). Initiation condition and mode of back discharge. *J. Electrostatics*, 4, 35.

Masuda, S., and A. Mizuno (1978). Flashover measurement of back discharge. *J. Electrostatics*, 4, 215.

Masuda, S., and Y. Nonogaki (1980). Detection of back discharge in electrostatic precipitators. Rec. IEEE/IAS 1980 Annual Conf., Cincinnati, Ohio, pp. 912–917.

Masuda, S., and Y. Nonogaki (1981), Sensing of back discharge and bipolar ionic current. *J. Electrostatics*, 10, 73.

Masuda, S., and Y. Nonogaki (1986). Bipolar structure of a back-discharge field in an electrostatic precipitator. *IEEE-IA Trans.*, IA-22, 4 (July/August), 602.

Masuda, S., and N. Sugita (1981). Electrostatically augmented air filter for producing ultra-clean air. Proc. 74th Annual Meeting of Air Pollution Control Association, Paper No. 81-45.3.

Masuda, S., T. Onishi, and H. Saito (1966). Inlet-gas humidification system for an electrostatic precipitator. *Industrial and Engineering Chemistry—Process Design and Development*, 5, 2, 135.

Masuda, S., S. Ago, T. Itoh, H. Saito, and N. Furuya (1976). Hybrid-type electrostatic precipitator. Proc. 69th Annual Meeting of APCA, Portland, Oregon, Paper No. 76-42.1.

Masuda, S., T. Obata, and J. Hirai (1978). A pulse voltage source for electrostatic precipitators. Rec. IEEE/IAS 1978 Annual Conf., Toronto, Canada, pp. 23–30.

Masuda, S., K. Akutsu, Y. Kanno, and M. Ko (1979a). Motion of small particles inside an electrostatic precipitator. Rec. IEEE/IAS 1979 Annual Conf., Cleveland, Ohio, pp. 139–145.

Masuda, S., A. Mizuno, and M. Akimoto (1979b). Effects of gas composition on sparking characteristics of back discharge—preliminary study. *J. of Electrostatics*, 6, 333.

Masuda, S. T. Itagaki, S. Noso, O. Tanaka, K. Hironaga, and N. Fukushima (1984). Bipolar current probe for measuring space charge potential and back corona severity in electrostatic precipitators. Proc. 2nd Int. Conf. on Electrostatic Precipitation, Kyoto, Japan, pp. 210–218.

Masuda, S., S. Hosokawa, and H. Nakatani (1985). Corona transmission line energized by very short pulse high voltages as applied in electrostatic precipitators, IEEE-IA Trans., IA-21, 6, 1377.

Masuda, S., T. Itagaki, and J.-Z. Wang (1987a). Role of dust space charge in electrostatic precipitation and its measuring method. Proc. 3rd Int. Conf. on Electrostatic Precipitation, Padova/Abano, Italy, pp. 519–526.

Masuda, S., S., Hosokawa, N. Tachibana, T. Ando, and Y. Matsumoto (1987b).

Fundamental behavior of direct-coupled submicrosecond pulse energization in electrostatic precipitators. *IEEE-IA Trans.*, IA-23, 1, 120.

Masuda, S., S. Hosokawa, T. Ohtani, X.-L. Tu, M. Tsutsumi, and N. Matsuda (1993a). The performance of an integrated air purifier for control of aerosol, microbial and odor. *IEEE-IA Trans.*, 29, 4, 774.

Masuda, S., S. Hosokawa, X. Tu, and Z. Wang (1993b). Cold plasma technologies for pollution control. Proc. 2nd Int. Conf. on Applied Electrostatics, Beijing, China, Beijing Institute of Technology Press, pp. 1–24.

Matts, S. (1978). Some experiences with increased electrode spacing. Proc. CSIRO Conf. on Electrostatic Precipitation, N.S.W., Australia, Paper No. 13-1.

Matts, S., and P. Ohnfeld (1964). Efficient gas cleaning with SF electrostatic precipitator. *SF Review* (1964–65).

Mayer-Schwinning, G. (1990). Treatment of flue gas and residues from municipal and industrial waste incinerators. Proc. 4th Int. Conf. Electrostatic Precipitation, Beijing, China, pp. 187–196.

Milde, H. I., and P. L. Feldman (1978). Pulse energization of electrostatic precipitators. Rec. IEEE/IAS 1978 Annual Conf., pp. 66–70.

Milde, H. I., and H. E. Van Hoesen (1979). Application of fast rising pulses to electrostatic precipitators, Rec. IEEE/IAS 1979 Annual Conf., Cleveland, Ohio, pp. 158–162.

Misaka, T., and H. Yubata (1993). Application of moving electrode type electrostatic precipitator for 500 MW coal-fired boiler. Proc. 5th Int. Conf. on Electrostatic Precipitation, Washington D.C.

Neulinger, F. (1990). Precipitators with intelligent energization. Proc. 4th Int. Conf. on Electrostatic Precipitation, Beijing, China, pp. 431–437.

Oglesby, S., Jr, and G. Nichols (1978). *Electrostatic Precipitation*. Marcel Dekker, New York.

Paulson, C. A. J., E. C. Potter, and K. Kamus (1978). Pilot-scale electrostatic precipitator tests on copper convertor flue gas. Proc. International Clean Air Congress, Brisbane, Australia, pp. 487–502.

Paulson, C. A. J., A. J. Prokopiuk, and R. Morrow (1993). The performance of a pilot-scale electrostatic precipitator using continuous, intermittent and pulsed energization. Proc. 5th Int. Conf. on Electrostatic Precipitation, Washington D.C.

Pauthenier, M. (1961). Lois de charge des particules spheriques conductrices dans un champ electrique biionisé. *La physique des forces electrostatiques et leurs application*, CNRS, pp. 279–281.

Pauthenier, M., and M. Moreau-Hanot (1932). La charge des particules spheriques dans un champ ionisé. *J. Phys. Radium*, 7, 12, 590.

Pauthenier, M., and M. Moreau-Hanot (1939). La theorie de la charge electrique des poussières de la générateur de haute tension à courant gazeux-resultats généraux. *Revue Générale die L'Electricité*, XLV, 18, 583.

Penny, G. W. (1937). A new electrosttic precipitator. *A.I.E.E. Trans.*, 56, 159.

Penny, G. W. (1951). Electrostatic precipitation of high resistivity dust. *A.I.E.E. Trans.*, 70, 1192.

Porle, K. (1988). Pulsed Energization of electrostatic precipitators-a review of worldwide experience. Proc. Int. Conf. on Modern Electrostatics, Beijing, China, pp. 9–13.

Potter, E. C. (1977). Electrostatic precipitation progress at the CSIRO minerals research laboratories in Sydney, Australia. Proceedings of the 4th International Clean Air Congress, pp. 848–851.

Potter, E. C. (1980). Surface chemistry of fly ash and electrostatic precipitation. *Proc. Institute of Electrostatics Japan*, 4, 4, 216 (in Japanese).

Potter, E. C., and C. A. J. Paulson (1974). Improvement of electrostatic precipitator performance by carrier gas additives and its graphical assessment using an extended Deutsch equation. *Chemistry and Industry*, 1974, 532.

Rinard, G. A., M. D. Durham, and D. E. Rugg (1981). Two-stage electrostatic precipitation. Proc. Int. Conf. on Electrostatic Precipitation, Monterey, California, pp. 178–191.

Simm, W. (1962). Die elektrische Eigenschaften des Staubes im Hinblick auf die Abscheidung im Elektrofilter. *Staub*, 22, 11, 463.

Sproull, W. T., and Y. Nakada (1951). Operation of Cottrell precipitators—effects of moisture and temperature. *Industrial and Engineering Chemistry*, 43, 6, 1350.

Szirmai, S. G., and E. C. Potter (1974). Measurement of powder strength at elevated temperatures by a new method. Proc. National Chemical Engineering Conf. 1974—Process Industries in Australia—Impact and Growth, Surfers Paradise, Queensland, Australia, pp. 304–411.

Tachibana, N., and H. Fujishima (1988). Application of Electrostatic precipitation with the intermittent energization. Proc. Int. Conf. on Modern Electrostatics, Beijing, China, pp. 14–19.

Tanaka, T., H. Fujishima, and Y. Tsuchiya (1993). Development of advanced dust collecting system for coal-fired power plant. Proc. 5th Int. Conf. Electrostatic Precipitation, Washington D.C.

Tassicker, O. J. (1978). Rapping reentrainment losses in full-scale electrostatic precipitators. Proc. of CSIRO Symposium on Electrostatic Precipitation, N.S.W., Australia.

Turnhout, J. v., W. J. Hoeneveld, J. W. C. Adamse, and L. M. Rossen (1979). Electret filters for high-efficiency and high-flow air cleaning. Rec. IEEE/IAS 1979 Annual Conf., Cleveland, Ohio, pp. 117–125.

Turnhout, J. v., J. W. C. Adamse, and W. J. Hoeneveld (1980). Electret filters for high-efficiency and high-flow air cleaning. *J. Electrostatics*, 8, 369.

Walkenhorst, W., and G. Zebel (1964). *Staub-Reinhaltung der Luft*, 24, 444.

White, H. J. (1951). Particle charging in electrostatic precipitation. *AIEE Trans.*, Pt. I, 70, 1186.

White, H. J. (1962). *Industrial electrostatic precipitation*. Addison-Wesley, Reading, Mass.

White, H. J. (1981). Review of the state of the technology. Proc. Int. Conf. on Electrostatic Precipitation, Monterey, California, pp. 17–53.

This Page Intentionally Left Blank

22

Modeling of Electrostatic Precipitators and Filters

Phil A. Lawless and Toshiaki Yamamoto

Research Triangle Institute
Research Triangle Park, North Carolina

Yoshio Otani

Karazawa University
Karazawa, Japan

> The choice is always the same. You can make your model more complex and more faithful to reality, or you can make it simpler and easier to handle.
>
> ——*Gleick, 1987*

I. INTRODUCTION

The electrostatic precipitator (ESP) is a real challenge to the modeler. It requires knowledge of many fields: electrostatics, physics, fluid mechanics, mechanical and electrical engineering, adhesion, cohesion, and aerosol behavior. A model can be simple enough to describe with a few equations but can also require the capacity of a large computer to calculate in detail. The science in ESP modeling is well established; the art consists of finding the proper level of detail for the various parts of the model.

The ESP is primarily an electrical device and must be characterized by its electrical parameters first. It is designed to collect aerosol particles, that is, particles small enough to remain suspended in a still gas for up to tens of seconds. The characteristics of the aerosol are next most important. The removal of the particles from a flowing gas must be accomplished

in a relatively short treatment time to minimize the size and cost of the ESP. The gas flow is important, especially the level of turbulence, because the electrical forces on the particles are not very strong and may be overwhelmed by aerodynamic forces. Finally, since the ESP may be removing tons of material from the gas each day, other (nonelectrical) methods for disposing of the collected material have to be considered and modelled.

The fundamental equation in ESP modeling is the particle drift velocity equation, an equation derived from balancing the electrical force on a charged particle with the aerodynamic drag due to the particle's motion through a gas:

$$w = \frac{qEC}{6\pi\eta r} \tag{1}$$

where w is the particle velocity, q is the charge on the particle, E is the electric field in which it moves, C is the Cunningham slip correction factor, η is the gas viscosity, and r is the particle radius (see Oglesby and Nichols, 1978, Chapter 21.) This equation neglects the forces of gravity and inertia and assumes that the particle moves through the gas without a turbulent wake. For most of the particles collected in ESPs, these are valid assumptions.

Equation 1 points out the first two areas to be modeled: particle charging and electric field values, with particle-size dependencies playing potentially important roles. The slip correction becomes important when particle sizes approach the mean free path between gas molecules; it serves to increase the drift velocity appreciably for particles smaller than about 0.5 μm in diameter.

Equation 1 describes the movement of a particle with respect to the gas surrounding it. The motion of the gas itself must also be modeled, an endeavor that ranges from extreme simplicity to full solutions of Navier-Stokes equations. This is the third area that will be discussed.

Once the motions of the gas and particles have been determined, the questions of immediate and ultimate collection performance must be addressed. Immediate collection is the first capture of a particle on a collecting surface; ultimate collection is its fate after being dislodged to fall into a hopper for disposal. Typically, the modeling of the nonideal effects is considered after the ideal mechanisms have been discussed, but, as will be shown, the nonideal effects are fundamentally intertwined with the ideal.

ESP design and performance are usually expressed in terms of efficiency—the fraction (or percentage) of the inlet dust load that is removed from the gas stream. Models, on the other hand, are more reasonably developed in terms of penetration, the fraction of the inlet loading that

emerges from the outlet. Emissions (upon which regulations are based) are proportional to penetration and the inlet loading. Penetration will be used in the remainder of this chapter.

If the ideal collection performance of an ESP is denoted by p_0, then there are two general nonideal processes that reduce the ultimate collection performance. The first is any process that allows a portion of the particles to avoid treatment altogether. In chemical reactor terminology this is called *bypassage*, and in ESP terminology *sneakage*. The second general process is one that operates on previously collected particles and causes them to become reentrained in the gas stream. Naturally called *reentrainment*, it can be caused by the rapping required to dislodge the dust cakes, mechanical vibrations, turbulence-induced aerodynamic forces, or electrical forces. Typically, rapping is the dominant cause of reentrainment.

The basic equation that incorporates these nonideal effects is

$$p_N = SN + (1 - SN)[p_0 + RR(1 - p_0)] \tag{2}$$

where p_N is the nonideal penetration, SN is the sneakage fraction, and RR is the reentrainment fraction. This equation may be used for the whole ESP or one of its sections. It describes the gross effects of the nonideal factors, but it does not include second-order effects, such as the impact of gas sneakage on the gas velocity in the collection zone. If the ideal penetration is zero, it is clear that sneakage and reentrainment limit the ultimate collection performance of the ESP. Many models do not use this form but account for nonideal factors with other parameters that degrade performance below the ideal value.

II. CHARGING

Charging of particles has two principal components (Chapters 3 and 21), field charging and diffusion charging. Field charging is due to the flow of ions along electric field lines to the surface of the particle. Diffusion charging is the thermally driven accumulation of ions on the particle in the absence of a field; once the ions come near the surface, they are bound there by their image charge. In the ESP, the two mechanisms operate simultaneously under most conditions.

A. Field Charging

For field charging, the electric field at the surface of the particle is evaluated as the sum of the external (uniform) field, the polarization field of the particle itself, and the radially symmetric field due to any charge on

the particle (Oglesby and Nichols, 1978). Field charging is a classical application of electrostatics and has been amply verified for spherical particles in the classical regime (on the order of millimeters in diameter.)

The charge on a particle $q(t)$ as a function of time is given by

$$q(t) = q_s \frac{t}{t + \tau} \tag{3}$$

where q_s is called the saturation charge, t is the exposure time to the ionic current, and τ is the charging time constant. The saturation charge is given by

$$q_s = 12 \frac{\kappa}{\kappa + 2} \pi \epsilon_0 r^2 E \tag{4}$$

where κ is the relative dielectric constant, ϵ_0 is the free space permittivity, and E is the applied field at distances far from the particle. Conductive particles, which have relaxation times that are short compared to the time for charging, should substitute the value 1 for $\kappa/(\kappa + 2)$. The charging time constant is given by

$$\tau = \frac{4\epsilon_0}{\rho_0 \mu} \tag{5}$$

where ρ_0 is the ionic space charge density and μ is the ionic mobility. The product $\rho_0 \mu$ is also equal to the quotient j/E, where j is the ionic current density.

B. Diffusion Charging

Diffusion charging is commonly described by a relation derived by White (1963) or alternatively by another described by Gunn (1955, Chapter 3). The White expression is based on a discrete kinetic model of the ions; the Gunn expression on a continuum diffusion model. The White expression for charging rate is

$$\frac{dq}{dt} = \pi r^2 \rho_0 v \exp\left(-\frac{qe}{4\pi\epsilon_0 rkT}\right) \tag{6}$$

where v is the mean thermal speed of the ions, e is the electron charge, and k is Boltzmann's constant. This expression may be integrated to give a closed form expression for $q(t)$.

The Gunn charging rate is given by

$$\frac{dq}{dt} = \frac{q\rho_0 \mu}{\epsilon_0} \left[\exp\left(\frac{qe}{4\pi\epsilon_0 rkT}\right) - 1\right]^{-1} \tag{7}$$

The similarities between the White and Gunn expressions are obvious and are discussed in more detail by Fjeld and McFarland (1988). The two diffusion models are not, however, equivalent.

C. Combined Models

In the ESP, most particles and electric fields are of such values that neither pure field nor pure diffusion charging is applicable. As a result, several theories have been developed for combined charging, most of which require numerical integrations of the charging rate equations. Smith and McDonald (1975) developed a widely used theory that combines field charging, field-modified diffusion charging, and pure diffusion charging over distinct regions of the particle. Liu and Kapadia (1978) developed a continuum field-diffusion theory that was refined and extended to bipolar charging by Fjeld et al. (1983). Cochet (1956) developed a charging expression similar to the field charging expression, but which included thermal diffusion and image forces. Finally, there is the widely used observation that the sum of field and diffusion charges, calculated independently, is a good approximation to the measured values.

There are other theories that refine charging calculations by including more detailed phenomena, but for ESP modeling, the ones cited here are most frequently used. All predict charges on particles that agree with experimental values at about the same level of accuracy. The charging data are not precise enough to distinguish between them. In many cases, the speed of computation is the criterion that will be used to select between them.

III. ELECTRIC FIELD

Particle charge and collection both depend strongly on the electric field, and calculations of electric field strength have received considerable attention. Modeling the electric field in the ESP is complicated by the presence of both ionic and particulate space charges. The ions move with the electric field, and the ionic space charge modifies the field. The particles are usually assumed to be immobile for the purpose of calculating the ion distribution, but the particulate space charge also modifies the electric field. The resulting electric field has been modeled both numerically and with analytic approximations.

The numerical methods are the standards against which the approximations can be judged. In recent years, numerical models of the wire-plate ESP have been given considerable attention. Finite difference methods were employed by Leutert and Böhlen (1972) and improved upon by

McDonald et al. (1977). Lawless and Sparks (1980) developed an electric field formulation that was a hybrid between finite difference and finite element techniques. Butler et al. (1989) completed work begun earlier by Davis and Hoburg (1983) and Hoburg and Davis (1986) using finite element techniques to solve for the electric field and the method of characteristics to solve for the ion motion. The third major method for the electrostatics problem is the charge simulation method, used by Elmoursi and Castle (1987) and refined by Elmoursi and Speck (1988). The boundary element method (similar to charge simulation) and the method of characteristics have been used together by Adamiak (1991).

The choosing between numerical methods is difficult and to some extent arbitrary. They all rely on evaluating fields and ionic currents at points on some sort of grid. The spacing of the grid influences the accuracy of the calculation and the time involved in reaching the results. The coupling between electric field and ionic space charge is so strong that much of the computation time is spent achieving self-consistent solutions. As a result, the numerical methods in practical models have so far assumed symmetrical arrangements of wires to reduce the computations.

The analytic approximations began with the work of Cooperman (1960), who developed a series expression for the Laplacian field (zero space charge) in an infinite array of wires-between-plates and then added a contribution due to ionic space charge. This approach is theoretically accurate if the space charge is uniform throughout the duct volume. Such would be the case at very low current densities, in which the ions follow the electric field lines without perturbing them, or if the particulate space charge were uniform. However, at current densities typical of ESP operation, the high values of ionic space charge make this approximation fail. Cooperman (1981) extended the approach to normal current densities and beyond with good results.

Lawless and Sparks (1986) approached the analytic approximation in a different way. Reasoning that the electric field directly opposite the wire in wire-plate geometry is not too different from the electric field in the wire-cylinder geometry, they computed a current density and electric field directly under the wire (with a correction factor to make the Laplacian field agree with Cooperman's Laplacian field). The electric field and current density on the collecting plate at locations away from the maximum were approximated with Warburg-like (Sigmond, 1982) distributions:

$$E(\theta) = E(0) \cos^n(\theta) \tag{8}$$

and

$$j(\theta) = j(0) \cos^m(\theta) \tag{9}$$

where θ is the angle with respect to the normal from the wire to the point of interest, and n and m are exponents describing the variation. The electric field exponent is approximately 2, while the current density exponent varies between 2 and 4, depending on the magnitude of the current density. McLean et al. (1986) extended this type of approximation to the corona formed in tufts on the electrode with negative polarity.

In general, these approximations perform well enough to be substituted for the numerical approaches when speed of computation or complexity of geometry are important. The numerical methods remain the fundamental methods for calculating electric field and current density.

IV. V-I OPERATING POINT

By themselves, none of the electric field methods are capable of predicting the whole V-I curve of an ESP or the voltage and current at which it will operate. The reason is that the voltage and current are determined by boundary conditions at the electrodes. Boundary conditions are not part of the electric field models but must be determined separately. The usual boundary conditions that are specified are the electric field at the wire surface and the ionic space charge density near the wire. These determine corona onset and the V-I curve.

A. Corona Discharge

The only model for corona initiation on smooth, round wires is that of Peek (1929), who measured corona onset voltages in wire-cylinder geometry to evaluate the electric field at the inner electrode surface. His result was

$$E_c = 3.0 \times 10^6 \left(\delta + 0.03\sqrt{\frac{\delta}{a}}\right) \tag{10}$$

where E_c is the field strength (V/m), δ is the air density relative to one atmosphere pressure and 298K, and a is the wire radius (m). More careful determination of the constants in the equation show slight polarity effects. This relation has been approximated theoretically by Cobine (1958). Surprisingly, there has been little further research into the electric field at the corona wire since Peek's initial effort. The electric field models assume that the Peek value for field is constant at the wire's surface at applied voltages well above corona onset. However, Waters and Stark (1975) provide some evidence that this assumption is not consistent with careful measurements.

B. Corona Structure

The negative corona obeys Peek's relation when the corona wire is small in diameter and smoothly polished. Corona wires operated in air for long periods of time, or those that collect dust particles on their surface, commence corona generation at much lower fields than those given by Peek's relation. The tuft corona forms by a more efficient mechanism than the glow corona of Peek's relation. Lawless et al. (1986), McLean et al. (1986), and Yamamoto and Sparks (1986) have modeled the tuft corona as measured in clean air. The structure of the tufts under high particulate space charge conditions is as yet undertermined by theory or experiment.

The ionic space charge near the wire is usually modeled by assuming that the current density is the product of electric field, ionic space charge, and mobility (using a mobility appropriate to the dominant gaseous ions). The latter is a weak assumption, because the corona contains a variety of ions (of both polarities) and electrons in its active zone. Nonetheless, the single mobility assumption produces good representations of experimental *V-I* curves.

C. Operating Points

A good ESP model should be able to predict the actual operating voltages and currents for all sections of the ESP. This goal has not been completely attained, but progress is being made. ESP electrical sections usually operate in one of three modes: the voltage is raised until electrical sparks occur; the voltage is raised to the limit of the power supply (either voltage or current); or the voltage is controlled at some lower value to prevent the formation of back corona or minimize power consumption.

Sparking is modeled as occurring when the value of the electric field near the plate reaches a critical value, based upon the experimental work of Phelps and Griffiths (1976). A correlation fitting their results is

$$E_s = 5.075 \left(\frac{259}{T}\frac{P}{1.0135}\right)^{1.48} + 0.063 x_w \left(\frac{298}{T}\frac{P}{1.0135}\right) \tag{11}$$

where E_s is the sparking field in kV/cm; T, the gas temperature in kelvins; P, the gas pressure in mbar; and x_w, the water vapor fraction in the gas. (The units are important because of the fractional exponent.)

It is important to realize that sparking is not a precise phenomenon. When the field at the plate is less than the sparking value, almost no sparks will occur; if it is equal, occasional sparks will occur; if it greatly exceeds the value, rapid sparking will occur. It is also important to realize that voltage waveform plays a strong role in sparking, because sparking will

usually occur at the peaks of the waveform. Peak voltage duration will also influence the formation of sparks.

Power supply limitations are easily modeled under most conditions. The *V-I* curve can be generated at increasing voltages until either the voltage or the current reaches its maximum value. What is not readily recognized is that the peak voltage may reach its limit before the average voltage, because of waveform effects. That is, the voltage rating of a power supply may be specified in terms of sinusoidal wave forms. The wave forms in ESPs may be far from sinusoidal in character (Oglesby and Nichols, 1978).

Back corona is a dust layer breakdown phenomenon that seriously degrades ESP performance. It is a function of layer resistivity and the current density through the layer. Modelling a back corona limit is equivalent to fixing the maximum current density at any location in the electrical section; this is well within the capabilities of the electric field models. The best experimental evidence suggests that dust layer breakdown occurs when the average electric field across the layer reaches 10 kV/cm (the actual value is a weak function of temperature). With this critical field, the current density permitted for any given layer resistivity is quickly computed.

Modeling the operating point at a minimum acceptable power level requires a complete ESP model, because "acceptable" has either an opacity or a mass emission interpretation. The model must be able to compute the emissions and evaluate opacity before any change to the operating voltage can be considered.

V. PARTICLE COLLECTION

Particle collection depends on the gas flow velocity and turbulence level. With laminar flow and steady velocity profiles, the particle trajectories are completely determined by the gas velocity and the drift velocity. Because of costs, ESPs are almost invariably operated in a higher velocity, turbulent regime. The degree of turbulence determines the kind of model that is applicable.

A. Turbulent Flow

From the earliest attempts to characterize ESP operation, the penetration has been modelled as an exponentially decaying function along the length of the ESP (White, 1963):

$$p = e^{-\mathrm{De}} \tag{12}$$

where De is a parameter called the Deutsch number, after one of the earliest ESP modelers, Walter Deutsch. White has shown that the exponential behavior can be derived under the assumption that the particles in the gas stream are uniformly mixed at all times. The resulting penetration can be expressed in terms of two parameters, a migration velocity ω and a specific collecting area SCA:

$$\text{De} = \omega \times \text{SCA} \tag{13}$$

The SCA is plate area divided by the volume of gas treated per unit time and has the units of inverse velocity; the Greek ω is chosen to resemble the particle drift velocity w discussed in Eq. 1. This migration velocity is, however, a parameter incorporating many effects, not a single physically meaningful quantity. Nonetheless, models often use the Deutsch equation (Eq. 12) as a reasonable description for individual particle sizes whose migration velocity is indeed equal to the drift velocity. Such a collection process is called an ideal Deutsch collection.

B. Finite Diffusivity Flow

The turbulence levels in conventional ESPs are far below what would be required to assure uniform mixing of the particles within a short length. In fact, it is far more reasonable to model the flow in an ESP as one with a finite eddy diffusivity. In such a model (Self et al., 1984), the particle concentration is no longer uniform across the width of the duct but builds a characteristic profile that migrates toward the collection plate down the length of the ESP. The overall effect is of collection at a much greater rate than the Deutsch equation permits.

This improved collection can be seen in Fig. 1, where the penetration is plotted as a function of Deutsch number and the electric Peclet number, defined as

$$\text{Pe} = \frac{wd}{D} \tag{14}$$

where d is the wire-plate spacing and D is the eddy diffusivity.

The Peclet number is an indicator of the relative strengths of the drift motion and the diffusive motion. This reduction in penetration for high Peclet numbers has been verified in low turbulence laboratory ESPs. The problem in applying the model to full-scale ESPs is in predicting the appropriate diffusivity to use, since diffusivity is a function of the turbulence intensity, a quantity that must usually be measured. In spite of this, Fig. 1 shows that ESPs with Peclet numbers of only 1 or 2 should collect particles more efficiently than the Deutsch equation predicts.

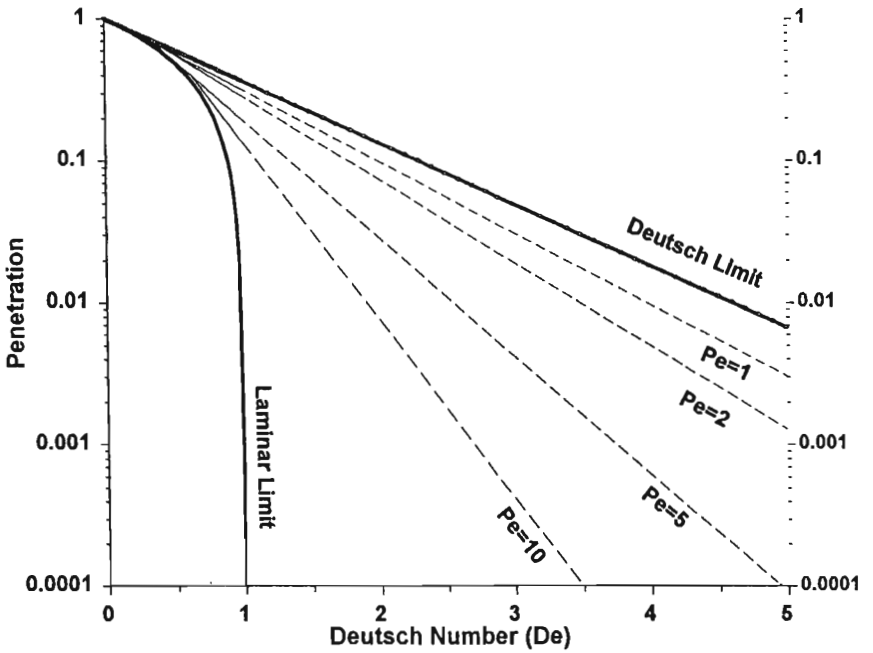


Figure 1 Penetration as functions of Deutsch and Peclet numbers.

C. Electrohydrodynamics

The ESP flow is further complicated by the fact that the ions and charged particles in the gas stream exert a force on the gas itself. The force is due to the drag of the gas on the ions or particles. When only the ions are considered, the motion of the gas that results from the ion drag force is called the corona wind. The study of the general interaction between the charged species and the neutral gas is called electrohydrodynamics (See Chapters 7 and 8.) Yamamoto and Velkoff (1981), Leonard et al. (1983), and Okubo et al. (1985) have modeled the electrohydrodynamic flow without the effects of particulate space charge and found, in general, that at normal ESP gas velocities (1–1.5 m/s) the disturbance of the flow streamlines is small. However, at velocities on the order of half that, the flow is perturbed significantly, and some forms of corona generate a strong turbulence. Section 6.B considers the effects of particulate space charge on electrohydrodynamics.

Yamamoto (1989) has further extended the finite diffusivity model to include electrohydrodynamics in the ESP. For the wire-plate ESP, it was

found that the collection is primarily unaffected by the turbulence intensity and secondary flows when the turbulent diffusivity is below 0.001 m^2/s. The collection is sharply reduced when the diffusivity exceeds that level. In practice, it is important to maintain a low turbulence level in the ESP.

Although the electrohydrodynamic effects can be described in great detail under carefully controlled conditions, the flows are very sensitive to geometrical considerations and end effects. It is therefore very difficult to apply electrohydrodynamics to practical ESP models, where much of the required information is simply not known.

VI. INTERACTIONS AND NONIDEAL EFFECTS

The previous sections describe the fundamental processes that take place in the ESP. This section describes the interactions that take place and the modeling of nonideal effects.

A. Particulate Space Charge

Since the goal of the ESP is to charge particles, and the particulate space charge can affect the electric field, the particulate space charge must be evaluated. The common assumption for modeling is that all particles of a given size have the same charge, so that the particulate space charge S_p is the sum over all sizes of the product of concentration and charge:

$$S_p = \sum_r N(r)\, q(r) \tag{15}$$

where $N(r)$ is the local concentration of particles of radius r, and $q(r)$ is their charge state. The effect of a uniform particulate space charge is to raise the effective corona onset potential by the amount

$$V_s = \frac{S_p d^2}{2\epsilon_0} \tag{16}$$

where V_s is the potential offset due to space charge S_p.

Because the space charge raises the corona onset voltage, it causes a reduction in available charging current at a fixed voltage. Therefore the charging must be evaluated in the presence of a space charge that is increasing because of the charging and may be decreasing due to the collection of particles. Withers and Melcher (1981) modeled the charging and collection of a monodisperse aerosol under multiple conditions of particle concentration and electrical conditions and performed experiments for comparison. They observed the phenomenon of "corona quenching" and the variation of current density along the collector as the particles were removed from the gas. Lawless and Sparks (1988) devised a graphical

approach for the solution of this problem, using an iterative solution. Lawless (1989) refined the approach and demonstrated solutions for a single wire. The space charge interaction is almost always confined to full ESP models because of the detailed particle charging calculations that depend on the particle size distributions.

B. Particle-Induced Turbulence

Atten et al. (1987) have examined the electrohydrodynamic (EHD) interaction of the charged particles with the gas and concluded that particles below about 5 μm in diameter are so strongly coupled to the gas that their motion is the primary cause of turbulence in the ESP. This would be true for particulate space charge densities that are comparable to the ionic space charge density (that is, for the inlet fields of the ESP). Estimates of the electric Peclet number for which this effect is important give values of about 1, corresponding to near-Deutsch collection (see Fig. 1). They conclude that the particle-induced turbulence will overwhelm any attempts to improve the gas flow quality.

Withers and Melcher (1981) predicted that under some conditions of particle concentration, concentration shock waves could develop because the particles that receive the highest charge overtake the slower-moving particles with lower charge. This is not an EHD effect, but it would have an influence on the gas turbulence.

C. Sneakage

Although sneakage was introduced as a fitting parameter in Eq. 2, little theoretical or experimental work has been done. Yamamoto et al. (1986) related gas sneakage to the pressure drop in the direction of flow. The simple model predicted sneakage flows of the order of 10% of the main gas flow; more important, it predicted sneakage variations with plate height, plate spacing, and degree of baffling within the collection zone.

D. Reentrainment

Reentrainment of collected particles, whether by rapping or by continuous processes, has received mainly experimental attention. The modeling of reentrainment has been mostly addressed toward using experimental results in full ESP models. Gooch and Marchant (1978) report the bulk of the experimental data and show the structure of the model for rapping reentrainment. The mass fraction of material reentrained is related to the mass calculated to be on the plates of the last section of the ESP by

$$y = Ax^z \tag{17}$$

where y is the amount reentrained, x is the amount collected on the last section, and A and z (approximately 0.1 and 1, respectively) are fitting constants that depend on the conditions under which the ESP operates. Lawless and Sparks (1984) used Eq. 2 in a simple model, equivalent to a linear reentrainment model:

$$y = RR \cdot x_s \tag{18}$$

where RR is the reentrainment fraction (typically 0.1), as before, and x_s is the mass of material collected on the plates of any single section of the ESP. The distinction between the two models is that material reentrained from upstream sections may be recollected, while that from the last section is emitted from the ESP.

The size distribution of reentrained particles was measured by Gooch and Marchant to have a characteristic mass median diameter of about 6 μm and a geometric standard deviation of about 2.5. More recent fits to the data show that the geometric standard deviation is about 1.4–1.6, which is a relatively narrow particle size distribution. Such size distributions have been informally shown to arise from the size-dependent collection of the ESP, but the size distributions are primarily empirical.

VII. MODELS

The final section summarizes the models that have been developed for ESPs. The two broad classes are the analytic models, for which penetration can be written as an explicit equation, and the computer models, for which similar equations apply, but whose operation depends on fine subdivisions of particle size distributions and electrode spacings. The analytic models may be further subdivided into simple models and sectional models, the first referring to the whole ESP and the second to the sections of the ESP. However, the analytic models make no pretense of calculating electric fields, relying on the user to supply that information.

A. Analytic Models

The foremost of the analytic models is the Deutsch model, given by Eqs. 12 and 13. It is followed in acceptance by the Matts-Öhnfeldt model (Matts and Öhnfeldt, 1963–1964) which resembles the Deutsch model:

$$p = e^{-(\mathrm{De})^k} \tag{19}$$

where k is a fractional exponent of 0.4–0.6, according to application. This model was derived to account for the effects of particle size distribution on the Deutsch number. It inadvertently includes other nonideal effects

that reduce the sensitivity of the penetration to the specific collecting area. The Cooperman model (Cooperman and Cooperman, 1982) uses the Deutsch expression, as in Eq. 12, but computes the migration velocity in Eq. 13 as

$$\omega_c = v\left[\left(\left(\frac{vd}{2D}\right)^2 + \frac{2(1-f)dw}{2D}\right)^{0.5} - \frac{vd}{2D}\right] \tag{20}$$

where ω_c is the Cooperman migration velocity, v is the gas velocity through the ESP, and f and D are fitting parameters representing the ratio of particles moving away from the walls to those moving toward the walls and the diffusivity coefficient, respectively. The Cooperman migration velocity modifies the Deutsch migration velocity by including the nonideal effects of reentrainment and diffusion.

The last simple analytic model is that of Robinson (1967):

$$p = (1 - B)\, e^{-A\mathrm{De}} + B \tag{21}$$

where A is related to the variation of dust concentration across the width of the duct and B is related to reentrainment of the collected dust. Robinson's model was one of the first to account specifically for concentration variations and for reentrainment.

The only sectional analytic model that has been published is the RTI Sectional model (Lawless and Sparks, 1984). That model uses the following equation for the penetration through the whole ESP, p_t:

$$p_t = \prod_{i=1}^{n} p_i \tag{22}$$

where there are n sections with individual penetrations p_i. The section penetrations use Eq. 2 to calculate p_i, with the p_0 terms calculated from Eqs. 12 and 13. The major innovation in the RTI model is that the average particle size is varied from section to section for calculating the particle drift velocity.

B. Numerical Models

The primary numerical ESP model, in terms of usage and impact, is the Southern Research Institute (SoRI) model (McDonald, 1978; Faulkner and DuBard, 1984). This model uses the charging model of Smith and McDonald, finite difference evaluations of the electric field, and Deutsch collection for individual particle sizes and incremental lengths through the ESP. Nonideal corrections are applied after the theoretical penetrations for each particle size have been calculated. Because of a consistent dis-

crepancy between theoretical predictions and measurements for particles smaller than about 2 μm diameter, the model also applies an empirical correction to the drift velocity in this size range, perhaps its weakest calculation. The model requires input of voltage and current operating points, although there is a facility for calculating a *V-I* curve in Revision 1. The space charge interaction is avoided by assuming an effective ion mobility that is a function of the particulate concentration in the gas stream.

A second numerical model is named ESPVI 1.0 (Lawless and Sparks, 1986). This model uses summed field and diffusion charging, analytic approximations for the electric field, and turbulent collection. A factor is introduced to multiply the SCA by a constant amount to account for finite diffusivity values. The nonideal effects were incorporated as in the RTI Sectional model, that is, in each section of the ESP. The associated *V-I* model could calculate *V-I* curves for each section, including an exponential decay of space charge along the length of each section. A sparking criterion could be invoked to determine the operating point. This model assumes filtered dc energization and predicted average voltages based on the sparking far in excess of typical values.

Development of published models was dormant until recently, although there has been continuous activity in modeling since the first publications. The SoRI model has been updated to include a self-consistent calculation of the space charge interaction (Faulkner et al., 1989). This model retains most of the features of the previous versions but is capable of more accurately calculating the space charge suppression of corona current.

Holstein et al. (1991) have presented a numerical model similar in structure to the SoRI models but with several modifications. The space charge interaction has been included in the field and charging calculations. Nonrapping, or continuous, reentrainment has been modeled. The empirical migration velocity correction was reduced but not eliminated. A rapping reentrainment factor and size distribution were determined for a dry sorbent mixed with fly ash, because the model was developed to explain measurements for that type of ESP operation.

Finally, two numerical models based on ESPVI 1.0 have been presented. Lawless and Plaks (1992) developed ESPVI 4.0, based on summed field and diffusion charging and turbulent collection with the turbulence confined to the core of the flow. Lawless and Altman (1990) developed ESPM, which uses a combined charging model and a multiple laminar zone collection model. Both models allow calculation of the sparking voltage and the back corona onset to determine operating voltage. Both models, for the first time, incorporate energization waveform with peak-to-average voltage ratio as an important input parameter. The first model

(Lawless and Plaks, 1992) allows the use of round wires, flat plates, and wire-between-pipes as elements of a corona electrode; with these elements, many different types of electrodes may be simulated. The second model (Lawless and Altman, 1990) accommodates only single diameter wire electrodes as corona electrodes. Finally, both models include the space charge interaction on a wire-by-wire basis; full *V-I* curves may be generated with the effect of space charge included at each voltage.

Details of the waveform model may be found in Lawless and Altman (1991). The new models also include a new nonideal condition, electrode misalignment, in which the electrodes deviate from their position in the center of the duct; this is modelled in Lawless et al. (1991). While it is not a universal defect, misalignment occurs often enough to be of concern to ESP users.

C. Comparison with Measurements

The data available for testing ESP models are relatively scarce. This is partly because of the expense of full-scale testing and because tests are not always designed to measure the parameters pertinent to modeling. Therefore comparison of model results with experimental results requires a degree of interpretation. One intercomparison of models and experiments was performed by Lawless and Sparks (1984), using published data for 13 cases. Their result is that the best model, the RTI Sectional model, has a standard deviation of 14% for the relative mass penetration ([predicted—measured]/measured) with a single set of nonideal parameters. DuBard and Dahlin (1987) compare the SoRI model with measured performances in a proprietary database. They conclude that measured ESP performance is best categorized by two sets of fitting parameters: one for ESPs with penetrations greater than 0.01 and another for those with less penetration. They interpret this to mean that older designs, targeted to meet a less stringent standard, had less attention paid to nonideal factors. For the newer designs, they conclude that the accuracy of the model prediction, including its sensitivity to poorly known nonideal factors, is of the same order as the day-to-day variations in the measurements of ESP emissions.

VIII. SUMMARY FOR ESP MODELING

Modeling of electrostatic precipitators has been a challenging field for many years. Particle charging has received considerable attention and is the most mature. Electric field modelling has also been highly developed. The gas flow conditions, including electrohydrodynamic effects, have

been studied extensively but are not well-integrated into full ESP models: most full models continue to use the Deutsch collection mechanism. Recently, the space charge interaction has been incorporated into the full ESP models, and first attempts at modeling voltagewave form effects have been made.

Modeling of the nonideal factors is not well developed at all. Rudimentary attempts have been made at modelling gas sneakage and electrode misalignment, but reentrainment is incorporated almost entirely by empiricism. Yet, in high-efficiency ESPs, the sneakage and rapping losses may account for the majority of emissions.

Full models are able to compute ESP performance satisfactorily with only a few fitting parameters. That is, for most ESPs in a particular application, the range of parameter variation is small. Once such an application is "calibrated," the models can predict variations in performance with particle or electrical conditions quite well. If the application pushes beyond the bounds of normal operation, the models must be changed to accommodate new effects that are encountered.

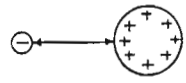
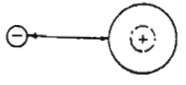
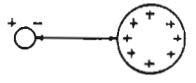
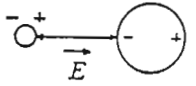
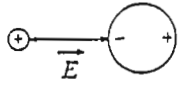
At present, there is a good balance between model approximations and the fitting parameters. Improving the approximations would not improve the overall level of model performance because of the uncertainties in the nonideal effects. However, in laboratory situations, more detailed modeling may be required to model observed effects, because the nonideal factors can be eliminated or significantly reduced. Better understanding of nonideal effects may force a revaluation of the approximations.

IX. ELECTROSTATIC FILTERS

In the collection of particles by fibrous filters, there exists a most penetrating particle size at which none of the mechanical collection mechanisms such as diffusion, interception, and inertial impaction are effective for particle collection. Electrostatic force can cover the transition region of these mechanical collection mechanisms, and various types of electrostatic filters have been devised. Electrostatic forces exerted between particles and fibers can be classified into five forces depending on the electrically charged states of particle and fiber as well as the existence of an external electric field. Table 1 illustrates the five electrostatic forces in the presence and absence of an external electrical field.

Electret filters, which consist of fibers with self-retained charge, have attracted great attention because they require no electrodes for the external electric field and they collect charged particles by a strong Coulombic force and even neutral particles by the induced force. Electret filters can achieve a high collection efficiency at a lower pressure drop than mechani-

Table 1 Electrostatic Forces Acting Between Fiber and Particles[a]

Charged state	Electrostatic force	Equation	Dimensionless parameter
With external electrical field			
Charged particle Charged fiber	Coulombic force 	$F\bar{r} = -\frac{qQ}{\pi\epsilon_0 d_f \bar{r}}$ $F_\theta = 0$	$K_C = \frac{C_C qQ}{3\pi^2\epsilon_0\mu d_f u_0}$
Charged particle Neutral fiber	Image force 	$F\bar{r} = -\left(\frac{\epsilon_f - 1}{\epsilon_f + 1}\right)\frac{q^2}{4\epsilon_0 d_f^2(\bar{r}-1)^2}$ $F_\theta = 0$	$K_C = \left(\frac{\epsilon_f - 1}{\epsilon_f + 1}\right)\frac{C_C q^2}{12\pi^2\epsilon_0\mu d_p d_f^2 u_0}$
Neutral particle Charged fiber	Induced force 	$F\bar{r} = -\left(\frac{\epsilon_p - 1}{\epsilon_p + 2}\right)\frac{Q^2 d_p^3}{\pi\epsilon_0 d_f^3 \bar{r}^3}$ $F_\theta = 0$	$K_I = \left(\frac{\epsilon_p - 1}{\epsilon_p + 2}\right)\frac{C_C Q^2 d_p^2}{3\pi^2\epsilon_0\mu d_f^3 u_0}$
Without external electrical field			
Neutral particle Neutral fiber	Gradient force 	$F = \frac{\pi\epsilon_0 d_p^3}{4}\left(\frac{\epsilon_p - 1}{\epsilon_p + 2}\right)\nabla\lvert E\rvert^2$	$K_C = \frac{2}{3}\left(\frac{\epsilon_p - 1}{\epsilon_p + 2}\right)\left(\frac{\epsilon_f - 1}{\epsilon_f + 1}\right)\frac{C_C\epsilon_0 d_p^2 E^{2*}}{\mu d_f u_0}$
Charged particle Neutral fiber	Coulombic force 	$F = qE$	$K_{EC} = \frac{C_C q\bar{E}^*}{3\pi\mu d_p u_0}$

[a] E: average electric field in the filter (V/m); ϵ_0: space permittivity (C/Vm); ϵ_f: dielectric constant of fiber; ϵ_p: dielectric constant of particle; q: particle charge (C), and Q: fiber charge (C/m).

cal filters. Figure 2 illustrates how the electret filter is effective for particle collection. When neutral particles are collected by neutral fibers, the particle penetration curve is concave against the particle diameter because interception is dominant for large particles and Brownian diffusion for small particles. When fibers are charged, induced force exerts on the neutral particles, and thus the penetration of a particle with a larger diameter is lowered. When charged particles with an elementary charge are filtered by a charge filter, additional Coulombic force acts on particles, yielding a low particle penetration in the entire particle size range.

There are two types of electret filters, split fiber filters and melt-blow fiber filters. The former is produced by splitting a sheet of electret into fibers with rectangular cross-sections, while the latter is manufactured by blowing melted electret material through an electrically discharging nozzle in order to implant electrical charge in the fibers. Most electret filters are made of polypropylene because it retains implanted electrical charge for a long period of time.

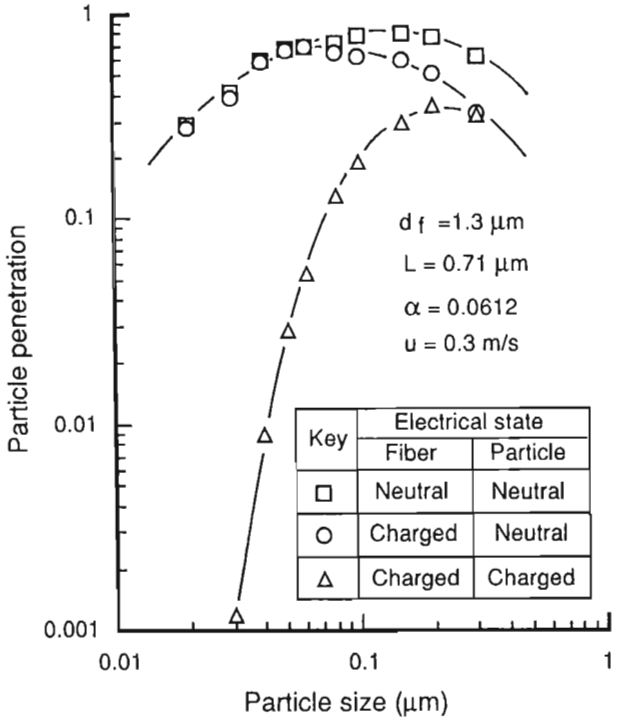


Figure 2 Effect of fiber and particle charges on particle penetration.

A. Initial Collection Efficiency of Electret Filters

In the same manner as mechanical filters, the collection efficiency of an electret filter E is related to the single fiber collection efficiency η by

$$E = 1 - \exp\left[-\frac{4}{\pi}\frac{\alpha}{1-\alpha}\frac{L}{d_f}\eta\right] \tag{23}$$

where α is the packing density of the filter, d_f the fiber diameter, and L the filter thickness. If we assume additivity of the collection efficiencies due to Coulombic force, induced force, and mechanical mechanisms, η_C, η_{In}, η_M, the single fiber efficiency is calculated by

$$\eta = \eta_C + \eta_{In} + \eta_M \tag{24}$$

In the collection of charged particles, all three terms in the preceding equation must be included, while the first term is omitted in the collection of neutral particles.

Initial single fiber collection efficiency of an electret filter with a uniform charge distribution along the circumferential direction of fibers was theoretically studied by Pich (1978). For an electret filter with dipole charge, Brown (1981) introduced the particle stream function and theoretically obtained the following expression of single fiber collection efficiency for charged particles when interception effect is negligible:

$$\eta_c = 0.59\, h_K^{-0.17} K_C^{0.83} \tag{25}$$

where h_K is the hydrodynamic factor given by Eq. 26 for Kuwabara flow (Kuwabara, 1959), and K_C is the Coulombic force parameter defined by Eq. 27.

$$h_K = -0.5 \ln \alpha + \alpha - \alpha^2 - 0.75 \tag{26}$$

$$K_c = \frac{C_C n_p e \bar{\sigma}}{6\epsilon_0(1+\epsilon_f)\mu d_p u} \tag{27}$$

C_C is the Cunningham slip correction factor, $n_p e$ the particle charge, $\bar{\sigma}$ the average surface density, ϵ_0 the space permittivity, ϵ_f the dielectric constant of the fiber, μ the viscosity, and u the filtration velocity. In electret filtration, contrary to mechanical filtration, the limiting trajectory of a particle is such that the particles pass through a point at which particle velocity vanishes. Therefore the particle with the limiting trajectory is transported toward the fiber surface in the normal direction of the fiber from the zero velocity point and then collides on the surface. Consequently, interception plays no role when a particle's radius is smaller than the distance between the zero velocity point and the fiber surface. This implies the existence

of a critical value of the interception parameter, below which interception does not affect the single fiber collection efficiency.

Pich et al. (1987) derived the Coulombic and interception single fiber efficiency at a fiber orientation by assuming that a particle with limiting trajectory has vanishing tangential velocity at a particle radius away from the fiber surface. Then they obtained the following average Coulombic interception single fiber efficiency by integrating it over all dipole orientation presuming that dipole orientation is random in the filter.

$$\eta_{CR} = \eta_R + \left(\frac{1}{1 + R} - \frac{\eta_R}{(1 + R)\eta_R + K_C}\right) K_C \tag{28}$$

where R is the interception parameter ($= d_p/d_f$) and η_R is the interception efficiency, which is given for Kuwabara flow as

$$\eta_R = \frac{1}{2h_K}\left[\frac{1}{1 + R} - (1 + R) + 2(1 + R)\ln(1 + R)\right] \tag{29}$$

Later, Otani et al. (1992) pointed out that particle tangential velocity vanishes at a particle radius away from the fiber surface only when the interceptional parameter is larger than the critical value given by

$$R_C = 0.66(h_K K_C)^{0.64} \tag{30}$$

Therefore Eq. 28 is valid only when $R > R_c$; otherwise Eq. 25 has to be used in the prediction of Coulombic collection efficiency.

Induced force, which is responsible for the collection of neutral particles, is a function only of the distance between the particle and the electret fiber and does not depend on the dipole charge orientation. Therefore the limiting trajectory always ends at the rear stagnation point of the fiber. By making use of this, Brown (1981) analytically obtained a point on the axis at which the particle velocity vanishes and numerically traced the particle trajectory backwards to obtain the original position of particles upstream of the fiber. The single fiber efficiency for a neutral particle is given by

$$\begin{aligned} \eta_{In} &= 1.48\, K_{In}^{0.93} && 10^{-4} < K_{In} < 10^{-2} \\ &= 0.51\, h_K^{-0.35} K_{In}^{0.73} && 10^{-2} < K_{In} < 1 \\ &= 0.54\, h_K^{-0.60} K_{In}^{0.40} && 1 < K_{In} < 100 \end{aligned} \tag{31}$$

where K_{In} is the induced force parameter defined by

$$K_{In} = \frac{(\epsilon_p - 1)C_C \pi^2 \bar{\sigma}^2 d_p^2}{6(\epsilon_p + 2)\epsilon_0(1 + \epsilon_f)^2 \mu d_f u} \tag{32}$$

According to a similar discussion for charged particles, there exists a critical interception parameter in the collection of neutral particles. The critical interception parameter given by Brown (1981) is

$$R_c = (h_K K_{In})^{1/2} \tag{33}$$

When we want to calculate the single fiber efficiency either by Eq. 25 or by Eq. 31, the main question that arises is how we know the average charge density of the electret fiber. There have been several attempts to measure the electret charge. Brown (1979) used ions to neutralize the electret charge and obtained the value of 34.2 nC/m which gave an average surface charge density of about 800 $\mu C/m^2$. Baumgartner et al. (1986) applied a single fiber technique by which the displacement of a single electret fiber in an external electret field was measured. The other approach was to obtain the effective charge so as to fit the experimental collection efficiency by Eqs. 25 or 31. Recently, Baumgartner et al. (1993) directly measured the particle trajectory around the electret fiber and suggested that the effective charge density is between 100 and 500 $\mu C/m^2$ for a split fiber filter and about 200 $\mu C/m^2$ for cylindrical electret fibers.

B. Stability of Electret Charge

As described in the preceding section, electret filters have very high initial collection efficiency compared to conventional mechanical filters. However, since the electret charge is not permanent, the problem arises of how long the initial collection efficiency is maintained in terms of practical use. Otani et al. (1992) studied the stability of the electret charge when it was exposed to particle-free humid air and liquid and solid particles. They found that the electret charge is fairly stable in humid air, but that the collection efficiency of droplets gradually decreases with particle load because captured droplets covered the fiber surface and thus weakened the electrical field around the fibers. In the filtration of solid particles, the collection efficiency may increase or decrease with dust load, depending on the effects of captured particles, which lead to both an increase in interceptional collection efficiency and a reduction of collection efficiency by the neutralization of electret charge.

REFERENCES

Adamiak, K. (1991). Simulation of corona in wire-duct electrostatic precipitator by means of the boundary element method. Conference Record, Industry Applications Society IEEE-IAS-1991 Meeting, pp. 610–615.

Atten, P., F. McCluskey, and A. Lahjormi (1987). Electrohydrodynamic simula-

tion of electrostatic precipitation. *IEEE Trans. on Industry Applications*, IA-23, 705.

Baumgartner, H., F. Löffler, and H. Umhauer (1986). Deep-bed electret filters—the determination of single fiber charge and collection efficiency. *IEEE Trans. Electr. Ins.*, 21, 477.

Baumgartner, H., C. Piesch, and H. Umhauer (1993). High-speed cinematographic recording and numerical simulation of particles depositing on electret fibers. *J. Aerosol Sci.*, 24, 945.

Brown, R. C. (1979). Electrical effects on dust filters. Proc. 2nd World Filtration Congress, London, pp. 291–301.

Brown, R. C. (1981). Capture of dust particles in filters by line-dipole charged fibers. *J. Aerosol Sci.*, 12, 349.

Butler, A. J., Z. J. Cendes, and J. F. Hoburg (1989). Interfacing the finite element method with the method of characteristics in self-consistent electrostatic field models. *IEEE Trans. on Industry Applications*, 25, 533.

Cobine, J. D. (1958). *Gaseous conductors—theory and engineering applications*. Dover, New York.

Cochet, R. (1956). Theory of charging of submicron particles in electrically ionized fields: rate of precipitation of the particles. *Compt. Rend. Acad. Sci.*, 243, 243.

Cooperman, G. (1981). A new current-voltage relation for duct precipitators valid for low and high current densities. *IEEE Trans. on Industry Applications*, IA-17, 236.

Cooperman, P. (1960). A theory for space-charge-limited currents with application to electrical precipitation. *A.I.E.E. Transactions*, 79, 47.

Cooperman, P., and G. D. Cooperman (1982). Precipitator efficiency for log-normal distributions. *Atm. Environment*, 16, 307.

Davis, J. L., and J. F. Hoburg (1983). Wire-duct precipitator field and charge computation using finite element and characteristics methods. *J. Electrostatics*, 14, 187.

DuBard, J. L., and R. S. Dahlin (1987). *Precipitator performance estimation procedure*. CS-5040. Electric Power Research Institute, Palo Alto, CA.*

Elmoursi, A. A., and G. S. P. Castle (1987). Mapping of field lines and equipotential contours in electric field problems using the charge simulation technique. *IEEE Trans. on Industry Applications*, IA-23, 95.

Elmoursi, A. A., and C. E. Speck (1988). Simulation of space charge fields in unbounded geometries. *IEEE Trans. on Industry Applications*, IA-24, 1699.

Faulkner, M. G., and J. L. DuBard (1984). *A mathematical model of electrostatic precipitation (revision 3)*. EPA-600/7-84-069a,b,c (NTIS Nos. PB84-212-679,687).

Faulkner, M. G., J. L. DuBard, and L. S. Hovis (1989). A self-consistent Deutschian ESP model. In Proceedings: EPA/EPRI Seventh Symposium on the Transfer and Utilization of Particulate Control Technology, San Diego, CA, Paper no. 7A5, Electric Power Research Institute, Palo Alto, CA.*

Fjeld, R. A., and A. R. McFarland (1988). Evaluation of select approximations for calculating particle charging rates in the continuum regime. *Aerosol Sci. and Technology*, 10, 535.

Fjeld, R. A., R. O. Gauntt, and A. R. McFarland (1983). Continuum field-diffusion theory for bipolar charging of aerosols. *J. Aerosol Sci.*, 14, 541.

Gleick, J. (1987). *Chaos*. Viking, New York, p. 287.

Gooch, J. P., and G. H. Marchant (1978). *Electrostatic precipitator rapping reentrainment and computer model studies*. FP-792. Electric Power Research Institute, Palo Alto, CA.*

Gunn, R. (1955). The static electrification of aerosols by ionic diffusion. *J. Colloid Science*, 10, 107.

Hoburg, J. F., and J. L. Davis (1986). Finite element/method of characteristics computations of self-consistent charge density—electric field structures. *Computational Electromagnetics*, 217.

Holstein, D. B., D. E. Rugg, and M. D. Durham (1991). Development of an ESP model for dry scrubbing applications. Proceedings: Ninth Particulate Control Symposium, Williamsburg, VA, Paper No. 4A1, Electric Power Research Institute, Palo Alto, CA.*

Kuwabara, S. (1959). *J. Phys. Soc. Japan*, 14, 527.

Lawless, P. A. (1989). Modeling particulate charging in ESPs II. Analytic approximations and refinements. Proceedings IEEE Industry Applications Society Annual Meeting, No. 89CH2792-0, p. 2154.

Lawless, P. A., and R. F. Altman (1990). An integrated precipitator model for microcomputers. Proceedings of the Eighth Symposium on the Transfer and Utilization of Particulate Control Technology, San Diego, CA, Paper No. 4A2, Electric Power Research Institute, Palo Alto, CA.*

Lawless, P. A., and R. F. Altman (1991). Modeling the effects of electrode misalignment. Proceedings of the Ninth Particulate Control Symposium, Williamsburg, VA, Paper No. 2A3, Electric Power Research Institute, Palo Alto, CA.*.

Lawless, P. A., and N. Plaks (1992). ESPVI 4.0—Electrostatic Precipitator V-I and Performance Model User's Manual. EPA-600/R-92-104a. U.S. Environmental Protection Agency. Research Triangle Park, NC. ESPVI 4.0 (program and manual) is available for downloading from the OAQPS Technology Transfer Network (select CTC bulletin board) (Modem: (919) 541-5742 @ 14400, N, 8, 1; voice: (919) 541-5384).

Lawless, P. A., and L. E. Sparks (1980). A mathematical model for calculating effects of back corona in wire-duct electrostatic precipitators. *J. Applied Physics*, 51, 242.

Lawless, P. A., and L. E. Sparks (1984). A review of mathematical models for ESPs and comparison of their successes. *Proceedings: Second International Conference on Electrostatic Precipitation* (S. Masuda, ed.), Kyoto, p. 513.

Lawless, P. A., and L. E. Sparks (1986). *An Interactive Model for Calculating V-I Curves in ESPs. Version 1.0*. EPA-600/8-86-030. (NTIS PB87-100046/AS).

Lawless, P. A., and L. E. Sparks (1988). Modeling particulate charging in ESPs. *IEEE Trans. on Industry Applications*, IA-24, 922.

Lawless, P. A., K. J. McLean, L. E. Sparks, and G. H. Ramsey (1986). Negative corona in wire-plate electrostatic precipitators. Part I: Characteristics of individual tuft-corona discharges. *J. Electrostatics*, 18, 199.

Lawless, P. A., N. Plaks, and R. F. Altman (1991). Modelling wave form effects in ESPs: the algorithm in ESPM and ESPVI. Proceedings of the Ninth Particulate Control Symposium, Williamsburg, VA Paper No. 2A1, Electric Power Research Institute, Palo Alto, CA.*

Leonard, G. L., M. Mitchner, and S. A. Self (1983). An experimental study of the electrohydrodynamic flow in electrostatic precipitators. *J. Fluid Mechanics*, 127, 123.

Leutert, G., and B. Böhlen (1972). The spatial trend of electric field strength and space charge density in plate-type electrostatic precipitators. *Staub Reinhalt. Luft.*, 32, 27.

Liu, B. Y. H., and A. Kapadia (1978). Combined field and diffusion charging of aerosol particles in the continuum regime. *J. Aerosol Sci.*, 9, 227.

McDonald, J. R. (1978). *A mathematical model of electrostatic precipitation (revision 1)*. Vols. I and II, EPA-600/7-78-111a,b (NTIS Nos. PB284-614,615).

McDonald, J. R., W. B. Smith, H. B. Spencer III, and L. E. Sparks (1977). A mathematical model for calculating electrical conditions in wire-duct electrostatic precipitation devices. *J. Appl. Phys.*, 48, 2231.

McLean, K. J., P. A. Lawless, L. E. Sparks and G. H. Ramsey (1986). Negative corona in wire-plate electrostatic precipitators. Part II: Calculation of electrical characteristics of contaminated discharge electrodes. *J. Electrostatics*, 18, 219.

Matts, S., and P. Öhnfeldt (1963–1964). Efficient gas cleaning with SF electrostatic precipitators. *Flakt*, 93.

Oglesby, S., Jr, and G. B. Nichols (1978). *Electrostatic Precipitation*. Marcel Dekker, New York.

Okubo, T., H. Yano, K. Nomoto, and T. Adachi (1985). Analysis of flow for the wire-plate electrode geometry. Proceedings of the Ninth Annual Meeting of the Institute of Electrostatics, Japan, pp. 17–20.

Otani, Y., H. Emi and J. Mori (1992). Initial collection efficiency of electret filter and its durability for solid and liquid particles. *Kagaku Kogaku Ronbunshu*, 18, 240.

Peek, F. W. (1929). *Dielectric Phenomena in High-Voltage Engineering*. McGraw-Hill, New York.

Phelps, C. T., and R. F. Griffiths (1976). Dependence of positive streamer propagation on air pressure and water vapor content. *J. Appl. Phys.*, 47, 2929.

Pich, J. (1978). Theory of electrostatic mechanism of aerosol filtration. In *Fundamentals of Aerosol Science* (D. T. Shaw, ed.). John Wiley, New York, pp. 325–367.

Pich, J., H. Emi, and C. Kanaoka (1987). Coulombic deposition mechanism in electret filters. *J. Aerosol Sci.*, 18, 29.

Robinson, M. (1967). A modified Deutsch efficiency equation for electrostatic precipitation. *Atm. Environment*, 1, 193.

Self, S. A., M. Mitchner, K. D. Khim, D. H. Choi, and R. Leach (1984). Effects of turbulence on precipitator performance. *Proceedings: Second International Conference on Electrostatic Precipitation* (S. Masuda, ed.). Kyoto, p. 249.

Sigmond, R. S. (1982). Simple approximate treatment of unipolar space-charge-

dominated coronas: the Warburg law and the saturation current. *J. Appl. Physics*, 53(2), 891.

Smith, W. B., and J. R. McDonald (1975). Calculation of the Charging Rate of Fine Particles by Unipolar Ions, *J. Air Pollution Control Assoc.*, 25, 168.

Waters, R. T., and W. B. Stark (1975). Characteristics of the stabilized glow discharge in air. *J. Phys. D: Applied Physics*, 8, 416.

White, H. J. (1963). *Industrial Electrostatic Precipitation*. Addison-Wesley, Reading, Mass.

Withers, R. S., and J. R. Melcher (1981). Space-charge effects in aerosol charging and migration. *J. Aerosol Sci.*, 12, 307–331.

Yamamoto, T. (1989). Effects of turbulence and electrohydrodynamics on the performance of electrostatic precipitators. *J. Electrostatics*, 22, 11.

Yamamoto, T., and L. E. Sparks (1986). Numerical simulation for three-dimensional tuft corona and electrohydrodynamics. *IEEE Trans. on Industry Applications*, IA-22, 880.

Yamamoto, T., and H. R. Velkoff (1981). Electrohydrodynamics in an electrostatic precipitator. *J. Fluid Mechanics*, 108, 1.

Yamamoto, T., P. A. Lawless, and L. E. Sparks (1986). Model study of gas sneakage in electrostatic precipitators. Proceedings World Congress III of Chemical Engineering, Vol. III, Tokyo, pp. 651–654.

*EPRI documents are available from Research Reports Center (RRC), Box 50940, Palo Alto, CA 94303, (415) 965-4081. There is no charge for reports requested by EPRI member utilities and affiliates, U.S. utility associations, U.S. government agencies (federal, state, and local), media, and foreign organizations with which EPRI has an information exchange agreement. On request, RRC will send a catalog of EPRI reports.

This Page Intentionally Left Blank

23

Transducers

T. Oda

The University of Tokyo
Tokyo, Japan

I. INTRODUCTION

A transducer is a device that changes certain physical values to other physical values. There are very many kinds of transducers related to electrostatics. They include electrostatic sensors, electric energy converters, and electric actuators. Typical examples are acoustic transducers made of electrets, one of which is called an electret microphone and is widely used in the compact cassette tape recorder. Other transducers include electromechanical converters, electrostatic sensors, and capacitive converters and are introduced in this chapter.

II. TRANSDUCERS MADE OF ELECTRET FILMS

A. Electret

1. Electret Film

The word *electret* (Sessler, 1987; Hilczer and Maleki, 1986; Gerhard-Multhaupt, 1987) was first proposed by Heaviside (1885) for a dielectric material with permanent electric dipole moment, on the analogy of the magnet, which is magnetic material with permanent magnetic dipole moment. In 1919, Eguchi (1919, 1925) manufactured an artificial electret made of waxes or other materials for the first time, by using thermal charging.

There are now two kinds of electrets, or two different charge storage mechanisms. One is electrically permanent polarized material, which is closely related to magnetically permanent polarized material, called the magnet. The lifetime of the polarized electret is not so long as that of the magnet or the second type of electret. The second type of electret is charged material with real (true) charge storage in bulk or on the surface of a dielectric material. Those charge storage mechanisms are shown in Fig. 1. Two different real charges are illustrated. In Fig. 1b, charges are injected from the surface of the material by a strong external electric field. Some ions, such as impurities, can move a little bit under a strong electric field and/or at high temperature, as shown in Fig. 1c. Most practical electrets are not polarized ones but second type ones with real charge storage. Thermal charging by application of a high dc electric field to a dielectric film at high temperature can make a very stable electret called a thermo-electret, but corona charging with or without a surface charging potential control grid is a typical charging method as a commercially available electret manufacturing method, because charging time of corona charging is much smaller than that of thermal charging.

2. Electret Analysis

A few fundamental charge analyzing methods are established to understand the charge storage mechanism of the electret. Thermally stimulated discharge current (TSDC) (Sessler, 1987), which is due to the relaxation phenomena of stored charges and polarization by increasing electret temperature, is useful for analyzing charge in an electret. One example of the automatic system developed by Oda et al. (1984) is shown in Fig. 2. Instead of thermal stimulation, the optical photon is also effective in exciting trapped charge, which is called photo-stimulated discharge current (PSDC); this is also very useful in the understanding of charge behavior. An example of a PSDC measuring system developed by Oda and Utsumi (1988) is seen in Fig. 3. Pressure wave propagation in a dielectric film can produce

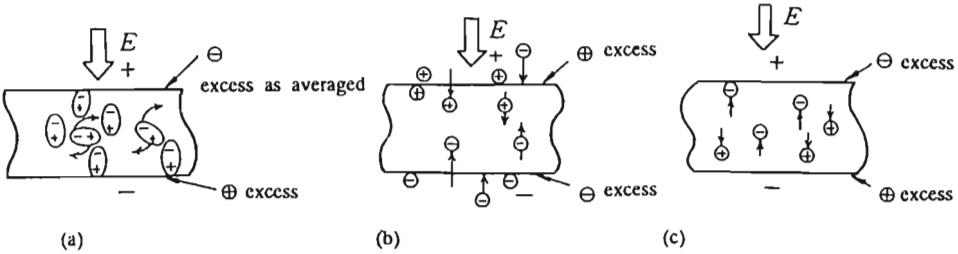


Figure 1 Different kinds of electrets.

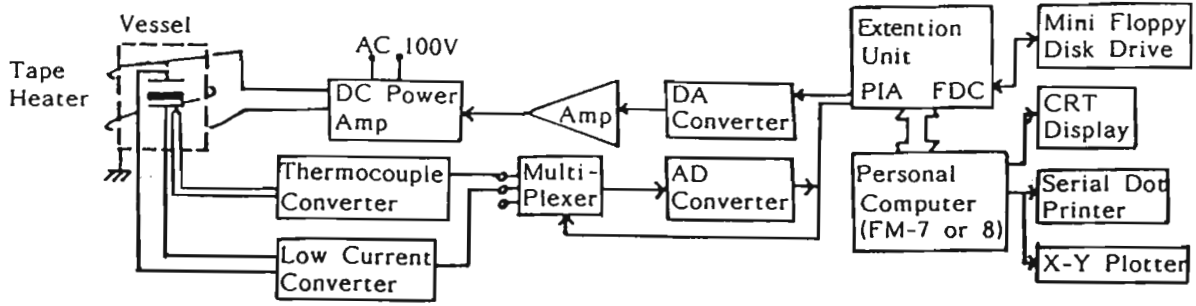


Figure 2 Schematic diagram of digital automatic TSDC analyzer. (Oda et al., 1984.)

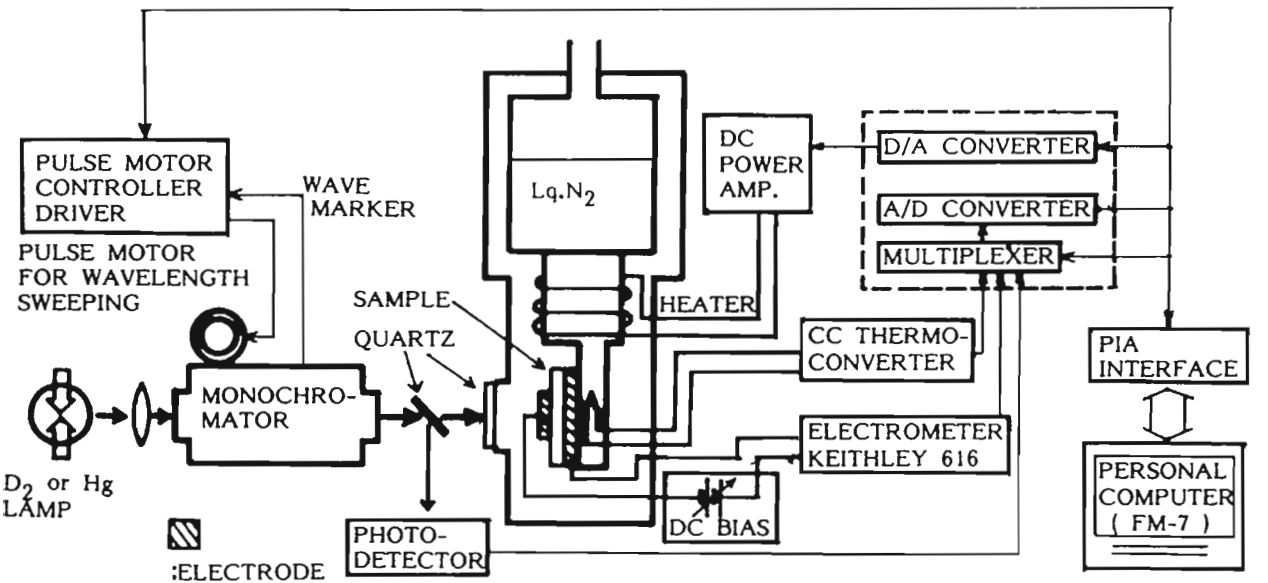


Figure 3 Schematic diagram of the UV-PSDC measuring system constructed by Oda and Utsumi (Utsumi and Oda, 1988.)

useful lateral distortion into the film to find out space charge distribution in a charged film. A short-pulse high-power laser (pulse width is 20 nanoseconds or 100 picoseconds typically with a total energy of 1 J or 20 mJ, respectively) can easily generate a fast-rising pressure wave, which propagates into the film. This method was proposed as a LIPP (laser-induced pressure pulse) method by Sessler et al. (1982) and by Gerhard-Multhaupt (1987). A piezoelectric element can also produce such pressure, as was first proposed by Eisenmenger and Haardt (1982). Takada and Sakai (1983) proposed a similar method, called the electroacoustic stress pulse method. Many similar charge analyzing methods have been proposed by many researchers; most of them are cited in the review article by Gerhard-Multhaupt (1987).

3. Use of the Electret

The electret can be used as a high-impedance and high-voltage power supply, though not with direct current. In other words, the electret is a condenser in which the stored charge is stable and its relaxation time is long. The electret application field is very wide now and includes fields those of such as acoustic transducers, electret machines (generator and motor), electret air filters, electrophotography, and biology. One of the important points for practical electret application is high stability or long lifetime of the charge. That is, the charge of the electret in an open state in natural air is easily relaxed by the humidity effect. Leakage current is large for high humidity. However, in closed circumstances, such as in a capsulate microphone, the humidity is controlled to be low, and dusts and ions are also very few. The lifetime of such an electret is assumed to be more than 100 years. Physical properties of electrets in detail are in cited references (Heaviside, 1885; Sessler, 1987; Hilczer and Malecki, 1986; Gerhard-Multhaupt, 1987).

B. Various Acoustic Transducers

1. The Electret Microphone

Eguchi et al. (1926) submitted a patent for an electret microphone and speaker using a thick electret (wax; not a film) as a biasing high-voltage supply for a condenser microphone or speaker (Nishikawa and Nukiyama, 1928). Some researchers reported the idea that was not practically realized. Although the fundamental concept of the electret microphone was established in the first half of the twentieth century, the development of a practical microphone started after the appearance of a high-resistivity polymer film that can store a large amount of charge with a long lifetime. Sessler and West (1962, 1963, 1973) reported the first practical electret

microphone by using a polymer film (charged mylar) that did not need external dc bias. The fundamental structure of the electret microphone is shown in Fig. 4. They used a mylar electret film as a vibrating film (diaphragm) by sound at first, then FEP teflon and others were now also used. A first commercial electret microphone was presented in 1968 by Sony corporation, which had long experience in condenser microphone engineering. The average signal sensitivity of 12 microphones (Sony ECM-19B) decreased only one db after 50,000 hours as reported by Imai (1978). Kubota (1976) reported a new type of electret microphone, the back electret. In this microphone, a diaphragm consists of a metalized polymer film (thin polyester; nonelectret) whose frequency response for sound was much better than the former electret foils such as polyacrylonitride, polycarbonate, and some fluoric resins. An electret film is laid on a thick dielectric back plate with an acoustic resister. After some tests, gold was found to be the best metalization material for a diaphragm. In the new microphone, the life time of the electret should be long, because it is shielded and far from an environmental natural air atmosphere. The performance of the new back electret microphone is roughly as same as that of the professional condenser microphone but with much cheaper cost and smaller weight. Figure 5 shows a schematic diagram of such a commercial microphone and its frequency response cited from the *Sony Microphone Handbook* (1983–84). A silicon oxide electret is manufactured by Sprenkels and Bergverd (1988) as a diaphragm of an electret microphone in which silicon integrated circuit process technology, such as photolithography, is utilized.

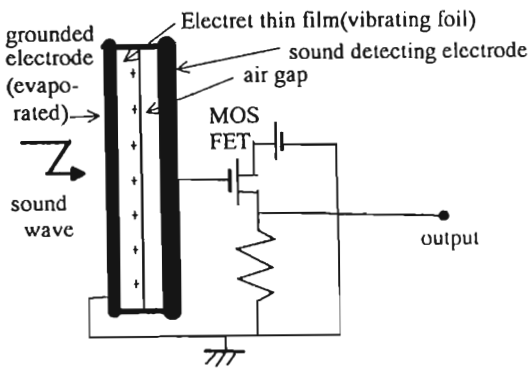
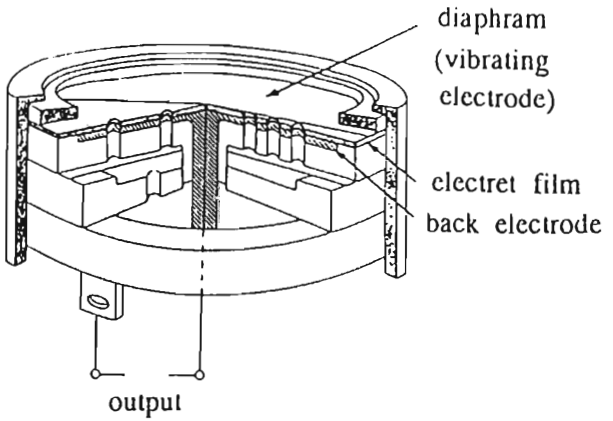
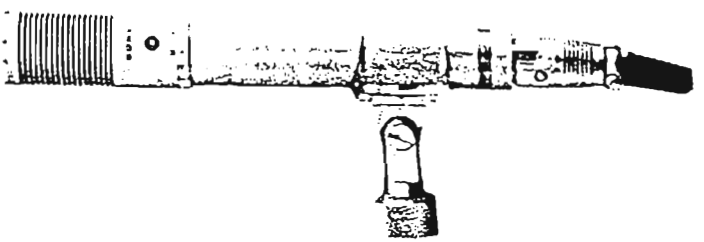


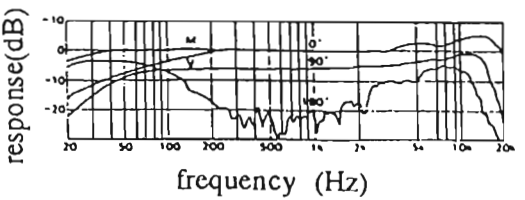
Figure 4 Basic structure of an electret microphone.



(a)



(b)



(c)

Figure 5 Basic structure of an electret microphone. (a) Schematic diagram of a backed electret microphone. (b) Photo of backed electret microphone (S-ECM-23F). (c) Frequency response of such a commercial microphone. (*Sony Microphone Handbook,* 1983.)

2. The Electret Pickup Cartridge

Following the appearance of the electret microphone in the marketplace, the first commercial electret phone pickup cartridge was developed in 1969. It used a backed electret for self-biasing and was reviewed by Watanabe (1980). Movement of a pickup needle tracking grooves in a phonograph record was transmitted to a moving aluminum electrode through a cantilever as shown in Fig. 6. The electret film is fixed on a thick metal electrode connected to a high-input impedance amplifier. When the needle vibrates, the capacitance between the moving electrode and the fixed metal electrode changes, and electrical current corresponding to the vibration is generated. By using four fixed electrodes, two with positive electrets and two with negative electrets, a push-pull type stereo electret cartridge is easily constructed. A special (monopole) push-pull stereo cartridge is illustrated in Fig. 7a. The frequency response of the electret cartridge is very good, but the sensitivity is not so high because the electrode size should be less than 1 mm^2, which requires a very high manufacturing technology. Another disadvantage of the electret pickup cartridge is that one must install an FET input amplifier. Thus an electric power supply for the amplifier is necessary; and the practical population of this cartridge is not as large as that for the electret microphone. A most delicate push-pull complementary type pickup cartridge may have high sensitivity and high quality but is very difficult to manufacture; its structure is illustrated in Fig. 7b.

3. Electret Loudspeakers and Headphones

A condenser type speaker (diaphragm type) may be manufactured that does not use a moving coil or a magnet. As such a speaker should be very simple and light in weight, the frequency response must be wide, but the output power of the speaker is not so large because the electrostatic force is not so much as the magnetic force in air, indicating that the electret speaker may be suitable for headphones or earphones. Figure 8 shows

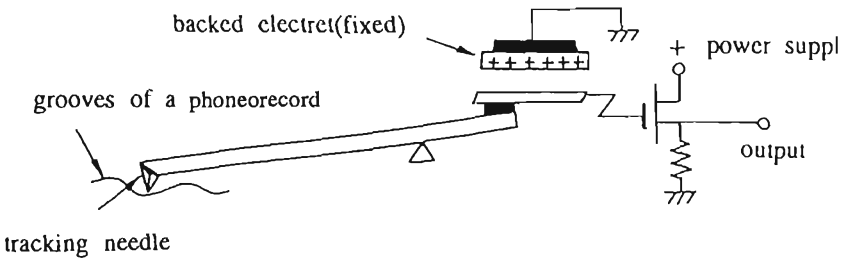


Figure 6 Principle of an electret pickup cartridge.

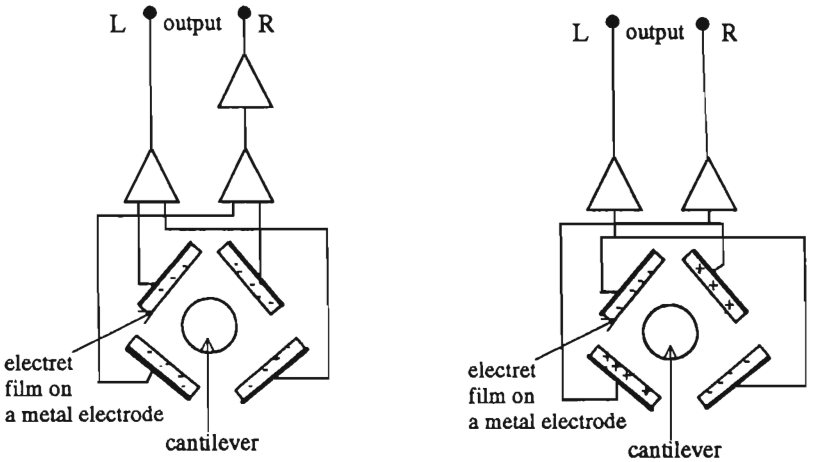


Figure 7 Practical electret cartridge. (Watanabe, 1980.)

one example of such electret headphones, introduced by Watanabe (1980). A simple electret speaker uses an electret film as a vibrating film in which both sides are capacitively coupled to metal electrodes connected to an audio power amplifier output. Mechanical performance of a vibrating film

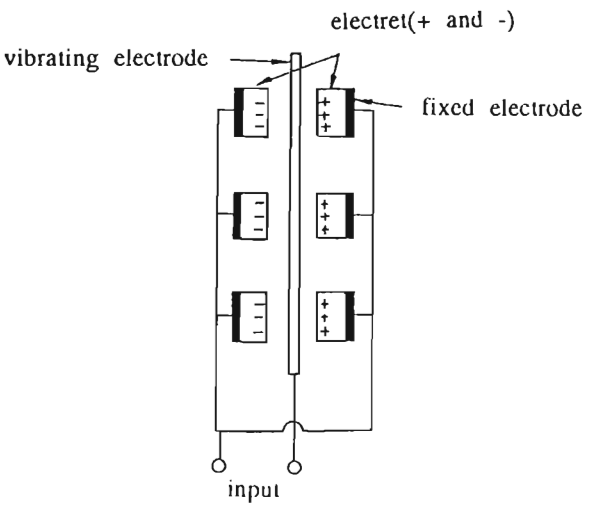


Figure 8 Electret headphone. (Watanabe, 1980.)

is very important to improve the frequency performance. A backed electret film fixed on a thick metal, as a fix electrode, is typically used where a thin vibrating film with very thin metal coating films on both sides is used as a diaphragm. In the figure, the best type, that is, a complemental backed electret type speaker, is shown.

C. Electret Motors, Generators, and Switches

As an electrostatic-field to mechanical-strength transducer, the corona motor (Moore, 1973) is a famous and interesting device in which the corona repulsion force is changed to rotating moment; details of such machines will be shown in Sec. VI. However, the corona motor or other electrostatic motor needs a high-voltage power supply and generates many ions that may produce harmful ozone and nitric oxide in air. A motor using a direct electrostatic force is theoretically possible but needs a high-voltage supply, many sleeves, and a high-voltage exchanger at times. Electrets can replace some parts of a high-voltage supply, and the operating voltage may be much reduced by using an electret. In 1961, Gubkin reported an electret motor consisting of a capacitance stator and an electrets rotor with a commutator. In 1970, Jefimenko and Walker developed a slot-effect electret motor with almost perfect shielding. Figure 9 is one example of such an electret motor. The output power of the motor is not high, but its very simple construction and nonmagnetic mechanism may be useful. By a similar construction, if a disk rotates, an electrostatic inductive voltage appears. That is, the electret motor can easily work as an electret high-voltage generator with a very simple construction. Without a commutator, the output is semi-sine-wave high voltage whose frequency is in proportion to the rotating speed. Tada (1981, 1982, 1986) proposed such a motor as a practical rotation sensor that is shown in Fig. 10. Sato

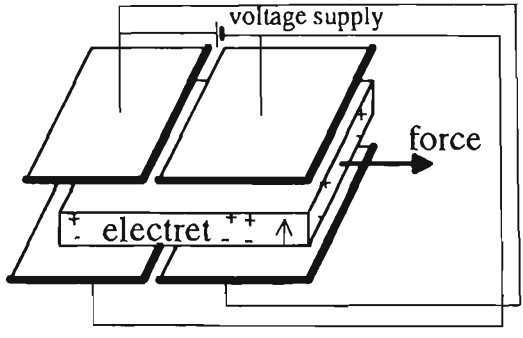


Figure 9 Basic concept of a slot effect electret motor. (Moore, 1973.)

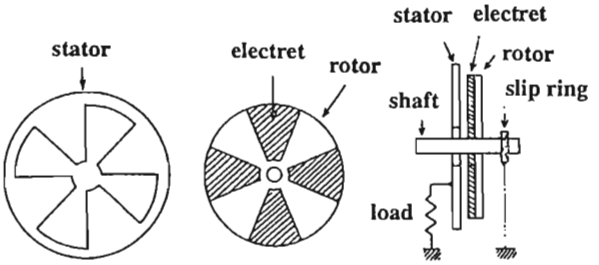


Figure 10 Electret generator. (Tada, 1981.)

and Takamatsu (1986) reported an electret switch that is illustrated in Fig. 11, where a very compact and economical switch is realized if a high-voltage drive is used. The switch is stable but the electrostatic force is not strong.

D. Electret Dosimeters

Radiation of x-rays, optical photons, electrons, or ions can induce charge storage, relaxation, polarization, or depolarization of dielectric material (Sessler, 1987), meaning that an electret can be applied as a radiation detector for dosimetry. Thermoluminescence (optical radiation by the recombination effect of an electron and a hole in a radiation-exited dielectric material by increasing material temperature) is already used in practical dosimetry. The charge decay of the electret is roughly in proportion to the radiation dose, and thermally stimulated discharge (depolarization) current (TSDC) analysis of an irradiated electret can be used as a dosimetry method, though it is not so practical and is not yet commercialized. Ikeya (1983) proposed a new type of electret detector as shown in Fig.

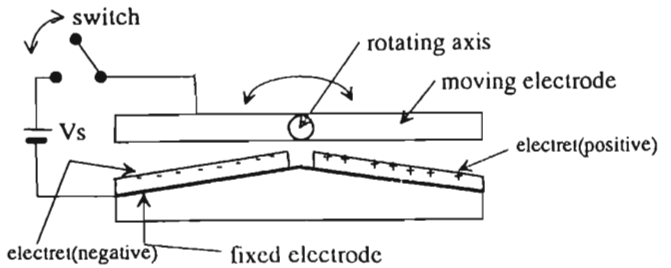


Figure 11 Schematic diagram of an electret switch. (Sato and Takamatsu, 1986.)

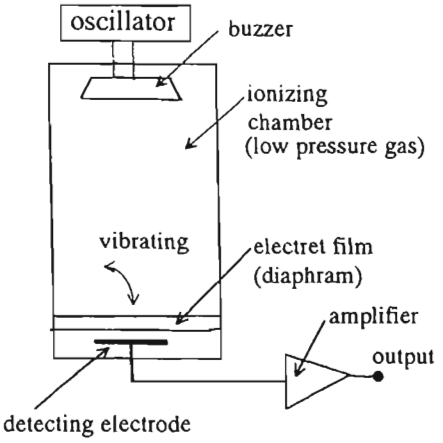


Figure 12 Electret dosimeter. (Ikeya, 1983.)

12. Radiation-induced ions in a gas area are collected to reduce the electret surface charge, which is monitored as a surface potential decay of the electret. The electret vibrates acoustically similarly to the electret microphone, and the ac signal is roughly in proportion to the surface potential, which is the reverse of the amount of radiation. Electret dosimetry is not yet in use commercially, but a cheap electret film could surely be used instead of a film badge as an x-ray detector.

III. PIEZO- AND PYROELECTRICITY

Polyvinylidene fluoride (PVDF) is the first piezoelectric polymer whose resistivity is not so high and depends on many factors, such as humidity, environmental gasses, pressure, and so on. Therefore real charges stored in PVDF are not so stable, but on the other hand, the polarization of PVDF is very stable. A polymer film is very light and flexible compared with ceramic piezoelectric materials in general; a comparison is shown in Table 1 by Sato and Murayama (1987). This polymer piezoelectric film is already utilized as a vibrating film of a speaker or a headphone; both are commercially available. As acoustic applications, a PVDF microphone, a transmitter for a telephone, etc., are under development.

As the PVDF material has acoustic impedance similar to that of liquid or biological materials, utilization of the PVDF as an ultrasonic generator is also being investigated. An ultrasonic transducer with signal transmitter and receiver functions has also been made by a PVDF array as a robot

Table 1 Characteristics of Piezoelectric Materials

	Unit	PVDF	Quartz	PZT	$BaTiO_3$
Density	ρ: 10^8 kg/m^3	1.78	2.65	7.5	5.7
Modulus of elasticity	c: 10^9 N/m^2	3.0	77.2	83.3	110
Relative dielectric constant	ϵ_r	13	4.5	1200	1700
Piezoelectric constant	d: 10^{-12}C/N	30	2	110	78
	e: 10^{-2}C/m^2	9	15	920	860
	g: 10^{-3}Vm/N	260	50	10	5
	h: 10^7V/m	80	390	95	60
Coupling coefficient	k: %	15	8.8	30.8	21.1

Source: Sato and Marayama (1987).

sensor by Kroemer and Manthy (1988). A vibrating sensor, a shock wave sensor by Granz (1988), a pressure sensor, a touch sensor, and a stress sensor by Rossi et al. (1988) have been developed. By using two detecting films that can detect the X or Y position of a pressed point, a signature recognition system is proposed by Bruyne (1988). A low-current-drive fan is realized in which many fins on PVDF bimorphs vibrate and produce wind by an ac voltage supply. As small elements on PVDF bimorphs can move with little power, a reflection type video display can be constructed by using as elements many small optical shutters [shown in Fig. 13 and demonstrated by Toda and Ohshima (1978)].

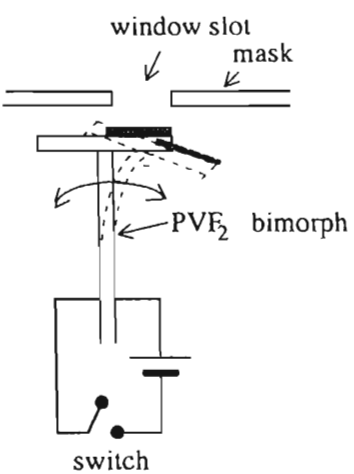


Figure 13 Display element of bimorph. (Toda and Ohsaka, 1978.)

Usage of pyroelectricity in an infrared detector, a fire sensor, and a pyrovisicon is also being investigated. A PVDF pyrosensor array is being developed to detect human body positions and moving speeds (Freitag and Meixner, 1988).

Recently, copolymers and blends of vinylidene fluoride (VDF) and trifluoroethylene (TrFE) were also developed that may have high electromechanical coupling factors. Date et al. (1988) has proposed a digital memory using PVDF polarization by using laser scanning. A digital-to-analog converting earphone is also reported (Gerhard-Multhaupt, 1987).

IV. SENSOR OF ELECTRIC CHARGE AND ELECTRIC FIELD

A transducer is also very important for the measuring of the charge of an electrostatic field. The MOSFET transistor is a real electric field transducer to electric current signals as impedance converting amplification. As this method is very sensitive to small changes in the electrostatic field, and as the spatial resolution of the field is also very high, the surface potential profile can be observed by scanning the detector over some area (Oda and Ueno, 1986). The small mechanical vibration of the electrode, where a typical vibration driver is a piezoelectric ceramic, is useful as a practical stable and reproducible charge or surface potential detector. The scanning system of such a probe can measure surface potential profiles or identify top and back surface charge density profiles; one example of the system is shown in Fig. 14 by Oda and Sato (1991).

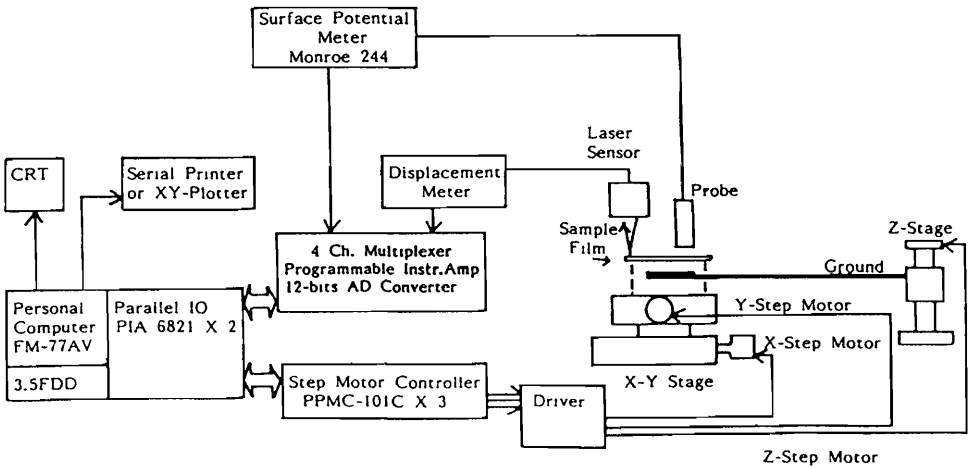


Figure 14 Automatic measuring system of surface charge density profiles of top and bottom of a charged film. (Oda et al., 1991.)

V. CAPACITIVE TRANSDUCER

As with a microphone, the capacitance between two electrodes presents us with important information and is widely applied in many sensors. A pressure change through a thin metal film can be detected as the change of capacitance; thus the capacitance pressure sensor or transducer. A direct capacitance measurement between target-conductive material and a sensing electrode is also a good indicator of gap length with a resolution in the micrometer range, which is already widely used commercially. A pressure-sensitive MOSFET using polymer electret fixing on the gate of the MOSFET was also tested by Voothuyzen and Bergverd (1988); the sensitivity is very high, but the thermal stability is not so good, and the introduction of the electret to the MOS structure is not easy.

VI. ELECTROSTATIC MOTORS AND GENERATORS

The history of electrostatic motors and generators is long. Jefimenko classified electrostatic motors into five groups, that is, contact motors, spark motors, corona motors, induction motors, and electret motors. Electrostatic motors as electric bells were invented by A. Gordon in the eighteenth century. A metal ball suspended by a silk string hits two opposite polarity plates alternately because the charge of the ball changes at the hit and electrostatic repulsion force operates. This swing motion was converted to rotating motion by Dailey and Dailey in 1880. A spark motor uses noncontact charge exchange by spark discharge, and practical output power can be generated. A corona motor as shown in Fig. 15 utilizes a more nearly constant discharge and generates a constant torque. Details of such motors are cited in Chap. 7 of Moore (1973). The typical principle of the electrostatic generator is charge separation that generates high voltage. The Van de Graaff generator (the charge carrier is a belt) is still one

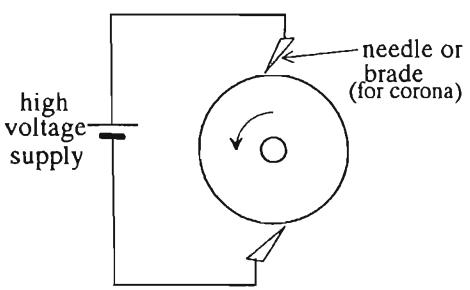


Figure 15 Corona motor.

of the best electric generators for making extremely high voltages. A high-speed rotating charge carrier can increase the output power of the generator. The usage of the electrostatic generator is restricted to special fields, because an electric field in air is limited and the space efficiency of the electrostatic generator is not good.

VII. CONCLUSIONS

As transducers related to electrostatics are now widely developed, it is difficult to introduce all of them here, and many kinds of useful transducers are passed over in this chapter. For example, optical image sensors and displays by electron flight are typical transducers that may be described in other chapters. Many electrostatic detectors are also not explained here. As typical electrostatic transducers, electret transducers are prominent in this chapter. Some other popular transducers are added but not systematically and in detail. The author hopes that readers interested in transducers will examine the cited references.

ACKNOWLEDGMENT

The author wishes to thank Mr. Takada of Sony for preparing some useful references.

REFERENCES

Bruyne, P. De (1988). Piezoelectric film as a sensor element in signature verification. *Proc. ISE*, 6, 229.

Date, M., T. Furukawa and T. Yamaguchi (1988). Opto-ferroelectric memories using vinylidene fluoride copolymers. *Proc. ISE*, 6, 298.

Eguchi, M. (1919). Variation of electrical conductivity of oils and waxes. *Proc. Phys.-Math. Soc. Jpn..*, ser. 3, 320.

Eguchi, M. (1925). On the permanent electret. *Philos. Mag.*, 49, 178.

Eguchi, M., S. Nishikawa, and D. Nukiyama (1926). Condenser-type transceiver using permanent charged materials—Electret. *Japan Patent No. 69025*. Publication No. 8500 147; submission was Aug. 6th, 1925 (in Japanese).

Eisenmenger, W., and M. Haardt (1982). Observation of charge compensated polarization zones in poly vinylidenefluoride (PVDF) films by piezo-electric acoustic step-wave response. *Solid State Commun.*, 41, 917.

Freitag, R., and H. Meixner (1988). PVDF sensor array for human body detection *Proc. ISE*, 6, 374.

Gerhard-Multhaupt, R. (1987). Electrets: dielectrics with quasi-permanent charge or polarization. *IEEE Trans. on EI*, EI-22, 531.

Granz, B. (1988). PVDF hydrophone for the measurement of shock waves. *Proc. ISE*, 6, 223.

Heaviside, O. (1885). Electromagnetic induction and its propagation-electrization and electrification. Natural electrets. *Electrician*, 230.

Hilczer, B., and J. Malecki (1986). *Electrets*. Studies in Electrical and Electronic Engineering 14. Elsevier.

Ikeya, M. (1983). Electret radiation dosimetry. *Proc. Inst. Electrost. Jpn.*, 7, 107 (in Japanese).

Imai, T. (1978). Design of condenser microphone using back plate electret. ASA & ASJ Joint Meeting, 29th November.

Kroemer, M., and W. Manthey (1988). Ultrasonic transducers using piezoelectric PVDF films. *Proc. ISE*, 6, 379.

Kubota, T. (1976). Back electret, a method to improve performance of condenser microphone of electret design. An Audio Engineering Society Preprint at the 55th Convention, Oct. 29.

Moore, A. D., ed. (1973). *Electrostatics and Its Applications*. John Wiley, New York.

Nishikawa, S., and D. Nukiyama (1928). A Use of the electret in a condenser transmitter. *Proc. Imp. Acad. Jpn.*, 4, 290.

Oda, T., and Y. Sato (1991). Noncontact surface charge density profiles measurement on top and bottom of a charged film. *IEEE Trans. Ind. Appl.*, 1A-27, 488.

Oda, T., and K. Ueno (1986). Surface charge density measurement of dielectric films using ultrasonic vibration. *IEEE Trans. on Elect. Ins.*, EI-21, 375.

Oda, T., and T. Utsumi (1988). Observation of UV photo-stimulated currents of teflon electrets. *Proc. ISE*, 6, 142.

Oda, T. S. Masuda, and T. Takahashi (1984). TSDC measurements of fly ashes from pulverized coal combustion. Proc. 2d Int. Conf. on ESP, 540.

Rossi, D, A. De Nannini, C. Domenici, and R. Francesconi (1988). Detection of stress field shear components by a piezoelectric polymer tactile sensor. *Proc. ISE*, 6, 234.

Sato, Y., and S. Maruyama (1987). Functional polymer electret-PVDF. *Proc. Inst. Electrost. Jpn.*, 11, 422 (in Japanese).

Sato, T. and T. Takamatsu (1986). An electret switch. *IEEE Trans. on Electr. Ins.*, EI-21, 449.

Sessler, G. M. (1963). Electrostatic microphones with electret foil. *J. Acoust. Soc. Am.*, 35, 1354.

Sessler, G. M., ed. (1987). *Electrets*. 2d ed. Topics in Applied Physics 33. Springer-Verlag.

Sessler, G. M., and J. E. West (1962). Self-biased condenser microphone with high capacitance. *J. Acoust. Soc. Am.*, 34, 1787.

Sessler, G. M., and J. E. West (1973). Electret transducers: a review. *J. Acoust. Soc. Am.*, 53, 1589.

Sessler, G. M., J. E. West, and R. Gerhard (1982). High-resolution laser-pulse method for measuring charge distributions in dielectrics. *Phys. Rev. Lett.*, 48, 563.

Sony Corp. (1983–1984). *Sony Microphone Handbook*.

Sprenkels, A. J., and P. Bergverd (1988). The use of silicon technology for an electret microphone construction. *Proc. ISE*, 6, 593.

Tada, Y. (1981). Electret generator. *Proc. '81 Ann. Meeting of IESJ*, 94 (in Japanese); (1982) Theoretical characteristics of rotating type electret generator. Ibid., 270 (in Japanese); (1986) Theoretical characteristics of generalized electret generator, using polymer film electrets. *IEEE Trans. on Electr. Ins.*, EI-21, 457.

Takada, T., and T. Sakai (1983). Measurement of electric fields at a dielectric/electrode interface using an acoustic transducer technique. *IEEE Trans. Electr. Ins.*, EI-18, 619.

Toda, M., and S. Ohsaka (1978). Displays using PVF_2 bimorph. *Proc. IEJ*, 2, 331 (in Japanese).

Voorthuyzen, J. A., and P. Bergveld (1988). An electret-based pressure sensitive MOS transistor. *Proc. ISE 6*, 587.

Watanabe, S. (1980). Electret acoustic equipment. *Proc. Inst. Electrost. Jpn.*, 4, 281 (in Japanese).

24

EHD Enhanced Mass Transfer Operations and Chemical Reactions

Wuhai He and Jen-Shih Chang

McMaster University
Hamilton, Ontario, Canada

I. INTRODUCTION

In the chemical processing industry, the efficiency of the operation performance is generally based either on the energy input or on the external forces applied. The majority of conventional chemical processing operations applies mechanical or thermal energy in combination with pressure or gravity forces. The ability of superimposed electric fields to improve several separation processes has been well known and widely used for many years. The familiar industrial applications range from solid-solid separation in the beneficiation of ores in the mining industry and cleaning of exhaust gases from solid particles in the energy and other industries (see also Chapter 21) to coalescence of water-in-oil emulsions in the petroleum industry (see also Chapter 18).

Over the past two decades an extensive effort has been made to explore the potential applications of electric fields in mass transfer enhancement as well as chemical reactions. There are several advantages in directly using electrical energy, especially in multiphase systems:

Electrical energy supplied to a system interacts selectively with an interface and to a lesser degree with the bulk phases. This can enhance the rate of mass transfer across the interface.

A superimposed electric field exerts electrohydrodynamic forces, which include several components (see also Chapters 7 and 8) and contribute to the existing gravity force either to levitate the dispersed phase or to enhance the dispersions.

Due to the reversible nature of the electric stresses, the work done by electric forces is nondissipative. Therefore the energy efficiency of electrically driven operations should be higher in terms of the second law compared to traditional mechanical or thermal driven operations.

In spite of these advantages, little is known either of the mechanism of electrically aided operations or of the important parameters responsible for the electric field effects. In this chapter we mainly discuss the electrohydrodynamic effects on the rate of mass transfer and chemical reactions, and we review various potential engineering applications in terms of performance of the electric field aided equipment used for different process operations.

II. MIXING FOR HOMOGENEOUS OPERATIONS

A. Background

The problem associated with the mixing of fluids during a chemical reaction is important for extremely fast reactions in homogeneous systems, as well as for all heterogeneous systems. This problem has two overlapping aspects (Levenspiel, 1972):

Degree of segregation. Mixing occurs on the microscopic level (mixing of individual molecules) or on the macroscopic level (mixing of clumps, groups, or aggregates of molecules). A real fluid exhibits partial segregation behavior, depending on its properties and the kind of mixing taking place.

Earliness of mixing. Fluid mixes early or late as it flows through the vessel due to the different flow patterns. Although there is a clearly defined residence time distribution (RTD) for each flow pattern of fluid through the vessel, each RTD does not define a specific flow pattern; therefore a number of flow patterns, some with earlier and others with later mixing of fluids may be able to give the same RTD.

The degree of segregation and the earliness of mixing can influence the performance of the reacting systems, with respect to both product distribution and capacity.

1. Self-Mixing of A Single Liquid

According to Levenspiel (1972), although segregation and earliness of mixing can usually be ignored when treating single reactions, this often is not the case with multiple reactions, where the effect of these factors on product distribution can be of dominating importance even at low conversion levels.

2. Mixing of Two Miscible Liquids

When two miscible fluids A and B are mixed, we normally assume that they first form a homogeneous mixture, which then reacts. However, when the time required for A and B to become homogeneous is not short with respect to the time for reaction to take place, reaction occurs during the mixing process, and the problem of mixing becomes important. Such is the case for very fast reactions or with very viscous reactant fluids.

B. EHD Enhanced Convective Mixing

There have been several investigations on the mechanisms of EHD enhanced mixing in the past two decades (Peters et al., 1980a, 1980b; Melcher, 1976; Schneider and Watson, 1970; Watson et al., 1970; Atten et al., 1987; Felici and Lacroix, 1978; Cross and Wang, 1991). When an electric field is applied to a liquid, free ions, which may be due to dissociation or to injection from the electrodes, will start to move. They transfer momentum to neutral molecules, and this results in bulk movement of the liquid, which is known as electroconvection (Peters et al., 1980a, 1980b). The character of this macroscopic motion is determined by the dielectric constant gradient, by the direction and magnitude of the free charge flow, and by the geometry of the electrodes (Schneider and Watson, 1970).

Compared to conventional mechanical mixing, two types of EHD enhanced mixing, the dielectric type (Chang, 1989) and the charge injection type (Hoburg and Melcher, 1976), have been proposed. The dielectric type is based on the temperature or material gradient effect of the dielectric constant, while the charge injection type is based on space charge gradient driven flows. Typical conventional type and EHD type mixers are shown schematically in Fig. 1.

1. Dielectric Type Convections

In order to have a net rotational force for generating convective flow by dielectric type components of EHD forces, both an inhomogeneous permittivity (for example due to a temperature gradient) and a nonparallel grad ϵ and grad $\mathbf{E}^2$ are required.

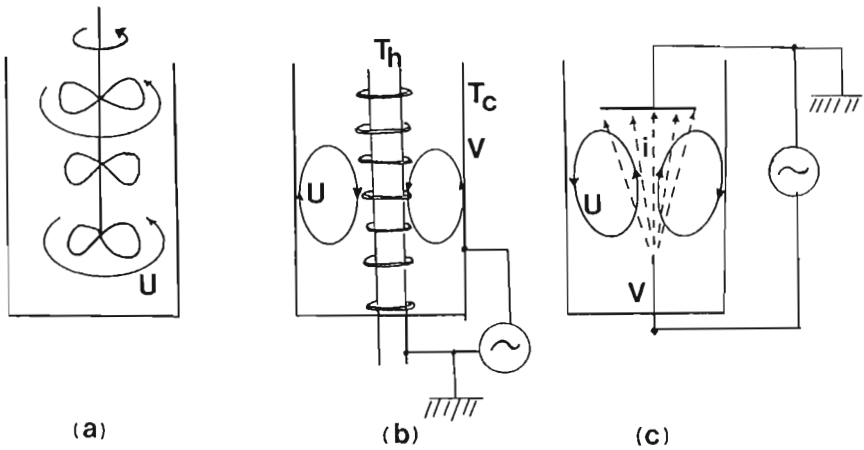


Figure 1 Conventional and EHD mixers. (a) Mechanical mixing; (b) dielectric type EHD mixing; (c) charge injection type EHD mixing.

For dielectric liquids, $\nabla\epsilon$ can be described as

$$\nabla\epsilon = \left(\frac{\partial\epsilon}{\partial T}\right)_\rho \nabla T + \left(\frac{\partial\epsilon}{\partial\rho}\right)_T \nabla\rho \tag{1}$$

Accordingly Ahsmann and Kronig (1951) defined an electric Rayleigh number through dimensional analysis by assuming a laminar incompressible flow as

$$E_{11} = \left(\frac{\partial\epsilon}{\partial T}\right)_\rho \Delta T_{oi} L^2 \frac{E_s^2}{\nu^2\rho} \tag{2}$$

and

$$F_E = -\frac{1}{2} E_s^2 \left(\frac{\partial\epsilon}{\partial T}\right)_\rho \nabla T \tag{3}$$

where ΔT_{oi} is the temperature difference between the inner and the outer electrode. The additional effect of fluid conductivity was characterized by Bonjour et al. (1962) as

$$E_{12} = \left(\frac{d\epsilon}{dT} + \frac{\epsilon_s\epsilon_0}{\sigma_0}\frac{d\sigma}{dT}\right) L^2 \Delta T_0 \frac{E_s}{\nu^2\rho} \tag{4}$$

where σ is the conductivity and a linear temperature dependence was assumed.

The numerical analysis has been done by Ogata and Chang (1985) for an annulus in both vertical and horizontal geometries. Figure 2 shows typical flow patterns for the vertical annulus geometry; there are significantly different flow patterns with a horizontal annulus geometry (Ogata and Chang, 1985).

2. Charge Injection Type Convections

In the case of a uniform dc electric field applied to a dielectric liquid, the dominant destabilization force causing electroconvection is the Coulomb force resulting from the interaction of the electric field with free space charge, which is nonuniformly distributed in the liquid. There are two generally accepted versions about the origin of the distribution of net space charge; one assumes that the distribution results from the thermally induced variation in electric conductivity of the liquid, and the other assumes injection of charge from either or both electrodes as the cause of the distribution (Schneider and Watson, 1970; Fernandez and Poulter, 1987; Fujino et al., 1989; Peters, 1980a).

Figure 3 shows the typical radial convective flow pattern of transformer oil in a wire-cylinder electrode geometry without any heating under a 30 kV dc electric field.

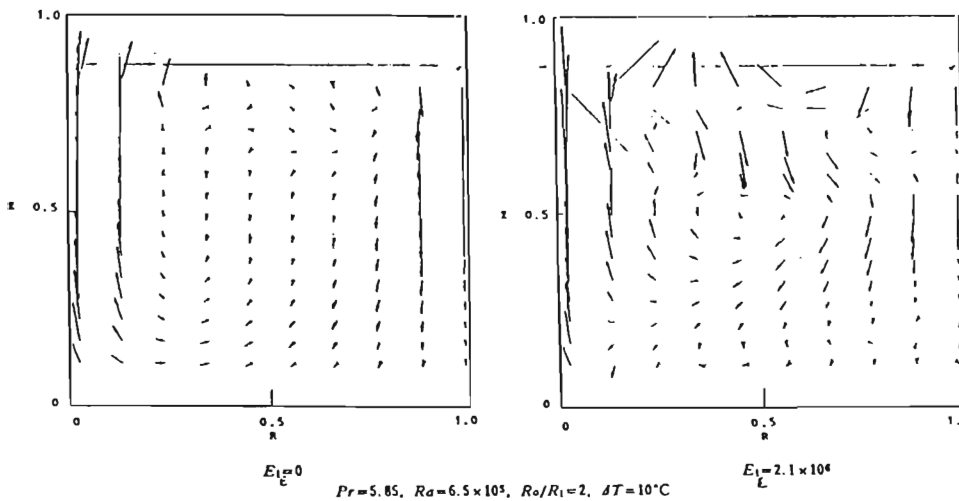


Figure 2 Velocity vector profiles inside vertical cylindrical annulus. $E_{1\epsilon}$: electric Rayleigh number ($=R_i^3(\partial\epsilon/\partial T)_\rho(T_i - T_o)E_i^2/\nu^2\rho$); Pr: Prandtl number ($=\nu/\alpha$); Ra: Rayleigh number ($=g\beta(T_i - T_o)R_i^3/\nu\alpha$); R_o: radius of outside cylindrical annulus; R_i: radius of inside cylindrical annulus. (From Ogata and Chang, 1985.)

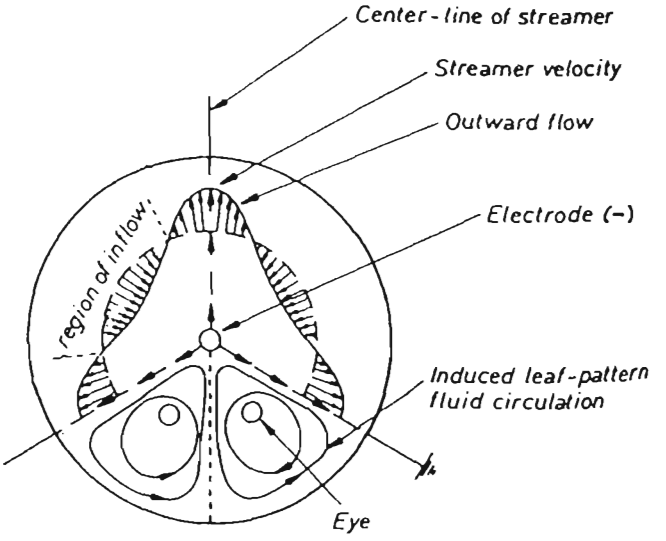


Figure 3 EHD induced convective flow pattern. (From Fernandez and Poulter, 1987.)

The Coulomb force exerted by an electric field on free charges injected into an insulating liquid may cause motion of the liquid. The effect of this convection is examined in two cases: a planar electrode geometry and a forced flow through a wire-cylinder geometry. In both cases the turbulent motion is essentially induced by the Coulomb force. Based on the work shown in Fig. 4, Peters (1980a) suggested two basic driving mechanisms governing bulk electroconvection. The first dominates low-field motion: the diffuse charge in the liquid close to the wall is swept away by the tangential component of the field. The second is manifest at high field strengths and is caused by the injection of free charge from electrodes.

Various studies in the field of EHD indicate that the application of an electrostatic potential to a dielectric liquid flowing in a duct can induce a complex secondary flow within the main stream that results in an enhanced convection effect. It should be mentioned that the secondary flow is little affected by the temperature field in the liquid, as clearly shown in Fig. 5.

An externally applied dc electric field across a plane layer of a dielectric liquid is known to cause an instability in the layer that is sometimes also called electroconvection. Electroconvection seems to be an attractive tool for enhancing convective heat transfer, particularly in the low Reynolds number flow of a dielectric liquid through a narrow space, where the

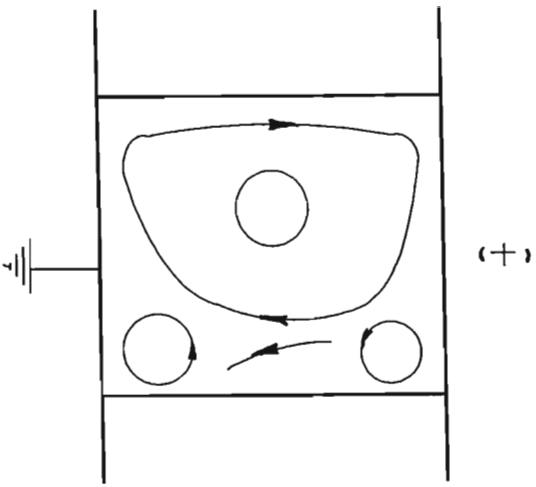


Figure 4 Electroconvective motion of carbon tetrachloride and kerosene mixture with polyethylene particles, 5 kV dc field. (From Peters, et al., 1980a.)

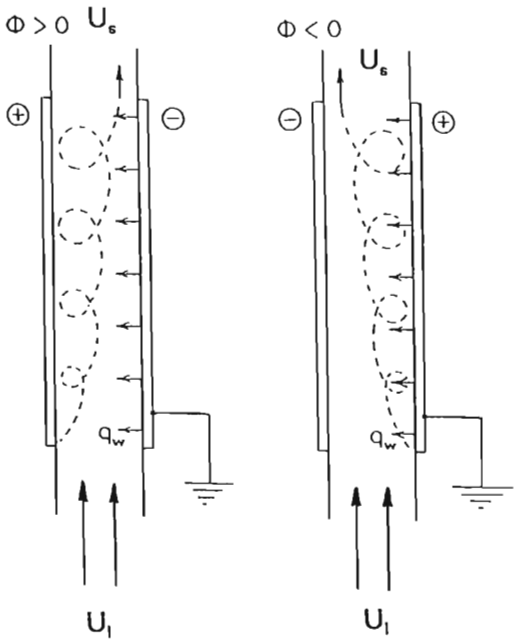


Figure 5 Electric field effect on induced secondary flow. ϕ: voltage applied to the electrode; q_w: heat flux at the heated electrode surface; U_l: liquid main stream flow; U_s: electric field induced secondary flow. (From Fujino et al., 1989.)

application of any convectional passive enhancement methods is neither easy nor effective.

III. GAS-LIQUID OPERATIONS

The gas-liquid operations include humidification and dehumidification, gas absorption and desorption, and distillation as well as chemical reactions. The operations in their various forms all have in common the requirement that a gas and a liquid phase be brought into contact for the purpose of a diffusional interchange between the two phases. The rate of mass transfer or chemical reaction is directly dependent upon the interfacial surface exposed between the phases; the nature and degree of dispersion of one fluid in the other are therefore of prime importance. The equipment can be broadly classified according to whether its principal action is to disperse the gas or the liquid:

Gas dispersed: bubble columns; sieve tray columns; mixing vessels, etc.
Liquid dispersed: spray columns; packed columns; falling film columns, etc.

Generally, the enhancement of equipment efficiency can be obtained by producing a large interfacial area for diffusional mass transfer and a higher degree of turbulence within and around bubbles or drops for eddy diffusion. The requirement for making turbulence coupled with a large interfacial area is relatively difficult because these features are incompatible in the sense that small bubbles and drops do not have high relative velocities nor do they exhibit marked internal circulation patterns. The application of an electric field as a technique to overcome these problems has been proposed by some investigators (Harker and Ahmadzadeh, 1974; Yamaguchi et al., 1982; Carleson and Berg, 1983; Sato et al., 1983; Ogata et al., 1985; Carleson and Fuller, 1987; Vasishtha and Someshwar, 1988).

A. Bubble Columns

Bubble columns are widely used in chemical process industries for carrying out gas-liquid operations because of their simple construction and the absence of moving parts. Various types of traditional bubble columns used in chemical process industries are described by Shah et al. (1982). The main needs for the better design of mass transfer bubble columns, other than more energy efficiency, are better insight concerning residence time, uniformity of bubble distribution, and the gas-liquid interfacial area. Currently existing bubble dispersion technique, based on the applied electric field method and dispersion fluid, is shown in Fig. 6; the basic bubble

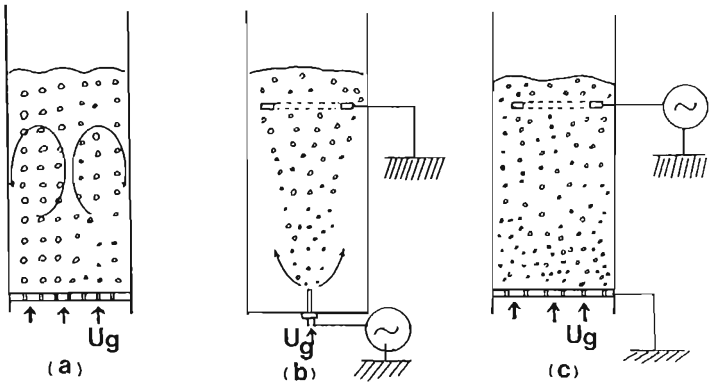


Figure 6 Schematics of EHD bubble columns. (a) Conventional bubble column; (b), (c) EHD bubble columns.

disruption and dispersion mechanisms, as well as system efficiency enhancement by an applied electric field, may differ depending on electrode geometry and the gas injection system (Ogata et al., 1985; Sato et al., 1979).

1. Bubble Disruption via Bubble Elongation Due to the Applied Electric Field

This process has been analyzed by Garton and Krasucki (1964). The elongation of a bubble due to the electric field in a gas-liquid system can be expressed by

$$\mathbf{E} = \left(\frac{\sigma}{\epsilon_0\epsilon_1\epsilon_2}\right)^{1/2}\left(\frac{\epsilon_1}{\epsilon_1 - \epsilon_2} - G\right)\left[\left(\frac{8A^2B}{3\gamma(\epsilon_1 - \epsilon_2)}\right)^{1/4}\cosh^{1/2}\theta \right. \tag{5}$$

where

$$3\theta = \cosh^{-1}\left\{\frac{Pr_0}{\sigma}\left[\left(\frac{27\gamma^5}{2(1+\gamma^2)^3}\right)^{1/2}\right\}\right.$$

$$A = 2\gamma - 1 - \frac{1}{\gamma^2}$$

$$B = 2\epsilon_1\gamma^3 - \epsilon_2(1+\gamma^2)^3$$

$$G = \frac{1}{\gamma^2 - 1}\left[\left(\frac{\gamma\cosh^{-1}\gamma}{(\gamma^2-1)^{1/2}} - 1\right)\right.$$

Here γ is the ratio of the major to the minor semiaxis, σ is the surface tension, P is the pressure within the bubble, r_0 is the radius of the bubble without an electric field, and ϵ_1 and ϵ_2 are the relative permittivities of liquid and gas respectively. Typical results are shown in Fig. 7 (Ogata et al., 1985).

2. Interfacial Instabilities

Instability of interface, which leads to bubble disruption, can be obtained from the Kelvin-Helmholtz instability analysis (Ogata et al., 1985; Chang, 1989) as follows:

$$(u_g - u_l)^2 F_0 + \frac{\sigma}{\rho_1}\frac{\partial^2 \xi}{\partial x^2} - g\xi\left(1 - \frac{\rho_2}{\rho_1}\right) \geq \frac{1}{2\rho_1}(\epsilon_2 - \epsilon_1)\frac{(\epsilon_1 + 2\epsilon_2)}{3\epsilon_2}\mathbf{E}_{int}^2 \tag{6}$$

where ξ is the wave height in the gas-liquid interface, u_g and u_l are local gas and liquid velocity, F_0 is a constant dependent upon bubble size, g is the gravitational acceleration, $\mathbf{E}_{int}$ is the electric field at the interface, and ρ_1 and ρ_2 are the density of liquid and gas respectively. The bubble disrupted when ξ equals the minor axis of the elongated bubble.

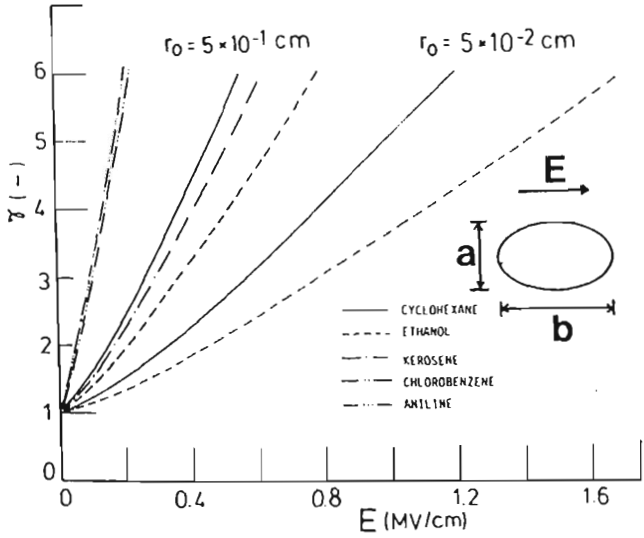


Figure 7 Elongation of bubbles in a uniform electric field for various fluids. r_0: original bubble radius without applied voltage; **E**: applied electric field; γ: ratio of bubble elongation ($=b/a$). (From Ogata et al., 1985.)

The mechanism of bubble dispersion can be a combination of the two effects, i.e., EHD flow and the enhancement of the interfacial drag forces due to the bubble disruptions. Typical flow velocity enhancement observed is shown in Fig. 8 (Ogata et al., 1985) where U_e is the enhanced bubble velocities in the presence of an applied electric field, while U_c is the bubble terminal velocities in the absence of electric field and M_0 is the volumetric gas flow rates. By combining these bubble dispersion and disruption effects due to the applied electric field, the energy efficiency η in current system can be defined as follows

$$\eta = \frac{\text{consumed energy for surface enlargement}}{\text{total energy added to the system}} = \frac{6\sigma \cdot M/\bar{d}_B}{V \cdot i + P \cdot M} \times 100\% \tag{7}$$

The first term of the denominator shows electrical energy, while the second is mechanical energy. The average diameter $\bar{d}_B$ (Sauter mean diame-

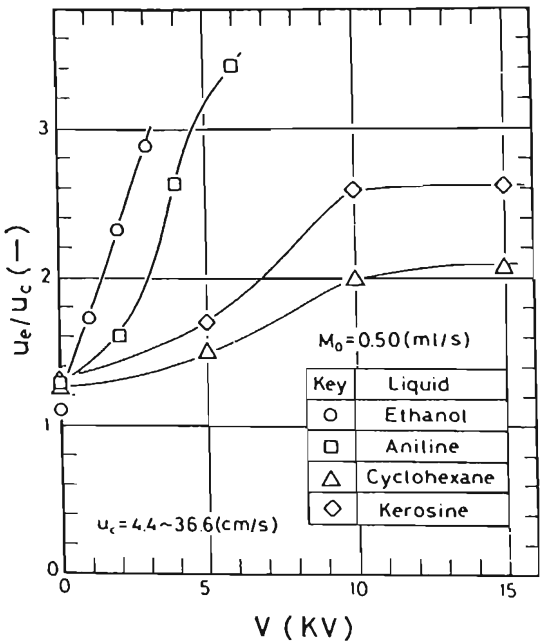


Figure 8 Normalized bubble rising velocity as a function of applied voltage. M_o: gas flow rate; V: applied voltage; U_c: bubble terminal velocity without applied voltage; U_e/U_c: relative bubble velocity with the applied voltage. (From Ogata et al., 1985.)

ter) is

$$\bar{d}_B = \frac{\sum_{i=1}^{N} d_{Bi}^3}{\sum_{i=1}^{N} d_{Bi}^2} \tag{8}$$

The other advantage of the EHD effect in a bubbly column reactor is mass transfer enhancement due to the interfacial velocity enhancement in inner bubbles (Chang and Berg, 1985), but no direct experimental result is presented in this moment.

B. Falling Film Columns

A thin film of liquid running down the inside of a vertical pipe, with gas flowing either concurrently or countercurrently, constitute a falling film column, also called a wetted wall column. Such devices have been used for theoretical studies of mass transfer because the interfacial area between the phases is readily kept under control and is measurable. Industrially, they have been used as absorbers for hydrochloric acid, where absorption is accompanied by a very large evolution of heat. In this case the column is surrounded with rapidly flowing cooling water. Many wetted wall devices have also been used for distillation, where the liquid film is generated at the top by partial condensation of the rising vapor. Gas pressure drop in these columns is probably lower than in any other gas-liquid contacting device, for a given set of operation conditions.

For the falling film column aided by an applied electric field, the gas-liquid interface becomes significantly rippling due to the surface waves; hence the interfacial area, and therefore the overall efficiency for mass transfer, is expected to be enhanced. Another advantage of the EHD falling film column is control of flooding phenomena (Diehl and Coppany, 1969), since the flow rate of the falling liquid film is limited by the gas flow rate. The relationship between liquid and gas flow rates in a general two-phase countercurrent flow system is shown in Fig. 9. Region 1 represents the flow regime where the stable operation of the system can be observed. In region 2, the continuous operation of the two-phase countercurrent flow system is not possible. Thus, for a given liquid flow rate, there exists a limit to which the gas flow can penetrate through the channel and vice versa. The locus of these flooding points forms an envelope of all maximum flow rates of the two-phase flow system, and this curve is called the "flooding curve." In Fig. 10 we have shown the flooding curve for various applied electric fields obtained by Revankar and Chang (1984). It is clear from the figure that the effect of the electric field is to reduce the flooding point. For smaller liquid flow rates, i.e., for small normalized

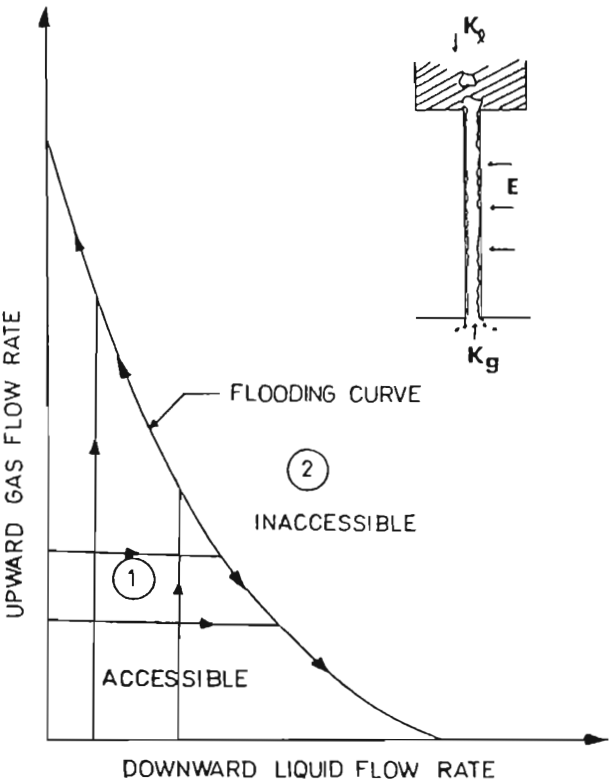


Figure 9 Flooding curve for a vertical two-phase counter-current flow. E: applied electric field; K_g: dimensionless velocity for upward gas flow ($= U_{g,c}/U_g$); K_l: dimensionless velocity for downward liquid flow ($= U_{l,c}/U_l$). (From Revankar and Chang, 1984.)

liquid flow velocity K_l, the enhancement of flooding due to electric field predominates.

IV. LIQUID-LIQUID OPERATIONS

Liquid-liquid operations include solvent extraction as well as some multiphase chemical reactions with two liquid phases involved; they are basically very similar to gas-liquid operations. One liquid phase is dispersed into the other continuous liquid phase. Spray columns, packed columns, various tray columns, etc., have been extensively used for liquid-liquid operations.

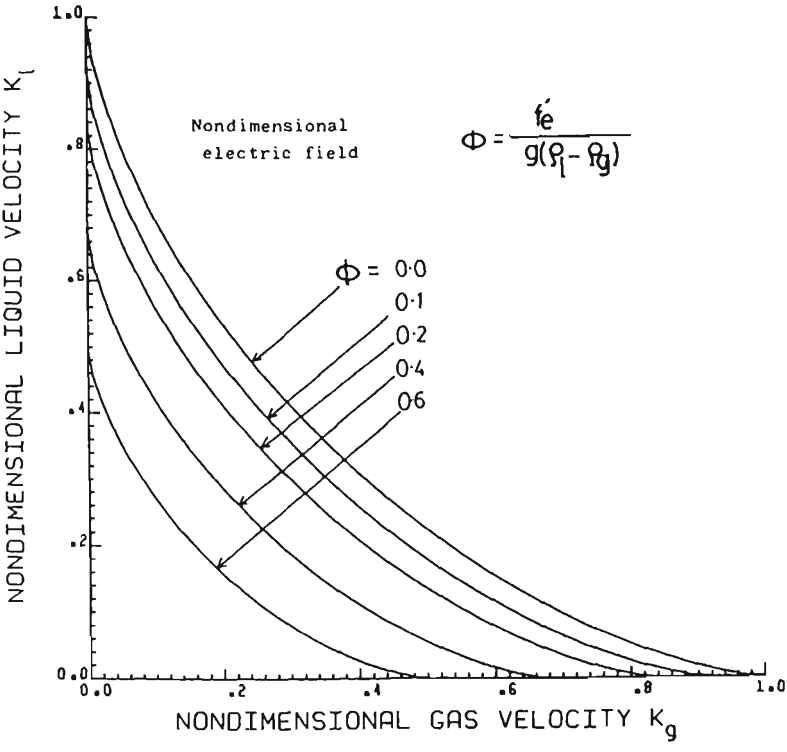


Figure 10 The effect of an applied electric field on flooding characteristics. (From Revankar and Chang, 1984.)

The application of a high voltage electric field to enhance the rate of mass transfer in liquid-liquid extraction has been an active subject of investigation for the past 25 years. Among the many of published works there have been several review papers and short articles that have summarized most of the work done to date (Thornton, 1968; Baird, 1983; Scott, 1989; Weatherley, 1992; Ptasinski and Kerkhof, 1992). The general idea of directly using an electric field to improve the performance of mass transfer in liquid-liquid extraction was initially described by Stewart and Thornton (1967). The improvement of interfacial mass transfer may be achieved in several ways due to the additional electrohydrodynamic (EHD) forces on the droplet-continuum interface: (1) reducing the effective interfacial tension, (2) increasing interfacial area for mass transfer, and (3) enhancing interfacial disturbance and drop circulation.

The effect of electrohydrodynamic (EHD) phenomena on mass transfer in solvent extraction is of increasing importance, since the EHD forces induced by an electric field at liquid-liquid interfaces form the basis for the exploration of the potential applications of electric fields in solvent extraction processes. The most important case for the EHD forces enhanced mass transfer in solvent extraction is that of relatively conducting droplets dispersed in a nonconducting continuous phase under the influence of an imposed electric field.

A. Electric Field Effects on Charged Droplets in Liquid-Liquid Systems

The formation and motion of a liquid droplet in another immiscible liquid are of importance in the understanding of solvent extraction processes, since an effective dispersion of one liquid phase into the other is one of the important factors determining the performance efficiency of the particular solvent extraction system. Figure 11 is a schematic diagram depicting the common features important to liquid-liquid mass transfer processes, including interfacial area (droplets) formation, free droplet-continuum interaction, and coalescence for phase separation.

When an electric field is applied across a dielectric liquid in which a charged droplet of a relatively conductive liquid is suspended, its behavior will be influenced by an applied electric field due to the EHD phenomena. The electric field acting on this charged droplet produces EHD forces in the outward direction on the droplet-continuum interface. Since the normal pressure component is in the direction opposite to the inward-acting interfacial tension, the charged droplet would behave as one with a lower effective interfacial tension under the applied electric field. Also, the tangential stress component is balanced by droplet surface motion in the neighborhood of the interface. All of these factors are beneficial for mass transfer enhancement. One of the advantages of using an imposed electrostatic field for droplet dispersion in the continuous phase is that it allows the production of smaller size droplets together with enhanced relative droplet velocity and reduced interfacial tension (He et al., 1991, 1993). Therefore for such a system both larger interfacial area and less mass transfer resistance can be achieved. A second feature is that the energy input in this process is extremely efficient because the electric field acts only on the droplet-continuum interface rather than throughout the bulk of the liquid phases. An additional feature is that there are no mechanical moving parts in the extraction system, so it is easy to maintain the operation process.

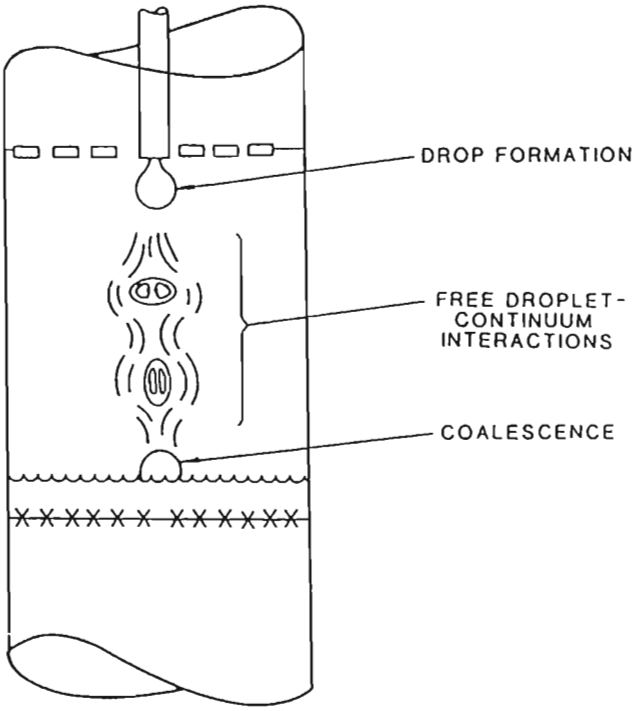


Figure 11 Schematic of solvent extraction processing. (From Scott, 1989.)

Figure 12 shows two distinctly different electric techniques that have been examined to create large interfacial areas in liquid-liquid systems: (a) droplets form directly at hollow electrode nozzles or orifices; (b) droplets form by strong electrical stresses to rupture a liquid-liquid interface.

B. Liquid-Liquid Extractions Controlled by an Imposed Electric Field

Currently there are no industrially significant solvent extraction systems that are controlled by applied electric fields. However, several applications of electric field systems to enhance emulsion coalescence, mainly in the petrochemical industry, are now in operation (see also Chapter 18).

Three general types of electrically controlled extraction contactors have been proposed and tested on the laboratory scale. The first kind is based upon the formation of millimeter sized droplets at nozzles and is designed to operate in vessels resembling sieve plate columns. The second

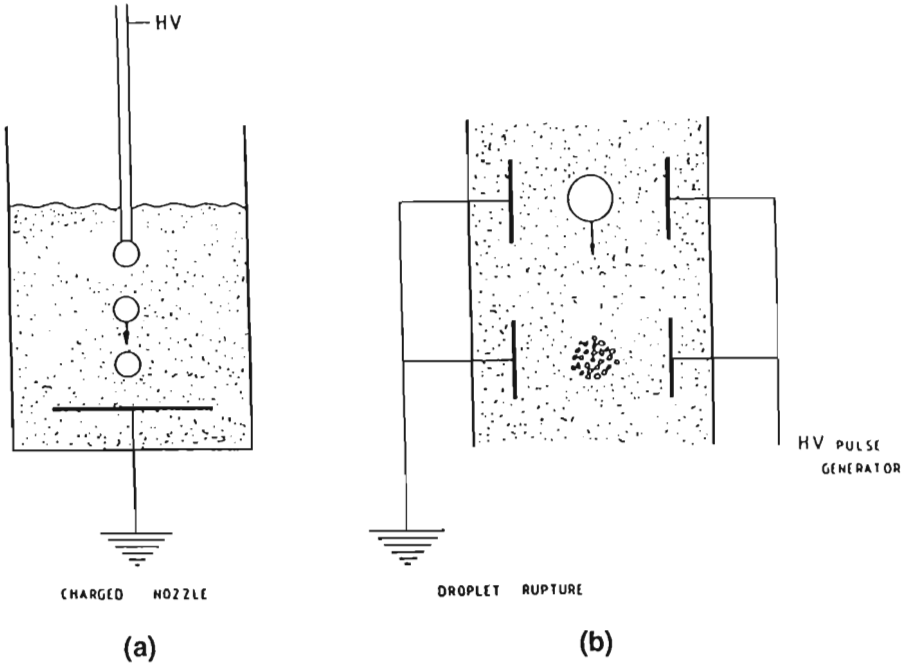


Figure 12 Surface area generation in an electric field. (From Ptasinski and Kerkhof, 1992.)

is based on the liquid film being disrupted into droplets in the other liquid by an electric field and is designed to operate in an inclined rectangular device. The third is based on electric field emulsification/coalescence phenomena and may require new equipment configurations.

1. Contactors Related to Millimeter Sized Droplets

Several examples of charged nozzle devices have been reported in the literature (Stewart and Thornton, 1967; Yamaguchi et al., 1985; Wham and Byers, 1987). The devices designed by Thornton and Bailes represent a single stage in a sieve plate column as shown in Fig. 13. The factor of three was obtained by comparison of the electric field to the no-field case in Thornton's particular apparatus. Then Bailes made a modified design to provide purged nitrogen gas in the gap between the top electrode and the upper surface of the continuous phase (Bailes, 1981). The reported results were in terms of the Murphree tray efficiency for the single stage device. No comparison was made to the performance of existing industrial devices. A related extractor geometry has been suggested that contains

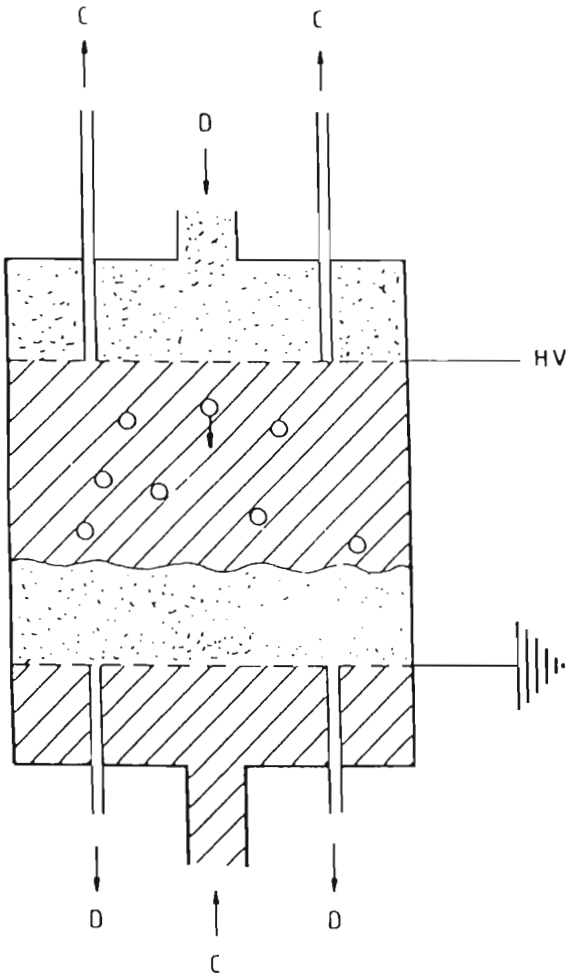


Figure 13 Schematic of electric field driven extractor. (From Bailes, 1981.)

four vertical-rod electrodes as schematically shown in Fig. 14 (Kowalski and Ziolkowski, 1981; Yamaguchi et al., 1988, 1989). Two electrode-rods opposite one another serve as positive poles, while the other pair act as negative poles. A 50 Hz ac electric power supply was used in the device made by Kowalski and Ziolkowski, while a dc electric field generator was used in the device designed by Yamaguchi et al. The electric field caused the formation of relatively small droplets from the sieve-tray plate or spray head and then aided in translating the droplet down the column in the

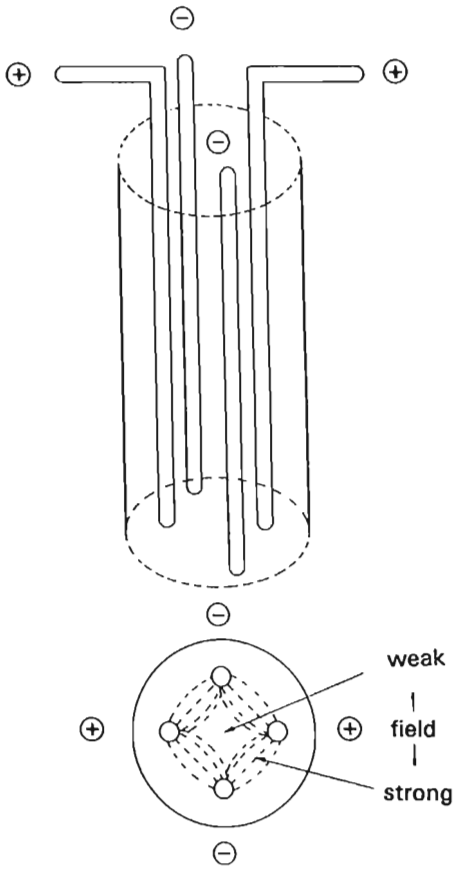


Figure 14 Vertical rod electrode extraction column. (From Kowalski and Ziolkowski, 1981; Yamaguchi et al., 1988, 1989.)

presence of the countercurrent flow of the continuous phase. Another example of vertical liquid-liquid extraction columns using an electric field was designed by Martin et al. (1983). Eight pairs of electrode rods were assembled in parallel along two sides of the column wall. The same voltage was applied to these eight stages of electrodes.

2. Contactor with Inclined Geometry

This kind of contactor deals with electric dispersion from a water film flowing down an inclined plate electrode into a stagnant dielectric liquid as seen in Fig. 15. At first the bottom electrode plate was made with flat

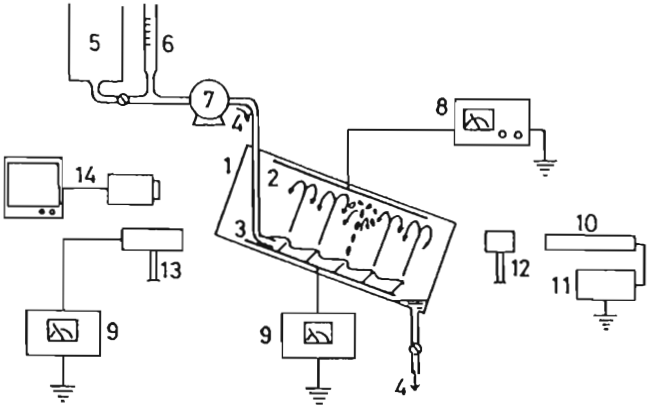


Figure 15 Schematic of inclined type contactor. (From Yoshida et al., 1986, 1988.)

flashboards (Yoshida et al., 1986); later it was modified with notched flashboards to stabilize the formation and motion of the droplets (Yoshida et al., 1988).

The results of this experimental investigation include the droplet size distribution, average droplet velocity, hold-up of the dispersed phase, and phase separation.

3. The Emulsion-Phase Contactor

This type of contactor, as schematically shown in Fig. 16, is based on the simultaneous emulsification/coalescence phenomena under the influence of a strong electric field. During operation, the electric field is used to create a high-surface-area emulsion, to hold the emulsion in place against the upward flow of the continuous phase, and to induce coalescence. Therefore the system achieves dispersion to form a large amount of interfacial area, coalescence, and phase separation in a single vessel utilizing a single electric field (Scott and Wham, 1989). Another alternative design of the emulsion phase type contactor is based on the principle of mixer/settler. It consists of an electrically enhanced mixing chamber to mix two liquid phases by applied electric field and a settling section located above the mixing chamber (Millar and Weatherley, 1989).

Recently there have two review papers (Scott, 1989; Ptasinski and Kerkhof, 1992) published in this area. Both have included much of the work to date and have discussed the potential applications of EHD techniques in several processes including solvent extraction, emulsion coalescence, and electrofiltration. Prospects for further research have also been mentioned in these two papers.

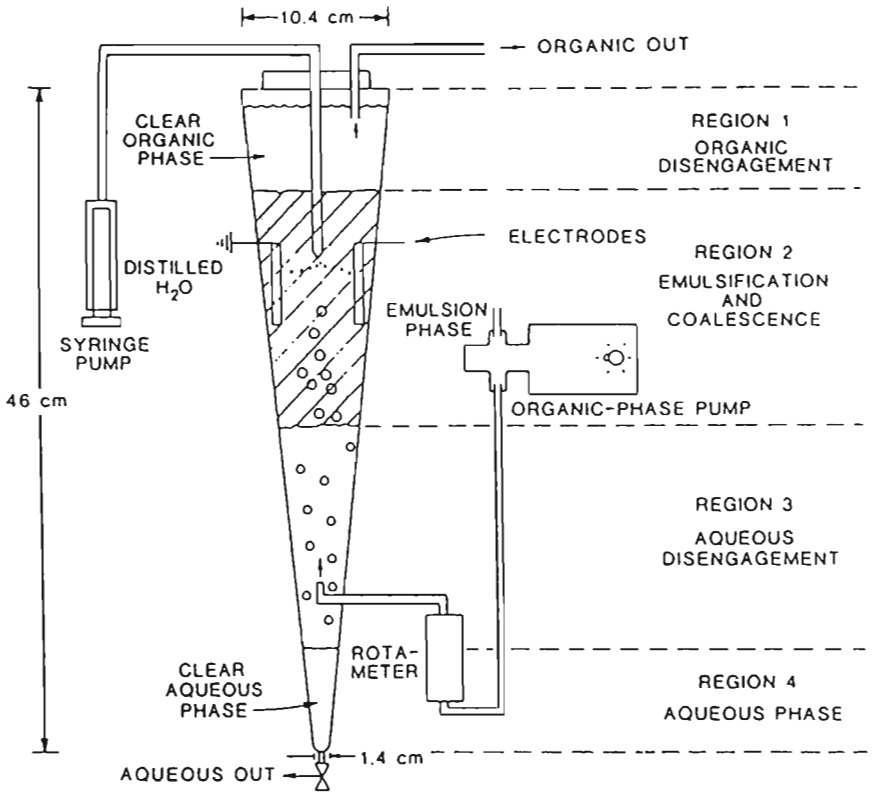


Figure 16 Schematic of emulsion-phase contactor. (From Scott, 1989.)

V. GAS-SOLID OPERATIONS

Heterogeneous catalytic chemical reactions with gases as both reactants and products, while using specially fabricated solid particles as catalyst to enhance the rate of reaction, are in this category. Mass transfer operations in this category include adsorption-desorption and drying. The two types of equipment widely used in gas-solid operations, especially for gas-solid chemical reactions, are packed beds and fluidized beds. However, investigations undertaken so far on the effect of electric fields on both packed and fluidized beds have been restricted in their electrohydrodynamic behavior, without chemical reaction or mass transfer involved.

When an electric field is applied to a packed bed or a fluidized bed, the resultant interparticle electrical forces can have important consequences for the bed dynamics. Dietz and Melcher (1978) developed a model for the electrical interparticle force in both fixed and fluidized beds.

In their model, the force results from the current constriction in the vicinity of the particle-particle contacts. In packed and electropacked beds, frictional forces restrain particle motions. As a result, the local interparticle force can be transmitted through normal and shear stresses to the walls. The experiments conducted by the Dietz and Melcher (1978) supported the validity of their model.

A. Packed Beds

Robinson and Jones (1984a) measured the yield stress of a brass sled in packed beds of powder (glass beads and sand) when an electric field was applied perpendicular to the direction in which stress was applied. Robinson and Jones (1984b) also measured the angle of repose of a packed bed of the same materials as a function of the electric field. All the experiments found that the normal stress was a linear function of the electric field, but there was considerable variation in the amount of stress applied by a given electric field.

B. Fluidized Beds

Two different types of electrofluidized beds (Johnson and Melcher, 1975) have been investigated as follows. In the coflow EFB, gas flow and electric field are in the same directions. In the crossflow EFB, gas flow and electric field are at a 90° angle. For the crossflow EFB with cylindrical reaction chambers, Ogata et al. (1980) defined concentric flow EFB. With an external bipolar ion injection, Mochizuki et al. (1992) named plasma EFB. All of these electrofluidized beds are shown schematically in Fig. 17.

The total pressure drop as a function of superficial gas velocity is shown in Fig. 18 for fluidized beds with and without bipolar ion injections. The location of the first maximum in the total pressure drop is generally called

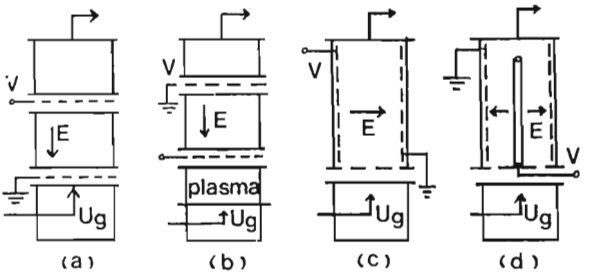


Figure 17 Schematics of electrofluidized bed reactors: (a) coflow; (b) plasma coflow; (c) crossflow; (d) concentric EFB.

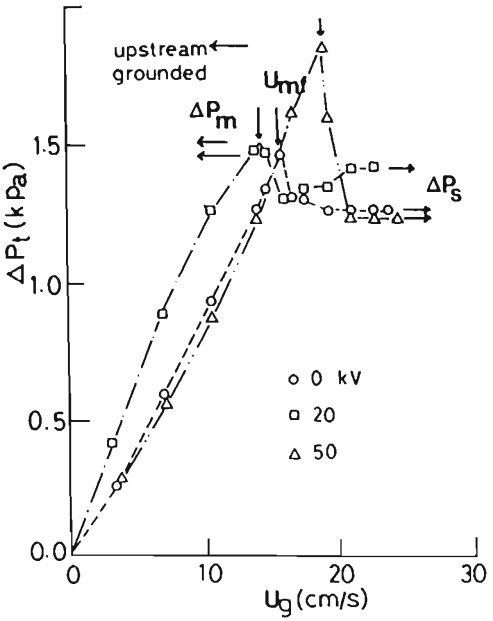


Figure 18 Typical fluidization characteristics of crossflow type EFB. (From Chang et al., 1990.)

the minimum fluidizing velocity U_{mf}, where the bed fluidizes. Further increasing the gas velocity will generate slug flow. In this fluidization region, the total pressure drop ΔP_s is fluctuating with time due to the gas slug motions. The maximum pressure drop in Fig. 18 is ΔP_m, and the time averaged pressure drop in the saturation region is ΔP_s. From the volume-dimensional mixture momentum conservation model of two-phase flow (Chang et al., 1990), the pressure drops inside the fluidized bed can be expressed by

$$\frac{dp_\Phi}{dz} = \tau_{w\Phi} - \rho_\Phi g + \mathbf{F}_\Phi(\mathbf{E}) - \frac{d(G_\Phi^2 V')}{dz} \tag{9}$$

$$p_\Phi = \alpha_g p_g + \alpha_p p_p \tag{10}$$

$$\rho_\Phi = \alpha_g \rho_g + \alpha_p \rho_p \tag{11}$$

$$G = \alpha_g \rho_g u_g + \alpha_p \rho_p u_p \tag{12}$$

$$V' = \frac{\alpha_g \rho_g u_g^2 + \alpha_p \rho_p u_p^2}{\alpha_g \rho_g u_g + \alpha_p \rho_p u_p} \tag{13}$$

The presence of ions in the system may equally influence all three terms, the ions not only changing net charge density ρ_c but also modifying the electric field, as can be expected from Poisson's equations:

$$\bar{\nabla}^2\chi = -\left(\frac{L}{\lambda_D}\right)^2 (n_i - n_e) = \bar{\nabla}\cdot\eta \tag{14}$$

In Eq. 14, the effect of bipolar ions on the second and third terms is only important for $(L/\lambda_D) \geq 1$. Here we must note that $n_i - n_e \neq 0$ due to the applied field and the onset of corona discharges near electrodes in the present system. The electrostatic adhesive force between wall and particle and/or particle and particle (Johnson and Melcher, 1975; Ogata et al., 1980; Ogata et al., 1984) clearly dominated to prevent fluidizations. Therefore the minimum fluidization velocity becomes larger in spite of the total pressure being only slightly influenced. However, once the superficial velocity is exceeded by this minimum fluidization velocity, the total pressure drop is substantially reduced due to the enhancement of local particle and gas velocities by EHD flow (Ogata et al., 1982). These opposite influences of the applied electric field method are applied in a particle-to-surface reaction enhancement without fluidizations (Chang et al., 1990),

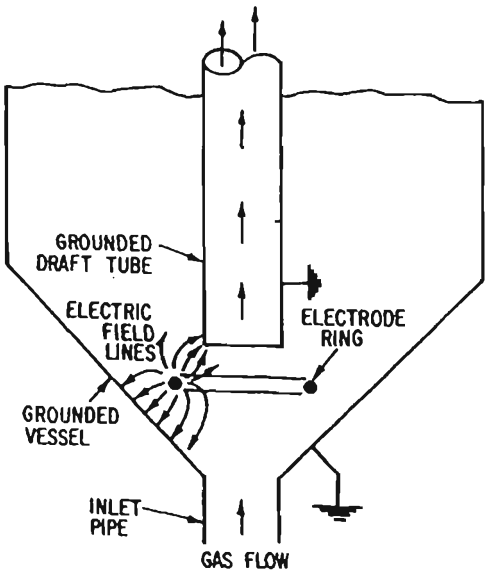


Figure 19 Schematic of electrospouted bed equipped with ring electrode. (From Talbert et al., 1984.)

and particle mixings (Ogata et al., 1982) and segregations (Kiewiet et al., 1978; Ogata et al., 1982). More recently, the electrospouted bed has been proposed, as shown in Fig. 19, by Talbert et al. (1984). The bed has a draft tube and side exits to reduce gas bypassing. A high voltage electrode ring, inserted below the draft tube, sets up an electric field between the ring and the draft tube and between the ring and the bed walls. These fields modify the flow of the particles, resulting in voltage-controlled particle entrainment and circulation. This technique may be applied more effectively on gas-particle reactions under fluidizations.

REFERENCES

Ahsmann, G., and R. Kronig (1951). The influence of electric fields on the convective heat transfer in liquids. *Appl. Sci. Res.*, A2 (1950), 235–244; erratum in A3 (1951), 85–88.

Atten, P., F. M. J. McCluskey, and A. C. Lahjomri (1987). The electrohydrodynamic origin of turbulence in electrostatic precipitator. *IEEE Trans. Ind. Appl.*, IA-23, 705–711.

Austin, L. J., L. Banczyk, and H. Sawistowski (1971). Effect of electric field on mass transfer across a plane interface. *Chem. Eng. Sci.*, 26, 2120–2122.

Bailes, P. J. (1981). Solvent extraction in an electrostatic field. *Ind. Eng. Chem. Process Des. Dev.*, 20, 564–570.

Baird, M. H. I. (1983). Special techniques, in *Handbook of Solvent Extraction* (T. C. Lo, M. H. I. Baird, C. Hanson, eds.), John Wiley & Sons.

Bonjour, E., J. Verdier, and L. Well (1962). *Chem. Eng. Progress*, 58, 63–66.

Carleson, T. E., and J. C. Berg (1983). The effect of electric fields on the absorption of pure sulfur dioxide by water drops. *Chem. Eng. Sci.*, 38, 871–876.

Carleson, T. E., and E. Fuller (1987). The effects of electrical charge upon mass transfer from drops exhibiting interfacial turbulence. *Chem. Eng. Comm.*, 57, 277–287.

Chang, J. S. (1987). EHD chemical reactors: a critical review. *Conf. Rec. IEEE IAS 1987 Annual Conference*, pp. 1471–1479.

Chang, J. S. (1989). Electrohydrodynamic control of fluid flow and heat transfer. *Trans. Chem. Eng. Japan*, 53, 24–27.

Chang, L. S., and J. C. Berg (1985). Electroconvective enhancement of mass or heat exchange between a drop or bubble and surroundings in the presence of an interfacial tension gradient. *AlCh.E J.*, 31, 149–151; 551–557.

Chang, J. S., S. Mielke, S. Ogata, and R. C. Scott (1990). Electromechanics and fluidization characteristics of co-flow type electrofluidized beds. *J. Electrostatics*, 24, 135–144.

Cross, J. D., and H. T. Wang (1991). Interfacial instability—a new approach to transient EHD motion with unipolar injection. *IEEE Trans. Elec. Insu.*, 26, 641–646.

Diehl, J. E., and C. R. Coppany (1969). Flooding velocity correlations for gas-liquid counter-flow in vertical tubes. *Chem. Eng. Prog. Symp. Ser.*, 65, 77.

Dietz, P. W., and J. R. Melcher (1978). Interparticle electrical forces in packed and fluidized beds. *Ind. Eng. Chem. Fundam.*, 17, 28–32.

Felici, N., and J. C. Lacroix (1978). Electroconvection in insulating liquids with special reference to uni- and bi-polar injection. *J. Electrostatics*, 5, 135–144.

Fernandez, J. L., and R. Poulter (1987). *Int. J. Heat Mass Transfer*, 30, 2125–2136.

Fujino, T., Y. Yokoyama, and Y. H. Mori (1989). Augmentation of laminar forced-convective heat transfer by the application of a transverse electric field. *Journal of Heat Transfer*, 111(5), 345–351.

Garton, C. G., and Z. Krasucki (1964). Bubble in insulating liquids: stability in an electric field. *Proc. Roy. Soc.* (London), A280, 211.

Harker, J. H., and Ahmadzadeh (1974). The effect of electric fields on mass transfer from falling drops. *Int. J. Heat Mass Transfer*, 17, 1219–1225.

He, W., M. H. I. Baird, and J. S. Chang (1991). The effect of electric field on droplet formation and motion in a viscous liquid. *Can. J. Chem. Eng.*, 69, 1174–1183.

He, W., M. H. I. Baird, and J. S. Chang (1993). The effect of electric field on mass transfer from drops dispersed in a viscous liquid, *Can. J. Chem. Eng.*, *71*, 366–376.

Hoburg, J. F., and J. R. Melcher (1976). *J. Fluid Mech.*, 73, 333.

Johnson, T. W., and J. R. Melcher (1975). Electromechanics of electrofluidized beds. *Ind. Eng. Chem. Fund.*, 14, 146–153.

Kiewiet, C. W., M. A. Bergougnou, J. D. Brown, and I. I. Inculet (1978). Electrostatic separation of fine particles in vibrated fluidized beds. *IEEE Trans. Ind. Appl.*, IA-14, 526–529.

Kowalski, W., and Z. Ziolkowski (1981). Increase in rate of mass transfer in extraction columns by means of an electric field. *Int. Chem. Eng.*, 21, 323–327.

Levenspiel, O. (1972). *Chemical Reaction Engineering*, 2d ed. John Wiley, New York.

Lo, T. C., M. H. I. Baird, and C. Hanson, eds. (1983). *Handbook of Solvent Extraction*. John Wiley, New York.

Martin, L., P. Vignet, C. Fombawlet, and F. Lancelot (1983). Electrical field contactor for solvent extraction. *Separation Sci. Tech.*, 18, 1455–1471.

Melcher, J. R. (1976). Electric fields and forces in semi-insulating liquids. *J. Electrostatics*, 2, 121–132.

Melcher, J. R. (1981). *Continuum Electromechanics*. MIT Press, Cambridge, Massachusetts, 3.1–3.26.

Millar, M. K., and L. R. Weatherley (1989). Whole broth extraction in an electrically enhanced liquid-liquid contact system. *Chem. Eng. Res. Des.*, 67, 227–231.

Mochizuki, Y., S. Ono, S. Teii, and J. S. Chang (1992). Fluidization and plasma characteristics of medium pressure RF glow discharge fluidized bed reactor. *J. Adv. Powder Tech.*, 5, 2–15.

Ogata, S., and J. S. Chang (1985). Effect of DC electric field on vertical annulus heat exchange system. *Proc. Japanese Electrostatic Soc.*, 9, 277–280.

Ogata, S., K. Tagama, K. Yamada, M. Fujino, and H. Shinohara (1980). An

experimental investigation of the dynamics of an electrofluidized bed. *Powder Eng.* (Japan), 17, 620–630.

Ogata, S., M. Fujino, and J. S. Chang (1982). Mixing and segregation properties in co-flow type electrostatic fluidized bed. *Proc. Inst. Electrostatics Japan*, 6, 180–185.

Ogata, S., T. Oshio, and J. S. Chang (1984). Electromechanics and fluidization characteristics of cross flow type electrofluidized beds. *Trans. IEEE Ind. Appl.*, IA-20, 1584–1590.

Ogata, S., K. Tan, K. Nishijima, and J. S. Chang (1985). Development of improved bubble disruption and dispersion technique by an applied electric field method. *A.I.Ch.E. J*, 31, 62–70.

Peters, J. M. H., J. L. Sproston, and G. Walker (1980a). Preliminary observations on bulk electroconvection in electrically stressed liquid insulants. Part II, Theoretical Investigation. *J. Electrostatics*, 9, 1–14.

Peters, J. M. H., J. L. Sproston, and G. Walker (1980b). Preliminary observations on bulk electroconvection in electrically stressed liquid insulants. Part I, Experimental investigation. *J. Electrostatics*, 8, 139–152.

Ptasinski, K. J., and P. J. A. M. Kerkhof (1992). Electric field driven separations: phenomena and applications. *Sep. Sci. Tech.*, 27, 995–1021.

Revankar, S. T., and J. S. Chang (1984). Countercurrent flooding phenomenon in gas-liquid two-phase flow under an electric field. Part 1, Theoretical analysis for adiabatic case in vertical tube. *J. Electrostatics*, 16, 47–68.

Robinson, K. S., and T. B. Jones (1984a). Particle-wall adhesion in electropacked beds. *IEEE Trans. Ind. Appl.*, IA-20, 1573–1577.

Robinson, K. S., and T. B. Jones (1984b). Slope stability of electropacked beds. *IEEE Trans. Ind. Appl.*, IA-20, 253–258.

Sato, M., S. Miyazaki, M. Kuroda, and T. Sakai (1983). Formation of uniformly sized bubbles in synchronization with an AC frequency. *Int. Chem. Eng.*, 23, 72–77.

Sato, M., M. Kuroda, and T. Sakai (1979). Effect of electrostatics on bubble formation. *Kaguka Koguka Ronbushu*, 5, 380–384.

Saville, D. A., and O. A. Palusinski (1986). Theory of electrophoretic separations. *AIChE. J.*, 32, 207–214.

Schneider, J. M., and P. K. Watson (1970). Electrohydrodynamic stability of space-charge-limited currents in dielectric liquids I. Theoretical study. *Physics of Fluids*, 13, 1948–1954.

Scott, T. C., and R. M. Wham (1989). An electrically driven multistage countercurrent solvent extraction device: the emulsion-phase contactor. *Ind. Eng. Chem. Res.*, 28, 94–97.

Scott, T. C. (1989). Use of electric fields in solvent extraction: a review and prospects. *Sepa. and Purif. Methods*, 18, 65–109.

Scott, T. C. (1987). Surface area generation and droplet size control using pulsed electric fields. *AIChE J.*, 33, 1557–1559.

Shah, Y. T., B. G. Kelkar, S. P. Godbole, and W. D. Deckner (1982). Design parameter estimations for bubble column reactors. *A.I.Ch.E. J.*, 28, 353–379.

Stewart, G., and J. D. Thornton (1967). Charge and velocity characteristics of electrically charged droplets. Part I, Theoretical considerations. Part II, Preliminary measurements of droplet charge and velocity. *I. Chem. E. Symposium Series*, No. 26, 29–42.

Suzuki, M. (1984). Separating device for an insulating gas-liquid two-phase fluid. U.S. Patent 4472278.

Talbert, C. M., T. B. Jones, and P. W. Dietz (1984). The electrospouted bed. *IEEE Trans. Ind. Appl.*, IA-20, 1220–1223.

Thornton, J. D. (1968). The application of electrical energy to chemical and physical rate processes. *Rev. Pure and Appl. Chem.*, 18, 197–218.

Vasishtha, N., and A. V. Someshwar (1988). Absorption characteristics of sulfur dioxide in water in the presence of a corona discharge. *Ind. Eng. Chem. Res.*, 27, 1235–1241.

Watson, P. K., J. M. Schneider, and H. R. Till (1970). Electrohydrodynamic stability of space-charge-limited currents in dielectric liquids II. Experimental study. *Physics of Fluids*, 13, 1955–1961.

Weatherley, L. R. (1992). Electrically enhanced extraction. In *Science and Practice of Liquid-Liquid Extraction*, Vol. 2 (J. D. Thornton, ed.). Oxford.

Wham, R. M., and C. H. Byers (1987). Mass transport from single droplets in imposed electric fields. *Separations and Technology*, 22, 447–466.

Yamaguchi, M., H. Sugaya, and T. Katayama (1989). Liquid-liquid extraction characteristics of a spray column with a D.C. electric field. *J. Chem. Eng. Japan*, 22, 25–29.

Yamaguchi, M., H. Sugaya, and T. Katayama (1988). Hydrodynamic behavior of dispersed phase in a spray column with an electric field for liquid-liquid extraction. *J. Chem Eng Japan*, 21, 179–183.

Yamaguchi, M., T. Takamatsu, F. Yoshida, and T. Katayama (1985). An experimental study of mass transfer rate in the dispersed phase for single charged drops in a dielectric liquid under a uniform electric field. *J. Chem. Eng. Japan*, 18, 325–330.

Yamaguchi, M., Y. Hashimoto, T. Takamatsu, and T. Katayama (1982). Gas absorption by single charged drops during their formation in a uniform electric field. *Int. J. Heat Mass Transfer*, 25, 1631–1639.

Yoshida, F., M. Yamaguchi, and T. Katayama (1988). Characteristics of electrical dispersion from water film flowing down an inclined plate into a dielectric liquid phase: drop diameter, drop velocity and dispersed-phase holdup. *J. Chem. Eng. Japan*, 21, 123–129.

Yoshida, F., M. Yamaguchi, and T. Katayama (1986). An experimental study of electrohydrodynamic dispersion from a liquid film flowing down an inclined plate into a continuous liquid phase. *J. Chem. Eng. Japan*, 19, 1–7.

25

Heat Engineering

Akira Yabe

Ministry of International Trade and Industry
Tsukuba, Japan

I. INTRODUCTION

The promotion of global energy conservation and environmental protection requires the critical utilization of waste heat (below 100°C) exhausted by factories. For this purpose, high-performance compact heat exchangers are desperately needed due to the small temperature difference between the heat transfer fluids used in heat exchangers. Recently, by taking advantage of the small electrical conductivity of organic media, such as CFC alternatives, using electric fields to enhance heat transfer has become not only feasible but desirable as well (Yabe et al., 1987a).

Active heat transfer enhancement techniques utilizing electric fields have the following advantages:

1. There is simplified implementation, using only a small transformer and an electrode (e.g., needles, wire, or mesh).
2. There is rapid control of heat transfer coefficients by monitoring the electric field strength.
3. There is localized cooling of complex curved passages, a common difficulty when using a blower or pump.
4. They are suitable for application to special environments (e.g., zero-gravity space).
5. CFC alternatives (e.g., HCFC123, HFC134a), oil, liquids with rela-

tively small electrical conductivity, and gases are acceptable working fluids at the present level of EHD technology.

6. Only negligible electric power consumption is required in many applications.
7. They have the possibility of heat transfer control, resulting in longer life span of electronic equipment due to the minimization of temperature fluctuations.

Generally speaking, any heat transfer mechanism is complicated when an electric field is applied. Complex interactions between electric, flow, and temperature fields, require, in some cases, that the governing equations be solved simultaneously. However, in the case of forced convection heat transfer with negligible natural convection, the temperature fields are determined theoretically by the flow fields. In cases of condensation heat transfer, the flow of condensate determines the heat transfer rate. Therefore, heat transfer enhancement techniques utilizing electric fields are frequently called electrohydrodynamical (EHD) augmentation methods of heat transfer.

This chapter discusses EHD effects in liquids, where complex interactions between the differing fields (electric, flow, and temperature) become important. Also discussed here are the EHD effects on the gas-liquid interface, where field interactions increase. The EHD liquid jet is examined as a typical example of an applied EHD mechanism involving a liquid. The EHD enhancement technique is also applied to condensation heat transfer and is illustrated here as a typical example involving the gas-liquid interface by utilizing the EHD extraction phenomenon along with EHD pseudo-dropwise condensation. Also discussed are the EHD effects on nucleate boiling heat transfer. Furthermore, this paper investigates the possibility of heat transfer control by applying varying electric fields.

II. INTERACTIONS AMONG ELECTRIC FIELDS, FLOW FIELDS, AND TEMPERATURE FIELDS

A. Forces Exerted on a Fluid in Electric Fields and Some Characteristics of the Governing Equations

The body force *fe* that acts on a fluid under the influence of electric fields can be derived by considering the change of the Helmholtz free energy for virtual work with the energy $\frac{1}{2}\epsilon E^2$ stored in the fluid under an electric

field (see details in Chaps. 7 and 8 in Panofsky and Phillips, 1962). The derived expression is

$$fe = \rho eE - \frac{1}{2} E^2 \nabla \epsilon + \frac{1}{2} \nabla E^2 \rho \frac{\partial \epsilon}{\partial \rho} \tag{1}$$

The first term states that the Coulomb force acts on the net charges, and the charge density ρe is the sum of the charges of positive and negative ions and electrons within a unit volume. This term becomes important for such cases as the corona wind that accompanies a corona discharge in gases and liquids. The second term represents the force produced by the spatial change of dielectric constant ϵ. The third term represents the force caused by the inhomogeneity of the electric field strength and is called the electrostriction term.

Physically, the sum of the second and third terms gives the force exerted on dielectric materials. Although the net charge is zero in the case of polarization of dielectric materials (see Fig. 1), the polarized charges yielded at the stronger electric field are forced more strongly than the ones yielded at the weaker electric field. Therefore by the resultant force, which is the sum of the forces exerted on each polarized charge, the fluid element is also forced to the stronger electric field region. In other words, these two terms can be expressed by $(k \cdot \nabla)E_0$. This expression means the polarized charge k is forced by the gradient of electric field strength.

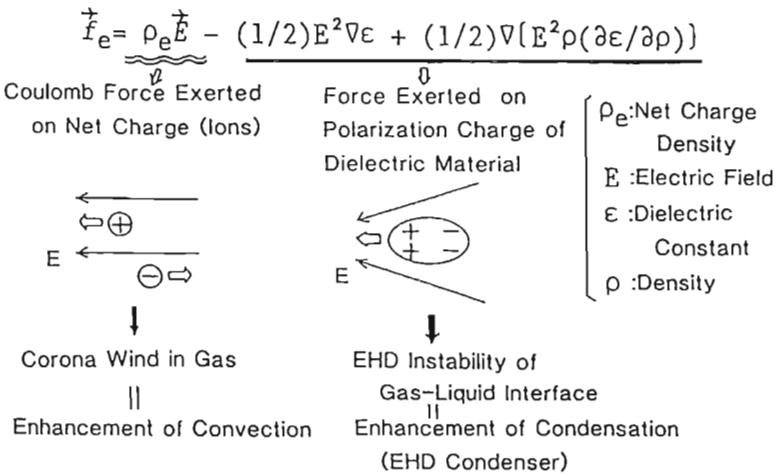


Figure 1 Body force generated in a fluid under electric fields.

However, in this case E_0 is not the electric field strength at the considered point but one in the case where there is no fluid only at the considered point and is given by $E_0 = E + k/(3\epsilon_0)$ for nonpolar fluids. These two terms become important in the case of EHD phenomena in liquids as well as the gas-liquid interface.

The electrostriction force is simplified in the case of nonpolar fluids by utilizing the Clausius-Mossotti law and is given by

$$\nabla\left[\frac{E^2(\epsilon - \epsilon_0)(\epsilon + 2\epsilon_0)}{6\epsilon_0}\right]$$

But for polar fluids, simplified expressions are difficult to obtain, since e is dependent on ρ, T, and p. Furthermore, since the electrostriction force is the gradient force (which is the same as a pressure term), it cannot cause any vorticity in the fluid. But, like the pressure, this electrostriction force is necessary when considering the force balance at the interface between different fluids. The body force fe can be transformed into the surface stress form by using Gauss' theorem as follows:

$$Tij = -\frac{1}{2}\left[\epsilon E^2 - E^2\rho\left(\frac{\partial\epsilon}{\partial\rho}\right)\right]\delta ij + \epsilon Ei Ej \tag{2}$$

where i and j are the components of the coordinates and δij is the Kronecker δ. This stress is called the Maxwell stress and this form is useful when examining EHD surface instabilities.

Concerning the governing equations of EHD phenomena, the Maxwell stress term should be added to the external force term of the Navier-Stokes equation to account for the effect of an electric field. The effect of a magnetic field, which is generated by the current, is negligible compared with the pressure generated by the electric field and the atmospheric pressure.

In our analysis we assume the fluid is incompressible, that the viscosity μ and the thermal conductivity λ are constant, and that the viscosity dissipation term is negligible. The resulting EHD governing equations can then be summarized in Table 1.

The first term of Eq. 9 (Table 1) is called the convection current, and the second term is called the conduction current. As seen from the governing equations, the complexity of the EHD phenomena is partly caused by the coupling of equations. One typical example of this is that the electric body force fe is included as the external force term in the Navier-Stokes equation of flow fields (Eq. 4), and that, at the same time, the fluid velocity

Table 1 Governing Equations of EHD Phenomena

Conservation equations	
Equation of continuity: $\nabla \cdot u = 0$	(3)
Navier-Stokes equation:	
$\rho \partial u/\partial t + \rho(u \cdot \nabla)u = -\nabla p + \mu \nabla^2 u + \rho g + fe$	(4)
Energy equation: $\rho c_p \partial T/\partial t + \rho c_p (u \cdot \nabla)T = \lambda \nabla^2 T$	(5)
Equation of state: $p = \rho RT/M$	(6)
Maxwell equations	
Poisson's equation: $\nabla \cdot \epsilon E = \rho_e$	(7)
Conservation of electric current: $\partial \rho_e/\partial t + \nabla \cdot i = 0$	(8)
Definition of electric current: $i = \rho_e u + \sigma_e E$	(9)
Definition of electric potential: $E = -\nabla \Phi$	(10)

u is included as the convective current term in Eq. 9 of the Maxwell equations.

In the steady state, without any convection,

$$\rho_e = -\left(\frac{\epsilon}{\sigma_e}\right) E \cdot \nabla \sigma_e \tag{11}$$

which is derived from Eq. 7 through Eq. 9. This means that the electric charges are generated by the gradient of the electrical conductivity. Since the electrical conductivities of liquids are generally dependent on temperature, Eq. 11 means that the temperature gradient generates the electric charges and that the Coulomb force acting on the generated electric charges becomes effective.

B. Relaxation Time of Electric Charges

To estimate the required time for realizing the steady state in the electric fields, we assume an instantaneous insertion of a liquid column, having an electrical conductivity σ_e and a dielectric constant ϵ, in a uniform electric field E_0. To investigate the change of the electric field, one-dimensionality is assumed (quasi-electrostatic induction in this case). As shown in Fig. 2, true electric charges generated on the interface ρ_{es} are derived as the difference of the electric flux density through the interface: $\rho_{es} = \epsilon_0 E_0 - \epsilon E$. Since the value of ρ_{es} would be equivalent to the total amount of

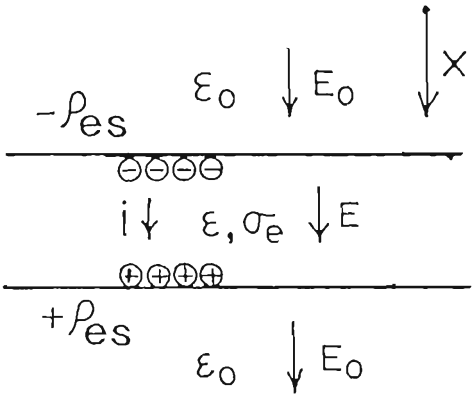


Figure 2 Relaxation phenomenon of electric charges.

the stored electric charges on the interface as the result of the electrical conduction, we find that $d\rho_{es}/dt = i = \sigma_e E$. The initial condition, $\rho_{es} = 0$ at $t = 0$, is based on the assumption that no true electric charge exists at the interface at the instant of applying an electric field. It also assumes that the only polarization charges appear at that given moment. Accounting for these assumptions, ρ_{es} becomes

$$\rho_{es} = \epsilon_0 E_0 \left\{ 1 - \exp\left(\frac{-\sigma_e}{\epsilon \cdot t} \right) \right\}$$

This means that the true electric charges increase with time and that ρ_{es} becomes $\epsilon_0 E_0$. This also occurs in the case of an existing electrical conductor. The characteristic time t_c is called the relaxation time of the electric charge and is defined by $t_c = \epsilon/\sigma_e$. It is a measure of the time period to realize the steady state in the electric field. The values of t_c are approximately 1 ms for distilled water, 10 ms for HCFC 123, and 10 s for CFC 113.

We utilize the ratio of t_{EHD} to t_c. In the case where $t_{EHD} << t_c$, the fluid can be assumed to be a dielectric substance. The electric field can, therefore, be determined by solving Eq. 7. In the case where $t_{EHD} >> t_c$, the fluid can be assumed to be electrically conducting. The electric field can then be determined by solving

$$\nabla \cdot \mathbf{i} = \nabla \cdot (\rho_e u + \sigma_e E) = 0$$

In the case where t_{EHD} is of the same order as t_c, the conservation equation of the electric current should be solved by accounting for the transient state of the amount of electric charges.

C. Interactions Among Electric Fields, Flow Fields, and Temperature Fields—Their Types and Mechanisms

Typical interactions among the electric, flow, and temperature fields are shown in Fig. 3. In case of a gas as the fluid, where the dielectric constant of the gas is nearly equal to 1, the Coulomb force generated on the true charges is important. But in the case of a liquid as the fluid, the force generated on the polarization charges would be of the same order of magnitude as the force generated on the true charges. Furthermore, if there is an interface typical to the phase change heat transfer, several additional interfacial forces would be generated to realize several kinds of EHD phenomena. Therefore the most effective EHD phenomenon to maximize the heat transfer is system specific. Typical EHD phenomena applicable to heat transfer enhancement and heat transfer control are shown in Table 2 for various kinds of heat transfer.

The typical EHD phenomenon involving gases is the enhancement of convective heat transfer by the use of a corona wind. This is also important in the flow of the electrostatic precipitation for capturing submicron particles. Experimental and theoretical research on corona wind has previously been performed and its mechanism quantified (Chattock, 1899; Yabe et al., 1978a; Yabe et al., 1978b; Kulacki, 1983). However, the application of wire electrodes to maximize the enhancement effects is still difficult (Tada et al., 1991).

The mechanism and characteristics of corona wind can be explained physically in the following discussion, as a typical example of EHD phenomena involving gases. A corona discharge occurs in the narrow region close to a needle or wire electrodes, where ions are produced by the ionization of a gas in a high electric field. These ions, controlled by the Coulomb force, migrate to the electrode plate without recombination. If the wire is an anode, the electrons are captured by the wire electrode. During the migration to the plate electrode, the ions transfer their momentum to neutral molecules via collision. A bulk flow of neutral molecules is thus created (Fig. 4). This flow undergoes forced convection, which augments heat transfer coefficients. Since the corona wind can reach a velocity approximately 2 ms^{-1}, heat transfer coefficients can be increased by a facter of 10 compared to those due to natural convection. Therefore

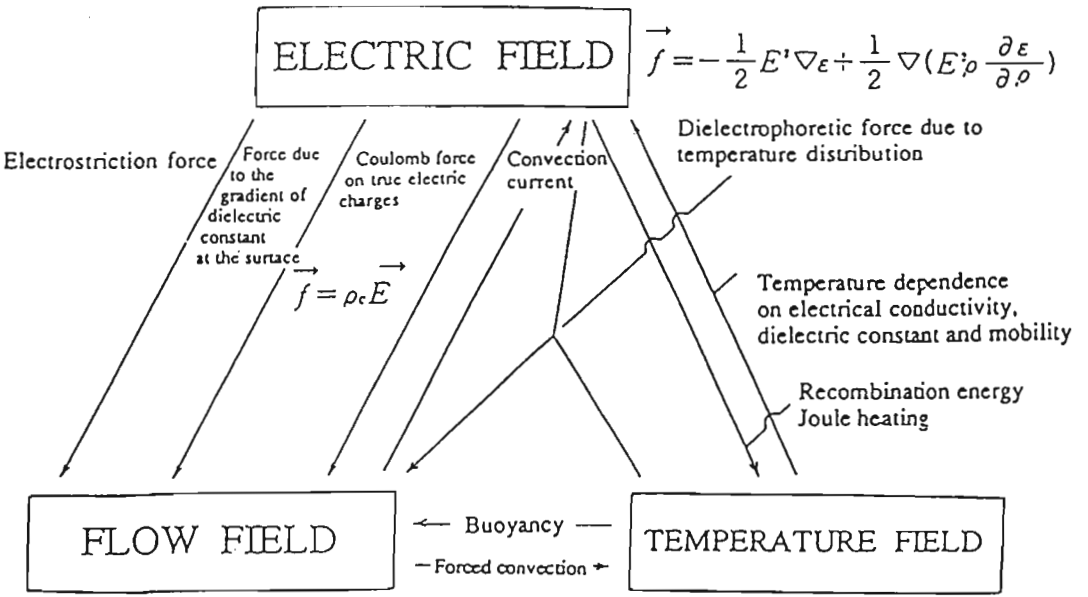


Figure 3 Interactions among electric field, flow field, and temperature field.

Table 2 Typical EHD Phenomena Applicable to Heat Transfer Enhancement

Convection (gas)
Corona wind generated by corona discharge (~3 m/s)
Convection (liquid)
Convection generated by electric charge injection of Corona discharge in liquids (~0.5 m/s)
Convection and turbulence generated by charge injection from electrodes
EHD liquid jet by applying nonuniform electric fields (about 1 m/s)
Boiling (convection in liquid is also effective)
Active movement of boiling bubbles on the heated surface by Maxwell stress
Deformation of boiling bubbles to make the bottom of the bubble spread on the boiling surface by the existence of thermal boundary layer
EHD promotion effects on Taylor instability to realize the breakup of bubbles into several bubbles
Evaporation
Flying of small liquid particles between the heat transfer surface and the opposing electrode by electrostatic atomization
Increase of heat transfer surface by the EHD extraction phenomenon of liquid
Condensation
Decrease of condensate film thickness by the removal of condensate from the condensing surface utilizing EHD extraction phenomenon of liquid
EHD pseudo-dropwise condensation
Dispersion of condensate from the condensing surface by electrostatic atomization

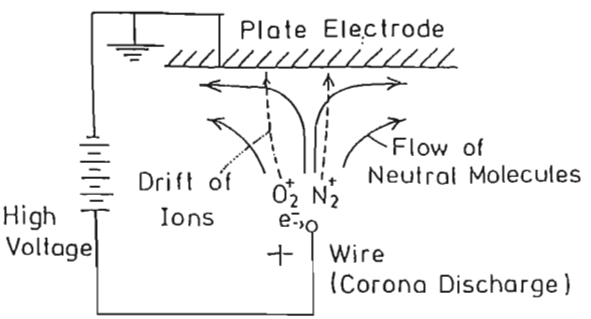


Figure 4 Mechanism of corona wind generated by corona discharge.

although the energy conversion efficiency of corona wind generation is less than 5%, it has the advantage of controlled localized cooling. This is particularly important when encountering complex curved passages not easily cooled with conventional fans.

III. AN EHD (ELECTROHYDRODYNAMICAL) LIQUID JET AND ITS APPLICATION TO CONVECTIVE HEAT TRANSFER ENHANCEMENT

Since all the terms of fe expressed by Eq. 1 are important in liquids, many kinds of EHD convection should occur. The convection caused by the corona discharge in liquids is also important (Stuetzer, 1960). However, the corona discharge in a liquid is not of practical use due to the degradation of the heat transfer medium. When a temperature distribution is established in the liquid, meaning that heat transfer is generated, electric charges are created by the gradient of electrical conductivity due to the temperature distribution as explained in Sec. II. Therefore the Coulomb force exerted on the space charges produces the convection. However, the resulting velocity of the liquid, in this case, would be less than a few centimeters per second (Turnbull, 1969). Furthermore, charge injection from the surface of the electrode without any electrical discharge could occur (Castellanos et al., 1984; Fujino and Mori, 1986), and the Coulomb force exerted on the injected space charges.

The EHD liquid jet was produced by applying a high electric voltage between the ring electrode and the plate electrode as shown in Fig. 5. The jet flow is ejected through the ring electrode in the direction away from the plate. This jet was first noted by Yabe (Yabe and Maki, 1988). It was shown experimentally that the flow velocity exceeded 1 ms^{-1} when the liquid mixture was CFC 113 and ethanol. This flow velocity was independent of the temperature distribution. This phenomenon was named the "EHD liquid jet" and was applied to the heat transfer augmentation of convection and the critical heat flux of the boiling heat transfer.

The EHD liquid jet velocity increases as the electrical conductivity of liquids increases. It becomes a maximum and saturates for electrical conductivity above 3×10^{-9} $(\Omega m)^{-1}$. Furthermore, CFC alternatives such as HCFC 123 have been utilized as the working fluid alone rather than a CFC 113–ethanol mixture. The velocity distribution was the reverse of the usual stagnation flow.

The main mechanism of the EHD liquid jet can be explained with respect to its governing equations. Although the external force generated in the liquid has contained various kinds of forces such as Coulomb force

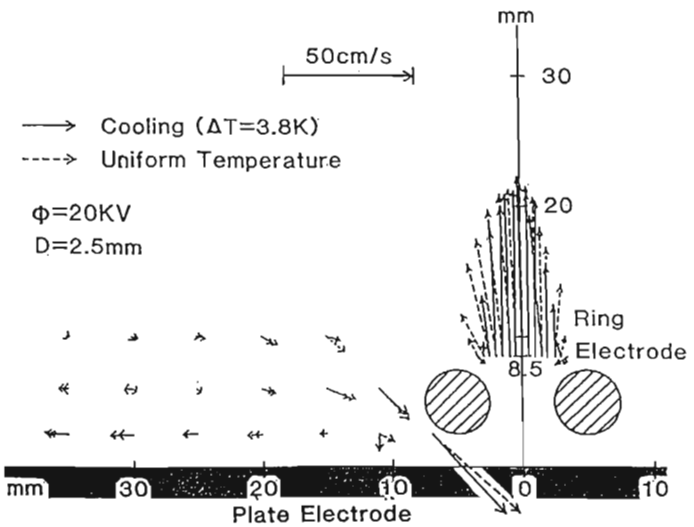


Figure 5 EHD liquid jet phenomenon.

and the force exerted on the polarized charges, the flow distribution of this EHD liquid flow has been explained mainly by electrostriction force. The fluid element is forced to migrate to the stronger electric field region by the electrostriction force (the third term of Eq. 1). The electric field is not symmetric for the ring and plate electrodes' arrangement with respect to the vertical plane includes the bottom edge of the ring electrode in the case of the upward-facing flat plate. Namely, in the outer region of the ring electrode, the electrostriction force makes the bottom edge of the ring electrode attract the fluid. This is caused by the larger magnitude. But in the region inside the ring electrode this force makes the bottom edge of the ring electrode attract the fluid. This is caused by the smaller magnitude. Therefore due to this asymmetrical distribution of the electrostriction force, the convection of an EHD liquid jet can occur. Since this electrostriction force is a gradient force, the initiation of the flow should occur by the instability due to the smaller Coulomb force around the electrodes, which is readily expected, based on the existence of the small amount of current. The electric potential and velocity distribution can be determined from the Navier-Stokes equation (Eq. 4) including the fe, the term of the electrostriction force, by assuming $tc \ll t_{EHD}$. This velocity distribution of the EHD liquid jet (see Fig. 6) agrees with those obtained experimentally.

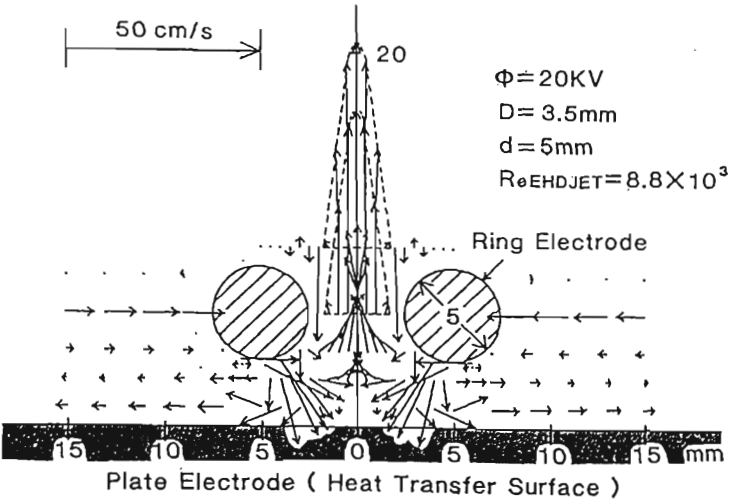


Figure 6 Velocity distribution of EHD liquid jet (theory).

The convective heat transfer coefficients from the plate increased in proportion to the electric field strength due to the effect of the EHD liquid jet as shown in Fig. 7. Compared to the natural convection heat transfer coefficients, the heat transfer coefficients increased by a maximum factor of 100. It was determined experimentally that the maximum heat transfer coefficients, exceeding 10^4 W/m^2 K, were caused not only by the velocity distribution of the EHD liquid jet but also by the turbulent heat flux due to its turbulent intensity.

IV. EHD PHENOMENA AT THE INTERFACE AND THEIR APPLICATION TO HEAT TRANSFER ENHANCEMENT

A. EHD Extraction Phenomenon of a Liquid from the Surface and the Enhancement of Condensation Heat Transfer

In the case of the heat transfer accompanying a phase change, the surface instability due to electric fields and the various EHD convection phenomena in liquids become important. In this section, augmentation of condensation heat transfer by the use of EHD surface instability on the gas-liquid interface is explained (see Fig. 8).

In many cases, the gas would be an electrical insulator and the liquid would be the electrical conductor (Melcher, 1961). Therefore by applying

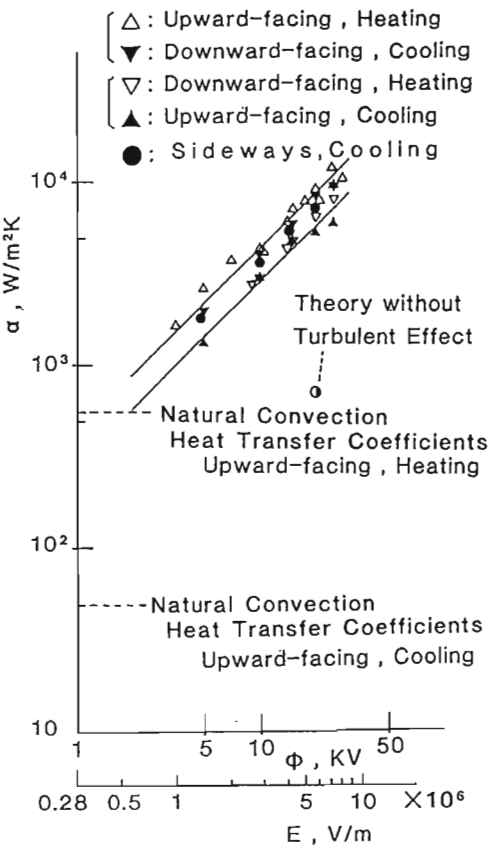


Figure 7 Convective heat transfer enhancement by applying EHD liquid jet.

the electric field for a time longer than t_c in a liquid, the electric field in the liquid would decrease to zero. The Maxwell stress on the liquid surface would have a horizontal component of nearly zero and a vertical component of $\frac{1}{2}\epsilon_l E_{l\perp}^2$. Physically, this means the product of the surface charge $\epsilon_l E_{l\perp}$ and the electric field on the surface $\frac{1}{2}E_{l\perp}$ and this force makes the liquid surface extend in the gas toward the electrode and away from the heat transfer surface. To determine the equilibrium condition of forces acting on the liquid surface, we assume the condition of an infinitesimal displacement of the liquid surface. This infinitesimal rise of the liquid surface causes an increase in the Maxwell stress and the raising of the liquid surface due to the decrease of the distance between the surface

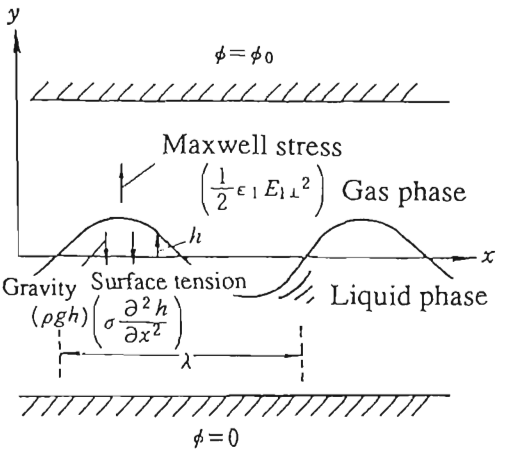


Figure 8 EHD instability on the gas-liquid interface.

and the electrode. Surface tension and gravity are the restoring forces. Therefore as the Maxwell stress becomes greater than the sum of the restoring forces, the upward attraction force increases, and consequently instability occurs.

Fundamental studies on the heat transfer augmentation of the filmwise condensation on the vertical surface by applying a nonuniform electric field have been carried out from the EHD viewpoint. This yields high-performance condensers that promote energy conservation. The liquid extraction phenomenon, applying nonuniform electric fields to create a liquid column between the electrodes, has previously been investigated (Yabe et al., 1982, 1987a, 1987b). This EHD liquid extraction phenomenon was explained quantitatively as a gas-liquid surface instability due to nonuniform electric fields in a theoretical study. Then, by applying this phenomenon to the condensation along a vertical cooled surface, the EHD augmentation phenomenon of removing some amount of condensate from the heat transfer surface was observed by the use of wire electrodes stretched horizontally and parallel to the surface. Furthermore, as a next forward step to apply this augmentation method to practical condensers, the augmentation effect of condensation outside of a vertical cooled tube was examined. By the use of a helical wire electrode optimized experimentally, about 95.8% of condensate could be removed from the condensation surface. Consequently heat transfer coefficients were up to 2.8 times larger than those without electric fields. This supports the effectiveness of the EHD augmentation method of condensation heat transfer.

B. EHD Pseudo-Dropwise Condensation and the "EHD Condenser"

A surface granulation phenomenon on the condensation surface, as can be seen in a dropwise condensation, could be observed in electric fields (Velkoff and Miller, 1965; Didkovsky and Bologa, 1982; Yabe et al., 1986). This EHD surface granulation phenomenon could be realized only for thin condensate film such as that produced by the above-mentioned EHD extraction technique. For ordinary condensate film, on the order of 200 μm, uniform electric fields create only the wavy motion of the condensate. This EHD surface granulation phenomenon can be applied even for condensation of fluorocarbons, which normally have surface tensions too low to realize ordinary dropwise condensation. The reason is that the EHD surface granulation phenomenon of a liquid film is qualitatively one type of gas-liquid instability in electric fields. Therefore the condensation heat transfer enhancement accompanied by this EHD surface granulation phenomenon is called EHD pseudo-dropwise condensation.

The EHD surface granulation phenomenon of the thin liquid film is the occurrence of liquid drops on the surfaces of liquid films whose thicknesses are below 100 μm. The liquid drops, whose diameters are on the order of a millimeter, have the shape of a hemisphere. EHD pseudo-dropwise condensation has been researched from the basic viewpoint. The EHD surface granulation phenomenon on a horizontal plate was investigated as a fundamental study (Yabe et al., 1986; Yabe, 1993). An experimental study of EHD pseudo-dropwise condensation heat transfer characteristics has been conducted (Sunada et al., 1991). Silicone oil instead of fluorocarbons was studied using this technique. The operating conditions were a uniform electric field of 16 kV/cm, an initial thickness of 20 μm for the liquid film, and a viscosity of 20 cSt for the liquid. The average diameter of the liquid drops was 2.3 mm with a standard deviation of 0.5 mm. The ratio of drop height to diameter increased with the increase of the electric field strength and di. Furthermore, the ratio of A_T/Ai was found to be over 0.5. The ratio of d_T/di decreased as di decreased. As well as when the electric field strength increased, di also decreased as the liquid viscosity decreased. This ratio, d_T/di, was minimized at approximately 20% during the basic experiments.

The combination of the EHD extraction phenomenon of the CFC 113 liquid (using a helical wire electrode) and the EHD pseudo-dropwise condensation (using a perforated curved plate) resulted in an increase in the condensation heat transfer coefficients by a factor of 4.5 over measured coefficients without the influence of an electric field (see Fig. 9). Furthermore, the heat transfer characteristics of the EHD pseudo-dropwise con-

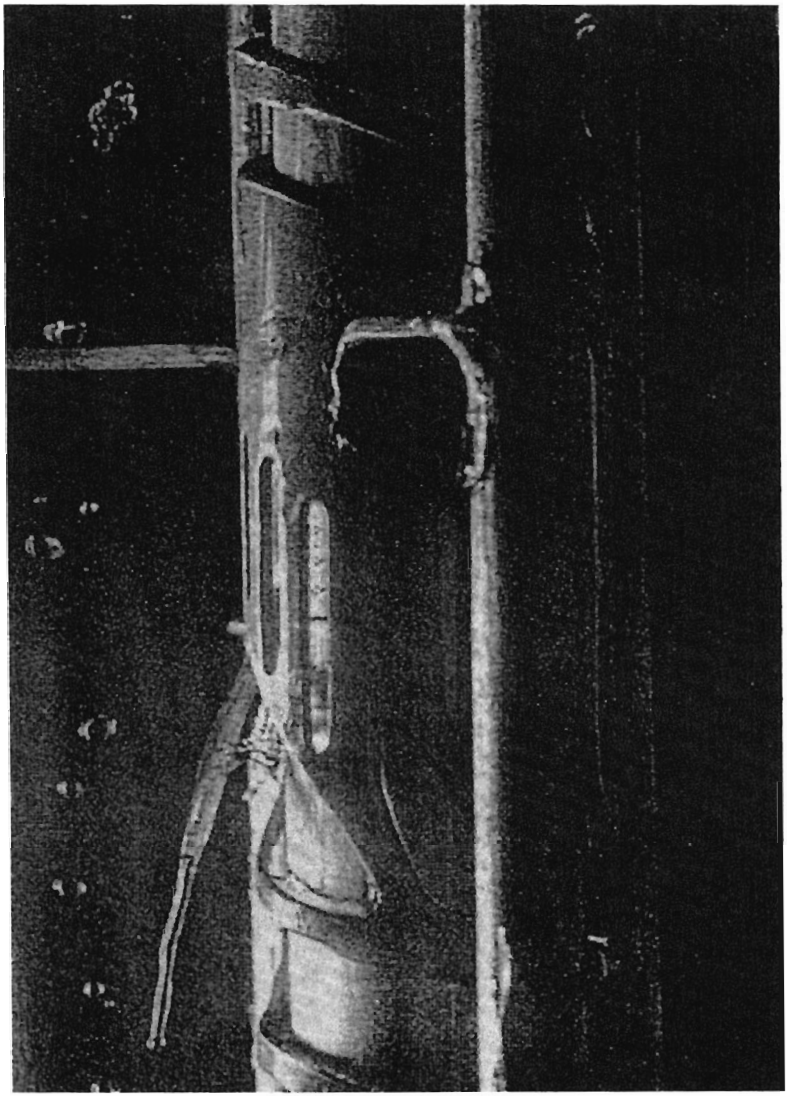


Figure 9 EHD extraction phenomenon of liquid and EHD pseudo-dropwise condensation.

densation were experimentally studied by utilizing a vertical heat transfer plate. When the electric field strength was greater than about 4 MV/m, EHD pseudo-dropwise condensation phenomenon occurred. At this point, the condensation heat transfer coefficients increased with increased electric field strength. The maximum local heat transfer coefficients exceeded 11,000 W/m²K for HCFC 123, as shown in Fig. 10. The enhancement ratio was over 4 times, for the lower part of the heat transfer surface, compared to the ratio without electric fields. Furthermore, if the amounts of the falling condensate are the same, the heat transfer coefficients become the same for the same electric field strength and are independent of the surface temperature of the heat transfer plate and the distance from the top of the plate. The above-mentioned large enhancement ratio has been obtained so far, which would have a large potentiality for heat transfer control by changing the electric fields.

The high-performance condenser utilizing the combination of the EHD extraction phenomenon and EHD pseudo-dropwise condensation is called an EHD condenser and has been developed for use in high-efficiency, high-temperature heat pump systems. Such a system was implemented in

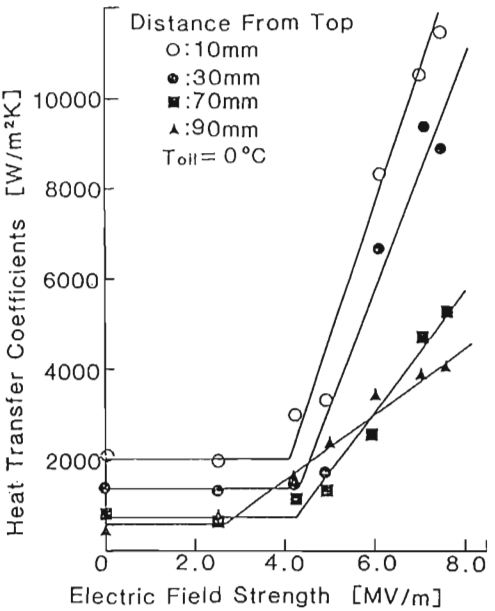


Figure 10 Condensation heat transfer enhancement by realizing EHD pseudo-dropwise condensation (working fluid: HCFC 123).

a large-scale national research and development project, the Super Heat Pump Energy Accumulation System, which is included in the Japanese national energy conservation program (Moonlight Project) sponsored by the Ministry of International Trade and Industry. The results of a test include a thermal output of 50 kW at a temperature of about 150°C. The resulting high-performance heat transfer characteristics are shown in Fig. 11. For working fluids of C_6F_{14} (perfluorohexan) and CFC 114, a heat transfer enhancement of 6 times (compared to those without electric fields) was achieved for a shell and tube type EHD condenser with a vertical condensing length of 1400 mm (Yamashita et al., 1991). The enhancement technique of condensation heat transfer becomes more effective for relatively high film Reynolds numbers (Ref* > 1000). As the vertical tube length increases or the latent heat of the working fluid decreases, this EHD enhancement technique becomes more effective.

V. EHD EFFECTS ON BUBBLES AND ENHANCEMENT OF NUCLEATE BOILING HEAT TRANSFER

When bubbles are present in the liquid, EHD phenomena become more complex. The sources of the EHD phenomena to be considered are instability due to liquid extraction phenomena, stability of the gas-liquid interface, occurrence of convection due to the Maxwell stress (including Coulomb and electrostriction force), migration of bubbles in electric field gradients, and electric charging of the bubbles (Berghmans, 1976; Allen

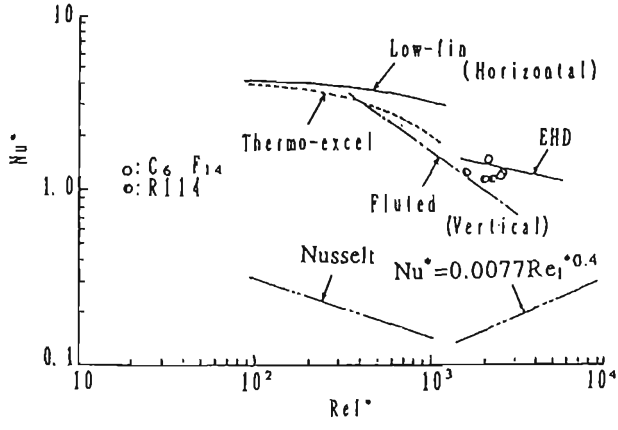


Figure 11 Heat transfer characteristics of "EHD condenser" compared with those of other enhanced tubes.

and Cooper, 1987; Ogata et al., 1985; Jones, 1978). Therefore since the presence of bubbles causes the EHD phenomena to become more complex compared to the case of pure liquid, clarifying specific EHD phenomena and techniques for utilizing EHD effects for heat transfer enhancement techniques is important.

The EHD effect on bubbles can be used to explain the deformation and the behavior of the bubbles, the temperature distribution effects on the EHD behavior, and the enhancement effect of nucleate boiling heat transfer. In conventional boiling phenomena, bubbles are generated on a superheated surface and grow until the buoyancy exceeds the interfacial tension on the heated surface. The repetition of this cycle is the familiar boiling phenomenon. However, in the presence of electric fields, several EHD effects appear in this boiling cycle and change it drastically. Figure 12 shows the EHD effect on nucleate boiling in which the boiling has been enhanced largely by applying an electric field. Considering the boiling curve of the pool boiling, the effects of EHD enhancement helped attain

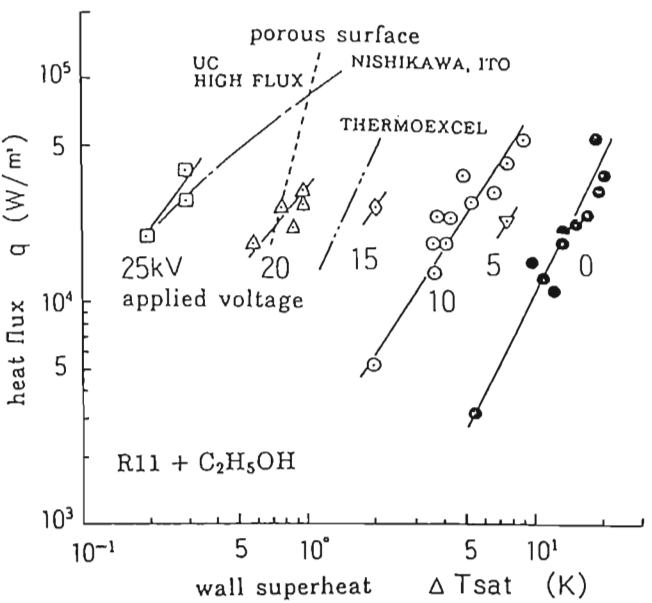
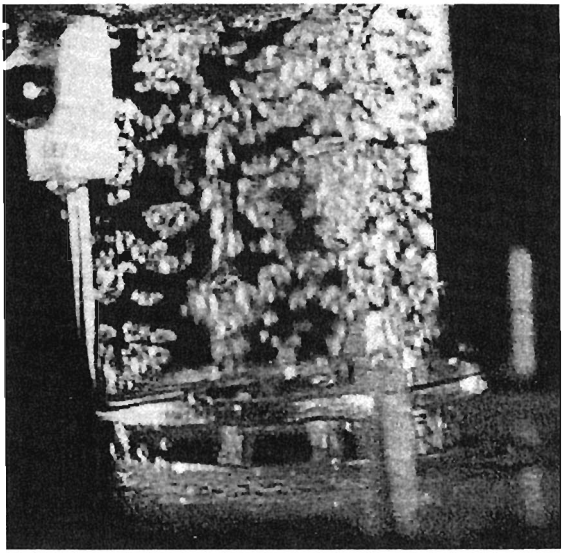


Figure 12 EHD effect on nucleate boiling heat transfer enhancement (electrode distance: 5mm; working fluid: mixture of CFC 11 and ethanol, which has the electrical conductivity of 4×10^{-8} [1/Ω m]; nearly the same phenomenon occurs for HCFC 123).

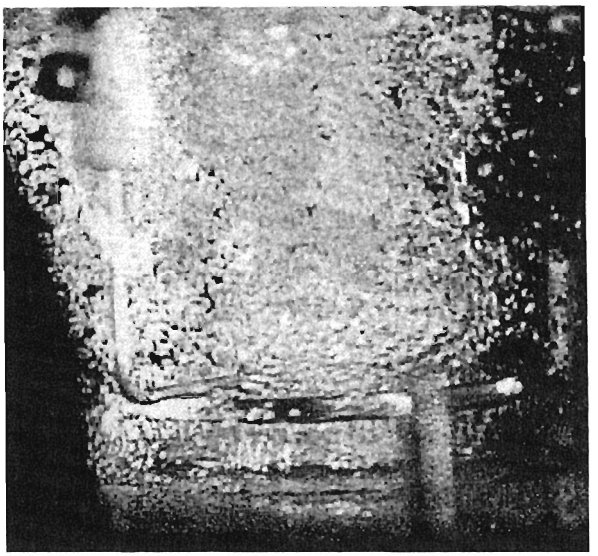
maximum heat transfer compared with experiments carried out thus far. These experiments included various manufactured boiling surfaces, as shown in Fig. 13. The condition of a superheated wall necessary for specific boiling heat flux decreased to below 1/50 for the applied electric field of 5 kV/mm (Ogata and Yabe, 1991, 1993a, 1993b). This boiling heat transfer augmentation effect increased with increasing electrical conductivity. It was at a maximum when the relaxation time of electric charges t_c in liquid was less than the characteristic time of bubble detachment from the surface (approximately tens of milliseconds). This is suitable for HCFC 123, the mixture of CFC 11 and ethanol, and other CFC alternatives. This means that the magnitude of the EHD effects determined whether the distribution of the electric field strength could follow the change of the bubble shape or not.

EHD influence on the behavior of bubbles in a boiling cycle was analyzed by utilizing a high-speed video system and by numerical simulation. On the vapor-liquid interface of the generated bubbles the Maxwell stress is effective. Since the line of the electric force should be vertical on a boiling surface made of metal, the electric field at the lower part of the bubble becomes weaker than that at the upper part of the bubble. Therefore the bubble is pressed on the heating surface by the dielectrophoretic force of Maxwell stress. The bubble also moves around the heat transfer surface, actively driven by the radial component of the Maxwell stress. This radial component is parallel to the surface in cases where asymmetrical deformation of the bubble occurs, while the bubble is pressed by the vertical component of the Maxwell stress. Since the electric field strength in the superheated liquid layer is weaker than that of the saturated region, due to the increase of electrical conductivity for the higher-temperature region, the bubble is pushed toward the heat transfer surface. This causes the bottom of the bubble to spread out on the heat transfer surface. As the result, the area of the thin liquid film under the bottom of the bubble increases, making the boiling heat transfer greatly augmented. Furthermore, by applying an electric field, the breakup of bubbles into several bubbles is activated due to the Taylor instability in the electric field on the vapor-liquid interface of the bubble. Consequently, the number of bubbles on a heat transfer surface increases as if new bubbles appeared on the boiling surface. The above EHD effects would make another boiling cycle that would also make a large amount of the boiling heat transfer enhancement.

This EHD enhancement effect of boiling has been researched and developed for high-performance evaporators of heat pump systems that utilize river water as their heat source. Also this effect would be effective



(a)



(b)

Figure 13 EHD effects on nucleate boiling enhancement [boiling curve for the mixture of CFC 11 and ethanol; electric conductivity 7×10^{-8} (1/Ω ml)]. (a) Electric field: 2 kV/mm. (b) Electric field: 5 kV/mm.

for augmenting the evaporation of the nonazeotropic mixtures in thermal cycles, thus promoting energy conservation.

VI. FUTURE APPLICATION FIELDS OF EHD ENHANCEMENT TECHNIQUES

EHD enhancement techniques can be successfully applied to various heat transfer mechanisms. Therefore, a large number of application fields exist for EHD enhancement techniques. Future application fields, where the mechanism or the effect of the EHD enhancement techniques have not yet been investigated, are briefly explained below.

The possible effect of an electric field on frosting phenomena needs investigation, since the defrosting problem possibly is the most important problem encountered by heat pump systems applying for colder regions. The dendritic crystal, which is generated at crystal growth period, has been shown to be affected by an applied electric field, and to be grown by repetition of the generation, growth, and removal cycle from the dense sublayer crystal (Munakata and Yabe, 1991).

The heat transfer characteristics of nonazeotropic mixtures for heat pump cycles and electric power generation cycles would be largely deteriorated, and therefore the enhancement of condensation and boiling have been seriously requested for realizing high-performance thermal cycles. The main reason for the deterioration would be the accumulation of one component of the working fluid having less potential for the condensation or the evaporation. Therefore since the EHD effects on the vapor-liquid surface would promote surface instability, causing mixing of the components of nonazeotropic mixtures, EHD enhancement techniques would be effective for the enhancement of condensation or boiling (Yabe et al., 1992).

There are some positive results in experiments involving EHD effects on the preservation of food. Accompanying the corona discharge in gases, ions and electrons as well as several chemical species (e.g., ozone) are generated. The occurrence of ozone and certain ions would be effective for pasteurization, but the exact mechanism has yet to be clarified (Asakawa 1981).

We still need much research on EHD effects on heat and mass transfer, where large EHD effects or interesting EHD phenomena may be expected. These include evaporation enhancement (Yabe et al., 1980), effects on gas-solid two-phase flow (Yoshida et al., 1990), enhancement effects on convection heat transfer and the effect generating the turbulence (Perez et al., 1988; Ishiguro et al., 1991), and the enhancement of combustion (Bradley, 1986; Hijikata et al., 1989).

VII. CONCLUSIONS

In this chapter, the characteristics of active heat transfer enhancement techniques by applying electric fields have been clarified. Furthermore, the present state of research on EHD heat transfer enhancement techniques was systematically described from the EHD viewpoint. This was done with respect to the convective heat transfer in liquids and phase change heat transfer of condensation and boiling. We conclude the following.

(1) The convective heat transfer coefficients (with an EHD liquid jet) are enhanced by a factor of over 100 compared to the natural convection heat transfer coefficients. Maximum heat transfer coefficients exceeding 10^4 W/m^{2}K are caused not only by the forced convection of the EHD liquid jet but also by the turbulent heat flux due to its turbulent intensity.

(2) The heat transfer characteristics of an EHD condenser attained the heat transfer increase of 6 times at most for the same film Reynolds number compared to that without electric fields, as a typical example of EHD phenomena at an interface. This enhancement of condensation heat transfer was developed utilizing the combination of the EHD extraction phenomenon of a liquid from the surface and the EHD pseudo-dropwise condensation.

(3) The nucleate boiling heat transfer was enhanced by a factor of 50 for the electric field of 5 kV/mm. This was based on the EHD effects causing the active movement and deformation on the heated surface of boiling bubbles. The bottom of the bubble spread out on the heat transfer surface, and the area of the thin liquid film under the bottom of the bubble would be increased.

Concerning the possibility of heat transfer control, rapid change (within milliseconds) of the heat transfer characteristics and the control of localized cooling of the system at an arbitrary point would be possible.

Since these EHD active heat transfer enhancement and control techniques have been widely researched, and efforts to develop actual heat exchangers actively pursued, we can expect practical use of these techniques for energy conservation and global environmental protection.

REFERENCES

Allen, P. H. G., and P. Cooper (1987). The potential of electrically enhanced evaporators. *Proc. 3rd Int. Symp. on the Large Scale Applications of Heat Pumps*, pp. 221–229.

Asakawa, Y. (1981). Promotion and retardation of vaporization as an effect of application of electric field. *Proc. 18th National Heat Transfer Symposium of Japan*. Sendai, D101, pp. 466–468.

Berghmans, J. (1976). Electrostatic fields and the maximum heat flux. *Int. J. Heat Mass Transfer*, 19, 791–797.

Bradley, D. (1986). The effects of electric fields on combustion processes. *Advanced Combustion Methods* Academic Press, pp. 331–393.

Castellanos, A., P. Atten, and M. G. Velarde (1984). Oscillatory and steady convection in dielectric liquid layers subjected to unipolar injection and temperature gradient. *Physics Fluids*, 27, 1607–1615.

Chattock, A. P. (1899). On the velocity and mass of ions in the electric wind in air. *Philosophical Magazine*, 48, pp. 401–420.

Didkovsky, A. B., and M. K. Bologa (1982). Vapor film condensation heat transfer and hydrodynamics under the influence of an electric field. *Int. J. Heat Mass Transfer*, 24(5), 811–819.

Fujino, T., and Y. H. Mori (1986). The effect of a transverse electric field on laminar channel flow with constant heat rate. *Proc. 4th Int. Symp. on Flow Visualization*, pp. 643–648.

Hijikata, K., T. Nagasaki, and H. Ohya (1989). A study on the enhancement of catalytic combustion by electric field. *Trans. JSME Ser. B*, 55, (514), 1698–1704.

Ishiguro, H., S. Nagata, H. Yabe, and H. Nariai (1991). Augmentation of forced-convection heat transfer by applying electric fields to disturb flow near a wall. *Proc. 3rd ASME/JSME Thermal Engineering Joint Conf.*, Reno, U.S.A, March 17–22.

Jones, T. B. (1978). Electrohydrodynamically enhanced heat transfer in liquids—a review. *Advances in Heat Transfer*, vol. 14, pp. 107–148. Academic Press, New York.

Kulacki, F. A. (1983), "Augmentation of low Reynolds number forced convection channel flow by electrostatic discharge." *Low Reynolds Number Flow Heat Exchangers*. (S. Kakac, ed.). Hemisphere, Washington, D.C., pp. 753–782.

Melcher, J. R. (1961). EHD and MHD surface waves and instabilities. *Physics Fluids*, 4, 1348–1354.

Munakata, T., and A. Yabe (1991). Effect of electric fields on frosting phenomenon. *Proc. 3rd ASME/JSME Thermal Engineering Joint Conf.*, Reno, U.S.A, March 17–22.

Ogata, J., and A. Yabe (1991). Augmentation of nucleate boiling heat transfer by applying electric fields (EHD behavior of boiling bubble). *Proc. 3rd ASME/JSME Thermal Engineering Joint Conf.*, Reno, U.S.A, March 17–22.

Ogata, J., and A. Yabe (1993a). Augmentation of boiling heat transfer by utilizing EHD phenomena. *Int. J. Heat Mass Transfer*, 36(3), 775–782.

Ogata, J., and A. Yabe (1993b). Augmentation of boiling heat transfer by utilizing EHD effect (EHD behavior of boiling bubbles 3rd heat transfer characteristics). *Int. J. Heat Mass Transfer*, 36(3), 783–791.

Ogata, S., K. Ten, K. Nishijima, and J. S. Chang (1985). Development of improved bubble disruption and dispersion technique by an applied electric field method. *A.I.Ch. E.Jl* 31, 62–69.

Panofsky, W., and M. Phillips (1962). Classical electricity and magnetism," 2d ed. Addison-Wesley, pp. 107–116.

Perez, A. T., P. Atten, B. Malraison, L. Elouadie, and F. M. J. McCluskey (1988). Heat transfer augmentation induced by electrically generated convection in liquids. *Experimental Heat Transfer, Fluid Mechanics, and Thermodynamics* (R. K. Shah, E. N. Ganic, and K. T. Yang, eds.) Elsevier, pp. 407–417.

Stuetzer, O. M. (1960). Ion drag pumps. *J. Appl. Phys.*, 31, 136–146.

Sunada, K., A. Yabe, T. Taketani, and Y. Yoshizawa (1991). Experimental study of EHD pseudo-dropwise condensation. *Proc. 3rd ASME/JSME Thermal Engineering Joint Conf.*, Reno, U.S.A, March 17–22.

Tada, Y., A. Takimoto, and Y. Hayashi (1991). Heat transfer enhancement in a convective field by applying ionic wind. *Proc. 3rd ASME/JSME Thermal Engineering Joint Conf.*, Reno, U.S.A, March 17–22.

Turnbull, R. J. (1969). Free convection from a heated vertical plate in a direct-current electric field. *Physics Fluids*, 12, 2255–2263.

Velkoff, H. R., and T. H. Miller (1965). Condensation of vapor on a vertical plate with a transverse electrostatic field. *Trans. ASME Ser. C*, 87, 197–201.

Yabe, A. (1993). Mechanism of electro-hydrodynamically (EHD) enhanced boiling and condensation. *Computers and Computing in Heat Transfer Science and Engineering* (W. Nakayama and K. T. Yang, eds.). CRC Press, pp. 331–348.

Yabe, A., and H. Maki (1988). Augmentation of convective and boiling heat transfer by applying an electro-hydrodynamical liquid jet. *Int. J. Heat Mass Transfer*, 31(2), 407–417.

Yabe, A., Y. Mori, and K. Hijikata (1978a). EHD Study of the corona wind between wire and plate electrodes. *AIAA J.*, 16(4), 340–345.

Yabe, A., Y. Mori, and K. Hijikata (1978b). Heat transfer augmentation around a downward-facing flat plate by non-uniform electric fields. *Proc. 6th Int. Heat Transfer Conf.*, Toronto, vol. 3, pp. 171–176.

Yabe, A., Y. Mori, and K. Hijikata (1980). EHD augmentation effect on vaporization. *Trans. Jp. Soc. of Mech. Eng. Ser. B*, 46(406), 1161–1171.

Yabe, A., K. Kikuchi, T. Taketani, Y. Mori, and K. Hijikata (1982). Augmentation of condensation heat transfer by applying non-uniform electric fields. *Heat Transfer 1982*. Hemisphere, Vol. 5, pp. 189–194.

Yabe, A., K. Kikuchi, T. Taketani, Y. Mori, and H. Maki (1986). Augmentation of condensation heat transfer by applying electro-hydrodynamical pseudo-dropwise condensation. *Heat Transfer 1986*. Hemisphere, Vol. 6, 2957–2962.

Yabe, A., Y. Mori, and K. Hijikata (1987a). Heat transfer enhancement techniques utilizing electric fields. *In Heat Transfer in High Technology and Power Engineering* (W. J. Yang and Y. Mori, eds.). Hemisphere, Washington, D.C., pp. 394–405.

Yabe, A., T. Taketani, K. Kikuchi, Y. Mori, and K. Hijikata (1987b). Augmentation of condensation heat transfer around vertical cooled tubes provided with helical wire electrodes by applying non-uniform electric fields. *Heat Transfer Science and Technology* (Bu-Xuan Wang, ed.). Hemisphere, Washington, D.C., pp. 812–819.

Yabe, A., T. Taketani, T. Maki, and H. Aono (1992). Experimental study of EHD condenser for non-azeotropic mixtures. *Trans. of ASHRAE*, 98(2), 455–461.

Yamashita, K., M. Kumagai, S. Sekita, A. Yabe, T. Taketani, and K. Kikuchi

(1991). Heat transfer characteristics of an EHD condenser. *Proc. 3rd ASME/JSME Thermal Engineering Joint Conf.*, Reno, U.S.A, March 17–22.

Yoshida, H., T. Komuro, and R. Echigo (1990). Heat-transfer control in a turbulent pipe flow with gas-solid suspensions by electric field. *Tran. JSME Ser. B*, 56(525), 226–234.

SYMBOLS

Ai	total film area (EHD surface granulation phenomenon)
A_T	thin film area
c_p	specific heat of fluid
di	initial film thickness (EHD surface granulation phenomenon)
d_T	thin film thickness
fe	body force generated in fluid under electric fields
k	polarized charge $[=(\epsilon - \epsilon_0)E]$
M	molecular weight
p	pressure
R	gas constant
T	temperature
t	time
t_c	relaxation time of electric charges in the working liquid
t_{EHD}	characteristic time of EHD phenomena
u	velocity
ϵ	dielectric constant of fluid
ϵ_0	dielectric constant of vacuum
λ	thermal conductivity
μ	viscosity
ρ	density of fluid
ρ_e	true electric charges
ρ_{es}	true electric charges at the interface
σ_e	electrical conductivity

26

Ozone Generation and Applications

U. Kogelschatz and B. Eliasson

Asea Brown Boveri
Baden, Switzerland

I. INTRODUCTION

Ozone was identified as a new chemical compound by Schönbein in 1839 (Schönbein, 1840). Its composition as a three-atomic version of the normally two-atomic oxygen molecule was suggested by Soret (1865). While Schönbein obtained traces of ozone by the electrolytic decomposition of water, Werner von Siemens (1857) found a method of reliably generating larger amounts of ozone by passing air or oxygen through a special electrical gas discharge. This silent discharge, which is also referred to as the dielectric barrier discharge, is a high-pressure nonequilibrium discharge. It is still used for large-scale industrial ozone production.

Ozone has a characteristic pungent odor and is a practically colorless gas. However, it exhibits an extremely strong ultraviolet absorption band at about 250 nm (Harley band). It is responsible for the strong filtering action of the stratospheric ozone layer protecting the biosphere against the dangerous short-wavelength radiation of the sun. The strong UV absorption is also made use of for measuring ozone concentrations in water and in the gas phase.

Ozone is a strong oxidizing and bleaching agent. Its germicidal and viricidal effects found early applications in protecting drinking water supplies endangered by cholera and typhus epidemics. Especially in Europe there has been a long tradition of utilizing ozone for the purification of

potable water. The first major ozone installations went into operation in Nice (France) in 1907 and in St. Petersburg (Russia) in 1910. Today, a large number of ozone installations are being used worldwide for water treatment.

II. PHYSICS OF OZONE GENERATION IN ELECTRICAL DISCHARGES

Although it is possible to produce small amounts of ozone by certain chemical reactions, in reality there is no alternative to using electrical discharges for the generation of larger ozone quantities. Glow discharges (Sabadil et al., 1980), corona discharges (Peyrous and Millot, 1981; Lécuiller and Goldman, 1988), pulsed high pressure discharges (Hosselet, 1973; Salge et al., 1980; Rosocha and Fitzsimmons, 1981), special double discharge techniques (Yamabe et al., 1987) as well as electron-beam controlled discharges (Fournier et al., 1979) and surface discharges (Masuda et al., 1988) have been investigated. A fairly recent proposition with surprisingly high ozone-generating efficiency is the use of a low-temperature glow discharge (Masuda et al., 1988; Chang and Masuda, 1988). It is operated at cryogenic temperatures at which ozone is extracted in liquid or solid form.

Today's industrial ozone production is exclusively based on silent discharges. For a detailed discussion of the older literature the reader is referred to the Gmelin *Handbook* article (1960) and to Lunt (1959). More recent scientific literature was reviewed by Kogelschatz (1983, 1988) and by Eliasson et al. (1987, 1991a,b) as well as in the two Russian books by Filippov et al. (1987) and Samoilovich et al. (1989). More technical aspects are addressed in the *Handbook of Ozone Technology and Applications* edited by Rice and Netzer (1982, 1984), in a book entitled *Ozone* by Horváth et al. (1985), and in *Ozone Science and Engineering*, the journal of the International Ozone Association, which first appeared in 1979.

A. The Silent Discharge Configuration

The historical experiment of Siemens consisted of two coaxial glass tubes forming an annular discharge gap. An alternating electric field was applied through the glass walls between external cylindrical electrodes. Air or oxygen passing through the annular discharge space in the axial direction was subjected to the action of the silent discharge and was partially converted to ozone.

In today's technical ozone generators a simpler configuration just employing one dielectric barrier is used (Fig. 1). The feed gas, oxygen or dried air, flows through a narrow discharge gap of about 1–2 mm in width. One side of the gap is formed by a metal electrode at ground potential, the other by a dielectric, normally glass, in contact with the high-voltage electrode. An alternating high voltage is applied to this configuration. The resulting alternating electric field in the discharge space must be high enough to cause electrical breakdown. Since ozonizers operate at pressures of a few bars, peak voltages of several kV are required to ignite the discharge.

B. Microdischarge Properties

From analyzing current oscillograms (Klemenc et al., 1937; Suzuki and Naito, 1952; Gobrecht et al., 1964), Lichtenberg figures (Buss, 1932; Bertein, 1973), and image intensifier recordings (Tanaka et al., 1978; Heuser, 1985), it was established that silent discharges under these conditions exhibit a discrete structure. The current flows across the gap through a large number of microdischarges or current filaments of typically nanosecond duration. Each microdischarge consists of a thin cylindrical conductive plasma column and spreads into a surface discharge at the dielectric boundary. Figure 2 shows a Lichtenberg figure obtained by placing a photographic plate into a small plate ozonizer with the emulsion facing the discharge space. After running the discharge for one half-wave, the plate was developed to show the "footprints" of individual microdischarges. Figure 2 clearly demonstrates the discrete nature of the silent discharge.

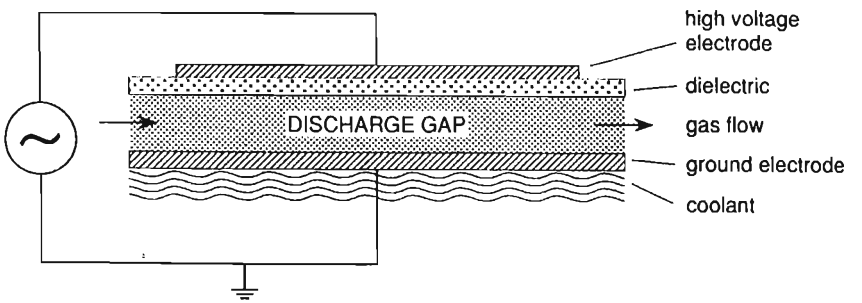


Figure 1 Electrode configuration of the silent discharge or dielectric barrier discharge.

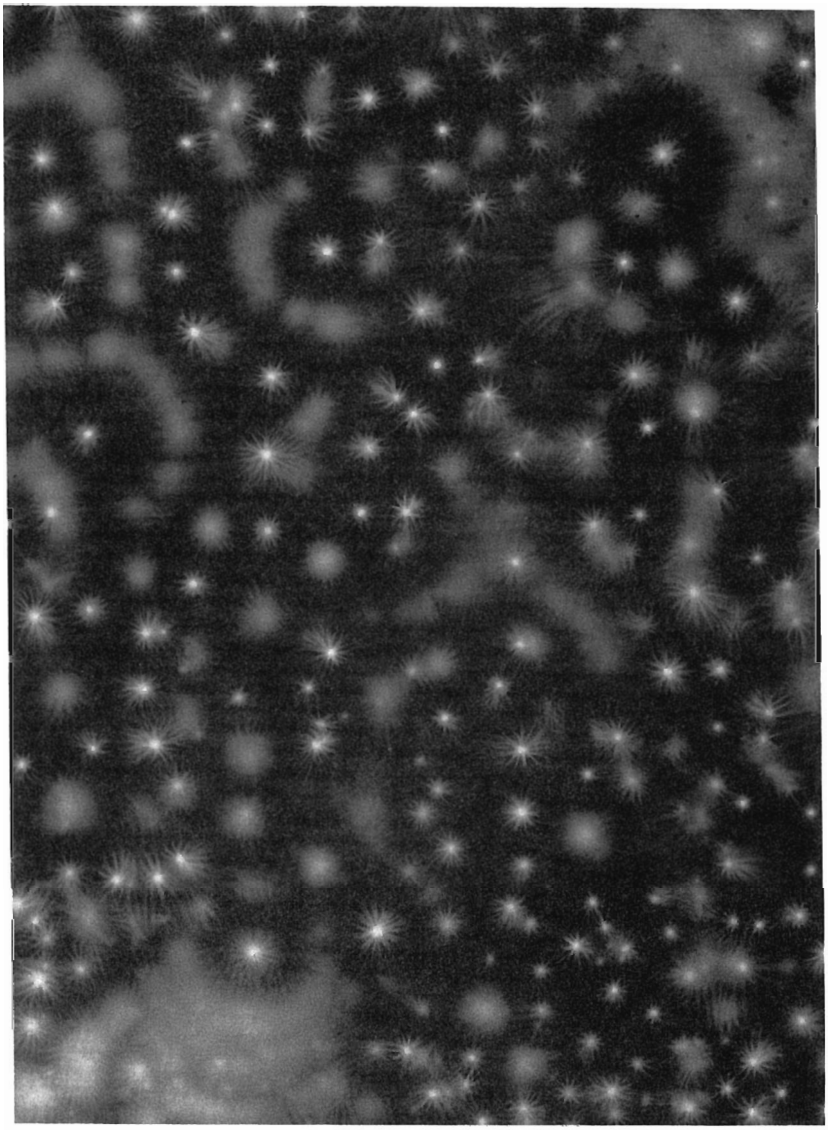


Figure 2 Photographic Lichtenberg figure showing the "footprints" of individual microdischarges (original size 7 × 10 cm). (From Kogelschatz, 1988.)

Detailed investigations into the properties of microdischarges have been carried out in recent years (Hirth, 1981; Drímal et al., 1987; Samoilovich et al., 1989; Mechtersheimer, 1989; Eliasson and Kogelschatz, 1991). The order of magnitude of different microdischarge parameters is listed in Table 1.

Knowledge of the plasma conditions inside the microdischarge columns is of eminent importance for modeling the reaction kinetics of ozone formation. The electrons generated in a microdischarge have certain mean energies and initiate all chemical reactions. They excite the neutral molecules leading e.g. through dissociation to atomic species that subsequently form ozone. The generation of the final product, ozone, can be optimized by influencing the plasma parameters in the microdischarges. This can be achieved by adjusting the operating parameters pressure and/or gap width as well as the properties of the dielectric barrier (permittivity, thickness). We can summarize the most important characteristics by stating that the microdischarges stay in a state of weakly ionized plasma with mean electron energies of a few eV while their gas temperature is close to the average temperature in the discharge gap.

The electron energy distribution and the mean electron energy are determined by the reduced electrical field E/n. At breakdown its value is given by the Paschen curve (about 100–150 Td, 1 Townsend = 10^{-17} V cm^2). It is a function of the product nd (particle density times gap spacing) and can be influenced by changing the pressure and the geometry. As long as current flows through the microdischarge, charge is accumulated on the dielectric. The charge generates an electrical field opposed to the original field and, after a few nanoseconds, results in the choking of the current flow at this location. As long as the external voltage is rising, additional microdischarges will occur at different locations. Thus the dielectric serves two functions. It limits the amount of charge and energy that goes into an individual microdischarge and it distributes the micro-

Table 1 Characteristic Microdischarge Properties

Duration	1–10 ns
Filament radius	0.1 mm
Peak current	0.1 A
Current density	100–1000 A/cm^2
Total charge	100–1000 pC
Electron density	10^{14}–10^{15} cm^{-3}
Electron energy	1–10 eV
Gas temperature	25–100°C

discharges over the entire electrode area. Changing the thickness of the dielectric or its permittivity will have a direct influence on microdischarge properties. Humidity changes the surface conductivity of the dielectric and also has a drastic influence on the microdischarges.

C. Average Quantities and Power Formula

Although the current flows in a large number of individual microdischarges, the overall electrical behavior of the discharge can be described quite adequately by average quantities. We introduce the discharge voltage U_{Dis} as the average voltage across the discharge gap during the active phases of the discharge and relate it to the power P.

$$P = \frac{1}{T}\int_0^T UI\,dt = \frac{U_{Dis}}{\Delta T}\int I\,dt \tag{1}$$

where ΔT is the time interval during which the discharge is active and the second integral is extended over the two active phases of the cycle. I is the discharge current and T the period of the applied alternating voltage. If C_D and C_g are the capacitances of the dielectric barrier and the discharge gap, respectively, $f = T^{-1}$ is the applied frequency, and $\hat{U}$ is the peak voltage, then the dissipated power is given by

$$P = 4fC_D U_{Dis}\left(\hat{U} - \frac{C_D + C_g}{C_D}U_{Dis}\right) \tag{2}$$

This power formula is valid for $\hat{U} \geq U_{Dis}(C_D + C_g)C_D^{-1}$ and was first derived by Manley (1943). Since U_{Dis} cannot be measured directly, it is sometimes advantageous to express the power P by measurable quantities.

$$P = 4fC_D\frac{C_D}{C_D + C_g}U_{Min}(\hat{U} - U_{Min}) \qquad \hat{U} \geq U_{Min} \tag{3}$$

where U_{Min} is the minimum external voltage necessary to sustain the discharge. At the moment U_{Min} is reached, microdischarge activity starts and continues until the peak voltage is reached (Fig. 3). This is repeated in analogous fashion in the negative half-wave.

All important quantities can be derived from a voltage-charge Lissajous figure (U-Q diagram), which is a useful tool in ozonizer research and development (Fig. 4). The U-Q diagram of a well designed ozonizer is an almost ideal parallelogram. During one period we see two passive phases ($1 \rightarrow 2$, $3 \rightarrow 4$) in which there is no discharge and the slope corresponds to the total capacitance $C_{tot} = (C_g^{-1} + C_D^{-1})^{-1}$.

During the active phases ($2 \rightarrow 3$, $4 \rightarrow 1$), the discharge voltage is U_{Dis} and the slope corresponds to the capacitance of the dielectric C_D. The

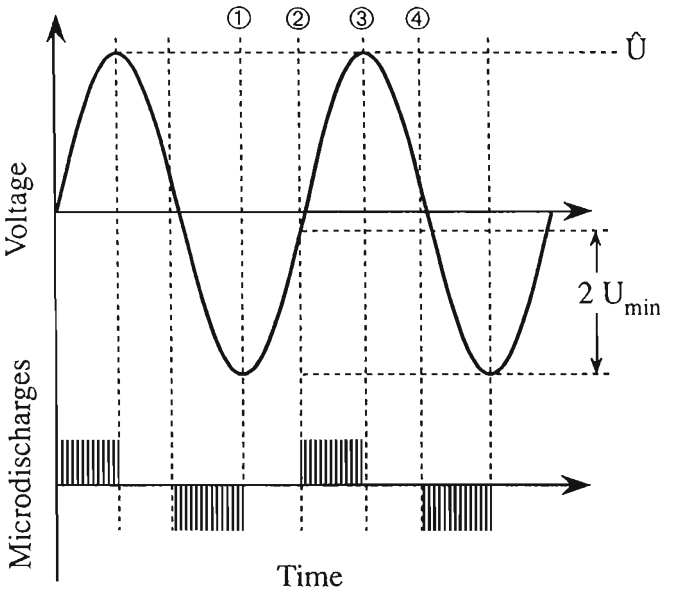


Figure 3 Schematic presentation of driving voltage and microdischarge activity.

area inside the parallelogram is proportional to the power dissipated during one cycle.

Such a discharge can be represented by a simple equivalent circuit (Fig. 5) with two antiparallel Zener diodes limiting the gap voltage to $\pm U_{Dis}$. As long as the external voltage is below U_{Min}, the device behaves like a

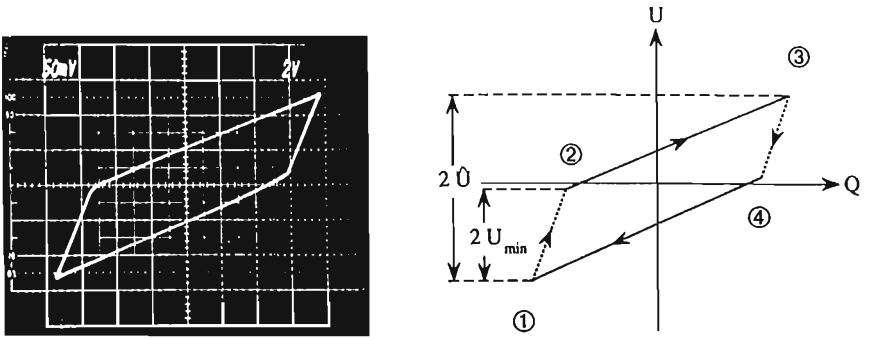


Figure 4 Voltage-charge Lissajous figure (U-Q diagram) of a laboratory ozonizer. (From Kogelschatz, 1988.)

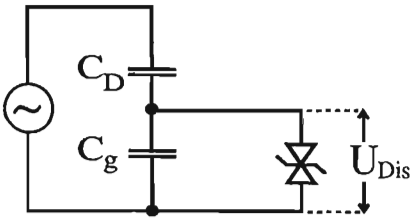


Figure 5 Simple equivalent circuit of a silent discharge configuration.

pure capacitance C_{tot} and no power is dissipated (passive phases). During the time when $U > U_{Min}$ the gap voltage is fixed at $\pm U_{Dis}$ and the power is given by the discharge current multiplied by U_{Dis} (active phases). The active phase is always terminated at the extreme values of the external voltage. At these points $dU/dt = 0$ and there is no displacement current across the dielectric.

From the power formula Eq. 2 some important conclusions can be drawn.

For a given geometry (C_D, C_g) the power depends only on the frequency f, the peak voltage $\hat{U}$, and the discharge voltage U_{Dis}. The shape of the feeding voltage is irrelevant.

For a fixed peak voltage and a given discharge configuration the power is strictly proportional to the frequency.

The discharge voltage is a derived quantity that can be calculated once U_{Min} is measured. U_{Dis} depends on the nature of the feed gas, the gap spacing, and the pressure.

III. CHEMISTRY OF OZONE FORMATION

A. Electron Kinetics in Oxygen and Air

Local electrical breakdown and microdischarge formation leads to the creation of a short current pulse. Detailed calculations of the electronic and ionic collision processes and reactions show that mainly the electrons are important for ozone formation (Gibalov et al., 1981; Eliasson et al., 1987; Braun et al., 1991). The electron energy distribution for a given reduced electric field E/n and the rate coefficients for the different processes can be calculated once the collision cross-sections of the different feed gas components are known.

The first step toward ozone formation is the generation of oxygen atoms. In pure oxygen, dissociation of O_2 molecules proceeds via two excited states.

$$e + O_2 \rightarrow e + O_2(A^3\Sigma_u^+) \rightarrow e + O(^3P) + O(^3P) \quad (4a)$$

$$\rightarrow e + O_2(B^3\Sigma_u^-) \rightarrow e + O(^3P) + O(^1D) \quad (4b)$$

The energy thresholds for these reactions to occur amount to 6 eV and 8.4 eV, respectively (Kogelschatz, 1983).

If air is used as a feed gas, the nitrogen molecules cannot be regarded as a passive carrier gas. Electrons in the above-mentioned energy range can excite nitrogen molecules to their triplet states, which are capable of dissociating oxygen molecules.

$$e + N_2 \rightarrow e + N_2(A^3\Sigma_u^+) \quad (5a)$$

$$\rightarrow e + N_2(B^3\Pi_g) \quad (5b)$$

$$N_2(A, B) + O_2 \rightarrow N_2 + 2O \quad (6a)$$

$$\rightarrow N_2O + O \quad (6b)$$

Also dissociation of N_2 molecules by electron impact and subsequent nitrogen atom reactions add to ozone formation (Eliasson et al., 1984).

$$e + N_2 \rightarrow e + 2N \quad (7)$$

$$N + O_2 \rightarrow NO + O \quad (8)$$

$$N + NO \rightarrow N_2 + O \quad (9)$$

In air about half of the ozone formed can be traced to reactions with excited nitrogen molecules and nitrogen atoms.

Electron kinetics in oxygen and in air has been treated by several authors (Yagi and Tanaka, 1979; Bonnet et al., 1980; Penkin et al., 1982; Eliasson et al., 1984, 1986, 1987; Rutscher and Wagner, 1985; Yoshida and Tagashira, 1986; Okazaki et al., 1988; Peyrous et al., 1989). Most models treat the reactions following a short electron pulse in a homogeneous medium. More advanced model calculations treat the temporal and spatial development of different particle species during the formation of a microdischarge (Eliasson and Kogelschatz, 1991a,b; Braun et al., 1991; Gibalov et al., 1991).

Predictions of the maximum efficiency can be given for the limiting case of small atom concentrations. In this case practically every oxygen atom reacts to form an ozone molecule. The efficiency of ozone formation is normally related to the enthalpy of formation of 1.48 eV/O_3 molecule or 0.82 kWh/kg ozone. An efficiency of 100% would consequently correspond to 0.68 O_3 molecules per eV or 1.22 kg/kWh. Figure 6 gives theoretical upper limits for the ozone formation efficiency in oxygen and in air. The curves suggest that in oxygen, reduced fields above 50 Td are required, while in air higher reduced fields above 150 Td are desirable. The theoretically achievable efficiencies correspond to 33% (400 g/kWh) in oxygen and 17% (200 g/kWh) in air.

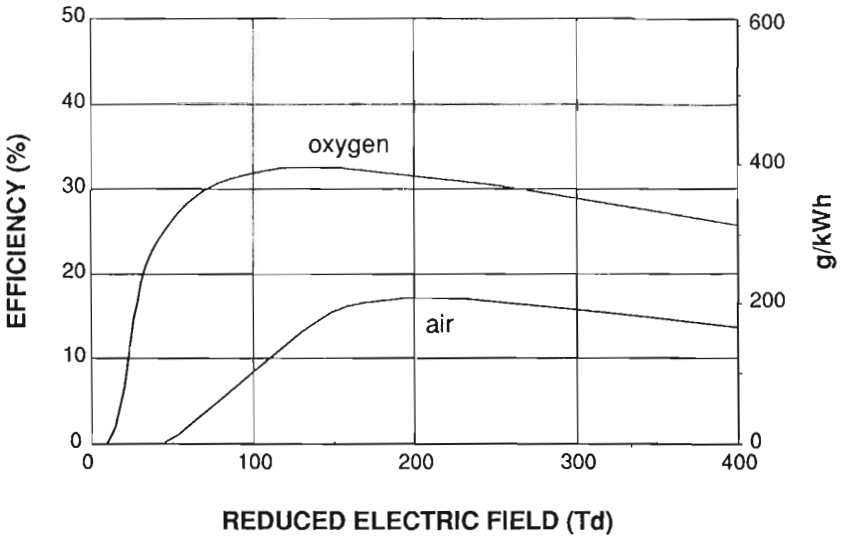


Figure 6 Theoretical prediction of maximum ozone generating efficiency in oxygen and air. 1 Td = 10^{-17} V cm^2. (Oxygen from Eliasson et al., 1987; air from Braun et al., 1991.)

The upper curve of Fig. 6 can be obtained from a simple approximation (Eliasson and Kogelschatz, 1981; Kogelschatz, 1983):

$$\eta = \frac{2\rho_D}{ev_d E/n} \tag{10}$$

where the efficiency η is given as the number of oxygen atoms produced per eV, ρ_D is the total dissociation rate coefficient ($4a + 4b$), e is the charge of an electron, and v_d is the electron drift velocity. The flat part in the efficiency curve results from the fact that the dissociation rate coefficient ρ_D has approximately the same dependence on the electron energy as the product $v_d E/n$.

Calculations with a comprehensive set of 70 rate equations (Eliasson et al., 1987) in oxygen show that the approximation Eq. 10 agrees within a few percent with the complete solution as long as the atom concentration is small ($[O]/n < 10^{-4}$) and energy losses due to ions can be neglected. The lower curve for the maximum efficiency in air was taken from Braun et al. (1991).

B. Free Radical Chemistry of Ozone Formation

While the electrons in a microdischarge attach within nanoseconds, some excited and atomic species can persist for much longer times. Another important difference is that electron collisions are mainly two-body reactions with rate coefficients depending on electron energy. Neutral particle reactions can be either two-body or three-body reactions, which implies that their relative importance depends on pressure. Their rate coefficients can also show a strong dependence on the gas temperature.

The main ozone formation process is the three-body reaction

$$O + O_2 + M \rightarrow O_3^* + M \rightarrow O_3 + M \tag{11}$$

where M is a third particle that is not changed in the reaction but is participating in the energy and momentum transfer. In ozonizers M can stand for O_2, N_2, or O_3. O_3^* is a transient excited ozone molecule, the initial reaction product. The ozone formation reaction Eq. 11 is favored over two-body reactions at higher pressures. This is one of the reasons why low pressure glow discharges are normally not used for ozone generation.

In oxygen at about atmospheric pressure, reaction Eq. 11 takes about 10 μs. In air it takes about twice that time (Sugimitsu and Okazaki, 1982; Eliasson et al., 1984). During this time oxygen atoms are present and can perform undesired side reactions like recombining to form O_2 molecules.

$$O + O + M \rightarrow O_2 + M \tag{12}$$

This side reaction puts an upper limit on the useful instantaneous atom concentration in a microdischarge. Since the O concentration enters quadratically in reaction Eq. 12 and only linearly in the ozone formation reaction Eq. 11, lowering the O concentration reduces the effect of recombination. Consequently, larger ozone concentrations have to be built up by a large number of relatively weak microdischarges.

As soon as there is a background ozone concentration the efficiency of ozone formation decreases because electrons, atoms, and excited species can destroy previously generated ozone molecules. With rising ozone concentration a monotonic decrease of efficiency is observed until, at the saturation concentration, the efficiency approaches zero. At this stage each subsequent microdischarge destroys as much ozone as it creates. This equilibrium state depends strongly on the temperature in the discharge gap. Higher temperatures lead to lower saturation concentrations.

For practical purposes a normalized efficiency versus concentration curve can yield a meaningful description of ozonizer performance (Fig. 7). The efficiency is normalized by the maximum obtainable efficiency $\eta(0)$ at vanishing ozone concentration, and the concentration axis is nor-

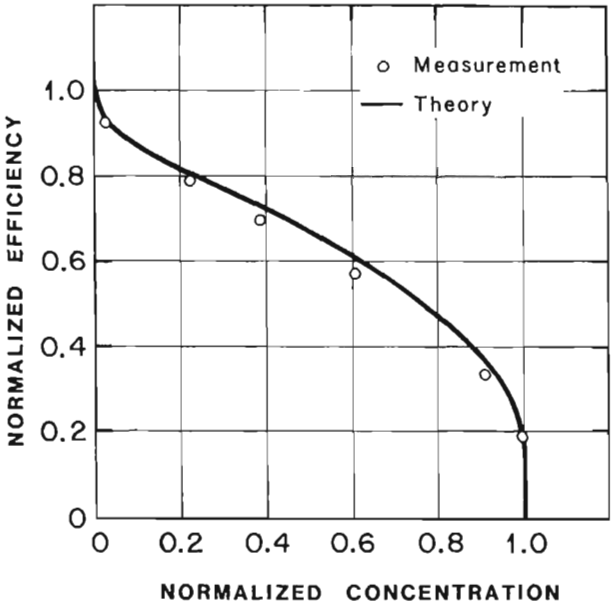


Figure 7 Normalized efficiency versus concentration curve of ozonizers. (From Kogelschatz, 1988.)

malized by the saturation concentration c_s representing the maximum attainable ozone concentration for the given geometry and operating conditions. The curve in Fig. 7 was calculated by solving a large system of differential equations describing ozone formation and ozone destruction processes in a large sequence of microdischarges in pure oxygen. Measurements follow the calculated curve closely.

The shape of the curve can be approximated by the following formula based on a simple plug flow model first proposed by Wassiljew et al. (1936) and later used by Filippov and Emel'yanov (1961):

$$\frac{\bar{\eta}(c)}{\eta(0)} = \frac{c/c_s}{\ln(1 - c/c_s)} \tag{13}$$

where c_s is the saturation concentration and $\bar{\eta}(c)$ is the efficiency of an ozonizer with an output ozone concentration c.

Ozonizers with different geometries and different operating conditions can have vastly different efficiencies $\eta(0)$ and saturation concentrations c_s. Nevertheless, the normalized efficiency curve Eq. 13 will represent the performance with reasonable approximation (Kogelschatz, 1983).

C. Nitrogen Oxides

When a silent discharge is running in air, traces of nitrogen oxides are also formed. Under typical ozonizer conditions nitrous oxide N_2O and dinitrogen pentoxide N_2O_5 can be detected in the output at concentrations that lie two orders of magnitude below the ozone concentration. For most applications, especially in water treatment, these concentrations are of no concern.

Reactions involving nitrogen oxides have become a major research goal in connection with atmospheric chemistry, smog situations, and flue gas cleaning processes. If ozonizers are operated at higher temperatures or higher specific energies (power/mass flow), NO_X concentrations increase, and finally ozone production breaks down completely. This state is referred to as "ozoneless mode" or "discharge poisoning." In the intermediate range, the nitrogen oxides N_2O, NO, NO_2, NO_3, and N_2O_5 could be detected (Yagi et al., 1979; Gibalov et al., 1985; Kogelschatz and Baessler, 1987; Eliasson and Kogelschatz, 1987) and simulated by model calculations (Samoilovich and Gibalov, 1986; Eliasson and Kogelschatz, 1986, 1987; Braun et al., 1988). At higher NO_X concentrations catalytic cycles involving oxygen atoms and O_3 molecules, also known from stratospheric chemistry, become important.

$$\begin{array}{lll} O + NO + M \rightarrow NO_2 + M & & NO + O_3 \rightarrow NO_2 + O_2 \\ \underline{O + NO_2 \quad \rightarrow NO + O_2} & & \underline{O + NO_2 \rightarrow NO + O_2} \\ O + O \quad \rightarrow O_2 & & O + O_3 \quad \rightarrow 2O_2 \end{array} \tag{14}$$

The left cycle results in enhanced "catalytic" recombination of oxygen atoms; the right cycle results in enhanced ozone destruction. The effect is quite dramatic and can easily be demonstrated in an ozonizer. Adding 0.1% of NO or NO_2 to the feed gas, air or oxygen, will completely inhibit ozone formation (Yagi et al., 1977; Hirth, 1981; Kogelschatz, 1983) irrespective of the applied power.

IV. TECHNICAL OZONE GENERATORS

A. Design Aspects

Most technical ozone generators make use of cylindrical discharge tubes of about 20–50 mm diameter and 1–2 m length. Glass tubes are mounted inside stainless steel tubes to form a discharge gap of 1–2 mm spacing (Fig. 8). The high voltage electrode is formed by a conductive coating, e.g., a thin aluminum film on the inside of the glass tubes. The preferred dielectric material is borosilicate glass (Pyrex, Duran). Other dielectrics, for instance ceramic tubes or enamel coatings on steel tubes, have found

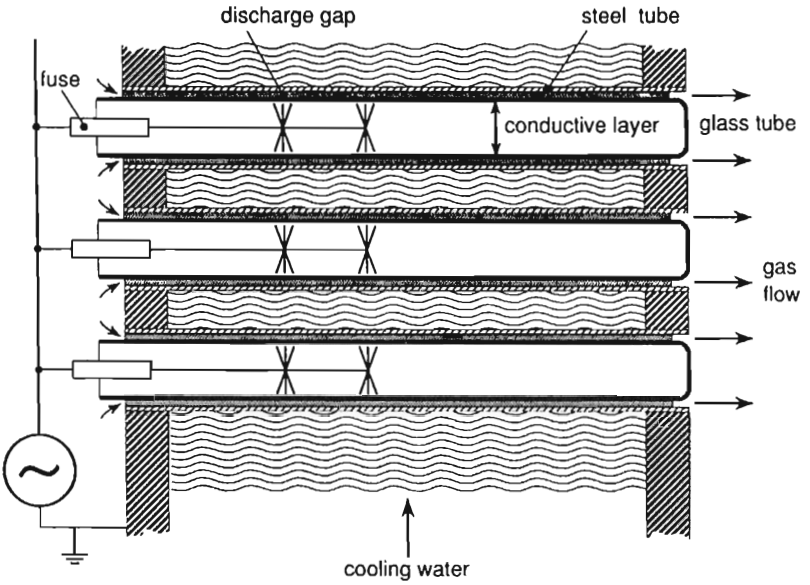


Figure 8 Schematic diagram of discharge tubes, gas flow, and cooling water flow in technical ozone generators (not drawn to scale).

only minor acceptance. Layered enamel coatings with optimized dielectric characteristics are under consideration again to meet the special requirements of ozone generators for pulp bleaching processes (high ozone concentrations at high pressure).

In many cases the discharge tubes are protected by individual high-voltage fuses placed on the tube axis in the lead to the specially formed brush contacts (Figs. 8 and 9). In case of a tube failure the fuse blows and disconnects the faulty part while the rest of the ozone generator stays in operation. Larger ozone generators have several hundred discharge tubes in one steel tank to provide enough electrode area for mass ozone production. The steel tubes are welded between two end plates thus forming a hermetically sealed cooling compartment. They are submersed in water for efficient heat removal in a cross-flow heat exchanger configuration (Fig. 8).

The desired narrow width of the annular discharge gap puts stringent requirements on the tolerances of steel and glass tubes as well as on their mounting procedures. Any variation in the gap spacing will have an influ-

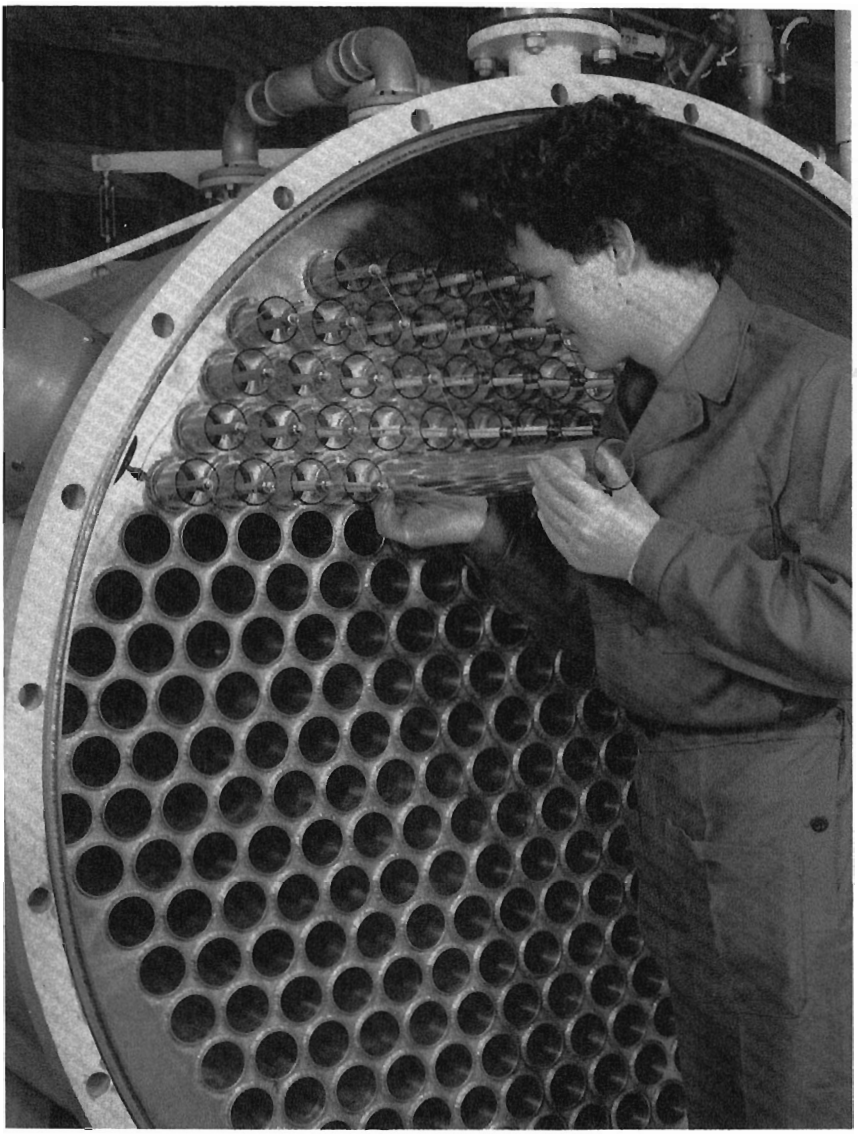


Figure 9 Entrance section of a medium-sized ozone generator with partially mounted glass tubes and high-voltage fuses.

ence on the electrical parameters (U_{Dis}, power density), on the heat transport, and on the gas flow.

B. Heat Balance

Ozone decomposes rapidly at elevated temperatures, and some of the rate coefficients describing ozone formation and destruction depend crucially on the gas temperature. Therefore it is essential that the heat generated by the discharge be removed in an efficient way. In the narrow annular gap after a few cm of entry length stationary radial profiles of the velocity and temperature distributions are established. The average increase of gas temperature ΔT_g is determined by a balance of the power not used for ozone formation—unfortunately the major part—and heat removal by radial heat conduction to the cooled steel electrode (Filippov and Emel'yanov, 1962; Pollo et al., 1985; Eliasson et al., 1987):

$$\Delta T_g = \frac{1}{3}\frac{d}{\lambda}\frac{P}{F}(1 - \eta) \tag{15}$$

where d is the gap spacing, λ the heat conductivity of the feed gas, P/F the power density referred to the electrode area, and η the efficiency of ozone generation. If the power, on a time average, is evenly dissipated in the gap volume, the resulting radial temperature distribution is a half-parabola with its peak value at the (uncooled) glass tube. The wall temperature T_w of the steel tube is determined by the cooling water. The average temperature in the discharge gap is given by

$$T_g = T_w + \Delta T_g = T_w + \frac{1}{3}\frac{d}{\lambda}\frac{P}{F}(1 - \eta) \tag{16}$$

With typical values for the operating parameters ($T_w = 20°C$, $d = 2 \times 10^{-3}$ m, $\lambda = 2.5 \times 10^{-2}$ W/mK, $P/F = 2$ kW/m^2, $\eta = 10\%$), we arrive at an average temperature of about 70°C in the gap. The peak value at the glass tube reaches approximately 90°C. According to Eq. 16, lowering T_w and using narrower discharge gaps will reduce the gas temperature. The most effective way of cooling the gap is the introduction of a second cooling circuit for the glass tube, which would reduce ΔT_g by a factor of four. Since this requires cooling of the high-voltage electrode, it is rarely done in technical ozone generators.

C. Power Supply Units

Traditionally, ozone generators were operated at line frequency. To increase the power, step-up transformers were used to raise the voltage to

about 20 kV. For smaller low-cost ozone installations this technique is still used. During the past decade modern high-power ozone generators switched to thyristor-controlled frequency convertors operating at frequencies between 0.5 and 5 kHz. According to the power formula Eq.2, the applied power is directly proportional to the driving frequency. Thus it was even possible to reduce the voltage to the range of 10 kV and still get a remarkable increase in power density. Typical values now reach 1–5 kW/m^2 of electrode area, which led to a drastic reduction in the size of ozone generating equipment. The lower voltages allow a much wider safety margin on the dielectric stress of the glass tubes, so that tube failure has become a rare event with well-designed medium-frequency ozone generators. A lower limit for the operating voltage is given by the requirement that the electric field in the gap be high enough to cause breakdown. This value depends on gap spacing and operating pressure. The preferred feeding circuits impress a square-wave current, in contrast to the sinusoidal feeding voltage used with line-frequency ozone generators. The higher frequencies brought the advantages of fast turn-off in case of emergency and less energy stored in the system. In addition, power supply units employing modern power electronics are more easily integrated into process automation and control systems.

D. Performance of Modern Ozone Generators

Modern ozone generators have profited from the better understanding of the ozone formation process in silent discharges and ways to influence microdischarge properties. The technical aim was attaining higher power densities, higher ozone generating efficiencies, and higher ozone concentrations.

For laboratory experiments the highest efficiencies at low ozone concentrations reach 8% (100 g/kWh) in air and 20% (250 g/kWh) in oxygen. Ozone concentrations as high as 6% (wt) in air and 20% in oxygen have been reported (Kogelschatz, 1988). These are, of course, extreme values reached in specially designed laboratory equipment and certainly do not correspond to economical operating conditions.

Typical figures for large ozone installations are given in Table 2.

The figures in Table 2 were taken from a comparison published by Erni et al. (1985). The numbers for the specific energy consumption include the preparation of the feed gas and auxiliary equipment.

Some points should be kept in mind. Ozonizers working with air operate at lower ozone concentrations and higher specific energies and corresponding cooling water requirements. Systems running on oxygen operate at higher ozone concentrations, have lower energy and cooling water re-

Table 2 Comparison of Ozone Generating Systems (300 kg ozone/h)

Feed gas	Air	Oxygen
Ozone concentration	2–3%	6%
Energy consumption per kg ozone	18–20 kWh	13–15 kWh
Cooling water consumption per kg ozone	2.5–3 m^3	1.5–2 m^3

Source: Erni et al., 1985.

quirements, but require about 50% higher investment costs to pay for the cryogenic air separation unit. The accuracy of such outlays has been demonstrated by the power evaluation of the Los Angeles oxygen-fed ozone system (Rakness and Stolarik, 1990). The ozone system has a capacity of 149 kg/h and has a tested specific energy consumption of 14.3 kWh/kg ozone in the concentration range of 5–6% (wt). Roughly half of this energy is spent on supplying the oxygen and the other half on the ozone generators. Figure 10 shows a photograph of the ozone generators. Since

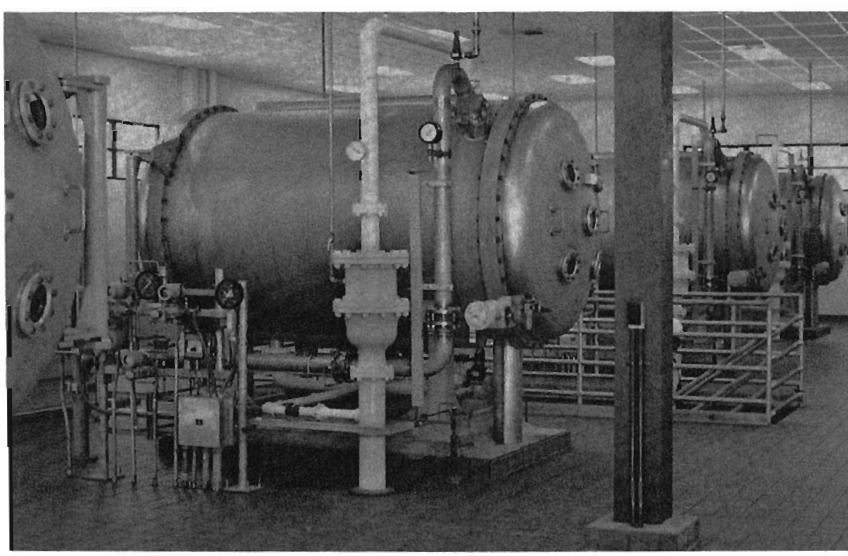


Figure 10 Ozone generators in the Los Angeles Aqueduct Filtration Plant. Six ozone generators are installed, each of which can produce 37.5 kg ozone per hour. (From Klein, 1990.)

oxygen is a considerable cost factor and only 5–6% is converted to ozone, more complex systems have been proposed that recycle the unconverted oxygen. This can be achieved either by recycling the off-gas, which normally requires a purification step, or by separating the oxygen from the ozone at the output of the ozone generators. This can be achieved in a pressure swing adsorption-desorption system in which ozone is preferentially adsorbed in silica gel columns at elevated pressure. Desorption is accomplished by depressurizing the saturated adsorber and using nitrogen from the cryogenic air separation stage as a carrier gas. During this process, the ozone concentration can be raised to about 8%. Readers interested in the economics of ozone generating systems of various sizes (1–100 kg/h) and different degrees of complexity are referred to Merz and Gaia (1990) and to Schulhof (1991).

Perhaps a remark is appropriate explaining why the simplest system producing ozone from air needs a feed gas preparation unit. The air fed into an ozone generator has to be free of dust and free of hydrocarbons and moisture. In the air preparation unit the dew point is lowered to about -60 or even -65°C, which corresponds to less than 5 ppm H_2O. Humidity interferes with the proper functioning of the dielectric as well as with the reaction kinetics by introducing additional species: H_2O, H, OH, HO_2, H_2O_2, HNO_2, HNO_3 (Peyrous, 1990). It leads to a drastic reduction of ozone generating efficiency and endangers the glass tubes by causing extremely strong microdischarges.

Large ozone installations produce some hundred kg ozone per hour at a power consumption of several megawatts. The capacity of one individual ozone generator operating at medium frequencies is today of the order of 30–50 kg/h and is likely to increase to a few hundred kg/h in the near future.

V. OZONE APPLICATIONS

A. Applications in Water Treatment

Ozone is a potent germicide and one of the strongest oxidants available. It is surpassed only by fluorine in its oxidizing power. Ozone molecules are only moderately stable and decay within a few days at room temperature. Elevated temperatures, ultraviolet radiation, or the presence of catalysts can accelerate this decay considerably. The natural decay products O_2 and, in the presence of organic compounds, also CO_2 cause no environmental problems. In addition, oxidation with ozone leaves no toxic residues that would have to be separated or disposed of.

Purification of drinking water has remained the major field of ozone application ever since its introduction at the beginning of this century. A recent survey (Tate, 1991) mentions more than 2000 water treatment plants using ozone worldwide, especially in Europe. The North American continent, due to its strong inclination toward chlorine disinfection, is lagging behind, with only about 90 ozone installations. This situation is changing rapidly as utilities are faced with the requirements of the Surface Water Treatment Rule, the Safe Drinking Water Act, and the impending Disinfection By-Products (DBP) Rule, as well as more stringent regulations for volatile and synthetic organic chemicals. The main targets for using ozone are disinfection, control of disinfection by-products (trihalomethanes), color, taste, odors, pesticides, and the removal of iron and manganese. In some cases pretreatment with ozone is reported to reduce turbidity and to result in higher filtration rates.

In addition to drinking water purification, ozone can also be used for the treatment of waste water (disinfection, removal of color and odor), of industrial wastes (phenolic and cyanide compounds), of contaminated ground water (volatile organics), and of cooling water circuits (control of microorganisms).

B. Applications in Pollution Control and Chemical Synthesis

Another important application of ozone is the treatment of off-gases. Due to its fast reaction rates even at diluted concentrations, ozone is used for the deodorization of gases containing hydrogen sulfide, mercaptans, or formaldehyde. Large-scale ozone applications have been suggested for the removal of NO_x from flue gases (Erni et al., 1985; Simachev et al., 1988; Klein, 1990; Saparov et al., 1990). Since nitric oxide (NO), the main NO_x component in flue gases, has a low solubility in water and cannot be directly removed by wet scrubbing, ozone is added to oxidize NO to NO_2 or N_2O_5. These components can be washed out with an ammonia solution to yield ammonium nitrate, which can be used as a fertilizer. In a similar way, SO_2 can be converted to ammonium sulfate.

Bleaching processes are other important applications where large amounts of ozone are used. Grey clay is bleached to yield white kaolin for making china and as an additive for high-quality white paper. Other examples are textiles, wax, effluents, and pulp. It has been suggested (Soteland, 1981; Klein, 1990; Sixta et al., 1991) that ozone can replace chlorine, which is still extensively used for bleaching in the pulp and paper industry. This way the discharge of organic chlorine compounds could be

eliminated. By combining oxygen, ozone, and hydrogen peroxide bleaches, pulp can be treated in a closed water circuit without using chlorine.

Ozone has also been used in chemical synthesis for the oxidation of oleic acid and the production of hydrochinon, certain hormones, antibiotics, vitamins, flavors, perfumes, and fragrances.

In all these applications ozone has definite advantages over other oxidizing agents. Only oxygen is added to the system and no objectionable side products or residues are formed. Ozone not used up in the process is taken care of in an ozone destruction unit which is based on thermal or catalytic ozone decomposition or a combination of both. As a consequence of its instability ozone is always produced on the site at a rate dictated by the process. No storage or transport of potentially dangerous chemicals is involved in ozone applications. As an additional advantage, ozone can be generated in remote locations or less developed countries wherever electricity is available.

REFERENCES

Bertein, H. (1973). Charges on insulators generated by breakdown of gas. *J. Phys. D: Appl. Phys.*, 6, 1910.

Bonnet, J., G. Fournier, D. Pigache, and M. Lécuiller (1980). Kinetics of species produced by an electron-beam controlled discharge in oxygen at atmospheric pressure. *J. Physique Lettres*, 41, L477.

Braun, D., U. Küchler, and G. Pietsch (1988). Behaviour of NOx in air-fed ozonizers. *Pure Appl. Chem.*, 60, 741.

Braun, D., U. Küchler, and G. Pietsch (1991). Microdischarges in air-fed ozonizers. *J. Phys. D: Appl. Phys.*, 24, 564.

Buss, K. (1932). Die elektrodenlose Entladung nach Messung mit dem Kathodenoszillographen. *Arch. Elektrotech.*, 26, 261.

Chang, J. S., and S. Masuda (1988). Mechanism of the ozone formation in a near liquid nitrogen temperature medium pressure glow discharge positive column. *Pure Appl. Chem.*, 60, 645.

Drímal, J., V. I. Gibalov, and V. G. Samoilovich (1987). The magnitude of the transferred charge in the silent discharge in oxygen. *Czech J. Phys.*, B 37, 1248.

Eliasson, B., and U. Kogelschatz (1981). Ozone production in an oxygen discharge: the rôle of electron impact dissociation of O_2 and O_3. Proceedings XV. Int. Conf. on Phenomena in Ionized Gases, Minsk, USSR, pp. 301–302.

Eliasson, B., and U. Kogelschatz (1986). N_2O formation in ozonizers. *J. Chim. Phys.*, 83, 279.

Eliasson, B., and U. Kogelschatz (1987). Nitrogen oxide formation in ozonizers. Proceedings 8th Int. Symp. on Plasma Chemistry, Tokyo, pp. 736–741.

Eliasson, B., and U. Kogelschatz (1991a). Modeling and applications of silent discharge plasmas. *IEEE Trans. Plasma Sci.*, 19, 309.

Eliasson, B., and U. Kogelschatz (1991b). Nonequilibrium volume plasma chemical processing. *IEEE Trans. Plasma Sci.*, 19, 1063.

Eliasson, B., U. Kogelschatz, and P. Baessler (1984). Dissociation of O_2 in N_2/O_2 mixtures. *J. Phys. B: At. Mol. Phys.*, 17, L797.

Eliasson, B., M. Hirth, and U. Kogelschatz (1987). Ozone synthesis from oxygen in dielectric barrier discharges. *J. Phys. D: Appl. Phys.*, 20, 1421.

Erni, P., M. Fischer, and H.-P. Klein (1985). Tonnage production of ozone for NOx removal from flue gas. Proceedings 7th World Ozone Congress, Tokyo, pp. 79–84.

Filippov, Yu. V., and Yu. M. Emel'yanov (1961). Electrical synthesis of ozone I: kinetics of the synthesis of ozone under flow conditions. *Russ. J. Phys. Chem.*, 35, 196.

Filippov, Yu. V., and Yu. M. Emel'yanov (1962). Electrical synthesis of ozone IV: effect of discharge intensity. *Russ. J. Phys. Chem.*, 36, 89.

Filippov, Yu. V., V. A. Boblikova, and V. I. Panteleev (1987). *Electrosynthesis of Ozone.* Moscow State University (in Russian).

Fournier, G., J. Bonnet, J. Fort, D. Pigache, and M. Lécuiller (1979). Towards a possible industrial production of ozone with an electron-beam controlled discharge. Proceedings 4th Int. Symp. on Plasma Chemistry, Zürich, pp. 742–747.

Gibalov, V. I., V. G. Samoilovich, and Yu. V. Filippov (1981). Physical chemistry of the electrosynthesis of ozone. The results of numerical experiments. *Russ. J. Phys. Chem.*, 55, 471.

Gibalov, V. I., V. G. Samoilovich, and M. Wronski (1985). Electrosynthesis of nitrogen oxides and ozone in an ozonizer. Proceedings 7th Int. Symp. on Plasma Chemistry, Eindhoven, pp. 401–406.

Gibalov, V., D. Braun, and G. Pietsch (1991). Spatial distribution of atomic oxygen concentration in barrier discharge channels. Proceedings 10th Int. Symp. on Plasma Chemistry, Bochum, pp. 3.2-7 p.1-3.2-7 p.6.

Gmelin Handbuch der Anorganischen Chemie (1960). Sauerstoff, Syst. Nr. 3: Ozon: Bildung und Zerfall auf elektrischem Wege. Verlag Chemie, Weinheim, pp. 1038–1077.

Gobrecht, H., O. Meinhardt, and F. Hein (1964). Über die stille Entladung in Ozonisatoren. *Ber. d. Bunsenges. f. phys. Chemie*, 68, 55.

Heuser, C. (1985). Zur Ozonerzeugung in elektrischen Gasentladungen. Ph.D. thesis, RWTH Aachen.

Hirth, M. (1981). Teilprozesse bei der Ozonerzeugung mittels stiller elektrischer Entladung. *Beitr. Plasmaphys.*, 20, 1.

Horváth, M., L. Bilitzky, and J. Hüttner (1985). *Ozone.* Elsevier Science, New York.

Hosselet, L. M. L. F. (1973). Increased efficiency of ozone production by electric discharges. *Electrochim. Acta*, 18, 1033.

Klein, H.-P. (1990). Commercial-scale generation and use of ozone. *ABB Review*, 1/90, 11 (Asea Brown Boveri, Baden, Switzerland).

Klemenc, A., H. Hinterberger, and H. Höfer (1937). Uber die Entladung in einer Siemens-Ozonröhre. *Zeitschr. Elektrochem.* 43, 708.

Kogelschatz, U. (1983). Ozone synthesis in gas discharges. Proceedings XVI Int. Conf. on Phenomena in Ionized Gases, Düsseldorf, Germany, Invited Papers, pp. 240–250.

Kogelschatz, U. (1988). Advanced ozone generation. In *Process Technologies for Water Treatment* (S. Stucki, ed.). Plenum Press, New York, pp. 87–120.

Kogelschatz, U., and P. Baessler (1987). Determination of nitrous oxide and dinitrogen pentoxide concentrations in the output of air-fed ozone generators of high power density. *Ozone Sci. Eng.*, 9, 195.

Lécuiller, M., and M. Goldman (1988). Analyse des régimes et des zones de la décharge couronne en termes de production d'ozone. *J. Phys. D: Appl. Phys.*, 21, 51.

Lunt, R. W. (1959). The mechanism of ozone formation in electrical discharges. *Adv. Chem. Ser.*, 21, 286.

Manley, T. C. (1943). The electrical characteristics of the ozone discharge. *Trans. Electrochem. Soc.*, 84, 83.

Masuda, S., K. Akutsu, M. Kuroda, Y. Awatsu, and Y. Shibuya (1988a). A ceramic-based ozonizer using high-frequency discharge. *IEEE Trans. Ind. Appl.*, 24, 223.

Masuda, S., S. Koizumi, J. Inoue, and H. Araki (1988b). Production of ozone by surface and glow discharge at cryogenic temperatures. *IEEE Trans. Ind. Appl.*, 24, 928.

Mechtersheimer, G. (1989). Influence of different dielectric materials on the ozone formation process. Proceedings 9th Ozone World Congress, New York, Vol. 2, pp. 1–12.

Merz, E., and F. Gaia (1990). Comparison of economics of various ozone generating systems. *Ozone Sci. Eng.*, 12, 401.

Okazaki, S., H. Sugimitsu, H. Niwa, M. Kogoma, T. Moriwaki, and T. Inomata (1988). Ozone formation from the reaction of O_2-activated N_2 molecules and a new type of ozone generator with fine wire electrode. *Ozone Sci. Eng.*, 10, 137.

Ozone Science and Engineering. Pergamon Press, New York (Now: Lewis Publishers, Boca Raton, FL). The official journal of the International Ozone Association.

Penkin, N. P., V. V. Smirnov, and O. D. Tsygir (1982). Investigation of the electrokinetic properties and of the dissociation of O_2 molecules in an oxygen discharge. *Sov. Phys. Techn. Phys.*, 27, 945.

Peyrous, R. (1990). The effect of relative humidity on ozone production by corona discharge in oxygen or air. A numerical simulation. *Ozone Sci. Eng.*, 12, 19 and 41.

Peyrous, R., and R. -M. Millot (1981). Ozone generation in oxygen by corona

discharges in a point-to-plane gap subjected to a chopped DC positive voltage. *J. Phys. D.: Appl. Phys.*, 14, 2237.

Peyrous, R., P. Pignolet, and B. Held (1989). Kinetic simulation of gaseous species created by an electrical discharge in dry or humid oxygen. *J. Phys. D: Appl. Phys.*, 22, 1658.

Pollo, I., J. Ozonek, and S. Fijalkowski (1985). Temperature distribution in the ozonizer. Proceedings 7th Int. Symp. on Plasma Chemistry, Eindhoven, pp. 407–411.

Rakness, K. L., and G. F. Stolarik (1990). Power evaluation of the Los Angeles oxygen-fed ozone system. *Ozone Sci. Eng.*, 12, 355.

Rice, R. G., and A. Netzer, eds. (1982, 1984). *Handbook of Ozone Technology and Applications*, vols. 1 and 2. Ann Arbor Science, Ann Arbor, MI, and Butterworth, Stoneham, MA.

Rosocha, L. A., and W. A. Fitzsimmons (1981). Criteria for the generation of homogeneous oxygen plasmas suitable for ozone synthesis. Proceedings 5th Int. Symp. on Plasma Chemistry, Edinburgh, pp. 421–426.

Rutscher, A., and H. E. Wagner (1985). The model of macroscopic kinetics in nonequilibrium plasma chemical reactions. *Beitr. Plasmaphys.*, 25, 315.

Sabadil, H., P. Bachmann, and H. Kastelewicz (1980). Reaktionskinetik der Ozonbildung in der Sauerstoffglimmentladung. *Beitr. Plasmaphys.*, 20, 283.

Salge, J., H. Kaerner, M. Labrenz, K. Scheibe, and P. Braumann (1980). Characteristics of ozonizers supplied by fast rising voltages. Proceedings 6th Int. Conf. on Gas Discharges and their Applications, Edinburgh, pp. 94–97 (IEE Conf. Publ. No. 189).

Samoilovich, V. G. and V. I. Gibalov (1986). Kinetics of the synthesis of ozone and nitrogen oxides in a barrier discharge. *Russ. J. Phys. Chem.*, 60, 1107.

Samoilovich, V. G., V. I. Gibalov, and K. V. Kozlov (1989). *Physical Chemistry of the Barrier Discharge*. Moscow State University (in Russian).

Saparov, M. I., S. S. Novoselov, S. A. Fadeev, and T. S. Gerasimova (1990). Reducing pollutant emissions to atmosphere from future coal-fired power stations. *Therm. Eng.*, 37, 41.

Schönbein, C. F. (1840). Beobachtungen über den bei der Elektrolysation des Wassers und dem Ausströmen der gewöhnlichen Electricität aus Spitzen sich entwickelnden Geruchs. *Poggendors Ann. Phys. Chem.*, 50, 616.

Schulhof, P. (1991). The price of ozonation in the Paris (France) suburbs. *Ozone Sci. Eng.*, 13, 607.

Siemens, W. (1857). Uber die elektrostatische Induction und die Verzögerung des Stroms in Flaschendrähten. *Poggendors Ann. Phys. Chem.*, 102, 66.

Simachev, V. Yu., S. S. Novoselov, V. A. Svetlichnyi, A. F. Gavrilov, M. V. Gorokhov, V. I. Semenov, V. A. Ryzhikov and V. V. Demchuk (1988). An investigation of the ozone-ammonia method of simultaneous desulphurisation and denitrification of flue gases when burning Donetsk coals. *Thermal Eng.*, 35, 171.

Sixta, H., G. Götzinger, A. Schrittwieser, and P. Hendel (1991). Medium consistency ozone bleaching: laboratory and mill experience. *Papier*, 45, 610.

Soret, J. L. (1865). Recherches sur la densité de l'ozone. *Ann. Chim. Phys.* (Paris), 7, 113.

Soteland, N. (1981). Potential use of ozone in the pulp and paper industry. Proceedings 5th Int. World Ozone Congress, Berlin, pp. 283–292.

Sugimitsu, H., and S. Okazaki (1982). Measurement of the rate of ozone formation in an ozonizer. *J. Chim. Phys.*, 79, 655.

Suzuki, M., and Y. Naito (1952). On the nature of the chemical reaction in silent electrical discharge II. *Proc. Jap. Acad.*, 28, 469.

Tanaka, M., S. Yagi, and N. Tabata (1978). The observation of silent discharge by image intensifier. *Trans. IEE of Japan*, 98A, 57 (in Japanese).

Tate, C. H. (1991). Survey of ozone installations in North America. *J. AWWA*, 83/5, 41.

Wassiljew, S. S., N. I. Kobosev, and E. N. Erjemin (1936). Reaktionskinetik in elektrischen Entladungen. *Acta Physicochimica U.R.S.S.*, 5, 201.

Yagi, S., and M. Tanaka (1979). Mechanism of ozone generation in air-fed ozonizers. *J. Phys. D: Appl. Phys.*, 12, 1509.

Yagi, S., M. Tanaka, and N. Tabata (1977). The influence of NOx diluent on the ozone generation by silent discharge. *Trans. IEE of Japan*, 97A, 609.

Yagi, S., M. Tanaka, and N. Tabata (1979). Generation of NOx in ozonizers. *Trans. IEE of Japan*, 99, 41.

Yamabe, C., M. Hayashi, Y. Tachioka, and K. Horii (1987). Ozone generation characteristics by new type double discharge ozonizer, Proceedings 8th Int. Symp. on Plasma Chemistry, Tokyo, pp. 742–747.

Yoshida, K., and H. Tagashira (1986). Computer simulation of ozone electrosynthesis in an N_2/O_2 mixture-fed ozonizer. *Memoirs of the Kitami Inst. of Technol.*, 18, 11.

This Page Intentionally Left Blank

27

Combustion Flue Gas Treatments

Massimo Rea

University of Padova
Padova, Italy

I. INTRODUCTION

The total electric power produced in 1990 has been 11,700 TWh; 64% of this electricity was produced by burning 1220 Mtoe of coal, 340 Mtoe of fuel oil, and 460 Mtoe of natural gas, and it produced over 7200 million tons of CO_2, about 40 million tons of NO_X, and a quantity of SO_2 ranging from 70 to 90 million tons (Khatib and Munasinghe, 1992).

As far as SO_2 is concerned, only 50% of worldwide production is presently removed, and there is a general demand for a larger reduction of emissions by adopting desulphurization plants based on several commercial processes. Such processes allow a removal efficiency of about 80%, but they require high investments, exhibit large operating costs, and produce by-products that need to be safely allocated.

The removal of NO_X from flue gas is also becoming important, and at present it is achieved to a certain extent by new combustion technologies, by catalytic reduction reactors, or by a combination of both.

Recently the possibility of removing gaseous noxious emissions with a pulse electrostatic technology has been verified. The main interest in such application is related to

1. The possibility of the simultaneous removal of NO_X and SO_2 by means of a dry, relatively simple, process

2. The similarity of this technology to the well-established electrostatic precipitator technology
3. The possibility of utilizing the end products, ammonium nitrates and sulphates, as fertilizers or soil conditioners

II. BASIC PHYSICAL PRINCIPLE

The effects of the irradiation of combustion gases were occasionally noticed by several researchers (Palumbo, and Fraas, 1971). The irradiation of a gas with electrons having high energy was deeply investigated by Kawamura et al. (1979) and by Tokunaga and Suzuki (1984). They stated that the irradiation produces ionized species and radicals capable of initiating chemical reactions leading to the oxidation of NO_X and SO_2 and, in the presence of ammonia, to the formation of ammonium nitrates and sulphates. The irradiation was first achieved using electron beams; then it was experimentally recognized that a corona discharge occurring in a high electric field can be a source of electrons with enough energy to produce active radicals (Mizuno et al., 1986; Masuda and Nakao, 1986; Civitano et al., 1986).

It is well known that the characteristics of a corona discharge strongly depend on the divergency of the electric field produced by the electrode arrangement and on the rate of rise of the applied voltage, and that the evolution of the corona discharge into a spark discharge depends on the duration of the applied voltage (Gallimberti, 1971).

In order to increase the number of electrons with higher energy, fast rising and short duration pulse voltages must be applied to electrode arrangements leading to high divergent electric fields, such as rod-plane or wire-plane geometries. The duration of the applied voltage must be short enough to prevent the thermalization of the corona streamers. The greater the voltage rise, the greater will be the electric field when the corona streamers develop and the higher will be the mean energy of the produced electrons. The role played by the geometry of the electrode arrangement is manifold: the divergency of the electric field, other conditions being equal, decreases the possibility of thermalization of the first corona streamers, but it is supposed to decrease the region where the first corona streamers develop in a high electric field.

In any case, only the first corona streamers are supposed to be effective in producing electrons with energy in the range 5 to 15 eV, able to interact with the gas molecules and to produce active radicals, while secondary corona streamers should be considered as a source of energy loss.

The fraction of energy absorbed by each gas component, when ionizing radiation interacts with a multicomponent gas system, is proportional to

its partial pressure. For a flue gas composition of 68% N_2, 15.5% O_2, 10.5% H_2O, and 6% CO_2 at 120°C, the primary processes have been summarized by Civitano et al. (1986) as in Table 1, in which the number in parentheses represents the G value, normalized to 100 eV, of each species, i.e., the number of molecules produced per 100 eV of energy absorbed by the system. The G value is better defined by

$$\frac{dX_i}{dt} = G \cdot \frac{D}{100 \cdot N}$$

in which dX_i/dt represents the production rate of the primary species i with the irradiation dose D ($V^{-1}\ s^{-1}$), N is Avogadro's number.

The secondary chemical reactions that lead to the formation of ammonium nitrates and sulphates are further complicated because of the presence of ammonia; they also depend on the temperature and the presence of liquid and solid aerosol particles (Chang, 1987, 1989).

Some attempts have been made to model the complex electrical and physicochemical processes, but they have had little or no success in predicting the removal rate in specified conditions (Gallimberti, 1991). It is believed that a deeper knowledge of the basic physical and chemical phenomena is required, and a number of laboratory-scale investigations are being carried out with this purpose.

III. BENCH SCALE TESTS

Following some laboratory experiments carried out by Masuda et al. (1987), which assessed the physical feasibility of the process, bench scale tests have been run with real gas. The greater bulk of the experimental data came from tests run in a test rig installed at the Marghera power station of ENEL (the electric power authority in Italy) and have been reported by Civitano et al. (1987) and Dinelli (1990). The test rig was installed in the slipstream of the flue gas duct from the outlet of the electrostatic precipitator installed downstream of a coal burner boiler of 70 thermal MW.

Table 1 Basic Processes

N_2		$N_2^+(2.27)$	$e^-(2.96)$	$N^+(0.69)$	$N(3.5)$	$N_2^*(0.29)$
O_2		$O_2^+(2.07)$	$e^-(3.30)$	$O^+(1.23)$	$O(1.41)$	$O_2^*(0.29)$
	100 eV →					
H_2O		$H_2O^+(2.56)$	$e^-(3.23)$	$H(4.07)$	$OH(4.17)$	$O(0.45)$
CO_2		$CO_2^+(2.24)$	$e^-(2.96)$	$CO^+(0.51)$	$O^+(0.21)$	$O(0.38)$

In Fig. 1 the experimental layout is presented and with special reference to the measuring system, while in Table 2 the characteristics of the main reactors used are reported.

The diameter of the emitting wire and the duct width are strongly correlated with the value of the applied voltage; 3 mm for the diameter of the emitting wires and 200 mm for the duct width proved to be a good compromise, with a crest value of the applied pulse voltage between 100 and 150 kV.

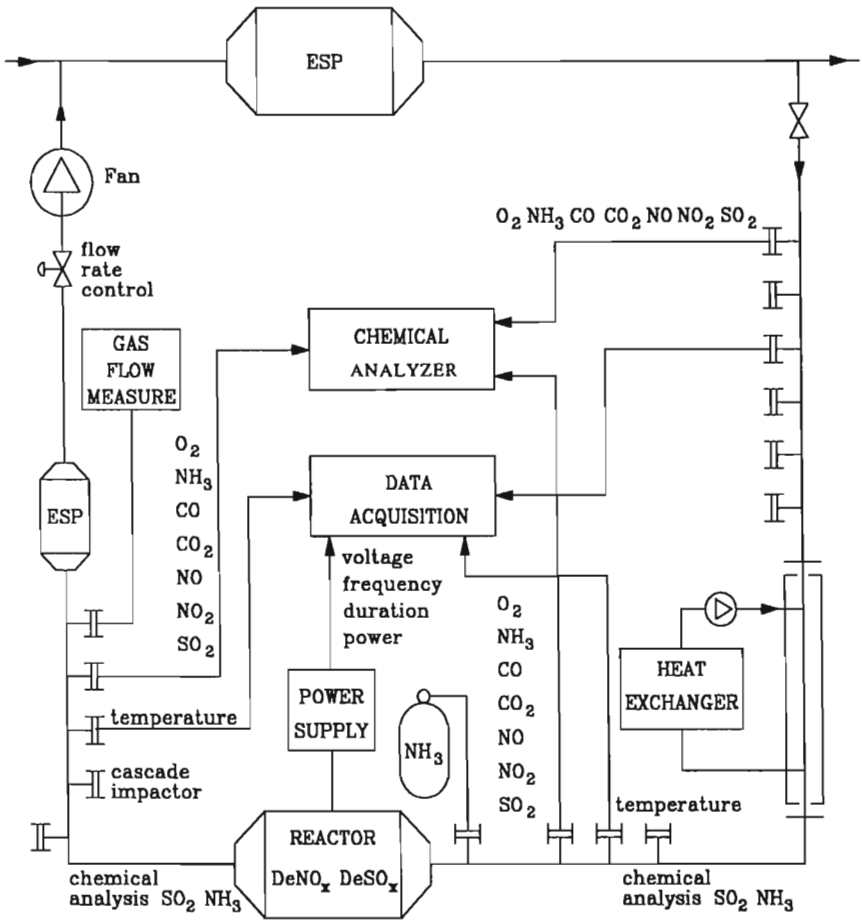


Figure 1 Experimental layout.

Table 2 Main Characteristics of the Reactors Used

	TR100/1	TR100/2	TR100/3		
Reactor geometry	parallel	parallel	cylindrical		
Channel length (m)	1.4	1.5	1.5		
Channel width or diameter (mm)	200	200	200		
Total plate surface (m^2)	8.4	12.0	8.5	13.2	15.1
Total volume (m^3)	0.84	1.2	0.42	0.66	0.75
Number of emitting wires	14	20	9	14	15
Distance between wires (mm)	200	200			
Emitting wire active length (m)	1.5	2.0	1.5		
Number of channels	2	2	9	14	15

In the case of parallel plate reactors it has been remarked that the corona streamers fill less than 20% of the total volume, while in case of the cylindrical reactor they fill all the volume.

In Table 3 the main flue gas experimental conditions are reported. The ammonia was injected upstream of the reactor, and it was from 0.7 to 0.8 times the molar ratio of NO_X plus SO_2.

The removal of SO_2 appeared to be governed mainly by the thermochemical reaction with ammonia, thus ensuring a rapid removal of SO_2

Table 3 Main Flue Gas Experimental Conditions

	TR1000/1	TR1000/2	TR1000/3
Flow rate (Nm^3/h)	600	470 & 600	500
Temperature (°C)	100 & 70	100	80 ÷ 100
Gas residence time (s)	3.7	5.4 & 6.9	3.4 & 7.0 & 5.4
Input NO_x ($mg(NO_2)/Nm^3$)	880 ÷ 1130	615 ÷ 1130	1030 ÷ 1130
(ppmv)	430 ÷ 550	300 ÷ 550	500 ÷ 550
Input SO_2	1030 ÷ 1430	1285	1000 ÷ 1140
	360 ÷ 550	450	350 ÷ 400
Solid particles (mg/Nm^3)	150	150	80 ÷ 120
Ammonia over (NO_x + SO_2) molar ratio (%)	0.7	0.8	0.8
Gas content N_2 (%)		73	
Gas content CO_2 (%)		13	
Gas content O_2 (%)		6	
Gas content H_2O (%)		8	

even without energization of the gas; it is however enhanced by the pulse corona energization, which ensures by itself (without ammonia injection) a removal rate of up to 20%. The SO_2 removal with ammonia injection and pulse corona energization was about 75% at a gas temperature of 100°C and about 90% at a gas temperature of 70°C.

In Fig. 2a,b the removal of NO_X is plotted versus the specific energy input to the gas for different reactors and different initial NO_X input concentrations.

It appears very clear that the removed quantity of NO_X depends on the energy absorbed by the gas as a consequence of the corona discharge. Thus the removal efficiency decreases as the initial NO_X concentration decreases.

Tests were also carried out with hydrated lime injection instead of ammonia injection; the results however indicated a much lower removal efficiency.

IV. TECHNICAL AND ECONOMIC PROJECTION

After the described preliminary tests, a technical projection was tried by Rea (1991), who suggested that an energy yield of about 14 Wh/Nm^3 would

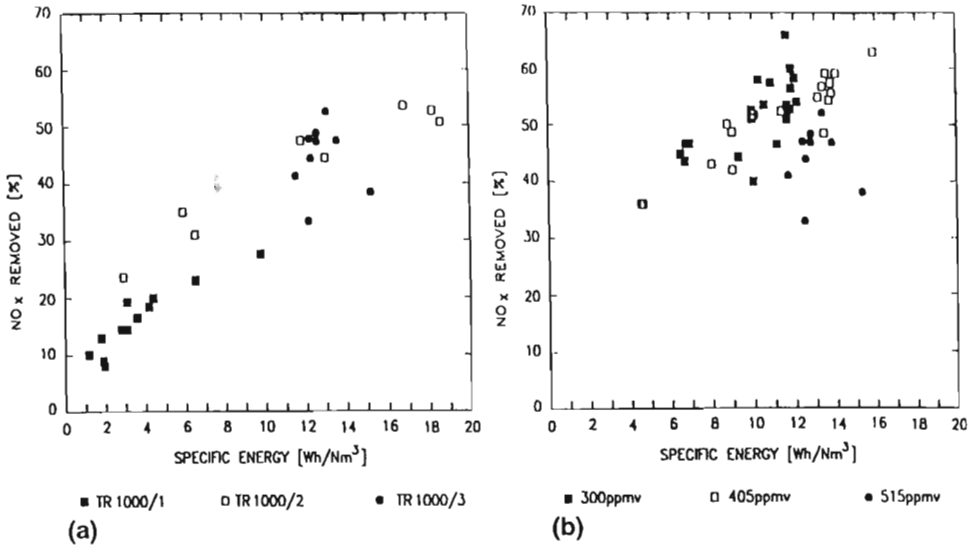


Figure 2 NO_x removal rate versus specific energy input (a) for different reactors and (b) for different input concentrations.

be required in order to reach a NO_X removal efficiency of 70%. Assuming an energy density of 2.4 J per meter of wire and per pulse, and a pulse repetition rate of 300 Hz, the power transfer would become 18 kW/m^3, and this would mean, for a 320 MW power station, a reactor volume of about 800 m^3.

Also an economic projection was made considering the following items:

Capital costs	Operating costs
Land	Ammonia consumption
Reactor	Electric energy consumption
Ammonia injection system	Maintenance
Pulse power supplies	

The land cost, although difficult to determine, should not be considered a penalizing factor, even in the case of retrofitting applications, because the reactor size is equal to or smaller than the size of the ESP installed for the removal of particulate matter. Also the reactor cost can be estimated on the basis of the cost of an equal-size precipitator, taking into account an increase of corrosion prevention criteria.

The cost of the pulse power supplies was very difficult to estimate because it involves new technologies. Assuming the worst case, it was estimated as the scale-up of the cost of the experimental pulse generator. Also the cost of ammonia consumption was evaluated pessimistically to be on the order of $0.60/kg.

The estimation of the electric energy cost implies the estimation of the pulse voltage generator efficiency. Although the efficiency of the experimental pulse voltage generator was lower, a figure of 0.75 was considered adequate. This means a need of electric power of 19 $W/(Nm^3/h)$, which corresponds to 20 MW for a 320 MW coal unit.

The preliminary analysis, as illustrated in Table 4, indicates, with reference to a power station of 320 electrical MW burning a low-sulfur coal, a capital investment lower than $10 million and an incidence cost in the order of 7 mills/kWh.

V. RECENT DEVELOPMENTS

The bench experiments described showed the need to optimize the process in order

Table 4 Tentative Economic Projection

Size of the boiler (MWe)	320
NO_x concentration (mg/Nm^3)	1200
SO_2 concentration (mg/Nm^3)	2000
Reactor volume (m^3)	2400
Electrical power (MW)	18
Ammonia consumption (Kg/h)	1550
Investment costs ($ million)	23.8
mechanical ($ million)	1.7
power generators ($ million)	20.0
additional ($ million)	2.1
Levelized operational costs ($ million)	8.8
energy ($ million)	3.5
ammonia ($ million)	5.3
Specific cost of plant ($/Kw)	74
Incidence on energy cost (mills/kWh)	5.0

To prevent any possible ammonia leakage
To reduce ammonia consumption
To increase the SO_2 and NO_X removal efficiency with higher temperature, lower energization, and lower humidity
To reduce the production of ozone and toxic by-products
To increase the collection efficiency of the ultrafine solid particles produced by the process

It was recognized that a deeper knowledge of basic phenomena was required; several laboratory-scale and bench-scale experiments have been started.

A better understanding of the chemical phenomena suggested a possible interaction between the oxidation of the sulphur and nitrogen oxides, and experimental evidence has been obtained, as reported by Civitano (1992), that a proper injection of oxygenated water at a given stage of the process would reduce to zero any ammonia leakage and increase the removal efficiency of NO_X at a given energization.

Also, a possible synergic effect is suspected and is presently being investigated between the plasma catalysis produced by corona discharge and a chemical catalysis produced by such elements as manganese and vanadium, which may exhibit different oxygen bonds.

A better understanding of the pulse corona discharge showed that the electrons produced by the first streamers, which develop in a few tens of

nanoseconds, have mean energies between 10 and 14 eV while the electrons produced by the secondary streamers have much lower mean energies. This suggests the use of corona discharges produced by very short voltage pulses, and the techniques for producing, with high energy efficiency, high-voltage pulses that last a few hundreds of ns and have dV/dt of on the order of 10^{13} V/s are now being investigated. A technique that has given good results is to superimpose the voltage pulses on a dc base voltage; using this technique it was possible to produce pulse corona discharges with an energy efficiency of up to 90% (Rea and Yan, 1992).

The technical feasibility of the process will be further investigated through the design and construction of pilot plants that will represent scale-ups of the bench experiment. In Italy ENEL is planning to set up a 10.000 Nm^3/h pilot plant, while in Japan Ebara is planning to set up two pilot plants, one of 2000 Nm^3/h supplied with flue gas from fossil fuel combustion and the other of 200.000 Nm^3/h supplied from a municipal refuse incinerator.

Further study is required for the industrial utilization of the process and is now in progress. Of great importance will be the qualification of the by-products in respect of the admissible content of solid particles; should the process installed for the cleaning of the flue gas from coal be burners, and should the content of heavy metals in the fly ash be low enough, it has been suggested to employ a mixture of fly ash and ammonium sulphates and nitrates as a soil softener for compact basic soils.

VI. OTHER APPLICATIONS

Although $DeNO_x/DeSO_2$ is thought to be the largest possible application of pulse corona discharges, other applications have been investigated by Masuda et al. (1987). An application receiving great interest is the possibility of decomposing volatile organic matter (VOC): cryogenic gases such as freon and organic solvents such as benzol, toluol, etc. (Chang et al., 1991; Yamamoto et al., 1992).

For a long time now nonequilibrium plasmas obtained at low pressure with radiofrequency voltages have been used for special surface treatment of dielectric materials; recently Masuda et al. (1991) successfully used pulse corona discharges for similar treatments at normal air pressure on wider surfaces.

REFERENCES

Chang, J. S. (1987). Mechanism of NH_4NO_3 aerosol particle formation by streamer corona discharges. Proceedings of the 3rd Int. Conference on Electrostatic Precipitation, Abano, 1987, pp. 653–665.

Chang, J. S. (1989). The role of H_2O and NH_3 on the formation of NH_4NO_3 aerosol particles and de-NO_x under the corona discharge treatment of combustion flue gases. *J. Aerosol Sci.*, 20, 8, 1087–1090.

Chang, J. S., P. A. Lawless, and T. Yamamoto (1991). Corona discharge processes. *Trans. IEEE*, PS-19, 1102–1166.

Civitano, L. (1992). Industrial application of pulsed corona processing to flue gas. *Non-thermal Plasma Techniques for Pollution Control*, NATO Advanced Research Workshop (in press).

Civitano, L., G. Dinelli, F. Busi, M. D'Angelantonio, I. Gallimberti, and M. Rea (1986). Flue gas simultaneous DeNOx/DeSOx by impulse energization. TEC-DOC-428, Final Report of a Consultants' Meeting on Electron Beam Processing of Combustion Flue Gases, Karlsruhe, 1986, pp. 55–84.

Civitano, L., G. Dinelli, and M. Rea (1987). Removal of NOx and SO2 from combustion gases by means of corona energization. Proceedings of the 3rd Int. Conference on Electrostatic Precipitation, Abano, 1987, pp. 677–687.

Dinelli, G., and M. Rea (1990). Pulse power electrostatic technologies for the control of flue gas emissions. *Journal of Electrostatics*, 25, 23–40.

Dinelli, G., L. Civitano and M. Rea (1990). Industrial experiments on pulse corona simultaneous removal of NOx and SO2 from flue gas. *Trans. IEEE*, IA-26, 535–541.

Frank, N. W., K. Kawamura, and G. A. Miller (1986). Design notes on testing conducted during the period of June 1985—September 1986 on the Process Demonstration Unit at Indianapolis, Indiana. IAEA-TECDOC-428. Final Report of a Consultants' Meeting on Electron Beam Processing of Combustion Flue Gases, Karlsruhe, 1986, pp. 119–134.

Gallimberti, I. (1972). A computer model for streamer propagation. *J. Phys. D, Appl. Phys.*, 5, 2179.

Gallimberti, I. (1991). Plasma catalysis reduction of NOx and SO2 in flue gases. Invited paper: HOKONE III Symposium on Plasma Chemistry, Strasbourg.

Kawamura, K., S. Aoki, H. Kimura, T. Fujii, S. Mizutani, T. Higo, R. Ishikawa, K. Adachi, and S. Hosoki (1979). Pilot plant experiment of NO_x and SO_2 removal from exhaust gases by electron-beam irradiation. *Radiat. Phys. Chem.*, 13, 5–12.

Khatib, H., and M. Munasinghe (1992). Electricity, the environment and sustainable world development. Proceedings of the 15th Congress of the World Energy Council, Commission Plenary Session 8, Madrid.

Masuda, S., and H. Nakao (1990). Control of NO_x by positive and negative pulsed corona discharges. *IEEE Trans.*, IA-26, 374–383.

Masuda, S., Y. Wu, T. Urabe, and Y. Ono (1987). Pulse corona induced plasma chemical process for DeNOx, DeSOx and mercury vapour control of combustion gas. Proceedings of the 3rd Int. Conference on Electrostatic Precipitation, Abano, 1987, pp. 667–676.

Masuda, S., I. Tochizawa, K. Kuwano, K. Akutsu, and A. Iwata (1991). Surface treatment of plastic material by pulse corona induced plasma chemical process—PPCP. Conference Record of the IEEE Industry Applications Society Annual Meeting, vol. 1, Dearborn, MI, pp. 703–707.

Mizuno, A., J. S. Clements, and R. H. Davis (1986). A method for the removal of sulphur dioxide from exhaust gas utilizing pulsed streamer corona for electron energization. *IEEE Trans.*, IA-22, pp. 516–521.

Palumbo, F. J., and F. Fraas (1971). The removal of sulphur from stack gases by electrical discharge. *J. Air Pollution Control Asso.*, 21, 143–144.

Ramsey, G. H., N. Plaks, C. A. Vogel, W. H. Ponder, and L. E. Hamel (1990). The destruction of volatile organic compounds by innovative corona technology. Proceedings of the Eighth Symposium on the Transfer and Utilization of Particulate Control Technology, San Diego, March, 1990.

Rea, M., and G. Dinelli (1990). Pulse power electrostatic technology for the simultaneous removal of NOx and SO2. Proceedings of the 4th International Conference on Electrostatic Precipitation, Beijing.

Rea, M., and K. Yan (1992). Energization of pulse corona induced chemical processes. *Non-thermal Plasma Techniques for Pollution Control*, NATO Advanced Research Workshop (in press).

Rea, M., and K. Yan (1992b). Evaluation of pulse voltage generators. Proceedings of IEEE-IAS Annual Conference, Houston, TX.

Tokunaga, O., and N. Suzuki (1984). Radiation chemical reactions in NO_x and SO_2 removal from flue gas. *Radiat. Phys. Chem.*, 24, 145–165.

Yamamoto, T., K. Ramanathan, P. A. Lawless, D. S. Ensor, J. R. Newsome, N. Plaks, and G. H. Ramsey (1992). Control of volatile organic compounds by an AC energized pellet reactor and a pulsed corona reactor. *Trans. IEEE*, IA-28, 528–534.

This Page Intentionally Left Blank

28

Atmospheric Electricity

Toshio Ogawa

Science Laboratory International
Kochi, Japan

T. Takeuti

Aichi College of Industry and Technology
Aichi, Japan

Z.-I. Kawasaki

Osaka University
Osaka, Japan

I. FAIR-WEATHER ELECTRIC FIELDS

A. Conductivity in the Atmosphere

The atmosphere may extend up to 30,000 km, but it is defined here as the space between the ionosphere and the ground. This region is composed of the troposphere, the stratosphere, and the mesosphere.

In discussing atmospheric electricity in fair weather it is necessary first to review the conductivity distribution in the atmosphere where the electricity will occur and propagate. The atmosphere is ionized by radioactivity, mainly α rays from the earth's crust, and by cosmic rays from space. Both electrons and primary positive ions thus produced react with atmospheric gases. The reactions continue until reaching the terminal negative and positive ions, respectively, within a few microseconds. Number densities of these ions are several 1000/cm^3 at ground level.

Ionic composition varies with altitude. From the ground level up to about 30 km, the major positive ions are composed of proton core ions

H^+ and attached water molecules $(H_2O)_n$. They are cluster ions of the type H_3O^+ $(H_2O)_n$, which are called proton-hydrate ions. A portion of the water molecules in the ions may be substituted by acetonitrile (CH_3CN). Near the ground, below about 6 km, NH_4^+ $(H_2O)_n$ may be the major ions (Eisele and McDaniel, 1986; Ziereis and Arnold, 1986).

The negative ions are composed of NO_3^- core ions and the attached $(HNO_3)_n$ and water molecules, below the 30 km level. Above that level the core ions HSO_4^- and the attached $(H_2SO_4)_n$ become dominant. In Fig. 1 are shown the principal ions and mean ion masses derived from models (Brasseur and Chatel, 1983; Swider, 1984; Arijs and Brasseur, 1986) and mass spectrometric data from ground level to 70 km (from Swider, 1988).

The atmospheric electric conductivity σ is given by

$$\sigma = \sum_i n_i \mu_i q_i \tag{1}$$

where the index i expresses the kind of ions and n_i is the number density of the i kind of ions. μ_i is the ion mobility. q_i is the ionic charge that the

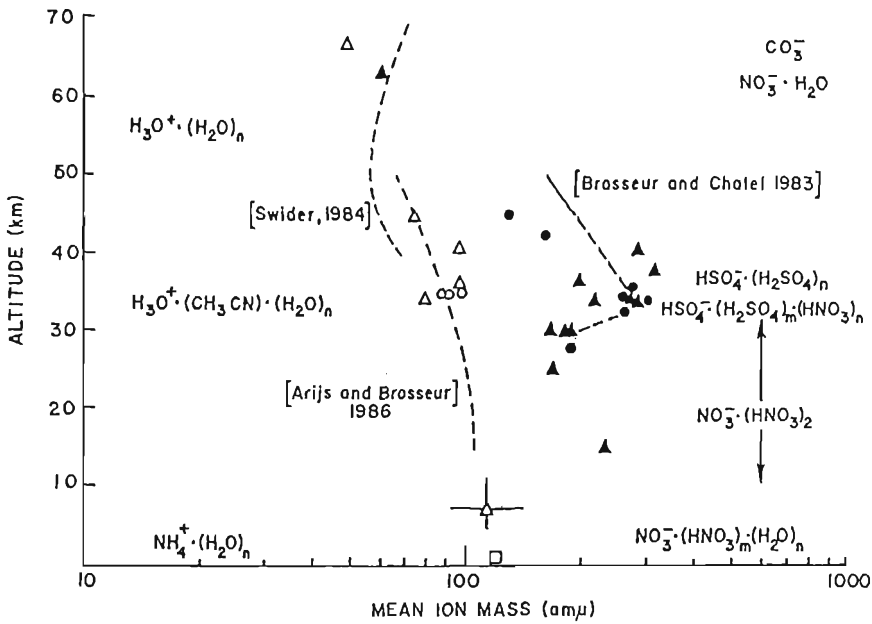


Figure 1 Atmospheric principal ions and mean ion masses as derived from models and mass spectrometric data from ground level to 70 km. (After Russell and Swider, 1991.)

ion carries and is given by $\pm Z_i |e|$, where Z_i is the number of elementary charges.

The ion mobility is the velocity of the charged particle that moves in the electric field of unit strength. The mobility μ_i is given by

$$\mu_i = \frac{q_i}{m_i \nu_i} \tag{2}$$

where m_i is the mass of the charged particle and ν_i is the collision frequency of the charged particle with the other kinds of coexisting particles.

The altitude profile of the atmospheric electrical conductivity was first calculated by using Eqs. 1 and 2 by Cole and Pierce (1965), and the derived profiles for day and night have been used by many authors. Then the measurements of conductivity by using balloons and rockets became popular, and the results of recent measurements under various geophysical conditions are given in Fig. 2. In Fig. 2 is also given the scale of relaxation time

$$\tau = \frac{\epsilon_r \epsilon_0}{\sigma} \tag{3}$$

where $\epsilon_r \epsilon_0$ is permittivity of the air. It is clear in Fig. 2 that the conductivity increases exponentially with altitude. It may be expressed by several exponential functions in the altitude ranges 0–5 km, 5–20 km, 20–40 km, 40–60 km, and 60–85 km, the lower boundary of the ionosphere, respectively. The conductivity changes from 10^{-14} S/m at the ground level to 10^{-4} S/m at the 85 km level. The earth's surface, the lower boundary of the atmosphere, has a conductivity on the order of 10^{-3}–10^{-2} S/m.

The conductivity in the altitude range up to 40 km is directly measured by using airplanes and balloons. Above that level it is measured by using rockets.

B. Mapping Theory

Electric fields are produced not only within but also outside the atmosphere, namely in the ionosphere and the magnetosphere, and in the earth's crust. The electric fields produced in various places in the earth medium propagate through the atmosphere. They are observed far from those origins. The propagation of the electric fields depends on the electric conductivity distribution that was discussed in Sec. I.A. The theory to estimate the order of attenuation of electric fields in the earth medium is called mapping theory. The quantitative order of attenuation is called the mapping factor. The larger is the field scale size, the smaller is the attenua-

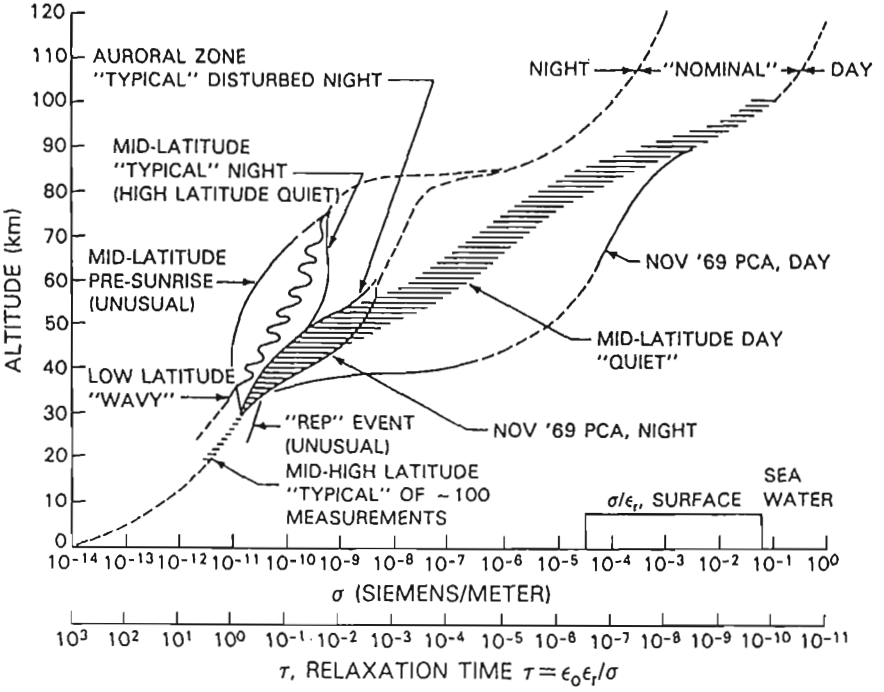


Figure 2 Atmospheric electrical conductivity and relaxation time under various geophysical conditions. (After Hale, 1984.)

tion of the electric fields. This is proved theoretically in the following. Isotropic conductivity is assumed here, but a similar consideration is possible for the atmosphere of anisotropic conductivity.

Here the atmospheric conductivity σ is simply assumed to increase exponentially from the ground, i.e.

$$\sigma = \sigma_0 \exp\left(\frac{z}{\alpha}\right) \tag{4}$$

where σ_0 is the conductivity at the ground level and α is the conductivity scale height. The three fundamental equations of the electric field

$$\mathbf{E} = -\nabla\Phi \tag{5}$$

$$\mathbf{J} = \sigma\mathbf{E} \tag{6}$$

$$\nabla\cdot\mathbf{J} = 0 \tag{7}$$

are solved together in the cylindrical coordinates (r, θ, z). The electrostatic potential Φ is obtained as

$$\Phi(r, z) = J_0(k_r r)\{A \exp(m_1 z) + B \exp(m_2 z)\} \tag{8}$$

From Eq. 8 the vertical and horizontal electric fields are derived respectively as

$$E_z(r, z) = -J_0(k_r r)\{m_1 A \exp(m_1 z) + m_2 B \exp(m_2 z)\} \tag{9}$$

$$E_r(r, z) = J_1(k_r r)k_r\{A \exp(m_1 z) + B \exp(m_2 z)\} \tag{10}$$

where J_0 and J_1 are the Bessel functions of the first kind of order 0 and 1, respectively. m_1 and m_2 are given respectively by

$$\begin{Bmatrix} m_1 \\ m_2 \end{Bmatrix} = -\tfrac{1}{2}\alpha \mp \{(\tfrac{1}{2}\alpha)^2 + k_r^2\}^{1/2} \tag{11}$$

where k_r is the wave number. It is interesting to see in Eqs. 9–11 that the electric fields do not depend on the conductivity value but only on the conductivity scale height α. When we examine the signs of m_1 and m_2, it is known that m_1 is negative and m_2 is positive. Therefore the value of the first term on the right-hand side in Eqs. 9 and 10 decreases with height, and the second term increases with height. From this fact the source of the first term of Eqs. 9 and 10 is in the atmosphere lower than a point of concern or inside the earth. The source of the second term is in the upper atmosphere above a point of concern or in space. If we consider the stratosphere or the mesosphere, the former may have thundercloud charges and the latter may come from the ionosphere, magnetosphere, or space.

The mapping factor calculated with a source at altitude 150 km is shown in Fig. 3, where the parameter λ is the wavelength given by $2\pi/k_r$. It is clear in Fig. 3 that the ionospheric electric field, the wavelength of which is larger than 200 km, maps in the lower atmosphere with little attenuation. This fact becomes the basis of the balloon measurement in the stratosphere of the horizontal electric field of ionospheric origin.

If we use the spherical coordinates (r, θ, ϕ), the mechanism of the atmospheric electric field mapping around the earth's surface can be understood. The atmospheric electric potential $\Phi(\sigma, \theta, \phi)$ is given by the next equation (Hays and Roble, 1979).

$$\Phi(\sigma, \theta, \phi) = \sum_{n=0}^{\infty} \sum_{m=0}^{n} [\{C_{Anm}\sigma^{(-1+\zeta_n)/2} + C_{Bnm}\sigma^{(-1-\zeta_n)/2}\}\overline{C_{nm}}(\theta, \phi) + \{S_{Anm}\sigma^{(-1+\zeta_n)/2} + S_{Bnm}\sigma^{(-1-\zeta_n)/2}\}\overline{S_{nm}}(\theta, \phi)] \tag{12}$$

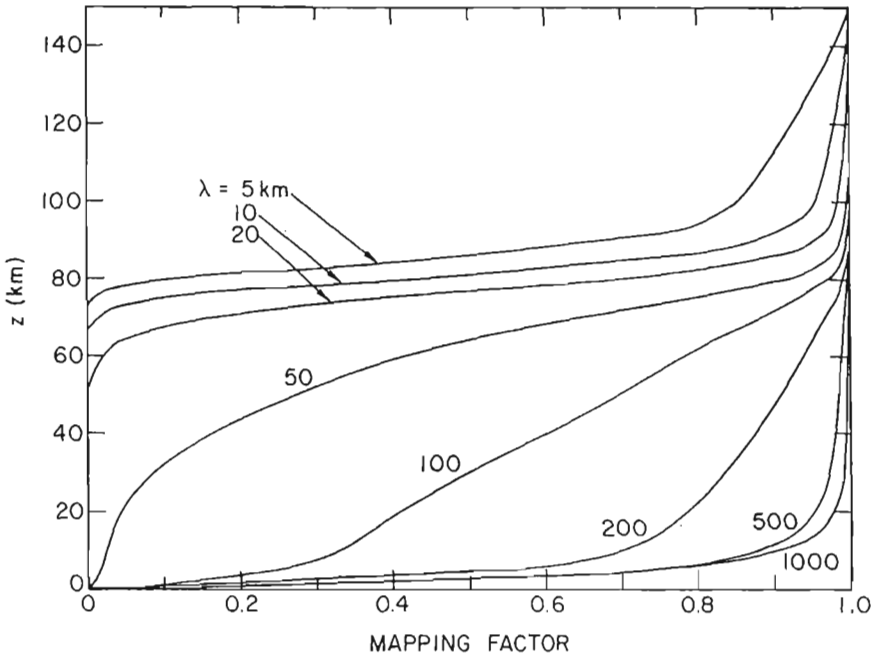


Figure 3 Mapping factor of the ionospheric horizontal electric field at 150 km with selected spatial wavelengths on a quiet night. (Park and Dejnakarintra, 1977.)

where the variable σ is used instead of r. ζ_n is given by

$$\zeta_n = \left\{\frac{1 + 4n(n+1)\alpha^2}{r_0^2}\right\}^{1/2} \tag{13}$$

where r_0 is the radius of the earth. C_{Anm}, C_{Bnm}, S_{Anm}, S_{Bnm} are the constants that must be determined from the boundary conditions. C_{nm}, S_{nm} in Eq. 12 are given respectively by

$$\overline{C_{nm}}(\theta, \phi) = \frac{1}{\pi^{1/2}} \overline{P_n^m}(\cos\theta)\cos m\phi \tag{14}$$

$$\overline{S_{nm}}(\theta, \phi) = \frac{1}{\pi^{1/2}} \overline{P_n^m}(\cos\theta)\sin m\phi \tag{15}$$

where

$$\overline{P_n^m}(\cos\theta) = \left\{\frac{2n+1}{2}\right\}^{1/2} \left\{\frac{(n-m)!}{(n+m)!}\right\}^{1/2} P_n^m(\cos\theta) \tag{16}$$

The $P_n^m(\cos\theta)$ in Eq. 16 is the associated Legendre function. The electric fields at a height in the atmosphere in any latitude ($90° - \theta$) and longitude ϕ are calculated by taking the differential of the electric potential $\Phi(\sigma, \theta, \phi)$ in Eq. 12. In the calculation the orographic features of the globe surface can be included.

C. Large-Scale Electric Fields

Thunderstorms are the largest source of atmospheric electric fields. Charge generation and charge separation in thunderstorm clouds will be discussed in the following section. The positive and negative charges generated are distributed in a cloud so that positive charges are in higher regions and negative charges in a lower regions in the cloud. This type of charge distribution is usual in thunderstorm clouds and is called the dipole distribution of positive polarity. In actual clouds a small pocket of positive charge occurs at the bottoms of the clouds. The electric field/current from such cloud charge distributions can be calculated. A model field/current distribution near a cloud is shown in Fig. 4, in which only the electric field/current direction is shown to see how the electric current

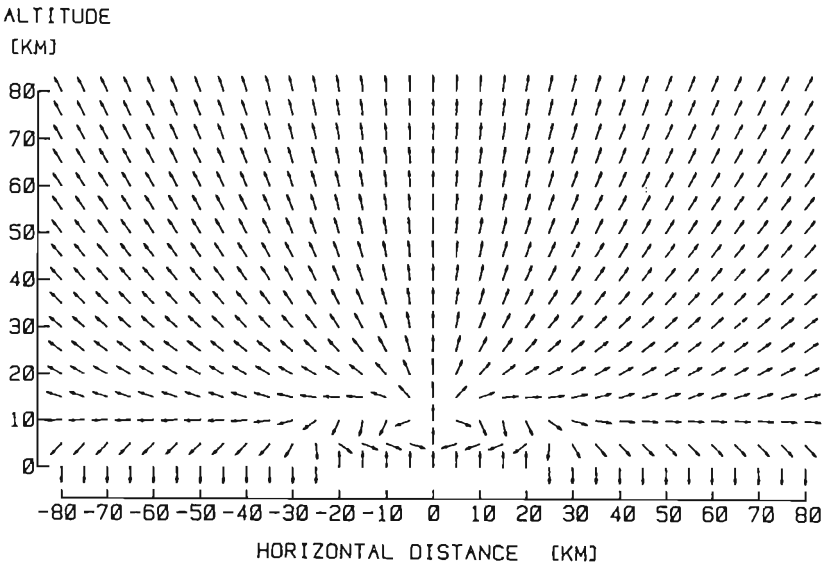


Figure 4 Electric current distribution from a model thunderstorm cloud with the positive charge 66 C at 8.5 km above ground and the negative charge −100 C at 6.0 km along a vertical line. (After Makino et al., 1980.)

flows out from a cloud into the atmosphere of real conductivity distribution. In this thundercloud model the positive and negative charges of +66 C and −100 C were assumed at 8.5 km and 6.0 km from the ground, respectively. The conductivity scale height was assumed to be 6.0 km. The electric field/current vector that was calculated every 5 km points upward in layers higher than 10 km. If the ionospheric potential of 300 kV is considered as an effect of all other global thunderstorm cloud charges, the electric field distribution near the cloud turns to be as shown in Fig. 5. It is clear in Fig. 5 that the direct effect of one average thunderstorm cloud spreads into the upper atmosphere but is confined within about 100 km distance from the cloud.

The mapping theory indicates that the higher is the thunderstorm cloud top, the larger is the rate of degree of the electric field mapping into the upper atmosphere. Such giant thunderstorms occur in tropical regions. One to two thousands of thunderclouds may be active simultaneously over the entire globe. Satellite experiments to measure this thunderstorm activity are under operation. An example of the result of experiments is shown in Fig. 6. This figure shows positions of lightning measured on a U.S. satellite DMSP. As had been supposed, the thunderstorm activity

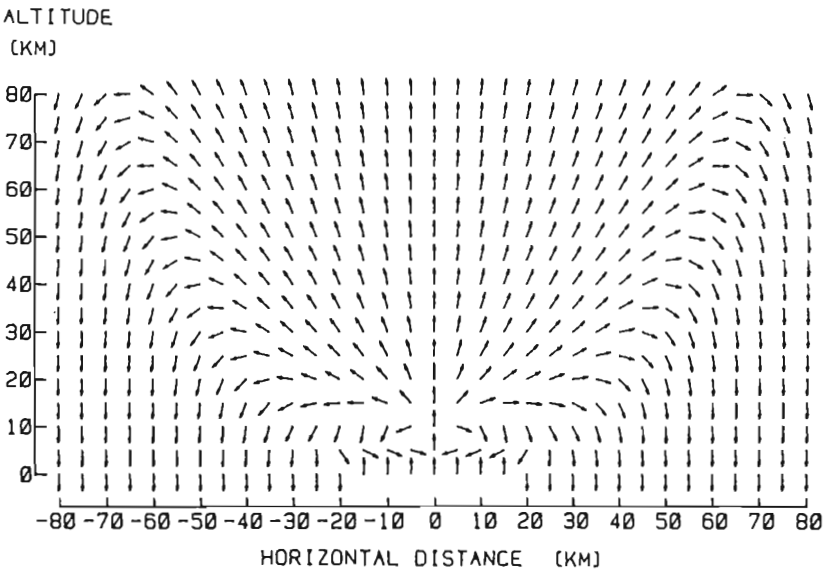


Figure 5 Electric current distribution from the model thunderstorm cloud as in Fig. 4 but assuming an ionospheric potential of 300 kV. (Makino et al., 1980.)

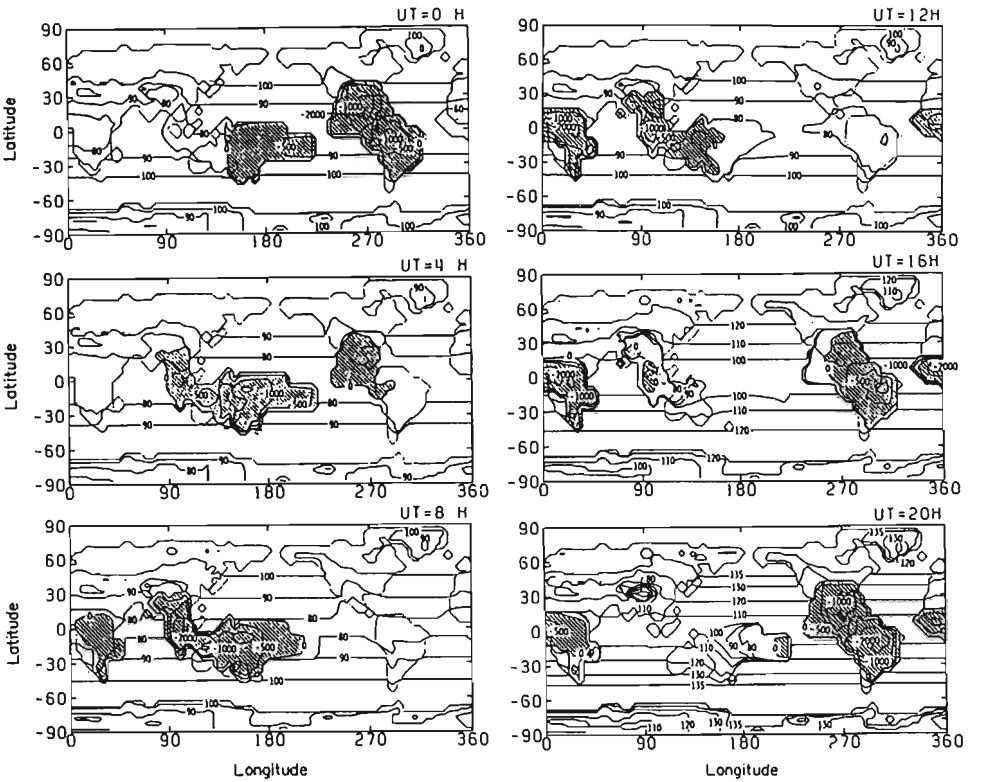


Figure 6 Occurrence of lightning as observed from a satellite DMSP September 10 through October 11, 1977. (After Edgar, 1978.)

was higher near the tropical zone, and more active on land than over ocean.

Using these data of lightning distribution, the global thunderstorm activity (charge distribution) is modeled. Then the global distributions of the atmospheric electric field and current were calculated based on the global electric circuit model. They are shown in Figs. 7 and 8, respectively. These results agree with the electric fields and currents that had been observed at various places on the ground. Thus the global circuit hypothesis proposed by Whipple and Scrase (1936), in which the atmospheric electric field was produced by global thunderstorm cloud charges, has been proved to be true.

The atmospheric electric field measured on the ground changes in time of various scales. A field amplitude to the period/frequency diagram is

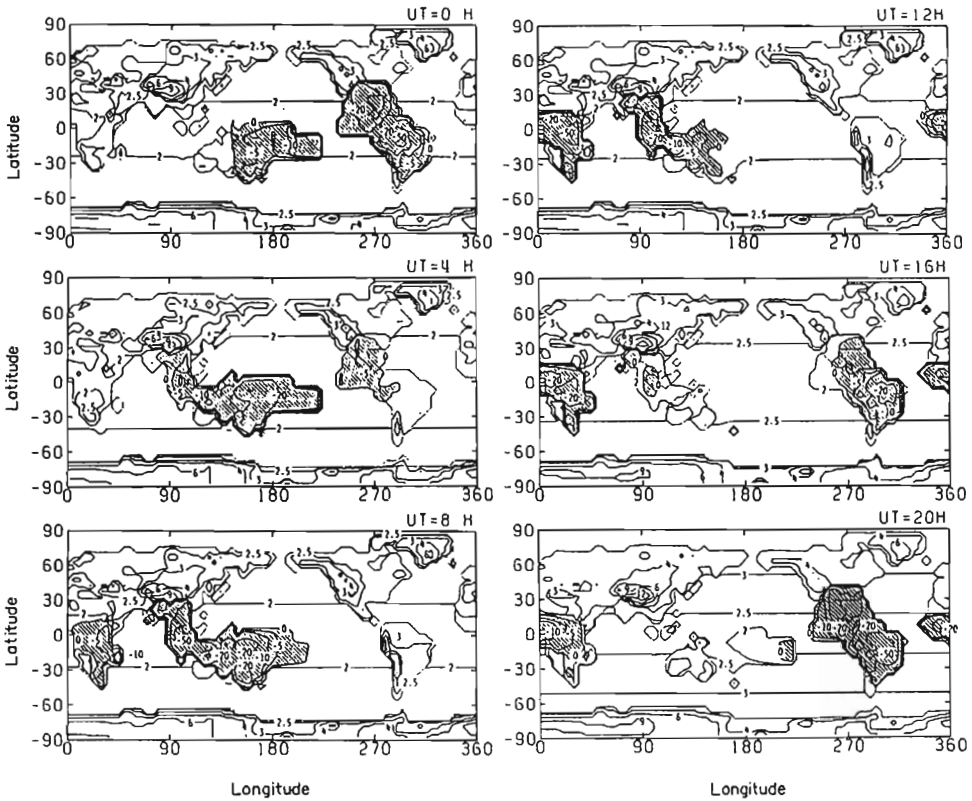


Figure 7 Global distribution of atmospheric electric field at ground level in V/m calculated every 4 h with model thunderstorm activity. (Makino and Ogawa, 1984.)

shown in Fig. 9 (Ogawa, 1973). The period/frequency ranges from 11 years, the solar cycle, to 100 MHz. The recognized amplitude of the solar cycle variation is on the order of 10 V/m, one tenth of the normal fair-weather electric field. The most apparent and clear variation is the diurnal variation. There are two kinds of diurnal variations, one in universal time and the other in local time. The universal time variation as shown in (a) of Fig. 10 (Parkinson and Torreson, 1931; Sverdrup, 1927) is of large scale and is caused by the global thunderstorm electrical activity as shown in (b) of Fig. 10 (Whipple and Scrase, 1936) and has been discussed above.

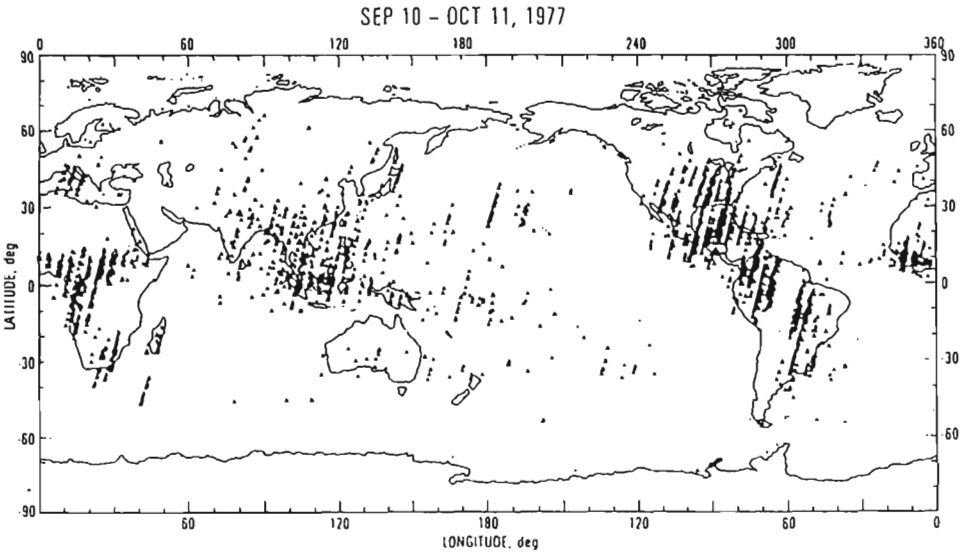


Figure 8 Global distribution of air-earth current in A/m^2 calculated every 4 h with the same model thunderstorm activity as in Fig. 7. (Makino and Ogawa, 1984.)

Large vertical electric fields were observed within the lower mesosphere by using rocket-borne field mills (Bragin et al., 1974; Tyutin, 1976). The order of the electric field strength is V/m. As to these unexpectedly large electric fields, many following experiments and discussions have been made and they are continuing (Goldberg and Holtzworth, 1991).

D. Small-Scale Electric Fields

The local time variation of the electric field as shown in Fig. 11 is of small scale and is caused by changes of conductivity in the atmosphere. The relation between the conductivity and the electric field is given by Ohm's law, that is,

$$J = \sigma E \tag{17}$$

where J is the air earth current density that is also expressed by

$$J = \frac{V}{R} \tag{18}$$

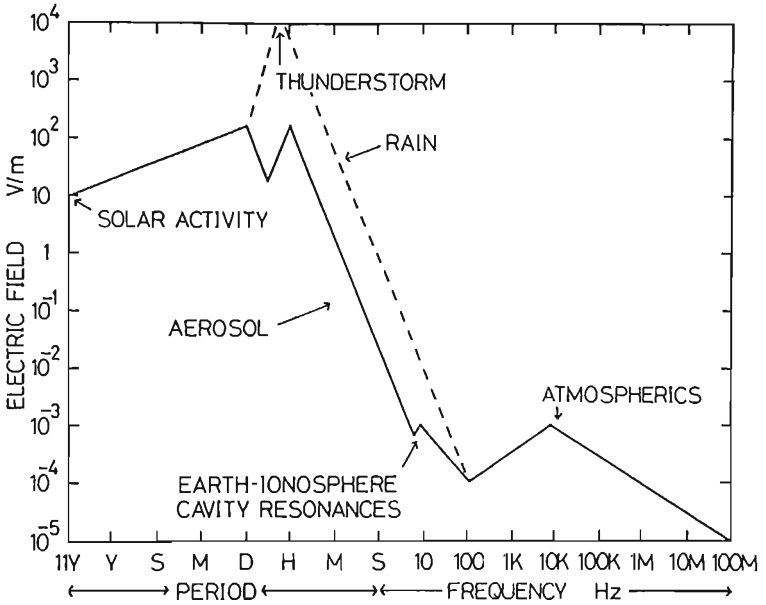


Figure 9 Atmospheric electric fields as a function of period/frequency. (Ogawa, 1973.)

where V is the ionospheric electric potential and R is the air columnar resistance. From Eqs. 17 and 18 we obtain

$$E = \frac{V}{\sigma R} \tag{19}$$

The atmospheric electric field is proportional to the ionospheric potential V and inversely proportional to both the local conductivity σ and the air columnar resistance R. R is the integrated resistance from the ground to the ionosphere of the air column with unit cross-section. Variability of R is smaller than σ. The electric field measured in an urban area depends more on the local conductivity than on the columnar resistance (Ogawa, 1960a, 1960b).

Two maxima of the electric field in the morning and in the evening in Fig. 11 are caused by the conductivity decreases due to increases in aerosol particles by human activity in an urban area. The depression of the electric field in midday is caused by diffusion of such aerosol particles by daytime air convection.

The electric field variations of short periods of an order of 10 min are

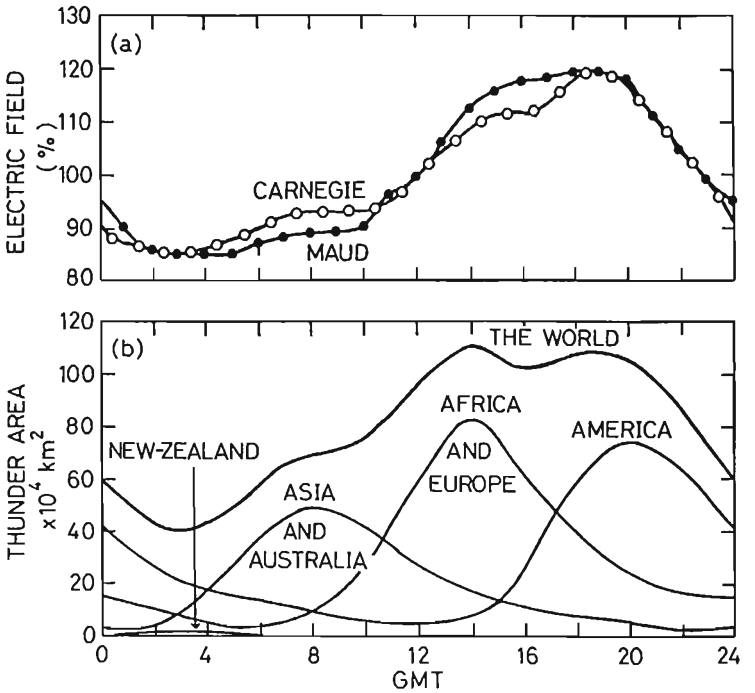


Figure 10 Diurnal variation of atmospheric electric field in universal time as observed (a) on board "Carnegie" and "Maud" on oceans. (After Parkinson and Torreson, 1931; Sverdrup, 1927). (b) Thunder areas for each continent and the world. (After Whipple and Scrase, 1936.)

caused by irregular distribution of space charges near the ground. The space charge ρ and the electric field E have the relation

$$\rho = \epsilon_r \epsilon_o \cdot \nabla \mathbf{E} \tag{20}$$

The space charges are produced from various human activities. Those well known are from factory chimnies, various fires, and exhaust gases from vehicles. The space charges decay during the flow with wind within the relaxation time τ (Eq. 3). The relaxation time of the air near the ground is 500–1000 s. The exhaust gases SO_2 and NO_x react with atmospheric gases and glow to heavy gases. They finally convert to atmospheric particles and affect the electric field.

There are direct charge generations in the atmosphere. Their mechanisms may be triboelectricity, the induction effect, and breakup charging,

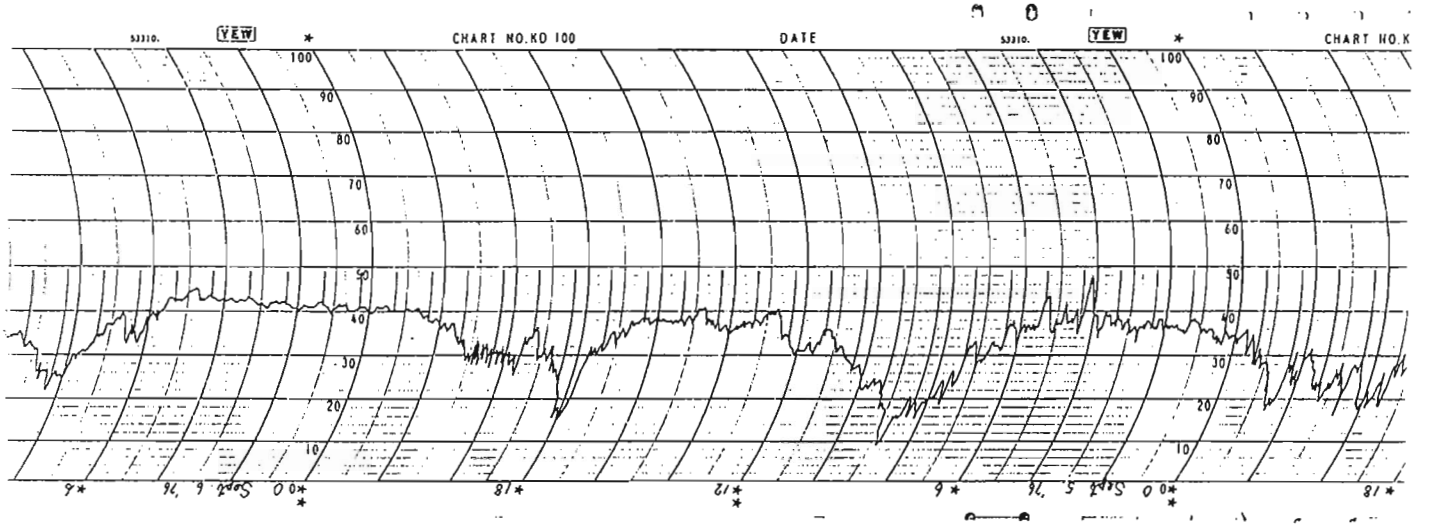


Figure 11 Diurnal variation of atmospheric electric field observed in Kyoto September 4 (19 JST) to September 6 (10 JST), 1976. Full scales are ±300 V/m in vertical axis and 39 h in horizontal axis.

just as in thunderstorm clouds. These mechanisms will be discussed in the following section.

Breakup charging is a common phenomenon, and an example is seen near a waterfall. A similar phenomenon is also seen in rain. When water drops hit the ground, the drops are broken into pieces and smaller fragments are spread into the atmosphere. In this process the smaller fragments of the water drops are charged negatively and the larger ones positively. The former are lighter than the latter and raised higher in the atmosphere. The size of the negative water fragments distributes in wide range extending to molecular size. These become ions in the atmosphere. The conductivity meter of the Gerdien type operating near the ground measures such negative ions, and the conductivity increases above the normal level. This causes variations of the electric field.

Various firing processes are not only a cause of ionization of the air but also a cause of the production of gases that convert to aerosol particles as described above.

A particular direct production of electricity is a corona discharge from high-tension power cables. Corona discharge produces space charges. This effect is enhanced during disturbed weather and observed downwind.

Volcanic ashes from volcanos have much electricity, and lightning flashes occur between ash clouds. This phenomenon may be caused by the triboelectricity between different types of ash. It was demonstrated by a laboratory experiment that larger and smaller ash particles have different signs of electric charges.

The effects of nuclear explosions were observed. The electric field decreased from the normal level by about 50% many thousands of kilometers downwind near the westerly jet stream.

E. Electric Fields from Outside the Atmosphere

Large-scale electric fields that occur outside the atmosphere are also subject to atmospheric electricity, because those electric fields map into the atmosphere. Such electric fields are Sq, L, S_q^p, DP1, and DP2 (Nishida, 1978).

Since the seventeenth century the earth's magnetic fields have been measured at many stations on the ground. About 200 observatories are working. In addition to these ground observations an onboard satellite magnetometer measures magnetic fields in space.

The earth's magnetic fields change in time of various scales. Geomagnetic daily variations are caused by the ionospheric electric currents, which are driven by dynamo action of the fluid plasma in the ionosphere by solar heating and tidal effects of the sun and the moon. These electric

current systems are called Sq and L, respectively. S means sun, q quiet, and L lunar. The diurnal variations can be detected only during quiet periods of geomagnetic activity. The dynamo current occurs at about 105 km of the ionosphere, where the Hall conductivity is the largest among the tensor components of conductivity. The electric field **E** is given in the equation

$$\mathbf{J} = (\sigma)(\mathbf{E} + \mathbf{v} \times \mathbf{B}) \tag{21}$$

where **J** is the ionospheric current, (σ) the tensor conductivity, **v** the ionospheric wind velocity, and **B** the geomagnetic flux density. The ionospheric electric current **J** can be estimated by measuring the geomagnetic field variation on the ground. The conductivity (σ) is estimated from the ionospheric electron density measured by rocket experiments. The plasma tidal velocity v is estimated by various experimental as well as theoretical methods. The electric field strength thus estimated is on the order of a few mV/m. Such an electric field is of global scale. Average ionospheric electrostatic potential as a function of magnetic local time is shown in Fig. 12. The total potential is estimated to be about 5 kV. According to the mapping theory described in Sec. I.A, this kind of large-scale electric field maps down with small attenuation in the stratosphere where a balloon measurement is possible. Such an electric field has not exactly been measured by previous balloon experiments. Instead an incoherent scatter radar at the equatorial region estimated electric fields by measuring the drift motion of the conductive fluid in the ionosphere. Such drift velocity is given by

$$\mathbf{v} = \frac{\mathbf{E} \times \mathbf{B}}{B^2} \tag{22}$$

An electric field occurs in the magnetosphere. The electric field is produced in interplanetary space by the solar wind interacting with the interplanetary magnetic field and maps in the magnetosphere. In such infinitely conductive space the relation

$$\mathbf{E} + (\mathbf{v} \times \mathbf{B}) = 0 \tag{23}$$

holds, where **v** is the solar wind velocity and **B** the interplanetary magnetic flux density. The magnetospheric electric field points westward in the equatorial plane. By this large-scale electric field a magnetospheric plasma convection occurs, by which the plasma drifts toward the earth. This drift motion velocity is given by the same expression as Eq. 22 that is equivalent to Eq. 23. Therefore it is not possible to determine which is the cause, the electric field or the plasma motion, and which is the effect.

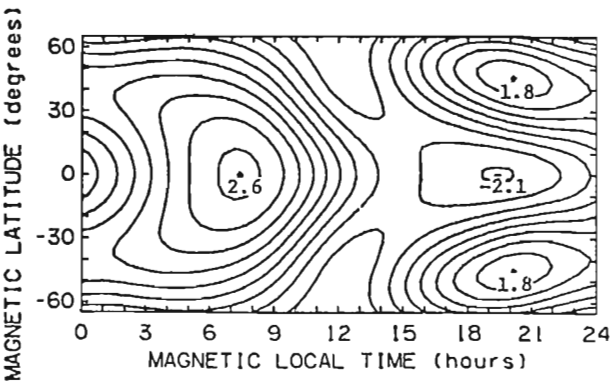


Figure 12 Average Sq electrostatic potential at 300 km altitude as a function of magnetic local time. (After Richmond et al., 1980.)

The magnetospheric electric field is mapped in the polar cap ionosphere through geomagnetic field lines. By this westward electric field the ionospheric plasma drifts beyond the pole from the day side to the night side (Eq. 22). In the equilibrium state, the drifted plasma in the night side auroral zone turns eastward in the morning side and westward in the evening side; then the plasmas meet at the subsolar point. This twin vortex plasma convection (Fig. 13) results in the polar cap ionospheric electric current. The current occurs inversely to the plasma convection under the influence of smaller electron collision frequencies with neutral gas particles than those of ions. This current system observed only during a geomagnetically quiet period is called S_q^p (Nagata and Kokubun, 1962), similarly named to Sq. In the auroral zone of the ionosphere the corresponding electric field is toward the equator in the morning side and toward the poles in the evening side. These ionospheric electric fields map down in the polar atmosphere, which can be measured again in the stratosphere by using balloons. During a geomagnetically disturbed period, the S_q^p cannot be seen, and polar ionospheric phenomena are all enhanced and disturbed. An enhanced current system during such disturbed period is called DP2 (polar disturbance 2). The disturbed polar ionosphere is more common than the quiet one. Mozer and Luct (1974) observed the horizontal electric fields covering one full day using six balloons successively at the northern auroral zone; see Fig. 14, where the fields were mapped in the magnetospheric equatorial plane along the geomagnetic field lines. The electric field strength in the magnetosphere is on the order of 1 mV/m. The total magnetospheric potential is estimated to be about 60 kV.

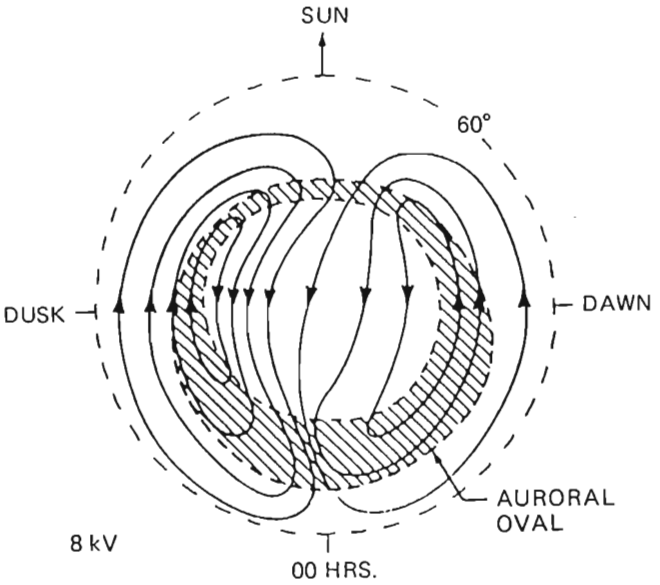


Figure 13 Schematic diagram of the polar ionospheric convection and the auroral oval. Total electric potential is estimated to be on the order of 8 kV. (After Burch, 1977; Richmond, 1986.)

During a period of high auroral activity in the polar night region, two kinds of strong electric currents occur in the auroral zone ionosphere. The stronger current is westward near the midnight zone and the other current is eastward near the dusk-to-midnight zone. They are called the westward and eastward auroral electrojets, respectively. These jet currents are caused by the Hall effect. The currents are driven by the equatorward and poleward electric fields, respectively. These electric fields can be measured by using stratospheric balloons as well as rockets. The electric fields are on the order of 10 mV/m and are called DP1 (polar disturbance 1) fields. In Fig. 15 is shown a model of auroral zone jet current system and geomagnetic field aligned currents connected to the magnetospheric equatorial current. The Sq current system is also shown in Fig. 15.

F. AC Electric Fields in Fair Weather

The quasi-dc components of the atmospheric electric fields have been discussed in the previous subsections, but a variety of ac phenomena can

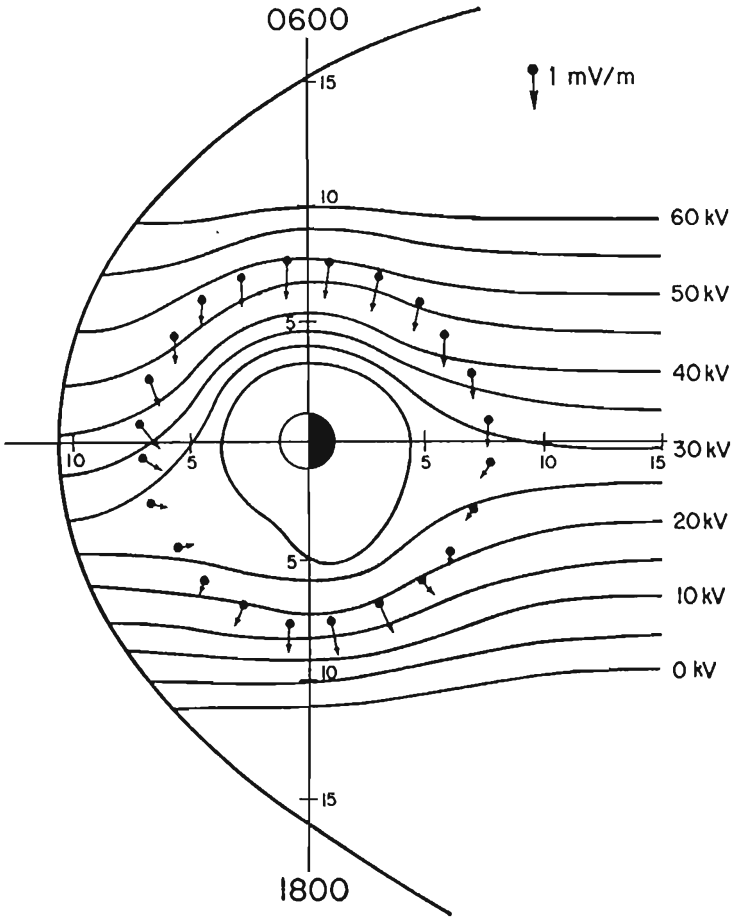


Figure 14 Magnetospheric equatorial electric fields as mapped from the polar stratosphere where the balloon measurements were made. (Mozer and Luct, 1974.)

also be observed in fair weather. A source of these ac phenomena is lightning discharges. A lightning channel of length 5–10 km may be a complex of a large number of radiation antennas with long and short wavelengths. Such a lightning channel radiates electromagnetic waves of various frequencies corresponding to the channel components. The tortosity of the lightning channel gives also a complex combination of radiations. The radiated frequencies may extend from ELF (3 Hz–3 kHz) to UHF (300 MHz–3000 MHz).

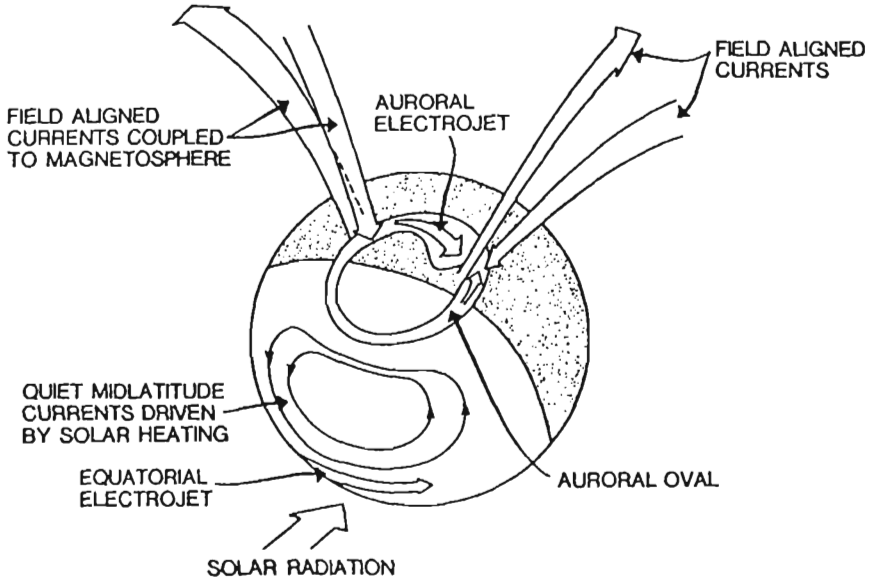


Figure 15 Schematic diagram of ionospheric electric currents (auroral electrojet, Sq current, and equatorial electrojet) and magnetic field aligned currents. (Richmond, 1986.)

There have been observed several interesting electromagnetic global phenomena. Schumann resonances are resonances in the spherical cavity between the lower boundary of the ionosphere and the earth's surface. Resonances can be seen for the first seven resonance modes. The first three resonance frequencies are 7.7, 14.1, and 20.3 Hz (Ogawa et al., 1968). The Q factors of these resonances are 3.3, 4.5, and 4.9 (Ogawa and Tanaka, 1970). The remaining resonance frequencies are seen at about 26, 33, 39, and 45 Hz (Ogawa et al., 1979). An example of Schumann resonances displayed on the frequency-time diagram (sonogram) is shown in Fig. 16.

Tweeks are the waveguide mode waves that propagate reflecting both at the lower boundary of the ionosphere and at the ground (Yano et al., 1989). The short dispersions of waves can be seen at about 2 kHz, 4 kHz, 6 kHz, etc. Examples of tweek atmospherics are given in Fig. 17.

Whistlers are phenomena of VLF waves propagating along geomagnetic field lines between the opposite hemispheres (Helliwell, 1965). Long frequency dispersion can be seen. Whistlers are observed in the evening

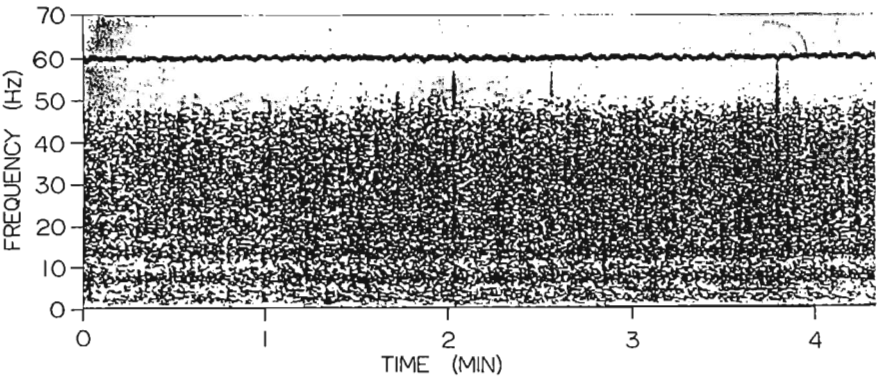


Figure 16 Schumann resonances as observed at 9 UT on July 16, 1967 in Kyoto displayed on sonogram.

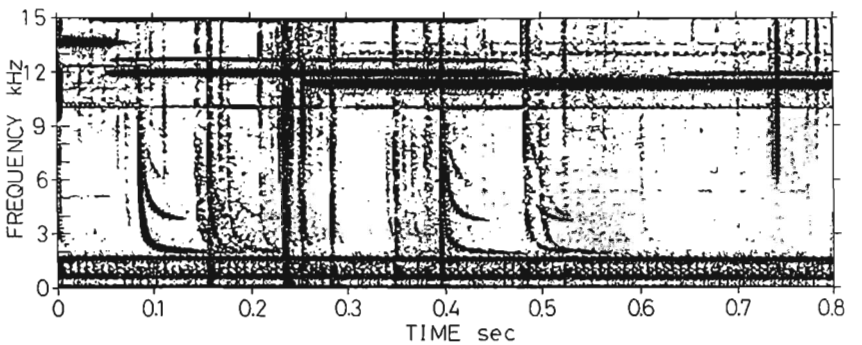


Figure 17 Waveguide mode tweek atmospherics as observed in Kochi displayed on sonogram.

and in early morning during the winter season (the summer season in the source region). Examples of whistlers are shown in Fig. 18.

Electromagnetic radiations are expected to occur from earthquakes. This is a related phenomenon to the breakup charging described in Sec. I.A. A model experiment was made to demonstrate emission from rock by hitting and breaking various kinds of rock in a laboratory (Ogawa et al., 1985; Ogawa, 1992). Breakup charging is one of the most important and interesting subjects in atmospheric electricity, and its physical mechanism should be investigated more carefully in the future.

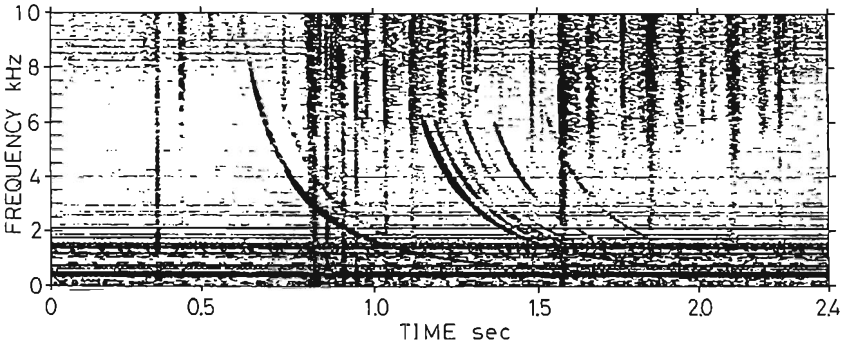


Figure 18 Whistler atmospherics as observed in Kochi displayed on sonogram.

II. THUNDERSTORM ELECTRICITY

A. Introduction

The thunderstorm is the most active electrical phenomenon in the natural world, and it has already been studied for more than two centuries. In spite of such a long history of thunderstorm research, the thunderstorm is still an object of research, especially that for protection against lightning damage. Electric fields are caused by the charge in the thundercloud and by lightning. The intensity or polarity of the electric field caused by the charge in a thundercloud changes slowly and that by lightning changes very fast.

B. Instruments

Many instruments other than electric ones are used in thunderstorm research. However, those instruments are not within our interest here.

1. Instruments for Slow Field Changes

Slow electric field changes are generally measured with two instruments, a field mill and an instrument for a point corona discharge current measurement. Though many types of field mill have been reported, every field mill is composed of some number of electrodes connected to a high resistance and the shielding metal plate over the electrodes. Fig 19 shows two examples of a field mill. Either the electrodes or the shielding plate are rotated; then the electrodes are repeated the exposure and shield to the electric field. During the exposure to the field, the charge proportional to the field intensity is induced through the high resistance on the electrodes. Following the exposure, the electrodes are shielded from the field

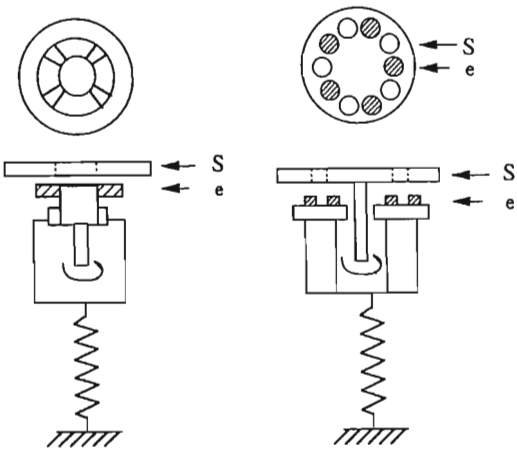


Figure 19 Examples of field mills (S = shielding plate; e = electrodes).

by the shielding plate; then the induced charges on the electrodes are removed through high resistance. This process results in alternative voltage proportional to the field intensity across the resistance. The voltage proportional to the field intensity is rectified synchronously to the exposure phase to indicate the sign and intensity of the field, and those are recorded with a pen recorder, etc. The field mill can measure from stationary electric fields to fast field changes. The time response of the mill is limited by the number of electrodes and the rotation velocity.

The field mill can precisely measure the electric field, but the long term of operation might occasionally result in some trouble by the rotary device. For this reason, the measurement of point discharge current is often applied instead of the field mill, though the relationship between the electric field intensity and the point discharge current is not so precise as with the field mill, as shown in Fig. 20. For example, Sakurano et al. (1989) have applied this corona current measurement for multisite measurements of the field during winter thunderstorms in Japan. They used nickel needles to keep these from rust. The radius of curvature of the needle point was 0.15 mm, and the needle was mounted on top of a pole with height of 5 m. The currents passed through a 10 K resistance to the ground and were recorded on battery operated pen recorders.

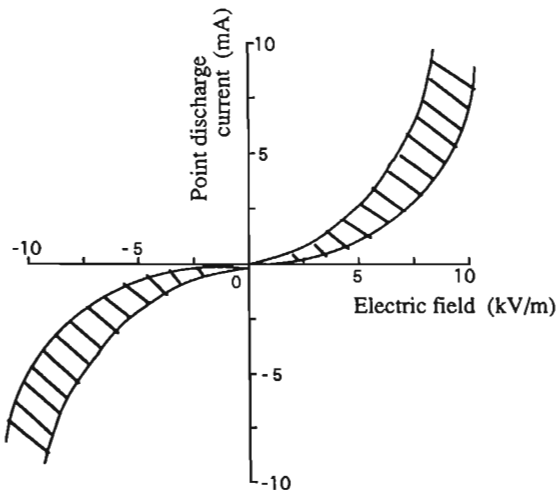


Figure 20 The relationship between the point discharge current and the electric field on the ground. (Courtesy Y. Kitoh, Nagoya University, Japan.)

2. Instruments for Fast Field Changes

Fast field changes are measured with many types of antenna, but most of the equivalent circuits of the antennas are similar to the circuit shown in Fig. 21. The upper limit of the frequency range of the instrument depends on the frequency range of the amplifier connected to the antenna circuit. The lower limit depends on the time constant CR of the antenna. C and R are the input capacity and the input resistance of the antenna, as shown in Fig. 21, respectively. The antenna gain G is

$$G = \frac{h_e C}{C + C_s} \tag{24}$$

where h_e and C_s are the effective height and stray capacity of the antenna, respectively. The gain of the instrument is controlled by changing the combination CR, as shown in Fig. 21.

Disturbance by corona discharge from an antenna under a very intensive field can be eliminated by the special configuration of Fig. 22. The frequency range of the instrument will be determined by the recording system. The field change up to about 1 MHz can be recorded with a modified video tape recorder. The field change in higher frequency ranges can be recorded by a transient memory with triggering circuit triggered by the electromagnetic field change caused by the lightning. This requires a larger memory to record for a sufficient duration.

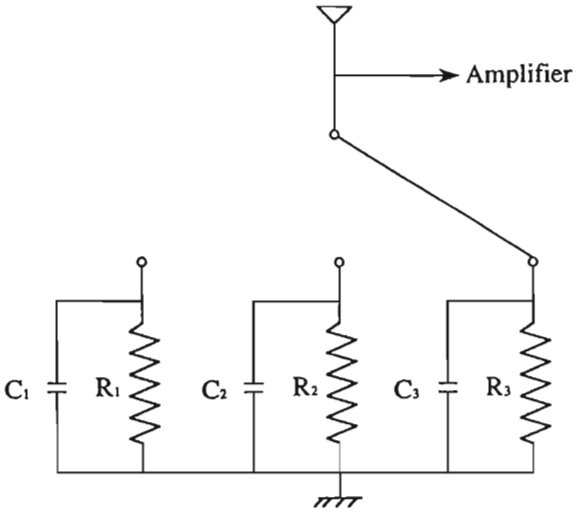


Figure 21 The equivalent circuit of the antenna for the measurement of fast field change.

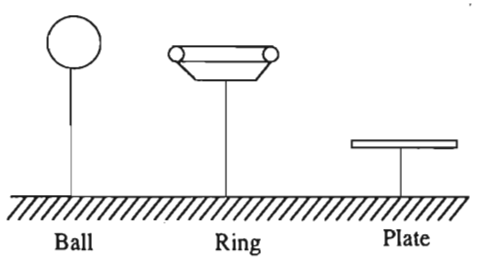


Figure 22 The antennae to eliminate corona discharge.

3. Measurement in Space

Electric fields caused by thunderstorms are generally measured on the ground. However, measurements in and around a thundercloud are also important for the study of thunderstorms. The fields are measured by instruments mounted on aircraft, rockets and balloons. Field mills on an aircraft should be mounted on multiple places to avoid the effect of the charge of the aircraft itself. A field mill under a captive or free balloon should be suspended by a long string to avoid the effect of the charge on the balloon surface. Fig. 23 is a field mill mounted ahead of a rocket for winter thunderstorm observation in Japan (Tatsuoka et al., 1991). The

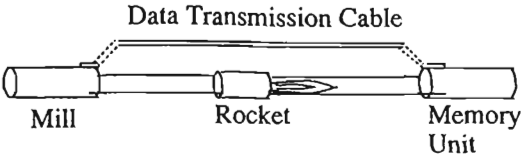


Figure 23 The field mill mounted on a rocket.

results obtained with both the balloon and the rocket are stored in a recording instrument on board or are sent by telemeter to the observation site.

C. Electric Fields Caused by Thunderstorms

Electric fields caused by thunderstorms are divided into two groups as described in Sec. II.A: electric fields caused by the charges in thunderclouds and those caused by lightning. The former change slowly and the latter fast.

1. Electric Fields Caused by the Charges in Thunderclouds

The typical charge distribution in the summer thundercloud is the electric dipole composed of an upper positive and a lower negative as shown in Fig. 24. There are some reports on the additional small positive charge under the main negative one. As the typical summer thundercloud passes through just above the observation site, a W type electric field as shown in Fig. 25 is occasionally recorded at the site. This seems to be evidence of an upper positive dipole with small positive charge. The charge distribu-

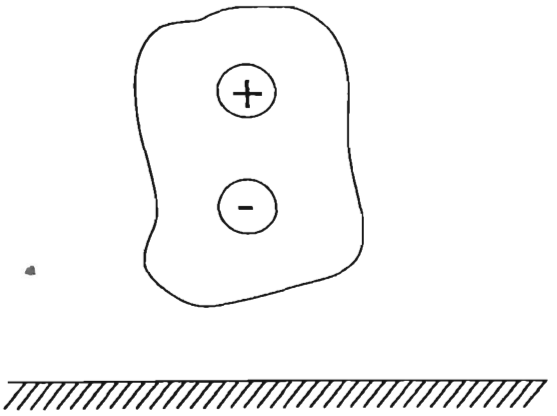


Figure 24 Typical charge distribution in the summer thundercloud.

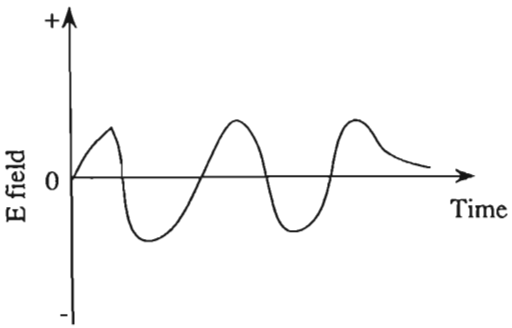


Figure 25 The W-type electric field by passage of the summer thundercloud over the observation site.

tion in the winter thundercloud is thought to be an upper positive dipole, as in the summer cloud, but the dipole axis is not vertical. We are not sure in the winter cloud about the existence of a small positive charge under the main negative one. The electric field intensity on the ground just under the summer thundercloud attains up to about 10,000 V/m, and that under the winter thundercloud up to 20,000–30,000 V/m because of lower charge location compared with the location in summer. Electric fields in thunderclouds are more intensive than those on the ground, as shown in Table 1.

2. Electric Fields Caused by Lightning Discharges

The frequency range of the electric field changes caused by lightning discharges extends from about 0.1 Hz to about 100 GHz. The upper limit of the frequency range is subject to other radio noises such as thermal noise of the instrument, cosmic noise, artificial noise, etc.

The fast field change caused by lightning is followed by a rather slow

Table 1 Electric Fields in Thunderclouds

Observer	Typical value	Max. value $\times 10^5$ V/m	Method
Winn et al.	0.5–0.8	2	Rocket
Winn et al.	—	1.4	Balloon
Rust et al.	1.5	3.0	Aircraft
Kasemir et al.	1	2.8	Aircraft
Imyanitov et al.	1	2.5	Aircraft
Fitzgerald	2–4	8	Aircraft

field change, a linear or an exponential change, ranging between 1 and 10 seconds. This is caused by regeneration of the charge in the thundercloud after the lightning, and it is called the recovery change. The rate of change is dependent on the distance between the lightning and the observation site, that is, there is a faster change for a closer lightning discharge.

The typical field change caused by an individual cloud discharge is a slow change between 0.1 and 1 superimposed on a fast change. It will be discussed here only for the slow change. The charge distribution in the thundercloud is assumed as a vertical dipole, upper positive with height h_1 and lower negative with height h_2; d is defined as the distance between the observation site and the projection point of the dipole axis on the ground. If d is less than r, where

$$r = h_1^{1/3} h_2^{1/3} (h_1^{2/3} + h_2^{2/3}) \tag{25}$$

the net field change should be positive, and vice versa.

Actually, the net slow changes caused by cloud discharge in a summer thunderstorm are generally positive for close discharges and negative for distant ones, coincident with the above discussion.

Amplitude of the net slow field change EV/m caused by cloud discharge can be roughly estimated by the following equation, assuming $d >> h_1$ and $d << h_2$. h_1, h_2, and d are in km and Q is in coulombs.

$$\Delta E_s = 2 \times 10^4 Q \frac{h_1 - h_2}{d^3} \tag{26}$$

Es observed in summer in Germany were roughly between 1000 V/m and 10,000 V/m for very close discharges and between 300 V/m and 3000 V/m for discharges at about 10 km from the observation site (Takeuti, 1987).

The ground discharges are divided into two groups, natural discharges and triggered ones. The triggered discharges are discharges starting from a high mast, a high building, etc., on the ground or those from aircraft, etc., in space. The natural discharge starts from the thundercloud as a stepped leader. If the leader starts from a negative charge region in the thundercloud, it is called a negative ground discharge, and if it starts from the positive charge region, it is called a positive one. The most frequent ground discharge is the negative natural discharge, so that the discussion will be limited to this discharge here.

Fig. 26 shows the typical process of the negative natural ground discharge, and Fig. 27 shows the field change corresponding to the negative natural ground discharge in a closed place.

The stepped leader starts down from the cloud to the ground emitting

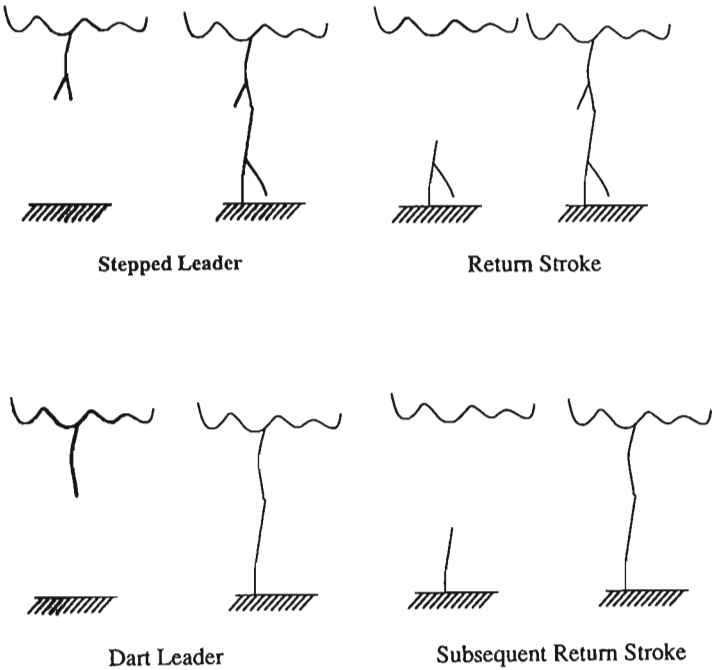


Figure 26 The time sequence of the typical negative natural ground discharge.

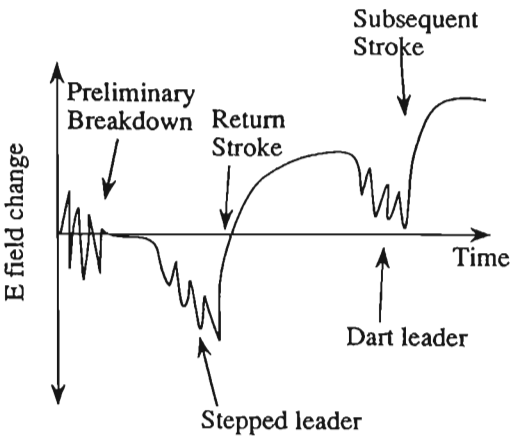


Figure 27 The field change caused by negative natural ground discharge in a closed place.

very fast regular electromagnetic pulses. When the leader arrives at the ground, a very bright return stroke from the ground arises and traces the channel ionized by the leader. The return stroke results in the fast electric field change. Some discharges finish the process at the arrival of the return stroke to the cloud, but in most cases the dart leader emitting regular pulses starts again from the cloud after the arrival of the first return stroke. When the dark leader arrives at the ground again, the second return stroke starts to the cloud. Such a process is repeated two to about ten times.

The most important and well discussed part of the field change caused by ground discharge is the change caused by the return stroke. Figure 28 is an example of electric field change caused by the first return stroke occurring within 5 km from the observation site. It is clear from Fig. 28 that the transition part can be divided into two groups, the fast transition part and the slow one. The rise time of the fast transition part of the field change with very high frequency component is important for the protection of a system from lightning damage. The return stroke current can be estimated from the field change, assuming the model of return stroke channel and current. One of the famous models is the transmission line model proposed by Uman et al.; however, it is not introduced here because the current is not within our interest.

The rise time of the fast transition part of the field change is dependent on the distance between the lightning and the site by the propagation effect, and it is also dependent on the conductivity of the surface. However, it is not dependent on the order of the return stroke. Table 2 shows 10–90% rise times of the fast transition part of the return strokes occurring at different distances (Oishi et al., 1986).

Table 3 shows the observed values of the electric field changes of the fast transition part caused by the return stroke (Oishi et al., 1986).

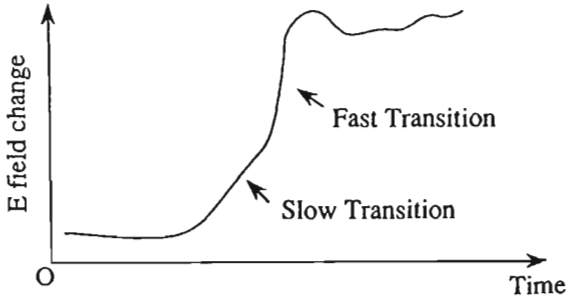


Figure 28 Field change caused by the first return stroke.

Table 2 10–90% Rise Times of the Fast Transition Part of the Return Stroke Fields

Distance (km)	Number of data	Rise time (μs)
2–10	5	0.345
3–15	5	0.74
10–20	10	1.37
20–30	19	1.40

Table 3 The Electric Field Changes of the Fast Transition Part of the Return Stroke

Lightning number	Intensity (V/m)	Distance (km)
1	471	1.0
2	371	1.0
3	92	3.3
4	99	3.3
5	218	1.6
6	141	1.0
7	126	3.0
8	372	2.3
9	186	3.0
10	231	2.3
11	278	2.0
12	93	1.0
13	512	2.0
14	164	3.3
15	134	3.3

D. Disturbances and Damages by Electric Fields

Intense electric fields by thunderstorms result in some disturbances and damages to electrical systems.

1. Corona Discharge

Corona discharge from the top of a receiving antenna mast by the intense electric fields induces in the input of the receiver a continuous electric noise in the low frequency range. Such corona discharge can be eliminated by a metal ball decreasing the field mounted on the top of the antenna.

2. Induction Field

Most damaging to power transmission lines and communications cables are direct lightning strikes. However, power lines with low voltage insulators and communications cables are also damaged by induced voltage by the field change caused by the return stroke. The induction voltages on the line and cable are dependent on the distance from the lightning and the return stroke current. Such an induction field also gives disturbances to some electronic instruments with semiconductors. Arresters, surge absorbers, shielding cases, etc., are recommended to avoid such damages and disturbances.

REFERENCES

Arijis, E., and G. Brasseur (1986). Acetonitrile in the stratosphere and implications for positive ion composition. *J. Geophys. Res.*, 91, 4003.

Bragin, Yu. A., A. A. Tyutin, A. A. Kocheev, and A. A. Tyutin (1974). Direct measurement of the atmospheric vertical electric field intensity up to 80 km. *Cosmic Res.*, 12, 276.

Brasseur, G., and A. Chatel (1983). A modelling of stratospheric ions: a first attempt. *Ann. Geophys.*, 1, 173.

Burch, J. L. (1977). The magnetosphere. *The Upper Atmosphere and Magnetosphere*. NRC Geophysics Study Committee, National Academy of Sciences, Washington, D.C., p. 42.

Cole, R. K., Jr., and E. T. Pierce (1965). Electrification in the earth's atmosphere for altitude between 0 and 100 kilometers. *J. Geophys. Res.*, 70, 2735.

Edgar, B. C. (1978). Space Sci. Lab. Rep., SSL-78(3639-02)-1, Aerospace Corp., Los Angeles.

Eisele, F. L., and E. W. McDaniel (1986). Mass spectrometric study of tropospheric ions in the northeastern and southwestern United States. *J. Geophys. Res.*, 91, 5813.

Goldberg, R. A., and R. H. Holtzworth (1991). Middle atmosphere electrodynamics. *MAP Handbook 32*, Part 1: MAP Summary (R. A. Vincent, ed.). SCOSTEP Secretariat, University of Illinois, p. 65.

Hale, L. C. (1984). Middle atmospheric electrical structure, dynamics and coupling. *Adv. Space Res.*, 4, 175.

Hays, P. B., and R. G. Roble (1979). A quasi-static model of global atmospheric electricity. 1. The lower atmosphere. *J. Geophys. Res.*, 84, 3291.

Helliwell, R. A. (1965). *Whistlers and Related Phenomena*. Stanford: Stanford University Press, p. 349.

Makino, M., and T. Ogawa (1984). Responses of atmospheric electric field and air-earth current to variations of conductivity profiles. *J. Atmos. Terr. Phys.*, 46, 431.

Makino, M., S. Hayashida, and T. Ogawa (1980). The electric field and current due to a model thunderstorm cloud in the global circuit. *Taiki Denki Kenkyu*, 23, 92 (in Japanese).

Mozer, F. S., and P. Luct (1974). The average auroral zone electric field. *J. Geophys. Res.*, 79, 1001.

Nagata, T., and S. Kokubun (1962). An additional geomagnetic daily variation field (S field) in the polar region on a geomagnetically quiet day. *Rep. Ionos. Space Res. Japan*, 16, 256.

Nishida, A. (1978). *Geomagnetic Diagnosis of the Magnetosphere*. New York: Springer-Verlag, p. 256.

Ogawa, T. (1960a). Types of diurnal variation of the air-earth current. *J. Geomag. Geoelectr.*, 11, 18.

Ogawa, T. (1960b). Diurnal variation in atmospheric electricity. *J. Geomag. Geoelectr.*, 12, 27.

Ogawa, T. (1973). Analyses of measurement techniques of electric fields and currents in the atmosphere. *Contributions, Geophys. Inst., Kyoto Univ.*, 13, 111.

Ogawa, T. (1992). ELF and VLF radio emissions from rocks. *Res. Lett. Atmos. Electr.*, 12, 275.

Ogawa, T., and Y. Tanaka (1970). Q factors of the Schumann resonances and solar activity. *Special Contributions, Geophys. Inst., Kyoto Univ.*, 10, 21.

Ogawa, T., Y. Tanaka, and M. Yasuhara (1968). Diurnal variations of resonant frequencies in the earth-ionosphere cavity. *Special Contributions, Geophys. Inst., Kyoto Univ.*, 8, 15.

Ogawa, T., K. Kozai, H. Kawamoto, M. Yasuhara, and A. Huzita (1979). Schumann resonances observed with a balloon in the stratosphere. *J. Atmos. Terr. Phys.*, 41, 135.

Ogawa, T., K. Oike, and T. Miura (1985). Electromagnetic radiations from rocks. *J. Geophys. Res.*, 90, 6245.

Oishi, Y., M. Nakano, T. Takeuti, and T. Nakai (1986). The risetime of the electric and the magnetic field changes caused by close lightning return strokes. *Research Letters on Atmospheric Electricity*, 6, 21–25.

Park, C. G., and M. Dejnakarintra (1977). The effect of magnetospheric convection on atmospheric electric fields in the polar cap. *Electrical Processes in Atmospheres* (H. Dolezalek and R. Reiter, eds.). Steinkopff, Darmstadt, p. 563.

Parkinson, W. D., and O. W. Torreson (1931). The diurnal variation of the electrical potential of the atmosphere over oceans. *Compt. Rend. de l'Assemblée de Stockholm, 1930, IUGG, Terrst. Magn. Electr. Bull.*, 8, 340.

Richmond, A. D. (1986). Upper atmosphere electric-field sources. *The Earth's Electrical Environment*. Geophysics Study Committee, National Research Council, National Academy Press, pp. 195–205.

Richmond, A. D., M. Blanc, B. A. Emery, R. H. Wand, B. G. Fejer, R. F. Woodman, S. Ganguly, P. Amaynec, R. A. Behnke, C. Calderon, and J. V. Evans (1980). An empirical model of quiet-day ionospheric electric fields at middle and low latitudes. *J. Geophys. Res.*, 85, 4658.

Russell, J. M., III, and W. Swider (1991). Structure and composition. *MAP Handbook 32*, Part 1: MAP Summary (R. A. Vincent, ed.). SCOSTEP Secretariat, University of Illinois, p. 1.

Sakurano, H., R. Matsubara, N. Murashita, and Y. Kito (1989). Presumption of regional distribution of the electric field polarity on the ground induced by winter thundercloud in Hokuriku District. *J.I.E.E. Japan*, 109-B, 355–360.

Sverdrup, H. (1927). Magnetic, atmospheric electric and auroral results, Maud expedition, 1918–25. *Publ. Carnegie Instn.*, Washington, D.C., No. 175, 6, 425.

Swider, W. (1984). Ionic mobility of the middle atmosphere. *Adv. Space Res.*, 4, 29.

Swider, W. (1988). Ionic mobility, mean mass and conductivity in the middle atmosphere from ground level to 70 km. *Rad. Sci.*, 23, 389.

Takeuti, T. (1987). *Lightning discharge*. Nagoya University Press, p. 75.

Tatsuoka, K., K. Nakamura, M. Minowa, and K. Horii (1991). Electric field measurement by rocket under the thunderclouds. Proceedings of 7th International Symposium on High Voltage Engineering.

Tyutin, A. A. (1976). Mesospheric maximum of the electric field strength. *Cosmic Res.*, 14, 132.

Whipple, F. J. W., and F. J. Scrase (1936). Point discharge in the electric field of the earth. *Geophys. Mem. Lond.*, 68, 1.

Yano, S., T. Ogawa, and H. Hagino (1989). Waveform analysis of tweek atmospherics. *Res. Lett. Atmos. Electr.*, 9, 31.

Ziereis, H., and F. Arnold (1986). Gaseous ammonia and ammonium ions in the free troposphere. *Nature*, 321, 503.

29

Biomedical Engineering

Akira Mizuno

Toyohashi University of Technology
Toyohashi, Japan

Masao Washizu

Seikei University
Tokyo, Japan

I. INTRODUCTION

There are needs in biotechnology for the manipulation of small objects, such as cells, chromosomes, biological membranes, and nucleic acid and protein molecules. Biological cells range in size from less than a micrometer to several hundred micrometers, and molecules are even smaller, measured in nanometers. Electrostatic forces, as has been discussed in previous chapters, are highly suitable for handling, characterization, and separation of these fine particles. With the use of electrostatic effects, these objects can be manipulated collectively or even individually. In addition, because electrostatic force is "surface force," distributed around the surfaces of objects, it enables gentle manipulation, without applying too much stress to the object.

Another aspect of electrostatic effects is associated with the breakdown of membranes. When a pulsed electric field of moderate magnitude is applied, a cell membrane breaks down and becomes permeable, but a resealing process follows due to the fluidity of the membrane. This process is called "reversible breakdown" and is used for bringing foreign material into the cell interior. Especially when this process is conducted in a DNA solution, it can be used to inject foreign genes into the cells (transfection). Or, when a partial breakdown occurs at the contact point of two cells,

they may fuse into one, to yield a hybrid between these two cells (electrical cell fusion). On the other hand, if the pulse is too strong, irreversible breakdown takes place, and the cell is destroyed. This effect can be used for sterilization.

This chapter mainly deals with the application of such ac and pulsed electric field effects to the manipulation of biological objects. Cell sorter technology, probably the most widely used application of electrostatic methods at present, will be treated in Sec. IV. No mention will be made of dc field effects, such as conventional gel electrophoresis, SDS electrophoresis, or isoelectric point electrophoresis, because there is an abundance of literature on these well-established techniques.

II. ELECTRICAL MODEL OF A CELL

A cell consists of a cytoplasmic interior and the cell membrane surrounding it. In the cytoplasm are suspended organelles such as the nucleus, the mitochondria, and the endoplasmic reticula. Some cells, such as bacterial, plant, and yeast cells, have cell walls outer to the cell membrane, while animal cells do not. The cytoplasm contains ions, about 1% by weight, and its resistivity is several tens of Ω cm, so that, from an electrostatic point of view, it can be considered as a conductor. The cell membrane is made up of a phospholipid bilayer about 10 nm in thickness, which is a fairly good insulator, with a membrane capacitance of about 1 $\mu F/cm^2$. Therefore animal cells or protoplasts (cells whose cell walls are enzymatically removed) are modeled at first approximation by a conductive sphere covered by an insulating layer (Fig. 1). The cell wall can be incorporated in such a model as an additional layer with a certain conductivity, but due to the complex structure of the cell wall its conductivity is difficult

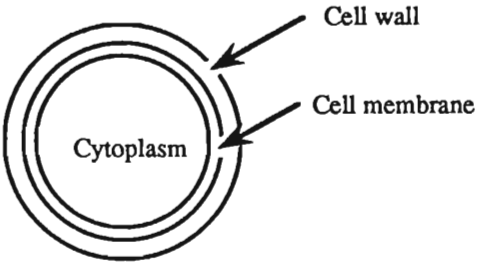


Figure 1 Electrical model of a cell.

to estimate accurately. In fact, the nature of the outermost layer is often reflected in the dielectric property of a cell as detected by dielectrophoretic measurements (Pohl, 1978; Pethig, 1979).

III. MANIPULATION AND CHARACTERIZATION

Because biological objects, such as cells or DNA, are in a form of suspension in aqueous solutions in most cases, special precautions against chemical reactions at the electrode-water interface must be made. Application of dc voltage to the electrodes immersed therein will cause electrolytic dissociation, so that these electrodes must somehow be separated from the area where the objects are manipulated. The use of an ac field can alleviate such problems. The ac field effects that can be used for the actuation of objects are summarized in Fig. 2.

A. Dielectrophoresis

Dielectrophoresis (DEP, Fig. 2(a)), developed and named by Prof. H. Pohl (Pohl, 1978), is a nonuniform field effect that yields translational motion of objects. In an electrostatic field, dielectric material polarizes, as seen in the figure, and equal amounts of positive and negative polarization charge appear on upstream and downstream sides of the particle. Because the field is nonuniform, there is an imbalance in Coulombic forces exerted on the polarization charges of both polarities, by which translational motion of the object is induced. This is the mechanism of DEP, and as well as other field effects depicted in Fig. 2, it is effective in ac fields also, because the polarity of the induced dipole alternates with the alternation of applied field.

The DEP force can conveniently be calculated by the "equivalent dipole moment" method (Jones, 1979). The equivalent dipole moment induced on a spherical particle of radius a in a uniform external field $\mathbf{E}$ is given by

$$\mathbf{p}_{eq} = 4\pi a^3 \epsilon_m K^* \mathbf{E} \tag{1}$$

where

$$K^*(\omega) = \frac{\epsilon_p^* - \epsilon_m^*}{\epsilon_p^* + 2\epsilon_m^*} \tag{2}$$

$$\epsilon_p^* = \epsilon_p - j\frac{\sigma_p}{\omega} \qquad \epsilon_m^* = \epsilon_m - j\frac{\sigma_m}{\omega} \tag{3}$$

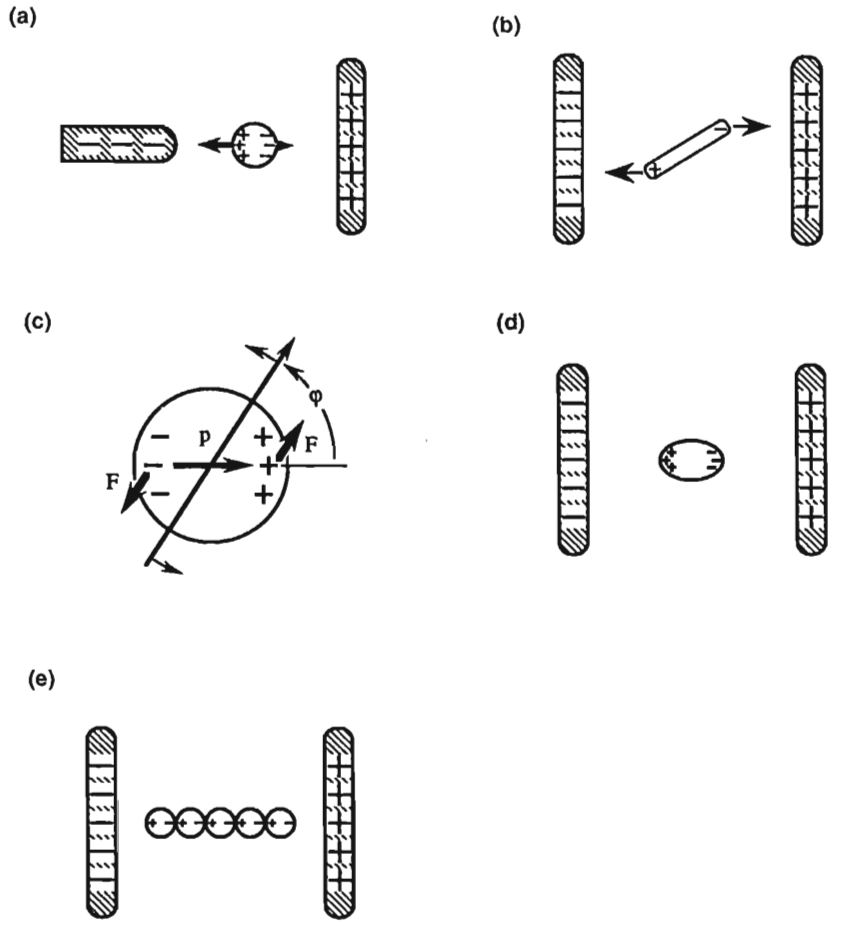


Figure 2 ac field effects for biomanipulations.

ϵ_p, ϵ_m being the dielectric constant of particle and medium; σ_p, σ_m the conductivity of particle and medium; and ω the frequency of the applied field; so that the mathematical expression for DEP force becomes

$$\mathbf{F}_d = \overline{(\mathbf{p}_{eq}\cdot\nabla)\mathbf{E}} = 2\pi a^3 \epsilon_m \mathrm{Re}[K^*(\omega)]\nabla(E^2_{rms}) \tag{4}$$

This equation states that

1. If $\mathrm{Re}[K^*(\omega)] > 0$, $\mathbf{F}_d$ is directed parallel to ∇E^2, i.e., the DEP force acts toward where the field is stronger (positive DEP).

2. If $\mathrm{Re}[K^*(\omega)] < 0$, $\mathbf{F}_d$ is directed antiparallel to ∇E^2, i.e., the DEP force acts toward where the field is weaker (negative DEP).
3. If $\mathrm{Re}[K^*(\omega)] = 0$, i.e., $\epsilon_p^* = \epsilon_m^*$, $\mathbf{F}_d = 0$.

Equation 2 is for the case when the particle is homogeneous and represented by only two parameters, ϵ_p and σ_p. For multilayered particles like cells, as shown in Fig. 3, the effective complex dielectric constant ϵ_{eff}^* can be derived by multiple use of the relation

$$\frac{\epsilon_{eff}^* - \epsilon_2^*}{\epsilon_{eff}^* + 2\epsilon_2^*} = \left(\frac{R_3}{R_2}\right)^3 \left[\frac{\epsilon_3^* - \epsilon_2^*}{\epsilon_3^* + 2\epsilon_2^*}\right] \tag{5}$$

However, in actual living cells, in addition to the interfacial polarization given by Eq. 2 or Eq. 5, many other polarization processes exist including that due to counterions. Therefore $K^*(\omega)$ shows complicated variation with the change in the frequency ω, which is referred to as "dielectrophoretic spectrum." In other words, the measurement of dielectrophoretic spectra gives some insight into the polarization process and can be used for characterizations of cells.

DEP can be measured by the observation of particle motion in any nonuniform field. Concentric cylinder or rod-to-plate electrodes can be used, but major problems with such field designs is that DEP force drops rapidly with distance. Isomotive fields on the other hand give uniform magnitude of DEP force in the entire volume between the electrodes (Pohl and Pollock, 1978).

Pohl introduced the dielectrophoretic collection rate (DCR; number of cells per pearl-chain on a pin electrode) as the measure of the magnitude of DEP and evaluated DEP force on various biological cells. He found that the DCR spectrum changes with the type of cells and their physiological conditions (Pohl and Crane, 1971). He also demonstrated the separation

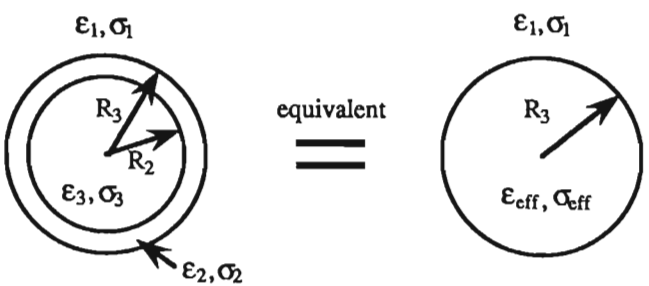


Figure 3 Equivalent model for a multilayered particle.

of cells according to the difference in DEP force using isomotive field geometry (Pohl and Kaler, 1979).

Pethig's approach was to measure the DEP spectrum using a microfabricated interdigital electrode system for generation of a nonuniform field (Pethig, 1990; Price et al., 1990). As DEP cell collection occurs, the cell suspension becomes more transparent, so that DEP can be measured by monitoring the time course of changes in light transmission. The advantage of the system is the simplicity and the adaptability to full automation of the measurement.

A system for the measurement of the DEP spectrum of the individual cell has been reported (Kaler and Jones 1990). Their method employs a vertical rod against horizontal plate electrode and levitates a cell therein with a feedback-controlled voltage. If the cell shows positive DEP, the cell's position in the horizontal direction is stable, because DEP force is directed to the center line of the electrode system. However, it is unstable vertically, because DEP force increases if the cell is perturbed upward and vice versa. Their method monitors the position of the cell and computer controls the voltage applied to the electrodes so that the cell is maintained at a predetermined location on the center line. The voltage applied then becomes the measure of the DEP force, which is in balance to the gravity on the cell. When negative DEP occurs, they employ a double-frequency method, where one frequency component is used for the measurement of DEP while the other frequency is chosen in the positive DEP region to stabilize the particle with the feedback system.

There have been attempts to use DEP phenomena for the manipulation of cells in microfabricated structures (Washizu et al., 1990d). Figure 4 is a device called a cell shift register. It consists of periodically arranged insulator walls (A–E) and electrodes (#1–#8) that are made by a photolithographic technique. Applying voltage between electrodes #2 and #4, a field maximum is created at the tip of A, and if the frequency is chosen so that the cell shows positive DEP, the cell is trapped here. To shift the cell one step to the right, the voltage is applied between #3 and #5. This kind of device, using electrostatic fields created in microfabricated structures for manipulation of particles, was named a fluid integrated circuit (FIC) (Masuda et al., 1989). It should be noted that precise design of the field pattern is essential in such a device. If there exists an unexpected field maximum, it would trap the cell and further cell motion would be hampered.

Figure 5 shows the method of cell transport and separation using the travelling field, developed by Fuhr et al. (1991). The potential ϕ traveling in the x direction

$$\phi = \phi_0 \exp(-ky) \cos(kx - \omega t) \tag{6}$$

yields a nonuniform field whose magnitude decreases with increase in y, which at the same time is a rotating field when it is seen at a fixed point in the field. If the frequency is chosen so that cells in this field show negative DEP, the cells are held at some distance from the electrode where DEP force balances gravity. Here, because of the delay in induced dipole as shown in the figure, DEP force acts in the negative x direction, and the cell is transported. In other words, the in-phase component of DEP force levitates the cell, while the out-phase component drives the cell horizontally. Difference in DEP force can thus be used for separation of cells.

B. Orientation

In early works by Teixeira-Pinto et al. (1960), it was reported that a variety of biological and nonbiological particles showed orientation phenomena under a high-frequency field. The theoretical background of this phenomenon was developed, in relation to safety issues in electromagnetic fields (Saito et al., 1966; Schwartz et al., 1965), and later modified by Jones (Jones, 1979; Miller and Jones, 1987).

Electrostatic orientation (Fig. 2(b)) occurs on an object that does not

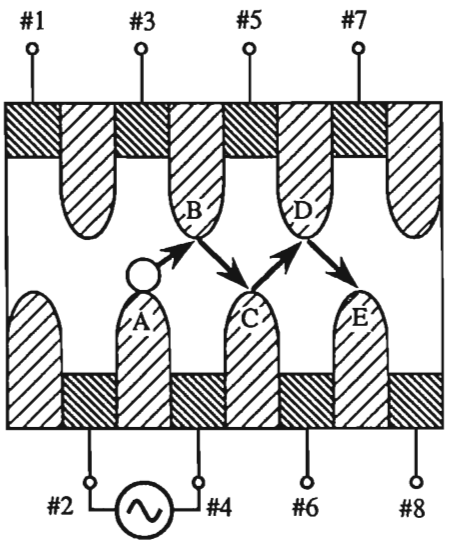


Figure 4 Cell shift register.

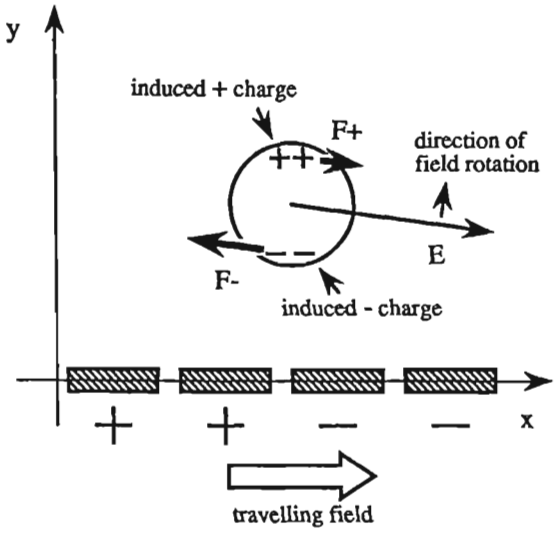


Figure 5 Transport of a cell in a travelling field. (After Fuhr et al., 1991.)

have spherical symmetry, where nonisotropicity in polarization yields orientation torque. For a spheroid with the three semiaxes a, b, and c, the equivalent dipole is given analytically:

$$p_i = \frac{4\pi}{3} abc\epsilon_m K_i^* E_i \tag{7}$$

where

$$K_i^* = \frac{\epsilon_p^* - \epsilon_m^*}{\epsilon_m^* + L_i(\epsilon_p^* - \epsilon_m^*)} \tag{8}$$

$$L_i = \frac{abc}{2} \int_0^\infty \frac{ds}{(s + r_i^2) R_s} \tag{9}$$

$$R_s = \sqrt{(s + a^2)(s + b^2)(s + c^2)} \tag{10}$$

and the suffix i indicates the a, b, or c direction; $r_i = a$, b, or c; and the torque on the spheroid is given as

$$\mathbf{T} = \mathbf{p} \times \mathbf{E} \tag{11}$$

Equation 7 states that $\mathbf{p}$ is not necessarily in line with $\mathbf{E}$, so that the particle rotates until one of its three axes becomes parallel to the field and $\mathbf{p} \parallel \mathbf{E}$

holds. All three orientations give $\mathbf{T} = 0$; which of them is realized must be determined by stability analysis. It is known that at the low and high frequency limits, i.e., $\omega \rightarrow 0$ and $\omega \rightarrow \infty$, the orientation with the longest axis parallel to the field is the stable orientation, and at ω between these limits, orientational changes occur depending on ω and ϵ on and σ of the particle and the medium.

A biological application of this phenomenon to the orientation of DNA has been reported (Washizu and Kurosawa, 1990a). DNA is a long flexible chainlike molecule on which genetic information is carried at the density of 2.9 kb (kilobase) per μm. A DNA molecule takes random coiled conformation due to thermal agitation in a solution. However, it has been shown that, with the application of ca. 1 MHz, 1×10^6 V/m field, it can be stretched straight. This is apparently because every part of the molecule tends to be parallel to the field. The orientation in combination with DEP can be used to position the stretched molecule to a predesigned high-field region, for instance onto a sharp electrode edge. The molecular size can be determined by measuring thus stretched length, or it can be cut at an arbitrary position with a sharp-focused laser beam. This method may also provide a technique for specimen preparation when biological molecules are to be observed with scanning tunnelling microscopes (STM) or atomic force microscopes (AFM).

C. Rotation

Electrorotation (Fig. 2(c)) is the rotation of an object in a rotating electric field. Because K^* in Eq. 1 or 7 is a complex constant, these equations show that there is a phase delay in induced dipole moment. This yields a rotational torque as shown in the figure. For a spherical particle in a rotating field

$$E_x = E_0 \cos(\omega t) \qquad E_y = E_0 \sin(\omega t) \tag{12}$$

the torque becomes

$$T_z = -4\pi a^3 \epsilon_m \mathrm{Im}[K^*(\omega)]\, E_0^2 \tag{13}$$

In comparison with Eq. 4, it is the real part of $K^*(\omega)$ that determines DEP force, while the imaginary part of $K^*(\omega)$ determines the rotational torque.

The physical interpretation of the delay in the induced moment of a cell is that it takes the time constant τ to charge the membrane capacitance through the resistivity of the suspension and the cytoplasm. Therefore the rotation is affected by the properties of the membrane such as changes in membrane area, so that the measurement of rotational speed against

the applied frequency (rotational spectrum) can be used for the characterization of the cell membrane (Arnold et al., 1989; Arnold and Zimmermann, 1988).

The application of electrorotation to cell separation has been reported by Fuhr et al. (1985). In their method, a mixture of two types of cells is placed on the surface of an agar plate, which is put in a rotating field. If the condition is so chosen that cofield and counterfield rotation occurs for the two types of cells, they roll to different directions, and the separation takes place. Such a separation is according to the imaginary part of $K^*(\omega)$, in contrast to that using the real part in DEP separation.

Another utilization of electric torque is exampled by the measurement of bacterial motor characteristics (Washizu et al., 1993). Some bacterial species, such as *Salmonella* or *E. coli*, swim by means of flagella that are rotated like a screw by the flagellar motor at the root of each flagellum. The difficulty with the measurement of its characteristics is the size; the bacterium itself is only a few micrometers and the motor is 30 nm in diameter. The experiment employs a conventional approach to motor characteristic measurement: apply external torque and measure the speed of rotation. Electrical torque due to electrorotation is used as the external torque here.

It should be added that cellular rotation is often observed in an alternating field, in such cases as pearl-chain formation prior to cell fusion. This cannot be explained merely by the above mathematical model, where no torque should appear under an alternating field. There have been a few models presented to explain the phenomenon. One is the model of Holzapfel et al. (1982), which attributes the rotation to the deformation of the field by adjacent cells, by which rotating field component is generated just as in a shading coil motor. Another is Turcu's (1987) stability analysis which shows that there is a region for a set of parameters ϵ, σ, and ω where the torque is zero for a cell at rest, but once it starts rotation, more torque is generated to result in spontaneous rotation. This mechanism is that of a single-phase induction motor. There is also a model to attribute the rotation to active ac dipole moments generated in living cells (Pohl, 1983).

D. Deformation

Protoplasts or liposomes (artificial small vesicles of phospholipid bilayer) are highly deformable vesicles that take spherical shape due to surface tension if there is no external stress. Animal cells are relatively less deformable because of reinforcement structures (cytoskeltons), but among

them erythrocytes are known to have high deformability, which makes them able to pass through a capillary smaller than the cell's diameter.

Under an electrostatic field, these objects can be elongated (Fig. 2(d)) or flattened due to electrical stresses (Maxwell stress). The application of this effect for desickling of sickled erythrocytes has been reported (Bogen et al., 1990; Ashe et al., 1987).

E. Chain Formation

Chain formation (Fig. 2e), or pearl-chain formation, results from attractive force between induced dipole moments of plural cells. Chains can be formed in both uniform and nonuniform fields, whether the particles show positive or negative DEP. The chain is more difficult to form for smaller particles where thermal randomization becomes more eminent. The threshold field strength E_{th} required to form a chain has been investigated by Schwan and Sher with its implications for nonthermal effects of electromagnetic waves (Schwan and Sher, 1969). The most important application of chain formation to biomedical engineering is found in the electrical cell fusion protocol, which we shall discuss later in this chapter.

F. Utilization of *Optical Pressure*

When a laser beam is scattered by an object, it imparts momentum and therefore force to the object by conservation of momentum. The force is called optical pressure or radiation pressure (Ashkin, 1970; Ashkin and Dziedzic, 1971). The force can be divided into two components (Ashkin and Dziedzic, 1989; Mizuno et al., 1991a). The first is the scattering force. It points in the direction of the incident laser and is proportional to the power. The other component is the gradient force that exists in beams with nonuniform intensity. It is proportional to the gradient of the intensity and points in the direction of the intensity gradient.

For Rayleigh-scattering regime particles, the scattering force is given by

$$F_{\text{scat}} = \frac{P_{\text{scat}}}{c} = \frac{I_0}{c} \frac{128\pi^5 r^6}{3\lambda^4} \frac{n^2 - 1}{n^2 + 2} \tag{14}$$

where P_{scat} is the Rayleigh scattered power, c the velocity of light, I_0 the incident intensity, λ the wavelength, n the index of refraction of the particle, and r radius of the particle. If a sphere is placed in a beam with an intensity gradient, it then experiences the additional gradient force component

$$F_{\text{grad}} = -\frac{1}{2}\alpha \nabla E^2 \tag{15}$$

$$\alpha = r^3 \frac{n_2 - 1}{n_2 + 2} \tag{16}$$

where α is the polarizability of the particle. Particles with high refraction index ($\alpha > 0$) are pulled into the high-intensity region of the beam. The optical pressure for larger particles can be calculated using the Mie scattering equation.

Figure 6 schematically shows the two components of the optical pressure. When a straight laser beam of Gaussian intensity distribution is used, particles are confined in the beam and are transported toward the incident direction. When a laser beam is strongly converged by a microscope lens with a large numerical aperture, the single-beam gradient trap can be made at a point where $F_{\text{grad}(z)}$ balances with $F_{\text{scat}(z)}$. This is called laser trapping and is useful for the micromanipulation of cells or particles (Ashkin et al., 1986).

Ashkin et al. applied laser trapping, using the apparatus shown in Fig. 7, for *Es. coli*, yeast cells, red blood cells of humans, and organelles within individual living cells of *Spirogyra*. Using an infrared red YAG laser, damage-free trapping can be achieved (Ashkin et al., 1987).

The optical pressure can also be used for transportation and sorting of single cells and fine particles (Buican et al., 1987). Figure 8 shows the velocity of optical transportation when an Ar ion laser of 20 μm beam

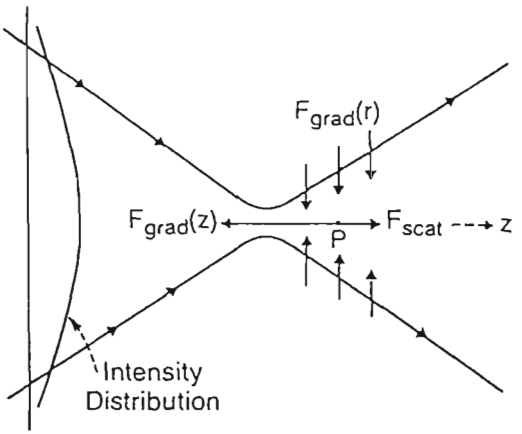


Figure 6 Optical pressure.

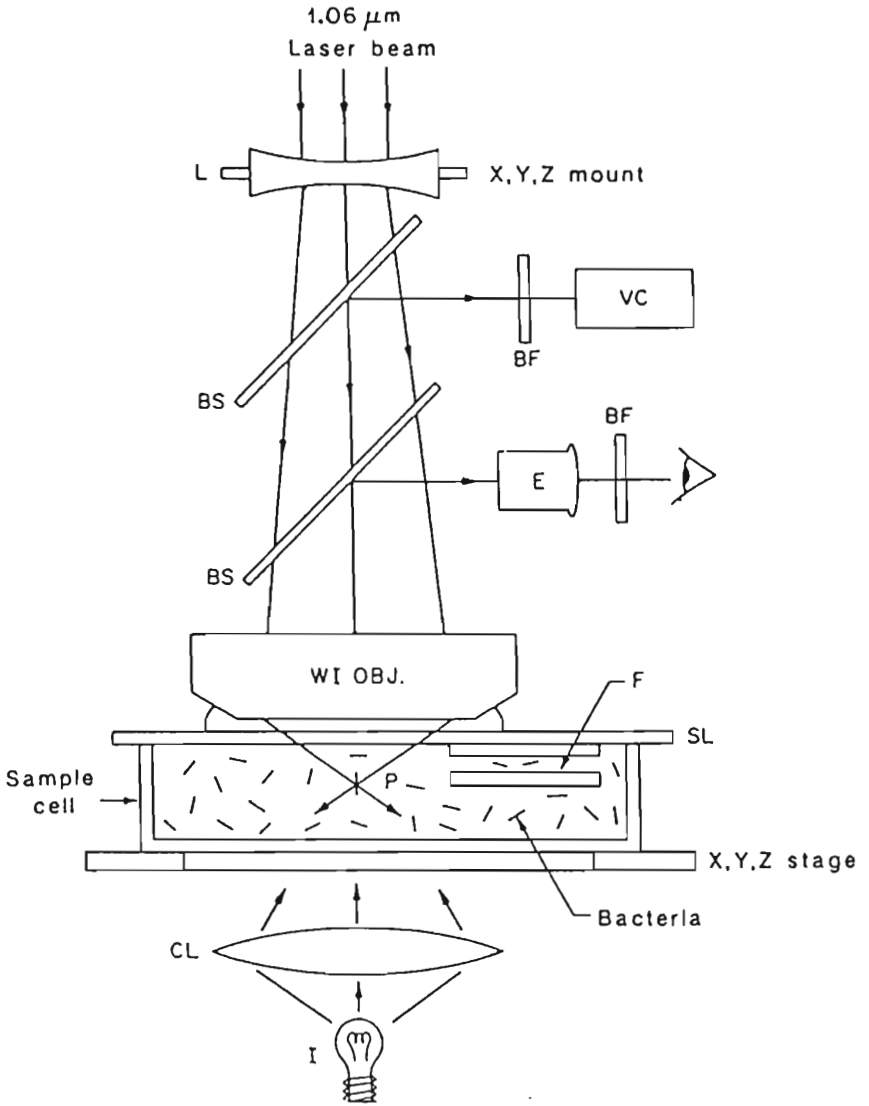


Figure 7 Laser trapping (laser tweezer).

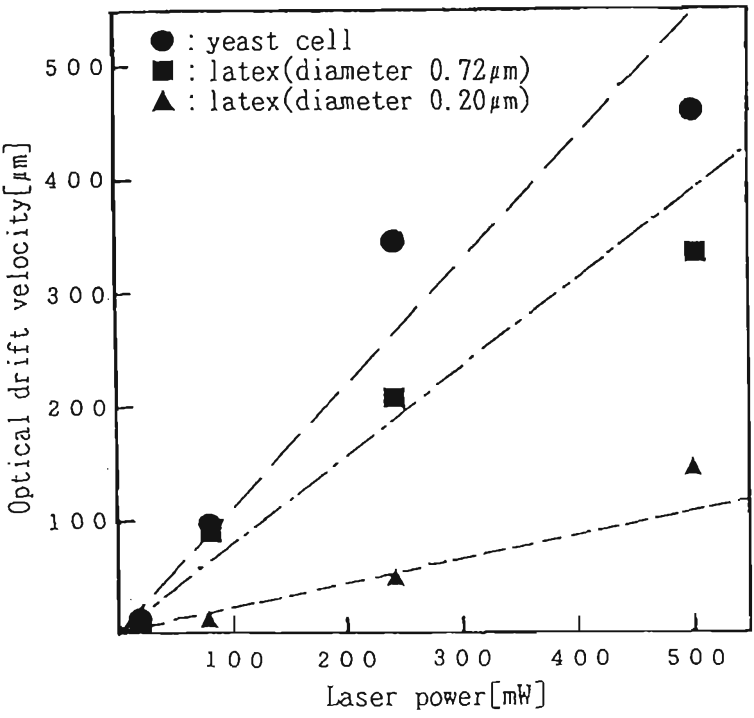


Figure 8 Velocity of optical transportation.

diameter was used (Mizuno et al., 1991a). Figure 9 shows a cell sorting method using crossed laser beams. Single cells are transported by a laser beam and sorted using another laser beam with higher intensity (Mizuno et al., 1991b).

The optical pressure provides a potential well for trapping and transportation of single cells. This is a distinctive property of the optical pressure, since the potential well for confinement of charged particles cannot be made electrostatically. The combination of optical pressure and electrostatic force, designated as optoelectrostatic micromanipulation, provides a more flexible micromanipulation of cells (Mizuno et al., 1991a).

1. Single-Cell Feeding Device

Figure 10 shows the single-cell feeding device. An insulating slit separates the cell storage chamber and the manipulation region. Cells usually have negative charge, and they cannot pass through the slit and are confined in the cell storage chamber by electrophoretic force. A laser beam is intro-

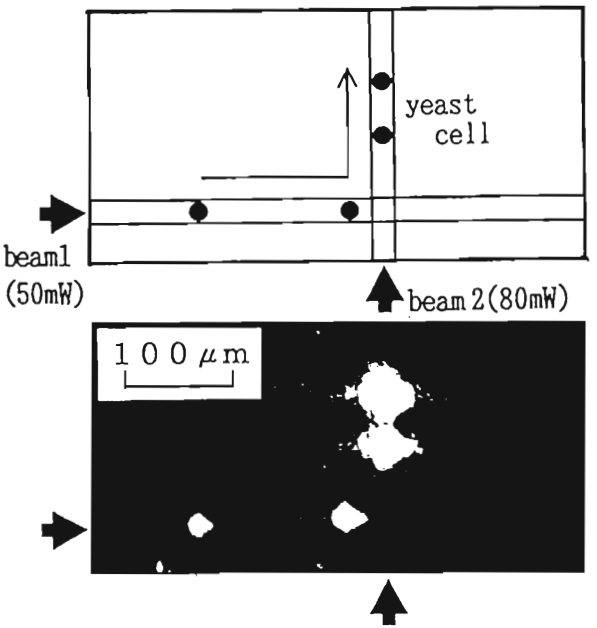


Figure 9 Cell sorting by crossed laser beam.

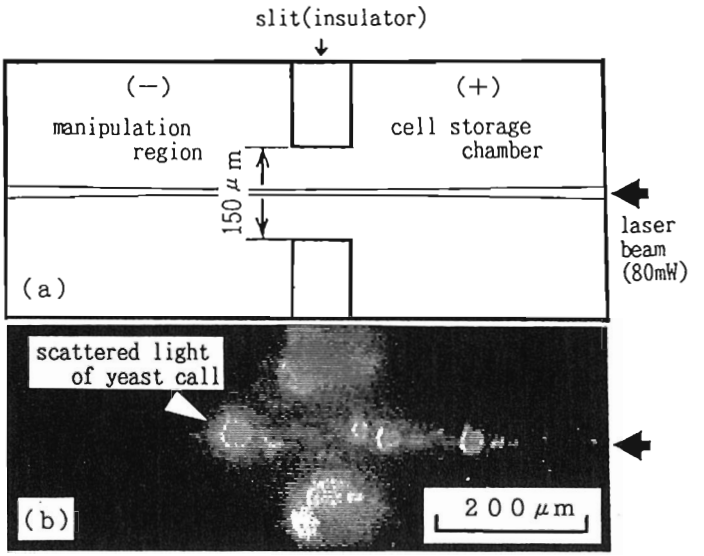


Figure 10 Single cell feeding device.

duced through the slit to the manipulation region. Single cells can be confined and pushed by the laser beam toward the manipulation region when the optical pressure is adjusted to be slightly larger than the electrophoretic force at the slit.

2. Positioning of an Injected Particle Inside a Cell

A carrot protoplast was fixed on the electrode surface electrostatically using dielectrophoretic force as shown in Fig. 11. Polystyrene latex particles (PSL) were transported to the surface of the protoplast by the laser beam. Pulsed voltages were then applied to inject the PSL into the protoplast. When the injection was made, the particles could be manipulated inside the protoplast using optical pressure.

3. Measurement and Sorting of Nonspherical Cells by Electrostatic Orientation

For an accurate measurement of configuration of nonspherical cells and chromosomes, the electrode system shown in Fig. 12 can be used. Single cells can be positioned at the center of the electrode system by laser trapping and can be oriented toward the field direction. High-frequency voltage of 1 MHz was used to form the electric field. The figure also shows the oriented yeast cell and the *E. coli* cell. Since fragile cells can be positioned and oriented by this method, configuration can be measured accurately. The trapped cell can then be sorted by optical transportation.

4. Rotation of Optically Trapped Cell

Using a photofabricated microelectrode as shown in Fig. 13, a cell can be rotated (Nishioka et al., 1991). The electrode system consists of three

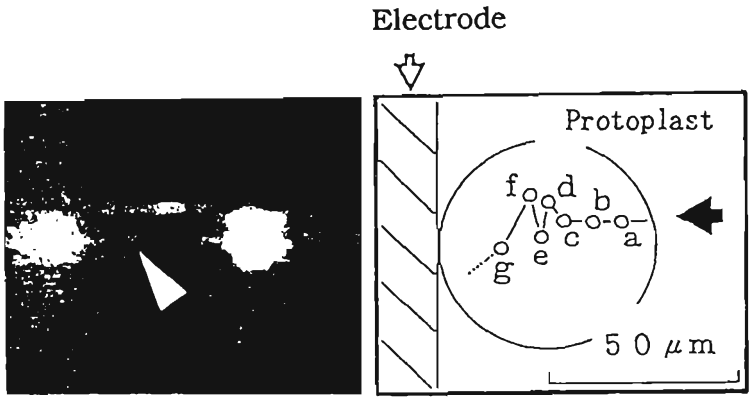
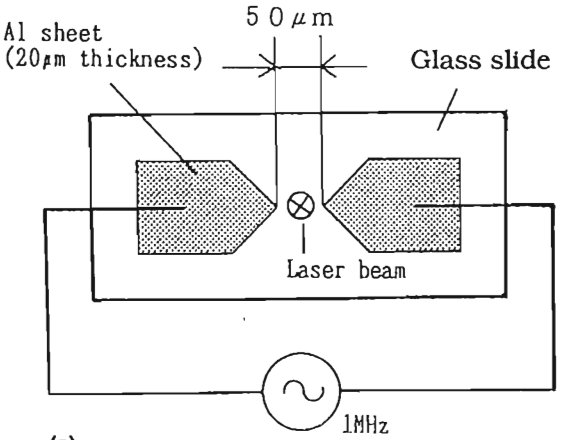
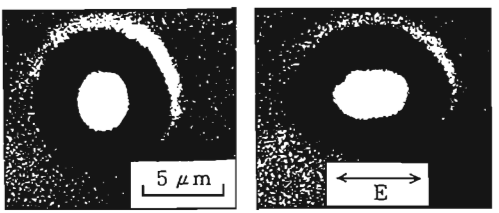


Figure 11 Positioning of an injected particle inside a carrot protoplast.

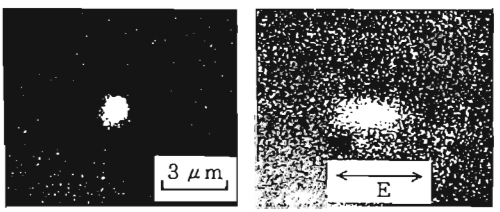


(a)



(i) (ii)

(b)



(i) (ii)

(c)

Figure 12 Measuring method utilizing laser trapping and electrostatic orientation. (a) Electrode; (b) yeast cell (i) t = 0 sec, (ii) t = 0.6 sec, E = 10^5V/m; (c) *E. coli* (i) t = 0 sec, (ii) t = 0.4 sec, E = 5×10^3V/m.

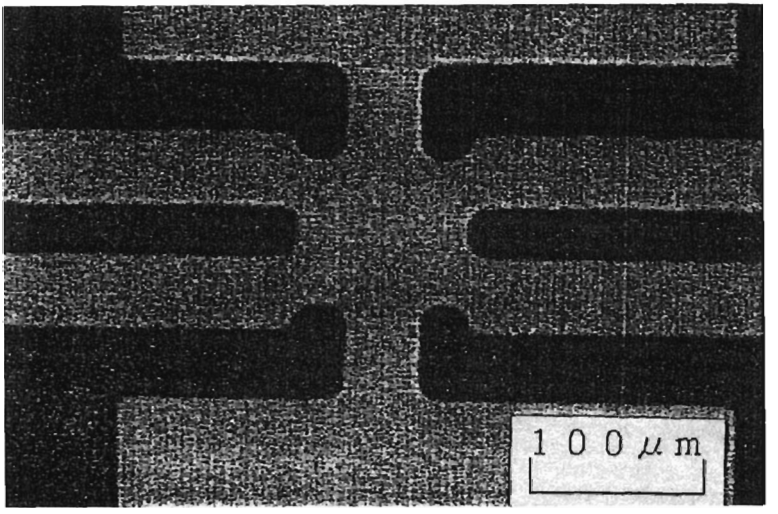


Figure 13 Microelectrode for rotation of a cell trapped by a laser beam.

pairs of electrodes, to which an ac voltage is applied in succession. A nonspherical cell is positioned at the center of the electrode system by laser trapping. Orientation of the trapped cell follows the rotating electric field direction. When an ac electric field of 1 MHz and 2×10^5 V/m intensity, a live *S. cerevisiae* cell could be rotated up to 130 rpm. The maximum rotating speed of a dead cell was smaller than that of a live cell (Nishioka et al., 1991).

IV. MEMBRANE ALTERNATION

A. Electrical Cell Fusion

Because the cell membrane is made of insulating lipid, when a cell is placed in a dc field, the voltage drop is concentrated on the cell membrane, and if this voltage exceeds the breakdown voltage V_b, the membrane punctures. The cell membrane is only 10 nm in thickness, and about 1 V is required to break down the membrane for most cells, whether natural or artificial, plant or animal. If the voltage far exceeds V_b or is maintained for a long period of time, the puncture develops until cell lysis occurs. However, because the membrane is a "two-dimensional fluid" and lipid molecules are rather free to move laterally, if the voltage is a short pulse slightly exceeding V_b, the membrane can reseal itself, a process called reversible breakdown.

The membrane voltage as a matter of fact does not build up instantaneously. When an external field E is applied stepwise at $t = 0$, the membrane voltage is given by

$$V_m(\theta) = 1.5\, a\, E \cos\theta \left[1 - \exp\left(-\frac{t}{\tau}\right)\right] \tag{17}$$

$$\tau = (\sigma_p + 2\sigma_s)^{-1} C_m a \tag{18}$$

where a is the cell radius, E is the magnitude of the applied field, θ is the angle between radius and field, and C_m is the membrane capacitance in F/m^2. Equation 14 shows that V_m is a maximum at the most upstream and downstream sides of the cell (poles) and is zero at $\theta = 90°$ (the equator). Therefore it is at the poles that membrane breakdown takes place.

Electrical cell fusion makes use of this reversible breakdown to create hybrids between two types of cells. The so-called Zimmermann protocol (Zimmermann et al., 1982) starts with the pearl-chain formation of the cell mixture suspended in isotonic nonionic solution (Fig. 14). Use of ionic high-conductivity solution is prohibitive because of the reduced DEP force in high-conductivity medium (cf. Eq. 2) and the high joule loss. When the cells in chains are in good contact to each other, a pulse voltage is applied. If the pulse amplitude is properly chosen, the reversible breakdown occurs, and during the resealing process the neighboring cell membranes fuse to form apocyte fusant.

A drawback of such a protocol is that the two types of cells to be fused are treated as a mixture, and how many of which types of cells fuse are unpredictable. To create exclusively a one-to-one hybrid, Sato et al. (1990) developed a system where two-dimensional arrays of microfusion chambers are employed. The chambers are microfabricated by a photolitho-

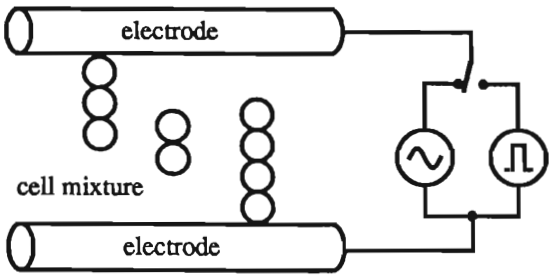


Figure 14 Electrical cell fusion.

graphic nonisotropic etching technique. Each chamber is equipped with a pair of electrodes, to which one cell from each cell type is fed using an array of micropipets, which are also photolithographically fabricated so as to fit into the array of fusion chambers. A pair of cells thus formed in each chamber is fused by the Zimmermann protocol to yield a one-to-one hybrid.

Another approach to obtain a one-to-one hybrid also uses microfabrication techniques (Masuda et al., 1989). The fusion is made in the chamber depicted in Fig. 15. Cells of types A and B are sent to this area through the fluid channel by micropumps installed at the upstream side of each channel (not shown in the figure). When high-frequency voltage is applied to the electrodes, field lines run through the small opening made at the center between the electrodes as shown in the figure, so that a field maximum is created here, and the cells are dielectrophoretically trapped here to form an AB pair. Then pulse voltage is applied to initiate membrane fusion. The fusants are sent to the outlet by activating the micropumps again.

B. Electroporation and Transfection

Electroporation uses membrane breakdown, not to fuse the membrane, but to allow the permeation of exogenous material into the cell interior by diffusion and/or electrophoresis. The method is just to apply pulsed

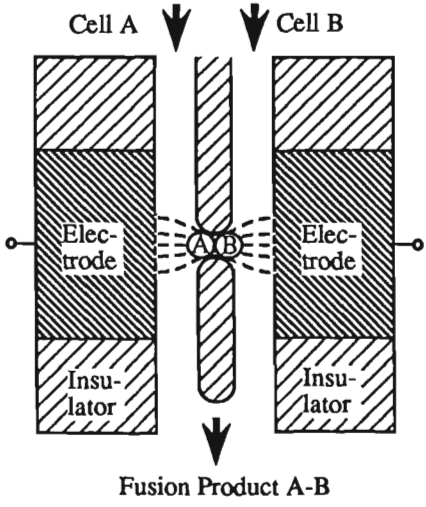


Figure 15 Fluid integrated circuit (FIC) cell fusion device.

voltage to the cosuspension of the cell and the particle or chemicals to be brought into the cell (Kinoshita and Tsong, 1977; Teissie and Tsong, 1981; Zimmermann and Arnold, 1988). The electrically punctured pores are stable and can be sustained for on the order of one second. In some cases, it allows the passage of particles as large as a cellular organelle. Therefore it could be caused not only by reversible breakdown but also by local irreversible breakdown, in which case the cytoskeletal protein network supports the membrane structure until the slow resealing process is completed (Chang and Reese, 1990).

Particularly important biochemical application of electroporation is found in electric transfection, where foreign genes are inserted into cells (Wong and Newmann, 1982).

C. Disinfection

High electric fields can be formed in liquids, and electrolysis can be reduced using a short-width pulsed voltage. A cell membrane breaks down when the voltage drop across the membrane exceeds 0.4–2 V, and reversible or irreversible breakdown takes place. Electrical cell fusion utilizes reversible breakdown.

Sale et al. and Hamilton et al. investigated the lethal effect of high electric fields on microorganisms. Applying high pulsed voltages of up to 25 kV/cm field strength and 40–100 ms pulse duration to suspensions of vegetative bacteria and yeasts in 0.85% NaCl solution, the authors have shown that death was not due to heating or electrolysis but was due to increased membrane potential that led to irreversible breakdown of the membrane structure (Sale et al., 1967; Hamilton et al., 1967). This method can be used for high-speed sterilization or low temperature sterilization to reduce damage by the medium. More detailed studies have been made on effectiveness and energy efficiency of this disinfection method (Sakurauchi et al., 1980; Mizuno and Hori, 1988; Sato et al., 1990; Matsumoto et al., 1991; Jayaram et al., 1991). Test results of high voltage disinfection by Matsumoto et al. (1991) are described in the following. Figure 16(a) shows a wire-cylinder electrode with a 20 mm inner diameter, a 110 mm length, and a wire diameter of 1 mm. Figure 16(b) shows the converged-electric-field type electrode system. An insulating plate with small holes (thickness 1 mm, hole diameter 1 mm) is placed between the parallel disc electrodes. Sample liquid is continuously introduced into the vessel through the hole of the disc electrode. The inner diameter of the vessel is 20 mm, and separation between the disc electrodes is 20 mm. In this electrode system electric current is converged into the small holes of the insulating plate where the cell suspension flows. Pulsed high voltages were

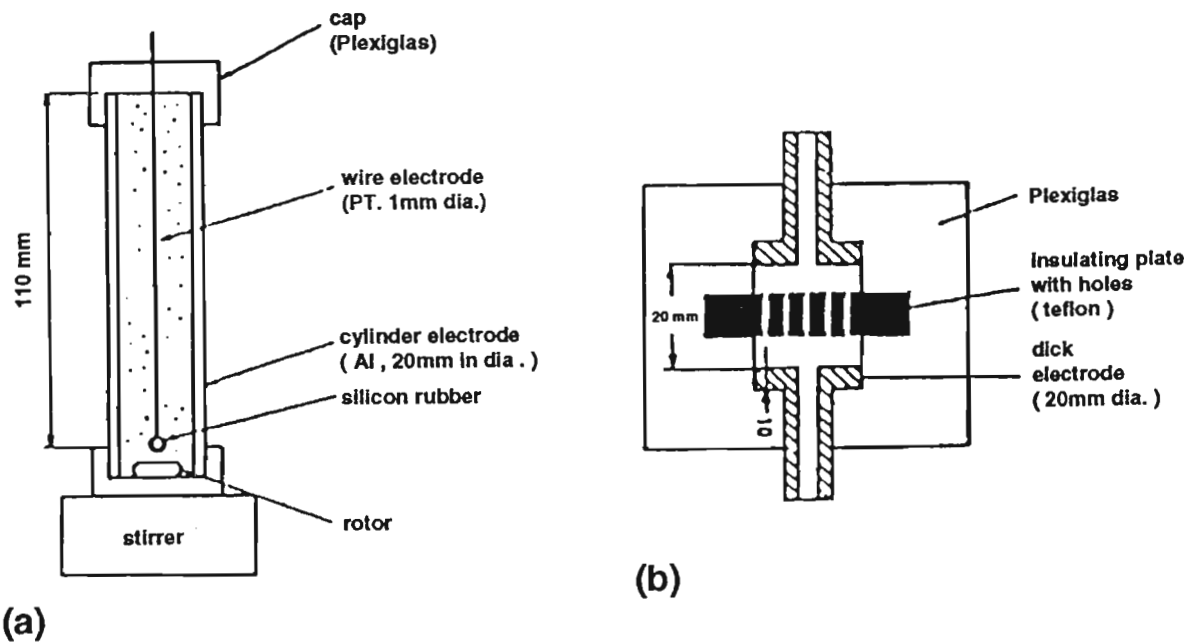


Figure 16 Electrode system for electrical disinfection. (a) Wire-cylinder electrode. (b) Converged-electric-field type electrode.

generated using a spark gap switch as shown in Fig. 17. Pulsed voltages with width of 2–250 μs were used.

The cells were suspended in phosphate buffer solution. The initial cell concentration was adjusted to be about 10^7 cells/cc. The conductivity of the sample was 500 to 5000 μS/cm. *S. cerevisiae*, *E. coli*, *S. aureus*, *A. niger*, and *B. subtilis* spores were tested.

The energy input to unit volume of the sample P is

$$P = 0.12\, CV^2 f/Q \tag{19}$$

where V is the charging voltage of the capacitance C (F) of the voltage generator, f is the frequency of the pulsed voltage, and Q is the sample flow rate.

Figure 18 shows the survivability of *S. cerevisiae* when the wire-cylinder electrode was used. The survivability was measured at $V = 20$ kV and $f = 25$ Hz. The solid line (A) in the figure shows that the pulsed high voltage could destroy the cell, and the survivability decreased to less than 1% in a short time. However, the destruction performance deteriorated with decrease of survivability. When the sample was stirred, the surviva-

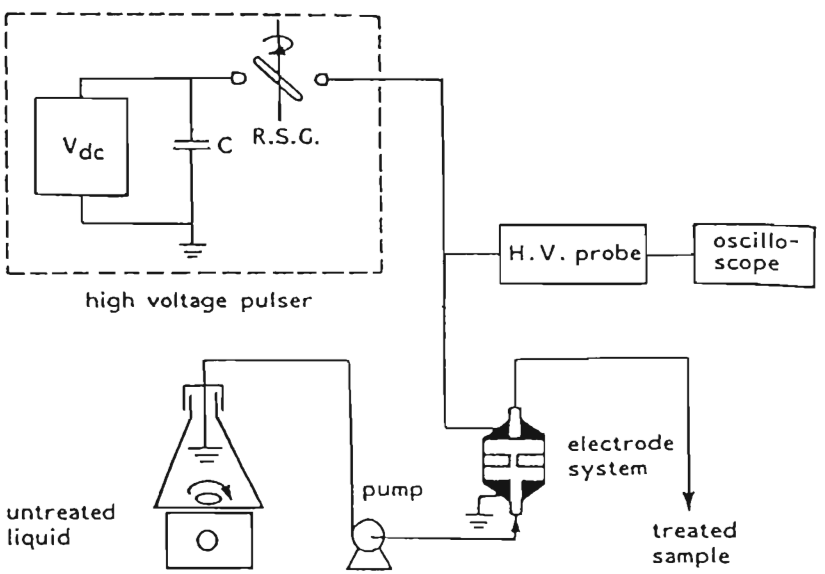


Figure 17 Schematic diagram of the experimental setup.

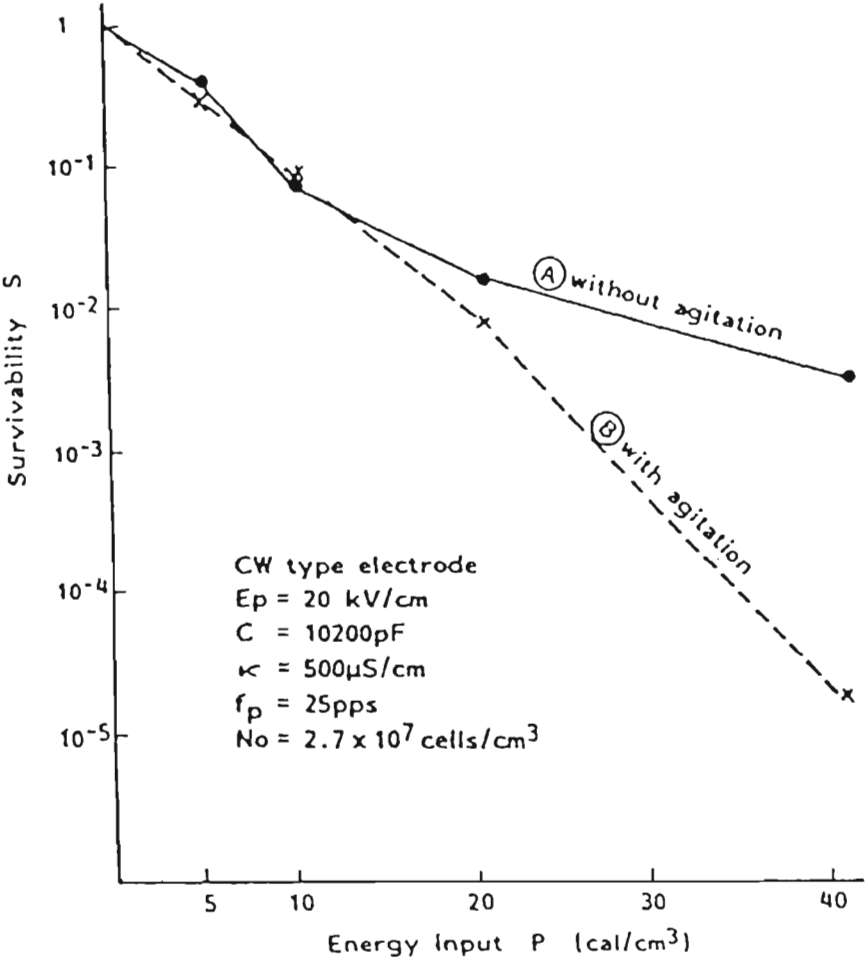


Figure 18 Survivability of *S. cerevisiae* with the wire-cylinder electrode.

bility decreased linearly. By continuous agitation of the sample liquid, the cells were exposed to the high electric field region near the wire electrode.

The converged-electric-field type electrode system was developed for continuous sterilization. Figure 19 shows the survivability of *S. cerevisiae* and *E. coli*. The survivability decreased almost linearly as an exponential function of input energy.

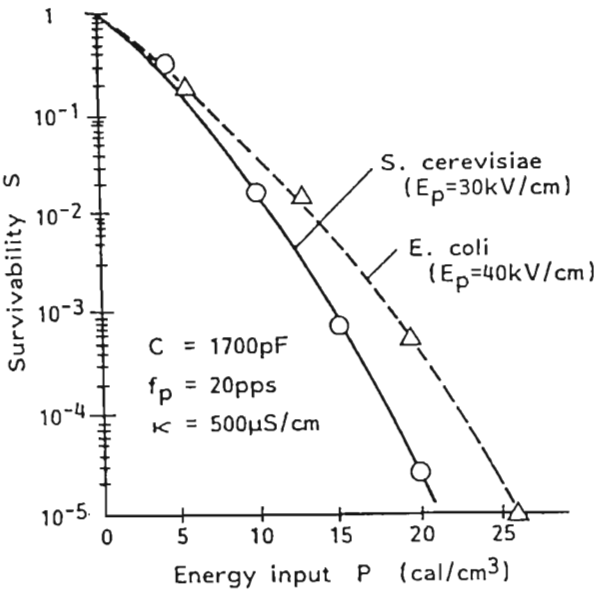


Figure 19 Survivability of *S. cerevisiae* and *E. coli* with the converged-electric-field type electrode.

This disinfection method, however, is not effective on every species. *B. subtilis* spores could not be destroyed by pulsed voltage application. It was also reported by Matsumoto et al. that *B. subtilis* spores could easily be disinfected by an intense ultraviolet ray associated with breakdown of liquid by pulsed voltage application.

Figure 20 shows photographs of *S. cerevisiae* cells before and after the pulsed high voltage sterilization process (Hayamizu et al., 1989). Almost all the cells did not change shape, but their surfaces became very rough, and fine debris was observed attaching to the cell surfaces.

A synergistic effect of temperature and pulse treatment on the destruction of *L. brevis* cells has been reported using a parallel plate electrode system (Jarayam et al., 1991). The survivability of *L. brevis* as a function of field at elevated temperatures is shown in Fig. 21. The destruction rate of cells was rapid with fields up to 15 kV/cm; however, at slightly higher field strengths, higher than 20 kV/cm, the destruction rate was reduced at 30 and 45°C. When the temperature of the medium was raised to 60°C, the survivability was reduced.

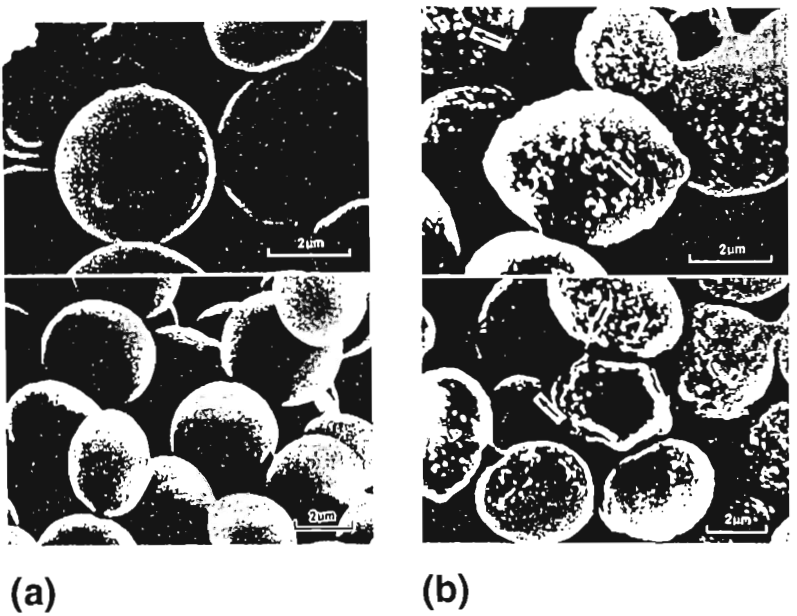


Figure 20 Effect of temperature for the destruction of *L. brevis* cells. (a) Normal *S. cerevisiae*. (b) Destroyed cells.

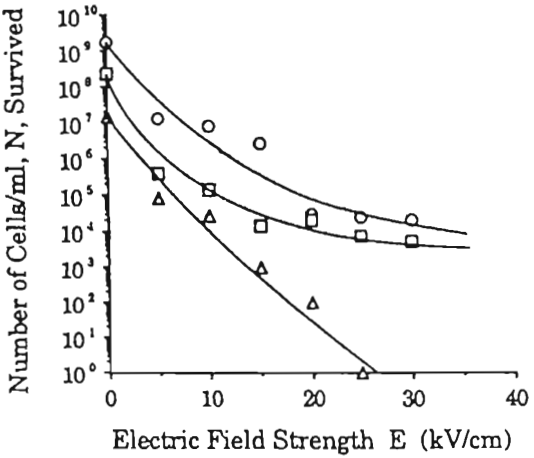


Figure 21 Effect of temperature for the destruction of *L. brevis*. ○, 30°C; □, 45°C; △, 60°C.

V. CELL SORTER

A. Principle

The fundamental concept of a cell sorter based on flow cytometry is shown in Fig. 22 (JASCO, 1984).

Sample flow suspending cells and sheath flow are introduced to the nozzle and are sprayed to form uniform droplets. The sheath flow surrounds the sample flow, and cells are aligned at the center of the flow by hydrodynamic focusing. Cell concentration should be so adjusted that a droplet contains less than one cell. Actually more than 10 vacant droplets should be formed between each droplet containing a cell.

The diameter of the nozzle typically ranges from 50 to 150 μm, and a typical velocity of the sprayed liquid jet is about 10 m/s. The nozzle incorporates a piezotransducer that generates uniform droplets at a stable breaking point. The droplet-forming frequency is typically 20 to 50 kHz.

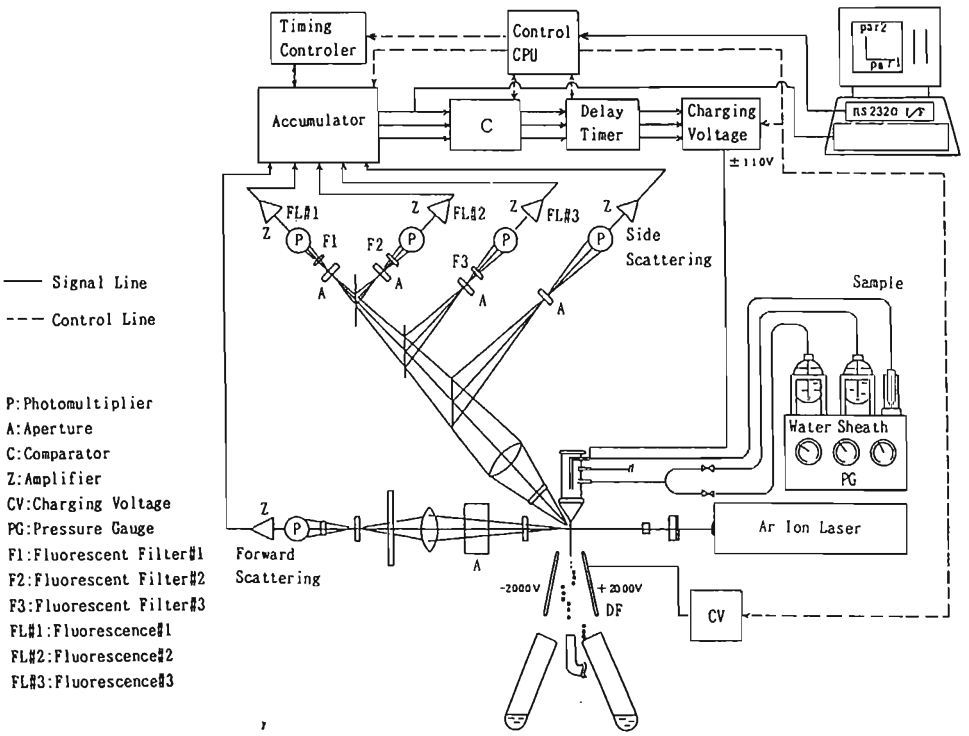


Figure 22 Fundamental concept of a cell sorter.

A laser beam is focused to the liquid jet at the outlet of the nozzle to measure optical characteristics of cells. Two or more lasers are used when necessary. A transparent nozzle can also be used, and the focal point of the laser is set inside the nozzle. Electrical cell sizing apparatus can be incorporated in the nozzle. Forward and side scattering light intensity as well as fluorescence are usually measured. These light signals are processed by comparing them with the reference value, and the droplet charging signal is generated accordingly.

The droplet charging signal is applied between an electrode that contacts the fluid in the nozzle and a counterelectrode surrounding the flow jet (not depicted in the figure). An electrostatic field is formed between the tip of the unbroken fluid jet and the counterelectrode. Induced charge appears on the surface of the tip, which is proportional to the charging voltage. Charged droplets are formed as the jet breaks when the charging voltage is applied. After charging, the droplets pass through a deflection electrode. The charging voltage should be applied after a certain delay time necessary for the cell to move from the signal detection point where the laser is focused to the breaking point of the flow jet. Since the delay time sometimes fluctuates within 1 or 2 droplet formation periods, usually two to four succeeding droplets are charged to sort one cell. In this case, the forward charged droplet induces an opposite polarity charge on the tip and affects the droplet charging. This interference should be compensated for by adjusting the waveform of the charging voltage to obtain the same deflection trajectory. A typical value of the charging voltage is 75 to 150 V, and the deflection voltage is + and −2000 to 3000 V.

At typical operating conditions, a cell sorter can measure and sort about 1000 cells/s. The cell preparation technique is very important in the use of the cell sorter. For the sample, a suspension of single cells should be prepared. To characterize the cell, usually fluorescence signals and forward/side-scattering signals are used. Details of cell preparation and staining methods are described by Melamed et al. (1990). Other types of cell sorters are also described in the same reference.

B. Cell Sorter for Plant Protoplasts

Techniques of flow cytometry and sorting were initially developed for animal cells with diameters in the 5 to 10 μm range. In bioengineering of plants, protoplasts are widely used for cell fusion or transfection, and sorting of protoplasts has been needed. Plant protoplasts have diameters in the 15 to 150 μm range, and they are very fragile in comparison to animal cells. Conventional cell sorters easily destroy plant protoplasts, mainly at the nozzle where the flow is squeezed and accelerates. Figure 23

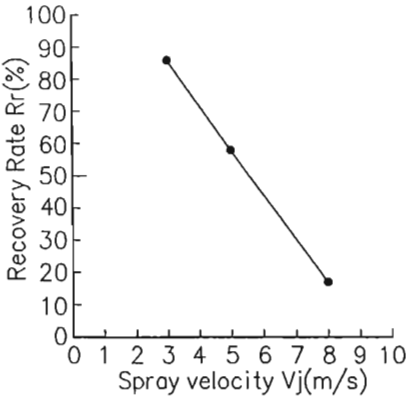


Figure 23 Recovery rate of cabbage protoplasts.

indicates an example of the recovery rate of cabbage protoplasts (diameter range of 15 to 40 μm) (Kawakami et al., 1992). It was observed that the protoplasts with larger diameters could be destroyed easily.

Galbraith et al. (1988) have reported on the sorting of plant protoplasts using nozzles with larger diameters, 100 to 200 μm, at reduced droplet formation frequency. It has also been reported that chilling and increased osmotic pressure could raise the recovering rate of viable protoplasts (Harkins et al., 1987).

When a nozzle with a large diameter is used to achieve a higher nondestructive rate, the droplet formation frequency decreases and the sorting speed reduces. The spray velocity should be decreased at the same time. Decreased spray velocity also results in reduced frequency of droplet formation. Figure 24 shows an air sheath nozzle, in which the flow jet is sprayed from the 250 μm nozzle at 3 m/s and the flow jet is squeezed to 150 μm diameter and 8.3 m/s velocity. The droplet formation frequency can be raised to 15 kHz. Fused protoplasts of cabbage and Chinese cabbage could be sorted using FITC fluorescent staining for cabbage and fluorescent of Chinese cabbage chlorophyll. The recovery rate was about 90%, and the fusant was condensed from 2 to 95% (Kawakami et al., 1993).

VI. CONCLUSION

For micromanipulation and measurement of cells, genes, membrane, or molecules, various novel tools and schemes have been developed. Electrostatic force and optical pressure, as mentioned in this chapter, are suitable means to treat very small objects. Micromanipulation can be used

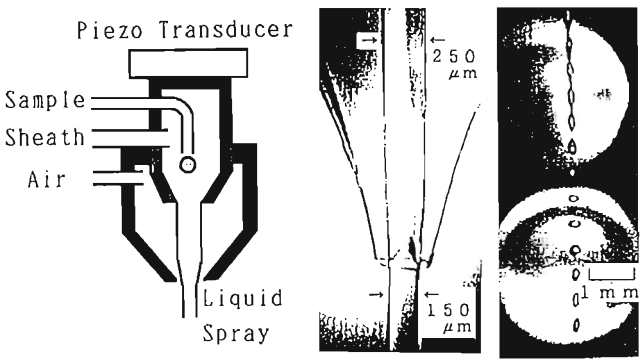


Figure 24 The air-sheath nozzle.

to fix single objects in order. This provides samples to be measured by microscopes with very high resolution such as scanning tunnelling microscopes or atomic force microscopes.

Electrostatic methods have been successfully used for cell fusion, transfection, and cell sorting. For incubation of cells, biocontamination should be avoided. Disinfection and gas cleaning are important, and electrostatic methods can also be applied in these fields.

REFERENCES

Arnold, W. M., and U. Zimmermann (1988). Electro-rotation: developments of a technique for dielectric measurements on individual cells and particles. *J. Electrostatics*, 21, 151–191.

Arnold, W. M., R. K. Schmitzler, S. Al-Hasani, D. Krebs, and U. Zimmermann (1989). Differences in membrane properties between unfertilised and fertilised single rabbit oocytes demonstrated by electro-rotation. *Biochim. Biophys. Acta*, 979, 142–146.

Ashe, J., S. Takashima, D. Bogen, and T. Asakura (1987). Desickling of sickled erythrocytes by means of low intensity, low frequency a.c. fields. Proc. 13th Ann. Northeast Bioeng. Conf., pp. 322–325.

Ashkin, A. (1970). Acceleration and trapping of particles by radiation pressure. *Phys. Rev. Lett., 24*, no. 4, 156–159.

Ashkin, A., and J. M. Dziedzic (1971). Optical levitation by radiation pressure. *Applied Physics Letters*, 19, no. 8, 283–286.

Ashkin, A., and J. M. Dziedzic (1989). Optical trapping and manipulation of single living cells using infrared laser beams. *Ber. Bunsenges. Phys. Chem.*, 93, 254–260.

Ashkin, A., and J. M. Dziedzic, J. E. Bjorkholm, and Steven Chu (1986). Observation of a single-beam gradient force optical trap for dielectric particles. *Optics Letters*, 11, no. 5, 288–290.

Ashkin, A., and J. M. Dziedzic, and T. Yamane (1987). Optical trapping and manipulation of single cells using infrared laser beams. *Nature*, 330, 24, 769–771.

Benguigui, L., and I. J. Lin (1982). More about the dielectrophoretic force. *J. Appl. Phys.*, 53, 1141–1143.

Benz, R., and U. Zimmermann, (1981). The resealing process of lipid bilayers after reversible electric breakdown. *Biochim. Biophys. Acta*, 640, 169–178.

Bogen, D. K., J. W. Ashe, and S. Takashima (1990). Deformation of biological cells by electric fields. Conf. Rec. Ann. Intl. Conf. IEEE/EMBS, 12, no. 4, 1519–1520.

Buican, T. N., M. J. Smyth, H. A. Crissman, G. C. Salzman, C. C. Stewart, and J. C. Martin (1987). Automated single-cell manipulation and sorting by light trapping. *Applied Optics*, 26, no. 24, 5311–5317.

Chang, D. C., and T. S. Reese (1990). Changes in membrane structure induced by electroporation as revealed by rapid-freezing electron microscopy. *Biophys. J.*, 58, 1–12.

Chiabrea, A., C. Nicolini, and H. P. Schwan, eds. (1985). Interactions between electromagnetic fields and cells. NATO ASI Series, Vol. 97. Plenum Press, New York.

Eigen, M., and G. Schwartz (1957). Orientation field effect of polyelectrolytes in solution. *J. Coll. Sci.*, 12, 181–194.

Fomchenkov, V. M., and B. K. Gavrilyuk (1978). The study of dielectrophoresis of cells using the optical technique of measuring. *J. Biol. Phys.*, 6, 29–68.

Fuhr, G., R. Hagedorn, and H. Göring (1985). Separation of different cell types by rotating electric fields. *Plant Cell Physiol.*, 26(8), 1527–1531.

Fuhr, G., R. Hagedorn, T. Müller, B. Wagner, and W. Benecke (1991). Linear motion of dielectric particles and living cells in microfabricated structures induced by travelling electric field. Proc. IEEE Micro Electro Mechanical Systems, pp. 259–264.

Galbraith, D. W., K. R. Harkins, and R. A. Jefferson (1988). Flow cytometric characterization of the chlorophyll contents and size distributions of plant protoplasts. *Cytometry*, 9, 75–83.

Glaser, R., and G. Fuhr (1986). Electrorotation of single cells—a new method for assessment of membrane properties. In *Electrical Double Layers in Biology* (M. Blank, ed.). Plenum Press, pp. 227–242.

Gruzdev, A. D. (1965). Orientation of microscopic particles in electric fields. *Biophysics*, 10, 1206–1208.

Hamilton, W. A. et al. (1967). Effects of high electric fields on micro-organisms. II, Mechanism of action of the lethal effect. *Biochim. Biophys. Acta*, 148, 789–800.

Harkins, K. R., and D. W. Galbraith (1987). Factors governing the flow cytometric analysis and sorting of large biological particles. *Cytometry*, 8, 60–70.

Hayamizu, M., T. Tenma, and A. Mizuno (1989). Destruction of yeast cells by pulsed high voltage application, *J. of Inst. Electrostatics Japan,* Vol. 13, No. 4, pp. 322–331.

Holzapfel, C., J. Vienken, and U. Zimmermann (1982). Rotation of cells in an alternating electric field: theory and experimental proof. *J. Membrane Biol.*, 67, 13–26.

JASCO (Japan Spectroscopic Co., Ltd.) (1984). Catalog of FCS-1 Cell Sorter.

Jayaram, J., G. S. P. Castle, and A. Margaritis (1991). Effects of high electric field pulses on *Lactobacillus brevis* at elevated temperatures. Conf. Rec. of IEEE/IAS Annual Meeting, pp. 647–681.

Jones, T. B. (1979). Dielectrophoretic force calculation. *J. Electrostatics*, 6, 69–82.

Jones, T. B. (1985). Multipole corrections to dielectrophoretic force. IEEE Trans. IA, IA-21, no. 4, 930–934.

Kaler, K. V. I. S., and T. B. Jones (1990). Dielectrophoretic spectra of single cells determined by feedback controlled levitation. *Biophys. J.*, 57, 173–182.

Kawakami, K., and A. Mizuno (1992). Analysis of membrane tension of plant protoplasts at a nozzle of a cell sorter. *J. of Inst. Electrostatics Japan,* Vol. 17, No. 1, pp. 55–64.

Kawakami, K., T. Kumagaya, L. Dayon, and A. Mizuno (1993). Development of a specialized cell sorter for plant protoplasts and its application in the separation of electrically fused plant protoplasts. *J. of Inst. Electrostatics Japan,* Vol. 17, No. 3, pp. 220–228.

Kinoshita, K., and T. Y. Tsong (1977). Formation and resealing of pores of controlled sizes in human erythrocyte membranes. *Nature*, 268, 438–441.

Mandel, M. (1981). The electric polarization of rod-like, charged macromolecules. *Mol. Phys*, 4, 792–795.

Masuda, S., M. Washizu, and T. Nanba (1989). Novel method of cell fusion in field constriction area in fluid integrated circuit. *IEEE Trans. IA*, 25, no. 4, 732–737.

Matsumoto, Y., N. Shioji, T. Satake, and A. Sakuma (1991). Inactivation of microorganisms by pulsed high voltage application. Conf. Rec. of IEEE/IAS Annual Meeting, pp. 652–665.

Melamed, M. R., T. Lindmo, and M. L. Mendelsohn (1990). Flow cytometry and sorting. 2d ed. John Wiley, New York.

Miller, R. D., and T. B. Jones (1987). Frequency-dependent orientation of ellipsoidal particles in AC electric fields. Conf. Rec. IEEE 9th Ann. EMBS Meeting, pp. 710–711.

Mizuno, A., and Y. Hori (1988), Destruction of living cells by pulsed high voltage application. *IEEE Trans. on IAS*, 24, no. 3, 387–394.

Mizuno, A., M. Imamura, and K. Hosoi (1991a). Manipulation of single fine particle in liquid by electrical force in combination with optical pressure. *IEEE Trans. on IAS*, 27, no. 1, 140–146.

Mizuno, A., H. Sakano, and Y. Ohno (1991b), Opto-electrostatic micro-manipulation of cells and fine particles. *Review of Laser Engineering*, 19, no. 9, 895–900.

Neumann, E. (1986). Chemical electric field effects in biological macromolecules. *Prog. Biophys. Molec. Biol.*, 47, 197–231.

Neumann, E., and A. Katchalsky (1972). Long-lived conformation changes induced by electric impulses in biopolymers. *Proc. Natl. Acad. Sci. USA*, 69, no.4, 993–997.

Nishioka, N., S. Matsumoto, Y. Ohno, and A. Mizuno (1991). A study on the micro-motor using the optical pressure and electrostatic rotating field. *Proc. 15th Annual Meeting of Inst. Electrostatics Japan*, pp. 229–232.

Pethig, R. (1979). Dielectric and electronic properties of biological materials. John Wiley, Chichester.

Pethig, R. (1990). Application of A. C. electrical fields to the manipulation and characterisation of cells. In *Automation in Biotechnology* (I. Karube, ed.). Elsevier, Amsterdam, pp. 159–185.

Pohl, H. A. (1978). Dielectrophoresis. Cambridge University Press, Cambridge.

Pohl, H. A. (1983). Natural oscillating fields of cells. In *Coherent Excitations in Biological Systems* (H. Fröhlich and F. Kremer, eds.). Springer-Verlag, Berlin.

Pohl, H. A., and J. S. Crane (1971). Dielectrophoresis of cells. *Biophys. J.*, 11, 711–727.

Pohl, H. A., and K. Kaler (1979). Continuous dielectrophoretic separation of cell mixtures. *Cell Biophys.*, 1, 15–28.

Pohl, H. A., and K. Pollock (1978). Electrode geometries for various dielectrophoretic force laws. *J. Electrostat.*, 5, 337–342.

Porschke, D. (1985). Effects of electric fields on biopolymers. *Ann. Rev. Phys. Chem.*, 36, 159–178.

Price, J. A. R., J. P. H. Burt, and R. Pethig (1990). Application of a new optical technique for measuring the dielectrophoretic behavior of micro-organisms. *Biochim. Biophys. Acta*, 1034, 93–101.

Saito, M., G. Schwartz, and H. P. Schwan (1966). Response of non-spherical biological particles to alternating electric fields. *Biophys. J.*, 6, 313–327.

Sakurauch, Y., and E. Kondo (1980). Lethal effect of high electric fields on micro-organisms. *Nippon Nogeikagaku Kaishi*, 54, no. 10, 837–844. Annual Meeting, pp. 713–719.

Sale, J. H. et al. (1967). Effects of high electric fields on micro-organisms. I, Killing of bacteria and yeasts. *Biochim. Biophys. Acta*, 148, 781–789.

Sato, K., Y. Kawamura, S. Tanaka, K. Uchida, and H. Kohida (1990). Individual and mass operation of biological cells using micromechanical silicon devices. *Sensors and Actuators*, A21–A23, 948–953.

Schwan, H. P., and L. D. Sher (1969). Alternating-current field-induced forces and their biological implications. *J. Electrochem. Soc.*, 116, no. 1, 22C–25C.

Schwartz, G., M. Saito, and H. P. Schwan (1965). On the orientation of nonspherical particles in an alternating electrical field. *J. Chem. Phys.*, 43, 3562–3569.

Takashima, S. (1989). *Electrical Properties of Biopolymers and Membranes*. Adam Hilger, Bristol and Philadelphia.

Teissie, J., and T. Y. Tsong (1981). Electric field induced transient pores in phospholipid bilayer vesicles. *Biochem.*, 10, 1548–1554.

Teixeira-Pinto, A. A., L. L. Nejelski, Jr., J. L. Cutler, and J. H. Heller (1960). The behavior of unicellular organisms in an electromagnetic field. *Exp. Cell Res.*, 20, 548–564.

Tombs, T. N., and T. B. Jones (1991). Digital dielectrophoretic levitation. *Rev. Sci. Instrum.*, 62(4), 1072–1077.

Turcu, I. (1987). Electric field induced rotation of spheres. *J. Phys. A: Math. Gen.*, 20, 3301–3307.

Washizu, M. (1990a). Handling of biological molecules and membranes in microfabricated structures. *Automation in Biotechnology* (I. Karube, ed.). Elsevier, Amsterdam, pp. 113–125.

Washizu, M. (1990b). Electrostatic manipulation of biological objects in microfabricated structures. *Integrated Micro-Motion Systems* (F. Harashima, ed.). Elsevier, Amsterdam pp. 417–432.

Washizu, M., and O. Kurosawa (1990c). Electrostatic manipulation of DNA in microfabricated structures. *IEEE Trans. IA*, 26, no. 6, 1165–1172.

Washizu, M., T. Nanba, and S. Masuda (1990d). Handling of biological cells using fluid integrated circuit. *IEEE Trans. IA*, 25, no. 4, 352–358.

Washizu, M., M. Shikida, S. Aizawa, and H. Hotani (1992). Orientation and transformation of flagella in electrostatic field. *IEEE Ttrans. IA*, 28, no. 5, 1194–1202.

Washizu, M., Y. Kurahashi, H. Iochi, O. Kurosawa, S. Aizawa, S. Kudo, Y. Magariyama, and H. Hotani (1993). Dielectrophoretic measurement of bacterial motor characteristics. *IEEE Trans. IA*, 29, no. 2, 286–294.

Wong, T., and E. Newmann (1982). Electric field mediated gene transfer. *Biochem. Biophys. Res. Commun.*, 107, 584–587.

Zimmermann, U. (1982). Electric field-mediated fusion and related electrical phenomena. *Biochim. Biophys. Acta*, 694, 227–277.

Zimmermann, U., and W. M. Arnold (1988). Biophysics of electroinjection and electrofusion. *J. Electrostatics*, 21, 309–345.

Zimmermann, U., B. Pilwat, and H. A. Pohl (1982). Electric field-mediated cell fusion. *J. Biophys.*, 10, 43–50.

30

ESD Hazards in the Electronics Industry

L. F. DeChiaro

Bell Communications Research
Red Bank, New Jersey

B. A. Unger

Burt Unger Associates
Monmouth Beach, New Jersey

I. INTRODUCTION

ESD (electrostatic discharge) is a significant cause of device failures at all stages of device and equipment production, assembly, test, installation, and field use. Even though device designs include protection circuitry, it is relatively easy to generate static potentials during handling and shipping that exceed the limits of the protection networks. Damage from ESDs can cause either complete device failure by parametric shifts or device weakness by locally heating, melting or otherwise damaging oxides, junctions, or parts of devices such as the metallized conductors. Electronic components can vary widely in their susceptibility to damage by ESD. Integrated circuits (ICs) in particular exhibit a delicate relationship between device design and ESD susceptibility. IC devices manufactured by two different vendors and claimed to be interchangeable may vary by a factor of 10 in their ESD susceptibilities. This chapter sets forth the fundamental principles of ESD in relation to the handling of modern electronic components.

Section II discusses the effects ESD can produce upon electronic components, particularly ICs. Section III provides background on practical aspects of ESD prevention such as static retardant materials and grounding techniques.

II. ESD MODELS AND TEST PARAMETERS

There are three generalized scenarios of charging and discharging that can give rise to damaging ESD events.

1. A charged source such as a person, cart, machine part, or other conductor touches a device or circuit board and discharges the stored charge to or through a device to ground. The human body model is a representation of one such scenario.
2. The device or circuit board can store charge on its conductive elements. Upon contact with an effective ground, the discharge pulse can create damage. The charged device model is an example of this event.
3. An electrostatic field is always associated with charged objects. Very sensitive devices placed in a particularly intense field can be damaged as a result of the potentials on junctions or oxides exceeding their breakdown potentials. However, a more common discharge event occurs when a device is grounded while in the presence of a field. This is an inductive discharge and falls under the heading of the field induced model.

This section describes these three primary ESD scenarios, their electrical parameters, and several of the physical failure mechanisms they tend to cause in semiconductor devices.

A. The Human Body Model

Historically, the first type of event to be studied was the human body ESD, which refers to charge transfer between a charged human operator and an IC device. The standard type of discharge in this case was appropriately called the human body model (HBM). Early oscilloscope measurements revealed that the human body ESD stressing waveform looks approximately like a decaying exponential. The standard ESD simulator chosen to produce this ideal HBM waveform is an RC discharge circuit as shown in Figure 1. The high-voltage power supply is adjusted to the desired stress voltage and then is allowed to charge slowly a standard capacitor through a high resistance (typically 10 megohms or more). The device under test (DUT) is connected to the output terminals of the simulator, and the stress is applied by energizing the relay, which discharges the capacitor into the DUT through the standard resistor. Figure 1 also shows an alternate load for the simulator circuit, which consists of a short circuit with a current probe. This alternate load is used for purposes of waveform calibration and standardization. Based upon studies performed

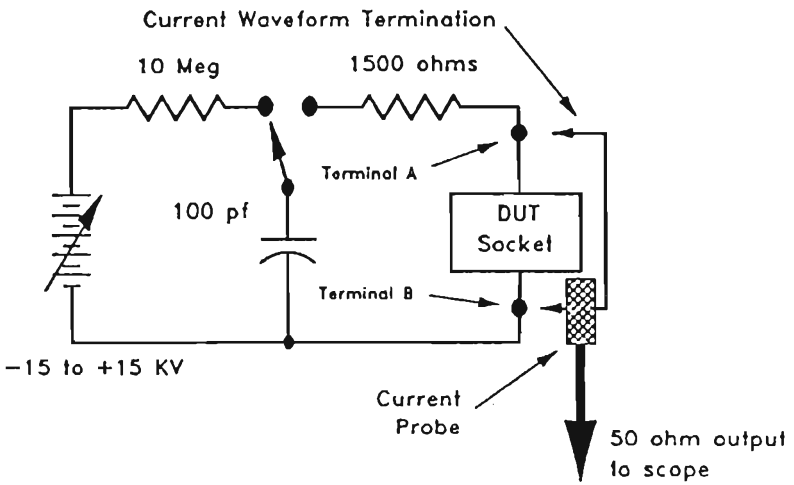


Figure 1 Schematic circuit diagram of standard HBM ESD simulator. The current probe and short circuit termination are used for waveform calibration.

with a number of human volunteers, a value of 100 picofarads was selected as the HBM circuit standard. With this value fixed, waveform observations enabled the determination of an average human resistance; and a value of 1500 ohms was selected for the HBM standard. These values give us a decaying exponential waveform with a decay time constant of 150 nanoseconds. Figure 2 shows the characteristics of the standardized HBM test waveform. Other equivalent electrical circuits are used to model a variety of capacitor discharge events such as discharges from furniture and machinery.

B. The Charged Device Model

Some ESD failures were traced to stress events that occurred when IC devices themselves became charged and then rapidly discharged. This type of stress was consequently called charged device ESD. A simulator was developed to reproduce the charged device model (CDM) stress event under controlled laboratory conditions. CDM stresses are simulated by slowly charging the leads of a device or circuit board and then discharging a lead through a low impedance path.

The energy stored on the conductive elements of the device (leads, interconnects, etc.) is discharged through the pin under stress, creating a rapid high-current event characteristic of a charged device ESD. The

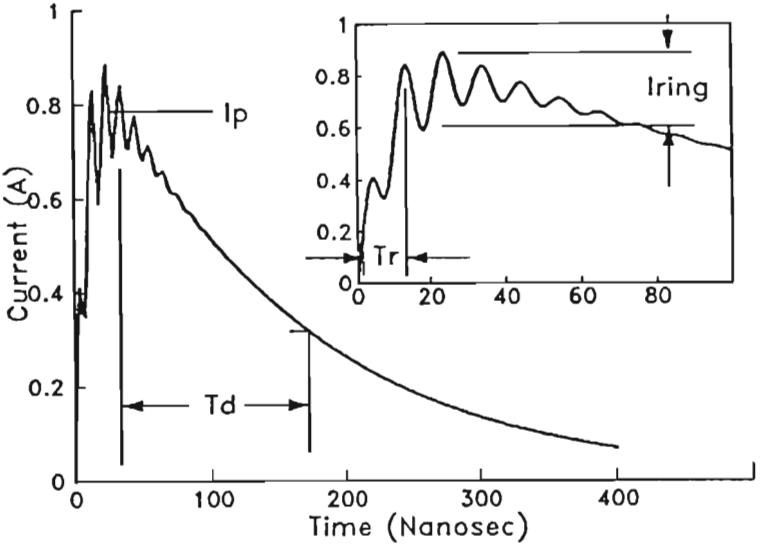


Figure 2 The HBM ESD waveform at 1500 volts stress.

simulator circuitry must be designed to minimize any parasitics that would attenuate the high frequency transients associated with a CDM discharge. This then provides the most damaging, worst-case CDM event. An example of a CDM waveform is shown in Figure 3.

C. The Field Induced Model

The field induced model (FIM) refers to stress events in which the IC device interacts with an externally applied electric field to cause a discharge. The most common type of field induced ESD is by induction. This occurs when a device is placed in an electric field and is brought into contact with a local ground. When this occurs, large transient currents can flow, creating a CDM-like event. If the device is subsequently discharged, another CDM-like ESD event can occur. This creates a kind of double jeopardy that can be highly destructive to ESD-sensitive devices. FIM ESD is the result of a combination of exposure to large fields and the grounding of the device while so exposed.

In some extreme cases where the field is very large and the device has some very sensitive junctions or very thin dielectric films, the local field at the device may be sufficient to cause dielectric or junction breakdown. In most cases, however, the interconnection of many elements on a circuit

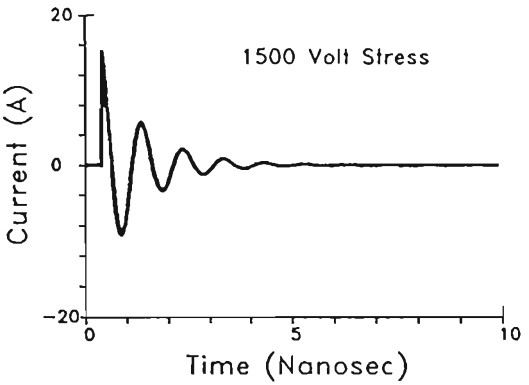


Figure 3 CDM ESD stress waveform. Note the high peak current, the excursions into negative polarity, and the short duration.

and the local parasitics mitigate against reaching breakdown potentials on any one element. If required, devices and circuit boards can be protected from strong fields by placing them in a package that screens out electric fields, such as a metallized package. Electric fields do not penetrate completely enclosed conductive containers. This is often referred to as a shielded container or a Faraday cage. A sensitive IC or circuit pack placed within the shielded container will not experience any electric field and will therefore be protected from FIM ESD while it is in the container.

D. The Electrical Parameters of ESD Stress

ESD causes the dissipation of modest (by macroscopic standards) amounts of energy within an IC device. However, since the physical dimensions of the circuit elements that dissipate this energy are measured in microns, the energy and power densities produced are very large, in many instances larger than the electrical or thermal limits of the materials used to fabricate IC devices. Before one can appreciate the impact of ESD on modern ICs, it is necessary to understand the electrical parameters of the stress. Such quantities as the peak current, total energy, rise time, and effective source impedance of the stress all exert an impact upon the failure threshold and mechanisms of a given device. Table 1 lists typical values for the important parameters of HBM and CDM ESD. The orders of magnitude shown for the current and time should illustrate the large differences in electrical parameters among the three types of stress. The CDM event exhibits the shorter rise time and duration and the larger current due to the very low impedance in the discharge path.

Table 1 ESD Stressing Parameters

Parameter	CDM	HBM
Stressing voltage	0–6,000	0–30,000
Source impedance (ohms)	<1	1500
Total energy (joules)	10^{-6}–10^{-5}	10^{-5}–10^{-4}
Rise time (nanoseconds)	0.05–0.5	~10
Duration (nanoseconds)	5	300
Peak current (amperes)	<100	<5

E. ESD Failure Mechanisms

When ESD currents enter or leave an IC device, they follow the path of lowest impedance and tend to cause failure at the first weak point encountered. The failure mechanism will be a very sensitive function of the device technology and most importantly, the device design and layout. Furthermore, the HBM and CDM/FIM models tend to produce different failure mechanisms at different locations on the component. There are two general categories of failure mechanisms: those caused by voltage or electric field and those caused by total energy deposited into a sensitive circuit. A number of well-known mechanisms have been produced by ESD transients and are summarized as

Gate oxide damage
Junction damage
Metallization damage
Arcing

The mechanism historically associated with ESD is gate oxide damage. Many complex ICs employ MOS technology, which requires the fabrication of insulated gate field effect transistors (IGFETs). In these devices, the impedance between the source and the drain terminals is controlled by the voltage applied to the gate terminal. The transistor gate is a conducting layer that is insulated from the rest of the device by a very thin layer (perhaps only 100 times the diameter of an atom) of insulating material such as silicon dioxide (SiO_2). The very small thickness of the oxide means that a moderate voltage of 5 V applied to the gate creates a very large electric field in the oxide. In fact, the transistor depends upon this field for its operation. Unfortunately the gate oxide, like all insulators, will remain undamaged only if the applied electric field is less than the maximum field strength for the material. Most dielectric oxides break down at field strengths of about 1×10^7 V/cm. This means that the gate must

never be exposed to voltages higher than about 20 V. If this voltage is exceeded, the gate oxide can be destroyed very rapidly. At sufficiently high stress levels, oxide destruction can occur in about 1 ns (1×10^{-9} seconds) or less, and the entire integrated circuit will then be permanently damaged.

The high voltage levels encountered on charged human operators or IC devices are many times larger than the gate oxide breakdown voltage. Fortunately for the IC industry, much of this voltage usually gets divided down and is dropped across the operator's impedance or the parasitic capacitance between an IC and local ground. As a result, the voltage actually reaching the sensitive gate is some fraction of the original voltage. Nevertheless, special circuits called protection networks are usually designed into modern ICs to protect the gate oxides. The design of these networks is a very difficult challenge, generally requiring a delicate tradeoff between ESD protection and required device operating speed. If these networks do not sufficiently attenuate the stress or if the discharge can circumvent the network, oxide damage can and will occur. Indeed, this mechanism is one of the leading causes of ESD failure in complex IC devices.

The next important failure mechanism is p-n junction damage. Essentially all active semiconductor components contain p-n junctions, and these junctions are susceptible to damage, especially if the applied voltage exceeds the reverse breakdown limit. For most modern IC devices, this limit lies between 10 and 100 volts. If a voltage higher than this limit is briefly applied, part of the junction may melt and then resolidify with a damaged crystal structure. This damaged structure acts as an electrical leakage path that degrades the performance of the IC.

The relation between the time duration and ESD stress current required to cause device failure are described by the Wunsch-Bell equation, which models heat transfer in one spatial dimension. Three distinct types of behavior are observed, each in its own time regime. For ESD stresses less than 1 microsecond in length, the failure threshold is inversely proportional to the stress duration. This is known as the adiabatic limit and corresponds to the case in which the device becomes damaged before thermal conduction can reduce the temperature at the failure site. For stresses in excess of 1 millisecond in length, the failure threshold becomes relatively independent of the stress duration. This occurs because the heat is removed from the failure site by thermal conduction at approximately the same rate at which it is generated by electrical power dissipation. In the intermediate region corresponding to stresses between 1 microsecond and 1 millisecond in length, the failure threshold varies roughly as the

square root of the stress duration. This corresponds to a case in which the rate of heat generation at the failure site is somewhat greater than the rate at which heat can be conducted away.

It must be remembered that many of these failure mechanisms are cumulative in nature. The cumulative nature of certain ESD failure modes is called latency and is to some extent inherent in the ESD phenomenon. This means that some supposedly good devices in the field can actually be "walking wounded" whose functionality may be unimpaired but which can fail during use with little or no additional stress. For these reasons, the topics of latency and cumulative failure mechanisms are of current interest for reliability professionals.

III. CONTROLLING ESD

A. Grounding

The most expedient method to minimize ESD damage is to minimize or prevent charge accumulation on devices or objects that may contact sensitive devices. A primary source of charge is from the person handling or working on or with devices. Two techniques are commonly available to prevent charge accumulation on human operators: the use of wrist straps and the use of conductive flooring in conjunction with conductive shoes.

The wrist strap is one of the first lines of defense against ESD damage. It is also one of the most cost effective countermeasures available to the electronics industry. When properly used, the wrist strap can minimize personnel voltages, thereby avoiding one of the most potent sources of ESD in the work environment. The wrist strap is composed of three components: the cuff, the strap, and the series resistor. The cuff is the component that is placed around the wrist and should make good electrical contact to the wrist. The strap is the component that connects the cuff with ground potential. The series resistor is included to provide personnel protection from an electric shock hazard.

Although wrist straps are highly effective in reducing HBM ESD, they are only part of a comprehensive ESD control effort. While manufacturing operators can be required to wear wrist straps, other personnel may occasionally enter a manufacturing area without taking proper precautions. The use of conductive flooring or conductive mats may be an excellent backup measure that can extend the protective zone beyond the reach of wrist straps. Topical floor treatments may also be effective in reducing charge levels within an existing facility. Several types of topical floor treatments are commercially available. Conductive paints or coatings are basically latex paints or acrylic materials that are loaded with finely di-

vided carbon granules. Topical antistats are also available for floor treatment.

Charge generation while walking is a function of the type of footware contacting the flooring. Shoe soles and heels that are made of either thick rubber or crepe are excellent insulators that are also prone to charge generation. Leather and some composite materials, on the other hand, are much less active. However, to minimize charge generation on conductive flooring, a grounding path between the body and flooring is required. It is possible to install commercially available conductive heel straps on shoes to provide a conductive path from the operator's foot to the grounded floor. In addition, special shoes can be purchased with rivets or other conductive inserts installed in the heel or sole to provide the ground path.

B. Packaging Materials

There are two primary requirements for packaging materials to minimize the potential for ESD damage. Packaging materials should be selected first, to minimize any charge accumulation (a triboelectric property) and second, to dissipate safely any charge that may be produced on the materials (a resistive or static dissipative property). This section discusses the materials and their properties that are available as packaging for sensitive components and circuit packs.

All packaging materials are divided into three general classes based upon their surface or volume resistivity. Table 2 contains the types and defining resistivity ranges. Materials used to package electronic parts should be selected to have surface and volume resistivities in the dissipative range. That is, the inner and outer materials should be capable of bleeding charge in a safe, slow fashion. This will permit any charge generated during shipment or handling to dissipate safely when grounded, prior to opening at the receiving end. If shielding is desired, a buried shielding layer could be incorporated but should not be permitted to contact the

Table 2 Classifications of Packaging Materials

Material class	Surface resistivity (ohms/square)	Volume resistivity (ohm-cm)
Shielding	10^4 or less	100 or less
Conductive	10^5 or less	10^4 or less
Dissipative	10^5–10^{12}	10^4–10^{11}
Insulative	greater than 10^{12}	greater than 10^{11}

item to be protected. This will prevent any possibility of a charged device model transient event.

The dissipative materials can safely drain an applied charge to ground slowly enough to avoid large and potentially damaging current surges. Dissipative materials can be used on static retardant work surfaces where they can be adequately grounded or on the outer layer of a laminated structure, provided that their triboelectric properties are favorable. These materials are well suited for use on the primary surfaces of automatic component handlers, because they can keep the components discharged and minimize the incidence of CDM ESD damage.

There is a family of materials in the dissipative range that incorporates an antistat that provides lubricious and conductive properties to the bulk. Such materials can be transparent, translucent, or opaque, depending upon the base plastic material. The reliability and lifetime of these materials is a strong function of the manufacturing process and can vary greatly among different materials vendors. These materials typically consist of an insulating plastic such as polyethylene that has been treated with an antistat compound. These compounds are called surfactants and have the property of being hygroscopic—that is, they attract water to the surface of the material. This water forms a thin film that provides two benefits. First, it lubricates the surface, reducing friction and thus triboelectric charging when the material contacts another surface. Second, the water layer is itself a weak conductor with some dissipational capability, generally resulting in a sheet resistivity between 10^9 and 10^{12} ohms per square. These materials are an attractive choice for use in direct contact with sensitive components or circuit packs and are frequently manufactured into bags for circuit board protection. Consequently, they are frequently laminated into the innermost layer of a multilayer structure. Their volume insulating capability prevents conduction of ESD energy to sensitive devices while their favorable triboelectric properties prevent charge buildup within the package.

There are other materials available with more permanent antistatic properties resulting from particular, usually proprietary, formulations. Many of these materials can be molded, laminated, or extruded to form boxes, bags, and IC carriers.

C. Discharging Methods

Although the charge removal and prevention technologies mentioned above have provided a major weapon in our arsenal against ESD, their effectiveness can be limited in certain cases. For example, automated IC handling systems contain mechanical parts that move at high speed and

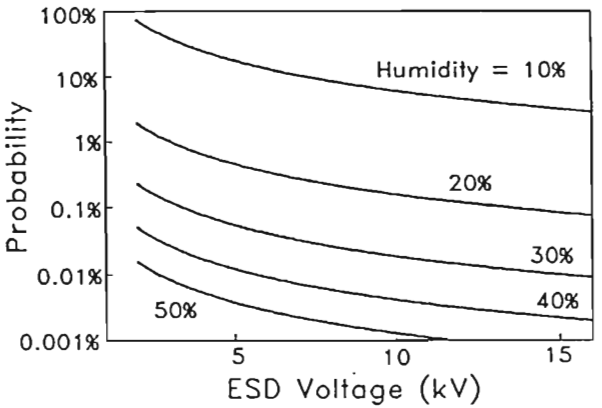


Figure 4 Probability of observing ESD stress events at voltages equal to or greater than the horizontal coordinate. Several plots are shown, each corresponding to a different value of relative humidity.

tend to collect charge. Sometimes, nonconductive surfaces must be used because of their chemical properties or other considerations. Contactless charge removal is required for best results in these cases. The best known examples of contactless charge removal are humidity and air ionization systems.

Atmospheric humidity tends to produce thin layers of mildly conductive moisture upon most solid objects. This layer can provide a leakage path that can slowly drain any accumulated charge to local ground. It follows that the amount of moisture in this layer is critically dependent upon the relative humidity. Studies cited by Mardiguian* imply that the probability of encountering an ESD event above any given voltage is a sensitive function of both the voltage (V) and the relative humidity (RH). The cumulative probability distribution function may be expressed as

$$P\,(\geq V) = \frac{1.71 \times 10^{10}}{V^{1.55} RH^{5.25}}$$

A plot of this function appears in Figure 4 and allows the reader to appreciate the rate at which the risk of ESD damage increases as the humidity drops below 20%.

The other primary means for contactless removal of charge involves

* Mardiguian, M. (1986). *Electrostatic Discharge: Understand, Simulate, and Fix ESD Problems*. Interference Control Technologies, Inc., p. 1.17.

the use of air ionizers. These systems generate large quantities of positively and negatively charged air ions. When ion clouds surround a charged object, the ions with opposite polarity are attracted to the object by the Coulomb force law, while the ions with identical polarity are repelled. The oppositely charged ions will then collide with the object, transfer their charge to it and thereby reduce or neutralize the charge on the object. Commercially available systems generally utilize one of two methods for ion generation: low-level radioactive emissions that ionize the surrounding air molecules and high-voltage point discharges.

REFERENCES

Failure Mechanisms

Avery, L. R. (1984). Electrostatic discharge: mechanisms, protection techniques, and effects on integrated circuit reliability. *RCA Review*, 45, June 1984.

Avery, L. R. (1987). CDM testing—trying to duplicate reality. EOS/ESD Symposium Proceedings, Orlando, FL, pp. 88–92.

Bowers, J. S., M. G. Rossi, and J. R. Beall (1983). A study of ESD latent defects in semiconductors. EOS/ESD Symposium Proceedings, Las Vegas, NV, pp. 198–204.

Chemelli, R. G., B. A. Unger, and P. R. Bossard (1983). ESD by static induction. EOS/ESD Symposium Proceedings, Las Vegas, NV, pp. 29–36.

Chemelli, R. G., and L. F. DeChiaro (1985). The characterization and control of leading edge transients from human body model ESD simulators. EOS/ESD Symposium Proceedings, Minneapolis, MN, pp 155–162.

Crockett, R. G. M., J. G. Smith, and J. F. Hughes (1984). ESD sensitivity and latency effects of some HCMOS integrated circuits. EOS/ESD Symposium Proceedings, Philadelphia, PA, pp. 196–201.

DeChiaro, L. F. (1981). Electro-thermomigration in NMOS LSI. International Reliability Physics Symposium, Orlando, FL, pp. 223–229.

Gammill, P. E. and J. M. Soden (1986). Latent failures due to electrostatic discharge in CMOS integrated circuits. EOS/ESD Symposium Proceedings, Las Vegas, NV, pp. 75–80.

Hughes, D. (1986). Guidelines for prevention of ESD damage to integrated circuits. Semiconductor International, May 1986.

Hull, R. (1988). Stress hardening of damage thresholds due to cumulative ESD pulse testing. EOS/ESD Symposium Proceedings, Anaheim, CA, pp 39–46.

Hyatt, H. (1984). Critical considerations for ESD testing. EOS/ESD Symposium Proceedings, Philadelphia, PA, pp 104–111.

McAteer, O. J., and R. E. Twist (1982). Latent ESD failures. EOS/ESD Symposium Proceedings, Orlando, FL, pp 41–48.

Rubalcava, A. L., and W. J. Roesch (1988). Lack of latent and cumulative ESD effects on MESFET-based GaAs ICs. EOS/ESD Symposium Proceedings, Anaheim, CA, pp. 62–69.

Shaw, R. N., and R. D. Enoch (1985). An experimental investigation of ESD-induced damage to integrated circuits on printed circuit boards. EOS/ESD Symposium Proceedings, Minneapolis, MN, pp. 132–140.

Shaw, R. N. (1986). A programmable equipment for ESD testing to the charged device model. EOS/ESD Symposium Proceedings, Las Vegas, NV, pp. 232–237.

Sim, S. P., and M. J. Robertson (1984). Catastrophic and latent damage in GaA1As lasers caused by electrical transients. *J. Appl. Phys.*, 55(11), 3950–3955 (June 1984).

Speakman, T. S. (1974). A model for failure of bipolar silicon integrated circuits subjected to electrostatic discharge. International Reliability Physics Symposium Proceedings.

Unger, B. A. (1981). Electrostatic discharge failures of semiconductor devices. International Reliability Physics Symposium Proceedings, Orlando, FL, pp. 193–199.

Unger, B. A. (1982). Electrostatic discharge (ESD) failure mechanisms and models. Nepcon West Proceedings 1982, Anaheim, CA.

Unger, B. A. (1988). Early life failures. *Quality and Reliability International* 4, 27–34.

Unger, B. A., R. G. Chemelli, and D. L. Hart (1986). Sheet resistance measurement of buried shielding layers. EOS/ESD Symposium Proceedings, Las Vegas, NV, pp. 59–61.

Woodhouse, J., and K. D. Lowe (1988). ESD latency: a failure analysis investigation. EOS/ESD Symposium Proceedings, Anaheim, CA, pp. 47–52.

Wunsch, D. C., and R. R. Bell (1968). Determination of threshold failure levels of semiconductor diodes and transistors due to pulse voltages. *IEEE Trans. Nucl. Sci.*, NS-15.

Input/Output Protection

DeChiaro, L. F. (1984). Device susceptibility testing and design hardening. EOS/ESD Symposium Proceedings, Philadelphia, PA, pp. 179–188.

Duvvury, C., and R. Rountree (1988). Output protection techniques for advanced CMOS processes. EOS/ESD Symposium Proceedings, pp. 206 hr ff.

Maloney, T. (1988). Designing MOS inputs and outputs to avoid oxide failure in the charged device model. EOS/ESD Symposium Proceedings, pp. 220 ff.

Rountree, R., C. Duvvury, T. Maki, and H. Steigler (1988). A process-tolerant input protection circuit for advanced CMOS processes. EOS/ESD Symposium Proceedings, pp. 201 ff.

Spacing, Dimension Effects on Failure Threshold/Damage

Avery, L. R. (1984). ESD protection structures to survive the CDM. EOS/ESD Symposium Proceedings, pp. 192 hr ff.

DeChiaro, L. F., R. G. Chemelli, and S. Vaidya (1986). Input ESD protection networks for fineline NMOS-effects of stressing waveform and circuit layout.

International Reliability Physics Symposium Proceedings, Anaheim, CA, pp. 206–214.
Duvvury, C., T. Taylor, J. Lindgren, J. Morris, and S. Kumer (1989). Input protection design for overall chip reliability. EOS/ESD Symposium Proceedings, New Orleans, LA, pp. 190–197.
Strauss, M. S., D. L. Lin, and T. L. Welsher (1987). Variations in failure modes and cumulative effects produced by commercial human body model simulators. EOS/ESD Symposium Proceedings, Orlando, FL, pp. 59–70.

Materials and Testing

Baumgartner, G. (1984). Electrostatic measurement for process control. EOS/ESD Symposium Proceedings, Philadelphia, PA, pp. 25–33.
Berkowitz, M. B. (1990). ESD controls in hazardous high voltage environments. EOS/ESD Symposium Proceedings, Lake Buena Vista, FL, pp. 27–35.
Chase, E. W., and B. A. Unger (1986). Triboelectric charging of personnel from walking on tile floors. EOS/ESD Symposium Proceedings, Las Vegas, NV, pp. 127–135.
Felt, F. S. (1983). Coplanar triboelectrification of selected materials. EOS/ESD Symposium Proceedings, Las Vegas, NV, pp. 95–101.
Gompf, R. H. (1984). Triboelectric testing for electrostatic charges on materials at Kennedy Space Center. EOS/ESD Symposium Proceedings, Philadelphia, PA, pp. 58–63.
Gompf, R. H. (1986). Robotic testing for triboelectric properties in a computer controlled environment at Kennedy Space Center. EOS/ESD Symposium Proceedings, Las Vegas, NV, pp. 151–155.
Havens, M. R. (1989). Understanding pink poly. EOS/ESD Symposium Proceedings, New Orleans, LA, pp. 95–101.
Huntsman, J., and D. Yenni, Jr. (1982). Test methods for static control products. EOS/ESD Symposium Proceedings, pp. 94 ff.
Keough, A. H., and G. T. Sydney (1990). The versatility of electron beam processing and the conversion of medium and high performance polymeric films for ESD protection. EOS/ESD Symposium Proceedings, Lake Buena Vista, FL, pp. 231–236.
Kolyer, J. M., and D. M. Cullop (1986). Methodology for evaluation of static-limiting floor finishes. EOS/ESD Symposium Proceedings, Las Vegas, NV, pp. 111–126.
Shah, B. M., P. L. Martinez, and B. A. Unger (1988). Test methods to characterize triboelectric properties of materials. EOS/ESD Symposium Proceedings, Anaheim, CA, pp. 77–83.
Shah, B. M., and B. A. Unger (1989). Test method to characterize triboelectric properties of adhesive tapes. EOS/ESD Symposium Proceedings, New Orleans, LA, pp. 102–106.
Unger, B. A., R. G. Chemelli, and D. L. Hart (1986). Sheet resistance measure-

ment of buried shielding layers. EOS/ESD Symposium Proceedings, Las Vegas, NV, pp. 59–61.

Unger, B. A., and D. L. Hart (1985). Triboelectric characterization of packaging materials. EOS/ESD Symposium Proceedings, Minneapolis, MN, pp. 107–110.

Human Body Model Test Equipment

Lonborg, J. O. (1983). Static survey meters. EOS/ESD Symposium Proceedings, Las Vegas, NV, pp. 63–66.

Shaw, R., and D. Enoch (1983). A programmable equipment for electrostatic discharge testing to human body models. EOS/ESD Symposium Proceedings, Las Vegas, NV, pp. 48–55.

EMI Effects of ESD

Dash, G. (1987). Standards and regulations for ESD testing at the system level. EOS/ESD Symposium Proceedings, Orlando, FL, pp. 115–123.

Honda, M., and T. Kawamura (1984). EMI characteristics of ESD in a small air gap—ARP governs the EMI. EOS/ESD Symposium Proceedings, Philadelphia, PA, pp. 124–130.

Honda, M., and Y. Nakamura (1987). Energy dissipation in electrostatic spark discharge and its distance effects. EOS/ESD Symposium Proceedings, Orlando, FL, pp. 96–103.

Honda, M. (1988). Evaluation of system EMI immunity using indirect ESD testing. EOS/ESD Symposium Proceedings, Anaheim, CA, pp. 185–189.

This Page Intentionally Left Blank

31

Static Electricity Hazards: Solid Surfaces and Gases

István Berta

Technical University of Budapest
Budapest, Hungary

I. THE HAZARDS

A. Basic Phenomena

Materials are electrically neutral if charge carriers of both positive and negative sign in equal quantities are distributed uniformly. Any disintegration of this neutral state, any local accumulation of unipolar particles, can result in electrostatic charging. Almost all of processes (both physical and chemical) in industry and in everyday life can cause electrostatic charging (see Chaps. 2–5), and depending on the circumstances more or less charge will remain on the materials. Charging in industrial electrostatics is always determined by two simultaneous phenomena:

1. Charge separation and accumulation
2. Charge dissipation or elimination

The level of resultant charging is determined by the ratio or the condition of equilibrium of these phenomena.

There are two main types of charging according to the carrying material:

1. Continous charging
2. Partical charging

In the first case charge accumulation takes place on the surface or inside of a continuous solid or liquid material. That is why these materials

have to be either insulating or insulated from ground. The resultant charging level is much affected by the resistivity (see Chap. 4) of these materials. The other main type, particle charging, is characteristic of two-phase streaming materials (powders or drops in a gas or a fluid). The small particles can become charged, but these charges cannot move independently of the material carrying them. That is why in this case the resultant charging level is almost independent of the resistivity of these materials. (E.g., floating conductive particles can charge in this way.) Usually the two main types of charging occur simultaneously, and the effects of both chargings have to be superposed in industry.

B. Electrical Properties of Materials

In order to determine the practical situations, e.g., both the buildup and the decay of electrostatic charges on solid materials, the electrical properties (surface resistivity ρ_s [Ω], volume resistivity ρ_v [Ωm], and permittivity ϵ [As/Vm]) of the materials have to be examined. However the connections between the charging phenomena and the above electrical properties are more complicated (Cross, 1987); the dissipation of charges is closely connected to the time constant

$$\tau = \rho_v \epsilon$$

of the charge decay on the materials. (τ is the time taken for the charge to reach approximately 37% of its initial value.) Based on the usual electrical definitions, there are conductive and insulating materials. On conductive materials (e.g., copper, 10^{-8} Ωm; graphite, 10^{-6} Ωm), the movement of charge carriers (electrons) is completely free; that is why the surface of electric conductors is always equipotential. Insulators (e.g., glass, 10^{9} Ωm; nylon, 10^{12} Ωm; amber, 10^{15} Ωm; polyethylene, 10^{18} Ωm) are materials that conduct no charge or almost no charge in practical cases. In industrial electrostatics one is interested in the movement of very small amounts of charge on the effect of relatively large voltages. That is why the ability of insulating materials to conduct slightly becomes extremely important.

In volume resistivity, antistatic materials are between insulating and conducting materials (Fig. 1). In the case of the usual charging phenomena in industry, or if the usual charge relaxation occurs, antistatic materials behave as electrostatic conductors. In case of discharges, when the movement of charge carriers is very fast (the time constant is well below 10^{-6} s), antistatic materials behave as electrostatic insulators. This means that antistatic materials combine the advantages of insulating and conducting materials.

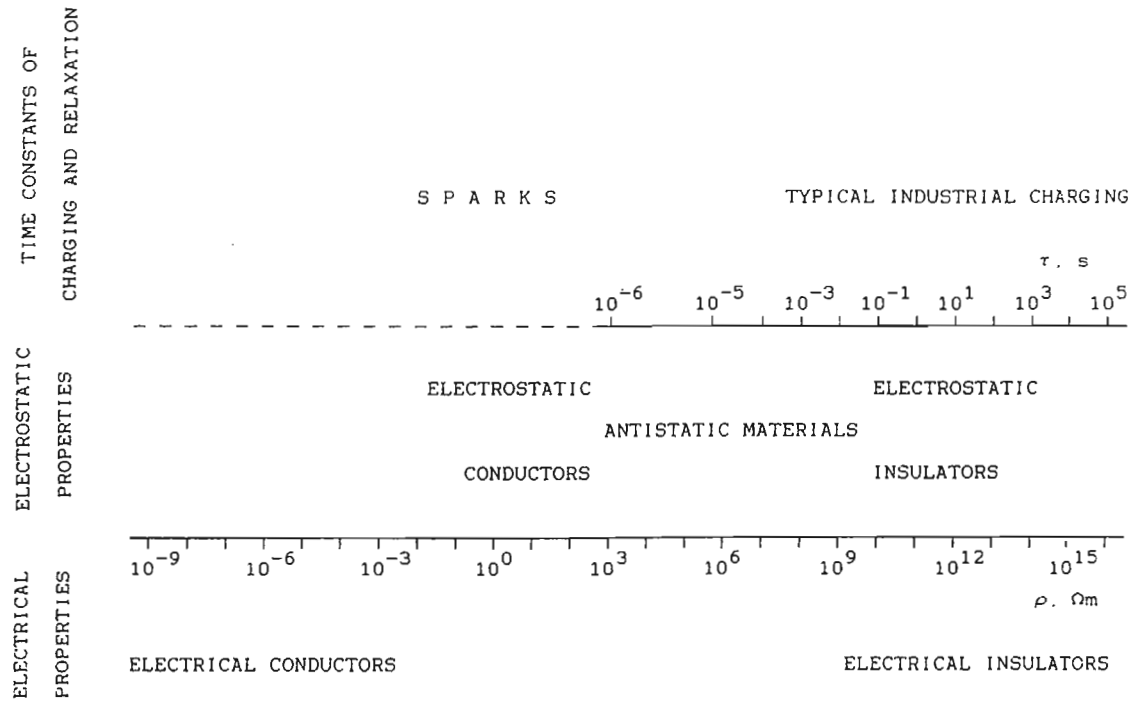


Figure 1 Volume resistivity of different materials compared to the time constants of dominant processes in industrial electrostatics.

C. Unwanted Effects

The unwanted effects of electrostatic phenomena occur in various branches of industry. Besides several manufacturing and technological problems (charged materials attract or repel each other, etc.), electrostatic discharges (see Chap. 30) can result in the most serious difficulties. Discharges can cause shocks or accidents or ignite flammable gases. In Fig. 2, typical energy levels of different types of electrostatic discharges are compared to the minimum ignition energy (see Chap. 11) of gases, vapors, and powders, and the resultant human reactions are given.

Corona discharge can be obtained on peaks or sharp edges of conductors e.g., those with radii of curvature less than 5 mm) in strong electric fields. Because the energy density of corona discharges both in space and

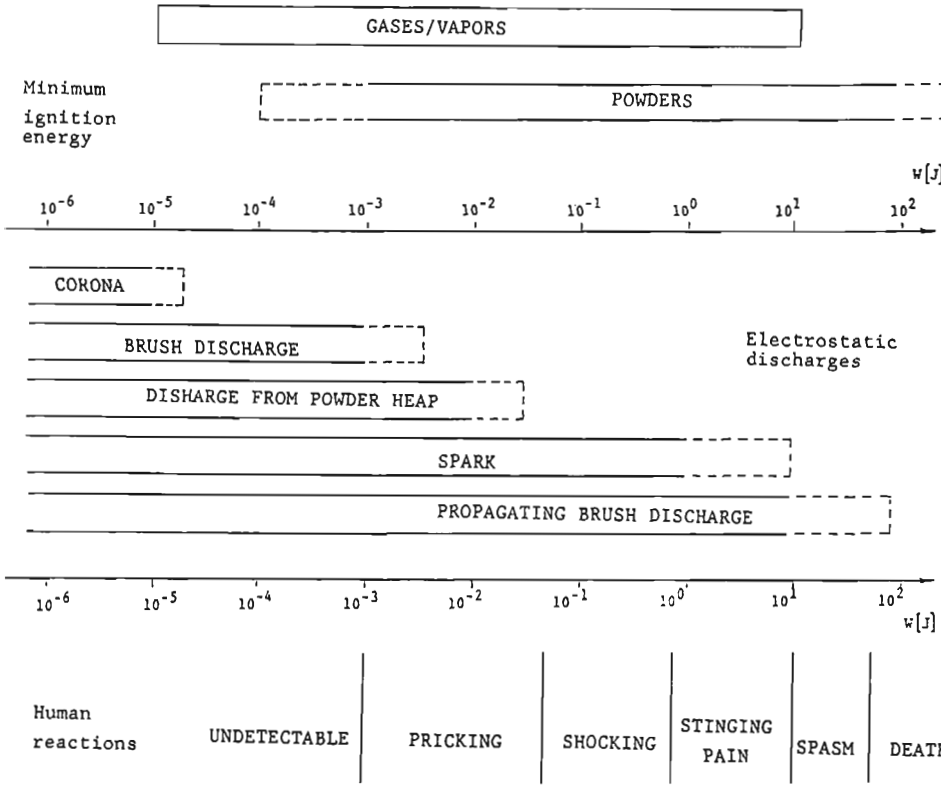


Figure 2 Hazards caused by different types of electrostatic discharges.

in time is very low, the hazard is usually negligible (Gibson and Lloyd, 1965).

Brush discharge is typical in the case of charged insulating surfaces approaching grounded metal electrodes (radius of curvature in the range 5–50 mm). The surface charge density has to be above 3.10^{-6} C/m^2 and the field strength above 5 kV/cm. The discharged area can be about 10^{-2} m^2, and the energy of the discharge can reach 1–3 mJ (Maurer, 1979; Berta et al., 1981; Lövstrand, 1981). The variety of the charge density (both in values and in polarities) observed on insulating surfaces can be explained as the effect of these discharges spreading over a limited part of the insulating surface (Zichy, 1973; Horváth and Berta, 1975).

Discharges along the surface of a powder heap in large silos were observed and examined by Maurer (1979) and by Glor (1985). The conditions for this type of discharge are as follows: continuous rapid inflow of charged particulate material in the size range of 1–10 mm with a specific charge less than 3.10^{-3} C/kg (see Chap. 27.III).

Sparks are typical capacitive discharges obtained in the gap of two conducting (usually metal) bodies. Sparks can come into existence if the potential of an ungrounded electrode exceeds 325 V (after Gibson, 1983; usually 100 V is used as a margin of safety). The energy of a spark is highly concentrated in space and in time in these discharges (breakdown in the air or flashover on insulating surfaces leading from one electrode to another). Because the energy supply is limited by the amount of the charges stored in the capacitance of the ungrounded electrode, arcs can never be formed from electrostatic sparks. As in all other electrostatic discharges, so in sparks; electron avalanches (collision ionization), streamers (photoionization), and leaders (heat ionization) are the basic physical phenomena (Kuffel and Zaengl, 1984).

Propagating brush discharge can be obtained on the surface of a charged thin insulating layer backed by a conductor. The thin insulating layer acts like a large distributed capacitor. The energy stored in this capacitor can be as high as several kJ/m^2, so the energy of the discharge, however distributed in space, can be extremely high. For getting brush discharges the surface charge density has to be higher than 2.5×10^{-4} C/m^2 and the thickness of the insulating layer less than 8 mm (Heidelberg, 1970; Blythe and Carr, 1981; Tolson, 1989).

Lightning-like discharges in industrial processes having never been reported in the literature, experimental tests and calculations show that these discharges cannot occur, if the volume of a spherical space charge is less than 60 m^3, or if the radius of a cylindrical space charge is less than 3 m (Boschung et al., 1977).

D. Typical Hazards

There is no doubt that sparks from ungrounded charged conductors are responsible for more than 90% of electrostatic fires and explosions. Though these electrostatic conductors are metal bodies in many cases, especially large numbers of hazardous situations are created by electrostatically conducting human bodies. People can be significantly charged by walking on an insulating floor, wearing nylon clothing, or moving among charged objects or touching them. During these processes the potential of a human body can reach 10–15 kV, and the energy of a possible spark is several mJ. (The peak value of the current in the breakdown channel is 10–100 A, but the spark lasts only 10^{-8}–10^{9} s.) By comparing these values to the minimum ignition energy of gases or vapors, or to the sensitivity of electronic devices (see Chap. 30), the hazard can be easily recognized. As moving and only occasionally grounded conducting bodies, vehicles also have to be mentioned. Constant and effective grounding (or at least discharging) of these objects is especially difficult for aircraft and spaceships (Taillet, 1991).

The second type of hazardous situation occurs on the surfaces of highly insulating materials, both solid and liquid (see Chap. 32). The hazard can reach an extremely high value if intensive charge generation and accumulation are present. Intensive generation can appear, e.g., because of high moving velocities, and accumulation on large surface capacitances can come into existence, e.g., in case of very thin insulating layers on metal surfaces. (A similar situation can appear on the inside surfaces of large silos because of the anticorrosive coating.)

Last but not least, gases have to be examined. Though the movement of pure gases or gas mixtures creates little if any static electricity, electrostatic charges can be carried on liquid or solid particles moved by the gas. The particles in this two-phase streaming material can be either extraneous matter (rust or water droplets) or a condensed phase of the gas itself (CO_2 "snow," liquefied gas mists or droplets in wet steam). Charges can accumulate either on ungrounded conductors or on the surfaces of insulators both inside the system and outside in the vicinity (BS 5958, 1991).

II. PROTECTION

After recognizing the electrostatic nuisances and hazards, protection is essential. There are no methods of protection that can be generally used, because of the variation in conditions leading to electrostatic charging. The method of protection that can be most effectively applied must suit the particular problem to be solved (Table 1).

Table 1 Protection Against Electrostatic Charging and Accompanying Hazards

Prevention of charge separation	Reduction of charging	Prevention of hazardous consequences
	Grounding of conductors	Prevention of incendiary sparks
	Drainage of charges from insulators	Prevention of flammable atmosphere
	Decreasing velocity	
	Increasing humidity	
	Antistatic materials	
	Neutralization of charges	

Generally, static charging can hardly be avoided, and prevention of incendiary sparks or flammable atmospheres is of uncertain effectiveness or very expensive. The most effective methods seem to be the reduction of charging by grounding and drainage or neutralization of charges.

A. Grounding

One of the main rules of static hazard prevention is to ensure good grounding of electrostatic conductors and antistatic materials. (Insulators cannot be grounded.) In Fig. 3 the simplified circuit diagram of the charging of a conductor is shown. In this schematic outline, C is the capacitance of the conductor, R is its leakage resistance, and S is the spark gap, where

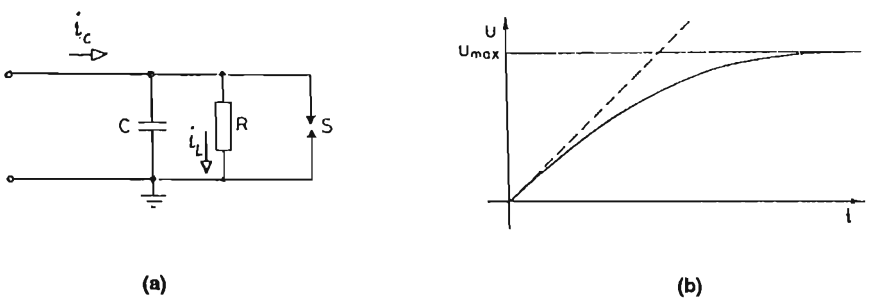


Figure 3 Equivalent electrical circuit for a conductor (a) and its voltage as a function of time while charging (b).

a discharge can appear. If the leakage current i_L is equal to the charging current i_C, the maximum potential of the conductor can be determined as

$$U_{max} = i_L R$$

The order of magnitude of the charging current in industry is generally about 10^{-6} A and it exceeds 10^{-4} A only in extreme cases. This way of thinking gives the possibility for the limitation of the potential of the conductor. If the aim is to avoid sparking, the recommended safe upper limit is 100 V, and the commonly used threshold value of electrostatic grounding 10^6 Ω is obtained. As is shown by Davies (1985), most sensitive devices can also be protected using this limitation (see Chap. 30).

If a spark can appear from an insulated conducting object to the surroundings, the entire energy of the conductor is discharged and its potential decreases to zero. The energy of the spark can be calculated as

$$W = \frac{1}{2} C U_{max}^2$$

The lower the grounding resistance, the lower the energy of the spark. Grounding is especially important in case of high charging currents and objects of high capacitance (Table 2). Based on the given minimum ignition energy of the surroundings and the capacitance of the conductive object, the threshold value of the leakage resistance can be theoretically determined (Fig. 4). One can see in the figure that 10^6 Ω, the commonly used maximum value of the leakage resistance, can be accepted even for very large capacitances (10^{-8} F) and in the presence of very sensitive atmospheres (10^{-4} J). Similarly to the aforesaid, estimating the order of magnitude of the breakdown voltage (10^4 V), the charging current (10^{-4} A), and the permittivity of the material ($1 \leq \epsilon \leq 2$), and knowing the minimum ignition energy of the surroundings, a threshold value can be determined for the materials. This threshold value means that in the presence of the given flammable atmosphere, materials with lower resistivity can be safely used (Fig. 5).

Table 2 Ground Capacitance of Typical Objects (pF)

Needlepoint	1
Hand tool	10
Human body	150
Car	500
Tank car	1000

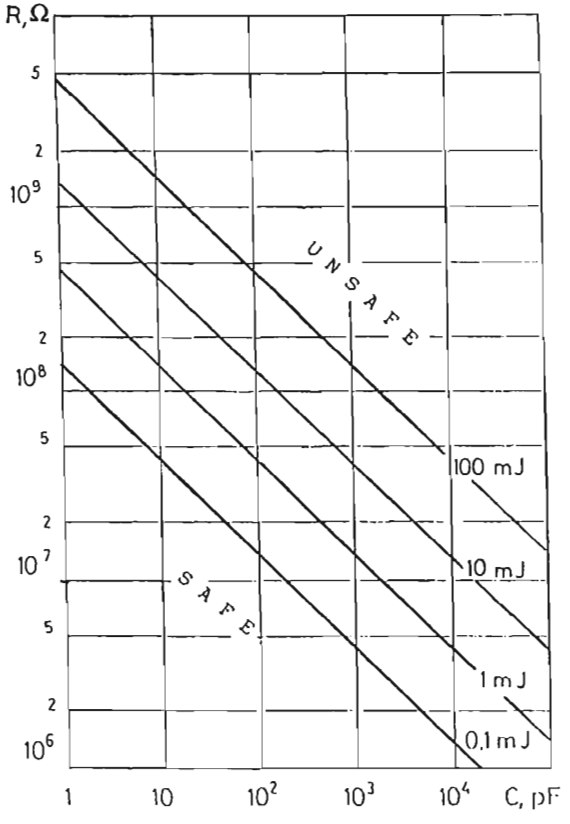


Figure 4 Leakage threshold R determined by the capacitance of the conductor C and the minimum ignition energy of the surroundings.

B. Resistivity and Velocity

One of the most important charging phenomena is contacting and parting of materials. During contact, exchange of charge carriers occurs, and when materials separate, part of the charge carriers attempt to flow back. If both of the objects are conducting, the neutral state will be removed. If at least one of the objects is insulating, the exchange of charges can remain to a certain extent. In case of continuous charging, the charge carriers can flow back to the earth either through the material or on its surface. That is why the surface and volume resistivity of the materials are determining factors of the charging phenomena. It is apparent that the parting velocity of the materials is an important factor, too. If this velocity

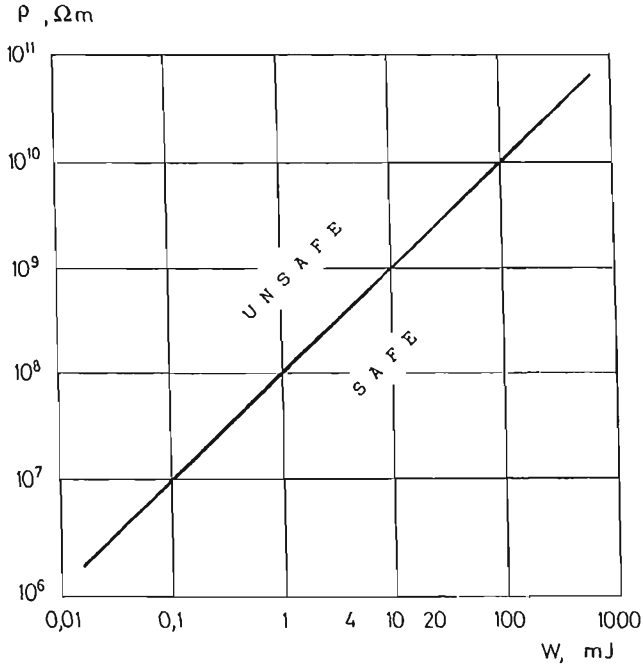


Figure 5 Resistivity threshold determined by the minimum ignition energy of the surroundings.

is low, there is more time for draining the charges. The relationship between the parting velocity and the draining velocity (closely connected to surface and volume resistivity of the materials) determines whether the insulators remain charged after contacting and parting or not (Berta et al., 1987). In case of particle charging there is no possibility for removal of charges after parting. Conductive particles (e.g., powder metal) can be charged when in contact with and parting from an insulating material, because after parting their charge cannot be drained through the medium (e.g., air) carrying the particles.

Models of typical charging and relaxation are to be seen in Fig. 6. In (a) a moving continuous material becomes charged and the charges are drained through the volume of the material. In (b) the surface decay of the charges is predominant. In (c) particle charging can be seen.

The equivalent electrical circuit and computed charging threshold for bulk decay of charges is given in Fig. 7. A typical example of the simultaneous importance of the velocity and the surface resistivity of the materials

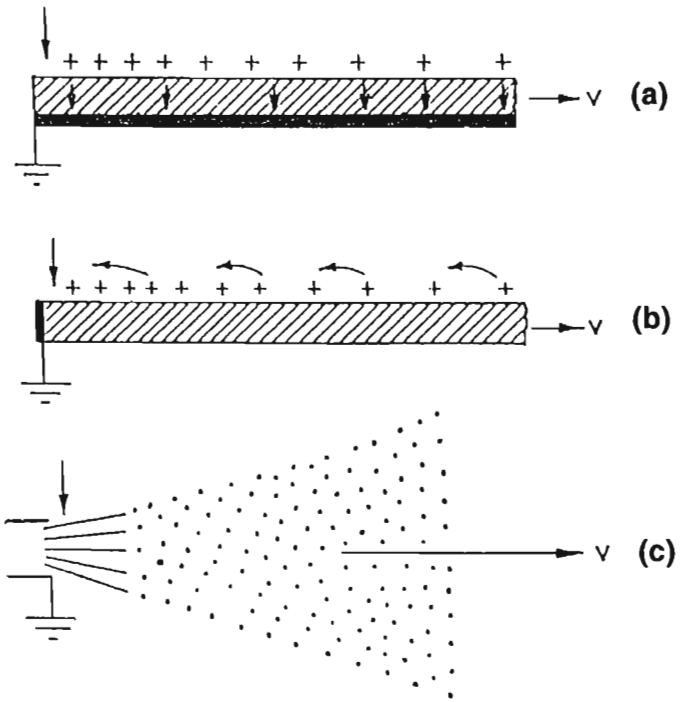


Figure 6 Bulk (a) and surface (b) decay of the charges compared with (c) particle charging.

can be the case of insulating films passing by grounded metal rollers (Horváth and Berta, 1975; Hughes et al., 1979; Ji et al., 1989). The equivalent circuit and the computed and measured charging threshold is given in Fig. 8.

One of the most common methods for draining charges in industry is to increase the humidity of the air. It is important to mention that in spite of the common misconception, when humidity is increased, electrostatic charges leak away not through the air, but through the moisture film absorbed on the charged surface.

One of the most important solutions to prevent electrostatic hazards (technological problems or fires and explosions) is the use of antistatic materials. As was shown in Fig. 1 (see Sec. I), antistatic materials combine the advantages of insulating and conducting materials. This means that antistatic materials can be grounded, and they can be used for earthing conducting objects, too (Fig. 9). The other important advantage of anti-

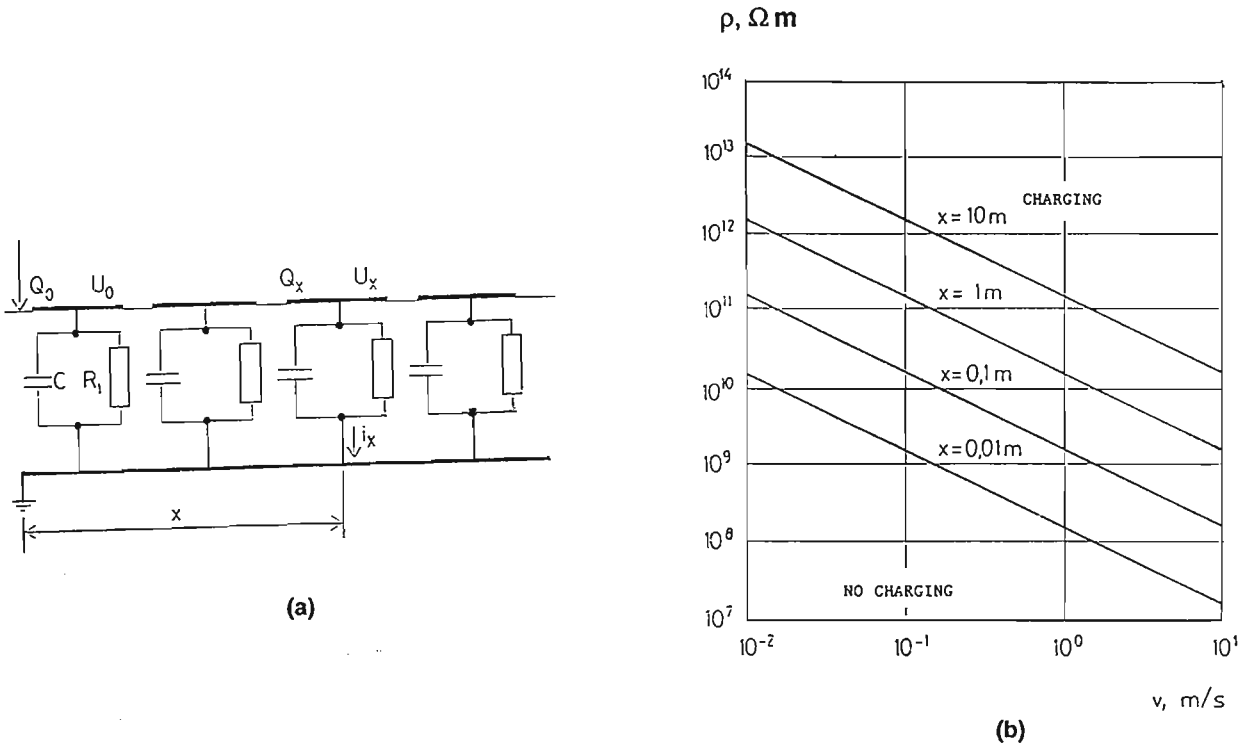


Figure 7 Equivalent circuit for bulk decay (a) and charging threshold, being the function of the distance measured from the place of charging (b).

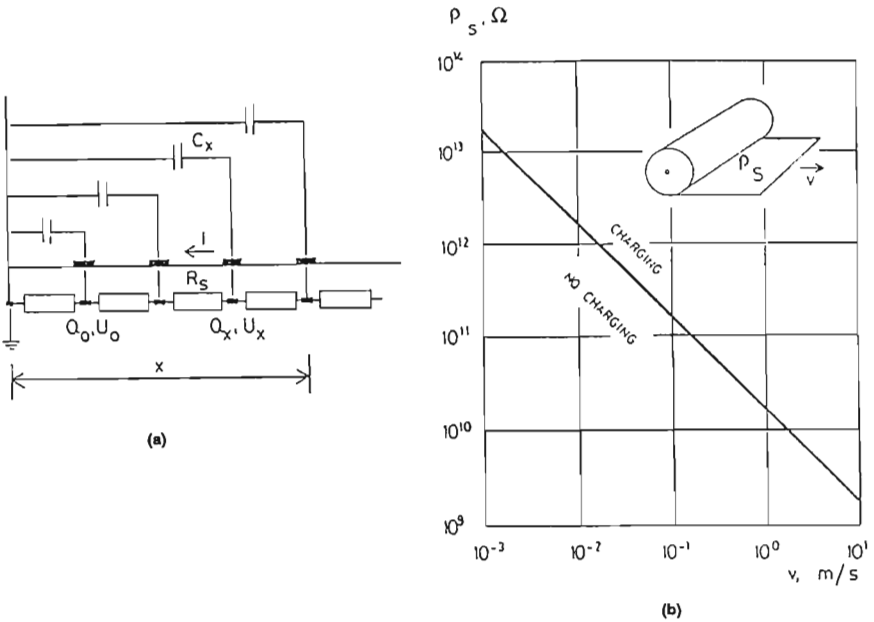


Figure 8 Equivalent electrical circuit (a) and charging threshold (b) for single film/roller contact.

static materials can be understood if discharges occur. A single spark generally discharges only a small part of the surface of a charged insulator (Berta and Gastanek, 1979), but it discharges practically all of the charges of an ungrounded conductor. Supposing the same conditions, a discharge derived from a charged conductor produces a more serious hazard than that derived from a charged insulator. As is shown in Fig. 9, the energy W_A derived from an ungrounded, charged antistatic body is also significantly lower than the energy W_c got from a similarly charged conductor. So antistatic materials are easy to handle (they can be grounded, unlike insulators) and produce far less hazard even if they are ungrounded (in comparison with conductors). This is the explanation for the urgent need and wide use of antistatic materials both in flammable atmospheres and in the presence of sensitive electronic elements everywhere in industry.

C. Neutralization

Electrostatic charges can be neutralized by eliminators (Table 3), producing charge carriers and neutralizing surface charges on solid materials or

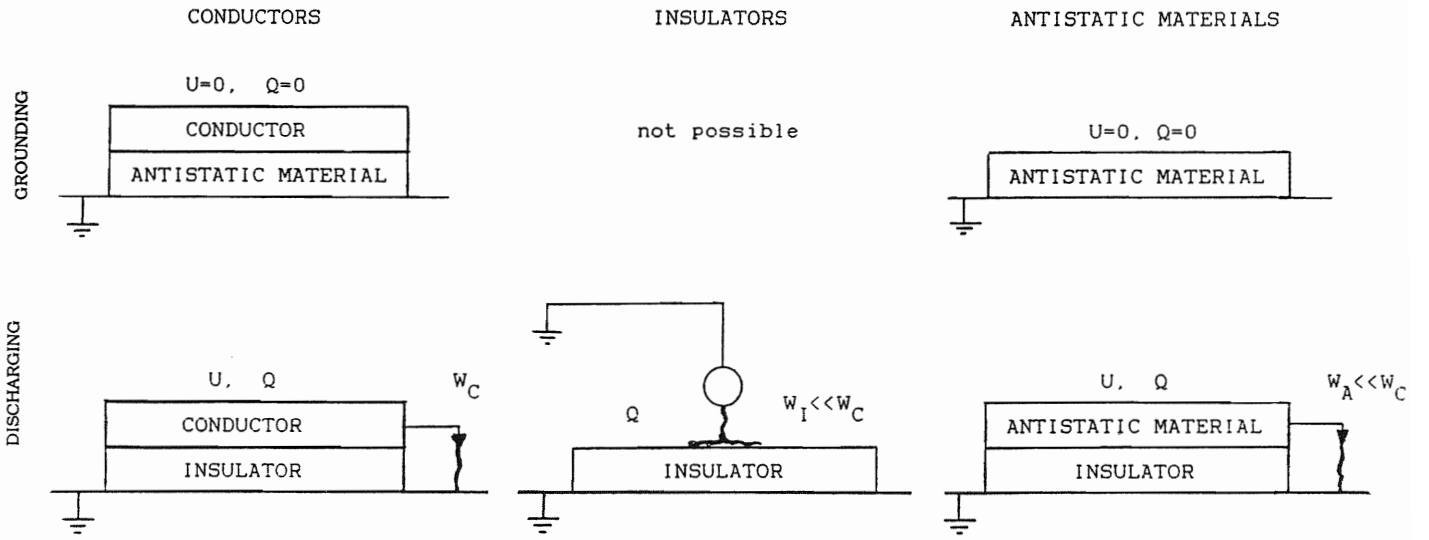


Figure 9 Comparison of grounding and discharging different materials.

Table 3 Main Types of Eliminators

Passive	Active		Radioactive	
	dc	ac	α	β
		Line frequency / High frequency		

space charges of two-phase streaming materials (contaminated gases or liquids). The simplest type of eliminator, the passive, i.e., induction, eliminator (grounded peaks or thin wires placed in the vicinity of the charges) produces charge carriers by means of corona discharges created by the charges to be neutralized. In case of active, i.e., high-voltage, eliminators (peaks or wires connected to a high voltage power supply and placed near the charges), the charge carriers are produced by the corona discharge coming into existence by virtue of the outer power supply. In radioactive eliminators (radioactive materials in safe metal housing placed facing the charges), the charge carriers are produced mostly by α or β rays.

The neutralizing efficiency of eliminators can be determined as

$$\eta = \left(1 - \left|\frac{\sigma_r}{\sigma_i}\right|\right) 100\%$$

where σ_i is the initial and σ_r is the residual charge density (before and after the eliminator). If all of the charges are neutralized ($\sigma_r = 0$), the efficiency of the eliminator is 100%. If the eliminator neutralizes only some of the initial charges ($\sigma_r/\sigma_i > 0$), or if opposite charging, so-called overcompensation, occurs ($\sigma_r/\sigma_i < 0$), η is less than 100%.

Induction eliminators are superior to other types in their simplicity of mounting, functioning, and reliability. They need neither power supply nor radioactive material. They can operate only if static charging exceeds a special threshold level, and they cannot reduce the charge density to zero. These eliminators can be successfully used where high velocities produce considerable charging.

Active eliminators can be easily controlled (dc eliminators must be controlled), and their efficiency is higher than that of any other type (the efficiency decreases with increasing frequency). They can be used for complete elimination of intense static charging. Using high-voltage eliminators, protection against electric shock and explosion hazard is essential.

Radioactive eliminators are simple and robust, and their shapes and dimensions can be changed easily. They must be strictly observed and

systematically renewed. They can be used for the complete neutralizing of moderate charging (rather low velocities) and are safe in flammable atmospheres, too.

For using the advantages of different types of the eliminators, combined eliminators (passive/active, passive/radioactive etc.) have been created. To give perfect neutralization of surface charges, in many cases charge carriers of both polarities have to be produced. To avoid recombination of these charge carriers (instead of elimination of static charges) the production of charge carriers of different polarities has to be separated in space and in time. In practice the conditions for elimination always change. This is why measuring and controlling systems are used (Fig. 10). Eliminators should be rugged, reliable, and effective. They have to be designed and chosen to be safe in flammable surroundings, grounded continuously, and located correctly. They must be carefully operated and regularly maintained to achieve maximum effectiveness (Horváth and Berta, 1982).

III. RISK

The different nuisances and hazards of electrostatic origin (see Chap. 30) have increased in recent years because of

1. The widespread use of flammable and explosive materials
2. The spread of sensitive electronic equipment

One has to recognize that the accumulation, the maximum level, and the dissipation of charges are affected by several conditions of processes (materials, contamination, speed of motion, etc.) and the surroundings (humidity, temperature, ion concentration, etc.). Some of these data are well-known, fixed, and monitored, but some conditions are not controlled or even unknown. That is why charging phenomena have to be handled as stochastic processes, and the charge level, varying in space and in time, must be treated using the methods of mathematical statistics.

The probability of fires and explosions can be discussed via Fig. 11. The independent probabilities of the formation of a flammable atmosphere $P(A)$ and of the electrostatic charging $P(B)$ can be estimated for a certain technology. The conditional probability of sparking $P(C/B)$ represents the probability of discharges if charging has occurred and the charges have accumulated. The probability of incendiary discharges $P(C/BC)$ is again a conditional probability supposing that the spark energy exceeds the minimum ignition energy of the surrounding atmosphere. The resultant proba-

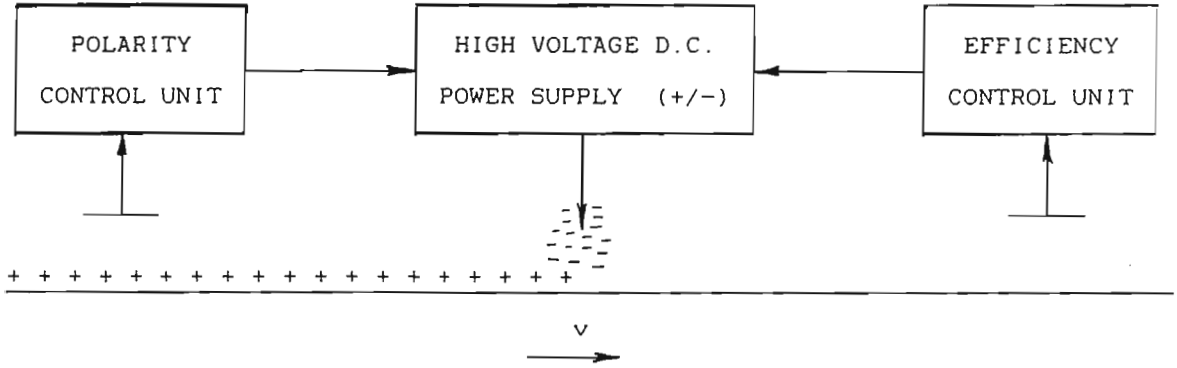


Figure 10 Elimination by a static control system.

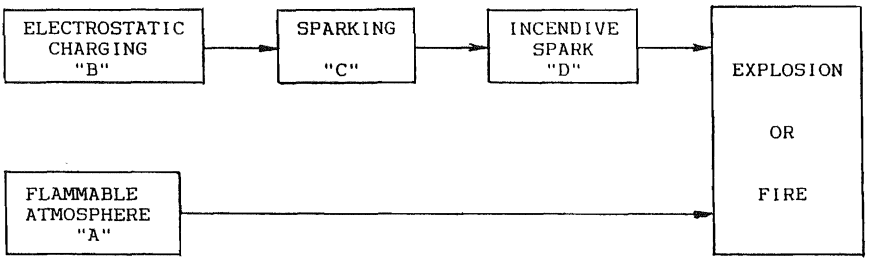


Figure 11 Conditions conductive to fire or explosion.

bility of occurrence of a fire or an explosion can be determined according to the theory of probability:

$$P(ABCD) = P(A)\cdot P(D/BC)\cdot P(C/B)\cdot P(B)$$

According to the aforesaid, a similar scheme can be drawn for determining the probability of failures or electrostatic damages of sensitive electronic devices and for all of the nuisances and hazards of electrostatic origin.

Practice can be complicated (e.g., the atmosphere can contain both gases and powders, several charging and discharging possibilities can be present), so the probability of occurrence of these single events cannot easily be measured, calculated, or estimated, and the probability of explosion or damage can be determined only in special situations. Regulations and standards (e.g., BS 5958, 1991; Richtlinien, 1989.) usually use a method of classification based on probabilities (Table 4).

In order to choose a method of avoiding electrostatic nuisances and hazards that shall be the most suitable, i.e., optimized both technically and economically, the electrostatic risk has to be determined. The risk is considered to be the harmful consequences of an optional strategy taking into account the probability of its appearance. The risk can be identified by the loss to be expected. This makes it possible to choose the static control strategy that is the most suitable for the practical problem at hand.

Table 4 Classification of Hazardous Areas

Zone 0	Explosive gas-air mixture is continuously present, or present for long periods.
Zone 1	Explosive gas-air mixture is likely to occur in normal operation.
Zone 2	Explosive gas-air mixture is not likely to occur in normal operation, and if it occurs it will exist for only a short time.

REFERENCES

Berta, I., and N. Gastanek (1979). The energy of electrostatic discharges. *Electrostatics '79*. Oxford, Inst. Phys. Conf. Ser. No. 48, pp. 67–72.

Berta, I., I. Fodor, and Gy. Clement (1981). Electrostatic sparks on charged insulating surfaces. *J. Electrostatics*. 10, 145–152.

Berta, I., I. Fodor, T. Jandó, T. Stelczer, N. Szedenik, and G. Woynárovich (1987). Testing of antistatic floor covers. *Electrostatics '87*. Oxford, Inst. Phys. Conf. Ser. No. 85, pp. 279–284.

Blythe, A. R., and G. E. Carr (1981). Characteristics of propagating electrostatic discharges on dielectric films. *J. Electrostatics*, 10, 321–326.

Boschung, P., W. Hilgner, G. Lüttgens, B. Maurer, and A. Widmer (1977). An experimental contribution to the question of the existence of lightning-like discharges in dust clouds. *J. Electrostatics*, 3, 303–310.

BS 5958 (1991). British Standard Code of Practice for Control of Undesirable Static Electricity. Part 1, General considerations. Part 2, Recommendations for particular industrial situations.

Cross, J. (1987). *Electrostatics: Principles, Problems, and Applications*. IOP Publishing, Bristol, p. 500.

Davies, D. K. (1985). Harmful effects and damage to electronics by electrostatic discharges. *J. Electrostatics*, 16, 329–342.

Gibson, N., and F. C. Lloyd (1965). Incendivity of discharges from electrostatically charged plastics. *Brit. J. Appl. Phys.*, 16, 1619–1631.

Gibson, N. (1983). Electrostatic hazards. *Electrostatics '83*. Oxford, Inst. Phys. Conf. Ser. No. 66, pp. 1–11.

Glor, M. (1985). Hazards due to electrostatic charging of powders. *J. Electrostatics*, 16, 175–181.

Heidelberg, E. (1970). Zündungen explosiver Gemische durch statische Elektrizität. *Advances in Static Electricity*. Proc of 1st Int. Conf. on Stat. El., Vienna, pp. 351–359.

Horváth, T., and I. Berta (1975). Mathematical simulation of electrostatic hazards. *Electrostatics '75*. Oxford, Inst. Phys. Conf. Ser. No. 27, pp. 256–263.

Horváth, T., and I. Berta (1982). *Static Elimination*. Research Studies Press, Chichester, p. 118.

Hughes, J. F., A. M. K. Au, and A. R. Blythe (1979). Electrical charging and discharging between films and metal rollers. *Electrostatics '79*. Oxford, Inst. Phys. Conf. Ser. No. 48, pp. 37–44.

Ji, X., Y. Takahashi, Y. Komai, and S. Kobayashi (1989). Separating discharges on electrified insulating sheet. *J. Electrostatics*, 23, 381–390.

Kuffel, E., and W. S. Zaengl (1984). *High Voltage Engineering*. Pergamon Press, Oxford, p. 498.

Lövstrand, K. G. (1981). The ignition power of brush discharges—experimental work on the critical charge density. *J. Electrostatics*, 10, 161–168.

Maurer, B. (1979). Discharges due to electrostatic charging of particles in large storage silos. *Ger. Chem. Engng.*, 2, 189–195.

Richtlinien für die Vermeidung von Zündgefahren infolge elektrostatischer Aufladungen (1989). Berufgenossenschaft der chemischen Industrie, Nr. 4, p. 78.

Taillet, J. (1991). Investigation procedures applied to major electrostatic accidents in complex systems. *Electrostatics '91*. Oxford, Inst. Phys. Conf. Ser. No. 118, pp. 63–70.

Tolson, P. (1989). High-energy discharges from plastic surfaces. *J. Electrostatics*, 22, 1–10.

Zichy, E. L. (1973). Antistatics for plastics. Elektrostatische Aufladung, Internationale Tagung der DECHEMA, Frankfurt/Main, Verlag Chemie, pp. 147–161.

32

Electrostatic Hazards During Liquid Transport and Spraying

A. G. Bailey

University of Southampton
Southampton, England

I. INTRODUCTION

Sea spray, waterfall spray, the spray from a domestic shower, or indeed any spray of liquid, either naturally or artificially generated, consists of electrically charged drops. Some of the earliest recorded observations of natural spray electrification were made by Elster and Geitel (1890), who detected considerable charge in the vicinity of waterfalls. It is believed that the charged spray and ions emanating from the oceans of the world contribute significantly to the electrification of the atmosphere. In a number of industrial situations jets or sprays of various liquids are used to clean down equipment, including the insides of storage and cargo tanks. During tank cleaning a residual amount of the previously stored product is usually present and may produce significant quantities of flammable vapor that can be ignited by electrostatic discharges of quite low energy. For example, a propane/air mixture, which may be present in a fuel oil tank, has a minimum ignition energy (MIE) of about 0.4 mJ, while naphtha may be ignited by discharges of energy of about half this value. When using liquid jets and sprays from nozzles it is therefore important to have an awareness of certain factors that tend to promote spray charging, so that this can be minimized if necessary.

Post et al. (1989) sprayed different liquids through simple nozzles at pressures up to 500 bar and measured the resultant spray electrification

by means of a field meter adjacent to the emergent jet. The charged sprays were collected in a vessel insulated from ground so that total charge "sprayed" as a function of time was monitored. The recorded electric field strengths ranged from less than 1 kV m^{-1} for sprayed toluene and acetone to about 10 kV m^{-1} for deionized water and up to about 90 kV m^{-1} for xylene containing particles of SiO_2. Relatively high charging was observed when emulsions such as water in toluene or two-phase mixtures of solid particles suspended in liquid were sprayed. Whether or not charged sprays lead to conditions enabling discharges to occur depends not only upon the spray liquid and spraying parameters but also on the geometry of the spray zone; during tank cleaning tank size is especially important, as larger tanks may contain a relatively large volume of charged spray, which results in high space potentials and fields, thus increasing the probability of discharges.

II. SUPERTANKER EXPLOSIONS

An industrial situation in which intense electrification may arise during spraying occurs during the water-jet washing of the oil cargo tanks of very large crude carriers (VLCCs). In 1969 three VLCCs exploded during tank washing operations. Powerful water jets, which are used to hose down the tank inner surfaces, generate a considerable amount of fine charged mist, which settles under gravity only very slowly. Within the tanks, which have capacities of approximately 24,000 cubic meters, space charge densities of 10^{-8} Cm^{-3} occur, leading to space potentials of several thousand volts and electric fields at tank walls of up to 30 kV m^{-1}. The question that arose was "Are electrostatic discharges of sufficient energy to ignite the residual crude oil vapor possible?" The posing of this question illustrated a situation that often pertains after an explosion, i.e., the cause is unknown and electrostatic discharge is one of several possible causes. The systematic work that led to an answer to the preceding question illustrates very well a number of basic electrostatic principles.

Prior to 1969, water washing of cargo tanks had been carried out safely for many years using portable washing machines. Jets of water at a pressure of 1000 kP were produced from 1.5 cm diameter nozzles at a flow rate of about 15 m^3 per hour. The machines were normally suspended into the tanks by hoses, several being required per washing operation. The explosions in 1969 occurred when new washing machines and procedures were being used. The new machines were designed to cope with the exceptionally large tank volumes of VLCCs and had throughputs of 175 m^3 per hour from 4 cm diameter nozzles. They were permanently mounted in the tanks and operated with recirculated water, i.e. water contaminated with

oil droplets. It was shown that several of these factors acting together may have led to the explosions.

From gas samples taken from a VLCC, the predominant gases were found to be propane and the isomers of butane, gases that have a minimum ignition energy of about 0.2 mJ. A coordinated experimental program was set up by Shell in 1970 with work being undertaken at laboratories in Amsterdam, the Thornton Research Centre in the UK, and the University of Southampton, UK. Studies on the safety of water washing were also supported by the International Chamber of Shipping (ICS) and the American Petroleum Institute (API). A primary objective was to determine whether any discharges of energy > 0.2 mJ could occur during tank washing operations. Laboratory experiments were small scale but sea trials were also conducted. An interesting observation by Bustin (1972) was that the potentials observed in tanks of various sizes during washing did not differ significantly. This finding correlated with the observation that the space charge density decreased in larger tanks as shown in Table 1. It should be noted that the space potential at the center of a tank depends upon the square of the tank radius (assuming a spherical tank), while the electric field at the tank wall depends only on the radius.

An experimental test tank of $2 \times 2 \times 3$ m^3 which was approximately 1/2000 scale was set up at Southampton (Hughes et al., 1973). To achieve a space potential of ~40 kV and a field of ~13 kV m^{-1}, which were of similar magnitudes to the values possible in a VLCC, it was necessary to inject a charged spray of density 10^{-6} C m^{-3} into the test tank. Preliminary investigations were concerned with the incendivity of discharges from charged mists to grounded objects. Neither spark nor lightninglike discharges were recorded under any conditions. However, the high field set up by the mist space charge was able to set up corona discharges on sharp grounded protrusions within the mist or at the edge of a tank. Van

Table 1 Space Charge Density in Tanks of Different Sizes

Vessel	Tank volume (m^3)	Max. charge density (nC m^{-3})
Shore tank	240	67
Small tanker	880	35
	1950	30
Large tanker	4640	15
	5300	17
VLCC	13000	10.7
	26000	3.8

de Weerd (1971) tested the incendivity of corona discharges at the end of a probe lowered into a 12,000 m^3 tank where the space potential was raised to 40 kV by steam injection. Propane gas seeped through holes at the surface of the probe, but the corona discharges that were readily detected did not ignite the gas. Since that time many ignition tests with corona discharges have proved that they are the most feeble type of discharge and are normally incapable of igniting dusts and vapors.

The experimental work at Southampton proceeded, after corona discharges had been ruled out as an ignition source, to consider whether an isolated piece of metal or slug of water passing through the charged mist might acquire charge, to be then discharged when passing close to a grounded protrusion from the tank wall. This possibility followed from experiments carried out by van de Weerd and van Laar (1973) of Shell. In these experiments a slug of water dropped out of a vertical pipe and fell through a cylindrical metal cage maintained at a high potential. The field from this cage polarized the slug, i.e., charge separation between its ends was induced. As the end of the slug passed close by a grounded probe a spark occurred that had sufficient energy to ignite a local propane/air mixture. A water slug could conceivably fall from the roof of a tank or be formed directly by the new water washing machines. Tests were carried out in which the whole test chamber contained a propane/air mixture.

The Southampton tests were conducted with 10 cm long metal cylinders and water slugs of 35 cm^3 volume. Both types, after falling through the charged mist, caused sparking to a grounded probe, which ignited the propane/air environment. The water slugs tested were always of the same volume, but elongation during the free fall to the probe occurred due to polarization forces in the space charge field. Elongation to about 35 cm was typical.

Even after having demonstrated that a conducting slug of water can initiate incendive discharges, the precise mechanisms leading up to discharge are complex and difficult to quantify. A volume of water falling through charged mist will intercept charged drops and so will charge according to the volume of mist swept through. Estimates of this charge, made by Hughes et al. (1973), give a value of approximately 2 nC, which is significantly less than the 40–50 nC of charge transfer from the slug to probe recorded experimentally. In fact, of various charging mechanisms considered, the only one that could explain the high charge transfers was induction charging. Induction charging is dependent upon the shape of the object being charged; an elongated slug polarizes much more strongly than the same mass of material in a spherical shape. A polarized slug may have a portion of its polarized charge at one end discharged as a spark if

the end passes close to a grounded probe, provided that the process occurs while the slug remains polarized in a local field. Alternatively, a slug falling from the roof of a tank, or being ejected from the nozzle of a washing machine, would take up a net charge by field induction and could subsequently discharge to a grounded probe even in a field free region.

The systematic investigations of electrostatic phenomena during tank washing operations proved that discharges of sufficient energy to cause an explosion in the "empty" tank of a VLCC could occur. The precise mechanism that caused the VLCC explosions was not proved but almost certainly was electrostatic in origin. It is interesting to note that the conclusions of API, after thorough investigations, were that *the probability that electrostatics was the cause was not necessarily higher than the probability of ignition from other causes such as human error or mechanical impact.*

III. ELECTROSTATIC CHARGING DURING FUEL FLOW

Whenever a liquid flows along a pipe, shearing of the electrical double layer at the liquid/wall interface causes charge of one polarity to be entrained in the liquid flow and leaves opposite charge on the pipe wall. Whether or not this effect is significant and leads to appreciable electrostatic charging depends upon several factors including pipe material (metal or insulator), liquid conductivity, flow rate, pipe diameter, and temperature. Liquid conductivity is extremely important, and only insulating liquids such as gasoline, kerosene, and others having a conductivity less than about 50 pS m^{-1} generate sufficient charge that a fire or explosion risk may arise unless appropriate measures are taken. In the following sections the operation of loading insulating fuel into a metal road or rail tanker is discussed and serves to illustrate a number of electrostatic hazards that may arise from incorrect system design and inappropriate operating procedures.

Insulating liquid pumped from a pipe into a tank will be charged according to the following equation by Schön (1965):

$$i = 3.7 \cdot 10^{-6} d^2 v^2 \left[1 - \exp\left(\frac{l}{v\tau}\right)\right] \tag{1}$$

where i = streaming current, d = pipe diameter, v = flow velocity, l = pipe length, and τ = fuel relaxation time. All units are S.I.

The streaming current represents the coulombs per second transferred by the liquid into the tank and is equal and opposite to the current flowing to ground from the pipe, assuming it to be metal. The equation shows

that if a pipe is sufficiently long the streaming current rises to a constant plateau value depending only on d^2v^2. Charging may be appreciably higher than indicated by the Schön equation if equipment such as a pump or strainer is present, especially near the pipe outlet. Very fine particle filters (<5 μm), for example, can be prolific charge generators, yielding charge densities in the range of 10–5000 Cm^{-3}, depending on flow velocity.

When charged liquid is loaded into a tank, a fire/explosion risk may arise if the criteria illustrated in Fig. 1 are satisfied. Tanks may be filled in different ways, some being more hazardous than others. Filling is normally by the feed pipe connected to the bottom of the tank, or alternatively the pipe protrudes into the tank from the top. With top filling, the pipe should extend to the bottom of the tank for safety reasons. To minimize charge accumulation on the liquid surface during filling, the flow rate should not be too high, and a central conductor or metal web from the top to the bottom of the tank will ensure that the potential is zero in the center region. With top filling, the conducting fill pipe, lowered to the tank bottom, serves this purpose. With bottom filling and no such central grounding object, liquid surface potentials can rise significantly higher than for top loading at the same rate. In addition, with any loading, splashing and foaming should be avoided, as charging levels are then increased.

In Fig. 1, the block at the top poses the question "Does charging occur?" From the foregoing it is clear that the answer to this question may be affirmative but dependent upon several parameters. This dependence may be illustrated by considering the guidance provided in national standards. Providing a liquid is conducting enough, charge accumulation

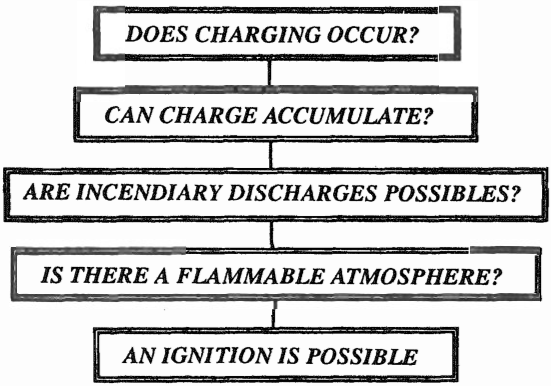


Figure 1 Criteria that may lead to an electrostatic ignition.

does not occur, and standards generally specify that it is only for fuels of conductivity <25 or 50 pS m^{-1} that precautions are required. The importance of good grounding of all conducting parts of a system is emphasized. Electrostatic hazards may arise during loading, gauging, and sampling. The latter two operations involve personnel who may be charged. When loading a single-phase liquid it is recommended in European standards that the pipe flow velocity should never exceed 7 ms^{-1}. A second condition includes pipe diameter d (in meters). Flow velocity should not exceed a value given by $u = N/d$ where the constant $N = 0.5$ m^2 s^{-1} when σ is larger than 5 pS m^{-1}, but if σ <5 pS m^{-1}, $N = 0.5$ in the UK but 0.38 in other standards. The more hazardous situations of two-phase liquids such as oils containing water or liquids containing particles or sediment in tanks are also considered in standards, and greater constraints on loading operations are specified.

The second block of Fig. 1 is concerned with charge accumulation. Liquid must be insulating for charge to accumulate. During loading an equilibrium is established between rate of charge accumulation in the liquid in the tank and the dissipation rate due to charge relaxation to the conducting tank walls. The time constant of the exponential relaxation process is inversely proportional to liquid conductivity. Antistatic additives may be used to increase liquid conductivity to say 50 pS m^{-1} so that significant charge accumulation does not occur. In large tanks, filled at the same rate as smaller tanks, the liquid surface level rises more slowly, giving more time for charge relaxation to occur before the surface reaches a critical level where a discharge could occur. For this reason it is possible to fill larger tanks at a greater rate provided the flow velocity is kept below 7 ms^{-1}.

The surface potentials that develop on a liquid during loading give a direct indication of charge accumulation and hence possible hazard. Walmsley (1990) has monitored potentials during normal and splash top loading of fuel into a tank as shown in Fig. 2. Bottom and normal top loading (pipe to bottom of tank) show similar potential rises during loading. During the bottom loading a central conductor was present; otherwise bottom loading potentials would have been greater. Splash loading surface potentials were 80% higher than nonsplash loading, illustrating the hazard of not lowering the fill pipe sufficiently. Walmsley (1990) also investigated the operating procedure of starting the tank filling slowly, until the liquid level had risen so that splashing was minimized, followed by an increase in filling rate. This was compared with filling entirely at the higher rate. Although potentials were maintained very low during the slow start (less than 1 kV), final potentials were the same for the two procedures (about 30 kV).

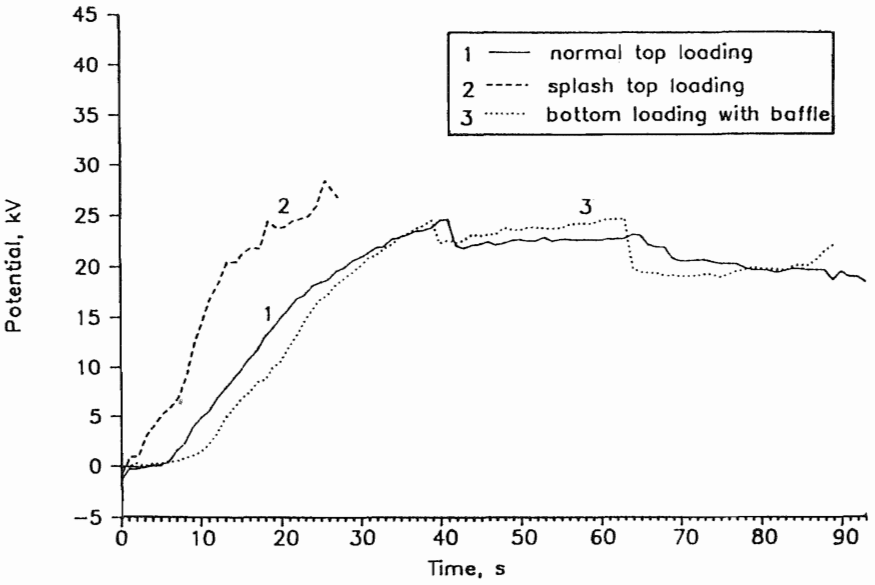


Figure 2 Space potentials within a tank during liquid filling. (From Walmsley, 1990.)

The third block of Fig. 1 is concerned with the probability of incendive discharges. A discussion of the various types of discharge that can occur during liquid transfer to a tank is beyond the scope of this article. Nonincendive corona discharges may occur, and incendive discharges of the spark and brush type occur unless precautions are taken.

The fourth block of Fig. 1 poses a more difficult question than might be expected. Most hydrocarbon liquids, when in equilibrium with their vapors, produce vapor concentrations outside the flammable range. Low flash point products such as gasoline produce an overrich vapor in a closed tank. However, at the start of a filling operation into a vapor-free tank the atmosphere rapidly becomes incendive and the vapor/air mixture may remain in the flammable range many minutes into the operation; it will eventually become overrich except possibly in the vicinity of air vents, etc. Some products such as toluene produce vapor within the flammable range even under equilibrium conditions. Liquids such as diesel fuel and heating oils have a high flash point, producing lean vapor/air mixtures in equilibrium. Despite this apparently safe situation, many fires and explosions have occurred during loading of these products. The problems generally arise when the practice of switch loading is carried out. Switch loading is the operation of loading an "empty" tank, which previously contained

a low flash point product such as gasoline, with a high flash point product such as diesel oil. The empty tank is likely to contain residual quantities of gasoline, and butane will be present in the tank atmosphere, which is likely to be overrich. During the subsequent loading, butane dissolves in the incoming product and the atmosphere enters the flammable range where it may remain for much of the filling operation.

Very many incidents have arisen during switch loading, and in concluding this section an example of an industrial accident is given. Bond (1991) cites a case in which an explosion occurred when kerosene was being bottom loaded into a road tanker that had previously contained gasoline. The filling rate was 97 $m^3\ h^{-1}$ through a 7.5 cm diameter (3 in.) hose. This is equivalent to a flow velocity of 6 ms^{-1}. The conductivity of the kerosene was less than 10 pS m^{-1}. As $\sigma > 5$ pS m^{-1}, the flow velocity should not have exceeded 6.6 ms^{-1}. At the operational flow velocity of 6 ms^{-1} the operation should have been safe. However, a microfilter was present in the pipeline and raised the charge to a dangerous level. It is not normal practice to use a microfilter in the line during road tanker loading. Aviation fuels, on the other hand, are normally filtered during loading, and due to this practice fuel conductivity should be increased to 25 or 50 pS m^{-1} or the fuel flow rate kept down to a relatively low level.

REFERENCES

Bond, J. (1991). *Sources of Ignition: Flammability Characteristics of Chemicals and Products*. Butterworth Heinemann, London.

Bustin, W. M. (1972). Electrically charged mist produced by water washing. Esso Research and Engineering Co., Report EE. 8 TMR. 72.

Elster, J., and H. Geitel (1890). Wien, Ber 94.

Hughes, J. F., A. W. Bright, B. Makin, and I. F. Parker (1973). A study of electrical discharges in a charged water aerosol. *J Phys D: Appl Phys*, 6, 966–975.

Post, L., M. Glor, G. Luttgen, and B. Maurer (1989). The avoidance of ignition hazards due to electrostatic charges occuring during the spraying of liquids under high pressure. *J Electrostatics*, 23, 99–109.

Schön, G. (1965). In *Handbuch der Raumexplosionen* (H. H. Freytag, ed.). Verlag Chemie, Weinheim.

van de Weerd, J. M. (1971). Electrostatic charge generation during the washing of tanks with water sprays. II. measurements and interpretation. *Inst. Phys. Conf. Series*, 11, 158–177.

van de Weerd, J. M., and W. A. van Laar (1973). Sparks generated by water slugs in tanks filled with electrostatically charged mist. III. Ignition experiments in a 2 m^3 tent setup. Koninklijke/Shell-Laboratorium, *Amsterdam report AMSR.0007.73*.

Walmsley, H. L. (1990). Electrostatic ignition risks in road tanker loading. *Petroleum Review*, 632–637.

This Page Intentionally Left Blank

33

Electrostatic Charge Elimination Techniques

C. G. Noll

The Simco Company
Hatfield, Pennsylvania

I. IMPORTANCE OF STATIC ELIMINATION

The management of electrical charge is critical to the success of electronic component manufacturing and assembly and to many general industrial processes. The problems usually arise from static charge on insulating materials. The electric field from these charge distributions can induce electrical charge separation on conductive objects, leading to secondary processes that may aid static elimination or introduce charge control requirements in themselves.

High static charge levels may trigger electrical discharges, provide electrical forces that attract particulate contaminants, or cause materials to stick together in undesirable ways. Electrical discharges, for example, can damage electronic devices and circuits, expose photographic film, or yield explosion- or accident-related safety hazards around industrial machinery. Particulate contaminants that are electrostatically drawn to sheets, film, or other insulating objects are troublesome in the photographic, packaging, printing, textile, and plastic products industries. High charge levels on sheets and films also cause these materials to be attracted to surfaces and rollers, causing difficulty in their handling. Pneumatically conveyed edge-trim fragments from web handling operations are particularly troublesome, leading to blinding of end-of-line cyclones, receiving vessels, and baling equipment.

Techniques to manage charge on insulating materials will be discussed in this chapter. We begin with ways to modify the conductivity of materials for those instances where such modification is commercially possible. Then, methods to ionize gases will be considered. Ionization gives free, mobile charge that can be drawn to electrostatically charged surfaces where recombination and neutralization can occur. Various generic equipment options for the neutralization of static charge will be discussed, as well as hazards and cautions that should be exercised in the electrostatic environment of industry.

II. CONDITIONING OF MATERIALS TO CONDUCT ELECTRICAL CHARGE

Electrical charge can accumulate to disturbing levels when the rate of charge separation exceeds its rate of recombination. Charge relaxation or redistribution is generally controlled by the electrical conductivity of the material itself and the material's bonding to ground. It is therefore natural to associate electrostatic processes with insulating materials, at least in a qualitative sense. The degree of conductivity associated with electrostatic processes is arbitrary, but it is loosely related to the speed of mechanical actions that might separate charge in the specific process. For example, electrostatic hazards are more likely to be present in high speed printing or film converting processes than in low speed ones.

Additives can sometimes be found to increase the conductivity of materials sufficiently to achieve charge recombination in a time scale that matters. These antistats may yield temporary static control or become an inherent part of the final product. Additives are available for solid (often fibrous), liquid, granular, and powder materials. Their use is limited to commercial requirements for the process and final product (Wilder, 1989; Modern Plastics Encyclopedia, 1993).

A. Extrinsically Conductive Materials

Conditioning agents (topical antistats) and other treatments are used to modify the surface of materials so that they will conduct electrical charge. They are also sometimes added to liquids such as fuels to assure safe handling and to transformer oil (Radwan et al., 1992) to prevent insulation breakdown. Fly ash conditioning with moisture, ammonia, or alkali (especially sodium) compounds increases conductivity of dust deposits, making electrostatic precipitation feasible for pollution control or process material recovery (White, 1963).

Extrinsic additives directly provide conductivity to an insulating material, without materially altering the insulator itself. They take the form of coatings and conductive additives to the material. Additives and treatments that increase lubricity stand out as key options for decreasing charging in the first place (Klein, 1991). Others bind moisture to the surface of the materials to improve surface conductivity and aid static control. The addition of moisture (humidity modification) for static control, by itself, is seldom a permanent solution. Humidity is, however, an important factor in static control (Kolyer and Rushworth, 1990).

1. Liquids

The resistivity of liquids can often be controlled by doping them with mild electrolytes or their dissociated components (Horvath and Berta, 1982). In some cases, polar liquids that are easily dissociated can be used as antistatic additives. This method is complicated and requires detailed investigation, particularly when materials are used to produce pharmaceutical or food products.

2. Powders

As solid material is divided into smaller and smaller parts, more surface area is exposed. Powders therefore offer the most severe test for the influence of antistats on surface conduction. Figure 1 shows an example of the electrical resistivity of a powder as a function of temperature and moisture content. The antistatic additive introduces surface electronic states that allow charge transfer between particles. These same surface electronic states are active in the enhancement of conductivity and cohesion within deposits. One is often troubled by changes in handling aspects of powders when introducing conditioning agents for static control. The additives also can become contaminants to the process or product.

3. Textiles

Antistatic additives are widely used in the textile industry, both to make certain manufacturing operations easier and to control uncomfortable nuisances from final products. Antistatic detergents, sprays, and dusters/brushes (containing antistatic additives) are commercially available. Antistatic additives for use with cellulose (Hellsten et al., 1989), wool (Brown and Pailthrope, 1988a, 1988b, 1988c), polyethylene terephthalate (PET) (Uchida et al., 1991; Abdul-Kadir et al., 1988), and acrylic fibers (Park et al., 1991), for example, are described in the literature.

Metallic and other conductive fibers are added to textiles to gain permanent conductivity. The resulting materials are used to make garments for use where electronic components are manufactured (clean rooms, packaging) and computer rooms. Others are used for electromagnetic interference

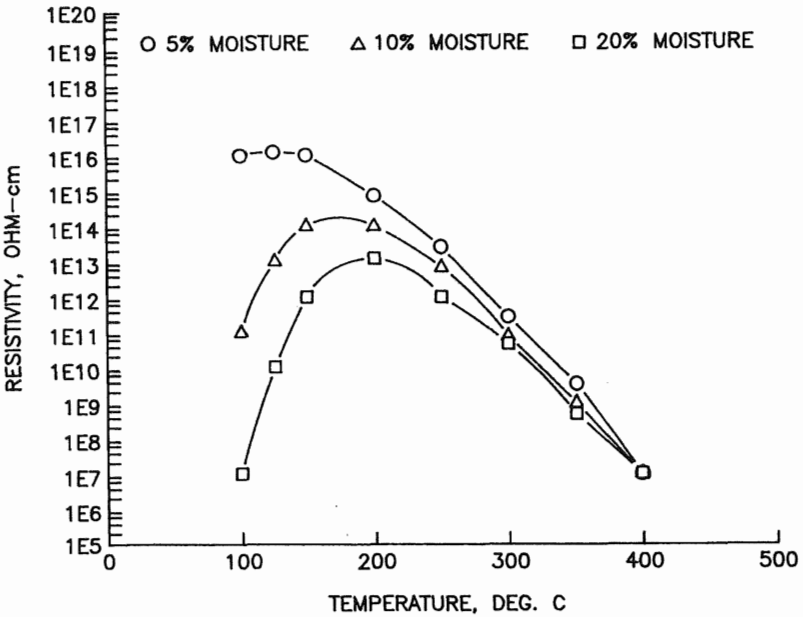


Figure 1 Electrical resistivity of a powder at elevated temperature.

(EMI) shielding (Marchini, 1991). Still others are used as filtration media in gas cleaning equipment.

4. Coated Solids

Another method of decreasing the surface resistivity of insulating materials is the deposition of thin metallic films. This method of charge control is widely used, e.g., on aircraft windshields, in cathode ray tubes (Rijnders and Van Der Voort, 1990; Van Den Eeden and Sluyterman, 1990), and in solar technology and electronics (Demchishin et al., 1988). It is rather difficult to protect these conductive films from damage. The same problem appears if conductive paints are used for surface treatments. Vapor phase photografting and chemical grafting have been used to add conductive layers to the surface on polypropylene (Morra et al., 1992).

At the present time organic and inorganic materials are widely used for antistatic floor coatings. To reduce the electrical resistance of coatings on such floors, it is possible to treat the surface with surface-active agents.

5. Solids

Conductive additives can be used to lower the volume electrical resistivity of insulators. Metal particles and carbon granules or filaments have been used. Threshold levels for conductivity enhancement are observed, because these additives act by direct contact conduction through the bulk of the material.

The decay of electrical charge from the surface of such a material depends on the method of charging. Charging with electrodes at the surface probes the conduction of the conductive component of the composite only, whereas charging with a corona results in two distinct processes: a screening of trapped charges by the conductive component and charge dissipation of the matrix (Ansermet and Kuttler, 1992).

A glycerine ester derivative, graphite, a metal powder, a metal oxide (Jando et al., 1989), and even ion beam radiation (Liu et al., 1989) have been shown to increase conductivity of polyvinyl chloride (PVC). Noncrosslinked high density expanded polypropylene doped with conductive carbon has been produced to offer cushioning, rigidity, and stable antistatic properties for cases and partitions used in packaging of electronic components and assemblies (Nojiri et al., 1991).

B. Intrinsically Conductive Materials

Intrinsic or internal antistatic additives are generally added chemically to the material and are an indistinguishable component of it. Materials containing these additives can resist even strong influences (wetting, rubbing, washing, or cleaning), and they are less inclined to age. The choice of an internal antistatic agent to provide resistivity control depends on the chemical structure of the antistat, the polymer type, polarity, and crystal structure, the type and concentration of other additives in the resin, and the fabrication and storage conditions of the resulting material (e.g., temperature and time) (Trotoir, 1988). Electroactive polymers (EAP) are also beginning to appear as conductive packaging materials.

III. USE OF BIPOLAR IONIZATION TO NEUTRALIZE STATIC CHARGE

Much effort has been expended toward developing materials that are electrically conductive, or treatments for materials to speed up charge recombination. Often such materials and treatments are inappropriate for a process or product, and one must find other methods to neutralize electric charge distributions on insulators.

The next consideration is the use of bipolar ionization. From bipolar ionizers, ions are distributed in the air or other gas surrounding the charged insulator. Coulomb forces attract those ions from the gas stream to neutralize the charge on the insulator and repel opposite polarity ions. There are usually grounded enclosures or other conductive objects around to capture the opposite polarity ions that are repelled during the recombination process. Bipolar ionizers eliminate static charge, not by material conductivity, but rather by the higher mobility of ionic charge in the gas stream, under the electric field of the charged insulator.

There are two factors that guide ionizer design and performance evaluations. The first is charge balance: the condition when the net free charge on a object equals zero in the presence of bipolar ionization from the ionizer. The second is charge decay time: the time for a static charge to be reduced to a given percentage of the charge's original level. Bipolar ionizers are usually rated by the time required to neutralize 90% of the charge on an isolated 20 picofarad metal plate from an initial potential of either 1 kV or 5 kV. The initial charge on this plate, of course, is the product of its capacitance and electric potential.

The performance of ionizers is reduced if the charge on an object does not produce electric field components directed toward the bipolar ionization. The terms field suppression and proximity effect are used to describe the observed reduction in electric field away from an object when the object is brought near a grounded or large polarizable object. The reduction in electric field is the result of an increase in capacitance between the charged object and ground with constant electrical charge on the object. The electric field lines are repositioned from radiating outward to image charges in the grounded or other polarizable object.

Most commercial ionizers depend upon electrical corona to produce bipolar ionization. The corona electrodes are driven with alternating potential (usually at line frequency, 50–60 Hz) or with a train of positive and negative square-wave potentials. The former are called AC ionizers and the latter pulse-DC ionizers. There are also double-DC ionizers that have continuously operating DC corona of each polarity.

An asymmetrical gap (e.g., needle-plate, wire-tube, etc.) is used to form corona electrodes in static eliminators. Either electrode may be fixed to ground potential, or both may float with a potential difference between them. The potential difference between the electrodes is raised to a level to produce electrical corona of alternating positive and negative polarity on the electrode with small radius of curvature.

Most static elimination is done in the air environment. In air, positive ions are formed by stripping electrons from atomic and molecular species and negative ions by electron attachment. Some gases such as nitrogen

do not attach electrons easily, and therefore negative corona in these gases is unstable. Corona type ionizers can operate unpredictably or not at all in these environments. The coating of the passive electrode with insulation will sometimes make AC ionizers operate in gases that are not electron attaching.

Gases containing oxygen, carbon dioxide, and water vapor will attach electrons and form stable negative ions and negative corona. High purity nitrogen, argon, and helium do not attach free electrons and do not form stable negative corona. In gases that are not electron attaching and in some other applications (possibly where intrinsic safety is required), radioactive sources are used. Charge neutralization is achieved by the electric field between the ions or free electrons and the charged object. Polonium-210, an alpha emitter, is the most common nuclear source for ionization products in the USA. Alpha radiation sources produce strong ionization in a well-defined space close to the radioactive source. Their penetration power through solid materials is also low.

IV. FIELD DRIVEN STATIC ELIMINATORS

There are two primary types of static eliminators: those using the electric field to move ions from the source to the charged object and those using flowing gases to move a bipolar ion cloud to the vicinity of the charged object, where the electric field will select ions to achieve static elimination. There are a few ionizers that use both mechanisms to achieve static control.

A. Induction Ionizers

When a sharp, grounded needle point is brought near a highly charged surface, it has induced in it a charge opposite that of the surface. If the charge concentration near the needle's tip is high enough, the surrounding air will break down. Ions will be injected toward the charged object of the essential polarity to neutralize the charge. The typical action of an induction bar is illustrated in Figure 2.

Induction ionizers are also known as passive eliminators since they do not have a power supply to elevate the minimum electrode potential to above the corona onset point. In particular, ionization will not be produced to neutralize a charged object, unless sufficient charge is induced on the needle electrode to initiate corona.

Induction ionizers are constructed as simple needle electrodes, arrays of needles (static bars), or brushes and tinsel.

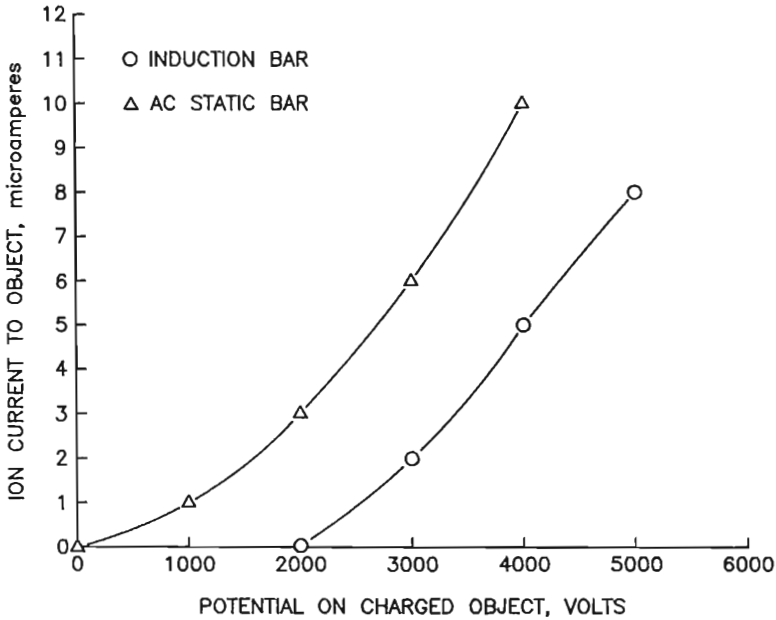


Figure 2 Ion injection from typical static bars.

In web processing (polymer films, for example), overcompensation can occur if the initial charge density on the web is high or the static eliminator is very close to the charged surface (Horvath and Berta, 1982). In overcompensation, the charged surface becomes oppositely charged after the supposed charge elimination. This occurs because some of the electric field lines of force from the eliminator to the charges on the surface intersect the surface where it is already discharged. Charge carriers following these electric lines of force reach the already discharged surface and charge it oppositely.

To avoid overcompensation, the electric field should be decreased at the eliminator by increasing the distance between the web and the eliminator, thus decreasing the number of lines of force intersecting the discharged surface.

B. Static Bars

The term static bar is usually applied to arrays of (corona or nuclear-element) ionizers that provide a source of ions for attraction to charged

objects. The purpose of the static bar is to inject ions even when the charge on the object is smaller than needed to produce ionization by induction. The ion injection current as a function of object charge is illustrated in Fig. 2 for a typical electrical (active) static eliminator.

Overcompensation can occur with these bars as with induction ionizers. Static bars are available in various lengths and in circular, square, hexagonal, and other shapes.

1. AC Static Bars

The main components of an AC static bar installation are the bar itself, the cable, and the power unit.

Typical AC static bars can have the needle electrodes directly coupled (hot bars), individually capacitively coupled (shockless bars), or individually resistively coupled (shockless bars) to the high voltage terminal. Directly coupled bars are referred to as hot bars, while the resistively and capacitively coupled bars are shockless and in some cases safe for hazardous work areas.

The electric cable used to energize high voltage AC static eliminators is sometimes shielded. This prevents the radiation of AC electric fields. Strong AC electric fields can be troublesome to delicate electronic circuits, such as computer lines. Corona-free shielded cable is used at times. It consists of a metal core, a conducting silicone layer, an insulating silicone layer, a conductive paint layer, a metallic braid layer, and a plastic sheath. The conducting silicone and conductive paint layers provide uniform, large-diameter surfaces that are most likely to be free from corona. The braid gives flexible shielding from electromagnetic interference and a sure ground contact for the paint.

Capacitive loading can be a problem with static eliminators that have long lengths of shielded cable or long lengths of high voltage cable in conduit. In capacitive loading, the capacitive reactance exceeds the inductive reactance, and the load draws the leading current. The excessive capacitive load can cause the operating voltage to rise or fall depending on circumstances of installation. If the operating voltage rises above acceptable limits, it can cause burnout of equipment. If the operating voltage falls below acceptable limits, it will reduce the ion output of the equipment.

Improved load regulation can be obtained by using a ferroresonant transformer as the power source. A ferroresonant transformer is a saturable device that regulates for changes in the magnitude of the input voltage. Ferroresonant transformers regulate the average value of the output voltage. Core saturation introduces waveform distortion that varies with the

input voltage. The rms value of the output voltage may therefore vary while the average value is held constant.

2. Dual-Phase Static Bars

As the speed of webs increases, the use of line-driven (50–60 Hz) static eliminators becomes less acceptable, since ionization is produced only during a portion of the waveform. By placing bars in series across a web and operating them out of phase, the maximum web speed for static elimination can be increased from about 800 to 1500 ft/min.

3. Double-DC Static Bars

The simultaneous use of steady DC of both polarities in a static eliminator allows use of static bars to web speeds of at least 2500 ft/min. Typically, the positive and negative corona ionizers are placed in series with the web's path. There are some static bar designs that have positive and negative ionizers placed alternately in a line along the length of the bar.

V. GAS DRIVEN STATIC ELIMINATORS

It is generally more efficient to attract ions directly from an ionizer to a charged object than to project them to a surface by a gas flow. However, there are many cases with space restrictions and with many charged, stationary objects or work surfaces that require the transport of bipolar ionization by gas currents.

A. Nozzles and Guns

Nozzles and guns are used in processing of insulating components and packaging to displace contaminants and prevent them from being attracted again to the work. Blow-off equipment is available for electronic assembly in Class 10 clean rooms, paint preparation rooms and tunnels, and the factory floor.

B. Ionizing Air Blowers

Larger work areas require blowers with electrostatic augmentation. Units for electronic assembly often contain heaters to warm the air stream. Most ionizing air blowers of this type have adjustable air speeds, built-in brushes for cleaning the electrodes, and either self-balance or electronic adjustment for charge balance in the air stream. Equipment is available for workbenches and industrial environments. There are even units that mount above the workbench blowing ionizing air down to the assembly

area, and grid units that mount to the outlet of HEPA filters in clean rooms.

C. Air Assisted Static Bars

It is often desirable to project a bipolar air stream as a sheet to form an ionized air curtain. The air curtain is used to blow particulate matter from work, or just to project ions where a static bar cannot be conveniently mounted. In these cases, static bars are fitted with tubes with equally spaced holes (air bars) or with air knives. Air knives eject high velocity sheets of air from a slit, thereby inducing a larger air flow. The air knife is also called an air amplifier because of the induced air flow.

VI. STATIC ELIMINATION IN CLEANING PROCESSES

Objects that are electrically charged will attract particulate matter by Coulomb or dipolar forces. Neutralization of this charge aids in cleaning and in maintaining the cleanliness of a surface.

A. Surface Cleaning

Surfaces can be cleaned by brushes or by gas streams that flow at speeds above the saltation and conveying velocities of the contaminants to be removed. Conductive (grounded) brushes with attached bipolar ionizers and ionized air guns are commonly used to displace particulate matter in manually operated systems. Other applications use nozzles and air knifes that are augmented with bipolar ionization.

B. Film and Web Cleaning

Films and webs are two dimensional, making them relatively easy to clean. Ionized air and/or brushes are used to dislodge contaminants from the film. The contaminants are then drawn by vacuum to a dust collector through an aperture placed above or below the film or web. Contaminants as small as 35 microns are removed by this equipment. Other cleaners combine static elimination with vacuum and wiping action.

C. Granule and Small Parts Cleaning

Pellets, granules, and small parts that are handled as bulk materials pose special cleaning problems. As bulk materials they contain a large amount of surface area, and those surfaces are for the most part hidden. One method of cleaning these materials is to suspend them in a fluidized bed

or elutriation column of bipolar ionized air. These cleaners separate shavings, fines, dust, and debris from granular material.

VII. STATIC ELIMINATION IN ASSEMBLY OF ELECTRONIC EQUIPMENT

The control of static charge in electronic assembly areas is discussed at length in several books (Boxleitner, 1988; Greason, 1987, 1992; Lacy, 1984; Matisoff, 1985; McAteer, 1990; and Sclater, 1990). There is also useful guidance in the standards and proceedings of the Electrostatic Discharge Association (ESD Assoc., 1993). Only brief comments will be made here to direct workers to the broad goals of static elimination in electronic assembly.

A. Workstation Considerations

In general, the goal is to prevent static charge from accumulating on workers, tools, and electronic components. This is done by using materials that dissipate charge rapidly and by grounding workers. The method of grounding should include resistive coupling, so that workers coming into contact with voltages in the assembly area are not directly connected to ground.

Static control programs typically include guidance for clothing, work surface materials, flooring, and shoes.

B. Room Air Ionization

The use of bipolar ionization for static elimination at the workstation was discussed in Sec. V.B.

As the work area becomes larger, recombination of ions becomes a critical issue. For this reason, many laminar-flow stations and room-area systems use pulsed-DC ionizers to inject successively layers of positive and negative ions into the room. These are chosen over alternating current (50–60 Hz) ionizers because of the longer time between pulses of ions of opposite polarity.

Some clean spaces demand very low levels of contaminants, and especially low levels of metallic contaminants. In these applications, the ionizing electrodes might be purged with dry air to prevent the formation of ammonium nitrates or be fabricated from nonmetallic materials. The latter materials might also be insulating to prevent spark discharge.

C. Packaging and Handling of Electronic Items

There are many types of static-shielding packaging available for transporting electronic items. The most common are conductive totes (rigid packages) and bags. In general, a conductive enclosure is formed that serves as a Faraday cage to protect the enclosed components and assemblies.

VIII. SPECIAL CONSIDERATIONS

A. Safety in Classified (Hazardous) Environments

Static elimination equipment is often purchased in industry to prevent spark discharges that might ignite vapors and fine particulate matter. Equipment especially designed for this purpose is tested in accordance with the requirements of the National Electrical Code (Earley et al., 1993).

B. Electrical Shock Hazards

Electrical ionization equipment typically operates in the voltage range from 4,000 to 7,000 V. This voltage is adequate to drive currents through the body far in excess of 0.5 mA, a level associated with perception of shock. To prevent shock hazards, some form of current limiting is necessary. Three methods are commonly used: current limited power sources, capacitive coupling to ionizers, and resistive coupling to ionizers.

Shockless static eliminating equipment employs current limiting at each emitting electrode. The short circuit current is generally limited to about 20 microamperes. This results in very little or no shock sensation when the electrodes are touched. The most common form of shockless equipment uses alternating current and capacitive coupling to individual needle electrodes. The high voltage cable is surrounded by a cylindrical metal annulus that contacts a single needle-electrode. Alternatively, resistors can be placed between the high voltage conductor and the individual needle-electrodes.

The high voltage electrodes can also be current limited for some control of shock hazard. This approach is less costly than shockless design and is adequate for static neutralizers with few corona electrodes. Generally, the output from the power source is connected to the corona electrodes through a current limiting resistor. The short circuit current is typically limited to a few hundred microamperes. The main concern at this current level is surprise, a reaction that may startle a person, causing an accident. Current limiting extends the useful life of electrodes and reduces the possibility of arcing and RFI emissions.

Static eliminating equipment is said to be hot when the ionizing electrodes are connected directly to the output of the high voltage transformer. This design yields high levels of ion output at a low cost. The current available at the ionizing point is whatever the high voltage transformer can deliver, typically a maximum of 5 milliamperes. This current level produces a very strong shock sensation. For this reason it is advisable to locate hot static eliminators where the operator cannot contact them or provide the static eliminators with guards and interlocks. The use of hot static eliminators is usually limited to industrial processes that operate at high speed, where guarding is mandatory for other than shock hazards. In these installations, operation of the static controls is interlocked with the operation of the machinery.

C. Environmental Issues

There are several environmental issues surrounding static elimination: ozone generation, radiation from nuclear ionizers, and electromagnetic interference.

Ozone is produced by electrical corona in air. Although the levels produced by air ionizers are low, one should consider their appropriateness for use in confined work areas. Ozone is a powerful oxidant that can affect materials in the work area and become an irritant to workers. Its pungent odor can be sensed at 10–20 ppb, a level well below the hazardous concentration of 100 ppb. Concentrations in the outdoor environment can exceed the levels found indoors around ionizers.

Nuclear ionizers produce ionizing radiation. They emit particles or photons that have sufficient energy to produce ionization directly in their passage through air. Nuclear ionizers are licensed to a site where they are used. The user must periodically exchange ionizing radiation sources and renew license agreements.

Electrical ionizers operate under conditions of controlled electrical discharge. Careful control of the discharge is essential to prevent transient fields that produce broad-spectrum electromagnetic interference. Corona-free high voltage cables, welded/rounded terminations, and shielding are used in static eliminators to reduce electromagnetic interference.

REFERENCES

Abdul-Kadir, N. M., R. H. Ihmayid, and A. S. Saadoon (1988). Electrostatics in polyethylene terphalate fibers. *Electrical and Electronics Engineering*, 17 n 4, 37–47.

Ansermet, J.-Ph., and A. Kuttler (1992). Charge screening in antistatic composites. *Journal of Electrostatics*, 27 n 3, 259–266.

Blitshteyn, M. (1984). Measuring the electric field of flat surfaces with electrostatic field meters. *Evaluation Engineering*, Nov. 1984.

Boxleitner, W. (1988). *Electrostatic Discharge and Electronic Equipment: A Practical Guide for Designing to Prevent ESD Problems*. Inst. Electrical.

Brown, D. M., and M. T. Pailthorpe (1988a). Antistatic wool. Part I. Polyethylene oxides and polyethoxylated amines as antistatic agents for wool. *Journal of the Textile Institute*, 79 n 2, 272–280.

Brown, D. M., and M. T. Pailthorpe (1988b). Antistatic wool. Part II. Quaternary polyethoxylated amines as antistatic agents for wool. *Journal of the Textile Institute*, 79 n 3, 349–355.

Brown, D. M., and M. T. Pailthorpe (1988c). Antistatic wool. Part III. Reactive quaternary ethoxylated amines as antistatic agents for wool. *Journal of the Textile Institute*, 79 n 3, 356–366.

Demchishin, A. V., V. N. Dobrovol'skii, L. V. Ishchuk, G. K. Ninidze, V. N. Rekichinskii, and V. V. Stetsenko (1988). Properties of transparent conducting films of indium oxide doped with tin. *Applied Solar Energy* (English translation of Geliotekhnika), 24 n 4, 65–68.

Earley, M. W., R. H. Murray, and J. M. Caloggero, eds. (1993). *The National Electrical Code Handbook*. 6th ed. National Fire Protection Association.

ESD Association (1993). Norstar Building, 200 Liberty Plaza, Rome, New York.

Greason, W. D. (1987). *Electrostatic Damage in Electronics: Devices and Systems*. John Wiley, New York.

Greason, W. D. (1992). *Electrostatic Discharge in Electronics*. Electronic and Electrical Engineering Research Studies, Electrostatics and Electrostatic Applications 12. John Wiley, New York.

Hellsten, K. M. E., A. W. Klingberg, and B. T. G. Karlsson (1989). Liquid detergents from cationic, anionic and nonionic surfactants adsorption, detergency and antistatic properties. *Journal of the American Oil Chemists' Society*, 66 n 9, 1381–1385.

Horvath, T., and I. Berta (1982). *Static Elimination*. John Wiley, New York, p. 25.

Horvath, T., and I. Berta (1982). *Static Elimination*. John Wiley, New York, pp. 56–57.

Jando, T., T. Stelczer, and F. Farkas (1989). Antistatic soft PVC materials for covering in building industry. *Journal of Electrostatics*, 23, Apr. 1989, 117–125.

Klein, W. G. (1991). Evaluating topical antistats. *Evaluation Engineering*, 30 n 2.

Kolyer, J. M., and R. Rushworth (1990). Coping with static electricity. Humidity and temperature effects on surface resistivity. *Evaluation Engineering*, 29 n 10.

Lacy, E. A. (1984). *Protecting Electronic Equipment from Electrostatic Discharge*. TAB Books, Blue Ridge Summit, Pennsylvania.

Liu, S. H., Z. C. Liu, B. X. Zhai, and Z. L. Wang (1989). Modification of polyvinyl chloride surface electrostatic properties by an ion beam. *Vacuum*, 39 n 2–4, 271–272.

Marchini, F. (1991). Advanced applications of metallized fibres for electrostatic

discharge and radiation shielding. *Journal of Coated Fabrics*, 20 Jan 1991, 153–166.

Matisoff, B. (1985). *Handbook of Electrostatic Discharge Control: Facilities Design and Manufacturing Procedures*. Van Nostrand Reinhold, New York.

McAteer, O. J. (1990). *Electrostatic Discharge Control*. McGraw-Hill, New York.

Modern Plastics Special Buyers' Guide and Encyclopedia (1993). Modern Plastics, Hightstown, New Jersey, p. 303.

Morra, M., P. Occhiello, and T. Garbassi (1992). Wettability and antistatic behavior of surface-grafted polypropylene. *Journal of Colloid and Interface Science*, 149 n 1, 290–294.

Nojiri, A., N. Suzuki, H. Shishikura, H. Komatsu, Y. Enomoto, and Y. Nomura (1991). Efcell semiconductive expanded polypropylene foam sheet. *Furukawa Review*, n 9, 74–80.

Park, Y. H., Y. K. Kim, and S. W. Nam (1991). Preparation and electrostatic properties of antistatic acrylics. *Journal of Applied Polymer Science*, 43 n 7, 1307–1313.

Radwan, R. M., R. M. El-Dewieny, and I. A. Metwally (1992). Investigation of static electrification phenomenon due to transformer oil flow in electric power apparatus. *IEEE Transactions on Electrical Insulation*, 27 n 2, 278–286.

Rijnders, J., and A. Van Der Voort (1990). Color monitor tubes with ARAS coatings. *Electronic Components and Applications*, 10 n 3, 85–89.

Sclater, N. J. (1990). *Electrostatic Discharge: Protection for Electronics*. TAB Books, Blue Ridge Summit, Pennsylvania.

Trotoir, J. P. (1988). Antifog/antistat eases processing problems. *Modern Plastics*, 65 n 10, 3.

Uchida, E., Y. Uyama, and Y. Ikada (1991). Antistatic properties of surface-modified polyester fabrics. *Textile Research Journal*, 61 n 8, 483–488.

Van Den Eeden, A., and S. Sluyterman (1990). Colour monitor tubes with magnetic-field suppression and antistatic coating. *Electronic Components and Applications*, 10 n 1, 48–52.

White, H. J. (1963). *Industrial Electrostatic Precipitation*. Addison-Wesley, Reading, Massachusetts, pp. 309–319.

Wilder, R. V. (1989). Antistats. *Modern Plastics*, 66 n 9.

Index

Abnormal dust deposition, 461
AC high voltage generation, 195
  cascaded, 195–198
  magnetization current, 197, 198
  oscillations, 200
  regulators, 198
  series resonance, 195–199
  single transformer, 195–197
  Tesla coil, 199, 200
  variable reactor, 198
Addressability, 300
Adhesion force, 347
Aerosol particles, 609
Aharonov-Bohm effect, 35, 37
Air-earth current, 629
Air toxics, 462, 471
Aliasing, 300
Ammonium nitrate, 600, 608
Antistatic-additives, 735
  floor coatings, 736
  materials, 709, 713
  sprays, 26
Apparent dust resistivity, 454, 455, 472
Arc
  current, 149
  definition, 149
  plasma, 149–152
  pressure, 149
  transferred, 152
  voltage drop, 149
Arcing, 692
Atmospheric electric conductivity, 620, 622
Atmospheric electric field, 627, 630
Atom
  energy levels, 157
  nucleus, 157
  structure, 157

Attachment, 181
dissociative, 182
radiative, 181
three-body, 183
Auroral zone jet current, 636
Autoionization, 181
Automatic voltage control, 458
Avalanche, 68, 72, 78

Back corona, 422, 453–458, 473, 489
general glow mode, 453, 473
initiation condition, 455
severity, 455, 474
streamer mode, 453
surface streamer mode, 453
Barrier effect, 70
Bernoulli, 106
Biionized, 444, 453, 455
Bingham plastic, 408
Bipolar current probe, 473
Blank's law, 167
Bond number, 102
Boxer-charger, 473
Breakdown, 71, 77, 78, 100, 101, 453, 455, 457, 653, 670
electric, 71, 78, 583
electromechanical, 79
field strength, 455
in nonuniform field, 74, 75
in uniform field, 72, 75
Breakup charging, 631, 639
Brush discharge, 707
Bubble, 535, 572
columns, 534
dispersion, 537
Built-in electric field, 32
Burst pulse corona, 152
Bushing chamber, 462
Bypassage, 483

Calcite, 461
Capacitance, 6, 272, 276–289
pressure sensor, 523
tomography, 285
Capacitive transducer, 523
Capacity coupled sensors, 238
Capillary condensation, 459
Catalytic recombination, 593
Catalyzer, 469
Cauchy problem, 89
Cell sorting, 667
Centrifugal cell, 474
Characteristic times,
charge relaxation, 124
Coulomb repulsion, 125
electroviscous, 127
ion diffusion, 125
ion transit, 125
magnetic diffusion, 123
mechanical, 122
period of the ac fields, 124
viscous relaxation, 127
Charge, 61
carriers, 61, 66
conservation of, 124
constant of diffusion charging, 446
control agent, 338
convection, 125
decay, 111
density, 123
fluctuations, 134
diffusion, 125
displacement, 52
dissipation, 703, 737
drift, 125
Charge exchange, 334
Charge injection, 285, 288, 529, 564
convection, 531
Charge-leakage resistance, 431
Charge neutralization, 739

Charge relaxation, 312, 704, 734
Charge separation, 703
Charge storage mechanisms, 510
Charge-to-mass ratio, 27, 340, 342, 414, 424, 475
Charge transfer, 185
  time constant, 421
Charged device model, 689
Charged droplet, 422, 680
Charged drops, 723, 726
Charged plumes, 140–142
  laminar, 142
  turbulent, 143
Charged wake, 144
Charging, 445–447
  bubbles, 572
  contact, 33
  continuous, 703
  diffusion, 445–457
  drops, 314, 318, 680
  electrochemical, 32
  electron, 445, 458
  electrostatic, 703, 709, 718, 727
  field, 445, 457
  induction, 421, 726
  oscillations, 35
  threshold, 715
  time constant of diffusion charging, 446
  time constant of field charging, 445
Charging devices, 419
Charging equation
  bi-ionized field, 455
  diffusion charging, 446
  field charging, 445
Chemically induced charging, 34
Chemical reactions, 170, 172–192
Chemistry of dust, 456
Crystallographic structure of dust, 457
Clausius-Mossotti law, 558
Cloud discharge, 646
Clustering, 185
CMYB four-colour printing system, 297
CMY subtractive primary system, 297
Coal conditioning, 457
  mixing, 457
Coalescence affected by 392, 546
  applied high voltages, 388
  electrode coating, 393
  phase ration, 393
  pulse frequency, 393
  thickness of electrode coating, 396
Coalescence, EHD enhanced, 388
  with chain formation, 389
  by dielectrophoresis, 390
  by electrophoresis, 391
  by random collision, 392
  with electrofining 392
  by intermolecular bonds, 389
Coenergy, 13
Collection efficiency, 451, 454, 462, 471
  performance, 451, 453
Collisions
  frequencies, 160, 621
  phenomena, 160
Complete thermodynamic equilibrium, 164
Conductance, 271, 276, 277, 281–285, 289
Conduction, 61, 62

Conduction of dust
electrolytic, 457
ionic, 455
repulsion, 112
surface, 455, 457
volume, 455
Conductivity, 8, 9, 123, 619, 629, 633, 634, 654, 734
Conservation laws, 160
Contact electrification, 331
Contactless charge removal, 697
Contact potential, 332
resistance, 456
Continuum diffusion model, 484
limit, 42
Convection (*see also* Electroconvection)
dielectric type, 529
inertially dominated, 135–138
length scale 135
manifest, 132–134
pattern, 130, 133, 134
planform, 129, 130
Rayleigh-Benard, 134
viscous dominated, 135–137
Convection-conduction number, 113
Convection-repulsion number, 113
Convective heat transfer coefficients, 566
Corona discharge, 152–154, 257, 444, 461, 487, 608, 615, 633, 640, 642, 649, 706, 717, 726
cell, 474
charging, 510
ionizer, 308
motor, 518, 523
needle, 288
negative, 443, 444, 453, 454
[Corona discharge]
onset potential, 492
origin of name, 152
positive, 443, 444, 468
quenching, 452, 461, 492
wind, 449, 557, 561
Coulomb
blockade, 36, 37
force, 126, 444, 460, 461, 532, 561
Coulombic interception single fiber efficiency, 502
Coulomb's Law, 1
Crank Nicholson method, 95
Cross-correlation method, 285–288
Cross section, 160
Cross-spectrum-coherence method, 286
Cunningham slip correction factor, 45, 448, 482, 501
Current, 8, 124, 125, 133
convective, 134–137
space charge limited, 137
transient, 130, 139

Dark discharge, 309
Dart leader, 647
DC high voltage generation, 200
Cockroft-Walton circuit, 203
delatron circuit, 205, 206
electrostatic generators, 207, 208
Felici, 208
van de Graaff, 207, 208
variable capacitance, 208
grading ring, 208
high voltage electrode, 208
rectifiers, 200, 201
full-wave, 200, 201

[DC high voltage generation]
half-wave, 200, 201
regulation, 203, 205
ripple factor, 201–203
tandem acclerator, 207
voltage doubler, 202
voltage multiplier, 204, 205
De-excitation reactions, 176
Degree of segregation, 528
Depolarization, 519
Detachment, 187
Deutsch number, 490
Dielectric, 57, 60, 69
barrier discharge, 581
constant, 3, 272, 277, 280, 281
nonpolar, 56
polar, 58
Dielectrophoresis, 60, 655
Dielectrophoretic collection rate, 657
Dielectrophoretic force, 10
Dielectrophoretic spectrum, 657
Differential type anemometer, 250
Diffuse layer, 84
Diffusion, 167–170, 498
ambipolar, 168, 170
Bronian, 500
charged particles, 167
charging, 40, 484
Dipole
coalescence, 391
moment, 11
Dirichlet problem, 89
Discharge, high pressure, 149
Displacement, 4
current, 588
Dissociation, 63
reactions, 176
Dithering, 300
Drift velocity, 166
Droplets, 543
Drops, 108
Dust
adehesion and cohesion, 462
adehesivity, 474
area-loading, 473
cohesivity, 459, 466, 474
mass-loading, 452, 472
resistivity, 453
seal, 460
Dynamo current, 634

Earliness of mixing, 528
Effect
of field-enhanced absorption, 70
Effective charging time
diffusion charging, 447
field charging, 445
Effective saturation charge
diffusion charging, 447
EHD (*see also* Electrohydrodynamics)
augmentation, 568
condenser, 557, 569, 572
convection, 564, 566
devices, 434
enhanced mixing, 529
extraction, 556, 569, 571
flow, 537, 550
forces, 529, 541
heat transfer enhancement, 577
liquid jet, 556, 564
liquid extraction, 568
method, 419
pseudo-dropwise condensation, 556, 569
pumps, 110
surface granulation, 569
surface instabilities, 558, 566
technology, 556

Einstein's relationship, 167
Elastic collisions, 162
Electret, 509
  dosimeters, 519
  fiber filter, 469
  filters, 513
  headphone, 517
  high-voltage generator, 518
  loudspeakers, 516
  machines, 513
  microphone, 513
  motors, 518
  pickup cartridge, 516
Electrical cell fusion, 670, 673
Electrical double layer, 33, 83, 388
Electrical shock hazards, 745
Electrical stresses, 528, 542
Electric Nusselt number Ne, 135–137
  transient, 139
Electric Peclet number, 490
Electric pressure, 100
Electric Rayleigh number, 530
Electric Reynolds number, 112, 316
Electric transfection, 673
Electric wind, 135
Electroacoustic stress pulse method, 513
Electroaerodynamics, 141
Electrocapillary number, 105
Electroconvection (*see also* Convection) 108, 133, 135, 138, 529
  cylindrical geometry, 138
  planar geometry, 138
  transient conditions, 138, 139
Electroconvective mobility, 108
Electroconvective number, 112
Electrode, 281, 288
  collecting, 443, 444, 449, 453, 459, 460, 461, 462, 464
[Electrode]
  discharge, 442, 443, 453, 454, 461, 462, 465
  plastic made, 468
  ring-type, 277, 281, 289
  strip-type, 281, 289
Electroluminescent displays, 357
Electromagnetic interference, 741
Electron, 157
  as intermediaries, 185
  beams, 608
  energy, 585
  impact ionization, 179
Electrofiltration, 546
Electrofluidized beds, 548
Electrography, 306
Electrogravity number, 103
Electrohydrodynamics, 99, 121, 491
  atomization, 435
  augmentation, 556
  forces, 540
Electrohydrostatics, 102
Electro-inertial number, 107
Electrolytic dissociation, 655
Electromagnetic interference, 746
Electromechanical coupling factors, 522
Electrophoresis, 382–384, 654
Electrophotographic process, 295
Electrophotography, 513
Electroporation, 672
Electroquasistatics, 122
Electrorheological effect, 399
  field strength, 399
Electrorheological fluids, 410
  bi-viscosity, 408
  compression, 410

[Electrorheological fluids]
doubling temperature, 401
particulate, 399
shear, 401, 408
tension, 410
viscosity, 401, 408
yield stress, 401, 408
Electrorotation, 661
Electrostatic devices, 291
Geiger-mueller tubes, 291
ionization chamber, 272, 291
photomultiplier tube, 291
proportional counter, 291
vidicon tube, 291
Electrostatic augmentation, 413, 462
Electrostatic cohesion force, 454
Electrostatic cohesivity, 459
Electrostatic control, 37
Electrostatic damages, 720
Electrostatic discharge, 281, 687, 707, 723
Electrostatic filters, 498
HEPA filters, 469
Electrostatic force, 498
Electrostatic generator, 523
Electrostatic induction, 432
voltage, 518
Electrostatic motors, 523
Electrostatic orientation, 659, 668
Electrostatic phase transitions, 30
Electrostatic Preagglomerator, 460
Electrostatic precipitators, 141, 481, 608, 609
air cleaning, 468
cylinder type, 442
dry, 459
[Electrostatic precipitators]
horizontal type, 462
hot, 457
industrial, 461, 462
multi-tube type, 462
one-stage type, 448, 452, 462
two-stage type, 448, 452, 457, 468
vertical type, 462
wet, 458, 460, 462, 464
wide, 462
Electrostatically augumented membrane filter, 471
Electrostatic separation
application, 365–385
coal industry use, 372–374
food industry use, 375–377
general separation method, 365–367
mining industry use, 367–372
solid-liquid separation, 382–383
waste processing industry use, 377–382
Electrostatic spraying, 429
Electrostriction, 60
force, 126, 558, 565
Electroviscous effect, 139
Elecroviscous number, 109
Emitter assembly, 265
Emulsion
breaking, 388
coalescence, 546
phase contactor, 546
Entrance length, 133
Equilibrium theory, 343
Equivalent dipole moment, 655
ESD stress, 691, 697
Euler method, 91
Excessive sparking, 453, 465
Exchange reactions, 176

Excitation reactions, 175
Extrinsically conductive materials, 734

Falling film columns, 534, 538
Faraday cage, 334, 691
Faraday shield, 280
Fermi energy, 34
Field charging, 46, 445, 457, 483
  effective, 42
  factor, 39, 46
Field induced model, 690
Field mill, 228, 641, 643
Field static eliminators, 739
Field stripping theory, 342
Finite difference method, 92
Finite element method, 93, 97
Flat CRTs, 352
Flat panel display, 352
Flooding phenomena, 538
Flow control, 407
  pressure drop, 407
  servomechanism, 407
Flow electrification, 85
Flow meter, 113
Fluidized beds, 547
Force, 1, 10, 60
  of attraction, 388
  of repulsion, 388
Forced flow, 133, 139, 144
  Couette, 133
  influence on convection pattern, 133
  Poiseuille, 133, 144
Force sensor, 226
Fowler-Nordheim field emission, 352
Free radical, 591
Frictional electrification, 331
Full dot-by-dot images, 299

Galerkin method, 94
Gas
  conditioning, 457, 460
  cooling, 458
  discharge, low pressure, 148–149
  distribution, 460
  driven static eliminators, 742
  humidification, 457
  kinetics, 160
Gassing, 80
Gate oxide damage, 692
Gauss-Seidel method, 97
Geiger tube, 152
Glow
  corona, 152
  discharge, 148–149, 582
    charged particle density, 149
    dc, 148
    degree of ionization, 149
    electron temperature, 149
    Faraday dark space, 149
    gas temperature, 149
    high frequency RF, 149
    luminous zones, 148
    microwave, 149
    negative glow, 149
    off-axis maxima, 149
    positive column, 149
Gradient force, 444, 461
Gravity pressure, 102
Gravity-capillary number, 102
Ground discharge, 646
Grounding, 708

Halftoning, 300
Heat transfer coefficients, 555
Helmholtz free energy, 556
Hermstein's glow, 454
High resistivity, 454

High voltage power supply, 443, 454
Hopper, 444, 459, 462, 464
Hopping, 460
  conductivity, 27
Human body model, 688
Humidity, 455

Image-intensifier, 473
Impact charging, 32
Impedance, 271, 277, 280, 290
Impulse generators, 208, 212, 217
  analysis, 213
  chopped impulses, 210
  control, front and tail time, 213
  definition, description, 208–212
  impulse generators
    single stage, 212
    multi-stage, 217
  Laplace transform, 214
  lightning impulses, 209, 210
  Marx generator, 217
  maximum transferred energy, 213
  multi-stage impulse generator (*see* Marx generator)
  resistors
    charging, 217
    damping, discharge, 213, 217
  surge impedance, 209
  switching surge, 212
  time
    front-time, 210, 212
    tail-time, 211–213
  trigatron, 217
  triggering, tripping, 218, 219
  virtual origin, 210
  voltage efficiency, 213
Indoor air toxics, 471
Induced corona, 426
Inductance, 276, 277
Induction charging, 421, 726
Induction ionizers, 739
Inductive technique, 285, 287
Inelastic collisions, 163
Inertial impaction, 498
Inertial pressures, 106
Inertial-viscous number 107
Injection, 61, 66, 125, 127, 128, 140
  autonomous, 129
  mechanisms
    electrochemical process, 127
    electronic process, 127
  parameter C, 125
Ink jet, 312
  printer, 109
  printing, 295, 303
In-situ resistivity cell, 473
Instability
  criteria, 129–133
  linear, 128, 129, 133
  nonlinear 130
  transient conditions, 132
  voltage, 129
    apparent, 131
Integrated air purifier, 444, 471
Interception, 498
Interfacial area, 534, 540, 542, 546
  instabilities, 536
  velocity, 538
Intermittent energization, 458
Intrinsically conductive materials, 737
Ion
  atom interchange, 185
  bombardment, 445
  depletion layer, 457

[Ion]
detector, 265
drift velocity, 248
flow anemometer, 247
flowmeter, 248
impact ionization, 179
interconversion processes, 183
molecule reactions, 185
positive, 453
sheath, 454
sinks, 187
sources, 181
Ionic current, 443, 458
distribution, 458
reactions, 175
Ionization, 67, 176, 633, 697, 739
autoionization, 181
bipolar, 737
by excited particles, 181
electron impact, 149, 179
ion impact, 179
potential, 457
thermal impact, 181
Ionization radiation, 746
Ionizers
AC, 738
double-DC, 738
nuclear, 746
pulse-DC, 744
Ionography, 306
Ionosphere, 619, 621, 635
field, 623, 635
potential, 630
Ion-transit time, 248
Ion-transit type anemometer, 265
Irreversible breakdown, 673

Jet, 108
Johnsen Rahbeck effect, 454
Junction damage, 692

Kelvin-Helmholtz instability, 536

Laminar flow, 85, 449
Laplace's equation, 5
Laser doppler anemometer, 450
Laser trapping, 664
Leaders, 77
Leakage resistance, 710
Leaking effects, 28
LED electrophotographic printers, 301, 308
Leeward air stream, 256
Lichtenberg figure, 584
Lightning 626, 633, 637, 640, 642, 707
discharges, 645
Lipschitz condition, 90
Liquid crystal displays, 360
Liquid-liquid
coalescence, 387, 388
dispersion, 387, 389
emulsions, 388
extraction, 387, 388, 396, 540, 542
Liquid membrane, 388, 396
Lissajous figure, 586
Load cell, 474
Local thermodynamic equilibrium, 151
Losses, 68, 69
conduction, 69
dielectric, 61, 68
Low resistivity, 454

Magnet, 510
Magnetic brush, 341
Magnetic field charging, 49
Magnetohydrodynamics, 123
Magnetosphere, 634
electric field, 635
plasma, 634

Mass transfer, 528, 534, 540
Matrix-addressed flat panel display, 359
Maxwell's equations, 123, 559
Maxwell-Boltzmann distribution function, 164
Maxwell stress, 558, 567, 574, 663
Mean free path, 162, 448, 457
Measurement for ESP, 471
Mesosphere, 619
Metallization damage, 692
Microdischarge, 583, 589
Mie scattering, 664
Migration velocity, 447, 449, 495
  apparent, 471, 472
  effective, 449, 450
  theoretical, 448, 449, 451
Millikan cell, 473
Mineral crystals, 465
Minimum fluidizing velocity, 549
Minimum ignition energy, 706, 708, 711, 723
Mobility, 9, 62, 108, 125, 131, 166, 167, 310, 422, 484, 488, 621
  apparent, 131
    steady state, 137, 138
    transient regime, 139
  hydrodynamic, 127, 134
  ion, 125, 131
  parameter M, 127, 134, 140
  small particles, 134
Modified Deutsch equation, 451
Molecule
  energy levels, 159
  structure, 159
MOSFET field sensing technique, 239
Multi-collector electrode, 256
Multiphase flow, 271–291
  film thickness, 286, 288–289
  flow regime, 273–275, 281–285, 288
  gas-liquid flow, 271–289
  gas-solid flow, 272–275, 281, 286–288
  interfacial area, 288–290
  phase distribution, 272, 281
  phase fraction, 271–289
  phase velocity, 271–273, 285–289, 291
Multiplication
  of charge carriers, 68
Mutual neutralization, 187

Navier-Stokes equation, 126, 482, 558, 565
Nematic phase, 361
Neutral reactions, 175
Neutralization, 424, 715
  of charges, 709
  by collision with wall, 192
  efficiency, 717
  of static charge, 734
Neutrons, 157
  labelled marker particle, 474
Nitrogen oxides, 593, 614
Nonequilibrium discharge, 581
Nonequilibrium plasma, 615
Nonimpact printing, 295

Ohm's law, 123, 629
Optical pressure, 664
Optoelectrostatic micromanipulation, 666
Ozone, 444, 469, 581, 588, 596, 614
Ozonizers, 583, 591, 597, 599

Packed beds, 547
Packed columns, 534

Parallel grid type anemometer, 248
Partial discharges, 70, 79, 156
Particle
  charging, 703
  flux density, 165
  penetration, 500
Paschen, 70, 73
  breakdown, 324
  curve, 585
  effect, 101
Pauli exclusion principle, 158
Peclet number, 39, 45
Penning effect, 181
Performance line, 451
Permittivity, 2, 3, 55
  complex, 58
Phase coalescence, 387
Phase separation, 546
Photodissociation, 185
Photoinduced discharge, 310
Photoionization, 176, 707
Photo-simulated discharge current (PSDC), 510
Piezo-electric, 272, 290, 520
  element, 513
Plasma, 585, 633
  average thermal energy, 147
  definition, 147
  electron
    density, 156
    temperature, 147, 154
  fourth state of matter, 147
  gas temperature, 147, 156
  parameters, 156
  sheath, 164
  thermal equilibrium, 147
Plasma displays, 354
PN-junctions, 32
Poisson's equation, 5, 96, 550
Polar cap ionosphere, 635
Polarization, 30, 54, 60, 360, 510, 519, 655
  interfacial, 657
Polarization catastrophy, 30
Polarization charges, 560
Polaron effect, 31
Positive ion sheath, 454
Positive streamer, 154
Potential, 5
Powder cloud theory, 343
Praegglomeration, 452, 453
  electrostatic, 452
  sonic, 452
Prebreakdown, 74, 76
Precharging, 457
Preduster, 452, 453
Pressure, 99
  mechanical, 126
  electrostrictive, 126
Pressure drop, 139
Probe, 276, 280, 285, 286, 289
  capacitance probe, 280
  double resistivity probe, 285, 289
  flush-wire probe, 289
  impedance probe, 280, 289
Protons, 152
Pulse application, 220
Pulse corona discharges, 615
Pulse energization, 458
Pulse high voltage, 458
Pulsed power supplies
  rotating spark-gap (RSG), 221
  Thryatron switched, 222
  Thyristor switched, 222
Pulseless corona, 152
Pyroelectricity, 520
Pyrosensor, 522

Quantum numbers, 158
Quasineutrality, 166

Radiation measurement, 290
Radiative
  attachment, 181
  recombination, 187
Radioactivity, 619
Rapping, 444, 458, 459, 460, 461
Rapture disk, 466
Rayleigh charge limit, 424
Rayleigh instability, 434, 437
Rayleigh limit, 316
Rayleigh-Ritz method, 94
Rayleigh-scattering, 663
Reaction rate coefficients, 172
Reaction rates, 170
Recombination, 62, 63, 165, 176
  dissociative, 187
  radiative, 187
  three-body ion-ion, 185
  volume, 185
Re-entrainment, 452, 454, 458, 459, 462, 474, 483, 493
  flow, 460
  rapping, 459
  resistivity, 460
Registration, 301
Relaxation, 57
Residence time, 534
  distribution (RTD), 528
Resistivity, 285, 286, 289
  cell, 472
  contral, 737
Return stroke, 647, 648
Reversible breakdown, 653, 670
Reynolds number, Re, 107, 127
  electric, 124
  forced flow, 133, 139, 144
  transition, 135
Rigidity, 71, 78
Rotary spark switch, 457
Runge-Kutta method, 90
Safety vent, 466
Saturation charge, 445, 455
  of field charging, 445
SCL (*see* Space charge, limited)
Schumann resonances, 638
Segregations, 551
Separatrix, 133
Sieve tray columns, 534
Silent discharge, 156, 581, 582
Single fiber efficiency, 502
Slip motion, 448
Slurry, 464
Smart materials, 37
Sneakage, 483, 493
Solvent extraction, 546
Soundwave measurement, 290
Sources of ions, 176
Space charge, 242, 486
  decay, 111
  density, 83, 424, 452, 472
  force field, 417
  limited (SCL), 129, 135
  current, 452
Spacecraft, 105
Space potential, 474, 724
Spark, 458, 462, 488, 707, 726
  definition, 154
  discharge, 152 ,154–156
  electron density, 156
    temperature, 156
  gas temperature, 156
  voltage, 443, 454
Specific collection area, 451
Speed ratio, 47
Spontaneous symmetry breaking, 31
Spray
  charging, 418
  columns, 534
  penetration forces, 415

Stability
  parameter T, 129
  time, 132
Static bars, 740
  AC, 741
  air assisted, 743
  double-DC, 742
  dual-phase, 742
Static charge, 738
  elimination, 733, 738
Stepped leader, 647
Stokes flow, 45
Stratosphere, 619
Stray capacitance, 281
Streamers, 77, 453, 608
  crona, 152
  positive, 453
  space, 453
  surface, 453
Streaming current, 727
Stress tensor, 12
Sub-critical bifurcation, 130
Successive overrelaxation method, 97
Suction Faraday cage, 472
Sumoto effects, 104
Surface
  charge density, 308, 707
  charging, 28
  chemistry of dust, 456
  discharges, 582
  force, 653
  tension, 102
Switching reactions, 185

Taylor series, 92
Temperature, 46, 455
Thermal charging, 509
Thermal-electret, 510
Thermaluminescence, 519
Thermophoresis, 165
Three-body
  attachment, 183
  collisions, 170
  ion-ion recombination, 185
Thunderclouds, 626, 643, 644
Thunderstorms, 625, 640
  electricity, 640
Toner, 326, 339
  charging, 329
Torque transmission, 409
  zero-field viscosity, 409
Total cross section, 163
Townshend, 73
Toxic by-products, 614
Trajectory of an emitted ion, 254
Transducer, 272, 276–288, 289
  capacitance transducer, 277–281, 286, 287, 289
  conductance transducer, 276, 289
  peizo-electric transducer, 272, 290
Transmission line, 458
  model, 648
Transport equations, 165
Travelling wave, 458
Treeing, 80
Triboelectricity, 631
Triboelectric series, 35
Triboelectrification, 32, 331
Trichel pulse corona, 152
Trihalomethanes, 600
Troposphere, 619
Turbulence (*see also* Convection, inertially dominated)
  fully developed, 137–139, 140
Turbulent flow, 85, 449
Tuft corona, 488
Tunneling currents 334
Two-body collisions, 170

Two-dimensional detection of wind, 256
Two-phase flow, 549

UHF aerial, 473
Ultrafine particles, 47
Unipolar conduction, 8
Unipolar injection (*see* Injection)

Vacuum, 75
van der Waals force, 341
Velocity
  fluctuations, 129, 134
  ion drift, 125
  liquid, 124
  meter, 285
  sound, 126
Vibration damping, 405, 409
  engine mount, 405
  resonance, 405
  shock absorber, 407
Viscous pressure, 107
Volatile organics, 600, 615
Volta-Helmholtz hypothesis, 33
Voltmeters, 226, 234
Volume charge density, 308

Walden's rule, 127, 129
Water-in-oil (w/o) emulsions, 388, 389
Water treatment, 599
Whistlers, 638
Wind velocity, 247
Work function, 333, 335, 352